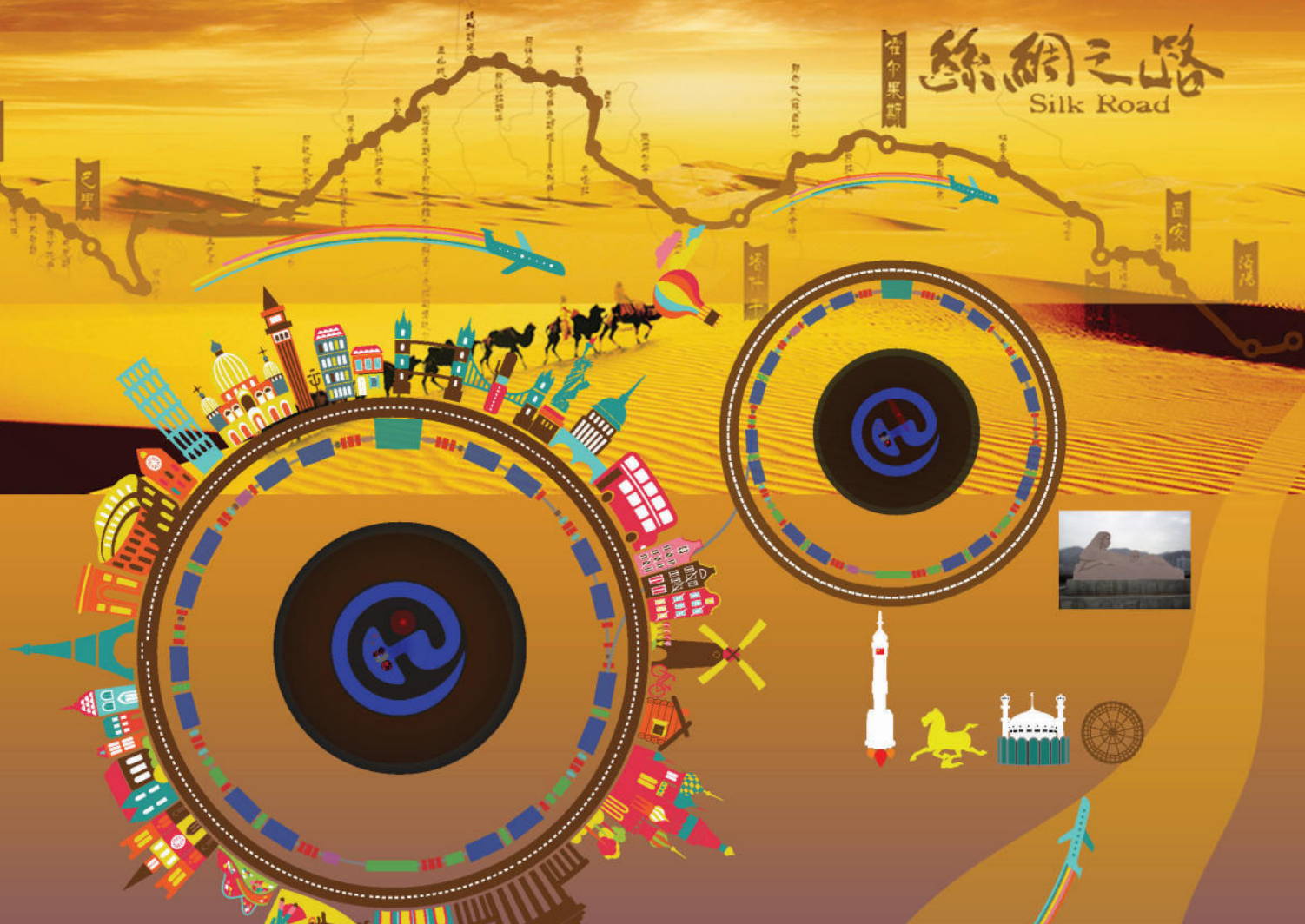


丝绸之路
Silk Road



HIAT 2018

LANZHOU, CHINA
Oct. 22 - 26, 2018

Conference Venue: 509 Nanchang Rd.
Hosted by Institute of Modern Physics,
Chinese Academy of Sciences
Conference Chair: Dr. Hongwei Zhao
co-Chair: Dr. Yuan He

14th International Conference
on Heavy Ion Accelerator Technology



<http://hiat2018.csp.escience.cn>



The 14th International Conference on Heavy Ion Accelerator Technology (HIAT2018)



Lanzhou, China, October 22-26, 2018

兰州重离子加速器国家实验室

HIRFL

江泽民



Preface

The 14th International Conference on Heavy Ion Accelerator Technology, HIAT'18, took place at Institute of Modern Physics (IMP) of the Chinese Academy of Sciences, China, from Sunday to Friday, 21st to 26th Oct., 2018.

HIAT conference provides a platform for scientists, engineers, students and industrial partners to present and discuss the latest developments of heavy ion accelerator. Over 100 delegates and 20 industry exhibits present at this conference. Following the tradition of the HIAT conference series, scientific program consists of invited and contributed oral sessions, poster sessions and discussion sessions.

IMP was founded in Lanzhou in 1957. As a national laboratory, IMP operates one major national research facility - the Heavy Ion Research Facility at Lanzhou (HIRFL). A series of remarkable results have been obtained at HIRFL. After a half century of development, IMP has become the most important research center for heavy ion sciences in China. Based on the developments and experience with heavy ion beam accelerators, IMP also takes charge of several new national projects: HIAF, CiADS. We have established active and fruitful collaboration with more than 40 universities and institutions in the worldwide.

We thanks for your participation. We are also deeply grateful to our Exhibitors and Sponsor companies for their financial support.

Sincerely,



Yuan He
Co-chair, HIAT2018

International Advisory Committee

Giovanni Bisoffi	INFN-LNL	Legnaro Italy
Yuan He	IMP	China
Oliver Kester	TRIUMF	Germany
Osamu Kamigaito	RIKEN	Japan
Brahim Mustapha	ANL	USA
Dinakar Kanjilal	IUAC	India
Maud Baylac	CNRS/IN2P3	France
Robert Laxdal	TRIUMF	Canada
Daniela Leitner	LBNL	USA
Nikolai Lobanov	Australian National University	Australia
Francis Osswald	IPHC/IN2P3	France
Zhaohua Peng	CIAE	China
Danilo Rifuggiato	INFN-LNS/Catania	Italy
Kimikazu Sasa	University of Tsukuba	Japan
Ludwig Beck	LMU	Munich Germany

Conference Chair

Hongwei Zhao (IMPCAS, China), Chair

Yuan He (IMPCAS, China), co-Chair

Liangting Sun (IMPCAS, China), Local Chair

Executive Board

Lu Li (Conference Secretary/Chief Editor)

Liang Lu (Industry Exhibition Manager)

Xinchen Hou & Yulu Huang (Foreign Affairs)

Junwei Guo & Wentao Guo (Lecture Hall Technical Support)

Qiangjun Wu (Conference Website Administrator)

Lixuan Li (Proceeding Room Technical Support)

Weihua Guo (Financial Management)

Teng Tan (Registration Management)

Yao Yang (Presentation Management)

JACoW Editorial Team

Jana Thomson (TRIUMF, Canada)

Maksim Kuzin (BINP, Russia)

Volker RW Schaa (GSI, Germany)

Lu Li (IMPCAS, China)

Contents

Preface

Foreword	iii
Committees	iv
Contents	v

Papers

MOXAA01 – Nuclear Physics Research at Heavy Ion Accelerators: Precision Studies with Stored and Cooled Exotic Nuclei	1
MOYAA01 – Advances of the FRIB Project	7
MOYAA02 – Status of the SPES Exotic Beam Facility	13
MOZBA01 – Present Status of HIRFL Complex in Lanzhou	18
MOOXA01 – Status of JINR FLNR cyclotrons	23
MOOYA01 – High Voltage Performance Degradation of the 14UD Tandem Accelerator	28
MOPB02 – Measurement Facility and Test Results for FRIB Superconducting Magnets at IMP	33
MOPB03 – The Superconducting Cyclotron RF System R&D	37
MOPB04 – Design of Fast Pulse Generator for Kicker Power Supply in HIAF	40
MOPB05 – Commissioning Progress of LEAF at IMP	42
MOPB07 – The Digital Controller for Power Supplies in HIAF	46
MOPB08 – The Multi-Physics Analysis of a Dual-Beam Linac	49
MOPB10 – Development of an All Permanent Magnet ECR Ion Source for Low and Medium Charge State Ions Production	53
MOPB15 – Development of a Pepper Pot Probe to Measure the Four-Dimensional Emittance of Low Energy Beam of Electron Cyclotron Resonance Ion Source at IMP	57
MOPB16 – Single Heavy Ion Bunch Generation Scheme in BRing at HIAF	61
TUXAA03 – ROSE - a Rotating 4D Emittance Scanner	65
TUYAA01 – Present Status of and Recent Developments at RIKEN RI Beam Factory	71
TUZAA01 – Development of RIKEN 28 Ghz SC-ECRISs for Synthesizing Super-Heavy Elements	77
TUZAA02 – Highly Charged ECR Ion Source Development at IMP	82
TUOXA01 – All-permanent Magnet ECR Ion Source DECRIS-PM	89
TUOZA01 – New Method to Design Magnetic Channels with 2D Optimization tools and Using Permendur Vanadium	92
TUOPA01 – Design of the Multi-Ion Injector Linac for the JLAB EIC (JLEIC)	97
WEOAA02 – Investigations on KONUS beam dynamics using the pre-stripper drift tube LINAC at GSI	102
WEOAA03 – Stochastic Cooling Simulation of Rare Isotope Beam and its Secondary Beam	107
WEYAA01 – Commissioning of China ADS Demo Linac and Baseline Design of CiADS Project	112
WEZAA01 – High-Brilliance Neutron Source Project	117
WEOXA01 – The Dc130 Project: New Multipurpose Applied Science Facility for FLNR	122
WEOYA01 – Mechanical Design of Single Spoke Resonator Type-2 (SSR2) Superconducting Cavity for RISP	125
WEOYA02 – First heavy ion beam acceleration with a superconducting multi gap CH-cavity	129
WEOYA03 – Design and Beam Commissioning of the LEAF-RFQ	135
WEPB03 – Multi-physics Analysis of a CW Four-rod RFQ	138
WEPB04 – New Type of Injector for Cancer Therapy	142
WEPB06 – Nb Sputtered 325 MHz QWR Cavities for CiADS	145
WEPB08 – Dynamics Study of a Drift Tube Linac for Both Heavy Ions and Proton	148
WEPB10 – Study on A HOM Type Buncher	152
WEPB12 – Error Analysis and RF Optimization of a Compact RFQ	155
WEPB13 – A New RF Structure: Bent-Vane Type RFQ	158
WEPB15 – Beam Commissioning in the First Chinese Demo Cancer Therapy Synchrotron	161
THOAA01 – High Resolution Mass Separator Dipole Design Studies for SPES Project	164
THOBA01 – Multipole Magnets for the HIAF Fragment Separator Using the Canted-Cosine-Theta (CCT) Geometry	170
THYAA01 – Novel Methods for the Production of Radionuclides of Medical Interest With Accelerators	175
THODA01 – Preliminary Design and Simulation Results of Ne ⁺ Beam Source	179
THOEA01 – JINR Heavy Ion Accelerators Application for SEE Testing in ISDE	183

Appendices	187
List of Authors	187
Institutes List	192
Participants List	197

NUCLEAR PHYSICS RESEARCH AT HEAVY ION ACCELERATORS: PRECISION STUDIES WITH STORED AND COOLED EXOTIC NUCLEI

Yuri A. Litvinov* and Thomas Stöhlker^{1,2}

GSI Helmholtzzentrum für Schwerionenforschung, 64291 Darmstadt, Germany

¹also at Helmholtz-Institut Jena, 07743 Jena, Germany

²also at Friedrich-Schiller-Universität Jena, 07743 Jena, Germany

Xin Wen Ma and Yu Hu Zhang

Key Laboratory of High Precision Nuclear Spectroscopy and Center for Nuclear Matter Science,
Institute of Modern Physics, Chinese Academy of Sciences, Lanzhou 730000, People's Republic of China

Takayuki Yamaguchi

Department of Physics, Saitama University, Saitama University, Saitama 338-8570, Japan

Abstract

This contribution is based on the plenary presentation at the 14th International Conference on Heavy Ion Accelerator Technology (HIAT-2018) in Lanzhou, China.

Heavy-ion storage rings offer unparalleled opportunities for precision experiments in realm of nuclear structure, atomic- and astrophysics. A brief somewhat biased review of the presently ongoing research programs is given as well as the future projects are outlined. The limited space does not allow for detailed description of individual experiments, which shall – to some extent – be compensated by extended bibliography.

INTRODUCTION

Atomic nuclei are many-body systems which are composed of two types of quantum mechanical particles protons and neutrons. The strong, weak and electromagnetic fundamental interactions are in play in the nuclei, which makes them extremely complex systems to describe. However, the nuclei are “natural laboratories” themselves, by studying which one learns about underlying fundamental interactions. The latter determine our world to be as it is and are thus the very reason for us to study them as good as we can.

Nuclear physics is more than 100 years old and is still one of the rapidly developing fields of research. This development is made possible by the progress in accelerator concepts and detector technologies, as were discussed *e.g.* at this conference. Today, scientists have created in laboratory about 3000 nuclides [1]. However, about 7000 nuclides are expected to exist with majority of yet unknown nuclei belonging to neutron-rich systems [2]. The path of the rapid-neutron capture process of element synthesis in cosmos is expected to be in this region [3–5]. There, the nuclear structure at large proton to neutron asymmetries is expected to change dramatically [6]. For instance, the nuclear shells in light neutron-rich nuclei are at different neutron numbers than the magic numbers established at stability [7, 8].

New-generation accelerator facilities aim at reaching further into the unknown nuclear territory. However, the yet

unknown nuclei have extremely small production cross sections and short lifetimes [9]. Sophisticated experimental techniques are needed to be able to produce and handle them, especially if their precision studies are aimed for. Here, heavy-ion storage rings coupled to radioactive ion beam facilities offer unique capabilities [10].

EXISTING HEAVY-ION STORAGE RINGS

If focusing on the radioactive-ion beam facilities, there are presently three operational heavy-ion storage rings [11]. These are the Experimental Storage Ring (ESR) at GSI [12], the experimental Cooler-Storage Ring (CSRe) at IMP [13], and the Rare RI Ring (R3) Facility at RIKEN [14].

Historically the first, the ESR at GSI is in operation with radioactive beams since 1992 [15, 16]. There, the exotic nuclei are produced at the Fragment Separator FRS [17] through fragmentation or in-flight fission of primary beams accelerated by the heavy-ion synchrotron SIS. The exotic nuclei are produced at high energies such that they emerge the production target as highly charged ions (HCI) [18–21]. The FRS can either be used as a pure magnetic rigidity ($B\rho$) analyser efficiently transmitting all produced nuclides within its $B\rho$ acceptance or, if a specially shaped degrader is employed, a pure mono-isotopic beam can be prepared by means of $B\rho - \Delta E - B\rho$ separation method, where ΔE stands for the energy loss in the degrader material. Also a direct, bypassing the FRS, injection into the ESR of primary and intense secondary beams is possible [22].

The ESR is a versatile machine offering numerous and flexible beam manipulation options. The ESR can store ions in a broad range of energies from about 3 A MeV to about 420 A MeV, corresponding to the maximum $B\rho(\text{ESR}) = 10 \text{ Tm}$. The average rest gas pressure of the ring is about $10^{-10} - 10^{-11} \text{ mbar}$. Such ultra-high vacuum environment sets strict constraints on experimental equipment that can be brought inside the vacuum.

Indispensable for experiments is the ability of cooling the secondary beams. The latter is especially important for radioactive beams which inevitably have a large momentum spread due to nuclear reaction process. Electron [23] and stochastic [24] cooling systems are routinely available.

* y.litvinov@gsi.de

Whereas the former cooling method is operational in the entire energy range of the ESR, the latter is fixed to a specific ion velocities of 400 A MeV. First laser cooling experiments were successfully performed [25–27]. Although the combination of stochastic pre-cooling and electron cooling has proven that hot ion beam can be cooled within about a second, this time is much too long for short-living rare ions [28, 29]. In the latter case, the isochronous ion-optical mode allows for (in first order) compensation of different particle momenta by orbit lengths in the ring [30]. This mode operates at the transition energy of the ring, γ_t .

A special attention is given to the ability to efficiently decelerate stored beams to low-energies. At present, the slowing down from the maximum to the lowest energy takes about a minute which limits the range of exotic nuclides that can be decelerated. A dedicated low-energy storage ring CRYRING has been installed behind the ESR [31]. It is being commissioned now. First experiments are planned for 2019. Worth noting is the HITRAP setup aiming at further slowing down and then trapping in a Penning trap HClS extracted from the ESR [32, 33].

The CSRe at IMP was taken into operation in 2007 [34, 35]. Secondary radioactive beams are produced by projectile fragmentation of primary beams accelerated by the synchrotron CSRm. They are analysed by the fragment separator RIBLL2 and injected into CSRe. Highly charged stable ions are produced in the same way with the only difference that thick production targets can be replaced by thin stripper foils. The CSRe is routinely operated in isochronous mode. Electron and stochastic cooling systems have been taken operation. Also the laser cooling of stored ions was demonstrated [36]. There are plans for establishing beam deceleration.

At RIKEN, the R3 ring is coupled to the presently most powerful radioactive ion beam facility, BigRIPS. The main accelerator at RIKEN is a superconducting cyclotron which is dramatically different from the facilities at GSI and IMP. Different to pulsed synchrotron beams, the cyclotron provides quasi-DC beam. Therefore a specific, single-particle injection scheme has been developed [37, 38]. Magnetic rigidities and energy deposition in special detectors along the BigRIPS provide particle identification (PID) for each secondary ion. A trigger signal can be send from the middle-focal plane of BigRIPS to the R3 injection kicker which arrives earlier than the particle itself. If the PID satisfies the set conditions, the injection kicker is armed and the corresponding particle is injected. The speciality of the ring is that it consists of dipole magnets only. Such lattice is very well-suited for isochronous ion-optical operation mode. The very first experiments at R3 have been successfully accomplished just during the time of the writing of this work [39].

EXPERIMENTAL INSTALLATIONS

Precision experiments require versatile experimental installations. They undergo steady development to meet the increasing requirements of experiments. Some examples are

listed below. The availability of setups in specific rings is indicated in the brackets.

- Internal gas-jet target is a supersonic jet of gas molecules crossing the vacuum pipe of the ring [40–42]. It enables reaction studies of stored beams with a windowless ultra-thin target. The combination of beam cooling and thin target allows for reaching very high energy and angular resolution in experiments. There are ports at several angles with view on the interaction region offering for optical and/or X-ray detection. (CSRe, ESR). We note, that at CRYRING a novel sophisticated detector system for nuclear and atomic reaction studies with the internal gas-jet is being constructed [43].
- Various detectors can be placed either in special vacuum pockets (scintillators, gas-filled multiwire chambers, silicon, diamond, etc.) [44–46] or directly into vacuum. (CSRe, ESR, CRYRING, R3)
- Laser beams can be merged with the stored ion beams along straight sections of the ring in both – co- and counter-propagating – directions [47]. (CSRe, ESR, CRYRING)
- Time-of-flight (ToF) detector is equipped with an extremely thin, a few $\mu\text{g}/\text{cm}^2$, carbon foil [48–51]. Secondary electrons emitted from the foil due to passing ions provide accurate timing signals which are used to determine particle revolution frequencies. (CSRe, ESR, R3)
- Schottky detectors are non-destructive monitors which are able to provide information on the frequencies and intensities of all particles stored in the ring [30]. The sensitivity of these detectors has been continuously improved over the last decade [52–56]. Present Schottky detectors allow for measurement of frequencies of single stored particles within merely a few ten ms. The dynamic range of Schottky detectors is such that single particles as well as beams with mA-intensities can be measured simultaneously. (CSRe, ESR, R3)

PRECISION EXPERIMENTS

Some examples of ongoing research are given below [57].

- Heavy-ion storage rings offer the possibility to store HClS in a specific high atomic charge state for an extended period of time. This capability enables measurements of weak decays of HClS [58–61]. Numerous experiments have been performed at the ESR and since recently also at the CSRe for investigations of continuum β -decay [62–65]. Of special interest are the two-body beta decays. These are the orbital electron capture (EC) [66] and bound-state β^- -decay (β_b^-) [67, 68]. Concerning the studies of EC decays the reader is referred to Refs. [69–84]. The bound-state β^- -decay was experimentally discovered in the ESR [85]. So far β_b^- -decay of fully-ionised $^{163}\text{Dy}^{66+}$, $^{187}\text{Re}^{75+}$, $^{205}\text{Hg}^{80+}$

- and $^{206,207}\text{Tl}^{81+}$ have been measured [85–90]. The next goal is the measurement of the β_b^- -decay of $^{205}\text{Tl}^{81+}$ [91], which is needed for Solar neutrino and s-process physics [92–96]. The corresponding experimental proposal is approved at GSI.
- Storage-ring mass spectrometry [30] is a very successful approach for measuring nuclear masses of short-lived nuclides. There are two approaches to perform such measurements. The Schottky mass spectrometry (SMS) is based on the electron cooling of the particles and Schottky detectors providing their revolution frequencies. Several hundred masses were obtained with this method [97–110]. The second method, the isochronous mass spectrometry (IMS), is based on the isochronous ion-optical setting of the ring. The cooling is then not required and the masses of nuclides with half-lives as short as a few ten μs can be addressed. TOF detectors are typically used for fast determination of revolution times. At CSRe the system of double TOF detectors allows in addition for an in-ring velocity measurement of each ion [111–115]. The IMS is pursued at all three storage ring facilities [11] and many highlight results have been achieved [116–137]. Both techniques are broad-band [138] and allow for addressing masses of many nuclei simultaneously. With the development of very sensitive and fast Schottky detectors, they are being considered in the IMS [65].
 - The high resolving power of storage ring mass spectrometry and especially the sensitivity to single ions allow for the search of very rarely produced long-lived isomeric states. Due to long half-lives and tiny production rates such states are very difficult to address with conventional gamma spectroscopy [139,140]. Several isomeric states were discovered in the past experiment as well as their decay properties as HCIs were studied [62, 141–151]. The region of interest of the future investigations are the neutron-rich nuclei around ^{188}Hf where isomers with exceptional properties are predicted to exist. Also proposed is the search for the exotic bound electron-positron decay [152].
 - Light-ion induced direct reactions, like elastic and inelastic scattering, transfer, charge-exchange, or knock-out reactions, are powerful tools for obtaining nuclear structure information [153–156]. Owing to the thin windowless targets and the beam cooling, high resolution measurements, even for very slow target-like recoil particles, can be achieved. Scattering of ^{56}Ni beam on the H_2 has been studied in the ESR proving the feasibility of such experiments [157–161]. Also the $^{20}\text{Ne}(p,d)^{19}\text{Ne}^*$ reaction was investigated at the ESR [162] which is the first step towards the measurement of the α -decay width of the 4.033 MeV state in ^{19}Ne . The latter is needed to conclude on the rate of the $^{15}\text{O}(\alpha,\gamma)^{19}\text{Ne}$ reaction in X-ray bursts. One shall

emphasise the complex detection systems developed for such reaction studies [163].

- Storage rings offer the possibility to address capture reactions on unstable ion beams. The proof-of-principle experiments addressing proton capture reactions relevant for the astrophysical p-process were performed in the ESR with decelerated ^{96}Ru [164, 165] and ^{124}Xe [166] beams. For these studies double-sided silicon strip detectors (DSSSD) were brought directly into the vacuum of the ring. In the future also (α,γ) and (p,n) reactions will be addressed. Still, the major goal is to perform these reaction studies on radioactive beams [167].
- The well-known in atomic physics dielectronic recombination (DR) process can be employed to measure isotope shifts (IS) and hyperfine splittings of radioisotopes as well as lifetimes of long-lived nuclear isomeric states [168, 169]. The highlights are the measured in the ESR DR resonances on exotic $^{237}\text{U}^{89+}$ and $^{234}\text{Pa}^{88+}$ [22, 170]. The latter isotope is a striking case since it has a low-energy isomeric level at $73.92+x$ keV with a half-life of 1.17 min. The signatures of both, the isomeric and ground, states could be seen. One of the future goals is to address ^{229}Th which has the isomeric state with lowest known excitation energy. If successful, this can pave the way to the separation of the isomer for further fundamental research studies. This goal is pursued at the CSRe and the ESR.

Apart from nuclear physics experiments, examples of which are given above, there is a broad range of experiments in realm of atomic physics, astrophysics as well as fundamental symmetries. For some examples of recent experimental results the reader is referred to Refs. [171–186].

FUTURE FAIR AND HIAF FACILITIES

The great success and the variety of the running research programs at the existing facilities is the motivation that heavy-ion storage rings are a central part of the future new-generation radioactive-ion beam facilities FAIR in Germany [187] and HIAF in China [188].

At FAIR, the present scope of the GSI storage rings will be extended by the collector ring CR and the high-energy storage ring HESR [189]. The CR is a dedicated machine for isochronous mass spectrometry [190–192]. Here the double-TOF system and a system of Schottky detectors shall enable direct mass and lifetime measurements of short-lived nuclides [193, 194]. The HESR will be used for accumulation and half-life measurement of long-lived radionuclides in high atomic charge states [193]. Furthermore, the HESR will offer cooled beams of HCIs accelerated to the maximal $B\rho = 50\text{ Tm}$ [195], which is a new energy regime for precision experiments in atomic physics [196–202]. These experiments are being prepared by the SPARC [203] and ILIMA [193] collaborations.

At HIAF, a novel concept of two storage rings coupled together for reaction studies of two co-propagating beams has been proposed [204]. The interest in the latter are the fundamental studies of critical and supercritical electromagnetic fields. Furthermore, each of the two storage rings can be run independently. Mass and lifetime measurements of short-lived nuclei are among the main physics cases.

LOW-ENERGIES

Experiments with stored HCIs at low energies have undoubtedly huge discovery potential. For instance, capture reactions can be addressed directly in the Gamow window of the corresponding astrophysical process [31, 167, 205]. Also for studying nuclear direct reactions, induced fission, etc. the ideal energy range is around 10 A MeV [206, 207]. Furthermore, low energies open possibilities for the search and detailed investigations of exotic decay modes [208], like for instance nuclear excitation by electron capture/transition (NEEC/T) [209, 210] and many more. Coupling of a storage ring with a source of slow neutrons is probably the only realistic approach for direct measuring of neutron-induced reactions [211–214]. Needless to say that high precision atomic physics experiments profit from low Doppler shifts. This rich physics program is the reason for installing the CRYRING at GSI. Unfortunately the slow deceleration process does not allow for experiments with nuclides living shorter than about a minute. Therefore, to enable these experiments there are several low-energy storage ring project that are initiated worldwide:

- A very detail concept for a storage ring at ISOLDE has been prepared [205]. A dedicated design of the ring fitting into the limited available space is ongoing [215].
- The new storage ring complex DERICA to be constructed at JINR in Russia has been proposed [216]. A low-energy storage ring is one of the central facilities [217].
- There is a proposal to transfer a low-energy storage ring TSR from Heidelberg to IMP in Lanzhou and to couple it to the existing CSRm facility. If realised this project could be the first in time and thus in the forefront of this research field. Furthermore, it would facilitate the optimisation of future low-energy facilities like for instance envisioned at HIAF.

CONCLUSION

In this contribution we provided a concise review of the experimental programs at the heavy-ion storage rings. The potential of the running research is still extremely large and it will enormously be extended by the future facilities. Whereas the higher energy regime will be covered at FAIR and to some extent also at HIAF, the present quest is to approach stored and cooled beams of short-lived nuclides at low-energies. Here, an exciting multidisciplinary physics program has been worked in details and awaits its realisation.

ACKNOWLEDGEMENTS

This work is supported by the European Research Council (ERC) under the European Union’s Horizon 2020 research and innovation programme (Grant No 682841 “ASTRUM”).

REFERENCES

- [1] *National Nuclear Data Center*, www.nndc.bnl.gov
- [2] J. Erler *et al.*, *Nature* **486**, 509 (2012)
- [3] E. M. Burbidge *et al.*, *Rev. Mod. Phys.* **29**, 547 (1957)
- [4] H. Schatz *Int. J. Mass Spectrom.* **349-350**, 181 (2013)
- [5] E. Pian *et al.*, *Nature* **551**, 67-70 (2017)
- [6] T. Otsuka, *Phys. Scripta* **T152**, 014007 (2013)
- [7] R. Kanungo *et al.*, *Phys. Rev. Lett.* **102**, 152501 (2009)
- [8] R. Kanungo, *Phys. Scripta* **T152**, 014002 (2013)
- [9] H. Geissel, *Prog. Part. Nucl. Phys.* **42**, 3 (1999)
- [10] Yu. A. Litvinov *et al.*, *Nucl. Instr. Meth. B* **317**, 603 (2013)
- [11] Y. H. Zhang *et al.*, *Phys. Scripta* **91**, 073002 (2016)
- [12] B. Franzke, *Nucl. Instr. Meth. B* **24/25**, 18 (1987)
- [13] J. W. Xia *et al.*, *Nucl. Instr. Meth. A* **488**, 11 (2002)
- [14] A. Ozawa *et al.*, *Prog. Theor. Exper. Phys.* **2012**, 03C009 (2012)
- [15] P. Kienle, *Forschung im Focus* (Interfrom, 1993)
- [16] H. Geissel *et al.*, *Phys. Rev. Lett.* **68**, 3412 (1992)
- [17] H. Geissel *et al.*, *Nucl. Instr. Meth. B* **70**, 286 (1992)
- [18] C. Scheidenberger *et al.*, *Nucl. Instr. Meth. B* **142**, 441 (1998)
- [19] H. Ogawa *et al.*, *Phys. Rev. A* **75**, 020703(R) (2007)
- [20] I. Tolstikhina *et al.*, *Phys. Usp.* **56**, 213 (2013); [2013 *Usp. Fiz. Nauk* **183** 225]
- [21] V. P. Shevelko *et al.*, *Nucl. Instr. Meth. B* **421**, 45 (2018)
- [22] C. Brandau *et al.*, *J. Phys. Conf. Series* **388**, 062042 (2012)
- [23] M. Steck *et al.*, *Nucl. Instr. Meth. A* **532**, 357 (2004)
- [24] F. Nolden *et al.*, *Nucl. Instr. Meth. A* **532**, 329 (2004)
- [25] W. Q. Wen *et al.*, *Nucl. Instr. Meth. A* **711**, 90 (2013)
- [26] W. Q. Wen *et al.*, *J. Phys. Conf. Series* **488**, 122005 (2014)
- [27] D. Winters *et al.*, *Phys. Scripta* **T166**, 014048 (2015)
- [28] H. Geissel *et al.*, *Nucl. Phys. A* **746**, 150c (2004)
- [29] H. Geissel *et al.*, *Eur. Phys. J. Special Topics* **150**, 109 (2007)
- [30] B. Franzke *et al.*, *Mass Spectrometry Reviews* **27**, 428 (2008)
- [31] M. Lestinsky *et al.*, *Eur. Phys. J. Special Topics* **225**, 797 (2016).
- [32] H.-J. Kluge *et al.*, *Adv. Quantum Chemistry*, **53** 83 (2008)
- [33] F. Herfurth *et al.*, *Phys. Scripta* **T166**, 014065 (2015)
- [34] H. S. Xu, *Int. J. Mod. Phys. E* **18**, 335 (2009)
- [35] H. S. Xu *et al.*, *Int. J. Mass Spectrom.* **349-350**, 162 (2013)
- [36] H. B. Wang *et al.*, *Nucl. Instr. Meth. B* **408**, 280 (2017)
- [37] Y. Yamaguchi *et al.*, *Nucl. Instr. Meth. B* **266**, 4575 (2008)

- [38] T. Yamaguchi *et al.*, *Int. J. Mass Spectrom.* **349-350**, 240 (2013)
- [39] A. Ozawa and S. Naimi, *private communications* (2018)
- [40] R. Grisenti *et al.*, *Europhys. Lett.* **73**, 540 (2006)
- [41] N. Petridis *et al.*, *Nucl. Instr. Meth. A* **656**, 1 (2011)
- [42] N. Petridis *et al.*, *Phys. Scripta* **T166**, 014051 (2015)
- [43] P. J. Woods, *private communications* (2017-2018)
- [44] O. Klepper *et al.*, *Nucl. Instr. Meth. B* **70**, 427 (1992)
- [45] O. Klepper and C. Kozhuharov, *Nucl. Instr. Meth. B* **204**, 553 (2003)
- [46] M. A. Najafi *et al.*, *Nucl. Instr. Meth. A* **836**, 1 (2016)
- [47] W. Nörtershäuser and R. Sánchez, *Phys. Scripta* **T166**, 014020 (2015)
- [48] J. Trötscher *et al.*, *Nucl. Instr. Meth. B* **70**, 455 (1992)
- [49] B. Mei *et al.*, *Nucl. Instr. Meth. A* **624**, 109 (2010)
- [50] W. Zhang *et al.*, *Nucl. Instr. Meth. A* **755**, 38 (2014)
- [51] W. Zhang *et al.*, *Nucl. Instr. Meth. A* **756**, 1 (2014)
- [52] F. Nolden *et al.*, *Nucl. Instr. Meth. A* **659**, 69 (2011)
- [53] F. Suzuki *et al.*, *Nucl. Instr. Meth. B* **317**, 636 (2013)
- [54] M. S. Sanjari *et al.*, *Phys. Scripta* **T156**, 014088 (2013)
- [55] M. S. Sanjari *et al.*, *Phys. Scripta* **T166**, 014060 (2015)
- [56] X. C. Chen *et al.*, *Nucl. Instr. Meth. A* **826**, 39 (2016)
- [57] F. Bosch *et al.*, *Prog. Part. Nucl. Phys.* **73**, 8 (2013)
- [58] Yu. A. Litvinov and F. Bosch, *Rep. Prog. Phys.* **74**, 016301 (2011)
- [59] F. Bosch *et al.*, *Int. J. Mass Spectrom.* **349-350**, 151 (2013)
- [60] D. Atanasov *et al.*, *J. Phys. B* **48**, 144024 (2015)
- [61] D. Atanasov *et al.*, *J. Phys. Conf. Series* **875**, 012008 (2017)
- [62] H. Irmich *et al.*, *Phys. Rev. Lett.* **75**, 4182 (1995)
- [63] F. Attallah *et al.*, *Nucl. Phys. A* **701**, 561c (2002)
- [64] L. X. Chen *et al.*, *Phys. Lett. B* **691**, 234 (2010)
- [65] X. L. Tu *et al.*, *Phys. Rev. C* **97**, 014321 (2018)
- [66] W. Bambynek *et al.*, *Rev. Mod. Phys.* **49**, 77 (1977)
- [67] R. Daudel *et al.*, *J. Phys. Radium* **8**, 238 (1948)
- [68] J. N. Bahcall, *Phys. Rev.* **124**, 495 (1961)
- [69] L. M. Folan and V. I. Tsifrinovich, *Phys. Rev. Lett.* **74**, 499 (1995)
- [70] Yu. A. Litvinov *et al.*, *Phys. Rev. Lett.* **99**, 262501 (2007)
- [71] Z. Patyk *et al.*, *Phys. Rev. C* **77**, 014306 (2008)
- [72] Yu. A. Litvinov, *Nucl. Phys. A* **805**, 260c (2008)
- [73] Yu. A. Litvinov *et al.*, *Phys. Lett. B* **664**, 162 (2008)
- [74] A. N. Ivanov *et al.*, *Phys. Rev. C* **78**, 025503 (2008)
- [75] Yu. A. Litvinov, *Int. J. Mod. Phys. E* **18**, 323 (2009)
- [76] N. Winckler *et al.*, *Phys. Lett. B* **679**, 36 (2009)
- [77] C. Giunti, *Nucl. Phys. B (Proc. Suppl.)* **188**, 43 (2009)
- [78] A. Merle, *Phys. Rev. C* **80**, 054616 (2009)
- [79] N. Winckler *et al.*, *Nucl. Phys. A* **834**, 432c (2010)
- [80] F. Bosch *et al.*, *Prog. Part. Nucl. Phys.* **64**, 435 (2010)
- [81] K. Siegien-Iwaniuk *et al.*, *Phys. Rev. C* **84**, 014301 (2011)
- [82] D. R. Atanasov *et al.*, *Eur. Phys. J. A* **48**, 22 (2012)
- [83] P. Kienle *et al.*, *Phys. Lett. B* **726**, 638 (2013)
- [84] A. Gal, *Symmetry* **8**, 49 (2016)
- [85] M. Jung *et al.*, *Phys. Rev. Lett.* **69**, 2164 (1992)
- [86] F. Bosch *et al.*, *Phys. Rev. Lett.* **77**, 5190 (1996)
- [87] F. Bosch *et al.*, *AIP Conf. Proc.* **477**, 344 (1999)
- [88] T. Ohtsubo *et al.*, *Phys. Rev. Lett.* **95**, 052501 (2005)
- [89] J. Kurcewicz *et al.*, *Acta Phys. Polonica B* **39**, 501 (2008)
- [90] J. Kurcewicz *et al.*, *Acta Phys. Polonica B* **41**, 525 (2010)
- [91] R. Singh Sidhu *et al.*, *EPJ Web of Conf.* **178**, 01003 (2018)
- [92] W. F. Henning *et al.*, *AIP Conf. Proc.* **126**, 203 (1985)
- [93] M. K. Pavićević, *Nucl. Instr. Meth. A* **271**, 287 (1988)
- [94] M. K. Pavićević *et al.*, *Nucl. Instr. Meth. A* **621**, 282 (2010)
- [95] M. K. Pavićević *et al.*, *J. Phys. Conf. Series* **888**, 012192 (2017)
- [96] M. K. Pavićević *et al.*, *Nucl. Instr. Meth. A* **895**, 62 (2018)
- [97] T. Radon *et al.*, *Phys. Rev. Lett.* **78**, 4701 (1997)
- [98] H. Geissel *et al.*, *AIP Conf. Proc.* **495**, 327 (1999)
- [99] T. Radon *et al.*, *Nucl. Phys. A* **677**, 75 (2000)
- [100] H. Geissel *et al.*, *Nucl. Phys. A* **685**, 115c (2001)
- [101] Yu. N. Novikov *et al.*, *Nucl. Phys. A* **697**, 92 (2002)
- [102] Yu. A. Litvinov *et al.*, *Nucl. Phys. A* **734**, 473 (2004)
- [103] Yu. A. Litvinov *et al.*, *Phys. Rev. Lett.* **95**, 042501 (2005)
- [104] Yu. A. Litvinov *et al.*, *Hyperfine Interactions* **173**, 55 (2006)
- [105] F. Bosch *et al.*, *Int. J. Mass Spectrom.* **251**, 212 (2006)
- [106] Yu. A. Litvinov *et al.*, *Nucl. Phys. A* **756**, 3 (2005)
- [107] Yu. A. Litvinov *et al.*, *Nucl. Phys. A* **787**, 315c (2007)
- [108] L. X. Chen *et al.*, *Phys. Rev. Lett.* **102**, 122503 (2009)
- [109] L. X. Chen *et al.*, *Nucl. Phys. A* **882**, 71 (20012)
- [110] D. Shubina *et al.*, *Phys. Rev. C* **88**, 024310 (2013)
- [111] H. Geissel and Yu. A. Litvinov, *J. Phys. G* **31**, S1779 (2005)
- [112] Y. M. Xing *et al.*, *Phys. Scripta* **T166**, 014010 (2015)
- [113] X. Xu *et al.*, *Chin. Phys. C* **39**, 104001 (2015)
- [114] P. Shuai *et al.*, *Nucl. Instr. Meth. B* **376**, 311 (2016)
- [115] R. J. Chen *et al.*, *Nucl. Instr. Meth. A* **898**, 111 (2018)
- [116] M. Hausmann *et al.*, *Nucl. Instr. Meth. A* **446**, 569 (2000)
- [117] M. Hausmann *et al.*, *Hyperfine Interactions* **132**, 289 (2001)
- [118] J. Stadlmann *et al.*, *Phys. Lett. B* **586**, 27 (2004)
- [119] H. Geissel *et al.*, *Hyperfine Interactions* **173**, 49 (2006)
- [120] B. H. Sun *et al.*, *Nucl. Phys. A* **812**, 1 (2008)
- [121] B. H. Sun *et al.*, *Int. J. Mod. Phys. E* **18** 346 (2009)
- [122] M. Wang *et al.*, *Int. J. Mod. Phys. E* **18**, 352 (2009)
- [123] X. L. Tu *et al.*, *Nucl. Instr. Meth. A* **654**, 213 (2011)
- [124] X. L. Tu *et al.*, *Phys. Rev. Lett.* **106**, 112501 (2011)
- [125] Y. H. Zhang, *Phys. Rev. Lett.* **109**, 102501 (2012)
- [126] H. S. Xu *et al.*, *Int. J. Mass. Spectr.* **349-350**, 162 (2013)

- [127] X. L. Yan *et al.*, *Astrophys. J. Lett.* **766**, L8 (2013)
- [128] X. L. Tu *et al.*, *J. Phys. G* **41**, 025104 (2014)
- [129] P. Shuai *et al.*, *Phys. Lett. B* **735**, 327 (2014)
- [130] X. Xu *et al.*, *Phys. Rev. Lett.* **117**, 182503 (2016)
- [131] R. Knöbel *et al.*, *Phys. Lett. B* **754**, 288 (2016)
- [132] R. Knöbel *et al.*, *Eur. Phys. J. A* **52**, 138 (2016)
- [133] P. Zhang *et al.*, *Phys. Lett. B* **767**, 20 (2017)
- [134] Y. M. Xing *et al.*, *Phys. Lett. B* **781**, 358 (2018)
- [135] C. Y. Fu *et al.*, *Phys. Rev. C* **98**, 014315 (2018)
- [136] Y. H. Zhang *et al.*, *Phys. Rev. C* **98**, 014319 (2018)
- [137] M. Z. Sun *et al.*, *Front. Phys.* **13**, 132112 (2018)
- [138] C. Trageser *et al.*, *Phys. Scripta* **T166**, 014062 (2015)
- [139] P. M. Walker and G. D. Dracoulis, *Nature* **399**, 35 (1999)
- [140] P. M. Walker and G. D. Dracoulis, *Hyperfine Interactions* **135**, 83 (2001)
- [141] Yu. A. Litvinov *et al.*, *Phys. Lett. B* **573**, 80 (2003)
- [142] B. H. Sun *et al.*, *Eur. Phys. J. A* **31**, 393 (2007)
- [143] B. H. Sun *et al.*, *Phys. Lett. B* **688**, 294 (2010)
- [144] B. H. Sun *et al.*, *Nucl. Phys. A* **834**, 476c (2010)
- [145] M. W. Reed *et al.*, *Phys. Rev. Lett.* **105**, 172501 (2010)
- [146] L. X. Chen *et al.*, *Phys. Lett. B* **691**, 234 (2010)
- [147] M. W. Reed *et al.*, *Phys. Rev. C* **86**, 054321 (2012)
- [148] M. W. Reed *et al.*, *J. Phys. Conf. Series* **381** 012058 (2012)
- [149] L. X. Chen *et al.*, *Phys. Rev. Lett.* **110**, 122502 (2013)
- [150] A. Akber *et al.*, *Phys. Rev. C* **91**, 031301(R) (2015)
- [151] Q. Zeng *et al.*, *Phys. Rev. C* **96**, 031303(R) (2017)
- [152] F. Bosch *et al.*, *EPJ Web of Conf.* **123**, 04003 (2016)
- [153] S. Ilieva *et al.*, *Eur. Phys. J. Special Topics* **150**, 357 (2007)
- [154] N. Kalantar-Nayestanaki *et al.*, *Int. J. Mod. Phys. E* **18**, 524 (2009)
- [155] H. Moeini *et al.*, *Nucl. Instr. Meth. A* **634**, 77 (2011)
- [156] T. Kröll *et al.*, *J. Phys. Conf. Series* **724**, 012026 (2016)
- [157] M. von Schmid *et al.*, *EPJ Web of Conf.* **66**, 03093 (2014)
- [158] M. von Schmid *et al.*, *Phys. Scripta* **T166**, 014005 (2015)
- [159] J. C. Zamora *et al.*, *Phys. Scripta* **T166**, 014006 (2015)
- [160] J. C. Zamora *et al.*, *Phys. Lett. B* **763**, 16 (2016)
- [161] J. C. Zamora *et al.*, *Phys. Rev. C* **96**, 034617 (2017)
- [162] D. T. Doherty *et al.*, *Phys. Scripta* **T166**, 014007 (2015)
- [163] M. Mutterer *et al.*, *Phys. Scripta* **T166**, 014053 (2015)
- [164] Q. Zhong *et al.*, *J. Phys. Conf. Series* **202**, 012011 (2010)
- [165] B. Mei *et al.*, *Phys. Rev. C* **92**, 035803 (2015).
- [166] J. Glorius, *private communications* (2018)
- [167] P. J. Woods *et al.*, *Phys. Scripta* **T 166**, 014002 (2015)
- [168] C. Brandau *et al.*, *J. Phys. Conf. Ser.* **194**, 012023 (2009)
- [169] C. Brandau *et al.*, *Hyperfine Interactions* **196**, 115 (2010)
- [170] C. Brandau *et al.*, *Phys. Scripta* **T156**, 014050 (2013)
- [171] W. Nörtershäuser *et al.*, *Phys. Scripta* **T156**, 014016 (2013)
- [172] P.-M. Hillenbrand *et al.*, *Phys. Scripta* **T156**, 014087 (2013)
- [173] P.-M. Hillenbrand *et al.*, *Phys. Rev. A* **90**, 042713 (2014)
- [174] P.-M. Hillenbrand *et al.*, *Phys. Rev. A* **90**, 022707 (2014)
- [175] M. Lochmann *et al.*, *Phys. Rev. A* **90**, 030501(R) (2014)
- [176] S. Tashenov *et al.*, *Phys. Rev. Lett.* **113**, 113001 (2014)
- [177] J. Ullmann *et al.*, *J. Phys. B* **48**, 144022 (2015)
- [178] H. F. Beyer *et al.*, *J. Phys. B* **48**, 144010 (2015)
- [179] R. Sanchez *et al.*, *Phys. Scripta* **T166**, 014021 (2015)
- [180] S. Tashenov *et al.*, *Phys. Scripta* **T166**, 014027 (2015)
- [181] P.-M. Hillenbrand *et al.*, *Phys. Rev. A* **91**, 022705 (2015)
- [182] P.-M. Hillenbrand *et al.*, *Phys. Rev. A* **93**, 042709 (2016)
- [183] R. Sanchez *et al.*, *J. Phys. B* **50**, 085004 (2017)
- [184] A. Gumberidze *et al.*, *Nucl. Instr. Meth. B* **408**, 27 (2017)
- [185] J. Ullmann *et al.*, *Nature Comm.* **8**, 15484 (2017)
- [186] T. Gassner *et al.*, *New J. Phys.* **20**, 073033 (2018)
- [187] *FAIR Green Paper: The Modularized Start Version* (2009)
- [188] J. Yang *et al.*, *Nucl. Instr. Meth. B* **317**, 263 (2013)
- [189] R. Maier *et al.* HESR Technical Design Report, (2008)
- [190] A. Dolinskii *et al.*, *Nucl. Instr. Meth. A* **574**, 207 (2007)
- [191] A. Dolinskii *et al.*, *Nucl. Instr. Meth. B* **266**, 4579 (2008)
- [192] S. A. Litvinov *et al.*, *Nucl. Instr. Meth. A* **724**, 20 (2013)
- [193] P. M. Walker *et al.*, *Int. J. Mass Spectrom.* **349-350**, 247 (2013).
- [194] I. Dillmann *et al.*, *Prog. Part. Nucl. Phys.* **66**, 358 (2011)
- [195] O. Kovalenko *et al.*, *Phys. Scripta* **T166**, 014042 (2015)
- [196] T. Stöhlker *et al.*, *Phys. Scripta* **T156**, 014085 (2013)
- [197] S. Hagmann *et al.*, *Phys. Scripta* **T156**, 014086 (2013)
- [198] T. Stöhlker *et al.*, *Hyperfine Interactions* **227**, 45 (2014)
- [199] A. Gumberidze *et al.*, *Phys. Scripta* **T166**, 014076 (2015)
- [200] T. Stöhlker *et al.*, *Phys. Scripta* **T166**, 014025 (2015)
- [201] P.-M. Hillenbrand *et al.*, *Phys. Scripta* **T166**, 014026 (2015)
- [202] T. Stöhlker *et al.*, *Nucl. Instr. Meth. B* **365**, 680 (2015)
- [203] T. Stöhlker *et al.*, *AIP Conf. Proc.* **1336**, 132 (2011)
- [204] Y. J. Yuan *et al.*, *Proc. HIAT2015*, TUM1101 (2015)
- [205] M. Grieser *et al.*, *Eur. Phys. J. Special Topics* **207**, 1 (2012)
- [206] P. Butler *et al.*, *Acta Phys. Polonica B* **47**, 627 (2016)
- [207] P. Butler *et al.*, *Nucl. Instr. Meth. B* **376**, 270 (2008)
- [208] Ch. J. Cerjan *et al.*, *J. Phys. G* **45**, 033003 (2018)
- [209] V. Goldanskii and V. Namiot, *Phys. Lett. B* **62**, 393 (1976)
- [210] A. Palfy *et al.*, *Phys. Lett. B* **661**, 330 (2008)
- [211] R. Reifarth *et al.*, *Phys. Rev. ST* **17**, 014701 (2014)
- [212] J. Glorius *et al.*, *Phys. Scripta* **T166**, 014088 (2015)
- [213] R. Reifarth *et al.*, *EPJ Web of Conf.* **146**, 01003 (2017)
- [214] R. Reifarth *et al.*, *Phys. Rev. ST* **20**, 044701 (2017)
- [215] M. Grieser, *private communications* (2018)
- [216] L. Grigorenko *et al.*, *Phys. Usp.*, (in press) (2018)
- [217] L. Grigorenko, *private communications* (2018)

ADVANCES OF THE FRIB PROJECT*

J. Wei†, H. Ao, S. Beher, N. Bultman, F. Casagrande, J. Chen, S. Cogan, C. Compton, J. Curtin, L. Dalesio, K. Davidson, A. Facco¹, V. Ganni, A. Ganshyn, P. Gibson, T. Glasmacher, Y. Hao, L. Hodges, K. Holland, H.-C. Hseuh, A. Hussain, M. Ikegami, S. Jones, T. Kanemura, P. Knudsen, R.E. Laxdal², J. LeTourneau, S. Lidia, G. Machicoane, I. Malloch, F. Marti, S. Miller, Y. Momozaki³, D. Morris, P. Ostroumov, J. Popielarski, L. Popielarski, J. Priller, H. Ren, T. Russo, K. Saito, S. Stanley, T. Xu, Y. Yamazaki,

Facility for Rare Isotope Beams, Michigan State University, East Lansing, MI, USA

K. Dixon, M. Wiseman, Thomas Jefferson National Laboratory, Newport News, VA, USA

M. Kelly, Argonne National Laboratory, Argonne, IL, USA

K. Hosoyama, KEK, Tsukuba, Japan

S. Prestemon, Lawrence Berkeley National Laboratory, Berkeley, CA, USA

¹ also at INFN - Laboratori Nazionali di Legnaro, Legnaro (Padova), Italy

² also at TRIUMF, Vancouver, Canada

³ also at Argonne National Laboratory, Argonne, IL, USA

Abstract

The Facility for Rare Isotope Beams (FRIB) Project has entered the phase of beam commissioning starting from the room-temperature front end and the superconducting linac segment of first three cryomodules. With the newly commissioned helium refrigeration system supplying 4.5 K liquid helium to the quarter-wave resonators and solenoids, the FRIB accelerator team achieved the sectional key performance parameters as designed ahead of schedule. We also validated machine protection and personnel protection systems that will be crucial to the next phase of commissioning. FRIB is on track towards a national user facility at the power frontier with a beam power two orders of magnitude higher than operating heavy-ion facilities. This paper summarizes the status of accelerator design, technology development, construction, commissioning, as well as path to operations and upgrades.

INTRODUCTION

The FRIB project started technical construction at the Michigan State University in August 2014 [1]. Three years later, the project entered the stage of phased commissioning with the heavy ion beams (Ar and Kr) following the completion of the room temperature part of the front end, as shown in Fig. 1 and Table 1. In this paper, we present the main results of the first two stages of beam commissioning that have been completed covering nearly all major accelerator systems including the electron cyclotron resonance (ECR) ion source, the Radio-frequency quadrupole (RFQ), the cryomodules of $\beta=0.041$ quarter-wave resonators, the liquid helium refrigeration plant operating at 4 K temperature, and supporting systems including RF, power supply, diagnostics, vacuum,

hardware and high level controls, machine protection, personnel protection, physics applications and integration.



Figure 1: FRIB driver linac viewed from the lower LEPT towards the superconducting linac in the accelerator tunnel at the beginning of beam commissioning in 2017.

Table 1: Stages of Accelerator Readiness (ARR) for the Phased Beam Commissioning of the FRIB Accelerator

Phase	Area with beam	Date
ARR1	Front end	2017-7
ARR2	Plus $\beta=0.041$ cryomodules	2018-5
ARR3	Plus $\beta=0.085$ cryomodules	2019-2
	Plus lithium charge stripper	2020-7
ARR4/5	Plus $\beta=0.29, 0.53$ cryomodules	2020-12
ARR6	Plus target and beam dump	2021-9

Subsequently, we discuss resolutions to some leading technical issues including low-sensitivity loss detection and machine protection, charge stripping with liquid metal, and microphonics suppression. We continue with status reports on infrastructure build-up of the MSU cryogenics initiative and the superconducting RF (SRF) Highbay. We conclude with challenges in the beam power ramp up and the path forward of beam energy upgrade.

* Work supported by the U.S. Department of Energy Office of Science under Cooperative Agreement DE-SC0000661 and the National Science Foundation under Cooperative Agreement PHY-1102511.

† wei@frib.msu.edu

PHASED COMMISSIONING

Front End Beam Commissioning

The main purpose of Front End (ARR1) commissioning was to integrate room-temperature accelerator systems together with the newly built civil infrastructure including electricity and water. For simplicity, we avoided cryogenics and focused on establishing needed processes for a newly constructed accelerator facility. Emphases were on hazard mitigation for personnel safety (electrical hazard from the high voltage platform and radiation hazard from the source plasma) and conduct of operations.

The ARR1 commissioning goals were promptly achieved with both Ar and Kr beams produced from the ion source, transported through the low energy beam transport (LEBT) with pre-bunching, and accelerated by the RFQ to beam energy of 0.5 MeV/u with full design transmission efficiency of about 85% [2] (Fig. 2).



Figure 2: Front End (ARR1) beam commissioning in 2017.

First Three Cryomodule Beam Commissioning

The main purpose of ARR2 commissioning was to perform integrated tests of nearly all accelerator systems with emphasis on cryogenics and cryomodules. Figure 3 shows the beamline layout extending from the ion source at the surface to the linac tunnel underground including three $\beta=0.041$ cryomodules and a temporary diagnostics station. After establishing the oxygen deficiency hazard control system [3], we first started the commissioning of the FRIB cryoplant at 4 K temperature (Fig. 4), followed by the commissioning of the cryo-distribution and the cool down of the cryomodules [4]. The tunnel access control system is activated for radiation hazard mitigation before we proceed with RF conditioning of the SRF cavities. As cryomodules have been 100% tested at multiple stages (cavity/couple/solenoid individual tests and cryomodule bunker tests), the conditioning in tunnel proceeded rapidly.

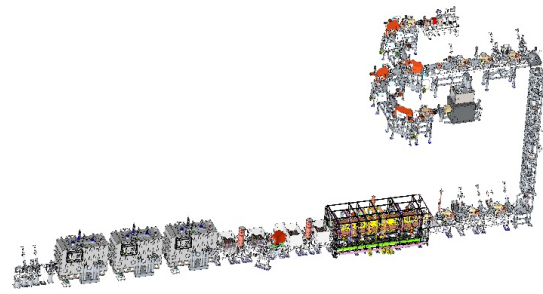


Figure 3: Scope of ARR2 beam commissioning in 2018 including the front end and the first three cryomodules.



Figure 4: Commissioning of the FRIB cryoplant at 4 K.

The ARR2 commissioning goals were again promptly achieved with both Ar and Kr beams from the Front End accelerated by the three cryomodules to beam energies above 2 MeV/u with 100% transmission efficiency (Fig. 5). The beam duty factor was gradually increased to 30% limited by the temporary beam dumping Faraday cup. The Ar⁹⁺ beam power of 66 W at 1.5 MeV/u would correspond to about 38 kW of power on the target had the beam been accelerated to the full energy of 285 MeV/u at 100% duty cycle. An unexplained observation was the neutron signal detected at unexpected low energy of 1.8 MeV/u [5].

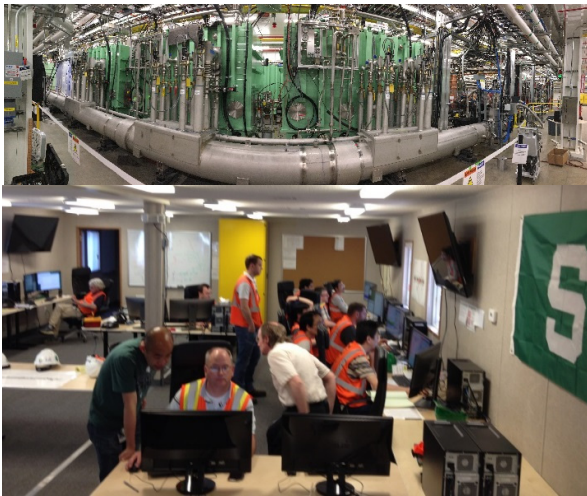


Figure 5: ARR2 beam commissioning in 2018 including both the front end and the first three cryomodules.

Forthcoming Beam Commissioning

ARR3 aims at accelerating the beams to ~ 20 MeV/u energy passing the charge stripper. All 15 cryomodules needed for ARR3 have been installed and being cooled down to 4 K temperature (Fig. 6). Subsequently, the carbon charge stripper installed for commissioning is planned to be replaced by the liquid lithium stripper. A warm up period of about 8 months is planned in-between facilitating installation, system reconfiguration and improvements.

ARR4/5 aims at further acceleration above 200 MeV/u meeting the facility requirements with SRF cavities operating at 2 K temperature. ARR6 integrates the driver linac accelerator with the target and beam dump of the experimental systems.



Figure 6: Cryomodules installed for ARR3 commissioning.

TECHNICAL ISSUE RESOLUTION

Major technical issues have been the focus of R&D since project start. These issues are being resolved and demonstrated during the staged beam commissioning.

Machine Protection and Low-sensitivity Beam Loss Detection

The issue of poor detection sensitivity of low energy heavy ions and the consequent challenges in machine protection is addressed by multi-layer, multi-time scale machine protection system designs [6]. The initially

installed beam attenuator for machine protection was removed after the beam chopper was validated and monitored limiting the beam duty cycle before the interim beam dump. The fast machine protection based on the differential beam current signal was demonstrated mitigating the stray beam within the required 35 μ s time duration (Fig. 7). In addition, the halo monitor rings installed between the cryomodules were highly sensitive to both ion and electron signals at nA level (Fig. 8). The fast thermometry sensors installed inside the cryomodule detected beam loss induced heating at 0.1 K level.

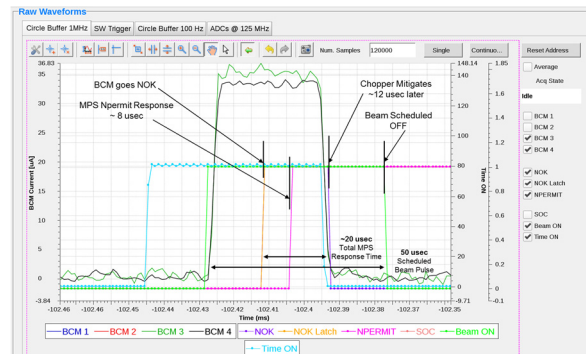


Figure 7: Demonstration of fast machine protection with the differential current monitor signal.

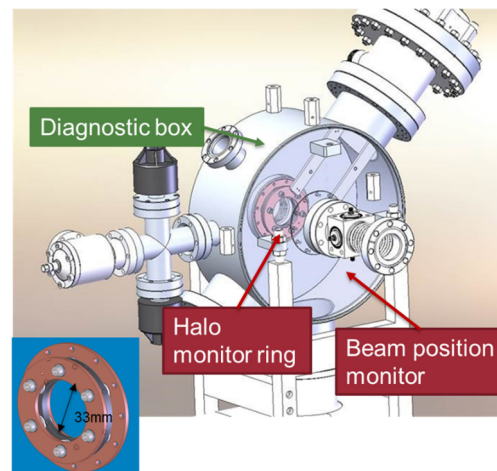


Figure 8: Halo monitor rings installed in the warm section between the cryomodules.

High-power Charge Stripping

Development of liquid lithium charge stripper capable of withstanding high beam power of heavy ions proceeded with demonstration of continuous lithium circulation with the electromagnetic pump. Lithium film was established inside the primary chamber housed inside the secondary vessel [7] (Fig. 9). Credited controls are implemented to ensure configuration management and conduct of operations.

Content from this work may be used under the terms of the CC BY 3.0 licence (© 2018). Any distribution of this work must maintain attribution to the author(s), title of the work, publisher, and DOI.



Figure 9: Liquid lithium charge stripper module (bottom) and the established lithium film (top).

Microphonics Suppression

Microphonics is known to compromise the performance of SRF resonators. The situation is more challenging for FRIB as the cryoplant containing noisy compressors is located in the same building of the FRIB accelerator (Fig. 10). Precautions in compressor design & installation is key to microphonics mitigation. Design of the innovative “bottom-up” cryomodule carefully incorporated microphonics suppressing considerations including top suspended cryogenic headers for vibration isolation [8 – 10]. Effectiveness of microphonics mitigation is monitored by tunnel measurement of vibrational spectrum (Fig. 10). SRF cavity locking issues that occurred at initial cool down were promptly resolved by iteration on valve controls logic and by provisions for liquid helium supply from a 10,000 liter Dewar.

INFRASTRUCTURE GROWTH

Michigan State University has heavily invested in the infrastructure necessary for FRIB development and for future research including funding of the cryogenics initiative, establishing the SRF Highbay for SRF resonator processing and certification at mass production capacity, and recruitment of subject matter experts from over the world covering all disciplines of accelerator physics and engineering needed for the development of high-power hadron accelerators.

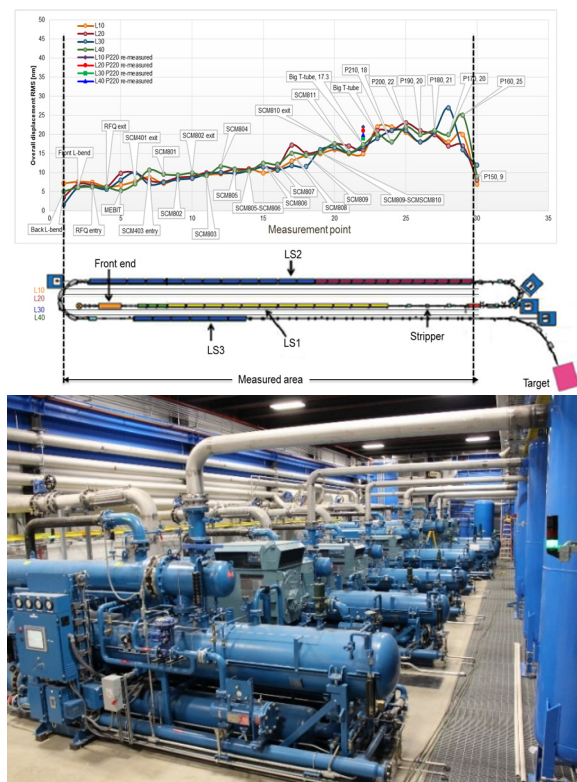


Figure 10: Cryoplant compressors located in the FRIB building (bottom) and the measured tunnel vibration (top).

The MSU Cryogenics Initiative

The MSU cryogenics initiative directed by R. Ganni aims at building up the national cryogenic knowledge base through education and training of cryogenic physicists and engineers, pursuing advanced cryogenic process design and state-of-the-art technology development, and supporting large-scale cryogenic systems associated with major accelerator facilities. Both regular university courses and condensed US Particle Accelerator School courses are offered along with traineeship programs. The initiative’s primary R&D areas are main compressor efficiency improvements, low level impurity removal, and small 2 K system for laboratory use (Fig. 11) [11].

SRF Highbay & Cryogenics Assembly Building

To meet the FRIB project schedule, MSU has built up the capacity of mass production and certification of > 1 cryomodules per month. The 2500 m² “SRF Highbay” houses areas for material inspection, cavity mechanical coordinate measurements, vacuum furnace degassing, chemical etching, high-pressure water rinsing, SRF coupler conditioning, cold mass assembly, and cryomodule testing (Figs. 12). This facility, together with the cryomodule assembly area and the machine shop, supports the production throughput of testing five cavities per week and one cryomodule per month [12]. In addition to the buffered chemical polishing (BCP) used for FRIB cavities, the

electro-polishing (EP) facility is being established to support FRIB upgrade. Furthermore, a new 1440 m² cryogenic assembly building is under constructed to house future cryomodule and superconducting magnet developments and production.



Figure 11: The MSU cryogenics initiative programs.



Figure 12: The SRF Highbay (top) and the cryomodule assembly area (bottom) housing six parallel assembly lines delivering more than one cryomodule per month.

POWER RAMP UP & UPGRADE

FRIB expects to ramp up beam power to 400 kW in about four years after the completion of the construction project (Fig. 13), which is about two order-of-magnitudes higher than any existing heavy ion accelerator in the power frontier [13]. Challenges include establishing the 28 GHz superconducting ECR ion source, the liquid lithium charge stripper, and the high-power charge selector, facilitating

beam halo cleaning and collimation, and improving the reliability and availability of the facility.

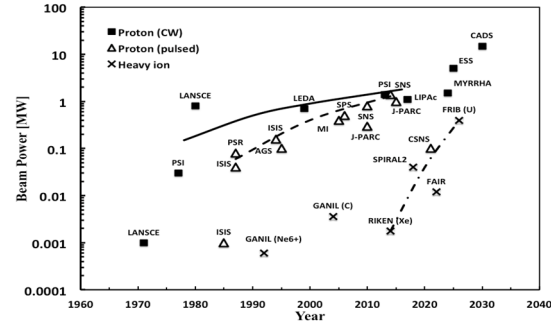


Figure 13: Evolution of hadron accelerator beam power.

The first step of FRIB upgrade is to double the driver linac output energy from the baseline to above 400 MeV/u. Space reserved in the FRIB tunnel will be filled with additional 11 cryomodules of $\beta=0.65$ elliptical cavities. Prototype cavities are being fabricated by the industrial vendors. In house BCP processing and certification results (Fig. 14) are to be benchmarked with those from Argonne using EP processing. The cryogenic distribution is configured so that the prototype cryomodule for FRIB upgrade can be readily connected after it is built. The raised energy is expected to significantly enhance the rare isotopes yield. It will also reduce the stress on the production target and the beam dump.



Figure 14: SRF cavity for FRIB upgrade being processed at MSU and Argonne National Laboratory.

ACKNOWLEDGMENTS

FRIB accelerator systems design and construction have been facilitated under work-for-others agreements with many DOE-SC national laboratories including ANL, BNL, FNAL, JLab, LANL, LBNL, ORNL, and SLAC, and in collaboration with institutes worldwide including BINP, KEK, IHEP, IMP, INFN, INR, RIKEN, TRIUMF, and Tsinghua University. The cryogenics system is developed in collaboration with the JLab cryogenics team. The recent experience gained from the JLab 12 GeV cryogenic system design is utilized for both the refrigerator cold box and the compression system designs. The liquid lithium charge stripping system is developed in collaboration with ANL.

REFERENCES

- [1] J. Wei *et al*, “FRIB Accelerator: Design and Construction Status”, in *Proc. HIAT'15*, Yokohama, Japan, Sep. 2015, paper MOM1|01, p. 6.
- [2] E. Pozdeyev *et al*, “First Acceleration at FRIB”, presented at LINAC'18, Beijing, China, Sep. 2018, paper WE2A01, unpublished.
- [3] M. Ikegami, “Machine and Personnel Protection for High Power Hadron Linacs”, in *Proc. IPAC'15*, Richmond, USA, May 2015, paper WEXC1, p. 2418.
- [4] F. Casagrande, in *Proc. IPAC'15*, Richmond, USA, May 2015, paper THYB1.
- [5] P. Ostroumov, “Overview of Worldwide High Intensity Heavy Ion Linacs”, presented at LINAC'18, Beijing, China, Sep. 2018, paper TU2A02, unpublished.
- [6] S. Lidia, “Diagnostics for High Power Accelerator Machine Protection Systems”, in *Proc. IBIC'14*, Monterey, USA, Sep. 2014, paper TU|YB1, p. 239.
- [7] T. Kanemura *et al*, “Construction Status of the FRIB Lithium Charge Stripper”, presented at INTDS'18, East Lansing, USA, Oct. 2018, unpublished.
- [8] A. Facco *et al*, “Superconducting Resonators Development for the FRIB and ReA Linacs at MSU: Recent Achievements and Future Goals”, in *Proc. IPAC'12*, New Orleans, USA, May 2012, paper MOOAC03, p. 61.
- [9] M. Johnson *et al*, “Design of the FRIB Cryomodule”, in *Proc. IPAC'12*, New Orleans, USA, May 2012, paper WEPPD006, p. 2507.
- [10] S. Miller *et al*, “Construction and Performance of FRIB Quarter Wave Prototype Cryomodule”, in *Proc. SRF'15*, Whistler, Canada, Sep. 2015, paper FRAA06, p. 1446.
- [11] V. Ganni *et al*, CEC-ICMC 59, 323 (2013).
- [12] T. Xu *et al*, “MSU RE-Accelerator ReA3 0.085 QWR Cryomodule Status” in *Proc. LINAC'14*, Geneva, Switzerland, Aug. 2014, paper MOPP044, p. 155.
- [13] J. Wei, “The Very High Intensity Future”, in *Proc. IPAC'14*, Dresden, Germany, June 2014, paper MOYBA01, p. 17.

BNL collaborated on the development of the alternative helium gas stripper. The SRF development benefited greatly from the expertise of the low- β SRF community. FRIB is collaborating with ANL on RF coupler and tuner developments, assisted by JLAB for cryomodule design, and by FNAL and JLab on cavity treatments. FRIB collaborated with LBNL on the development of VENUS type ECR ion source.

We thank the FRIB Accelerator Systems Advisory Committee for their valuable guidance, colleagues who participated in FRIB accelerator peer reviews including G. Ambrosio, J. Anderson, D. Arenius, W. Barletta, G. Bauer, G. Biallas, J. Bisognano, S. Bousson, P. Brindza, S. Caspi, M. Champion, D. Cossairt, M. Crofford, C. Cullen, D. Curry, R. Cutler, G. Decker, J. Delayen, J. Delong, G. Dodson, J. Donald, H. Edwards, J. Error, J. Fuerst, T. Khabiboulline, F. Kornegay, K. Kurukawa, J. Galambos, J. Galayda, G. Gassner, P. Ghoshal, J. Gilpatrick, C. Ginsburg, S. Gourlay, M. Harrison, S. Hartman, S. Henderson, G. Hoffstaetter, J. Hogan, S. Holmes, M. Howell, P. Hurh, R. Kersevan, A. Hodgkinson, N. Holtkamp, H. Horiike, C. Hovater, H. Imao, R. Janssens, R. Keller, J. Kelley, P. Kelley, J. Kerby, S.H. Kim, A. Klebaner, J. Knobloch, R. Lambiase, M. Lamm, Y. Li, C. LoCocq, C. Luongo, K. Mahoney, J. Mammosser, T. Mann, W. Meng, N. Mokhov, G. Murdoch, J. Nolen, W. Norum, H. Okuno, S. Ozaki, R. Pardo, S. Peggs, R. Petkus, C. Pearson, F. Pellemoine, T. Peterson, C. Pillar, J. Power, T. Powers, J. Preble, J. Price, D. Raparia, J. Rathke, A. Ratti, T. Roser, M. Ross, R. Ruland, J. Sandberg, R. Schmidt, W.J. Schneider, D. Schrage, S. Sharma, I. Silverman, K. Smith, J. Sondericker, W. Soyars, C. Spencer, R. Stanek, M. Stettler, W.C. Stone, J. Stovall, H. Strong, L.T. Sun, Y. Than, J. Theilacker, Y. Tian, M. Thuot, J. Tuozzolo, V. Verzilov, R. Vondrasek, P. Wanderer, K. White, P. Wright, H. Xu, L. Young, and A. Zaltsman, and colleagues who advised and collaborated with the FRIB team including A. Burrill, A.C. Crawford, K. Davis, X. Guan, P. He, Y. He, A. Hutton, P. Kneisel, R. Ma, K. Macha, G. Maler, E.A. McEwen, S. Prestemon, J. Qiang, T. Reilly, R. Talman, J. Vincent, X.W. Wang, J. Xia, Q.Z. Xing H.H. Zhang,. The FRIB accelerator design is executed by a dedicated team in the FRIB Accelerator Systems Division with close collaboration with the Experimental Systems Division headed by G. Bollen, the Conventional Facility Division headed by B. Bull, the Chief Engineer's team headed by D. Stout, with support from the FRIB project controls, procurement, and ES&H teams, and from NSCL and MSU.

STATUS OF THE SPES EXOTIC BEAM FACILITY

M. Comunian, A. Andrighetto, P. Antonini, C. Baltador, L. Bellan, D. Benini, J. Bermudez, G. Bisoffi, D. Bortolato, M. Calderolla, M. Cavenago, S. Corradetti, L. de Ruvo, A. Facco, E. Fagotti, P. Favaron, L. Ferrari, A. Galatà, F. Galtarossa, M. Giacchini, F. Gramegna, A. Lombardi, M. Maggiore, M. Manzolaro, D. Marcato, T. Marchi, P. Mastinu, P. Modanese, M. F. Moisisio, A. Monetti, M. Montis, A. Palmieri, S. Pavinato, D. Pedretti, A. Pisent, M. Poggi, G. Prete, C. Roncolato, M. Rossignoli, L. Sarchiapone, D. Scarpa, D. Zafiroopoulos, INFN-LNL, Legnaro, Italy. M. Bellato INFN- Sez. di Padova, Padova, Italy.

Abstract

At Legnaro National Laboratories of INFN it is under construction a Rare Isotope Facility called "Selective Production of Exotic Species" (SPES) based on a 35-70 MeV proton cyclotron, able to deliver two beams with a total current up to 0.75 mA, an ISOL fission target station and an existing ALPI superconducting accelerator as a post accelerator (up to 10 MeV/u for $A/q=7$). The paper will cover notably: the high-resolution mass separator, the CW RFQ (80 MHz, 727 keV/u, with internal bunching), the 1+ low energy transfer line and the injection line from Charge Breeder to ALPI under installation.

INTRODUCTION

SPES, acronym of Selective Production of Exotic Species, is a CW radioactive ion beam facility under construction at LNL INFN in Italy. It will produce and accelerate neutron-rich radioactive ions, to perform nuclear physics experiments, which will require beams above Coulomb barrier [1].

The main functional steps of the facility are shown in Fig. 1: the primary beam delivered by the cyclotron, the beam from the fission target (as an example, up to 10^{13} particle/s of ^{132}Sn), the beam cooler, the separators, the charge breeder and the accelerator (the existing ALPI with a new RFQ injector). The use of the continuous beam from the +1 source, which can use different configuration types LIS, PIS, SIS, maximizes the RNB efficiency but need a CW post accelerator (RFQ and ALPI). The beam is prepared for the post-accelerator stage with a charge breeder device. The energy from 20 to 40 kV on the transfer lines are determined by the chosen RFQ input energy (5.7 keV/u); for this reason, all the devices where the beam is approximately stopped (production target, charge breeder and RFQ cooler) lay at a voltage proportional to the ratio A/q . The charge state range ($3.5 < A/q < 7$) is bounded by the RFQ field level for the upper limit and by the minimum voltage on $q=1$ transport line.

THE CYCLOTRON AS PRIMARY DRIVER FOR SPES AND TARGET

The proton beam is accelerated by a 35-70 MeV, 700 μA commercial cyclotron C70 (Best Cyclotron Systems

Inc.). It offers simultaneous double extraction from two 180° apart exit ports, to be used for both fundamental nuclear science and medical and material research [2].

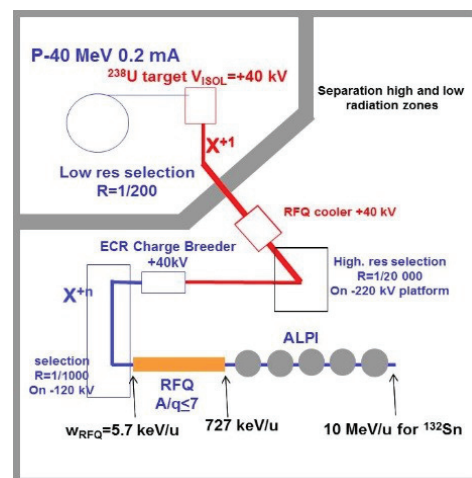


Figure 1: functional scheme of the SPES facility. There are two main areas: the 1+ line and the n+ line, where 1+ and n+ indicates the beam charge state.

C70 is an Azimuthally Varying Field (AVF) compact cyclotron with four sectors, with the main magnet energized by resistive coils.

Protons are extracted by H- stripping the electrons in a thin graphite foil. Installation and successful commissioning were accomplished in 2015-2017, driving the beam to a home designed and built beam dump.

Stability and reliability tests of C70 were conducted: e.g. in 5 days long run at 40 MeV, the average beam current was $201.18 \pm 0.97 \mu\text{A}$. Tests were then extended to 70 MeV - 500 μA with good stability and repeatability. Dual extraction was proven as well.

The cyclotron will impinge the production target (7 properly spaced UCx discs, 40 mm diameter, 0.8 mm thick), generating about 10^{13} fissions/s. RA isotopes produced by the ^{238}U fissions are delivered to the 1+ ion source where they are ionized and accelerated to 20-40 keV.

The target box must be kept a temperature of $2000 \pm 2200^\circ\text{C}$ in vacuum to enhance RA isotope mobility, extraction and ionization. This temperature is achieved by combining

Content from this work may be used under the terms of the CC BY 3.0 licence (© 2018). Any distribution of this work must maintain attribution to the author(s), title of the work, publisher, and DOI.

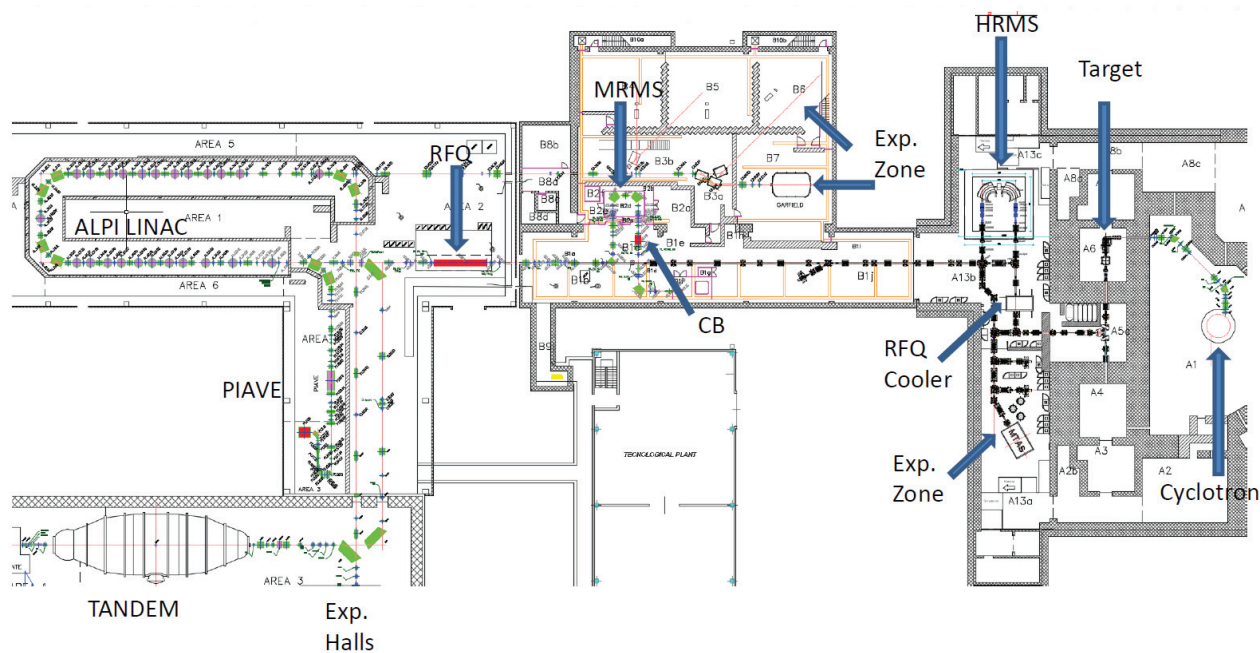


Figure 2: General SPES layout with main areas.

the 8 kW proton beam and Joule heating. Surface (SIS), plasma (PIS) and LASER (LIS) ionization sources will be used, aiming at maximum ionization efficiency, since the production rate of specific nuclei can be extremely low.

THE SEPARATION STAGES

The general layout of the SPES facility is presented in Fig. 2.

The reference beam for the beam dynamics simulations is chosen to be the ^{132}Sn , extracted at 40 kV at the end of the target extraction system. It has been chosen a $q=19$ after the charge breeder i.e. $A/q=6.9$, in such a way to test the maximum required electromagnetic fields of the line elements of the facility.

There are three normalized rms emittance regimes: after the target, it is chosen to be $\epsilon_{n,rms}=0.007$ mm mrad, with an equivalent geometric emittance at 99% of $\epsilon_{geo,99\%}=64$ mm mrad, assuming a gaussian distribution cut at 4σ . Then, the beam cooler prepares the beam to the high mass resolution stage, reducing the emittance down at least by a factor 5 and the energy spread by a factor 10 at the level of ± 1 eV rms. After the CB, the emittance for the BD calculation is assumed to be $\epsilon_{n,rms}=0.1$ mm mrad. As far as the longitudinal phase space is concerned, a uniform distribution between ± 10 eV is considered. After the CB, the energy spread is set to ± 15 eV. The low-resolution section (LRMS) is the part of the line between the target and the beam cooler. Two mass spectrometers are placed between the target and the beam cooler: the Wien Filter and a 90° dipole. The overall resolution is of 1/200 in mass, enough to separate the isobars from the other isotopes. Two similar type of spectrometers, the High-Resolution Mass Spectrometer (HRMS) and the Medium Resolution Mass Spectrometer (MRMS) are provided for the SPES project. Both are composed by two 90° magnet with a multipole

(up to 12° order pole) between them, placed onto platforms.

The HRMS is a full ions separator used to obtain the ions of interest, because it removes isobar ions coming from the source and the MRMS is used to clean the nominal beam from high intensity contaminants introduced by charge breeder [3].

After the 1/200 isotopes separator, the isobars separation is represented by HRMS placed on a -220 kV platform (the effect is a reduced divergence and energy spread). This separator is constituted by six quadrupole lens, two hexapole lens, two dipoles and one multipole lens placed in the symmetry plane of the system to fix the curvature aberration. The HRMS can separate different isobar with $\Delta M/M=1/20000$ and $\Delta W/W=\pm 1$ eV (this so low energy spread is due to the beam cooler) like shown in Fig. 3 below. The optics improvement is still ongoing, but it shows a fully resolving capability of isobars separated of 1/20000 in mass. An option to reduce the platform voltage for the HRMS down to -120 kV, like the MRMS, is ongoing. The code used for the design of HRMS/MRMS is TraceWin from CEA [4], and a full benchmark has been done, with the same results, by using COSY [5].

It is important to consider that the HRMS performance depend strongly on the beam cooler efficiency [6][7]. After the charge breeder, the next spectrometer is the MRMS, placed on a -120 kV platform (for the same reasons of the HRMS). The goal in resolving power of this spectrometer is 1/1000 with the interest beam in A/q fully separated. The Table 1 shows the overall capabilities of the two spectrometers. After the selection, the beam is sent to the CB through a periodic transport line.

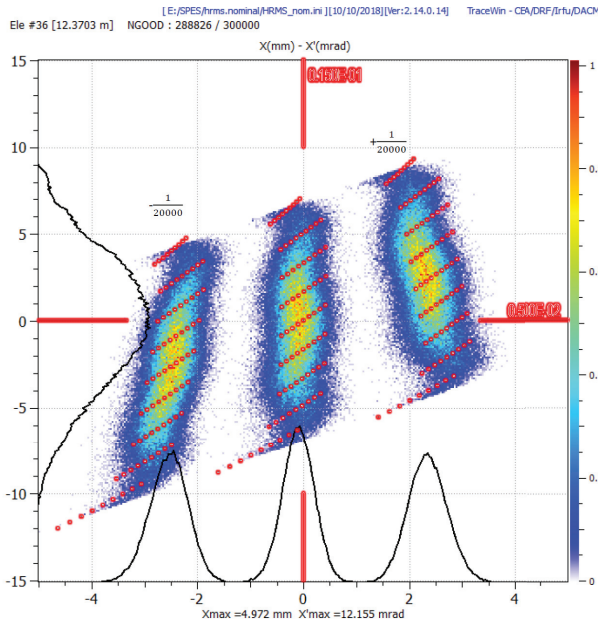


Figure 3: Phase Space (X, X') at HRMS image point of three beams separated of $1/20000$ on mass with $\pm 1\text{eV}$ RMS energy spread, with overlapped the results of COSY 5° order simulation, as red dots.

Table 1: Medium and High Spectrometer Performances

Parameter [units]	MRMS	HRMS
RMS Emit. nor. [mrad]	0.1	0.0014
Beam Energy [keV]	160	260
Nominal Resolution	1/1000	1/20000
RMS Energy Spread [eV]	± 15	± 1
90% Geom. Emit. [mrad]	56	2.8
(Geom. Emit.)/Resol.	56000	56000

THE CHARGE BREEDER

Charge breeding at SPES will be based on the ECR technique: the model adopted (SPES-CB) derives directly from the PHOENIX Charge Breeder installed at the Laboratoire de Physique et de Cosmologie. The SPES-CB was delivered to LNL at the end of 2015, after successful acceptance tests carried out at LPC [8].

Highly charged ion beams in the range $3.5 < A/q < 7$ will be extracted from this device through a three electrodes extraction system designed at LNL [9], and initially focused by two solenoids. It is well known that the breeding can introduce contaminants in the extracted beam, coming from two main sources: impurities present in the gas fed into the plasma chamber (normally oxygen),

or deriving from the outgassing of the surfaces exposed to vacuum, and the release of particles from the materials constituting the vacuum chamber due to their interaction with the plasma. To face with the first problem, special attention was paid to the surface treatments, in particular of the stainless steel plasma chamber and the iron plug at extraction (ARMCO). For the second one, a Medium Resolution Mass Spectrometer (MRMS) was designed with an expected resolving power of $\Delta(M/q)/(M/q)=1/1000$ will be installed downstream the charge breeder. Figure 4 show the installation zone of charge breeder.



Figure 4: Charge Breeder installation.

THE SPES RFQ

The SPES RFQ is designed to accelerate beams with A/q ratios from 3.5 to 7 from the Charge Breeder through the MRMS and the selection and injection lines up to the MEBT. The main parameters of the RFQ are listed in Table 2. The RFQ is composed of 6 modules about 1.2 m long each. Each module is basically composed of a Stainless-Steel Tank (AISI LN 304) and four OFE Copper Electrodes [10]. In Fig. 5 the transverse beam dynamics through the RFQ is show.

A copper layer will be electrodeposited on the tank inner surface and a spring joint between tank and electrode is used to seal the RF.

Table 2: Main RFQ Parameters

Parameter [units]	Design value
Operational mode	CW
Frequency [MHz]	80
In/out. Energy [keV/u]	5.7-727 ($\beta=0.0035-0.0359$)
Vane length L [m]	6.95
RF Power [kW] (+30%)	98

Content from this work may be used under the terms of the CC BY 3.0 licence (© 2018). Any distribution of this work must maintain attribution to the author(s), title of the work, publisher, and DOI.

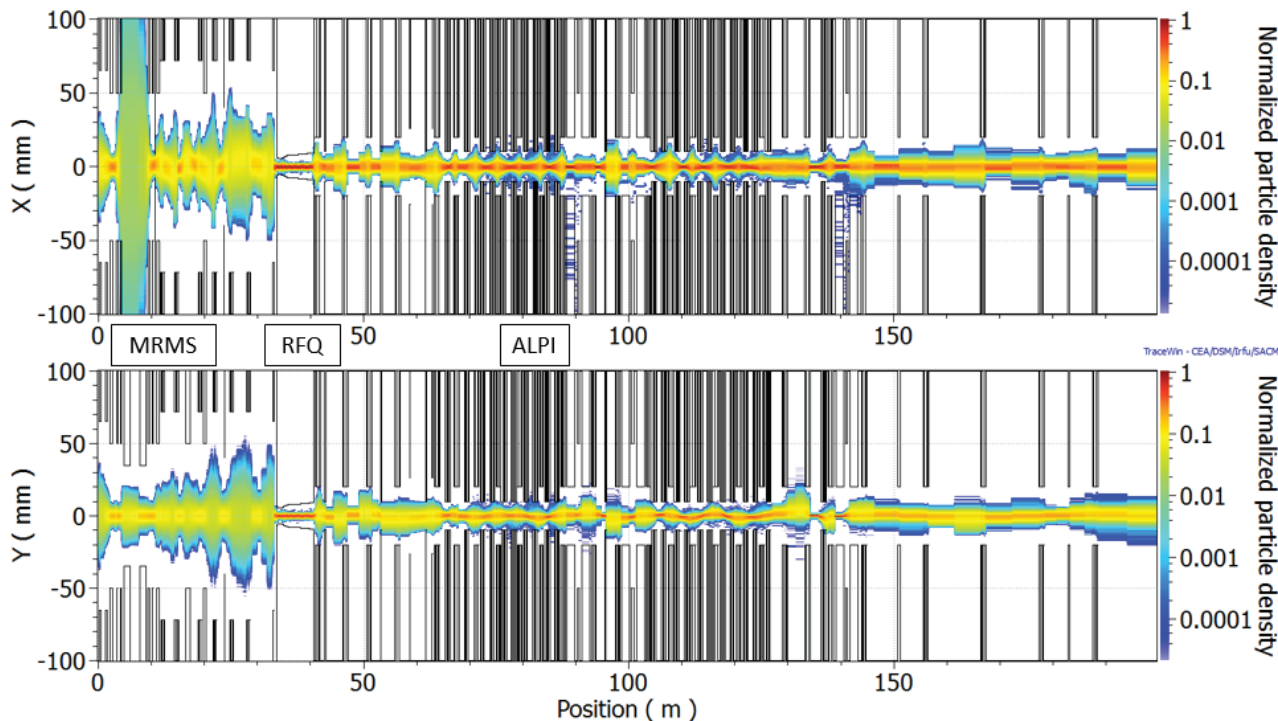


Figure 5: Multiparticle normalised-densities y and x of the whole line CB-RFQ-ALPI- Experimental hall.

The RFQ voltage law is a linear function along z $V(z)=V(0)+a \cdot z$ with $a=3.177$ kV/m and $V(0)$ depending on the A/q of the ion to be accelerated. Such law is implemented by designing the RFQ to obtain a constant TE_{21} cut-off frequency $f_c=79.5$ MHz along the structure and by properly shaping the vane undercuts at the Low and High Energy Ends of the RFQ. The compensation of the R_0 variations, is made with the capacitive region that is varied along the RFQ. The electrode thickness is equal to 48 mm and the tank inner radius R is equal to 377 mm.

The RFQ is in its construction phase: 20 out of 24 electrodes were finished, and tight mechanical accuracies were within specifications. Almost all scanned profiles of each electrodes follow tolerance on best fitted curve profiles (0.04mm) except for some small spot (Outliers <1 % of measured points). In Fig. 6 is show the RFQ electrode under measurements.

The tank machining tender was completed, and its construction is started. Support and alignment frames were meanwhile designed.

THE ALPI LINAC FOR SPES

After the SPES RFQ, a transport line, including 2 normal conducting quarter wave resonators (QWR) for longitudinal matching, delivers the exotic beam to the existing sc linac ALPI. Several upgrades are being implemented, to improve both the performance (in final energy and current values) and the reliability of ALPI [11] [12]. The complete refurbishment of the cryostats and cryogenic plant control systems was completed in 2017 and tested with success.



Figure 6: SPES RFQ electrode under measurements.

During 2018, several important milestones are planned: the replacement of 10 magnetic lenses with 50% higher gradient ones, expected to improve beam transmission along the machine; displacement of 2 QWR cryostats from the PIAVE stable beam injector to ALPI, to make them available to both stable and exotic beams and in 2020, we plan to add two fully new cryostats at the end of ALPI, so as to achieve the final energy of 10 MeV/A for the reference SPES beam ^{132}Sn .

All along the facility, proper beam instrumentation for both pilot and exotic beam must be provided, the beam current will be measured via normal Faraday cups, equipped with low noise amplifiers; position and transverse profiles via wire grids and MCP-based electron

monitors; emittances via wire-grid and Allison scanners. The first series of boxes will be completed in 2018 for the new SPES injector and the low-energy exotic beam transport line. Tape stations, based on γ -ray spectroscopy of the β -decaying RA nuclei, will be located after the LRMS, after the HRMS and at the end of ALPI, to identify the beam isotopic composition and intensity.

An end-to-end simulation from the CB to the end of ALPI has been performed by using TraceWin. The beam travels from the CB to the third hall. The final kinetic energy is 1.2 GeV ($\Delta E/E < \pm 0.4\%$) with total losses of 14% in the nominal case. In Fig. 5 the multiparticle densities are shown for the x and y coordinates.

CONCLUSIONS

Several highlights of the SPES project were shown. The high-resolution mass separator is under refinement while the WF and the LRMS are under procurement. The MRMS is going to be installed and the RFQ is under construction. An end to end simulation of the line from the CB to the experimental hall was done, showing an overall transmission $>85\%$ in the nominal case.

REFERENCES

- [1] G. Bisoffi et al. "Progress in the realization and commissioning of the exotic beam facility SPES at INFN-LNL", 2018 J. Phys.: Conf. Ser. 1067 052017.
- [2] M. Maggiore "Status of the high intensity beam Facility at LNL-INFN", Proceedings of Cyclotrons2016, Zurich, Switzerland, paper FRA03, p.394.
- [3] M. Comunian et al. "Design of high resolution mass spectrometer for SPES", In Proc. of IPAC'18, Vancouver, Canada, 2018, paper THPAK021, p.3252.
- [4] D. Utriot and N. Pichoff, "TraceWin", CEA Saclay, <http://irfu.cea.fr/Sacm/logiciels/index3.php>
- [5] M. Berz, COSY INFINITY, Version 10 User's Guide and Reference Manual, MSU, 2017.
- [6] M. Maggiore et al., "Plasma-beam traps and radiofrequency quadrupole beam cooler", Review of Scientific Instrument 85, AIP publishing, November 2013.
- [7] A. Nieminen et al., "Beam Cooler for Low-Energy Radioactive Ions", Nuclear Instruments and Methods in Physics Research A 469, August 2001, p. 244-253.
- [8] A. Galatà et al., The new ECR charge breeder for the Selective Production of Exotic Species project at INFN-LNL, Rev. Sci. Instrum. 87 (2016) 02B503.
- [9] A. Galatà et al., Status of the SPES-charge breeder (SPES-CB) and its beam line at INFN-LNL, Nucl. Instrum. Meth B376 (2016) 329.
- [10] L. Ferrari et al "Thermo-mechanical calculation of the SPES RFQ", In Proc. of HIAT'15, Yokohama, Japan, 2015, paper WEPB13, p.219.
- [11] M. Comunian et al., "Beam Dynamics Simulations of the Piave-Alpi Linac", In Proc. of IPAC'11, San Sebastian, SPAIN, 2011, paper WEPC014, p.2034.
- [12] A. Pisent et al. "SPES Beam Dynamics", In Proc. of HB'14, East Lansing, USA, 2014, paper TUO4AB01, p220.

PRESENT STATUS OF HIRFL COMPLEX IN LANZHOU*

Y. J. Yuan[†], D. Q. Gao, L. Z. Ma, L. J. Mao, R. S. Mao, J. Meng, Y. W. Su, L. T. Sun, Y. Y. Wang, J. X. Wu, Z. Xu, J. C. Yang, W. Q. Yang, Q. G. Yao, X. J. Yin, B. Zhang, W. Zhang, Z. Z. Zhou, H. W. Zhao, G. Q. Xiao, J. W. Xia, Institute of Modern Physics, CAS, Lanzhou, China

Abstract

Heavy Ion Research Facility in Lanzhou (HIRFL) is a cyclotron, synchrotron and storage ring accelerator complex, which accelerates ions of hydrogen to uranium from low to medium energy. Since the complete of HIRFL-CSR project in 2008, under the support from CAS, efforts have been put to improve the infrastructure for machine performance, including improvement of EMC environments, power distribution stations, PS stations, cooling water system, RF system of cyclotrons and adoption of EPICS control system, etc. New generation SC ECR source-SECRAL2 with high performance is put into operation. Experiments of electron cooling with pulsed electron beam are performed for the 1st time. Stochastic cooling and laser cooling are realized in CSRe. The performance of RIBLL2 and CSRe are gradually improved. The ISO mode of CSRe for precise atomic mass measurements is well studied and reaches state-of-art mass resolution of storage rings. The operation status and enhancement plan of HIRFL will be briefly reported in this paper.

INTRODUCTION

HIRFL[1,2] is one of the largest heavy ion research facility in China. It belongs to the National Laboratory of Heavy Ion Accelerator, which was established in 1991, at Institute of Modern Physics (IMP). HIRFL serves for the scientific researches in nuclear physics, atomic physics and nuclear science related interdisciplinary study.

HIRFL consists of two cyclotrons (SFC and SSC), one synchrotron (CSRm) and one storage ring spectrometer (CSRe), in chain, see Fig. 1. The SFC cyclotron was constructed in 1960s for light ions. It's upgraded in 1980s to accelerate heavy ions from hydrogen to uranium, as required to be an injector of cyclotron SSC. The CSR project, CSRm and CSRe are the major components, was constructed at the turn of this century, for higher energy pulsed beam and precise nuclear physics and atomic physics study at external target and in ring.

Within the half century construction period, the infrastructure of HIRFL has been improved gradually according to the development of technology. In recent years, under the strong support of the maintenance and renovation budget from CAS, we upgraded the power station of HIRFL, LLRF of cyclotrons, water-cooling systems [3] and intra-network; built up the environment control of power supply room of CSR and the monitoring systems of water-cooling, power station and water leakage detection; rearranged and rewired the cables of CSRe to improve the

EMC condition of CSRe. Above all, new generation super-conductive ECR source SECRAL-II as a back-up of SECRAL with better performance was constructed and put into operation this year [4,5]; EPICS was introduced to take over most of the control system [6].

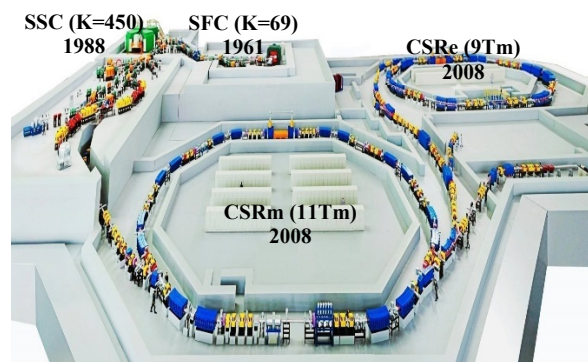


Figure 1: The layout of HIRFL complex.

To improve the performance of HIRFL, new technologies are researched and developed. Experiments of electron cooling with pulsed electron beam are performed for the 1st time for the development of e-coolers at future circular accelerator. The performance of RIBLL2 as on-line separator of secondary beams was gradually improved. The ISO mode of CSRe for precise atomic mass measurements is well studied and reaches state-of-art mass resolution of storage rings with unique two-TOF velocity measurement setups. The Stochastic cooling and laser cooling are realized in CSRe, which will help to extend the research ability of nuclear and atomic physics at CSRe.

Up to now, SFC is the only injector for both SSC and CSRm. This limited the total beam time of the HIRFL complex. To increase the beam time, new injectors are urgently needed. Under the support of CAS and IMP, a DC Linac injector of SSC is being developed since 2012, which will accelerate heavy ion beam to 1.024 MeV/u. New pulse Linac injector for direct injection to CSRm is designed and underdevelopment. With the new injectors the beam time for experiments will be increased dramatically.

OPERATION STATUS OF HIRFL

In last 5 years, the beam time requirement of HIRFL is increasing rapidly. New growth points mainly from anti-radiation testing and reinforcement study of circuits, pile radiation material study, production of super-heavy elements and experiments at storage rings. The machine time and beam time of HIRFL averaged to more than 7500 h/a and 5300 h/a separately. The failure time averaged to less than 250 h/a. With the only injector cyclotron SFC, beam time reached it's up-limit. Among the beam time provided, about 54 % is for nuclear physics and atomic physics, 16

* Work supported by NSFC: 11575265, U1232208, 10921504, 11320101003, 11375244, 10705039, 11275236, 11035007 and U1232123.

[†] yuanyj@impcas.ac.cn

% is for material science, 13 % is for space science, 8 % is for bio-science, the rest is for the machine study. More than 50 % of the beam time is provided for researchers outside IMP.

As an all-ion accelerator complex, HIRFL provides beams of nature exist ions from Hydrogen to Uranium. The provided ion beams are indicated Fig. 2, including some of their isotopes. According to the design parameters and the working condition limits (range of magnet field and RF frequency) of the cyclotrons, the energy range of available beams from SFC and/or SSC for different A/Q ratios of ions is shown in Fig. 3. It can be seen that the energy range of cyclotrons is still limited by the down-limit of present working field of SFC.

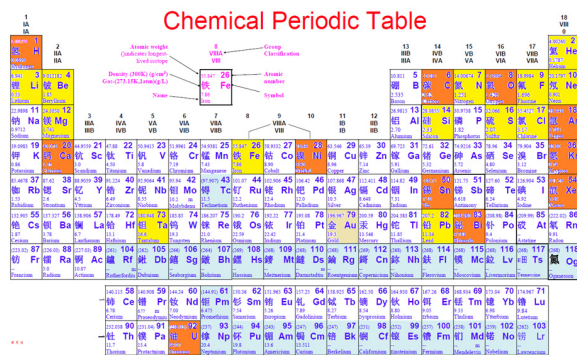


Figure 2: The accelerated primary beams at HIRFL in the chemical periodic table. The red blocked were accelerated in CSRm.

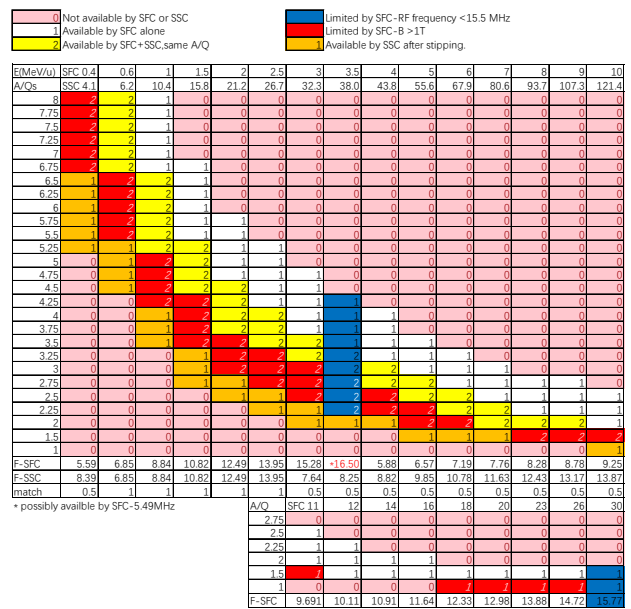


Figure 3: Energy range of beams from SFC and/or SSC for different A/Q ratios of ions.

UPGRADE OF INFRASTRUCTURES

As shown in Fig. 1, HIRFL was built-up in 3 periods, lasting about half century. In recent years, under the strong support of the national maintenance and renovation budget for large scale fundamental science and technology facilities from CAS, many aspects of the infrastructure of

HIRFL were upgraded or renewed to improve the operation stability and reduce the failure time.

Power Station The power station for SSC and the beam lines to terminals is replaced using new grid technology, to improve the reliability, safety and energy efficiency.

Water Cooling System The water-cooling systems of HIRFL were upgraded to increase the cooling resistance and heat exchange efficiency, which improved the working stability of power supplies. The resistance of inner circulating water reached above 1.0 MΩ·cm.

Intranet The backbone of intra-network was upgraded from 100 M to 10 G bandwidth according to the requirements for data transmission from control system, beam diagnosis system and physics experiments. With careful design, physical link network topology optimization, application of network expansion with virtualization technology, and rectification of the network cabinet and cables, the new network well meets the growing requirements. An online status inquiry system of network equipment was established along with the upgrading.

EMC Environment The signal cables and power cables of CSRe and RIBLL2 were rearranged and rewired to reduce the electromagnetic radiation interference and improve the EMC environment. The background noise levels of beam diagnosis and experiment detectors were reduced by more than one order.

Environment Control The power supply rooms of CSR were built up inside the CSR hall for more stable and reliable performance of the PS. New monitoring systems of water-cooling [3], power station and water leakage detection were built up to monitor the basic operation condition. The radiation protection system was also rebuilt.

IMPROVEMENTS OF PERFORMANCE

To improve the performance of HIRFL, new technologies are researched and developed.

New Control System The self-developed distributed control system of HIRFL was developed in many years part by part, and based on many kinds of platforms. It's not convenient for the operation and not easy to exchange signals and data. In last years, the open-source Experimental Physics and Industrial Control System (EPICS), developed at LANL and ANL, was adapted to take over most of the control system of HIRFL[6]. The structure of new control system based on EPICS is shown in Fig. 4.

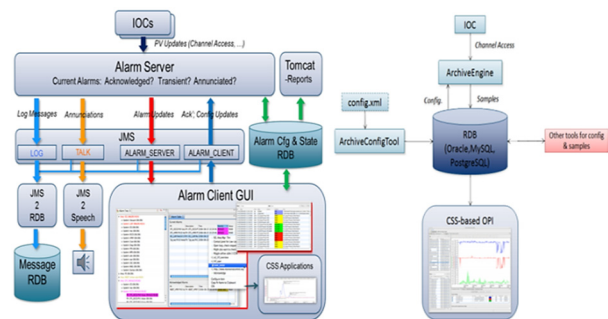


Figure 4: The structure of new HIRFL control system.

Content from this work may be used under the terms of the CC BY 3.0 licence (© 2018). Any distribution of this work must maintain attribution to the author(s), title of the work, publisher, and DOI.

Content from this work may be used under the terms of the CC BY 3.0 licence (© 2018). Any distribution of this work must maintain attribution to the author(s), title of the work, publisher, and DOI.

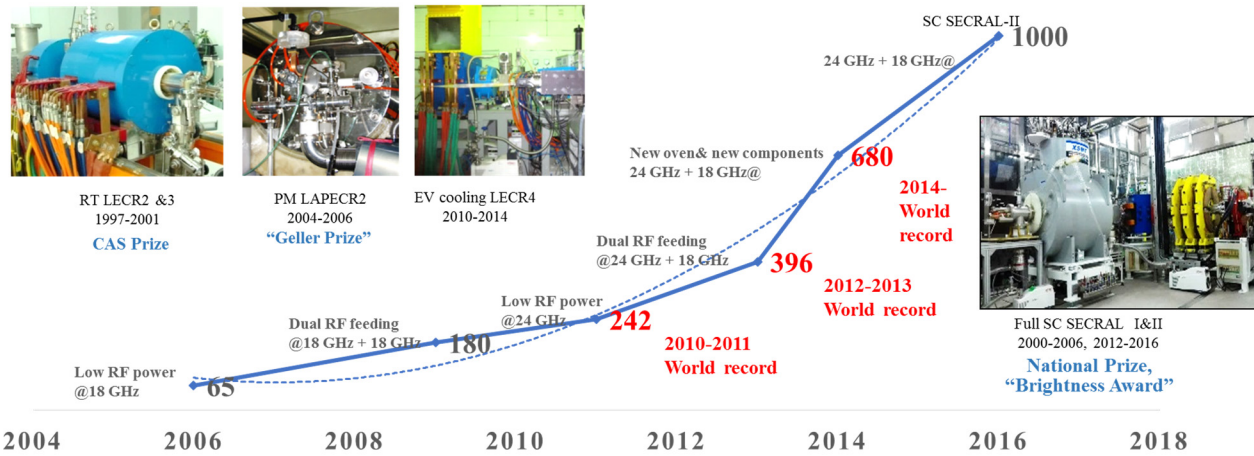


Figure 5: A brief summary of the development of ECR ion sources at IMP.

New control system of electron cooler at CSRm was built to replace the attached one to accommodate the up-graded electron cooler [7]. The LLRF of cyclotron RF systems and the PXI RF controller of CSRm were rebuilt to improve the operation stability, enhance the data-loading speed and reliability.

New SC ECR Ion Source A new generation superconductive ECR source-SECRAL-II as a back-up of the former SECRAL with better performance was constructed and put into operation this year [5]. With new structure, SECRAL-II created higher magnetic field and works at 18 GHz / 24 GHz microwave frequency. It sets a new beam current record of highly charged heavy ion beams. Figure 5 gives a brief summary of the development of ECR ion sources at IMP since 2004. With the state-of-art ECRIS technology, SECRAL-II will enable SFC cyclotron to accelerate heavy ions with higher charge state and intensity to higher energy, which benefits the accumulation and acceleration in synchrotron CSRm.

Pulsed Electron Cooling Experiments of electron cooling with pulsed electron beam are performed for the 1st time at CSRm [8,9]. New phenomena were observed. It was found that the modulation frequency should be near integer or half integer harmonic numbers of the revolution frequency of ions to maintain the life time of ions, otherwise the stored ions will lose rapidly. With the cooling of pulsed electron beam, the ions will be bunched inside the electron bunch and cooled. The experiment phenomena can be explained by space ME field of electron bunches in theory and proved by numeric simulations. The study of electron cooling with pulsed electron beam is important for the cooling of high energy bunched ion beam with high peak current electron cooler, at future ion circular accelerator or colliders.

RIBLL2 Improvement The performance of the 2nd radioactive isotope beam line at Lanzhou - RIBLL2 as an in-flight separator of relativistic projectile fragments was gradually improved. Figure 6 shows the design of RIBLL2 as the connection RIB line between CSRm and CSRe and RIB separation line to external target ETF [10]. There are 8 beam profile detectors newly installed along RIBLL2 for

both horizontal and vertical profiles. The core structure of detector is shown in Fig. 7. In the joint efforts of experimental teams, RIBLL2-ETF is capable of identifying clearly all ions up to Z=30, with the combination of the TOF and the MUSIC detectors [10]. Future upgrading of RIBLL 2 was planned.

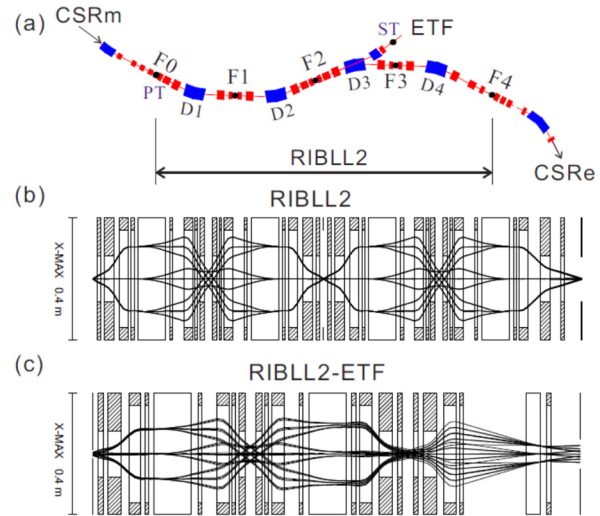


Figure 6: (a) A schematic layout of the RIBLL2 beam line. Horizontal beam trajectories with the first-order optics calculated by the GICOSY for the full RIBLL2 (F0 to F4) (b) and the first half of RIBLL2 and ETF (c).

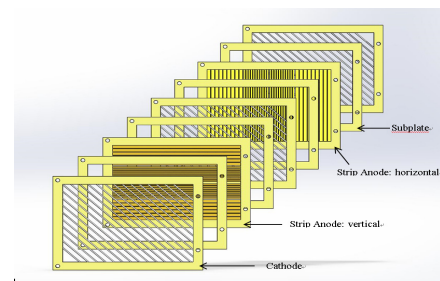


Figure 7: Core structure of BPD at RIBLL2.

Advanced Mass Spectrometry The ISO mode of CSRe for precise atomic mass measurements is well studied and reaches state-of-art mass resolution of storage rings with unique two-TOF velocity measurement setups (see Fig. 8). Following the ISO mode mass spectrometry at ESR@GSI, we explored deeply the mass spectrometry at CSRe. With the improvement of EMC environment and new dipole PS at CSRe, the signal-noise ratio was significantly improved. With the new idea of two-TOF detector at storage rings to measure the velocity of ions, the transition energy (γ), as a function of the closed orbit length or momentum deviation, can be measured precisely using the time spectra data of the ions cycling in CSRe [11]. The transition energy function can be monitored and optimized online to ensure stable and good isochronous condition. With the quadrupole magnets and sextupole magnets corrections, a mass resolution of 1.71×10^5 (FWHM) was reached [12]. Further non-linear optimization with higher order magnet field was planned.

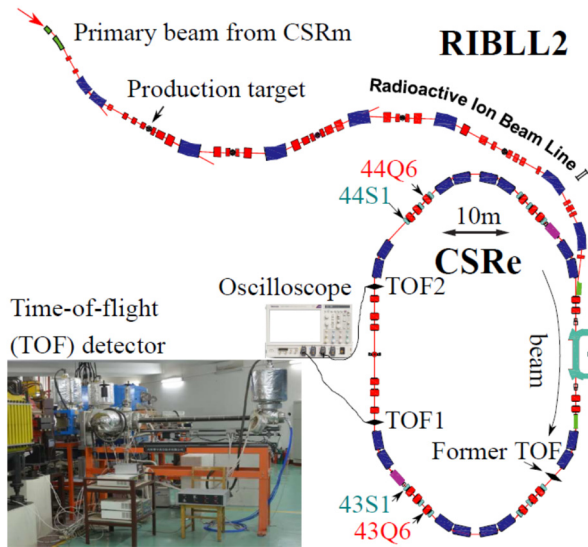


Figure 8: The layout of storage ring mass spectrometry with single TOF and double TOF detectors at CSRe. A picture of installed TOF detector is shown at the left bottom.

Stochastic Cooling and Laser Cooling The Stochastic cooling and laser cooling are realized in CSRe, which will help to extend the research ability of nuclear and atomic physics at CSRe. The beam after target with large emittance and momentum spread can be cooled down in seconds by stochastic cooling with slot line pickup and kickers [13]. Stochastic cooling will be used in the Schottky Mass Spectrometry (SMS) experiments. The relativistic Li-like O^{5+} beam, with energy of 280 MeV/u, was cooled by CW laser of wavelength 220 nm recently. It's up to now heavy ions with highest charge state and highest energy that ever been laser cooled. Figure 9 shows the setup of laser cooling at CSRe.

FUTURE DEVELOPMENTS

Up to now, SFC is the only injector for both SSC and CSRm. This limited the total beam time of the HIRFL

complex. To increase the beam time, new injectors are urgently needed. Under the support of CAS and IMP, a CW Linac injector of SSC is being developed since 2012, which will accelerator heavy ion beam to 1.024 MeV/u [14,15]. New pulse Linac injector for direct injection to CSRm is designed and underdevelopment. The operation modes of HIRFL will be enhanced with new injectors (see Fig. 10). With the new injectors the beam time for experiments will be increased dramatically.

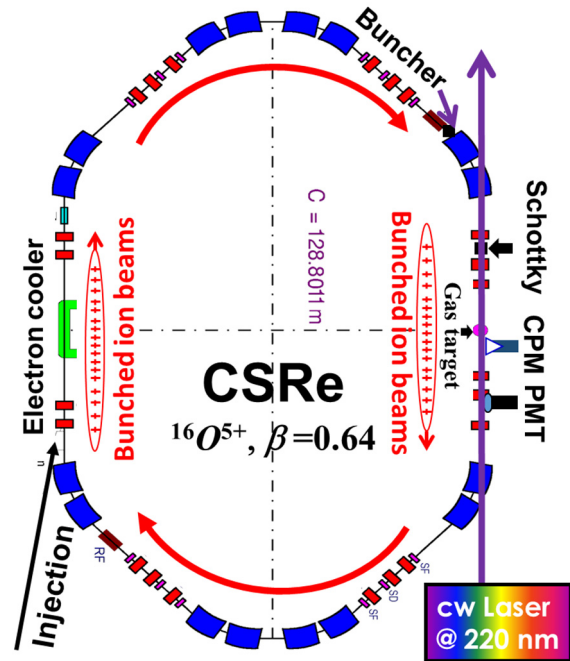


Figure 9: Experimental setup of laser cooling at CSRe.

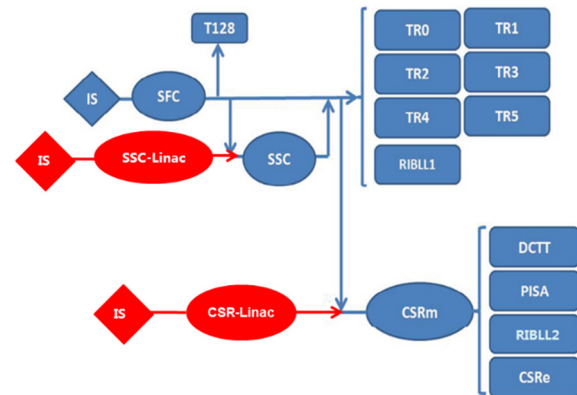


Figure 10: Operation modes of HIRFL with new injectors SSC-Linac and CSRm-Linac.

The first part of SSC-Linac [14,15], energy up to 580 keV/u was constructed off-site. We identified and solved the momentum resolution problem of high intensity heavy ion beam at Q/A selection system [16]. The updated Q/A selection system with additional solenoid reached sufficient Q/A resolution. It will be installed at SSC hall next year. The energy after further acceleration of SSC will be 6 MeV/u, compared with present 1 MeV/u of Uranium from SFC. The intensity will be increased 10~100 times.

Fig. 11 shows the design location of SSC-Linac and the off-site development of SSC-Linac. The beam lines with crossed vacuum chambers were ready for parallel operation with injectors SFC and SSC-Linac.

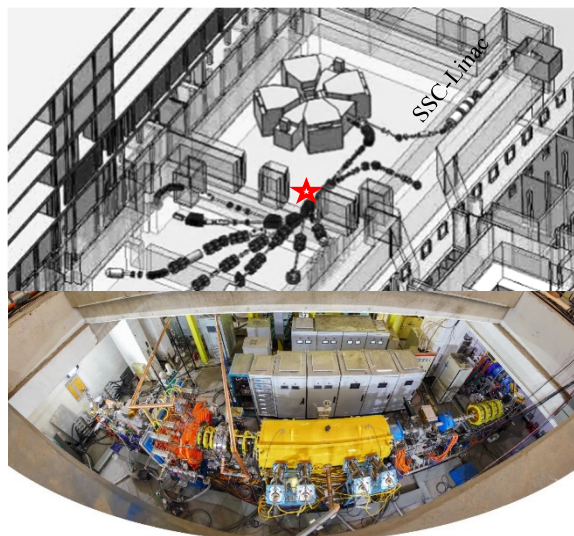


Figure 11: The design location of SSC-Linac (up) and the off-site development of SSC-Linac (down). At the red star position of the beam lines, the vacuum chamber is crossed for parallel operation of injectors.

CONCLUSION

We have detailed the present status of HIRFL complex. To match the increasing beam time and quality requirement of HIRFL, continual improvements of infrastructure remains an important aspect, developments and applications of new technologies are the other. Meanwhile, for the new project HIAF [17], which will break ground in 2018, many aspects of new technology should be studied by the construction group and some of them will be verified at HIRFL.

ACKNOWLEDGMENTS

HIRFL is managed by the National Laboratory of Heavy Ion Accelerator in Lanzhou and the Chinese Academy of Sciences. The authors would like to acknowledge the contributions from colleagues and friends especially from local experiment groups, GSI Helmholtz Centre, Jefferson Lab, RIKEN, Peking University and Beihang University.

REFERENCES

- [1] J.W. Xia et al., “The heavy ion cooler-storage-ring project (HIRFL-CSR) at Lanzhou”, Nucl. Instr. Meth. A 488(1–2), 11–25 (2002), DOI:10.1016/S0168-9002(02)00475-8
- [2] Y. J. Yuan et al., “Status of the HIRFL–CSR complex”, Nucl. Instr. Meth. Phys. Res. Sect. B, 317:214-217, DOI:10.1016/j.nimb.2013.07.040
- [3] Y. Li, Y. Wang, D. Zhou et al., “HIRFL cooling water-monitoring system design and construct”, Radiat. Detect. Tech. Meth. (2018) 2: 35. <https://doi.org/10.1007/s41605-018-0066-y>

- [4] L. T. Sun et al., “Technical approaches towards intense high charge state ion beam production with superconducting EC-RIS”, in Proc. of the 17th Int. Conf. on Ion Sources, AIP Conf. Proc., 2011(1):040022, DOI:10.1063/1.5053296
- [5] H. W. Zhao et al., “Intense highly charged ion beam production and operation with a superconducting electron cyclotron resonance ion source”, Phys. Rev. Accel. Beams, DOI: 10.1103/PhysRevAccelBeams.20.094801
- [6] Shi An et al., “Embedded EPICS Control System of High Voltage Power Supply for Extraction Deflector on HIRFL-CSR”, IOP Conf. Series Mater. Sci. Engi. 381(1):012148, DOI:10.1088/1757-899X/381/1/012148
- [7] J. Su et al., “Control system design for new electronic cooler of HIRFL-CSRm”, Radiat. Detect. Tech. Meth., 2018, 2 (2) :31, DOI: 10.1007/s41605-018-0061-3
- [8] H. Zhao et al., “Electron Cooling of Bunched Ion Beam in a Storage Ring”, Phys. Rev. Accel. Beams, 21, 023501, DOI:10.1103/PhysRevAccelBeams.21.023501
- [9] H. Zhao et al., “Simulation of Ion Beam Cooling with a Pulsed Electron Beam”, Nucl. Instr. Meth. Phys. Res., Sect. A, DOI:10.1016/j.nima.2018.03.048
- [10] B. H. Sun et al., “Towards the full realization of the RIBLL2 beam line at the HIRFL-CSR complex”, Science Bulletin 63(2), DOI:10.1016/j.scib.2017.12.005
- [11] R. J. Chen et al., “A method to measure the transition energy γ_t of the isochronously tuned storage ring”, Nucl. Instr. Meth. A, DOI:10.1016/j.nima.2018.04.056
- [12] W. W. Ge et al., “Experimental investigation of the transition energy γ_t in the isochronous mode of the HIRFL-CSR”, Nucl. Instr. Meth. A, DOI: 10.1016/j.nima.2018.07.059
- [13] G. Y. Zhu et al., “Stochastic cooling experiments for CSRe at IMP”, Nucl. Instr. Meth. Phys. Res., Sect. A, DOI:10.1016/j.nima.2018.09.023
- [14] X. Yin et al., “The R&D status of SSC-Linac”, in Proc. IPAC2014, Dresden, Germany, pp.3277-3279, ISBN 978-3-95450-132-8
- [15] H. Du et al., “Beam dynamics, RF measurement, and commissioning of a CW heavy ion IH-DTL”, Nucl. Sci. Tech. 29(3):42, DOI: 10.1007/s41365-018-0373-5
- [16] X. H. Zhang et al., “Analyzing and matching study of mixed high intensity highly charged ion beams”, in Proc. HB2016, Malmö, Sweden, July 2016, pp.422-426, ISBN 978-3-95450-178-6
- [17] J.C. Yang et al., “High intensity heavy ion accelerator facility (HIAF) in China”, Nucl. Instr. Meth. Phys. Res. Sect. B, 317:263-265, DOI:10.1016/j.nimb.2013.08.046

STATUS OF JINR FLNR CYCLOTRONS

I.V. Kalagin*, G.G. Gulbekian, S.N. Dmitriev, Yu.Ts. Oganessian, B.N. Gikal, S.L. Bogomolov, I.A. Ivanenko, N.Yu. Kazarinov, V.A. Semin, G.N. Ivanov, N.F. Osipov, Joint Institute for Nuclear Research, FLNR, Dubna, Moscow region, Russia

Abstract

Status of JINR FLNR cyclotrons and plans of their modernization together with plans on creation of new facilities will be reported. At present, three cyclotrons: U400, U400M and IC100 and MT-25 microtron are under operation at the JINR FLNR. U400 and U400M are the basic FLNR facilities that both are under operation is about 12000 hours per year. The U400 (pole diameter of $D=4$ m) was designed to accelerate ions from B to Bi up to 19 MeV/u. U400 reconstruction is planned. The U400M cyclotron ($D=4$ m) is used to accelerate ions from Li to Xe up to 60 MeV/u. U400M modernization is planned. The IC100 accelerator ($D=1$ m) is used for applied researches with Ar, Kr and Xe ions at energy of 1.2 MeV/u. Creation of the dedicated DC-130 cyclotron ($D=2$ m) with ion energies of 4.5 and 2 MeV/u is planned on the base of U200 cyclotron. The Super Heavy Element Factory (SHE factory) is the new FLNR JINR project. The DC-280 cyclotron ($D=4$ m) is the basic facility of the SHE factory, which will accelerate ions with energies 4 - 8 MeV/u cyclotron at intensities up to 10 pmkA for ion masses over $A=50$. The main systems of the DC-280 were assembled and tested, the cyclotron is preparing for commissioning.

INTRODUCTION

The scientific program of the Flerov Laboratory of Nuclear Reactions of the Joint Institute for Nuclear Research (FLNR JINR) consists of experiments on synthesis of heavy and exotic nuclei using ion beams of stable and

radioactive isotopes and studies of nuclear reactions, acceleration technology and applied research.

Presently, the FLNR JINR has four cyclotrons of heavy ions: U400, U400M, IC100 (IC-100), that provide performance of the basic and applied researches (Fig. 1). Total annual operating time of the U400 and U400M cyclotrons is more than 10000 for many years (Fig. 2).

The old U200 cyclotron will be reconstructed to the DC130 cyclotron for applied research.

At present time, the project of Super Heavy Element Factory is being performed at the FLNR JINR [1]. The project implies design and creation of the new experimental building with new DC280 cyclotron which has to provide intensities of ion beams with middle atomic masses ($A\sim 50$) up to 10 μ A.

U400 CYCLOTRON

The isochronous U400 cyclotron has been in operation since 1978. [2] The cyclotron produces ion beams of atomic masses $4\div 209$ with energies of $3\div 29$ MeV/nucleon. Before 2017 about 66% of the total time has been used for acceleration of $^{48}\text{Ca}^{5+}$ ions with intensities up to 1.2 μ A for synthesis of super heavy elements. New prospects for the synthesis of super heavy elements may appear to be connected with the usage of the intense beam of neutron-rich ^{50}Ti . The beam of $^{50}\text{Ti}^{5+}$ ions has been accelerated into the U400 cyclotron with extracted beam intensity is about 0.5 μ A [3]. In 2017, about 40% of the total time was used for $^{50}\text{Ti}^{5+}$ acceleration.



Figure 1: The layout of the Flerov Laboratory buildings, where: U400, U400M, IC100, DC280 are heavy ion cyclotrons, MT25 is microtron, SHE Factory is Super Heavy Element Factory, NC is Nanotechnology Centre.

* kalagin@jinr.ru

Content from this work may be used under the terms of the CC BY 3.0 licence (© 2018). Any distribution of this work must maintain attribution to the author(s), title of the work, publisher, and DOI.

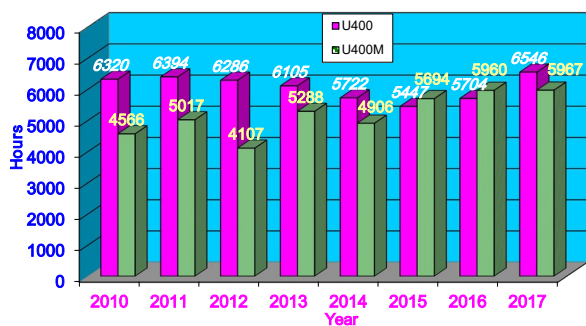


Figure 2: U400 and U400M operation in 2010-2017.

The U-400 modernization is planned to begin in 2021. The aims of the modernization are increasing the total acceleration efficiency and possibility to vary ion energy fluently at factor 5 for every mass to charge ratio (A/Z). The width of ion energy region will be $0.8 \div 27$ MeV/nucleon. The project of U400 modernization intends decreasing the magnetic field level at the cyclotron center from $1.93 \div 2.1$ T to $0.8 \div 1.8$ T, see Table 1 (U400R).



Figure 3: The sketch of the new U400 experimental hall.

The axial injection and ion extraction systems will be changed. For the ion extraction both the stripping foil and the deflector methods are considered. Moreover, the project intends changing the U400 vacuum, RF and power supply systems. The expected ion beam intensities will be at least 2.5 times more than U400 ones [1]. The U400 experimental hall will be essentially modernized in the period from 2020 to 2023. The total experimental building will be extended to about 2000 m². New halls will be attached to the old building from sides (Fig. 3). The new experimental area will consist of six separated halls located on two floors. Every hall will be radiation shielded.

U400M CYCLOTRON

The isochronous U400M cyclotron has been in operation since 1991. The cyclotron was intended for acceleration ion beams Li to Bi with $A/Z=3 \div 3.6$ (A - atomic weight of the accelerated ion; Z - ion charge when accelerated) at energies of $34 \div 60$ MeV/nucleon and ion beams with $A/Z=8 \div 10$ at energies of $4.5 \div 9$ MeV/nucleon.

The beam extraction method is performed by ion stripping method. At present, the U400M has two opposite directions of ion extraction with corresponding ion beam

transport lines. The cyclotron ion beams intended to carry out physical experiments on study properties and structure of light exotic nuclei, synthesis the new super heavy elements and applied researches. Two types of spiral inflectors are used in the U400M axial injection system for low and high energy regimes. To produce required ions the 14 GHz ECR ion source DECRIS-2 and the superconducting 18 GHz ECR ion source DECRIS-SC2 are being used [4].

Table 1: Comparative Parameters of U400 and U400R

Parameter	U400	U400R
	Value/Name	
Magnet weight	2100 t.	2100 t.
Magnet power	850 kW	200 kW
RF system power	100 kW	100 kW
Magnetic field level	$1.93 \div 2.1$ T	$0.8 \div 1.8$ T
The A/Z range	$5 \div 12$	$4 \div 12$
The frequency range	$5.42 \div 12.2$ MHz	$6.5 \div 12.5$ MHz
Harmonic modes	2	$2 \div 6$
The max extraction radius	1.72 m	1.8 m
Vacuum level	$(1 \div 5) \cdot 10^{-7}$ Torr	$(1 \div 2) \cdot 10^{-7}$ Torr
Ion extraction method	Stripping foil	Stripping foil Deflector
Number of ion extraction directions	2	2

The beam extraction method is performed by ion stripping method. At present, the U400M has two opposite directions of ion extraction with corresponding ion beam transport lines. The cyclotron ion beams intended to carry out physical experiments on study properties and structure of light exotic nuclei, synthesis the new super heavy elements and applied researches. Two types of spiral inflectors are used in the U400M axial injection system for low and high energy regimes. To produce required ions the 14 GHz ECR ion source DECRIS-2 and the superconducting 18 GHz ECR ion source DECRIS-SC2 are being used [4].

We plan to begin modernization of the cyclotron in 2019. The modernization will include replacement of the main coils of the cyclotron magnet, correction of the first harmonic of magnetic field at magnetic measurements, replacement of the vacuum pumping system with diffusion pumps to the system with cryopumps, modernization of RF- resonators and changing the analog RF control system to digital one. In the result, we expect to increase



Figure 4: The new DC-280 cyclotron, where: 1- Main magnet, 2- HV injection system, 3- RF resonator, 4- Flat-top resonator, 5- Vacuum pumps.

intensities and maximal energies of ion beams. We also consider the possibility to increase energies of light ions to 60+80 MeV/nucleon by using an electrostatic deflector for ion extraction from ultimate cyclotron radiuses.

U200 - DC130 CYCLOTRON

In 1968 the U-200 was put into operation in the FLNR. In 2013 it was decommissioned, because of being outdated physically and technologically. In 2019 we plan to begin creation of the new DC130 cyclotron which will be based of the U200 yoke. The cyclotron will be intended to provide ions from O to Bi with energies 2 and 4.5 MeV/nucleon for SEE testing of electronic components and 2 MeV/ nucleon for production of track membranes and research in the field of solid state physics.

IC100 CYCLOTRON

The isochronous IC100 cyclotron was put into operation the in 1985 with PIG internal ion source. Due to the upgrade in 2003 IC100 was equipped with external axial beam injection system and the superconducting ECR ion source (DECRI-SC) which allowed to produce intensive beams of highly charged ions of Xenon, Iodine, Krypton, Argon and other heavy elements of the Periodic Table with $A/Z=5,545,95$ at energies of $0,9\div 1,1$ MeV/nucleon.

The focusing system of injection line consists of a solenoidal lens and a quadrupole lens situated between the ECR and the 90° magnet, also three solenoids placed in the vertical part of the injection channel. Spiral inflector is installed into the center of the accelerator. The accelerated beam extraction system consist of electrostatic deflector and two focusing magnetic channels. In routine operation IC100 provides intensities of the $^{86}\text{Kr}^{+15}$ and $^{132}\text{Xe}^{+23}$ ion beams up to $3 \mu\text{A}$.

Special-purpose beam transportation line with polymer film irradiation unit and beam scanning system has been created as well as a box for heavy ion beam research.

DC280 CYCLOTRON

The Super Heavy Element Factory (SHE factory, Fig.3) is the new FLNR JINR project. The main task of the Factory is the synthesis of new chemical elements with atomic numbers 119 and higher, as well as a detailed study of the nuclear and chemical properties of previously discovered superheavy elements. The Factory will be equipped with target materials, new separators and detectors for the study of the nuclear, atomic and chemical properties of the new elements. The new DC280 (Fig. 4) will be the basic facility of the SHE factory.

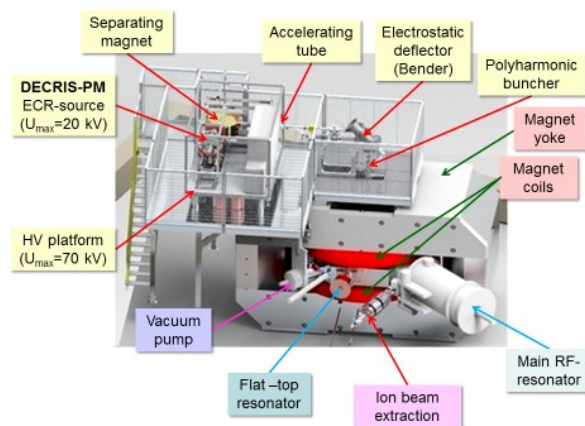


Figure 5: Configuration of the DC280 cyclotron.

The DC280 cyclotron will significantly increase the potential of the existing accelerator complex of the FLNR.

Content from this work may be used under the terms of the CC BY 3.0 licence (© 2018). Any distribution of this work must maintain attribution to the author(s), title of the work, publisher, and DOI.

The accelerator designed at the Flerov Laboratory of Nuclear Reaction of the Joint Institute for Nuclear Research in Dubna (FLNR, JINR, Dubna) is intended for carrying out fundamental and applied investigations with ions from He to U (masses from $A = 2$ up to 238).

Table 2: Design Parameters of the DC-280 Cyclotron

Parameter	Value/Name
Ion source	DECRIS-4
Injecting beam potential	Up to 80 kV
A/Z range	4÷7.5
Energy	4÷8 MeV/n
Magnetic field level	0.6÷1.3 T
K factor	280
Gap between plugs	400 mm
Valley/hill gap	500/208 mm/mm
Magnet weight	1000 t
Magnet power	300 kW
Dee voltage	2x130 kV
RF power consumption	2x30 kW
Flat-top dee voltage	2x14 kV

The parameters of the DC-280 cyclotron are shown in Table 2. The energy of the ions extracted from the cyclotron may vary from 4 up to 8 MeV/ nucleon. The expected intensity of extracted beam at DC280 is 10 pμA for ions with masses up to 50 [1]. The cyclotron was equipped with high voltage injection system (80 kV) with new permanent magnet ECR ion source, the RF- system with 2 main resonators and 2 flat- top ones, the electrostatic deflector for ion beams extraction (Fig. 5) and the beam transport system with 5 channels (Figs. 6 and 7) [5]. At present, launching and tuning works of the main systems of the DC-280 cyclotron are carried out as they are completed. In according to FLNR plans the cyclotron commissioning is planned in the end of 2018.

CONCLUSION

The Flerov Laboratory plans implies essential development of the cyclotron complex to 2023.

ACKNOWLEDGMENT

The authors would like to thank the excellent technical support from the FLNR JINR cyclotrons staff.

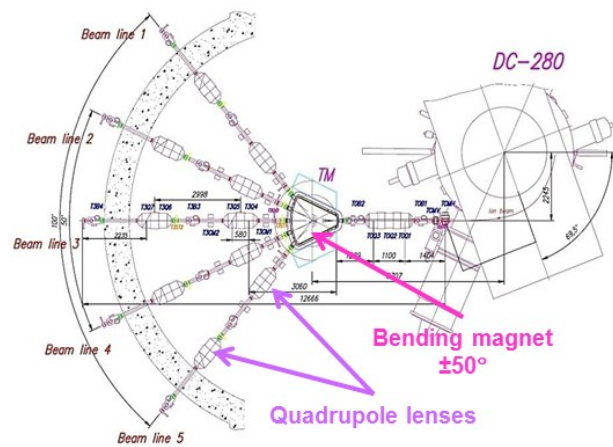


Figure 6: Scheme of beam transport.



Figure 7: Beam transport channels, where: 1- $\pm 50^\circ$ bending magnet, 2- quadrupole lenses.

REFERENCES

- [1] G. Gulbekyan, B. Gikal, S. N. Dmitriev, S. L. Bogomolov, O. N. Borisov, I. A. Ivanenko, N. Yu. Kazarinov, V. I. Kazacha, I. V. Kalagin, N.F. Osipov, A. V. Tikhomirov, J. Franko, "Development of FLNR JINR Heavy Ion Accelerator Complex in the Next 7 Years. Project of New DC-280 Cyclotron", Proc. of IPAC-2011, San-Sebastian, Spain, 2011, paper WEPS082, p.p. 2700-2702.
- [2] G. Gulbekian, *et al.*, "Status of the FLNR JINR Heavy Ion Cyclotrons" in Proc. of 14 Int. Conf. On Cyclotrons and Their Applications, Cape Town, South Africa, 1995, paper B-15, p.p. 95-98.
- [3] S. Bogomolov, A. Bondarchenko, A. Efremov, K. Kuzmenkov, A. Lebedev, K. Lebedev, V. Lebedev, V. Loginov, N. Yazvitsky, Z. Asfari, B.JP. Gall, "Production of ion beams from ECR ion sources by MIVOC method", Proc. of RUPAC-2014, Obninsk, Russia, 2014, paper THPSC47, p.p. 432-434.
- [4] S. Bogomolov *et al.*, "Resent Development in ECR Ion Sources at FLNR JINR" Proc. of RUPAC-2012, Saint-Petersburg, Russia, 2012, paper FRYOR01, pp. 203-207.

- [5] G.G. Gulbekian, S.N. Dmitriev, Yu.Ts. Oganessian, B.N. Gikal, I.V. Kalagin, S.L. Bogomolov, I.A.Ivanenko, N.Yu.Kazarinov, G.N. Ivanov, N.F.Osipov, "Status of the DC-280 cyclotron project", in Proc. of Int. Conf. On Cyclotrons and Their Applications, Zurich, Switzerland, 2016, paper THP25, p.p. 363-365.

HIGH VOLTAGE PERFORMANCE DEGRADATION OF THE 14UD TANDEM ACCELERATOR*

P. Linardakis[†], N. R. Lobanov, T. B. Tunningley, D. Tsifakis, S. T. Battisson, B. Graham, J. A. Bockwinkel, J. Heighway, Heavy Ion Accelerator Facility, Australian National University, Canberra, ACT, 2601, Australia

Abstract

The 14UD at the Australian National University's Heavy Ion Accelerator Facility (HIAF) operated at a maximum voltage of 15.5 MV after the installation of tubes with a compressed geometry in the 1990s. In recent years, the performance of the accelerator has shown a gradual decline to a maximum operation voltage of ~14.5 MV. There are some fundamental factors that limit the high voltage performance, such as SF₆ gas pressure, field enhancement due to triple junctions and total voltage effect. In addition, there are non-fundamental factors causing high voltage degradation. These are: operation with faulty ceramic gaps; operation at inappropriate voltage and SF₆ pressure combinations; SF₆ leaks into the vacuum space; use of SF₆ and O₂ as a stripper gases; poor electron suppression in the high energy stripper and frequent use of highly reactive ions such as sulphur and fluorine. In this paper we will discuss factors that limit the high voltage performance. The main outcomes of a preliminary investigation of titanium (Ti) electrodes removed from the accelerator after a few decades of operation will be reported. The investigation confirmed contamination of Ti electrodes with unstable films containing traces of oxides, sulphur and fluorine. The rehabilitation strategies for the accelerator will be discussed.

INTRODUCTION

The Heavy Ion Accelerator Facility (HIAF) at the Australian National University (ANU) operates a National Electrostatics Corporation (NEC) 14UD pelletron tandem electrostatic particle accelerator [1]. This accelerator has been in operation for over forty years after the first successful experiment in 1974. The original configuration used corona voltage distribution system, in which a maximum voltage of 14.8 MV was achieved for experiments in 1981. However, there was a consistent deterioration from this level that eventually lead to an examination of aging effects [2] and a major accelerator upgrade in around 1990 [3].

This upgrade was comprised of two components. The first was the installation of "compressed geometry" acceleration tubes that removed dead space and allowed the installation of additional acceleration tubes thereby reducing the field across each insulating gap. The second replaced the corona voltage distribution system that was causing corrosion of accelerator components [4] with a resistor grading system. With these upgrades, a peak conditioning

voltage of 16.7 MV was achieved, with experiments performed at 15.5 MV. However, the maximum voltage available for experiments has now degraded to around 14.5 MV.

Since January 2016, the 14UD has had voltage on its terminal for 56% of the total time, with 16% of the time spent on major accelerator maintenance and repairs. Of the time with terminal volts, 27% has been with terminal volts above 13.5 MV.

Even with continued operation near or above the original design voltage of the 14UD, user demand for both operational time and even higher terminal voltages is increasing. Therefore, the degradation mechanisms of the 14UD should be understood in order to extend the useful life of the accelerator.

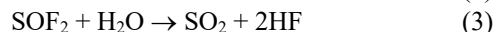
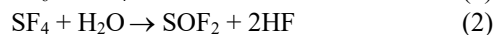
HIGH-VOLTAGE BREAKDOWN

Mechanical issues in an electrostatic accelerator can be readily dealt with, but it is the electrical breakdown mechanisms of the insulating gas and vacuum spaces that determine the limits on high-voltage performance. A thorough review of the mechanisms – and the damage created – is provided in [5] and discussed here with specific reference to the ANU 14UD.

SF₆ Breakdown

The insulating space between the accelerator column and the containing pressure vessel of the 14UD is filled with approximately 22 tonnes of sulphur hexafluoride (SF₆) gas at a pressure of 100 psia. Although considered to be inert, chemical reactions during and after electrical breakdown of SF₆ create long-lived toxic and corrosive by-products [6, 7].

The basic reaction scheme, even in high purity SF₆, is [8]:



where M is any exposed metal such as titanium electrodes or aluminium structural components. The breakdown product yield is influenced by the SF₆ pressure, H₂O content and spark discharge energy [6, 9].

In the era of corona voltage distribution in the 14UD, hydrofluoric acid (HF) products in particular may have caused repeated fracturing of the nylon links in the pelletron chains [4]. A move to resistor voltage distribution configurations ameliorated the problem, but the use of corona terminal voltage stabilisation and arc discharges of the terminal voltage between accelerator electrodes and to the

* Work supported by Australian Federal Government Superscience/EIF funding under the NCRIS mechanism

[†]peter.linardakis@anu.edu.au

tank wall still provide a means of breakdown product formation.

In addition to chemical breakdown products, voltage breakdown in the SF₆ space results in deposits on exposed metal surfaces and the dispersion of particulate material throughout the 14UD, which affect the insulating capabilities of the gas.

The SF₆ gas in the 14UD pressure vessel is recirculated continuously through alumina, with purity, SO₂ and moisture content analysed regularly using a Cambridge Sensotec Rapidox 3100CA system. Since 2014, the SF₆ purity, SO₂ content and H₂O content has averaged 96.6%, 2.2 ppmV and 5.7 ppmV respectively (at around 20°C and 14.3 psi). This moisture level is similar to that measured in gaseous nitrogen sourced from liquid nitrogen boil off.

Even with a low moisture content, significant breakdown products are still produced inside the 14UD, evidenced by the particulates discussed earlier, a pungent smell and the mild acidification of water used to clean the accelerator during periodic maintenance.

Vacuum Arcs

Even at 10⁻⁸–10⁻⁷ Torr, electrical breakdown can occur between the electrodes in the accelerator vacuum space. Breakdown is triggered via the release of electrons through [5, 10]:

- field emission from protrusions on electrode surfaces, either from manufacture or previous discharges;
- field emission from foreign particulates embedded in the electrode surfaces;
- ionisation of gas or other low vapour pressure contaminants desorbed from electrode surfaces that then cause micro-discharges;
- hot field emission from impacting particles that deform the electrodes and;
- ionisation of metal vapour from high-energy particle impact.

Clean electrode surfaces and good vacuum are therefore necessary prerequisites for good high voltage performance, both of which become more challenging as the 14UD ages even further.

Electrode surface conditioning is necessary to achieve good insulating strength. This is a process of safely removing protrusions and moving contaminants through the repeated use of electrical discharges. In operating accelerators, this is most often done in-situ, with or without sections of the accelerator column shorted. The terminal voltage is increased just until qualitative evidence of conditioning, such as x-ray emission from high-energy electron impact [10] and small vacuum excursions, is observed. This evidence will disappear as conditioning progresses. Overzealous attempts at conditioning can lead to dissipation of the majority or all of the stored energy in the accelerator and cause violent breakdown across other gaps in the accelerator column, distributing particles and damaging electrodes leading to deconditioning. Deconditioning can also occur through loss of vacuum from outgassing after discharges or from even the smallest vacuum leak.

Although conditioning can also be performed ex-situ via fast spark, glow or arc discharges or active gas preparation [5], removal of tubes from the accelerator inherently requires venting the acceleration tube and compromising the vacuum.

14UD DEGRADATION FACTORS

The factors of an aging accelerator that affect ultimate performance of the ANU 14UD are many and varied. For example, erosion of spark-gap electrodes in the SF₆ space due to breakdown products increases surface roughness and the likelihood of electron field emission precipitating breakdown. Issues such as this are relatively simple to diagnose, track and rectify during routine maintenance. However, others issues such as small vacuum leaks, the condition of ceramic insulators and the condition of internal acceleration tube electrodes, are not.

SF₆ Injection Into Vacuum Space

The Australian Nuclear Science and Technology Organisation (ANSTO) reported on the injection of SF₆ gas into the vacuum space for use as a gas stripper medium [11]. While there was no report of an effect on accelerator performance, installation of a similar system into the ANU 14UD resulted in a decrease in the ultimate achievable terminal voltage and in rapid deconditioning. The conditioning limit could not be sustained even after short operation at lower terminal voltages.

More recently, the 14UD has suffered from pressure-sensitive vacuum leaks from the SF₆ space into the acceleration tube vacuum. Residual Gas Analysis (RGA) of the vacuum at the both ends of the acceleration tube showed a sudden appearance and sometimes subsequent disappearance of SF₆ without relation to any external event. This occurred on multiple occasions accompanied by up to a one and a half order of magnitude degradation in vacuum. Even with a recovery in vacuum, and no significant levels of SF₆ detected with RGA scans, accelerator performance degraded in a similar manner to that observed when using SF₆ as a stripper gas. This perhaps suggests adsorption of the gas onto the electrode surfaces that is then involved in discharge events.

Ceramic Insulators

The ceramic insulators in the acceleration tubes and column support posts are of course a critical component in the operation of an electrostatic accelerator. The majority of these in the 14UD are original to the machine and some are showing their age. Over time, high-voltage insulators can degrade due to operation in polluted environments [12] and suffer x-ray radiation-induced degradation in resistivity in the presence of an electric field [13].

As with an earlier investigation into ageing ceramics in the 14UD [2], current leakage across insulation gaps in the supporting columns posts is still observed. It is often accompanied by feint cracks in the surface of the ceramic or metallic track marks that bridge the gap. Leakage currents up to tens of microamperes at five kilovolts are measured

Content from this work may be used under the terms of the CC BY 3.0 licence (© 2018). Any distribution of this work must maintain attribution to the author(s), title of the work, publisher, and DOI.

and are sometimes extremely dependent on the surrounding humidity.

Physical damage of the ceramic is also observed without current leakage, with significant amount of debris visible in the surrounding area.

As the posts form a structural component of the accelerator, damaged posts are replaced with urgency and exclusively with new posts. A previous programme to refurbish posts through sandblasting and high pressure rinsing seems to have had no benefit on extending the lifetime of older, used, post assemblies.

It is unclear if the mechanical failure of ceramics is due to electrical stresses from voltage breakdowns or from mechanical stresses from pressure cycling, movement of the terminal spinning during maintenance or from the release of energy during large terminal voltage sparks.

Current leakage is also measured across some ceramic gaps in the acceleration tubes. These are more problematic as the tubes cannot be removed as readily as posts and the only viable solution in the short-term is to electrically short those gaps. There are currently 21 shorted gaps of a total of 980 gaps in the 14UD. While in theory this is only a 2.1% reduction in the achievable terminal voltage, the shorted gaps are mostly grouped in particular regions and have a detrimental effect on the homogeneity of the voltage gradient throughout the acceleration column.

Unlike ceramic gaps on posts, there is sometimes no obvious external physical evidence accompanying a leaky ceramic gap in the acceleration tube, suggesting an issue in the vacuum space.

Electrode Surface Condition

The surface condition of electrodes has a great influence on the voltage at which conditioning will first appear in the vacuum space and therefore the achievable operational voltage. Unfortunately, the condition of electrodes in the vacuum space cannot be monitored in-situ and controlled testing at full operational voltages during maintenance periods is not possible, since the high breakdown voltage SF₆ insulating gas is replaced with atmospheric air to allow entry into the pressure vessel.

ELECTRODE SURFACE CONDITION

Five acceleration tubes were replaced with viable used spares during a maintenance period in 2016. The replacements were to troubleshoot and repair issues created by a poor high-energy stripper design that allows burst carbon foils to escape the region and electron emission to be unsuppressed (which is another limiting factor on voltage performance). Three eleven-gap tubes above the high-energy stripper were removed from unit 19 and two eleven-gap tubes were removed from below the stripper in unit 20. The titanium insert electrodes within the tubes were removed and examined using SEM EDX analysis.

Figure 1 and Fig. 2 show the top of the first titanium electrode in unit 19, acceleration tube 2 (exposed to the ion beam) and the bottom of the last electrode in the same tube (chiefly exposed to electron flux). SEM images of the same electrodes are shown in Fig. 3 through Fig 6. These images

show varied but common features observed, such as porosity, metal vaporisation and material build up. Titanium sheet samples were also analysed as a comparison (Fig. 7) and the surface was shown to be relatively pure, with sparse embedded particles with a high oxygen and carbon content.

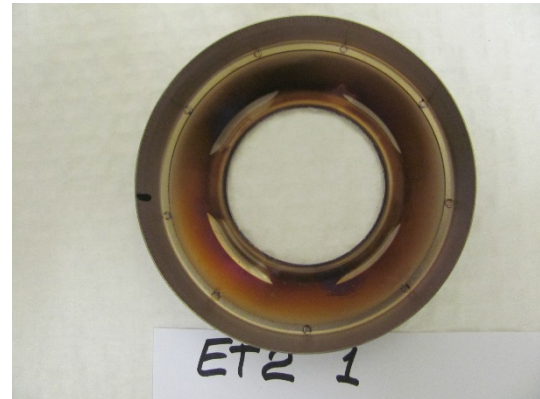


Figure 1: Top face of electrode 1 in unit 19, acceleration tube 2 after over 40 years of operation.



Figure 2: Bottom face of electrode 12 (last) in unit 19, acceleration tube 2 after over 40 years of operation.

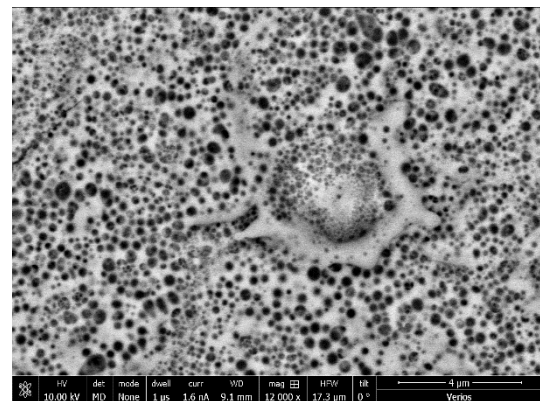


Figure 3: SEM image of the bottom of electrode 1 in unit 19, acceleration tube 2, showing metal vaporisation and surface porosity.

EDX analysis measured the composition at up to twenty radial points on the top and bottom of seven of the fifty-five electrodes removed. Three of these electrodes were the

first electrode in a tube, three the last and one from the middle of a tube. Within measurement taken from a single side of an electrode, the composition was relatively homogeneous, but small differences were observed between the top and bottom sides of the electrodes.

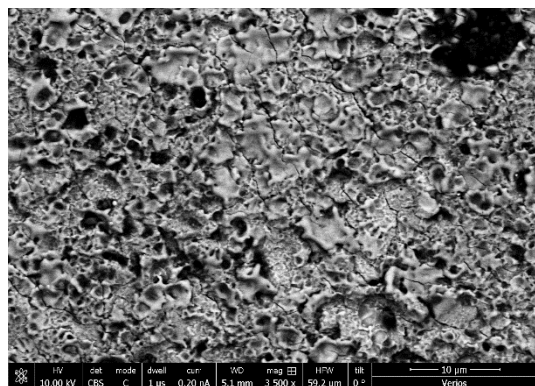


Figure 4: SEM image of the top of electrode 12 (last) in unit 19, acceleration tube 2 showing re-crystallisation of the surface layer of the Ti electrode.

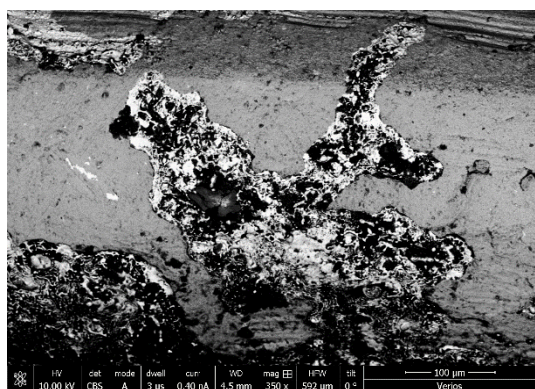


Figure 5: SEM image of the bottom of electrode 12 (last) in unit 19, acceleration tube 2, showing metal vaporisation.

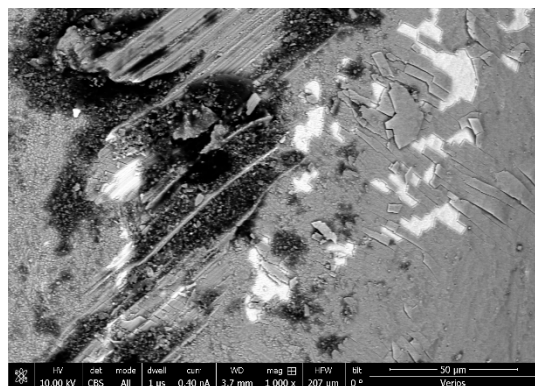


Figure 6: SEM image at the inner edge (toward the beam axis) of the bottom side of an acceleration tube electrode showing severe layer build up and subsequent possible flaking. The black regions are carbon rich layers and the white areas are pure Ti. The grey areas are loose films contaminated with O, F, S.

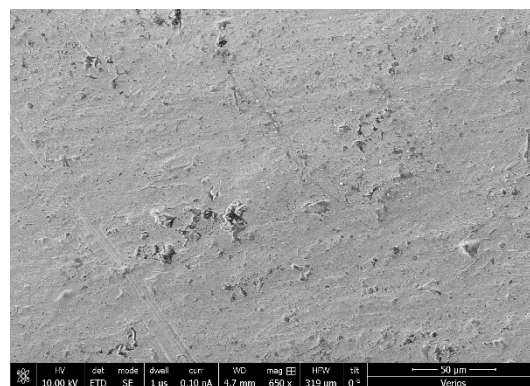


Figure 7: SEM image of titanium sheet as a comparison to used titanium electrodes in acceleration tubes.

Aside from titanium, the results showed the primary composition to be of oxygen, carbon, fluorine and aluminium, with trace amounts of silicon, argon, magnesium, sulphur, sodium calcium and iron. Across the seven electrodes analysed, oxygen percentages were 20–40% and generally higher on the underside of the last electrode in a tube. Carbon percentages were 10–20%. These are both more than double the amounts found on unused titanium. Fluorine, which is not seen on measurements of unused titanium, was found at percentages of 3–7%. Furthermore, very slightly higher levels of fluorine were found toward the axis of the acceleration tubes. Small amounts of aluminium were also detected, at 1–3%.

In combination with the SEM images, the oxygen and carbon content suggests a build-up of oxide and carbon layers, which aside from impacting the voltage gradient, would provide particulate material for increased initiation of vacuum breakdown. The supply of oxygen comes from residual gas in the acceleration tubes and oxygen gas that was historically used as a gas stripper medium. Most of the carbon contamination is likely to be from broken carbon stripper foils.

The presence of fluorine is further evidence of SF₆ leakage into the vacuum space.

Other features were also observed upon disassembly of the acceleration tubes. Pure physical damage to electrodes was observed, with craters in electrode surfaces and sputtering of titanium. This then creates protrusions that then act as a trigger for the release of electrons. An example of cratering is shown in Fig. 8.

REMEDICATION OPTIONS AND CONCLUSION

From the observed conditions of the accelerator tube insert electrodes, their remediation through cleaning or replacement should be a priority. However, even new electrodes may need processing. New tubes and electrodes installed during the compressed geometry upgrade of the 14UD were processed via magnetron sputtering using argon, followed by baking in a vacuum oven at 600 °C [3, 5].

NEC offer refurbishment of accelerator tubes via high pressure rinse of the tube and replacement or electro-polishing of the titanium insert electrodes. However, this does not remediate issues with possible deterioration of the bulk

dielectric properties of the ceramic insulation, nor any damage to the aluminium bonding layer between the titanium and ceramic.

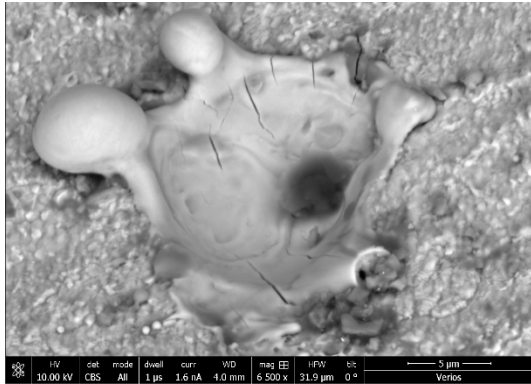


Figure 8: SEM image at the inner edge (toward the beam axis) of an acceleration tube electrode showing severe metal vaporisation.

The most obvious and efficient remediation option is the installation of new acceleration tubes. However, consideration of the large capital outlay required, facility downtime and the strategic future of the facility is necessary. Incremental replacement over time to reduce downtime requires regular venting of the vacuum space, compromising the good, low vacuum required to minimise vacuum breakdown.

REFERENCES

[1] T. R. Ophel, J. S. Harrison, J. O. Newton, R. H. Spear, E. W. Titterton and D. C. Weisser, “The 14UD pelletron accelerator at the Australian National University”, *Nucl. Inst. & Meth.*, vol. 122, p. 227, 1974, doi:10.1016/0029-554X(74)90485-6

[2] T. A. Brinley, G. P. Clarkson, M. D. Malev, T. R. Ophel, R. B. Turkentine and D. C. Weisser, “Ageing effects in the Canberra 14UD pelletron”, *Nucl. Inst. & Meth. in Phys. Reas Sec. A*, vol. 244, p.89, 1986, doi:10.1016/0168-9002(86)90744-8

[3] D. C. Weisser and M. D. Malev, “NEC accelerator tube upgrade: 16.7MV in a 14UD”, *Nucl. Inst. & Meth. in Phys. Reas Sec. A*, vol. 287, p.64, 1990, doi:10.1016/0168-9002(90)91767-6

[4] T. R. Ophel, D. C. Weisser, A. Cooper, L. K. Fifield and G. D. Putt, “Aspects of breakdown product contamination of sulphur hexafluoride in electrostatic accelerators”, *Nucl. Inst. & Meth.*, vol. 217, p. 383, 1983, doi:10.1016/0167-5087(83)90746-9

[5] T. Joy, “Electrostatic accelerator tubes — Recent progress and future directions”, *Nucl. Inst. & Meth. in Phys. Reas Sec. A*, vol. 287, p.48, 1990, doi.org/10.1016/0168-9002(90)91766-5

[6] J. Tang, X. Liu, X. J. Rao, F. P. Zeng, Q. Yao and Y. L. Miao, “Decomposition characteristics of SF₆ under different spark energies”, *IEEE Trans. on Dielectrics and Electrical Insulation*, vol. 23, p.3346, 2016, doi:10.1109/TDEI.2016.006143

[7] W. T. Tsai, “The decomposition products of sulfur hexafluoride (SF₆): Reviews of environmental and health risk analysis”, *Journal of Fluorine Chemistry*, vol. 128, p.1345, 2007, doi:10.1016/j.jfluchem.2007.06.008

[8] I. Sauers, H. W. Ellis, and L. G. Christophorou, “Neutral decomposition products in spark breakdown of SF₆”, *IEEE Transactions on Electrical Insulation*, vol. EI-21, p.111, 1986, doi:10.1109/TEI.1986.348932

[9] A. Derdouri, J. Casanovas, R. Grob and J. Mathieu, “Vacuum breakdown mechanisms, and X-ray pulses in accelerators”, *IEEE Transactions on Electrical Insulation*, vol. 24, p.1147, 1989, doi:10.1109/14.46349

[10] R. Morrow and D. C. Weisser, “Spark decomposition of SF₆/H₂O mixtures”, *Nucl. Inst. & Meth. in Phys. Reas Sec. A*, vol. 382, p.66, 1996, doi:10.1016/S0168-9002(96)00505-0

[11] M. A. C. Hotchkis, D. Child, D. Fink, D. Garton, V. Levchenko and K. Wilcken, “Sulphur hexafluoride as a stripper gas for tandem accelerators”, *Nucl. Inst. & Meth. in Phys. Reas B*, vol. 302, p.14, 2013, doi:10.1016/j.nimb.2013.03.029

[12] N. Bashir and H. Ahmad, “Ageing of Transmission Line Insulators: The Past, Present and Future”, in *Proc. 2nd IEEE International Conference on Power and Energy (PECon 08)*, Johor Baharu, Malaysia, Dec. 2008, pp. 30-34, doi:10.1109/PECON.2008.4762440

[13] S. J. Zinkle and E. R. Hodgson, “Radiation-induced changes in the physical properties of ceramic materials”, *Journal of Nuclear Materials*, vol. 191-194, p.58, 1992, doi:10.1016/S0022-3115(09)80011-1

MEASUREMENT FACILITY AND TEST RESULTS FOR FRIB SUPERCONDUCTING MAGNETS AT IMP

Wenjie Yang¹, Beimin Wu², Dongshen Ni, Wei Wu, Enming Mei¹, Lizhen Ma
 Institute of Modern Physics, Chinese Academy of Sciences, Lanzhou, China
¹University of Chinese Academy of Sciences, Beijing, China
²Lanzhou University, Lanzhou, China

Abstract

The superconducting magnets of the Facility of Rare Isotope Beams (FRIB) are used to focus and steer the heavy ion beams of the driver linac. All the magnets are designed as a solenoid with bucking coils to suppress the stray field. And all of the magnets have superconducting dipole correctors to steer both horizontal and vertical field. Two types of magnets are manufactured in China and most of them have been tested at Institute of Modern Physics (IMP). This paper describes the measurement facilities and magnetic axis measurement method. We also present a summary of the measurement process and test results of the magnetic performance for the magnets.

INTRODUCTION

The Facility for Rare Isotope Beams (FRIB) will be a new national user facility for nuclear science. It is funded by the DOE-SC, Michigan State University (MSU) and the State of Michigan. The driver linac of the FRIB facility can accelerate all stable isotopes to energies beyond 200 MeV/u at beam powers up to 400 kW [1].

FRIB SC magnet packages are used to focus and steer the heavy ion beams of the driver linac. 80 magnets have purchased from XSMT Co. Ltd, China. It Include 9 short and 71 long magnets. IMP undertook the design tasks. And, then 30 of the magnets tested at IMP.

Each FRIB SC magnet package consists of a main focusing solenoid, a pair of stray field bucking coil, a pair of SC dipole correctors both in the vertical and horizontal directions, a helium vessel, a passive quench protection device and the reference points for showing the magnetic axis of the solenoid coil. The solenoid coil length is 25cm and 50cm respectively [2]. The simulation model for 25cm solenoid coil is shown in Fig.1.

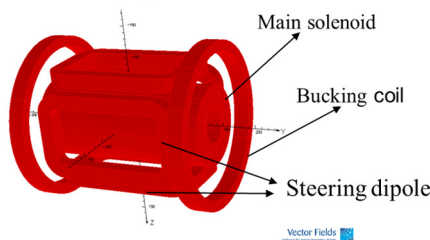


Figure 1: Simulation model of FRIB SC magnet package (25cm).

The FRIB SC magnet is designed as a bath-cooled magnet. The operating temperature of the liquid helium bath is

up to 5.0K. The peak field on the beam axis is approximately 8T. Table 1 summarizes the main parameters of the magnet.

Table 1: Parameters for the FRIB SC Magnet

Parameters	Unit	50cm	25cm
Main solenoid nominal current	A	90	90
Peak solenoid filed at I_{nom}	T	8	8
$\int B_z^2 dz$ at I_{nom}	T ² m	28.2	13.6
$\int B_z^2 dz$ uniformity within 80%×R	%	2	2
$\int B_x dz, \int B_y dz,$ integrated field strength	Tm	0.06	0.03
$\int B_x dz, \int B_y dz,$ Uniformity within 15mm	%	5	5
Maximum current of dipole	A	19	19

Due to the stringent space restriction inside the cryo-modules, the solenoids was designed as compact as possible. The inner diameter of the cold bore is 40mm. The mechanical lengths of the SC magnets are 589.53mm and 349.76mm respectively. The solenoid and dipole correctors are mounted inside the helium vessel which has a diameter of 304.8mm. Figure 2 shows the two types of SC magnets after assembly.

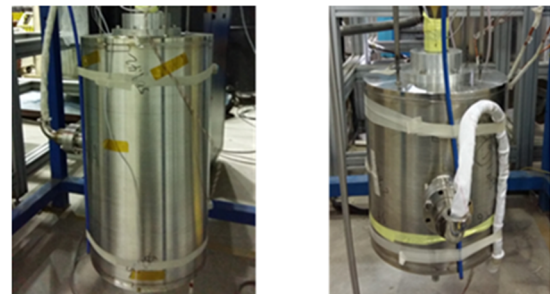


Figure 2: Two types of FRIB SC magnets after assembly and preparing for vertical test in the helium dewar. 50-cm solenoid package(left),25-cm solenoid package(right).

The design of the solenoids minimized the stray field in order to ensure the adjacent SC RF cavities exposed to a field less than specified. The stray field are suppressed by

Content from this work may be used under the terms of the CC BY 3.0 licence (© 2018). Any distribution of this work must maintain attribution to the author(s), title of the work, publisher, and DOI.

the bucking coils. When the solenoid and dipoles are all powered at the nominal currents, the maximum acceptable magnetic stray field is 270 Gauss for all points where $z \geq 390$ mm from the centre of the 50-cm solenoid and 240 Gauss for 25-cm type ($z \geq 260$ mm) [3].

The helium vessel was made of 316L stainless steel to minimize residual field and welding also be done in a way to reduce the residual field. The deviation of the field centre axis from the mechanical centre axis should be within 0.3mm.

MEASUREMENT FACILITY

Cryogenic Test Station

The cryogenic test station for the FRIB SC magnet base on an old Linde TCF10 helium liquefier which has a liquefaction capacity up to 39L/h. Figure 3 shows main parts of the station. There are three vertical test cryostats in this test station. The inner diameters of the cryostats are 300mm, 700mm, 800mm. The helium gas produced in the testing process is recovered by a 23 Nm³/h piston compressor. Then the gas is purified by the purifier in the TCF10 liquefier and liquefied again.

The magnets were pre-cooled by liquid nitrogen. Then the nitrogen was pressured out by helium gas. Before filling in the liquid helium the cryostat should be vacuumed and filled with pure helium. After the test and magnetic measurement, the liquid helium remaining in the test cryostat was pressured back into the helium storage-dewar. This step can save the liquid and reduce the time for warm up.



Figure 3: Cryogenic test station High pressure helium storage tank (1), Air bag (2), Compressor (3), TCF10 (4), Liquid helium dewar (5).

Vertical Measurement Setup

Due to the small bore size (40 mm), it is hard to develop and insert an anti-cryostat into the magnet for keeping the

measurement device at room temperature. So the measurement system are operated at cryogenic temperature. According to the performance requirements of the SC magnet, the key content of cryogenic test is to measure the integral fields of the main solenoid and steering dipoles. The deviation of the solenoid field centre axis from the mechanical centre are also determined by the field measurements.

The vertical measurement set up and measuring coordinate system are shown in Fig.4. The SC magnet was tested in the 700mm cryostat. There is a motion mechanism on the top of the cryostat which contains 4 motion axes. X&Y are manual axes and Z&C are motor drive axes. The C axis is used for rotation measurement and the Z axis is used for vertical direction mapping. The position resolution is 1 μ m and 1 seconds for Z and C axis respectively.

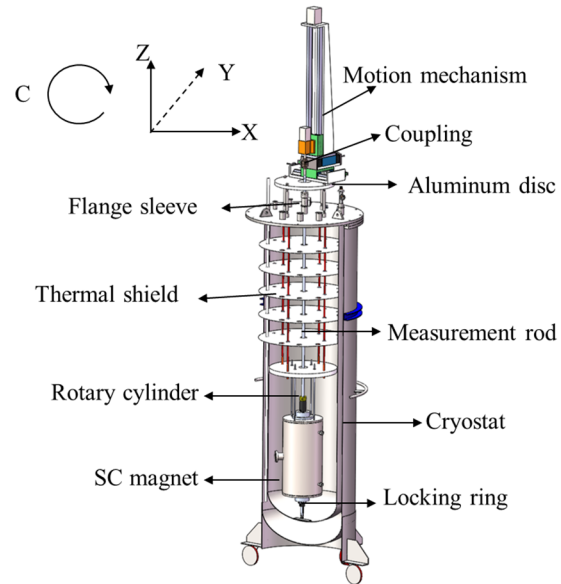


Figure 4: Measurement setup for cryogenic test.

The motion mechanism are mounted on a aluminum disc and connected to the measurement rod by a coupling. By adjusting X and Y axis the centre of the C axis can coincide with the centre of the measurement rod and can be coaxial with the magnet. We reserve a uniform gap between inner surface of the magnet and the rotary cylinder by precision machining. The bottom of SC magnet has a locking ring to keep the magnet stable during the measurement.

Measurement Rod and Rotary Cylinder

We used a long non-magnetic stainless steel tube as the measurement rod (diameter: 20mm length: 2.8m). The upper end is connected to the motor drive by a coupling and the bottom end has two Hall probes to measure the integrated field. The transverse Hall probes (B_r) can mapping the field of the steering dipoles and the axial probes (B_z) can measure the field of the main solenoid along the magnet centre. There is a small gap between the G10 wedge and cylinder's groove, which is shown in Fig.5. Based on this configuration, the measuring rod can be used as rotating shaft of the rotary cylinder simultaneously

Additional two transverse Hall probes (B_1 and B_2) are installed in the symmetrical position of the cylinder for determining magnetic centre axis. These two probes are rotated to scan B_r at both ends of the main solenoid where the radial field component is a maximum. At this position the B_r components are most sensitive for the deviation of magnetic field centre.

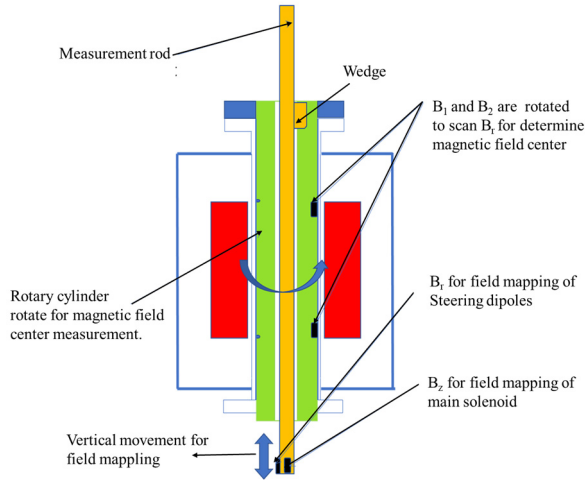


Figure 5: Measurement rod and rotary cylinder. Methods for measuring integral fields and magnetic field centre. Install position of Hall probes

Low temperature axial and transverse Hall probes from Cryomagnetics company are used. They were calibrated at 4.2K up to 9T. The linearity error of the probes are less than 0.2%, the sensitivity varies with the magnetic field are less than 1%. The core of the data acquisition system is a NI industrial PC, which is used to monitor the temperature and voltage, control the power supply and motor drive. A stable, low noise nanovoltmeter model 2182A from Keithley is used to measure the Hall voltage. The multi-channel acquisition can be reached via a multi-channel acquisition switch system, model 2700 also from Keithley.

MEASUREMENT RESULT

Training

We carried out the cold performance tests for all the SC magnet. During the initial cold tests, the number of the quenches to reach the nominal operating field at 4.5 K are recorded.

The solenoids and steering dipoles used a passive quench protection device. At 4.2 K, the solenoids are powered and ramped up to their nominal field with a minimum ramp rate of 0.5% of I_{nom} per second. After solenoid training, each steering dipole should be powered and ramped up to its nominal field separately. At last, all three coils (solenoid, horizontal steering dipole and vertical steering dipole) triple training at their nominal fields simultaneously.

Most of the SC magnet reached their nominal field without quenches. Some of the them needs two or three times training.

Magnetic Centre

The alignment scans are performed at both ends of the solenoid. The increments of measurement is set 45° with a current of I_{nom} (dipoles off) at both ends of the solenoid. The solenoid field B_r data is fitted using sine wave as shown in Fig.6. We compare theoretical results with actual measurements, to determine the displacement and orientation of the axis from the magnetic axis [4].

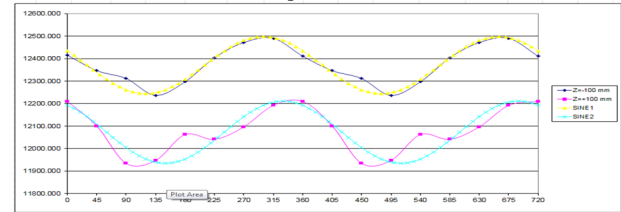


Figure 6: Fitted of the magnetic centre data.

The requirement of deviation of the field centre from the mechanical centre are smaller than 0.3 mm. After the cold test, we mark the field centre on the helium vessel for the solenoid alignment. The flanges are chosen to the location of the fiducials.

Integral Field

The solenoid field B_z shall be measured at I_{nom} every 5 mm along the Z-axis through $-400 \text{ mm} \leq Z \leq +400$ for the 50 cm solenoid and $-200 \text{ mm} \leq Z \leq +200$ for the 25 cm solenoid in order to obtain integrated squared field $\int B_z^2 dz$ [T^2m]. The measurement result of a 50cm magnet are shown in Fig.7. The results of series measurement result are 2% larger than the theoretical calculated value.

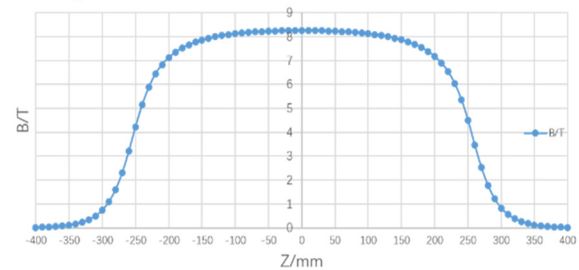


Figure 7: A 50cm magnet measurement result for the integral field of main solenoid.

The integral field of the steering dipole at I_{nom} be measured along the Z axis parallel to the centre of the magnet and at a distance $R=15\text{mm}$ from the beam axis. Rotating the measuring rod can measure $\int B_x dz$ and $\int B_y dz$ respectively as Fig.9. The series measurement result can reach the requirement defined in table1.

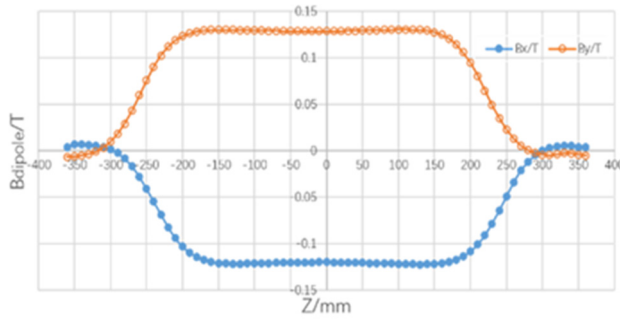


Figure 8: A 50cm magnet measurement result for the integral field of steering dipole.

CONCLUSION

It is the first time for serial cold test of SC magnet at IMP and all of the results are accepted by FRIB even some of the magnets have been already successfully commissioning.

The measurement facility works well during the test. The major flaw is that the stray field map and the uniformity cannot be measured. Because the roundness of the coil bobbins of the solenoid coils is on high machining accuracy that we can make sure the uniformity beyond the requirement.

The vertical test consumes much time and liquid helium, and has a great risk of failure. (Data acquisition failure move not smooth etc.). Maybe a horizontal test programme would solve these problems.

REFERENCES

- [1] J.WeI and H.alo, "FRIB ACCELERATOR: DESIGN AND CONSTRUCTION STATUS", in *Proc. HIAT2015*, Yokohama, Japan, JACoW, <http://www.jacow.org>
- [2] SOW for FRIB Solenoid Packages, FRIB-T30602-PD-000437-R002 Issued 30 September 2014.
- [3] Safwan Shanab and Kenji Saito, "Superconducting Solenoid Package Design, Fabrication, and Testing for FRIB", *IEEE Trans. Appl. Supercond.*, vol. 28, no. 2 March. 2018, no. 4004404.
- [4] Ahovi Kponou and Alexander Pikin, "Analysis of the Magnetic Field Measured by a Rotating Hall Probe in a Solenoid to Locate its Magnetic Axis" *AIP Conference Proceedings* 572, 178 (2001); doi: 10.1063/1.1390113 View online: <http://dx.doi.org/10.1063/1.1390113>.

THE SUPERCONDUCTING CYCLOTRON RF SYSTEM R&D*

Xianwu Wang[†], Xingli Jiang, Yong Qiao, Zhe Xu, Institute of Modern Physic, Lanzhou, China

Abstract

IMP is presently developing a 10MeV Superconducting Cyclotron (IMP-MK90) (see Fig. 1) for the nuclear pore membrane production and research purpose [1-5]. The cyclotron parameter see Table 1. The RF system comprises two separated resonators driven by independent amplifiers to allow for the phase and amplitude modulation technique to be applied for beam intensity modulation. The cyclotron works on 4th harmonic with Dee's voltage 70kV frequency 37MHz. According to the physical requirements of the superconducting cyclotron, the cavity is designed to be vertical 1/2 wavelength line structure. The RF system preliminary design has been completed (Fig. 2).



Figure1: The cyclotron structural model.

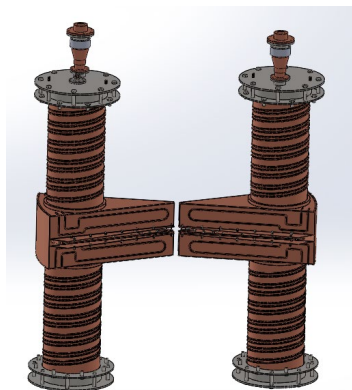


Figure 2: The RF cavity structural model.

THE CYCLOTRON AND RF SYSTEM DESIGN

On the basis of the physical design requirements, the relevant physical parameters shown in Table1.

* Work supported by IMP

[†] email address: wangxw@impcas.ac.cn

Table 1: RF System Specifications

■ Type of cyclotron	
Heavy Ion	$^{40}\text{Ar}^{12+}$, $^{86}\text{Kr}^{26+}$
■ Axial injection with ECR ion source	
Split beam with either Septum Magnet or QWR cavity	
Beam current	>3euA
Beam energy	10MeV/u
■ RF system parameter	
Resonant Frequency	37MHz
Dee Voltage	60-80KV
Dee Angle	33°
Extraction Radius	750mm
Injection Radius	35mm
Phase Stability	$\leq \pm 0.5^\circ$
Amplitude Stability	$\leq 1 \times 10^{-4}$
Frequency Stability	$\leq 1 \times 10^{-6}$
■ Magnet	
Magnet Coil	~300kAT
Maximum magnetic field	2.75T
Magnet Weight	~90 tons
■ Production Lines	
Multi-purpose Line	1 line
Industrial line	3 line with beam split

RF STRUCTURAL SIMULATION RESULTS WITH CST

According to the structure parameter, the three-dimensional model is founded, simulated and analyzed with CST. By changing and optimizing Dee's angel, stem dimension, stem height and position etc. parametrics of structure, The simulation results show that the resonant frequency is 37.05MHz, Q value is 7259 and power loss is 18kW. The voltage along the radial gap of Dee is from 82.25 kV in the center of Dee to 85.56 kV in the radius of Dee Extraction. The voltage distribution is uniformly rising along the radial gap of DEE. As shown in Fig. 3. The results shows that the voltage characteristics along the radius basically depend on the the position and diameter of the inner stem, and the Dee's angle. The electric field and magnetic field distribution map of the cavity are shown in Fig. 4 and 5. Surface current distribution result show in Fig. 6.

THE TUNING DESIGN OF THE RF CAVITY

The fine-tuning loop has been designed to meet the dynamically tuned requirements.the coarse-tuned with capacitor . The fine-tuning parameter shows in Table 2.

Content from this work may be used under the terms of the CC BY 3.0 licence (© 2018). Any distribution of this work must maintain attribution to the author(s), title of the work, publisher, and DOI.

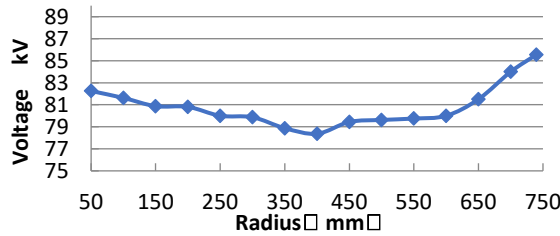


Figure 3: Voltage distribution along radius.

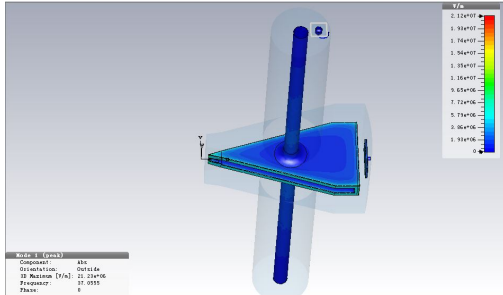


Figure 4: Electric field distribution.

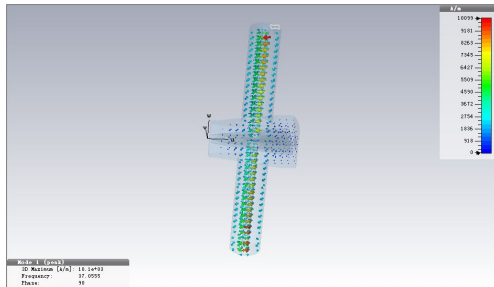


Figure 5: Magnetic field distribution.

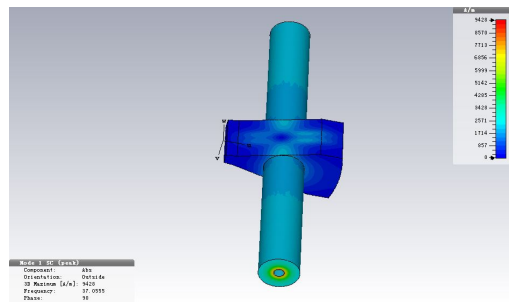


Figure 6: Surface current distribution.

Table 2: The Fine-Tuning Parameter

Parameter	Value
Tuning range (kHz)	120
Tuning resolution(Hz)	100
The rotation angle of the tuning ring (°)	90
Backlash Tolerance (°)	0.1

THE COUPLER DESIGN OF THE RF CAVITY

The coupler has been designed to be inductor coupler. The coupler maximum testing power is 30kW. Maximum power consumption on coupler is 0.5%. Maximum reflection power on coupler is 1%.

THE SAWTOOTH WAVE BUNCHER DESIGN

The design of buncher adopts small signal harmonic synthesis and wide band amplification and matching transmission. The buncher parameter shows in Table 3. The principle is shown in Fig. 7. the RF system block diagram.

Table 3: The Sawtooth Wave Buncher Parameter

Parameter	Value
Frequency (MHz)	37
Effective duty cycle	>60%
Buncher voltage(kV)	1.6
Linearity error	<1%

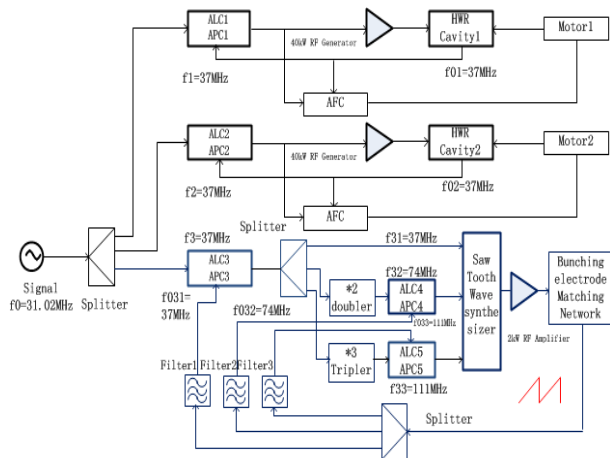


Figure 7: the block diagram of RF system composition.

CONCLUSIONS

The paper introduce the RF design of the 37MHz superconducting cyclotron cavity and RF system, including RF cavity simulation, the geometry structure of DEE is optimized repeatedly for the ideal voltage distribution, the buncher designing scheme and parameter etc.

The next step is to carry out the system optimization design, including the system cooling design coupling, and tuning optimization design, and the radio frequency splitter beam design, and the system engineering transformation work.

REFERENCES

[1] S. Shin, J. Lee, B.-N. Lee, D. Ha, H. Namgoong, Development of the RF cavity for the SKKUCY-9 compact cyclotron, Nuclear Instruments and Methods in Physics Research A, 795, 2015, pp.276-283.

- [2] H.S. Song, H.W. Kim, B.N. Lee, J.H. Oh, J.S. Chai. Design Of Rf Cavity For Compact 9 Mev Cyclotron. *In Proceeding of IPAC 2011*, San Sebastian, Spain, pp.151-153.
- [3] Y. Jongen, M. Abs, W. Kleeven, S. Zarembo, A.A. Glazov, S.V. Gurskiy, O.V. Karamyshev, G.A. Karamysheva, N.A. Morozov. RF Cavity Simulations for Superconducting Cyclotron C400. *Physics of Particles and Nuclei Letters*, Vol.8, No.4, 2011, pp.386-390.
- [4] V. Sabaiduc, G. Gold, B. Versteeg, J. Panama. Resonator system for the best 70 Mev cyclotron. *In proceedings of Cyclotrons 2013*, Vancouver, Canada, 2013, pp.153-155.
- [5] V. Afzalan, H. Afarideh, R. Azizi, M. Ghergherehchi, J.S. Chai. Design and simulation of cavity for 10 MeV compact cyclotron. *In Proceedings of Cyclotrons-2013*, Vancouver, Canada. 2013, pp.200-202.

Content from this work may be used under the terms of the CC BY 3.0 licence (© 2018). Any distribution of this work must maintain attribution to the author(s), title of the work, publisher, and DOI.

DESIGN OF FAST PULSE GENERATOR FOR KICKER POWER SUPPLY IN HIAF

Y. Liu^{†1}, J. Gao¹, D.Q. Gao, J.B. Shang-guan, J. Zhao

Institute of Modern Physics, Chinese Academy of Sciences, 730000 Lanzhou, China

¹also at University of Chinese Academy of Sciences, Beijing 100049, China

Abstract

Kicker power Supply is one of the key components in the injection and extraction system of HIAF (High Intensity Heavy Ion Accelerator Facility, the 12th five-year national big science project). The PFN-Marx generator technology based on solid-state switch IGBT will be applied to HIAF-Kicker power supply. Hundreds of fast pulse signals are required for these IGBTs' control. The PFN-Marx generator has many requirements for their control signals, such as adjustable pulse-widths and time-delay. The maximum value of adjustment accuracy of the pulse-widths and delay among multiple control signals need to be 10ns. In this paper, a fast pulse generator circuit with adjustable pulse-widths and time-delay is designed for HIAF-Kicker power supply. This design is based on an emerging ARM-embedded FPGA. And the test results shown that the design can meet the required performance.

INTRODUCTION

The High Intensity Heavy Ion Accelerator Facility (HIAF) is a new accelerator facility under design at the Institute of Modern Physics (IMP), Chinese Academy of Sciences [1]. The Kicker power supply is a device that provides excitation current for the pulsed magnet in the injection and extraction system of HIAF. HIAF-Kicker power supply will use a solid-state PFN-Marx structure as an energy storage system. Since the limited withstand voltage and current capability of a single solid-state switch IGBT, the quantity of IGBTs in solid-state PFN-Marx generator is very large. The control accuracy of PFN-Marx generator directly affects the beam injection efficiency. Therefore, the synchronous driving of multi-channel IGBT has become a technical difficulty problem that must be solved for HIAF-Kicker power supplies.

To reduce the time-delay caused by the dispersion of circuit parameters on FPN-Marx generator, people used

to adjust switches on and off manually. This method is time consuming and laborious. The switches cannot to be debugged online while the power supply is in operating. To solve these problems, we designed a fast pulse generator based on Cyclone V chip, which integrates FPGA and a dual-core ARM Cortex-A9 MP core processor. In this design, ARM is mainly used to upload and download the control data. The fast pulse generator circuit is designed to generate hundreds of fast pulse control signals. For such signals, the time-delay and pulse-widths are adjustable and the adjustment accuracy is 10 ns. The high-accuracy digital control design provide synchronous drive signals for multi-channel IGBT of FPN-Marx generator, which has a significant advantage over manual adjustment.

THE SOLID-STATE PFN-MARX GENERATOR ON HIAF-KICKER

Compared with FPN (Pulse-Forming Network) and PFL (Pulse-Forming Line), PFN-Marx generator is based on solid-state switch IGBT, which has advantages of smaller size, easy to repair and more flexible to adjust pulse-widths and delay. After the energy storage process has been completed in PFN-Marx circuit, the square wave excitation current can be generated by the solid-state switch IGBT for the magnet load [2].

The work principle of the solid-state PFN-Marx generator is: the charging power supply charges the PFN in parallel through the charging resistor. After the charging process has been completed, the solid-state switches are turned on at the same time. The charging resistor acts as an isolator, and the PFNs in each stage are discharged serially. Each level of PFN modulates the waveform and finally the approximate square wave pulse waveform is obtained on the load. The schematic of the solid-state PFN-Marx generator is shown in Fig. 1.

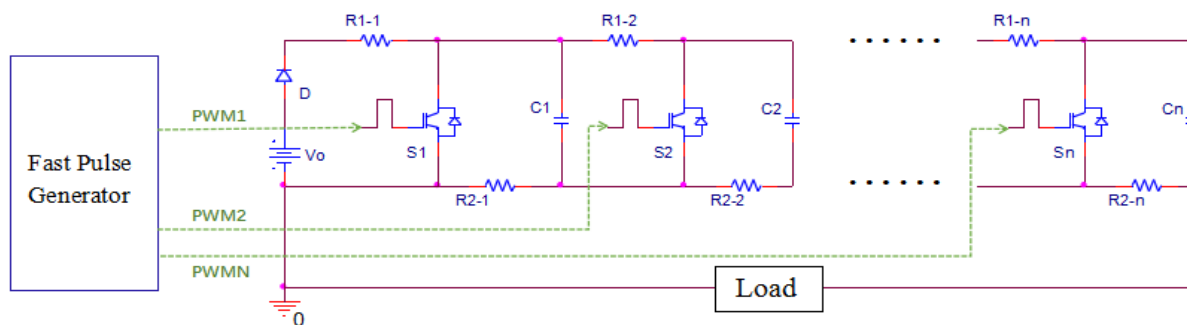


Figure 1: The schematic of the solid-state PFN-Marx generator.

[†] yanliu@impcas.ac.cn

THE CONTROL SYSTEM STRUCTURE

The entire control system of HIAF is an Ethernet-based distributed control system. The information such as voltage parameters and pulse-widths need to be quickly sent to Kicker power supply controllers through the Ethernet [3]. In order to make communication easier between the upper control system and the Kicker power supply controllers, we use the Cyclone V SX FPGA, which integrated with dual-core ARM Cortex-A9 MP Core processor.

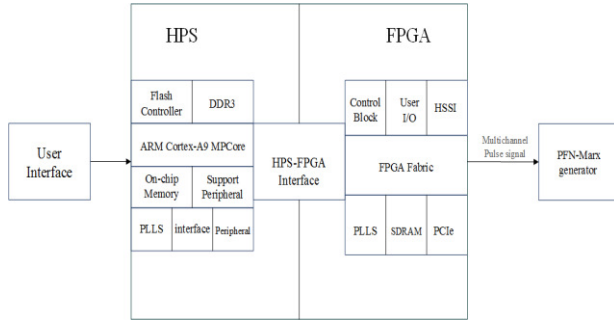


Figure 2: The control system structure.

The control system structure is showed in Fig. 2. In this control structure, the delay and pulse-widths data are sent by the user interface via Ethernet. The ARM stores this information and distributes them to different registers on the FPGA side through the AXI bus bridge. After receiving these data, fast pulse generator circuit on FPGA generate hundreds of fast pulse control signals. Then we convert these output pulse signals into multi-channel optical signals. These optical signals are transmitted through the optical fiber and then converted into current signals by optical transceiver to the PFN-Marx generator.

FPGA-BASED FAST PULSE GENERATOR

As shown in Fig. 3, the programming contents on FPGA include: the fast pulse generation module and Avalon bus interface module. The fast pulse generation module contains multiple 16-bit counters. These counters read the delay and pulse-widths data for counting. These data are written in some 32-bit registers on FPGA by ARM through the AXI bus bridge. Among this data the upper 16 bits data represent the delay information and the lower 16 bits data represent the pulse-widths information. After counting process is completed the fast pulse generation circuit outputs the fast pulse.

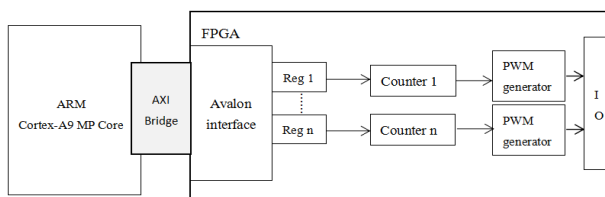


Figure 3: The fast pulse generator hardware structure.

For general external address space access, the CPU requires a user-defined interface control module. The

Avalon bus interface module is designed according to the CPU read/write timing. Then the two modules are attached to the AXI bus bridge via the Qsys component. We use the PLL cores in FPGA to multiply the clocks to 100MHz, so that the adjustment accuracy of the pulse-widths and delay reaches 10ns.

THE FAST PULSE OUTPUT SIGNALS

The design of fast pulse generator was used successfully to driving multi-channel IGBTs of PFN-Marx generator synchronously for HIAF. In this paper, we take three fast output pulses as an example. As shown in Fig. 4, the delay among each channel signals is adjustable with a time precision of 10 ns. The pulse-widths can also be adjusted according to the Kicker power supply's requirements with the same precision of 10 ns. All pulse-widths and delay information are sent through the Ethernet. The synchronization experiment show this design can meet the synchronous drive requirements of solid-state PFN-Marx generator for HIAF.

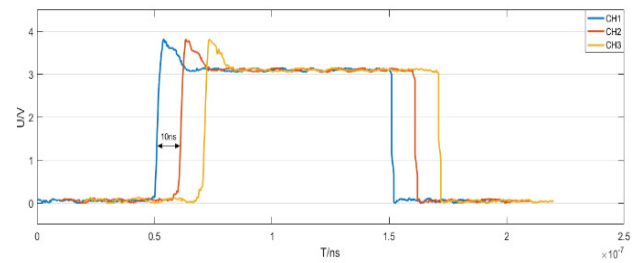


Figure 4: The multi-channel fast pulse output signals.

CONCLUSIONS

In this paper, a fast pulse generation circuit based on an ARM-embedded FPGA structure is designed to realize the synchronous driving for multi-channel IGBT of PFN-Marx generator for HIAF-Kicker. We use digital technology to accurately adjust the delay and pulse-widths of the drive pulses, effectively avoiding the shortage of manual adjustment. Moreover, the digital driving technology can improve the stability and synchronization of the injection and extraction system in HIAF. The following work will focus on integrating the fiber interfaces for hundreds of fast pulses into the controller of Kicker power supply systems and giving an optimized fan out scheme to reduce budget.

REFERENCES

- [1] J.C. Yang, J.W. Xia, G.Q. Xiao, et al., "High Intensity heavy ion Accelerator Facility (HIAF) in China", Nuclear Instruments & Methods in Physics Research, 2013, 317(5), pp. 263-265.
- [2] H. Li, H.J. Ryoo, J.S. Kim, et al., "Development of Rectangle-Pulse Marx Generator Based on PFN", IEEE Trans Plasma Sci, 2009, 37(1), pp. 190-194.
- [3] Yu. Guo, Yan Wang, D. Zhou, W.F. Liu, et al. "Design of Control System for Kicker Magnet Power Supply", Atomic Energy Science and Technology, 2013, 47(6), pp. 1070-1073.

COMMISSIONING PROGRESS OF LEAF AT IMP

Y. Yang[†], Y. H. Zhai, P. Y. Jiang, L. T. Sun, L. Lu, H. Jia, W. P. Dou, X. Fang, L. Jing, Y. Wei,
 W. Ma, L. P. Sun, W. Lu, Y. H. Guo, X. J. Liu, H. W. Zhao
 IMP/CAS, Lanzhou 730000, China

Abstract

A Low Energy intense-highly-charged ion Accelerator Facility (LEAF), which is mainly consist of an 45 GHz superconducting ECR ion source, LEBT and an 81.25 MHz 4-vane RFQ, was designed to produce and accelerate heavy ions, from helium to uranium with A/Q between 2 and 7, to the energy of 0.5 MeV/u. The typical beam intensity is designed up to 2 emA CW for the uranium beam. The project was launched in 2015 and has been successfully commissioned with He⁺ (A/Q=4), N²⁺ (A/Q=7) beam and accelerated the beams in the CW regime to the designed energy of 0.5 MeV/u. Beam commissioning results of He⁺ beam have been reported previously. This paper presents the details of N²⁺ commissioning and beam studies.

INTRODUCTION

LEAF (Low Energy intense-highly-charged ion Accelerator Facility, see Fig. 1) [1] has been successfully commissioned with A/Q=4 ion He⁺ and A/Q=7 ion N²⁺. Since the designed heaviest ion is Uranium with charge state of 34, N²⁺ could be a substitute of U³⁴⁺ to evaluate the accelerator performance due to the same rigidities. Studies of the facility were carried out by beam commissioning with different intensities. Beam characteristics from ECR were measured and discussed. Beam phase space re-construction was developed to study the evolution process of the beam from source to RFQ, contributing to LEBT tuning and particle cutting with collimators.

SOURCE RESULTS

A 14.5 GHz room-temperature permanent magnetic ECR ion source was fabricated and employed for the commissioning of LEAF. The source performance meets intensity requirements for commissioning. The source demonstrated ~5 emA of He⁺ beam, 1.5 emA of He²⁺ beam, 1.7 emA of N²⁺ beam and 0.16 emA of N⁵⁺ beam. Beam emittances were measured for N²⁺ beam with several intensities. As shown in Fig.2, beam emittance increase with the intensity. The main reason should be attributed to the plasma meniscus change, related with source tuning. Aberrations from the magnets and space charge effects also contribute to the beam emittance degradation [2,3]. Figure 3 demonstrates the measured

phase space distributions of N²⁺ beam with intensities of ~0.14 emA and ~1.52 emA, respectively. It is seen that by increasing the beam intensity the phase spaces are seriously distorted, resulting to emittance growth.

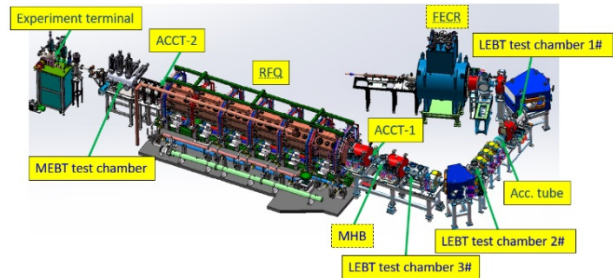


Figure 1: Layout of LEAF.

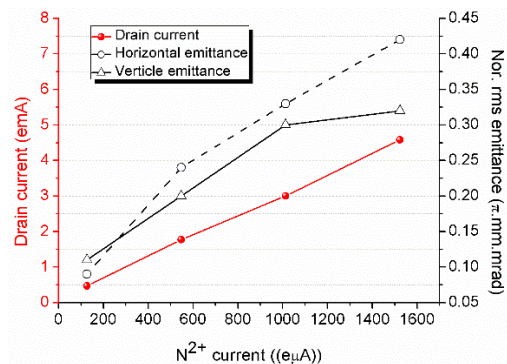


Figure 2: N²⁺ beam emittance versus beam current.

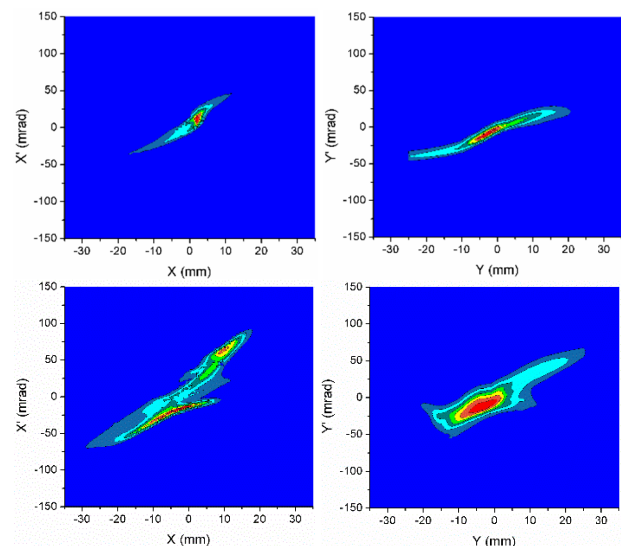


Figure 3: Measured beam phase space distributions for ~0.14 emA (up) and ~1.52 emA (down) N²⁺ beams.

* This work is supported by the National Nature Science Foundation of China (contract No. 11427904 and 11575265).

[†] yangyao@impccas.ac.cn.

BEAM COMMISSIONING

~0.1 emA of N²⁺ Beam Commission and Characteristics

The RFQ commissioning of N²⁺ beam started with ~0.1 emA. The slits in Q/A analyser of ECR were throttled to confine the emittance. Figure 4 shows the measured emittance, indicating 0.07 π .mm.mrad in horizontal and 0.05 π .mm.mrad in vertical. The beam, with energy of ~3.57 keV/u (25 kV extraction voltage of ECR), was pre-accelerated to the designed RFQ input energy of 14 keV/u by the accelerating tube and converted to an approximately axisymmetric beam by four quadrupoles in the LEBT line. Afterwards the beam was focused by two paired solenoids [2] and matched to RFQ. Beam transmission efficiency through LEBT reached 100%.

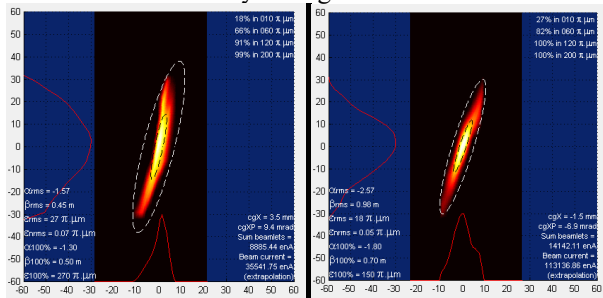


Figure 4: Emittance measurement for ~100 emA N²⁺ beam, throttled slits.

The RFQ was conditioned to 63 kW, corresponding to the vane voltage of 71.3 kV, which was slightly higher than the designed voltage of 70 kV to accelerate A/Q=7 ion beams. The measured transmission efficiency (including non-accelerated particles) was ~98%. The Multi-Harmonic-Buncher (MHB) has not been operational yet, therefore beam injected into the RFQ was a DC beam. The acceleration efficiency was of ~54.6% because the starting synchronous phase of the RFQ was set to -45 degree. The beam energy was measured with TOF monitor (two BPMs with a distance of 1.068 m between each other, see Fig. 5), satisfying the designed energy of 0.5 MeV/u.

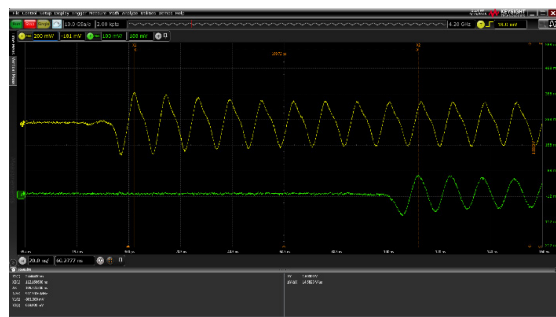


Figure 5: BPM signals (yellow: BMP-1, green: BMP-2).

Transverse emittances after RFQ were measured by using slit+slit+FC and plotted in Fig. 6. The measurements demonstrated rms emittances of 0.119 π .mm.mrad in horizontal and 0.088 π .mm.mrad in vertical. The phase

spaces were slightly distorted, which can be due to the factor that the injection beam had been aberrant. Simulations by TRACK code were also provided in Fig. 6, which indicated horizontal emittance of 0.119 π .mm.mrad and vertical emittance of 0.092 π .mm.mrad. Measurements have a good agreement with simulations. Besides, we observed that no emittance exchange between X&Y directions. That's because after ECR beam emittance measurement (at LEBT test chamber 1#, see Fig. 1) there is no element creating transverse coupling in LEBT and also no coupling in RFQ for such low-current beam.

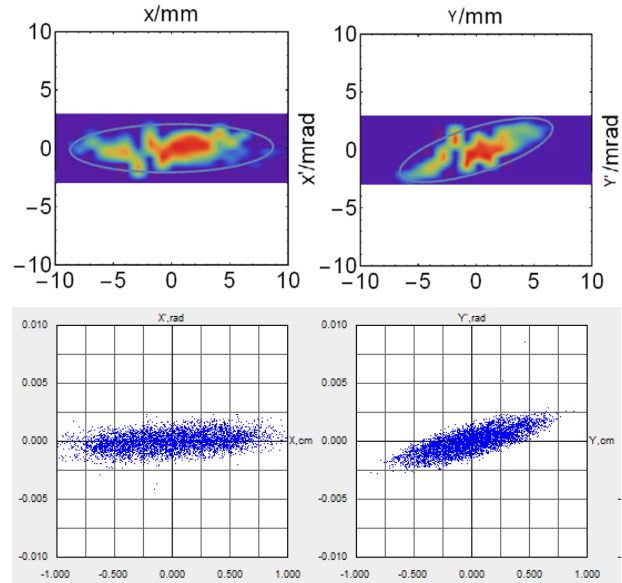


Figure 6: Measured (up) and simulated (down) beam emittance in MEBT test chamber after triplet focusing.

Beam bunch profile was measured by a Fast Faraday Cup (FFC) which has a time resolution of ~80 ps, as shown in Fig. 7. The measured FWHM (Full Width at Half Maximum) of the bunch length was ~1.9 ns, which was slightly larger than the simulated value of 1.5 ns (see Fig. 8).

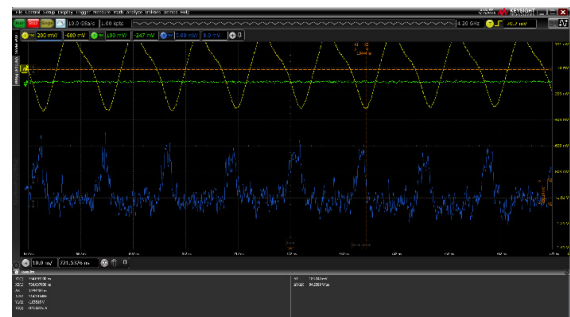


Figure 7: FFC signal.

Content from this work may be used under the terms of the CC BY 3.0 licence (© 2018). Any distribution of this work must maintain attribution to the author(s), title of the work, publisher, and DOI.

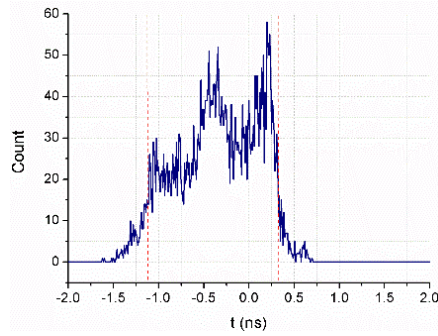


Figure 8: Simulated bunch profile.

Commission for Different-Current Beams

Further beam commissioning was to increase the beam current. The source intensity was enhanced from ~ 118 μA to 785 μA and the corresponding emittances were shown in Fig. 9. By slightly tuning the LEBT magnets to achieve maximum RFQ transmissions, the transmission efficiencies of the beam in LEBT and RFQ were measured and plotted in Fig. 10. One thing should be clear that the beam transmissions from LEBT test chamber 1# to 3# (see Fig. 1) always kept 100%, even for very high intensity as 1.7 emA. Some “tail” particles would be lost at RFQ entrance, leading to LEBT transmission efficiency (from LEBT test chamber 1# to ACCT-1) lower than 100%. The RFQ transmission decreased with the beam current. As seen from the plot, the RFQ transmission decreased to 82% while the beam intensity reached 785 μA . A collimator channel based on two sets of X&Y slits was designed and installed in LEBT test chamber 3# to remove the “tail” particles and improve the RFQ transmission so as to reduce the beam loss in RFQ. With the collimator on, $\sim 11.5\%$ (13.6%) of the particles were cut for initial 520 μA (785 μA) beam, while the RFQ transmission efficiency was improved from $\sim 88.5\%$ (82%) to $\sim 95.7\%$ (91%). Further transmission efficiency improvement requires the operation of MHB.

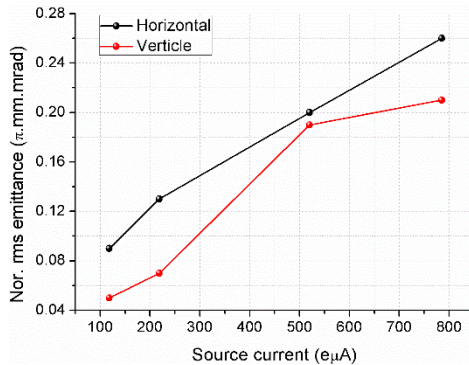


Figure 9: N^{2+} beam emittance versus beam current from source.

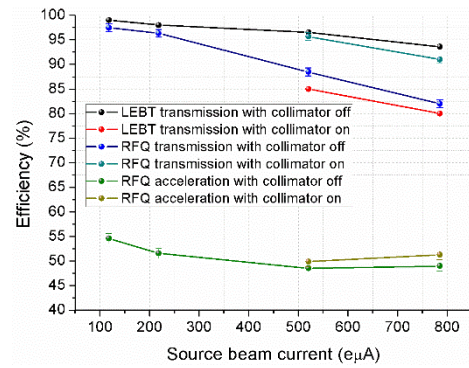


Figure 10: Transmission efficiencies in LEBT (from LEBT test chamber 1# to ACCT-1), RFQ (from ACCT-1 to ACCT-2), and acceleration efficiency of RFQ (from ACCT-1 to MEBT test chamber).

PHASE SPACE RE-CONSTRUCTION

Ion beams from ECR source are typically distorted with aberrations due to the magnetic confinement configuration. Beam simulation by using an imaginary initial distribution, such as water-bag distribution or Gauss distribution, can't well present the evolution process of the beam. Phase space re-construction based on emittance measurement is very necessary for simulations that are close to the realistic beam transport and machine studies, especially for those high-intensity beams. A code was developed to re-construct the projection phase space distributions based on Allison scanner measurements. Beam transverse coupling was not considered because no element after ECR beam emittance measurement in LEBT could produce transverse coupling to the beam under linear conditions. As an example, Fig. 11 illustrates the measured transverse phase space distributions with Allison scanner at LEBT test chamber 1# for N^{2+} beam with current of 785 μA . The re-constructed distributions are given below.

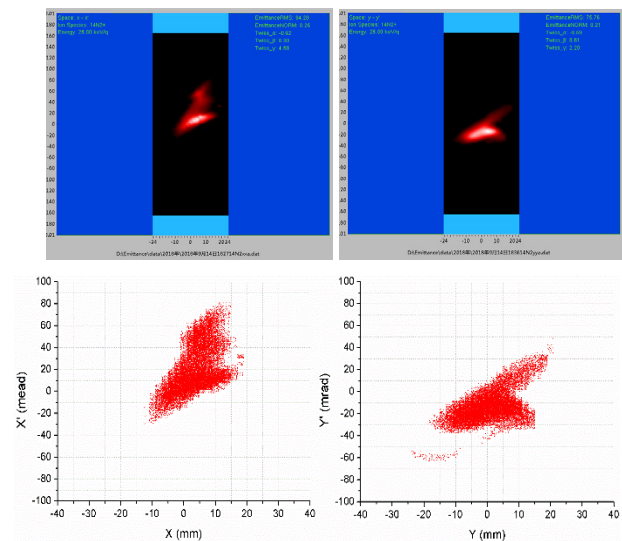


Figure 11: Measured N^{2+} beam phase space distributions with Allison scanner (up) and re-constructed distributions (down).

The artificial particle distributions were input in TRACK to perform the subsequent simulations. After LEPT transmission both measured and simulated phase space distributions at LEPT test chamber 3# were presented in Fig. 12. It is observed that the simulated distributions have very similar shapes with the measured ones, demonstrating that simulations based on phase space reconstruction could well predict the beam phase space profile at any location in LEPT, which is especially important and useful at the positions of beam collimators where particle “tails” are wanted to be cut by the slits. As shown in Fig. 12, it is possible to predict that the “tail” particles could be removed by the slits that located after the emittance measurement point.

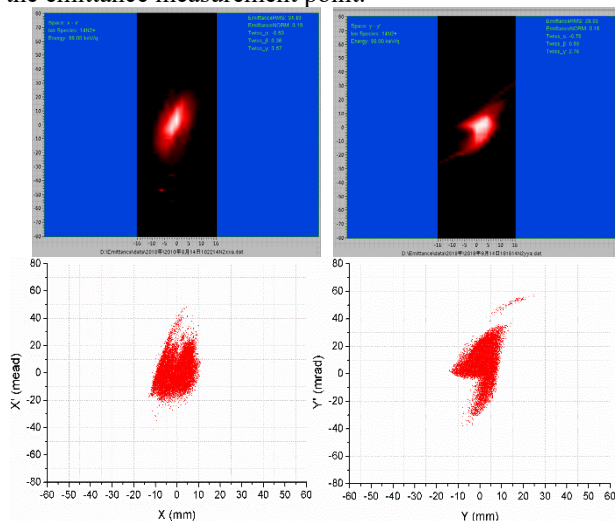


Figure 12: Measured beam phase space distributions with Allison scanner at LEPT Test chamber 3# (up) and simulated distributions based on phase space reconstruction (down).

CONCLUSIONS AND FUTURE PLANS

LEAF has been successfully commissioned with $A/Q=4$ ion He^+ and $A/Q=7$ ion N^{2+} . Key performance parameters demonstrated. MHB is now being installed and tested. Future beam commissioning will be carried out with MHB operational. Beam intensity will be increased step by step, from pulse to CW.

REFERENCES

- [1] Y. Yang, *et. al.*, “Initial Beam commissioning of LEAF at IMP”, in *Proc. the 29th Linear Accelerator Conf. (LINAC’18)*, Beijing, China, Sep. 2018, paper TUPO005.
- [2] Y. Yang, *et. al.*, “HIAF Front End for Transmission and Acceleration of $30 \mu\text{A } ^{238}\text{U}^{35+}$ ” in *Proc. 61st ICFA Advanced Beam Dynamics Workshop on High-Intensity and High-Brightness Hadron Beams (HB’18)*, Daejeon, Korea, Jun. 2018, paper WEA2WB03, (slides only).
- [3] V. Mironov, *et. al.*, “On Optical Properties of Ion Beams From an Electron Cyclotron Resonance Ion Source”, AIP Conference Proceedings 2011, 080008 (2018).

THE DIGITAL CONTROLLER FOR POWER SUPPLIES IN HIAF*

Yulian Tan^{† 1,2}, Yuan Cui¹, Daqing Gao, Yuzhen Huang, Jiqiang Li, Huajian Zhang, Shuai Zhang,
Institute of Modern Physics, Chinese Academy of Sciences, Lanzhou 730000, P. R. China

¹ also at University of Chinese Academy of Sciences, Beijing 100049, P. R. China

² also at Huizhou Ion Science Research Center, Huizhou 516300, P. R. China

Abstract

High Intensity Heavy Ion Accelerator Facility (HIAF) is a project proposed by Institute of Modern Physics, Chinese Academy of Sciences (IMP). This paper designs a digital controller for Bring in HIAF dipole power supplies system, which is several circuit boards consist of high precision ADC, optical fiber module, DDR3 SDRAM, Gigabit Ethernet module. It uses Cyclone V SX SoC FPGA, which integrated with dual-core ARM Cortex-A9 MP Core processor. This paper explains the hardware and software architecture of the controller and how can it improve power supplies performances. The FPGA finishes the PI regulating and PWM modulation. The ARM is responsible for data pre-setting, web service, database, and power supplies detection and protection management. At the end, this paper gives the output measurements when the controller is used in the prototype, which verifies the rationality and reliability of the design.

INTRODUCTION

HIAF [1] is a new facility for heavy ion researches [2], which consists of two ion sources, a high intensity Heavy Ion Superconducting Linac (HISCL), a 45 Tm Accumulation and Booster Ring (ABR-45) and a multifunction storage ring system. Because the Booster Ring has high quality requirement for beam, the power supplies for magnets should have high stability, reliability, and small tracking error, small current ripple. This paper describes a controller which is designed for Booster Ring dipole power supplies. The aim of the new controller is to improve the real-time performance, stability, and reliability.

HARDWARE ARCHITECTURE

This part describes the chip selecting of the controller and the main boards. Some papers have proposed the design of a new controller [3] uses Raspberry Pi and FPGA, which means that ARM and FPGA have both used in accelerator power supplies area. Further, this paper proposes SoC FPGA which integrates ARM and FPGA, which makes the design more reliable because of the simplicity.

Chip Selecting

The controller uses Cyclone V SX SoC FPGA, which has the main performance as: Hard memory controllers supporting 400 MHz DDR3 SDRAM with optional error correction code (ECC) support, PCI Express with multi-function support, variable-precision digital signal

processing (DSP) blocks, and HPS Dual-core ARM Cortex-A9 MP Core processor. In controller, it has DDR3 SDRAM, FLASH, fiber optic 88e1111, and Ethernet module. What the old one used is Cyclone II FPGA EP2C70 [4]. The differences of two FPGA resources between two controllers are listed as Table 1. The change of the chip can improve the speed of the controller.

Table 1: The Differences Between FPGAs

Items	Cyclone V	Cyclone II
LEs	68,416	110,000
Pins	499	422
Memory bits	5,662,720	1,152,000
DSP blocks	112	/
Multipliers	224	150
Total PLLs	15	4

Main Boards

Figure 1 shows that the controller has 5 boards, which consists of main board, mother board, ADC board, extended board, and PLC board. All these boards use high speed protocol to communicate with each other. GXB is used between mother board and ADC board. Except for GXB, this controller also uses industrial general protocol such as RS232, RS485, and CAN. The old controller [4] has 7 boards, including the boards the same as the new one and MCU boards, power board. Giving up redundant boards makes the system be more reliable.



Figure 1: The photos of the controllers.

SOFTWARE ARCHITECTURE

The software architecture of the controller has two parts, which is FPGA and ARM. The FPGA part uses Verilog

* Work supported by Pearl River Talent Scheme.

[†] tanyuilian@impcas.ac.cn.

HDL language to finish parallel program, and the ARM part which is embedded Linux uses C language for programming.

FPGA Part

The FPGA finishes the PI regulating and PWM modulation. FPGA is also responsible for communicating with PLC, and receiving some states such as overcurrent fault, overvoltage fault, interlock fault. Compared to the old one, the new controller using new series FPGA can be more flexible to finish some power on self-tests cooperating with ARM. And the greater memory resources make storage be more convenient.

ARM Part

The ARM is responsible for data pre-setting, web service, database, power on self-tests, and power supplies detection and protection management. To be real timing, the controller adopts White Rabbit timing System. All the read-back data have timestamps, which is convenient for the physicist to regulate beam. In the ARM, it runs an embedded real-time Linux. Compared to the old controller, it makes full use of Linux, and gives up the shortages of NIOS II.

The Communication Between FPGA and ARM

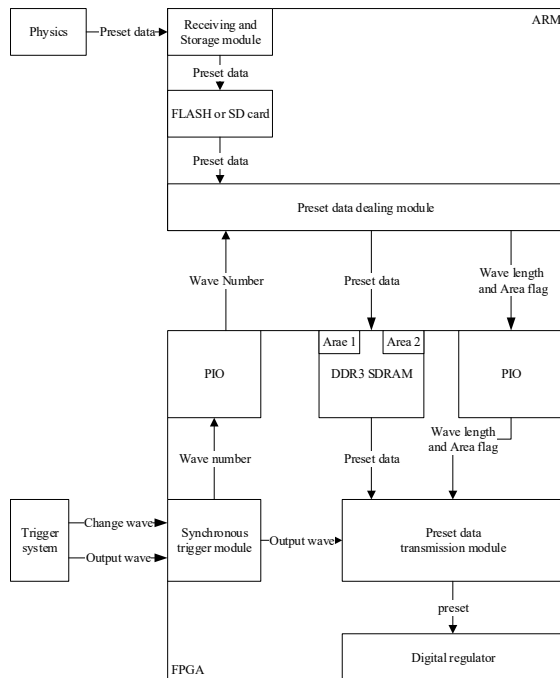


Figure 2: Pre-set data transmission flow.

The Hard Processor System (HPS, also called ARM) and FPGA communicate with each other through bus interfaces that bridge the two distinct portions. There are three bridges between HPS and FPGA, which are FPGA-to-HPS Bridge, HPS-to-FPGA Bridge, and Lightweight HPS-to-FPGA Bridge. This design uses HPS-to-FPGA Bridge to finish pass pre-setting data from ARM to FPGA. Except for that, Lightweight HPS-to-FPGA Bridge is used to transmit some enable signals and flag signals through PIO

to make sure the sequential between two parts is synchronous. The details about how the pre-set data transmits are listed as Fig. 2. And it uses FPGA-to-HPS Bridge to finish passing read-back data including currents, voltages, and states from FPGA to ARM DDR3 SDRAM, which is shown in Fig. 3. All these read-back data can be saved into file on SD card.

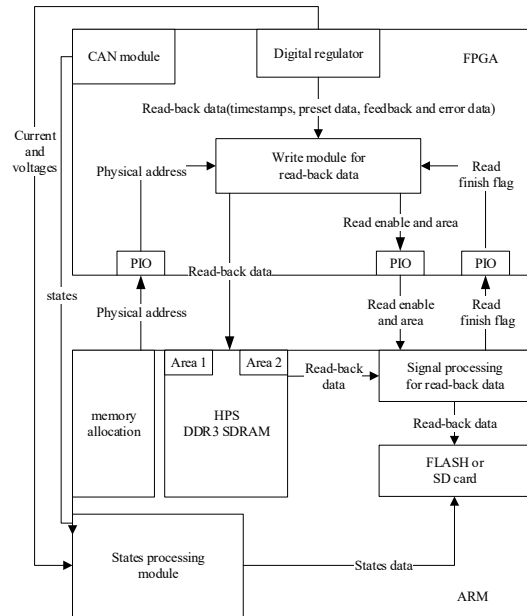


Figure 3: Read-back data transmission flow.

RESULT

Figure 4 gives the photos of debugging. The controller is used to control the prototype whose loads are quadrupole magnets, and the measurements screenshots from oscilloscope about output current is shown as Fig. 5 and Fig. 6.

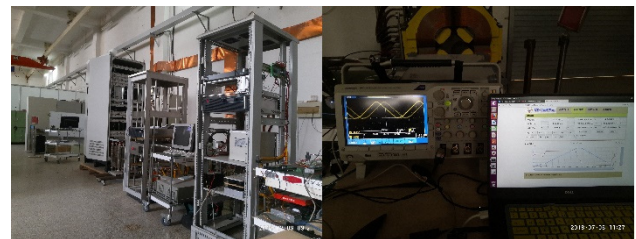


Figure 4: The photos of debugging.

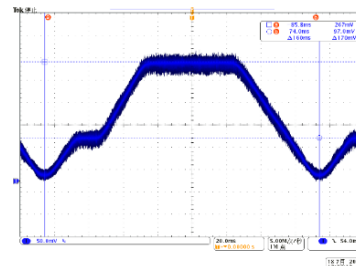


Figure 5: Oscilloscope screenshots (pulse current output, maximum current 15A).

Content from this work may be used under the terms of the CC BY 3.0 licence (© 2018). Any distribution of this work must maintain attribution to the author(s), title of the work, publisher, and DOI.

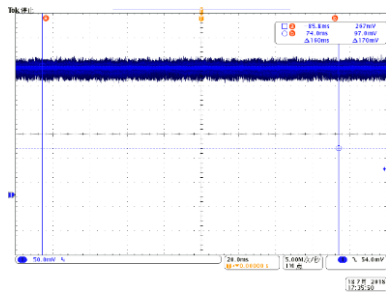


Figure 6: Oscilloscope screenshots (direct current output 15A).

This paper analyses the result from FPGA processing by Python in Linux and draws the error between given and output current as follow. Figure 7 is the data about 15A pulse current output. Figure 8 is the data about 15A direct current output. With the data from direct current output, it can make a conclusion that the stability is 0.05, calculating as Eq. (1). (MaxCur means the maximum output current, and MinCur means the minimum output current.) Because the prototype is 600A, the stability achieves the requirements. The error is lower than ±0.7A (pulse current) and ±0.0035A (direct current).

$$\begin{aligned}
 \text{Stability} &= \frac{\text{MaxCur} - \text{MinCur}}{\text{MaxCur} + \text{MinCur}} \\
 &= \frac{15.75 - 14.25}{15.75 + 14.25} = 0.05 .
 \end{aligned} \tag{1}$$

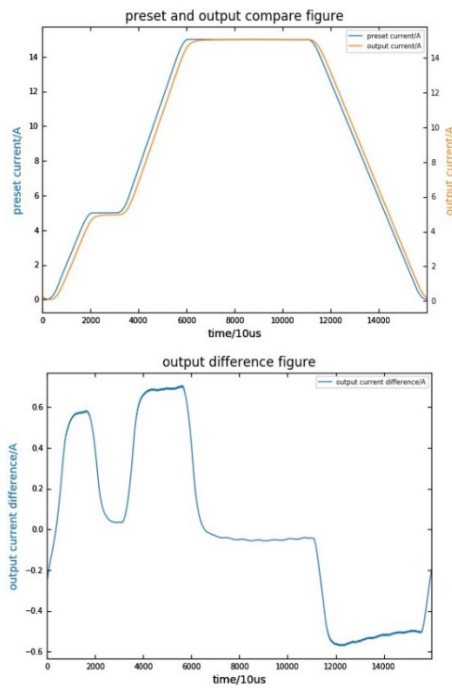


Figure 7: The pulse given and output current (the above one) and the error between given and output (the bottom one).

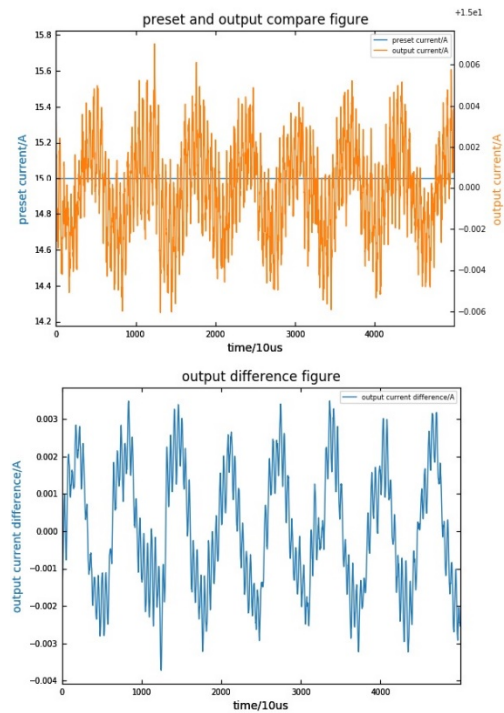


Figure 8: The direct given and output current (the above one) and the error between given and output (the bottom one).

CONCLUSION

This paper gives an architecture of the digital power supplies controller in HIAF. It proposes a new idea about using SoC FPGA in accelerator power supplies field. With reducing the boards number, the controller becomes more reliable. And it makes full use of embedded Linux, which means it can overcome the shortcoming of NIOS II. Finally, testing in prototype proves that this controller is qualified.

REFERENCES

- [1] J.C. Yang, J.W. Xia, G.Q. Xiao, *et al.*, “High Intensity heavy ion Accelerator Facility (HIAF) in China”, Nuclear Instruments & Methods in Physics Research, Vol. 317, p. 263-265 Part: B, Dec. 2013, doi: 10.1016/j.nimb.2013.08.046
- [2] Shuang R, Yang J, Zhang J, *et al.*, “Design of extraction system in BRing at HIAF”, Nuclear Instruments & Methods in Physics Research, vol. 892, p. 53-58, Jun. 2018, doi: 10.1016/j.nima.2018.02.052
- [3] Visintini R, Cleva S, Cautero M, *et al.*, “A New Concept of Controller for Accelerators’ Magnet Power Supplies”, IEEE Transactions on Nuclear Science, vol. 63, Issue. 2, p. 849-853, Part: 2, Special Issue: SI, Apr. 2016, doi: 10.1109/TNS.2015.2498480
- [4] Zhao J, Gao D, Chen Y, *et al.*, “Implementation of an FPGA controller for correction power supplies in heavy ion synchrotron”, Nuclear Instruments & Methods in Physics Research, vol. 777, p. 167-171, Mar. 2015, doi: 10.1016/j.nima.2014.12.115

THE MULTI-PHYSICS ANALYSIS OF A DUAL-BEAM LINAC *

Tao He¹, Liang Lu, Wei Ma, Lei Yang, Xianbo Xu, Liepeng Sun, Chaochao Xing,
 Institute of Modern Physics, Chinese Academy of Science, Lanzhou 730000, China
¹also at University of Chinese Academy of Sciences, Beijing 100049, China

Abstract

A prototype 81.25 MHz dual-beam drift tube linac (DB-DTL) is being designed to prove the feasibility of multi-beam type linac. The beam dynamics design and electromagnetic calculation have been completed [1]. The following step is the multi-physics analysis of the DB-DTL. The three-dimensional multi-physics analysis is very important for the design of the DB-DTL. The RF dissipated power will make the cavity temperature rise and cause cavity resonance frequency shifting due to the deformation of cavity structure. The distributions of cavity deformation and stress are calculated according to the cavity temperature distribution. All the simulation results, including cavity temperature rise, deformation and stress and the frequency shifting resulted in cavity deformation, should be within an acceptable range. The designing goal is to design the DB-DTL operated in pulse model with 1/1000 duty factor. The detailed multi-physics analysis of the prototype DB-TL will be presented in this paper.

INTRODUCTION

The DB-DTL project has been proposed to prove the feasibility of multi-beam type linac in middle energy region acceleration [2] [3], which will apply to the design of new heavy ion inertial confinement fusion (HIF) facility [4]. The layout of the DB-DTL test bench is shown in Fig. 1, which include a 1mA permanent magnet type PIG ion source, faraday cups for measuring beam transmission, an existing CW 162.5 MHz RFQ accelerator [5], the prototype DB-DTL and an analyzer magnet for measuring beam energy. The DB-DTL is able to accelerate 1 mA proton from 0.56 MeV to 2.5 MeV. The normalized power dissipation of the DB-DTL is 35.83 kW according to the electromagnetic calculation results of the DB-DTL [1]. The main parameters of the DB-DTL are listed in Table 1. The DB-DTL will be operated in room temperature. The power dissipated on the internal surface on the DB-DTL will make cavity temperature rise, which also result in structure deformation and resonant frequency shifting. It is important to simulate the temperature rise, deformation and frequency shifting of the DB-DTL cavity. Actually, the DB-DTL will be operated in pulse mode with a duty of 1/1000, with cooling-water channels but without cooling-water because of the limitation of funds. The multi-physics analysis is performed to explore the maximum operating pulse duty factor, which will apply to the beam experiment. The detailed three-dimensional multi-physics

analysis of the DB-TL will be presented in this paper, which is a coupled electromagnetic, thermal and structural analysis.

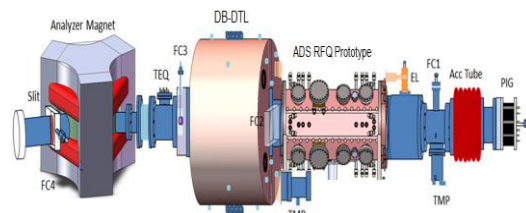


Figure 1: The layout of the DB-DTL beam test bench, which include a PIG ion source, faraday cups, the Prototype ADS RFQ, the DB-DTL and analyzer magnet.

Table 1: Main Parameters of the DB-DTL

Parameters	Value
Charge to mass ratio q/A	1
Frequency (MHz)	81.25
Beam current (mA)	1
Input/output energy (MeV)	0.56/2.5
Radius of beam-aperture (mm)	10
Maximum gap voltage (kV)	389.06
Transmission rate	34%
Operation mode	pulse
Cavity length	991.43
Shunt impedance (MΩ/m)	200.02
Normalized power dissipation (kW)	35.83

THE PROCEDURES AND GOAL OF MULTI-PHYSICS ANALYSIS

As shown in Fig. 2 [6], the procedures of multi-physics analysis include electromagnetic, thermal, structural and frequency shifting analysis. The ANSYS workbench [7] and CST Microwave Studio (MWS) [8] are utilized in the simulation. Firstly, the high frequency electromagnetic simulation is performed with the MWS and the distribution of RF thermal loss is simulated with ANSYS High Frequency Structure Simulator (HFSS) code. Based on the simulation results, the normalized cavity power dissipation is calculated, which is applied to the thermal analysis. The thermal analysis generate cavity temperature map according to the cavity internal surface heat flux. According to the distribution of cavity temperature, the distributions of structural stresses and deformations of the DB-DTL are calculated in structural analysis. Finally, the resonant frequency shifts, resulted in cavity the deformation, is simulated in HFSS code. The frequency sensitivity of cooling-water temperature and velocity are also

* Work supported by NSFC and CAS through Grant Nos. 11475232 and 11535016.

† email address: hetao0216@impcas.ac.cn

Content from this work may be used under the terms of the CC BY 3.0 licence (© 2018). Any distribution of this work must maintain attribution to the author(s), title of the work, publisher, and DOI.

simulated by using ANSYS. Through multi-physics analysis, appropriate parameters of cooling-water are chosen to satisfy the requirement for DB-DTL cavity operation. The deformation and stress of cavity and corresponding resonant frequency shifting of the DB-DTL should be within a proper range.

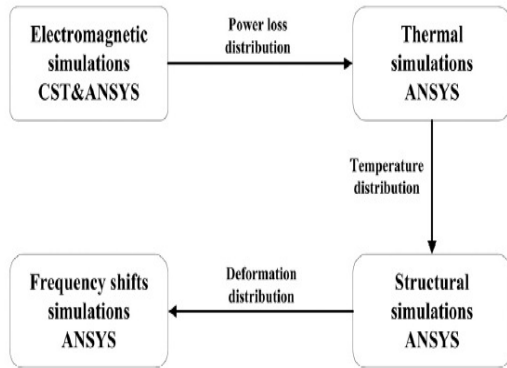


Figure 2: The multi-physics analysis scheme with MWS and ANSYS (Cited [6]).

HEAT TRANSFER THEORY OF COOLING-WATER

According to the heat conduction formula [9], the heat transfer coefficient h_c of cooling-water can be calculated.

$$h_c = \frac{KN_u}{D} \quad (1)$$

Here D and K is the diameter and the thermal conductivity of cooling-water, respectively. The value of K is $0.63 \text{ W/m}^0\text{C}$. The parameter N_u is the Nusselt number of cooling-water [10].

$$N_u = 0.023R_e^{0.8}P_r^{0.8} \quad (2)$$

The P_r represents the Prandtl parameter of cooling-water, where μ and C_p is dynamic viscosity coefficient and specific heat capacity of cooling-water, respectively.

$$P_r = \frac{\mu C_p}{K} \quad (3)$$

The R_e is the Reynolds number, here ρ and v is the density and average velocity of cooling-water, respectively.

$$R_e = \frac{\rho v D}{\mu} \quad (4)$$

In thermal analysis, the ambient temperature and cooling-water temperature are both set to be $20 \text{ }^0\text{C}$.

STRUCTURE MODEL AND LAYOUT OF COOLING-WATER CHANNELS OF THE DB-DTL

In multi-physics simulation, a half model of the DB-DTL cavity with the cooling-water channel is utilized, as illustrated in Fig. 3. The copper cavity model will be applied in thermal and structural analysis by using ANSYS. The octahedron structure shell of DB-DTL is applied for good stability and easily assembling. There are eight cooling-waterway channels for ridge and ten cooling-waterway channels for wall. The interface of coupler, Pickup and observing window is located at another sur-

face of the octahedron cavity. The main parameters of cooling-water are plotted in Table 2. Considering the limitation of water-supply machine, the velocity of cooling-water for ridge and wall are both set to be 2 m/s . The diameter of cooling-water channel is 15 mm . Therefore, the heat transfer coefficient h_c can be calculated by using the heat transfer theory of cooling water in chapter 3.

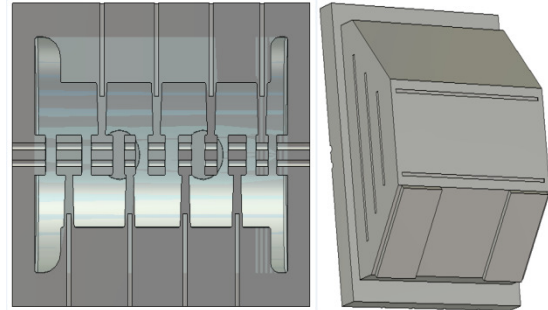


Figure 3: The cooling-water layout and structure model of the DB-DTL.

Table 2: Main Parameters of Cooling-Water

Parameters	Ridges	Walls
	Cooling-water	Cooling-water
D (mm)	15	15
v (m/s)	2	2
R_e	30000	30000
P_r	6.6349	6.6349
N_u	187.14	187.14
h_c ($\text{W/m}^2/0\text{C}$)	7860	7860

RF SIMULATION

The electromagnetic simulation is firstly performed by using MWS. Then, verification of electromagnetic calculation is simulated by using ANSYS HFSS. Table 3 gives a comparison of electromagnetic simulation between the MWS and ANSYS. The simulation results show that the difference between the two codes is enough small to ignore. The power dissipation of the DB-DTL is calculated with MWS and the surface loss density is simulated with ANSYS HFSS, as illustrated in Fig. 4, which will be applied to following thermal simulation. The normalized power dissipation of the DB-DTL cavity is calculated to be 35.83 kW . The beam power is 2 kW . According to the experience, the practical power loss is 1.2 times the simulated value [11]. The half model of the DB-DTL will dissipate 18.915 kW in multi-physics simulation

Table 3: The RF Simulation Results Comparison Between the MWS and the ANSYS HFSS

Parameters	MWS	ANSYS
F (MHz)	81.24993	81.9050
Q	13514	12860

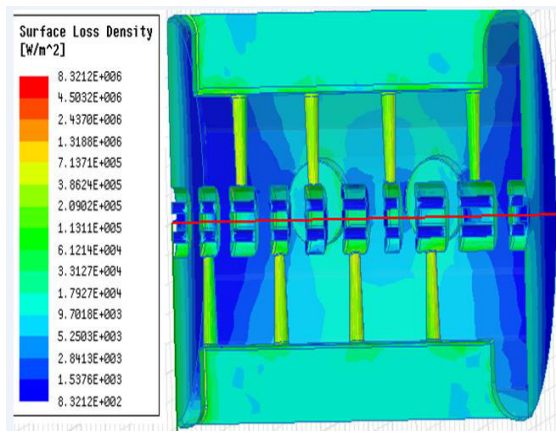
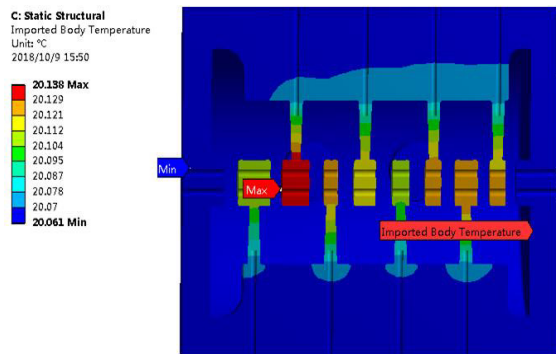
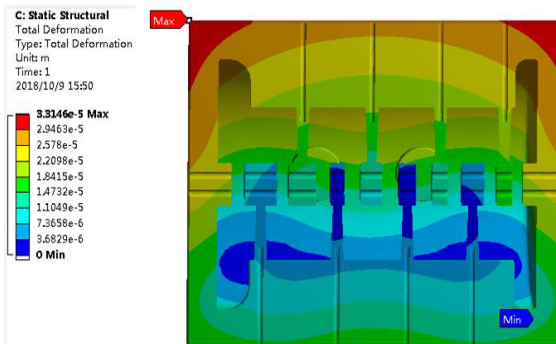


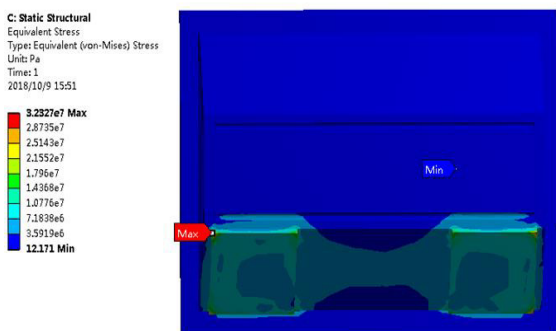
Figure 4: The power loss distribution on the internal surface of DB-DTL cavity.



A: The temperature distribution of DB-DTL cavity



B: The deformation distribution of DB-DTL cavity



C: The stress distribution of DB-DTL cavity

Figure 5: When the duty factor is 1/1000, the temperature (A), deformation (B) and stress (C) deformation distribution of the DB-DTL without cooling-water system.

THERMAL AND STRUCTURAL SIMULATION AND FREQUENCY SHIFTING CALCULATION

The thermal simulation is performed with the ANSYS Steady-State Thermal code, which generate the temperature map of the DB-DTL cavity. The cooling system and power dissipation is very important to simulate the temperature distribution of the DB-DTL. The cavity temperature distribution is applied to structural analysis in ANSYS Static Structural code for simulating the deformation and stress distribution of DB-DTL cavity.

The designing goal is that the DB-DTL operates in pulse model with a duty of 1/1000. In addition, there isn't cooling-water in the cooling-water channels because of the limitation of funds. Therefore, the power dissipation on the internal surface of the half model of the DB-DTL is firstly set to be $18.915 \times 1/1000$ kW in thermal simulation. The simulation results show that the maximum temperature is 21.38°C located at drift tube, the maximum deformation is $23.4\ \mu\text{m}$ located at upper cavity edge and the maximum stress is $22.942\ \text{MPa}$ located at fixed supporting plane edge, as illustrated in Fig. 5. The deformation of the DB-DTL cavity will cause frequency shifting. Based on the displacement result of the cavity, the frequency shifting is calculated with ANSYS HFSS code. The frequency shifting is $0.9\ \text{kHz}$. The frequency tubing ability of tuners is $9.65\ \text{kHz/mm}$, as shown in Fig. 6, which is applied in frequency tubing. All the simulation results are within an acceptable range, which meet the designing goal of the DB-DTL operated in pulse mode with a duty of 1/1000.

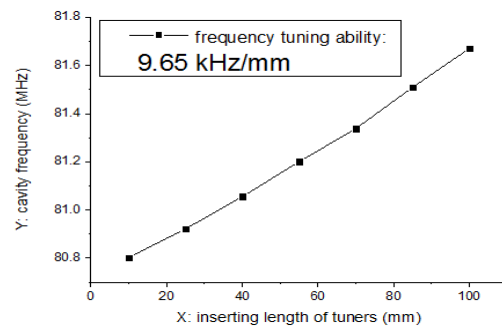


Figure 6: The frequency tubing capacity of tuners.

CONCLUSION

The designing goal is that the DB-DTL is operated in pulse model with a duty of 1/1000. There isn't cooling-water in the cooling-water channels of the DB-DTL for the limitation of funds. The multi-physics analysis results of the DB-DTL show that the maximum temperature is 21.38°C located at drift tube, the maximum deformation is $23.4\ \mu\text{m}$ located at upper cavity edge, the maximum stress is $22.942\ \text{MPa}$ located at fixed supporting plane edge and The frequency shifting is $0.9\ \text{kHz}$ caused by the cavity deformation. All the simulation results are within an acceptable range, which indicate that the designing goal of DB-DTL is achieved.

REFERENCES

- [1] T. He, L. Lu, W. Ma, et al., "Studying a Prototype of Dual-Beam Drift tube Linac", in *Proc. 9th Int. Particle Accelerator Conf. (IPAC'18)*, Vancouver, Canada, Apr.-May 2018, pp. 1020, doi:10.18429/JACoW-IPAC2018-TUPA1009
- [2] L. Lu, T. He, Toshiyuki, et al., "Study on a Super High Intensity Injector for HIF", the 22nd International symposium on Heavy-ion Fusion and Beam-Driven High Energy Density Science, Daejeon, Korea, HIF2018, 20-24 August 2018.
- [3] L. Lu, T. He, L. Yang, W. Ma, et al., "Research on a Two-Beam Type Drift Tube Linac", in *Proc. 28th Linear Accelerator Conf. (LINAC'16)*, East Lansing, MI, USA, Sep. 2016, pp. 989-991, doi:10.18429/JACoW-LINAC16-THPLR061
- [4] L. Lu, T. He, L. Yang, et al., "New developments of HIF injector", *Matter Radiat. Extremes*, vol. 1, pp. 50-59, Sep. 2017, doi:10.1016/j.mre.2017.09.003
- [5] Z. Zhang et al., "Design and beam test of a high intensity continuous wave RFQ accelerator", *Nucl. Instr. Meth. A*, vol. 763, pp. 383-387, Jun.2014, doi:10.1016/j.nima.2014.06.051
- [6] W. Ma, L. Lu, T. Liu, et al., "Three-dimensional multi-physics analysis and commissioning frequency tuning strategy of a radio-frequency quadrupole accelerator", *Nucl. Instr. Meth. A*, vol. 866, pp. 190-195, Jun. 2017, doi:10.1016/j.nima.2017.06.004
- [7] ANSYS. <http://www.ansys.com>
- [8] MWS CST Simulation packages. <http://www.cst.com>
- [9] Dittus, F. W., and L. M. K. Boelter. "University of California publications on engineering." University of California publications in Engineering 2 (1930): 371.
- [10] McAdams W H. Heat Transmission. 3rd. New York: McGraw-Hill, 1954.
- [11] F. Kreith, the CRC Handbook of Thermal Engineering, CRC Press, Boca Raton, 2000.

DEVELOPMENT OF AN ALL PERMANENT MAGNET ECR ION SOURCE FOR LOW AND MEDIUM CHARGE STATE IONS PRODUCTION

J. Q. Li[†], L. T. Sun, Y. Yang, Y. Cao, X. Z. Zhang, X. Fang, J. W. Guo, Y. H. Zhai, H. Wang, B. H. Ma, L. B. Li, W. Lu, and H. W. Zhao,
IMP/CAS, Lanzhou 730000, China

Abstract

An all permanent magnet Electron Cyclotron Resonance ion source-LAPECR1U (Lanzhou All Permanent magnet ECR ion source no.1 Upgraded), has been built at IMP in 2017 to satisfy the requirements of LEAF (Low Energy intense-highly-charged ion Accelerator Facility) for first two years commissioning. LAPECR1U was designed to be operated at 14.5 GHz to produce intense low and medium charge state ion beams. LAPECR1U features a compact structure, small size, and low cost. A cone-shape iron yoke in injection side and an iron plasma electrode in extraction side were used to enhance the axial magnetic field strength. The typical parameters and the preliminary beam results of the source are given in this paper.

INTRODUCTION

A Low Energy intense-highly-charged ion Accelerator Facility, LEAF, was launched at IMP in 2015 for researches of irradiation material, highly charged atomic physics, low energy nuclear astrophysics, *et. al.* The layout of LEAF is shown in Fig. 1. It mainly includes ECRIS, LEBT and a RFQ. The 4th generation ECR ion source FEER need to provide 2 emA U^{34+} beam with 45 GHz microwave heating. The design of FEER has been completed and the ion source is under construction. To satisfy the requirement of LEAF platform for first two years commissioning, a substitute ECR ion source, which must be compact structure and low cost, is in demand.

With the development of Lanzhou All Permanent Magnet Electron Cyclotron Resonance ion source (LAPECR) in Institute of Modern Physics (IMP) in the last decades, it has become the cost-optimal machine to produce high intensity and multiple charge state ion beams. LAPECR series are widely used for heavy ion accelerators, atomic physics research [1], and Heavy Ion Medical Machine (HIMM) [2] because of such advantages as compact structure, low cost and small size. We have built an upgraded all permanent magnet ECR ion source No.1, named LAPECR1U to satisfy the requirements of LEAF facility as ion injector for preliminary experiment.

LAPECR1U was designed to be operated at 14.5 GHz with the extraction HV 10-40 kV, and expected to produce intensity low and medium charge state ion beams. Especially, high intensity N^{2+} ion beam with high

beam quality was expected because of the same A/Q as U^{34+} .

LAPECR1U has successfully delivered He^+ and N^{2+} ion beams for RFQ commissioning. This paper will give the details of the design of LAPECR1U. Then, the preliminary commissioning results of LAPECR1U on LEAF platform were presented.

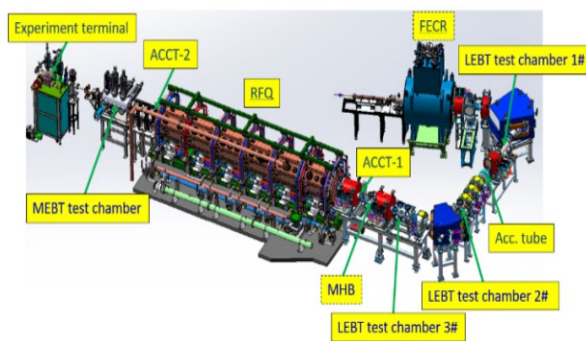


Figure 1: Layout of LEAF.

THE DESIGN OF LAPECR1U

LAPECR1U, which was designed based on older LAPECR1 [3], is a low and medium charge state ion source that can produce intense N^{2+} ion beam. In our design, the axial magnetic field is mainly produced by two permanent magnet rings and the radial magnetic field is provided by one hexapole. A 12-segmented axial magnetic ring at injection side provide the injection magnetic field with the peak up to about 0.63 T, and a 12-segmented cone shape magnetic ring at extraction side provide the extraction magnetic field up to 0.67 T. In order to improve the performance and control the size of LAPECR1U, a cone-shape iron yoke in injection side and an iron plasma electrode in extraction side were used to enhance the axial magnetic field strength, and the axial magnetic field can exceed 1.45 T at injection side and 0.72 T at extraction side. The B_{mini} field was optimized to 0.38 T by varying the space between injection ring and extraction ring. The radial magnet is a 12-segmented Halbach structure hexapole which provides a 0.94 T radial magnetic field at the inner wall of a 40 mm diameter plasma chamber, which is designed with double-wall structure allowing sufficient low conductivity water cooling. The typical parameters of LAPECR1U are given in Table 1. The schematic of LAPECR1U is shown in Fig. 2.

* Work supported by CAS (QYZDB-SSW-JSC025), MOST (contract No. 2014CB845500), and NSF (contract No. 11221064).

[†] lijiaqing@impcas.ac.cn.

Table 1: Key Parameters of LAPECRIU

B_{inj} (T)	0.63(1.45)
B_{ext} (T)	0.67(0.72)
B_{mini} (T)	0.38
Br of chamber surface (T)	0.94
Plasma chamber ID (mm)	40
R_f (GHz)	14.5
HV (kV)	40
L_{mirror} (mm)	78
L_{ecr} (mm)	46
Dimension (mm)	$\Phi 202 \times 210$

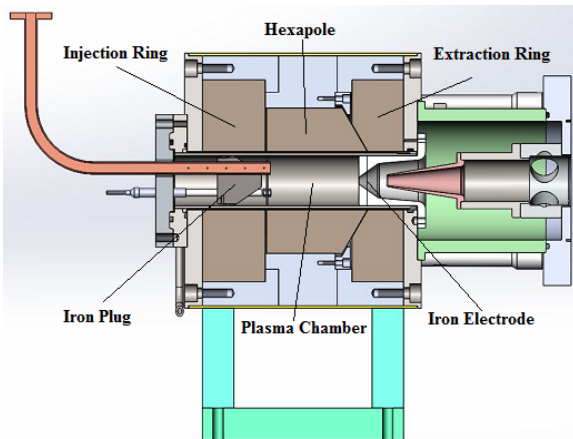


Figure 2: Schematic of LAPECRIU.

As shown in Fig. 2, LAPECRIU possesses more compact structure and higher axial magnetic field strength. Each of magnet rings next to another, and the male cone shape hexapole was cooperated with the inner cone shape extraction ring to compensate the radial field at extraction side. Figure 3 shows the contours map of LAPECRIU in x-z plane, and the total field $B=0.7$ T contours are well closed inside the plasma chamber. Figure 4 shows the axial magnetic configuration of LAPECRIU ion source.

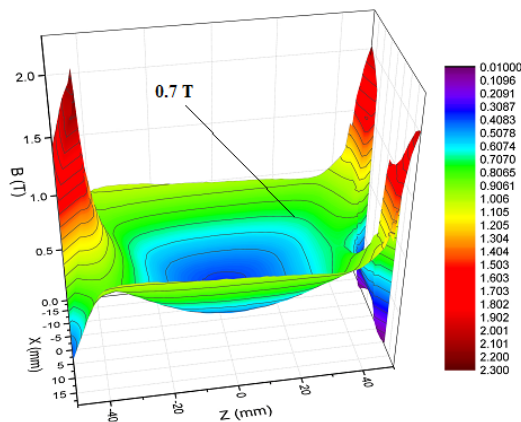


Figure 3: The contours map of LAPECRIU in X-Z plane.

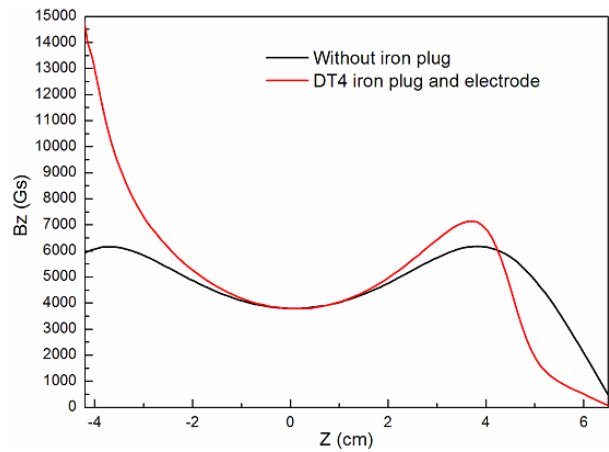


Figure 4: Axial magnetic configuration of LAPECRIU.

As shown in Fig. 4, due to the employment of iron plug and iron electrode, axial fields at injection side and extraction side were enhanced significantly, and the field gradient has increased. This will be beneficial for beam production of higher charge state ions according to the scaling laws.

PRELIMINARY COMMISSIONING RESULTS

LAPECRIU was installed at LEAF in December, 2017. The first beam was extracted on the end day of January, 2018. Figure 5 gives the photo of the source and Q/A analyser. The Q/A analyser consists of two solenoids and a 110° dipole. Beam diagnostic devices, located at the end of Q/A analyser, include a Faraday cup, X&Y Allison scanners and a beam profile viewer.

The source has passed the 30 kV insulation test without sparking, and it has been working well under 20 kV extraction voltage with the distance between plasma electrode and puller of 22 mm. The pore diameters of plasma electrode and puller were 6 mm and 8 mm respectively. Because of other more important missions of LEAF platform, we have not enough time to optimize the performance of this ion source, the optimization had been operated for only one week. During such a short period, we have tuned the helium ions and nitrogen ions. Microwave power was fed into the ion source from a 14.5 GHz TWT (Traveling-Wave Tube) amplifier. Finally, 5.0 emA of He^+ was measured by faraday cup with -200V biased voltage, when the total drain current was 12.1 emA and microwave power was 200 W. Under the same condition, 1.5 emA of He^{2+} were obtained under 420 W microwave power, while the total drain current was 7.2 emA.

Content from this work may be used under the terms of the CC BY 3.0 licence (© 2018). Any distribution of this work must maintain attribution to the author(s), title of the work, publisher, and DOI.

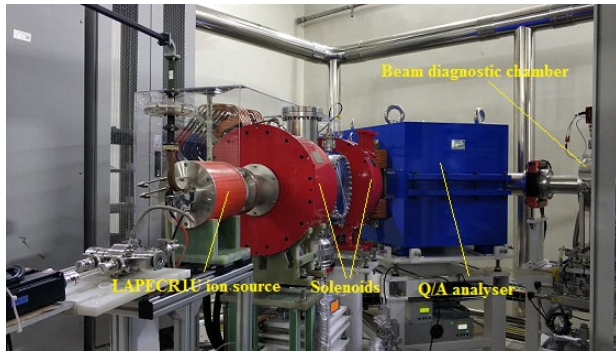


Figure 5: Picture of LAPECRIU and Q/A analyser.

For nitrogen ions beam production, two approaches were taken to optimize the beam intensity. During the first test, only nitrogen gas was fed into the source, 1.7 emA of N^{2+} was measured by faraday cup under RF power of 190 W. Obviously, it is not difficult to product such lower charge state ions, however, only 56 eμA of N^{5+} was measured. In order to enhance higher charged state ions production, helium was also fed into the source as supporting gas. Easy to see that the CSD (Charge States Distribution) was shifted to the high charge state ions when supporting gas was used, then 157 eμA of N^{5+} and 8 eμA of N^{6+} were obtained at 20 kV extraction voltage and 260 W rf power. Figure 6 shows the spectrum optimized on N^{5+} . The performance of the source for Helium and Nitrogen ion production was summarized in Table 2.

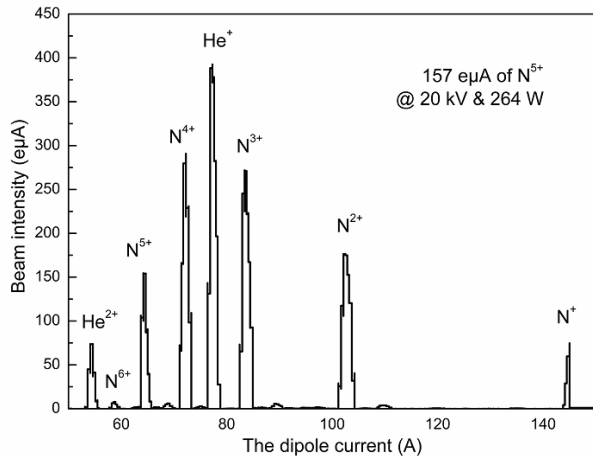


Figure 6: The CSD optimized on N^{5+} with mixed gas.

Table 2: Summary of Maximum Beam Current for Various Ions and Charge States (eμA)

	1	2	3	4	5	6	7
He	5100	1500					
N	1600	1700	828	424	157	8	

In order to investigate the beam quality of N^{2+} ion, beam emittances with several beam intensities were measured and plotted. As shown in Fig. 7, beam emittance increases with the intensity. Two reasons should be considered, the one is plasma status depended on source tuning, which decided the plasma meniscus [4]. Another

is aberrations from magnets and space charge effects [5]. Both of two reasons led to the growth of beam emittance. In addition, the measured phase space distribution of N^{2+} with beam intensity about 1.5 emA was displayed in Fig. 8. Not hard to see that the phase space was seriously distorted with such a stronger beam intensity. It is disadvantages to beam transportation. Fortunately, beam performance at a low intensity is enough to the early stage commissioning. Anyhow, some methods should be taken to optimize the beam quality in the future.

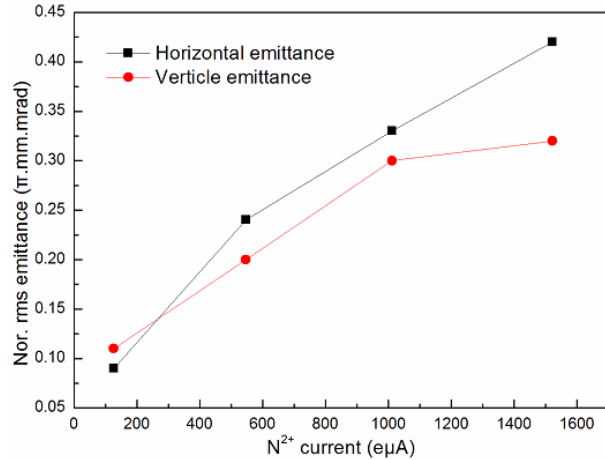


Figure 7: N^{2+} beam emittance versus beam intensity.

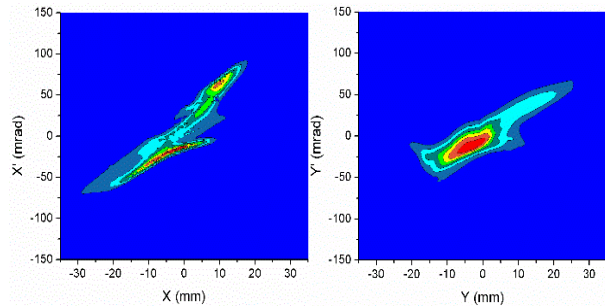


Figure 8: Measured phase space distributions for 1.5 emA N^{2+} beam.

CONCLUSIONS

A compact all permanent magnet ECR ion source for low and medium charge state ions has been successfully fabricated at IMP. The preliminary operation results of LAPECRIU for the LEAF platform have been presented in this paper. Performance of the ion source is good enough to meet the requests of LEAF project for preliminary commissioning.

REFERENCES

- [1] L.T. Sun *et al.*, "A latest development all permanent magnet ECRIS for atomic physics research at IMP", *Rev. Sci. Instrum.* 77, 03A319 (2006).
- [2] Y. Cao *et al.*, "An all permanent magnet electron cyclotron resonance ion source for heavy ion therapy", *Rev. Sci. Instrum.* 85, 02A960 (2014).

Content from this work may be used under the terms of the CC BY 3.0 licence (© 2018). Any distribution of this work must maintain attribution to the author(s), title of the work, publisher, and DOI.

- [3] Y. Shang *et. al.*, “Lanzhou All Permanent ECR Ion Source No. 1-LAPECR1”, *High Energy Physics and Nuclear Physics*. 31, (Supp. 1) 115-117 (2007).
- [4] V. Mironov *et. al.*, “On optical properties of ion beams extracted from an electron cyclotron resonance ion source”, *AIP Conference Proceedings* 2011, 080008 (2018).
- [5] Y. Cao *et. al.*, “Study of ion beam transport from the SECRAL electron cyclotron resonance ion source at the Institute of Modern Physics”, *Rev. Sci. Instrum.* 83, 02B726 (2012).

DEVELOPMENT OF A PEPPER POT PROBE TO MEASURE THE FOUR-DIMENSIONAL EMITTANCE OF LOW ENERGY BEAM OF ELECTRON CYCLOTRON RESONANCE ION SOURCE AT IMP

X. Fang[†], L. T. Sun, Y. J. Yuan, Y. Yang, Y. Cao, C. Qian, X. Z. Zhang, R. F. Chen,
J. X. Wu, X. X. Li, H. Wang, B. H. Ma, W. Lu, and H. W. Zhao
IMP/CAS, Lanzhou 730000, China

Abstract

The ion beams extracted from an Electron Cyclotron Resonance (ECR) ion source always exist strong transverse coupling effect that is caused by the field of the axis mirror magnets and the extraction solenoid. A Pepper Pot probe was developed and used to obtain the full four-dimensional (4D) phase space distribution of the low energy beam extracted from the ECR ion source at IMP. This paper describes the design of the Pepper Pot, the setup configuration, the detailed image processing procedure, especially the analysis results verification compared to another type emittance meter. The first 4D emittance is also determined through the Pepper Pot probe. The transverse phase space distribution measurement data of oxygen beams from the LECR4 experimental platform are presented and discussed.

INTRODUCTION

Electron cyclotron resonance (ECR) ion sources [1] were widely used in the particle accelerator because of their high performance on producing highly charged ions. During the last few years it became the evident that the ion beam extracted from the ECR ion sources excited complicated structure of phase space distributions [2]. The ion beam in the horizontal and vertical planes are strongly coupled due to the strength field of solenoid include extraction coil of the axial mirror magnets and the extraction solenoid [3]. In order to obtain the transverse distribution, some type of emittance device were previously used, like Slit to wire meter [4], Allison type meter [5], but these devices cannot provide full phase space distribution. Pepper Pot probe is another type emittance meter that can acquire 4D emittance. Another significant advantage of the Pepper Pot probe is the very short time of measurement progress. Pepper Pot probe were widely used to measure both electron [6] and heavy ion [7] emittance of the low energy beam transport line (LEBT). There were two types Pepper Pot probe, one is single-pass type [8] that the probe was rapidly insert to the beam center to measure whole beamlet [9] data, the laboratories like LBNL, ANL, RIKEN, BNL are all this type; the other is scanning type [10] that the beamlet data were obtained through probe moving step by step, KVI has designed this type probe and it was used to measure the beam transverse distribution. Most of exist Pepper Pot

probes have acquired the beam transverse distribution of LEBT that without the verification, in most case the results of Pepper Pot probe whether reliable is uncertain. In this paper the Pepper Pot probe result was compared to Allison Scanner in order to certify the accuracy.

THE SETUP OF PEPPER POT

The prototype of the Pepper-Pot meter which was recently designed and commissioned is shown in Fig. 1. It contains a Pepper-Pot mask with two copper frames, a square scintillator and a 45 degree stainless steel mirror. The Pepper-Pot mask is a tantalum foil with a thickness of 100 micrometers with holes of 100 micrometers diameter and distance between adjacent holes is 3 mm in both x and y direction. A round potassium bromide (KBr) is used for the scintillator (5 mm thickness) with 50*50 mm available size. The mask is mounted in the copper frame which has one blocked hole in the center to provide an absolute spatial reference for the data processing. There was no additional cooling of the mask because the beam is low energy during the tests. A 45 degree mirror reflects the appearing light pattern to the CCD camera seem like perpendicular at the beam. The exposure time and gain of the camera can be adjusted online via the user interface and a real-time image can be acquired. A code based on the Matlab software is designed for the transverse emittance calculation.

The Pepper Pot probe is located on the LEBT line of the LECR4 platform [11, 12] at IMP. The layout of the LECR4 platform is shown in Fig. 2. It contains a room temperature ECR ion source and a LEBT line which includes two solenoids and a 90 degree analysis magnet to focus and select the expected ion beam to the RFQ. The Pepper Pot probe was mounted in the diagnostic box behind the RFQ, two Allison scanners [13] were recently added to the same cube in order to compare the measurement results between two types device.

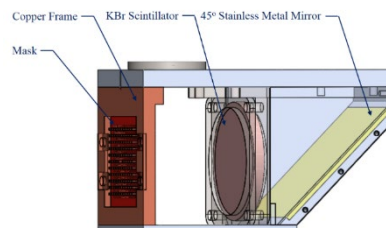


Figure 1: The draw of Pepper Pot probe with KBr scintillator at IMP.

* Work supported by CAS (QYZDB-SSW-JSC025), MOST (contract No. 2014CB845500), and NSF (contract No. 11221064).

[†] fangxing@impccas.ac.cn.

Content from this work may be used under the terms of the CC BY 3.0 licence (© 2018). Any distribution of this work must maintain attribution to the author(s), title of the work, publisher, and DOI.

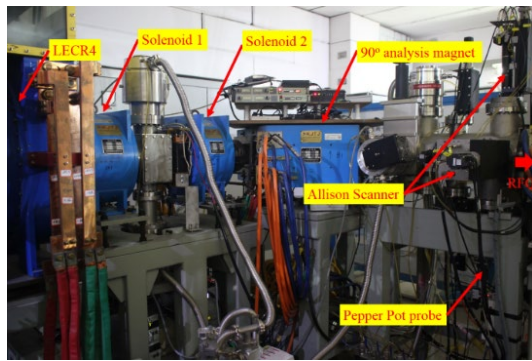


Figure 2: Layout of LECR4 experimental platform.

CONFIGURATION

Angular Resolution

The angular resolution of the Pepper Pot probe depends on the distance between the Pepper Pot mask and the scintillator screen. With increasing the distance, the absolute spot size on the final image increase, but the angular resolution decrease. In practice however, for a given mask, the distance depends on the expected maximum angle that the beam particles have and that beam spot do not overlap but far enough to ensure a good spot resolution. The distance of the Pepper Pot probe at IMP can be varied from 10 up to 40 mm. Table 1 shows the angler resolution for the different distance between the Pepper Pot mask and the scintillator screen.

Table 1: The Angular Resolution of the Probe that the Pixel Size is 52 μm

Distance (mm)	Angular resolution (mrad)
10	5.20
25	2.08
40	1.30

Linearity of the Light Yield

The linearity of the light yield of the different type scintillator were test in world laboratories [14, 15]. The material of scintillator of the Pepper Pot probe at IMP is KBr because of its highest light yield. The linearity of light yield of KBr screen interact with ion beam will be discussed in this section. Figure 3 shows the linearity of the light yield with the O^{5+} ions collision. One can see that nearly linear increase with the total generated light with the incident ion beam current with different threshold value. The light yield dependence means that the KBr scintillator shows a high saturation behind on the hundred micro-ampere ion beam current that the beam emittance measurement is credible, within the measured beam current no saturation effect was found.

IMAGE DATA PROCESSING

One version of the transverse emittance processing code has been developed to analyze the Pepper Pot beam image. The code is capable of extracting the full 4D phase space information from the captured light image. It includes noise treatment, production of the beam

distribution matrix, calculation of the transverse 4D sigma matrix and the phase ellipse parameters based on the root-mean-square algorithm [16], and saving the output results. The detail analysis steps of the code are described in the following.

The Noise Treatment

The noise of the Pepper Pot image were reduced including the background subtraction and Gaussian noise flitting. The procedure is that the beam image with beam collision subjects the dark image without beam collision, and both image is under same camera settings. Then pixel gray of the disposed image under the threshold sets to zero and the other pixel gray deducts the threshold. Finally, a 3*3 medial filter which is the effective technique in isolated pixels removing is used to filter the stochastic noise.

The Beam Matrix Calculation

The sensitive image contains whole beamlet collision is cut out by the code. Based on the image, the Decal coordinate (X_p, Y_p) of pixels can be defined through the relative center of the beam pattern and the pixel resolution. The beam momentums matrix on the both direction are obtained through the quotation $r'=(R-r)/L$. L is the distance between the front side of Pepper Pot mask and the detecting side of the KBr light pattern screen, R is the Decal coordinate of pixels, r is the Decal coordinate of the holes of the mask related to the pixels. So the beam distribution matrix $\rho(x, x', y, y')$ can be generated through sorting the data with one direction such as horizontal.

Beam emittance analysis

According to the beam distribution matrix, the phase space ellipse parameters can be calculated through quotation. The 4D emittance will be obtained synchronously. The emittance analysis will be discussed particularly on the next section of this paper.

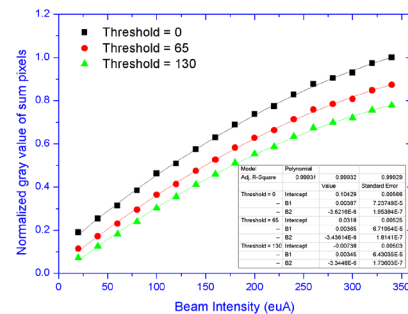


Figure 3: The light yield for the 15 keV O^{5+} beam with the gain is 400 and the exposure time is 1000 ms.

RESULTS CERTIFICATION

The final transverse distribution results of the Pepper Pot probe based on image processing are very sensitive with the external setting. However, there are almost no data on the certification of analysis results of the Pepper Pot probe. The detailed certification of the Pepper Pot results is discussed on this section.

Phase Ellipse Rotation Angle Comparison

Phase ellipse rotation angle [8] is used to a certification that verify the difference of the twiss parameters between the Pepper Pot probe and Allison Scanner. The ellipse rotation angle θ is shown in Fig. 4. Nine different phase space ellipse has been measured by both the Pepper Pot probe and the Allison Scanners with different focusing solenoids value. The ellipse rotation angle relationship between the Pepper Pot and the Allison Scanner is shown in Fig. 5. It can see that the difference of ellipse rotation angle between the two types emittance meter is less than 1.5% of the both phase space.

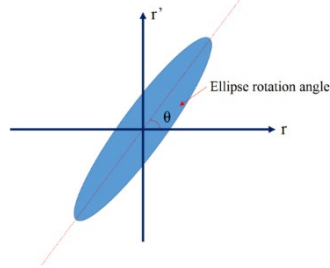


Figure 4: The ellipse rotation angle.

The Ellipse Parameters Comparison

The 2D transverse phase distribution contains the RMS emittance and the twiss parameters are compared to that of Allison scanner to certain the reliability of the results. The verification pattern is shown is Fig. 6, it can be seen that the difference of the RMS emittance is 18.73% in the horizontal and 4.18% in the vertical. The horizontal difference of twiss parameters is 20.22% with α , 18.80% with β and 14.90% with γ , these difference of vertical is 10.95%, 7.10% and 9.08%. The horizontal difference is The largest difference of the Pepper Pot probe results is not larger than about 20%, and the smallest is less than about 4%, so it is a conclusion that the Pepper Pot probe at IMP can be used to measure the beam transverse distribution and its processed results is reliable.

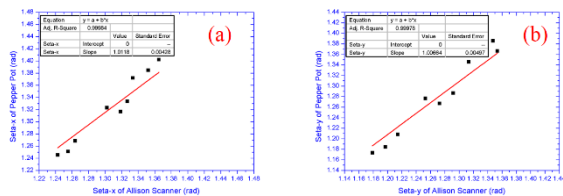


Figure 5: The ellipse angle comparison. The difference of the ellipse rotation angle is related to the slop of the red line in the pattern. (a) The rotation angle of space xx' (b) The rotation angle of space yy'.

4D EMITTANCE

The advantage of Pepper Pot probe in the measurement is the 4D emittance calculation. The 4D emittance results are shown in Fig. 7, it contains the 4D emittance acquired by the Pepper Pot probe, and the products on the two-dimensional emittance that processed by these two meters. One can see that the difference between the 4D emittance and the product of two-

dimensional emittance of Pepper Pot probe is lower than that of Allison Scanner, and the products of Allison Scanner is larger than the 4D emittance obviously.

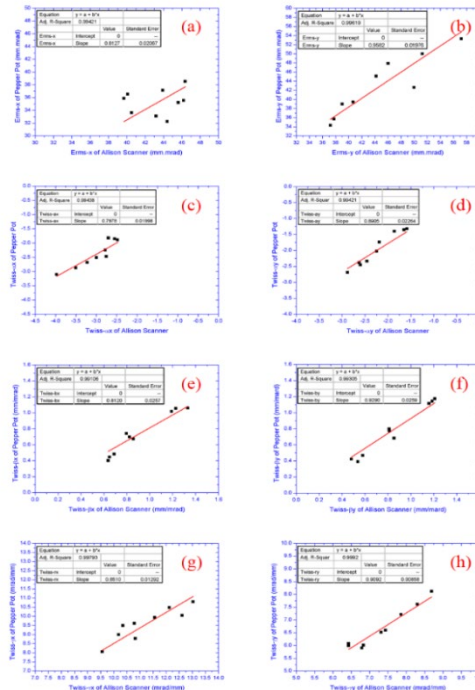


Figure 6: The comparison of the twiss parameters. The difference is related to the slop of the red line in the pattern. (a) The RMS emittance of space xx'. (b) The RMS emittance of space yy' (c) The twiss- α of space xx' (d) The twiss- α of space yy' (e) The twiss- β of space xx' (f) The twiss- β of space yy' (g) The twiss- γ of space xx' (h) The twiss- γ of space yy'.

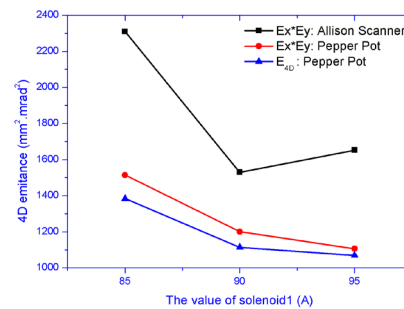


Figure 7: The 4D emittance processed by the Pepper Pot probe on different value of solenoid 1 that the value of solenoid 2 is fixed at 125A.

CONCLUSION

The design of Pepper Pot probe has been completed and the 4D transverse phase space distribution has been clearly demonstrated. The results of Pepper Pot probe is verified to that of Allison Scanner comprehensively. The verification shows a well property of Pepper Pot probe so that the transverse phase distribution base on the image process method is credible. Increasing the detecting range of the mask is the next optimizing work of the Pepper pot probe at IMP.

REFERENCES

- [1] A. Girard, G. Melin, “ECR ion sources today Physics, performance and technology”, *Nucl. Instr. Meth. A.* 382, 252-66 (1996).
- [2] P. Spadtke, K. Tinschert, R. Lang, et al., “Prospects of ion beam extraction and transport simulations”, *Rev. Sci. Instrum.* 79, 02B716 (2008).
- [3] Y. Yang, Y. J. Yuan, L. T. Sun et al., “Transverse coupling property of beam from ECR ion sources”, *Rev. Sci. Instrum.* 85, 113305 (2014).
- [4] J. Pogge, “Sns emittance scanner, increasing sensitivity and performance through noise mitigation, design, implementation and results”, in *proceeding of BIW2006*, Batavia, U.S, 435-44 (2006).
- [5] M. P. Stockli, R. F. Welton, R. Keller, and M. Leitner, “Emittance studies with an Allison scanner”, *Rev. Sci. Instrum.* 77, 03B706 (2006).
- [6] J. G. Power, M. E. Conde, W. Gai et al., “Peppet-pot based emittance measurement of the AWA photoinjector”, in *Proceedings of PAC*, Albuquerque, U.S, 4393-5 (2007).
- [7] S. Kondrashev, A. Barcikowski, B. Mustapha et al., “Development of a pepper pot emittance probe and its application for ECR ion beam studies”, *Nucl. Instr. Meth. A.* 606, 296-304 (2009).
- [8] S. Jolly, “Pepperpot Emittance Measurements of the FETS Ion Source”, Imperial College, London, 2007.
- [9] M. P. Stockli, “Measuring and Analyzing the Transverse Emittance of Charged Particle Beams”, in *Proceedings of BIW 2006*, Batavia, U.S, 25-62 (2006).
- [10] H. R. Kremers, J. P. M. Beijers, and S. Brandenburg. “A pepper-pot emittance meter for low-energy heavy-ion beams”, *Rev. Sci. Instrum.* 84, 025117 (2013).
- [11] W. Lu, B. Xiong, X. Z. Zhang et al., “Progress of a Room Temperature ECRIS using Evaporative Cooling Technology at Institute of Modern Physics”, *Rev. Sci. Instrum.* 85, 02A926 (2014).
- [12] X. H. Zhang, Y. J. Yuan, X. J. Yin et al., “Analyzing And Matching Study Of Mixed High Intensity Highly Charged Ion Beams”, in *Proceedings of HB2016*, Malmö, Sweden, 422-26 (2016).
- [13] Y. Cao, L. T. Sun, L. Ma, et al., “Experimental study on the electric-sweep scanner and ion beam emittance of electron cyclotron resonance ion source”, *Rev. Sci. Instrum.* 77, 03A346 (2006).
- [14] M. Strohmeier, J. Y. Benitez, D. Leitner et al., “Development of a pepper-pot device to determine the emittance of an ion beam generated by electron cyclotron resonance ion sources”, *Rev. Sci. Instrum.* 81, 02B710 (2010).
- [15] T. Nagatomo, V. Tzoganis, M. Kase et al., “Development of a pepper-pot emittance meter for diagnostics of low-energy multiply charged heavy ion beams extracted from an ECR ion source”, *Rev. Sci. Instrum.* 87, 02B920 (2016).
- [16] M. Zhang, ‘Emittance Formula for Slits and Pepper-pot Measurement’, 1996.

Content from this work may be used under the terms of the CC BY 3.0 licence (© 2018). Any distribution of this work must maintain attribution to the author(s), title of the work, publisher, and DOI.

SINGLE HEAVY ION BUNCH GENERATION SCHEME IN BRING AT HIAF*

D. Y. Yin[†], J. C. Yang, L.J.Mao, H. Du, G.D.Shen, Institute of Modern Physics, Lanzhou, China

Abstract

As the Booster Ring of the High Intensity Heavy-ion Accelerator Facility (HIAF), BRing is a synchrotron which can be able to accumulate and accelerate full ion species provided by iLinac to required energy with RF acceleration system. When accelerating uranium beam (e.g. $^{238}\text{U}^{35+}$), the variation range of the kinetic energy is 17MeV/u-830 MeV/u, and the corresponding revolution frequency f_{rev} range is 0.099MHz-0.447MHz. Because of the low frequency limit value of 0.099MHz, the RF frequency f_{RF} of RF cavity should be h (harmonic number) times of f_{rev} , thus, there will have h (is equal to harmonic number) bunches after acceleration. To satisfy the extraction requirement, the accelerated multiple bunches should be recollected in one bunch by means of longitudinal manipulation.

The different single bunch generation method of de-bunching and bunch merging are investigated separately, and the beam parameters in different cases are obtained, meanwhile, the optimized RF program during the de-bunching and bunch merging are presented.

INTRODUCTION

In China, the Heavy Ion Research Facility at Lanzhou (HIRFL) [1] is one major national research facility focusing on nuclear physics, atomic physics, heavy ion applications and interdisciplinary researches. A series of remarkable results have been obtained at HIRFL. Based on the developments and experience with heavy ion beam accelerators, a new project HIAF [2] was proposed by IMP in 2009. The facility is being designed to provide intense primary and radioactive ion beams for nuclear physics, atomic physics, application research sciences and so on. The schematic layout of HIAF project is shown in Fig. 1.

The HIAF project consists of ion sources, linac accelerator, synchrotrons and several experimental terminals. The superconducting ion Linac accelerator (iLinac) is designed to accelerate ions with the charge-mass ratio $Z/A=1/7$ (e.g. $^{238}\text{U}^{35+}$) to the energy of 17 MeV/u. Ions provided by iLinac will be cooled, accumulated and accelerated to the required intensity and energy (up to 1×10^{11} and 830 MeV/u of $^{238}\text{U}^{35+}$) in the Booster Ring (BRing), then fast extracted and transferred either to the external targets or the Spectrometer Ring (SRing).

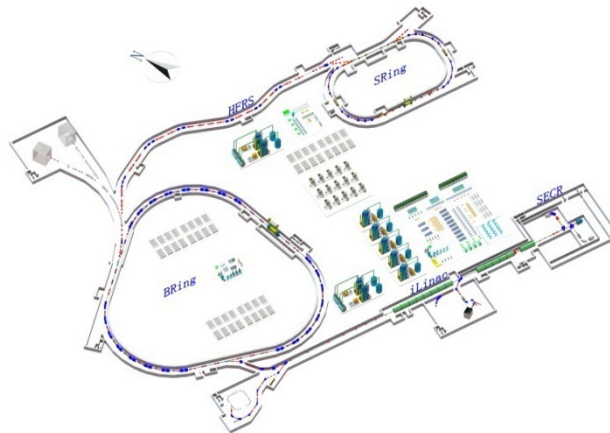


Figure 1: Layout of papers.

As a key part of the HIAF complex, BRing is a synchrotron which can be able to accumulate and accelerate full ion species with a circumference of 569 m and a maximum magnetic rigidity of 34 Tm, Table 1 shows the main configuration and parameters of the BRing.

Table 1: Main Parameters of BRing

Main parameters	Values
Circumference (m)	569
Maximum magnetic rigidity (Tm)	34
Accelerating rate (T/s)	12
Momentum acceptance ($\Delta p/p$)	$\pm 5.0 \times 10^{-3}$
Injection	
Ion	$^{238}\text{U}^{35+}$
Energy (MeV/u)	17
Revolution frequency(MHz)	0.099
Momentum spread ($\Delta p/p$)	$\leq \pm 2 \times 10^{-3}$
Extraction	
Maximum Energy (MeV/u)	830
Revolution frequency(MHz)	0.447
Particle number (ppp)	1.0×10^{11}

After two-plane painting injection and accumulation, the beam with the injection energy of 17 MeV/u is costing beam which will spread over 2π in rf phase and it has a momentum spread of $\Delta p/p = \pm 2 \times 10^{-3}$ (see Fig. 2). Due to the evolution frequency of 0.099MHz at injection energy is beyond the working frequency range of the cavity, so the RF cavity will work at the harmonic number greater than 1, based on experience and dynamics results,

* Work supported by National Natural Science Foundation of China(11705253)

[†] yindy@impcas.ac.cn

Content from this work may be used under the terms of the CC BY 3.0 licence (© 2018). Any distribution of this work must maintain attribution to the author(s), title of the work, publisher, and DOI.

the number will be selected as 3 or 4. Fig. 3a presents the bunch distribution at the end of acceleration at the harmonic number of 3, and Fig. 3b presents the bunch distribution at the end of acceleration at the harmonic number of 4.

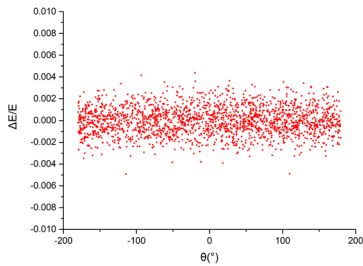


Figure 2: Initial distribution after accumulation.

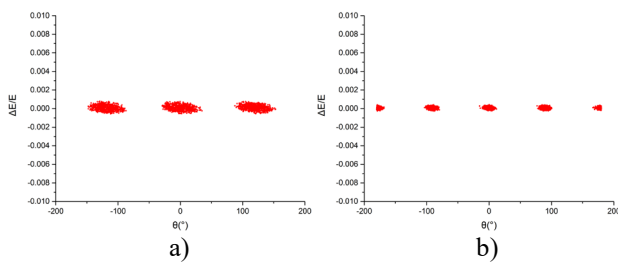


Figure 3: Beam distribution after acceleration. a) at the harmonic 3, and b) at the harmonic 4.

In order to meet the extraction requirement of the bunch number of one, multiple bunches which the number is equal to harmonic number of RF system should be converted to one. In general, there are two schemes to generate single bunch. The first one is firstly to debunch [3,4] multiple bunches to costing beam, then recapture the costing beam to one bunch, and the second one is to merge [5] the bunches through the RF manipulation.

DEBUNCHING

The conventional method for changing the longitudinal structure of the beam is to debunch by cancelling the voltage at the initial frequency, and then the beam will drift without longitudinal focusing, and then to rebunch with another RF frequency to one bunch. The voltage will be decreased adiabatically from the value which at the end of acceleration to that of cavity activation (close to 0v) within a period of time. Based on the beam parameters of $^{238}\text{U}^{35+}$ proposed by the BRing, the debunching process is simulated at the extraction energy of 830MeV/u. During the simulation process, we can know, the momentum spread decreasing with voltage decreasing. Fig. 4e-f show the longitudinal phase-space (azimuth – kinetic energy spread) distribution at the end of the beam debunching with different decreasing time(5ms, 10ms, 15ms, 20ms, 25ms and 30ms), and it is known from the figures, the multiple bunches can't be completely debunched if the debunching time is not enough. Figure 5 shows the momentum spread after debunching with

different debunching time. From the results mentioned above, the debunching time of 30ms is enough, and the momentum spread is 0.00014 rms, the beam is costing beam in this case. After that the costing beam will be recaptured at the fundamental harmonic by turn on the rf voltage adiabatically. From the Fig. 6 we can see clearly that the single bunch is generated from 3 bunches successfully. And Fig. 7 shows the RF program during the whole process including capture, acceleration, debunch and recapture.

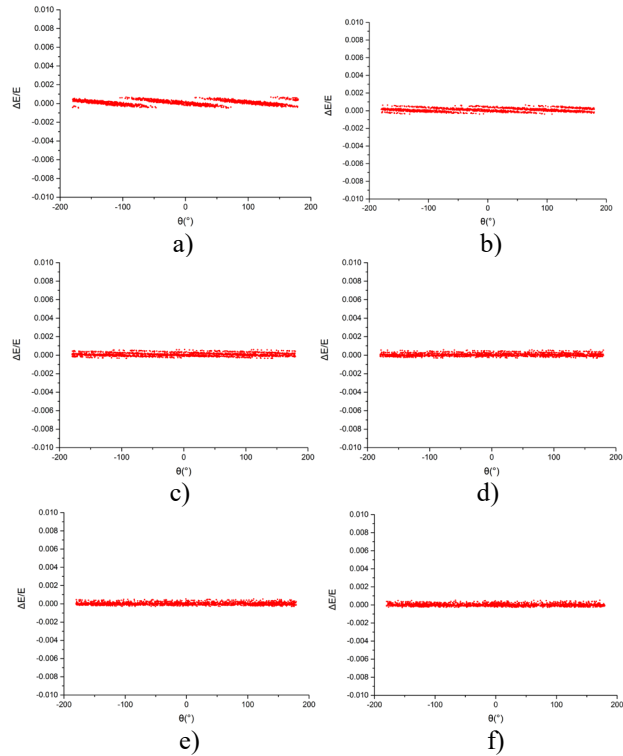


Figure 4: Beam distribution after debunching with different debunching time: a) 5ms, b) 10ms, c) 15ms, d) 20ms, e) 25ms, f) 30ms.

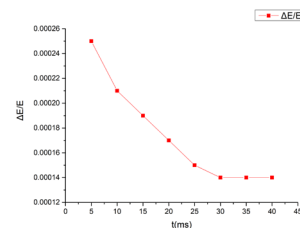


Figure 5: Momentum spread after debunching with different debunching time.

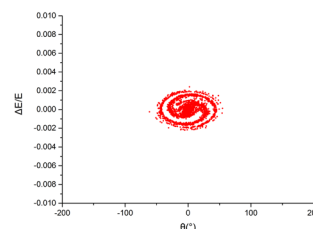


Figure 6: Beam distribution after recapture.

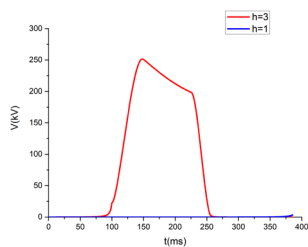


Figure 7: RF voltage program during the whole process. Red line is the RF voltage program with the harmonic 3, and the blue line is the RF voltage program with the harmonic 1.

There are two RF harmonics are used through this whole process, and the basic parameters of these RF system are listed in Table 2.

Table 2: Main Parameters of RF System of Debunching

Main parameters	Values
Ion species	U^{35+}
Energy (MeV/u)	830
Harmonic number h	4-1
Gap voltage(kV)	250-3.49

As the widely used way to generate single bunch, debunching can minimize emittance blow-up, however, this technique presents a number of drawbacks:

- RF voltages must be controlled down to small amplitudes in the presence of beam-loading,
- while drifting, the beam is left uncontrolled,
- the full circumference is filled with particles,
- the continuous beam has a very small $\Delta p/p$ which makes it prone to microwave instability.

BUNCH MERGING

Another convenient alternative method of generating single bunch is bunch merging, and the bunch number of merging pairs must be divided by 2 (or a power of 2). In this article, the beam is accelerated with RF system at harmonic 4, so, 4 bunches will be generated after acceleration, and the scheme of 4:2:1 bunch merging will be used to generate single bunch.

When the acceleration completed, there will 4 bunches held with an RF system on harmonic 4, RF voltage on harmonic 2 is slowly turned on while it is reduced on harmonic 4. With the correct phasing between both systems and sufficiently slow voltage changes, the 4 bunches merge into 2, and this process is shown in Fig. 8, after that, RF voltage on harmonic 1 is slowly turned on while it is reduced on harmonic 2, the 2 bunches merge into 1 this process is shown in Fig. 9. There are three RF harmonics are used through the whole process (see Fig. 10), and the basic parameters of these RF system are listed in Table 3.

Table 3: Main Parameters of RF System of Bunch Merging

Main parameters	Values
Ion species	U^{35+}
Energy (MeV/u)	830
Harmonic number h	4-2-1
Gap voltage(kV)	270-80-80

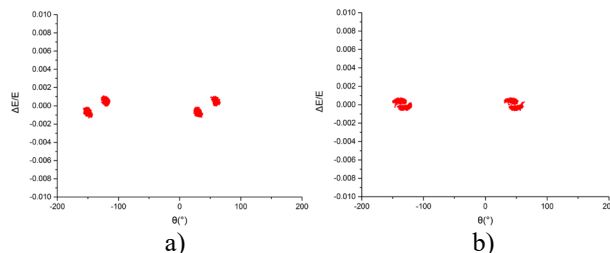


Figure 8: Bunch distribution during the bunch merging. a)-during the merging from 4 to 2 and b)-at the end of merging from 4 to 2

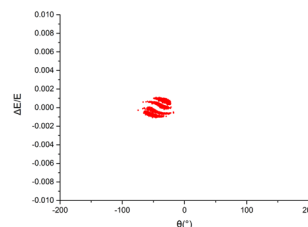


Figure 9: Bunch distribution after bunch merging.

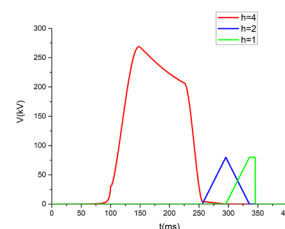


Figure 10: RF voltage program during the bunch merging process.

CONCLUSION AND OUTLOOK

Determination of single bunch generation scheme is a compromise of total operation cycle, RF system available, and so on. The study of this subject is just beginning, a more detail RF program and beam parameters will be presented in subsequent work.

REFERENCES

- [1] J. W. Xia et al., "The heavy ion cooler-storage-ring project (HIRFL-CSR) at Lanzhou", Nucl. Ins. and Meth. in Physics Research A488 (2002) 11-25.
- [2] J.C. Yang et al., "High Intensity heavy ion Accelerator Facility (HIAF) in China", Nucl. Ins. and Meth. in Physics Research B317 (2013) 263-265.
- [3] S.Y. lee, "Accelerator Physics", 2nd Ed. Singapore, World Scientific (1999) 242-243.

Content from this work may be used under the terms of the CC BY 3.0 licence (© 2018). Any distribution of this work must maintain attribution to the author(s), title of the work, publisher, and DOI.

- [4] K.Y. Ng, “Adiabatic Capture and Debunching”, FER-MILAB-FN-0943-APC (2012) 1-11.
- [5] I. Bozsik et al., “ Numerical investigation of bunch-merging in a heavy-ion-synchrotron”, Computing in Accelerator Design and Operation (1983) 128-133.

ROSE - A ROTATING 4D EMITTANCE SCANNER

M. Maier, L. Groening, C. Xiao, GSI Helmholtzzentrum für Schwerionenforschung GmbH,
 64291 Darmstadt, Germany

A. Bechthold, J. Maus, NTG Neue Technologien GmbH & Co. KG, 63571 Gelnhausen, Germany

Abstract

The detector system ROSE [1][2], allowing to perform 4D emittance measurements on heavy ion beams independent of their energy and time structure, has been built and successfully commissioned in 2016 at GSI in Darmstadt, Germany. This method to measure the four dimensional emittance has then been granted a patent in 2017. The inventors together with the technology transfer department of GSI have found an industrial partner to modify ROSE into a standalone, commercially available emittance scanner system. This is a three step process involving the hardware, the electronics and the software working packages. It is planned to have a configurable customer product ready by end of 2020. This contribution presents the actual status and introduces the multiple possibilities of this 4D emittance scanner.

INTRODUCTION

Usually just separated measurements of two-dimensional $x-x'$ and $y-y'$ sub phase-spaces (planes) are measured, as for simplicity correlations between the two planes, i.e. $x-y$, $x-y'$, $x'-y$, and $x'-y'$ are often assumed as zero. However, such inter-plane correlations may be produced by non-linear fields such as dipole fringes, tilted magnets or just simply by beam losses. Figure 1 shows the simulation of a coupled and an uncoupled beam with initially identical projected horizontal and vertical rms-emittances through a solenoid channel. This illustrates the fact that initial coupling influences the final horizontal and vertical beam size.

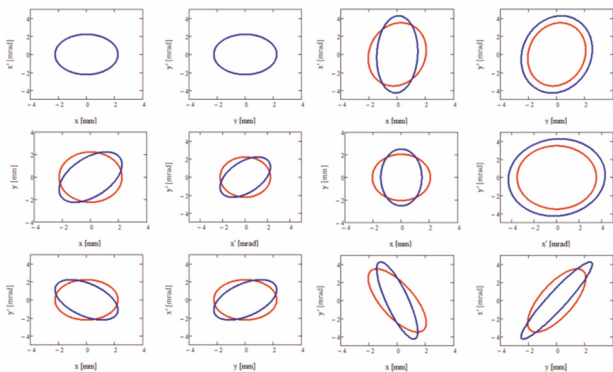


Figure 1: Simulation of an initially uncoupled (red) and coupled (blue) ion beam (left) at the exit of a solenoid channel (right).

For some applications, as for example matching the round transverse phase space of a linac beam Fig. 2 to the flat acceptance of a synchrotron [3], [4], inter-plane correlations are a prerequisite Fig. 3.

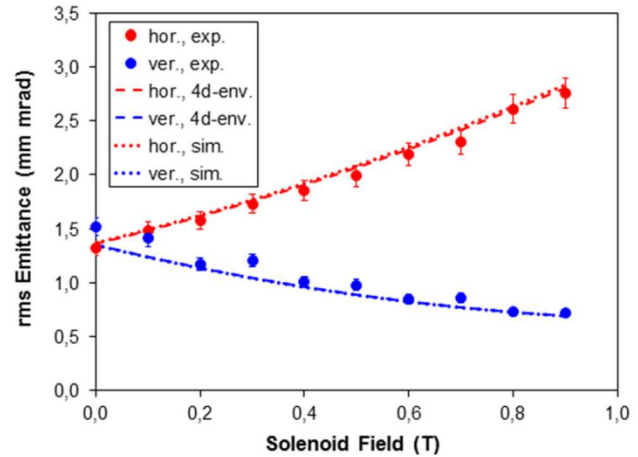


Figure 2: One knob emittance transfer using EMTEX [3].

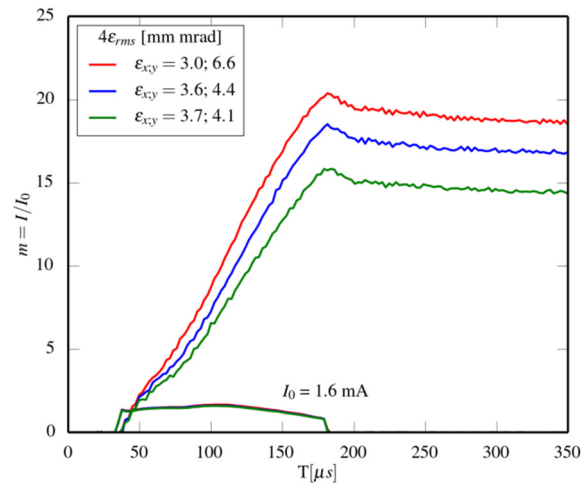


Figure 3: The emittance transfer using EMTEX directly translates in increased injection efficiency into SIS18 [4].

In order to remove correlations that do increase the projected rms-emittance, they must be quantified by measurements. This applies especially if space charge effects are involved as they cannot be calculated analytically. Using the skew triplet of the EMTEX setup we have measured the increase of the projected rms-emittance of a U^{28+} beam with 11.4 MeV/u to be in the order of 75%. Removing this inter-plane coupling could increase the beam brilliance and thus the injection efficiency into SIS18 by 75% [5].

There is considerable work on measuring four-dimensional distributions using pepper-pots [6] - [9] for electron beams or ion beams at energies below 150 keV/u, for which the beam is fully stopped by the pepper-pot mask. However, due to technical reasons this method is not

Content from this work may be used under the terms of the CC BY 3.0 licence (© 2018). Any distribution of this work must maintain attribution to the author(s), title of the work, publisher, and DOI.

applicable at energies above 150 keV/u, i.e., doubtful readout by temperature-dependent screens and fixed resolutions by holes and screens [10].

In the following we report about ROSE, an alternative method to measure the full 4D beam matrix that has been successfully commissioned and is currently modified to become a customer product in industry. This involves three working packages concerning the hard- and software and a stand-alone electronics to become independent of a specific accelerator control system.

ROSE PRINCIPLE

ROSE is a standard slit-grid emittance scanner using only one measuring plane which is rotatable around the beam axis. In combination with a magnetic doublet it allows to determine the full 4D beam matrix C (see Eq. 1) in approximately one hour with a minimum of four emittance measurements at three different angles.

$$C = \begin{bmatrix} \langle XX \rangle & \langle XX' \rangle & \langle XY \rangle & \langle XY' \rangle \\ \langle X'X \rangle & \langle X'X' \rangle & \langle X'Y \rangle & \langle X'Y' \rangle \\ \langle YX \rangle & \langle YX' \rangle & \langle YY \rangle & \langle YY' \rangle \\ \langle Y'X \rangle & \langle Y'X' \rangle & \langle Y'Y \rangle & \langle Y'Y' \rangle \end{bmatrix} \quad (1)$$

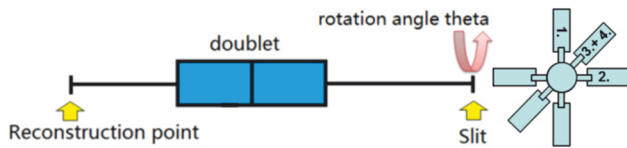


Figure 4: To obtain the beam matrix C at the reconstruction point four emittance values are measured using ROSE behind a magnetic doublet.

As shown in Figure 4 the emittance measurements are done using a magnetic setting (a) for the 0° , 45° , and 90° measurement and another magnet setting (b) for the 45° measurement. Four measurements are sufficient to measure the complete four-dimensional second-moments beam matrix.

1. 0° doublet setting (a)
2. 90° doublet setting (a)
3. + 4. 45° doublet setting (a) and (b)

The method and mathematics of ROSE is described in detail in [2].

DETECTOR SYSTEM – ROSE

A technical drawing of the ROSE detector is shown in Figure 5. The two ports housing the slit and grid mechanics are on opposite sides of the rotating chamber to minimize the torque. The turbo molecular pump is mounted on a separate vacuum chamber that does not rotate. Two gate valves are to separate ROSE from the accelerator vacuum during rotation and for maintenance. The slit and grid geometry is shown in Figure 6. The spatial resolution is given by the slit width of 0.2 mm, while the angular resolution is 3 mrad. If necessary the angular resolution may be increased to 0.3 mrad by using up to 9 intermediate grid steps, yet this lengthens the measurement time. The stepper motor used to rotate the chamber and an encoder to

determine the rotation angle allow for a precision better than half a degree. The disc brake is used to stabilize the chamber during the emittance measurement.

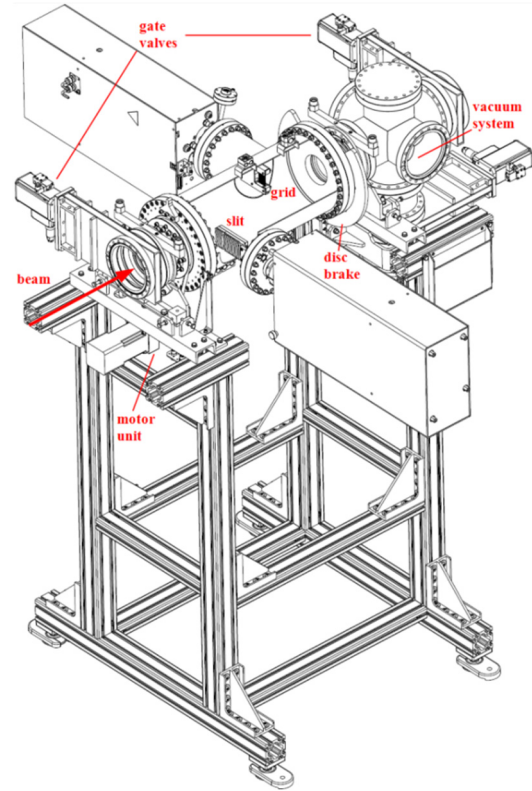


Figure 5: The ROSE detector system. The rotatable slit-grid vacuum vessel and the separate pumping chamber are installed between two gate valves to protect the accelerator vacuum during rotation. To avoid vibration during the measurement a disc brake system clutches the chamber.

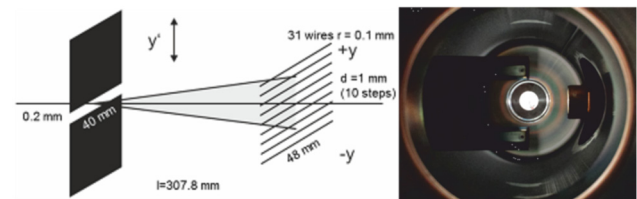


Figure 6: Schematic picture and photo of the slit and grid.

COMMISSIONING RESULTS

Beams of 1.4 MeV/u $^{40}\text{Ar}^{9+}$ and $^{136}\text{Xe}^{19+}$ from the high charge state injector HLI at GSI served to commission the hard- and software of ROSE to benchmark it against existing emittance scanners, and to proof its capability to measure the 4D beam matrix. To achieve this, an emittance scanner park shown in Figure 7 has been used.

It comprises a skew triplet to enforce and modify the coupling, a doublet to achieve the different magnetic settings that are required for the measurement, an existing standard high resolution emittance scanners called Mob-Emi, and ROSE. Throughout the beamline three current transformers and one end cup are used to measure and to ensure full beam transmission.

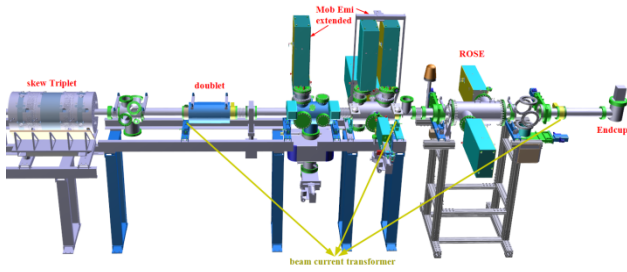


Figure 7: Experimental setup used for commissioning.

To first benchmark ROSE the emittance of a 1.4 MeV/u Ar^{9+} beam from the HLI ECR source has been measured horizontally using the well calibrated emittance scanner MobEmi and ROSE at 90° . To compare the results the emittance measured with MobEmi has been propagated to the ROSE slits. In a second step the horizontal and vertical emittances have been measured with both scanners for different quadrupole duplet settings (a) and (b). The comparison at the entrance of the quadrupole duplet is shown in Figure 8. The measured emittances at 0° (vertical) and 90° (horizontal) are in good agreement for all three emittance scanner set-ups. ROSE has been successfully benchmarked against the MobEmi emittance scanner.

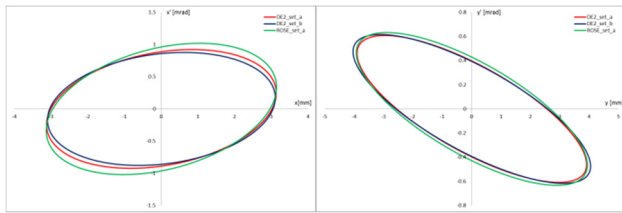


Figure 8: The beam emittance at the quadrupole duplet entrance, determined for different magnetic fields of the quadrupole duplet using ROSE and MobEmi.

To experimentally proof ROSE's capability to measure the 4D transverse beam matrix the inter plane correlations of the HLI of a 1.4 MeV/u Ar^{9+} beam have been measured. As no significant initial correlations were found to be present, controlled coupling of the planes by using the skew triplet has been enforced. Figure 9 shows the measured coupling moments and in Fig. 10 they are compared to the uncorrelated beam at the entrance of the skew triplet. For both skew quadrupole settings a full emittance scan using ROSE has been performed. As the beam parameters transformed back to the entrance of the skew triplet shown in Fig. 11 match very well, the reliability of the ROSE measurements is experimentally proven. The expected effect of the skew triplet has been confirmed with ROSE. Figure 12 shows the obtained eigen-emittances [11] of the HLI Argon beam. Applying error analysis, the obtained eigen-emittances are: $\varepsilon_1 = 2.43$ (0.19) mm mrad and $\varepsilon_2 = 2.04$ (0.17) mm mrad and the corresponding beam matrix C is given in Eq. 2 in mm mrad.

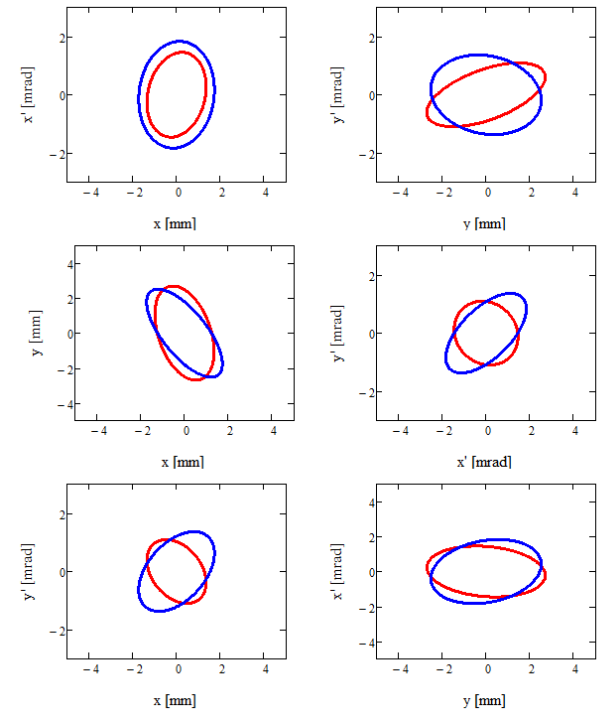


Figure 9: ROSE measurements of a 1.4 MeV/u Ar^{9+} for two different skew triplet settings (red off, blue on).

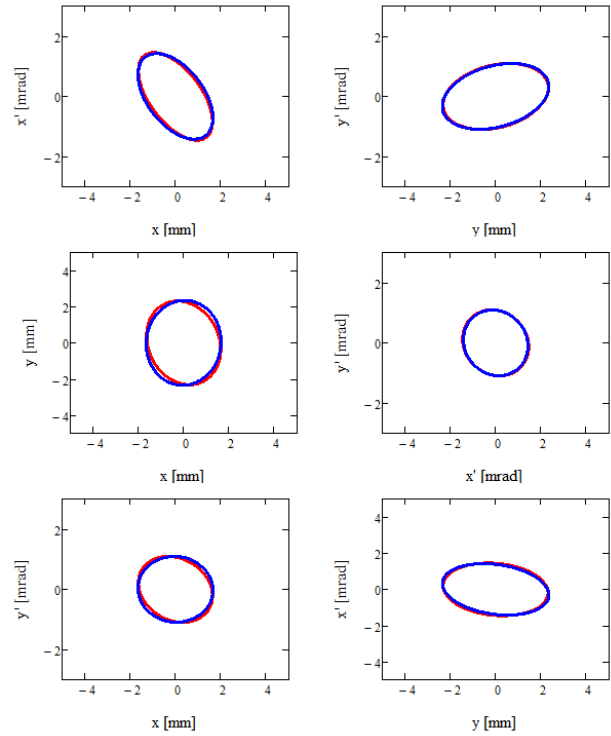


Figure 10: ROSE measurements shown in Fig. 9 transformed back to the entrance of the skew triplet.

$$C = \begin{bmatrix} 8.57 & -4.34 & -3.28 & -1.10 \\ -4.34 & 3.35 & -0.74 & 1.52 \\ -3.28 & -0.74 & 11.20 & -3.05 \\ -1.10 & 1.52 & -3.05 & 1.87 \end{bmatrix} \quad (2)$$

Content from this work may be used under the terms of the CC BY 3.0 licence (© 2018). Any distribution of this work must maintain attribution to the author(s), title of the work, publisher, and DOI.

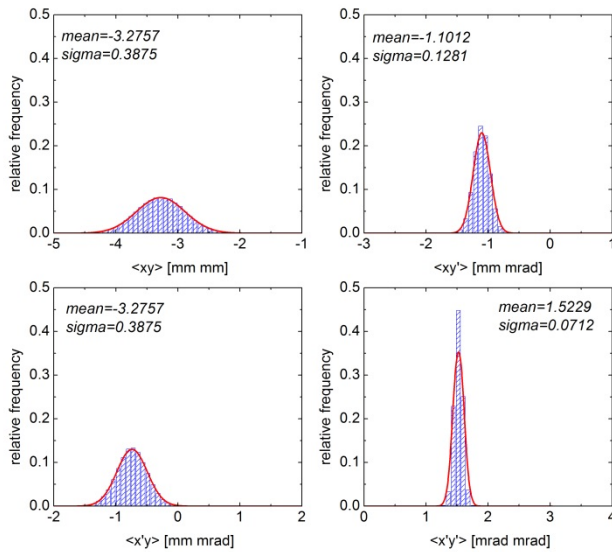


Figure 11: Measured moments with the skew triplet switched on.

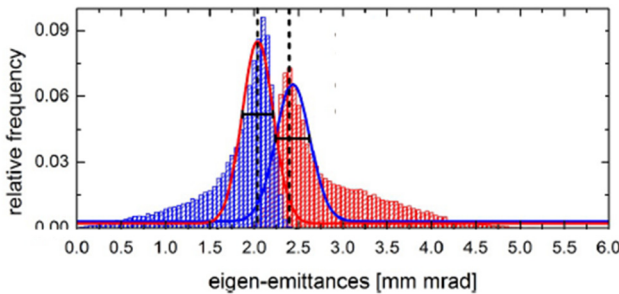


Figure 12: The two eigen-emittances being derived from the measurement of the HLI 1.4 MeV/u Ar⁹⁺ beam.

ELECTRONICS – ROBOMAT

For the commissioning of the prototype of ROSE the GSI control system has been used. However, ROSE as a mobile emittance scanner has to be independent of a specific control system. Thus ROBOMAT [12] was specified as standalone emittance electronics, independent of an accelerator control system to control the ROSE movements, measuring and saving the data as well as monitoring the ion beam current and vacuum conditions in the vessel. ROBOMAT itself has no special 4D feature and is a standard emittance scanner electronics with the additional degree of freedom to rotate the scanner freely around the beam axis. It comprises a housing rack, an integrated Beckhoff industrial PC, on which all the software for controlling the devices, data taking and handling as well as monitoring the interlock status is installed. As the cable length for the grid electronics is limited the user may connect to it via Ethernet. For data taking of the grid currents electronics by Pyramid F3200E has been chosen as it fulfills all requirements in accuracy, speed, and number of channels. It has arrived at NTG as shown in Fig. 13 and is currently prepared, tested and commissioned at NTG.

The three stepper motors and their controllers for moving the emittance slit, grid, and the rotation of the vessel have arrived as well and are shown in Fig. 14.



Figure 13: The grid electronics Pyramid F3200E that will be used has arrived at NTG and is currently prepared, tested and commissioned.



Figure 14: The stepper motor and associated controller units have arrived at NTG and will be integrated into ROSE to replace the GSI systems.

Because of economic and practical reasons NTG has decided to exchange the analog stepper motors of the existing prototype ROSE by a more modern digital type shown in Figure 14. These components have as well already arrived and should be integrated into ROSE by the end of October 2018. The technical details and requirements have been discussed with NTG and the colleges of the GSI beam diagnostics- and the Linac department. This resulted in a list of key features backing the offer of NTG. The key features of ROBOMAT and the different measurement modes are given in the following list.

ROBOMAT is:

- controlling all movements of ROSE,
- performing the emittance measurements,
- capable to measure DC and pulsed beam,
- covering beam currents ranging 10μA - 100mA,
- including ion current measurement,
- storing emittance data in XML format,
- visualizing the emittance measurements,
- handling the multiple internal and external interlock signals e.g.:
 - beam on
 - moving device
 - vessel vacuum pressure
 - slit water cooling
 - gate valve status

The possible measurement modes are:

- **Parallel:** slit and grid are moving in parallel.
- **Angular offset:** slit and grid constant offset.
- **Diagonal:** slit-grid offset as function of position.
- **Intermediate step:** fine extra grid steps to increase the angular resolution.
- **Double grid:** two grid positions to double the grid area
- **Ultrafast:** drive by measurement while moving.
- **Profile grid:** only the grid is in the beam.
- **Background:** measurement without beam.

SOFTWARE – ROSOFT

The software ROSOFT will provide the user with a tool to plan, perform, and evaluate 4D emittance measurements. It is going to be included into the base 2D functionality of ROBOMAT. It is supposed to perform the following actions sketched in Fig. 15 on a user configurable beam line, consisting of regular and skew quadrupoles, drifts and the emittance scanner. The user defines the beamline and maximum magnetic field strength available. Then with all magnets off, the measured horizontal and vertical projection of the beam emittance will be used by the software to calculate optimum settings for the 4d emittance scan which will guide the user through the measurement procedure. Once all required four emittance scans are performed, the software will generate an evaluation report. In case a skew triplet is available the software may suggest magnet settings for the skew triplet to reduce the inter-plane coupling to increase the beam brilliance.

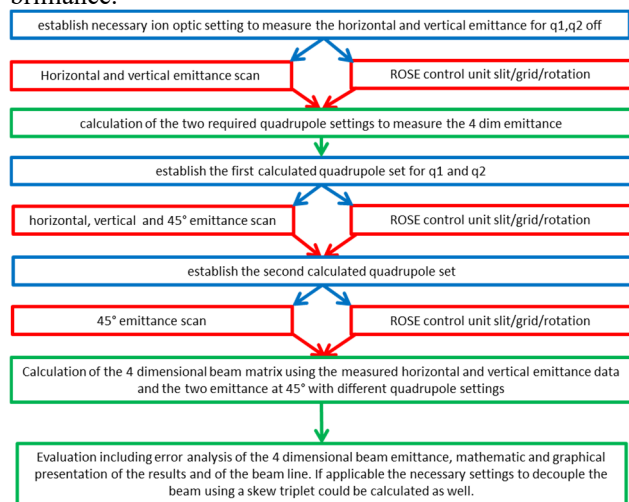


Figure 15: software flowchart: necessary actions within the external accelerator control system in blue, in red ROBOMAT functions and in green the ROSE software interaction.

TIMELINE

As we have a working prototype the next big step is the commissioning of the standalone electronics ROBOMAT which is scheduled for beginning of 2019. To develop a Software package with the full 4d capability will take approximately 2 years. NTG has applied for a third party funding which may be provided by the state of Hessen we

are waiting right now for the positive decision before we can start in this matter. In those two years in parallel to the software programming NTG may improve the hardware of ROSE for example by switching to a 2 chamber system. So we expect to be able to deliver our first customer product end of 2020.

CONCLUSION

We have invented, build and successfully commissioned a 4d-emittance scanner for heavy ion beams independent of their kinetic energy and time structure. We have found an industrial partner and together we are developing a turnkey 4d emittance scanner for the accelerator community. The project has started this year and we expect to have a configurable customer product ready in the end of 2020.

ACKNOWLEDGEMENTS

My special gratitude goes to all GSI staff involved in this project. This includes the technical infrastructure as well as the support in the mathematics and physics tasks. The technology transfer department has been very successful in raising funds and finding an industrial partner. Of course I'd like to thank the company NTG for their interest to realize this project together with us. And we would like to thank the Bundesministerium für Wirtschaft und Energie for the possibility to get third party funding for the development of ROBOMAT.

REFERENCES

- [1] Deutsche Patentanmeldung Nr. 102015118017.0 eingereicht am 22.10.2015 beim Deutschen Patent- und Markenamt Titel der Patentanmeldung: Drehmodul für eine Beschleunigeranlage.
- [2] C. Xiao, M. Maier, X. N. Du, P. Gerhard, L. Groening, S. Mickat, and H. Vormann, "Rotating System for Four-Dimensional Transverse rms-emittance Measurements", Phys. Rev. Accel. Beams 19, 072802 – Published 19 July 2016.
- [3] L. Groening, M. Maier, C. Xiao, L. Dahl, P. Gerhard, O.K. Kester, S. Mickat, H. Vormann, and M. Vossberg, "Experimental Proof of Adjustable Single-Knob Ion Beam Emittance Partitioning" Phys. Rev. Lett., 113, (2014) 264802.
- [4] S. Appel, L. Groening, Y. El Hayek, M. Maier, C. Xiao, Injection optimization through generation of flat ion beams: Nucl. Instr. and Meth. A 866, 36-39 (2017), DOI: 10.1016/j.nima.2017.05.041
- [5] C. Xiao, L. Groening, P. Gerhard, M. Maier, S. Mickat, H. Vormann, "Measurement of the Transverse Four-Dimensional Beam rms-Emittance of an Intense Uranium Beam at 11.4 MeV/u: NIMA 2016, doi: 10.1016/j.nima.2016.02.090
- [6] S. Kondrashev *et al.*, Nucl. Instrum. Methods Phys. Res., Sect. A 606, 296-304 (2009).
- [7] H.R. Kremers, J.P.M. Beijers, and S. Brandenburg, in Proc. DIPAC'07, Venice, Italy, pp.195-197.
- [8] T. Nagatomo, V. Tzoganis, M. Kase, O. Kamigaito, and T. Nakagawa, Rev. Sci. Instrum. 87, 02B920 (2016).

- [9] J.G. Wang *et al.*, *NIM A* 307, p. 190, (1991).
- [10] P. Forck, GSI, (Private Communication).
- [11] A. J. Dragt, General moment invariants for linear Hamiltoniansystems, *Phys. Rev. A* 45, 2572 (1992).
- [12] gefördert durch: Bundesministerium für Wirtschaft und Energie.

PRESENT STATUS OF AND RECENT DEVELOPMENTS AT RIKEN RI BEAM FACTORY

H. Okuno*, T. Dantsuka, M. Fujimaki, N. Fukunishi, H. Hasebe, Y. Higurashi, E. Ikezawa, N Ikoma, H. Imao, O. Kamigaito, M. Kidera, M. Komiyama, K. Kumagai, T. Maie, M. Nagase, T. Nagatomo, T. Nakagawa, M. Nakamura, J. Ohnishi, K. Ozeki, N. Sakamoto, K. Suda, U. Uchiyama, S. Watanabe, T. Watanabe, Y. Watanabe, K. Yamada, H. Yamasawa,
 RIKEN Nishina Center, Wako, Japan

Abstract

The Radioactive Isotope Beam Factory (RIBF) is a cyclotron-based accelerator facility that is used for nuclear science studies and was completed at the end of 2006. RIBF can produce the most intense RI beams using fragmentation or fission of high speed heavy ion beams. Ever since the first beam was produced, effort has focused on increasing the intensity of uranium beams. Ions beams with high intensity and high availability have been used to produce many important scientific achievements. Upgrade programs have been proposed to further expand scientific opportunities. These programs have two goals. The first goal is to find heavier elements than element 118, which is already named. The upgrade program for the heavy ion linac (RILAC), including installation of a superconducting linac, has been funded and is under construction. The second goal is to increase the intensity of uranium ion beams up to $1 \mu\text{A}$, thus facilitating further investigations into the physics of unstable nuclei. This program for uranium beams is still been unfunded. We are pursuing a budget-friendly version without changing the project goals.

INTRODUCTION TO RI BEAM FACTORY

The Radioactive Ion Beam Factory (RIBF) is a cyclotron-based accelerator facility that uses fragmentation or fission of heavy ion beams to produce intense radioactive ion (RI) beams over the entire atomic range [1]. RIBF is used to explore the inaccessible region of the periodic table, to discover the properties of unstable nuclei, and advance knowledge in nuclear physics, nuclear astrophysics, and applications of rare isotopes for society. The RIBF facility consists of four cyclotron rings (RRC [2], FRC [3], IRC [4], and SRC [5]) with three injectors, including two linacs (RILAC [6, 7] and RILAC2 [8]) and one AVF cyclotron (AVF) [9]. Cyclotrons cascades can provide heavy ion beams from H_2^+ to uranium ions at more than 70% of the speed of light to efficiently produce RI beams. Three acceleration modes are available, as shown in Fig 1. The first mode is primarily used for mid-heavy ions, such as Ca, Ar, and Zn. The second mode is used for light ions, such as O and N. The third mode is used for very heavy ions such, as Xe and U. Of course many researchers use beams from the injectors. For example, synthesis of super heavy elements uses beams from RILAC,

while beams from the AVF cyclotron are used for RI production. Table 1 lists the specifications of the four ring cyclotron in RIBF. RRC has been operating since 1986. FRC and IRC have structures similar to that of RRC. The weight per K-value is listed in the table, which clearly shows that FRC is very compact compared to the other cyclotrons. Obtaining an acceleration voltage of 640 MV for uranium acceleration up to energy of 345 MeV/u is the most challenging with SRC. Design and construction of RIBF accelerators began in 1997, and we obtained the first beam at the end of 2006.

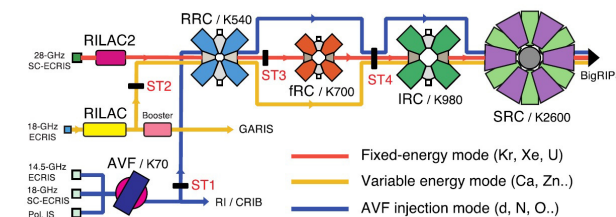


Figure 1: Acceleration modes for RIBF facility.

Table 1: RIBF cyclotron specifications. * in the table indicates that the values are shown for the case of uranium acceleration up to 345 MeV/u.

	RRC	fRC	IRC	SRC
K-value (MeV)	540	700	980	2600
R_{inj} (cm)	89	156	277	356
R_{ext} (cm)	356	330	415	536
Weight (ton)	2400	1300	2900	8300
K/W	0.23	0.54	0.34	0.31
N_{sec}	4	4	4	6
rf Resonator	2	2+FT	2+F	4+FT
Frequency range (MHz)	18–38	54.75	18–38	18–38
Total Acc. Volt. (MV)	2	2+FT	2+F	640
Acc. Volt. (MV/turn)*	0.28	0.8	1.1	2.0
Δr (cm)*	0.7	1.3	1.3	1.8
I_{sc} (μA)*	1.8	11.2	3.7	2.6

* okuno@riken.jp

SUCCESSFUL OPERATION FOR TWELVE YEARS

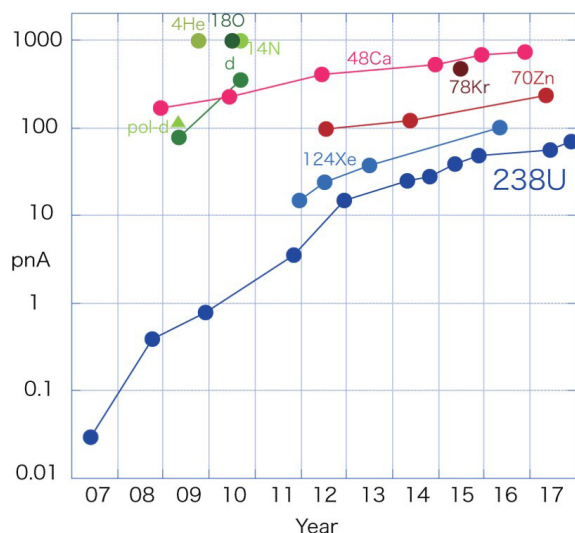


Figure 2: History of beam intensities at the RIBF accelerator.

Operations over approximately twelve years following production of the first beam were very successful. Our continuous efforts have increased the beam intensity, especially for very heavy ions like Xe and U, as shown in Fig 2. The currently available beam intensity of uranium ion is 71 pA, which is the world record. The beam availability has improved significantly, exceeding 90% since 2013. Such a supply of beams with high intensity and high availability have facilitated many important scientific achievements, such as obtaining the naming rights of element 113 [10], discovering 106 kinds of new isotopes [11], discovery of anomalies in magic numbers of neutron-rich nuclei [12], and cross section measurements of long lived fission products [13].

To many measures were taken to improve the accelerator performance, including upgrading the ion source and adding two charge strippers for uranium beam acceleration as follows. A 28 GHz ECR ion source using superconducting solenoids and sextuple magnets was constructed because powerful ion sources are essentially required to increase the uranium beam intensity [14, 15]. The operation of this ion source on the beam line started from 2011 with the new injector linac (RILAC2). Currently, approximately 150 $e\mu\text{A}$ of U^{35+} can be stably extracted with a high-temperature oven. Charge strippers are important devices for increasing the intensity of the uranium beam because they have a high risk of bottleneck problems due to their fragility against high-power beams. After much research and development [16, 17], we developed a new stripping system based on helium gas [18] for the first stripper and a new rotating disk stripper with a highly-oriented graphene disk for the second stripper [19]. These have worked well so far.

Here we summarize the lessons learned from operating RIBF. First, it is very difficult to operate an accelerator complex where four cyclotrons are connected in series, because

one must inject and extract the accelerated beams four times. Energy matching between the cyclotrons and single turn extraction requires the greatest care and effort. Second, multi-step charge stripping should be avoided, because charge stripping reduces beam intensity at every step due to charge dispersion. Furthermore, the thickness of the charge strippers should be as thin as possible because charge strippers are always sources of emittance growth. Third, the space charge effect in the low energy cyclotron (RRC) is very severe because of the low velocity and low RF voltage. Table 1 lists the space charge limit for the four cyclotrons in the case of uranium beam acceleration according to Baartman's paper [20]. The table clearly shows that the space charge limit in the RRC is small compared to the current required to reach 1 μA at the exit of SRC. The final point is that approximately 20% of the current from the ion source can reach the exit of SRC, excluding the charge stripping efficiency, as shown in Fig 3. This value is not particularly large, yet it is still large compared to that of other accelerators. In fact, 10 mA from the ion source is extracted to obtain 3 mA from the ring cyclotron in the case of the PSI machine. However, it is very important to understand beam loss mechanisms to improve and reduce uncontrolled beam loss.

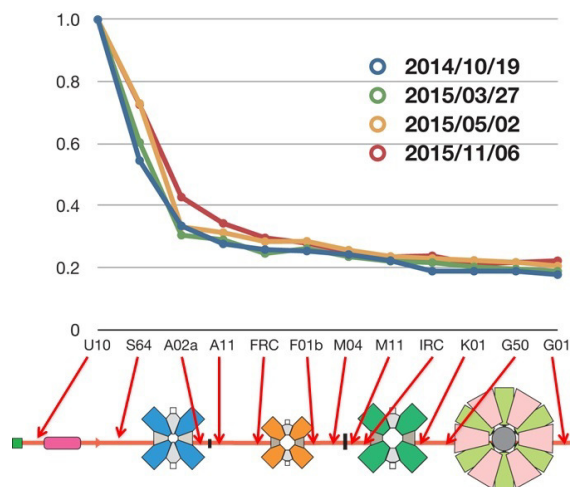


Figure 3: Transmission in the RIBF accelerator complex.

UPGRADE PLAN OF RIBF

Based on the lessons learned and scientific achievements described in the previous section, we define upgrade plans aimed towards the two following goals. The first goal is to obtain a 1 μA uranium beam with energy of 345 MeV/u. The second is synthesis of super heavy elements, such as 119 and 120.

The program consists of three primary components for achieving these two goals, as shown in Fig 4. The first stripper is skipped to avoid beam intensity reduction due to charge dispersion after the beam passes through the stripper. This requires replacement of the existing FRC with a new one that can accept the same charge (35+) as that of the ion source, while the existing FRC can accept 64+. Skipping

Content from this work may be used under the terms of the CC BY 3.0 licence (© 2018). Any distribution of this work must maintain attribution to the author(s), title of the work, publisher, and DOI.

the first stripper will improve the beam quality, especially in the longitudinal direction, because charge-exchange energy straggling in the first stripper is significant. This affects the extraction efficiency at the subsequent cyclotrons. The second component involves resolving problems relating to the space charge effect in the low energy cyclotron (RRC), which requires the RRC cavity be remodeled to obtain higher RF voltage. The third component focuses on an upgrade of RILAC by adding a superconducting RF linac, with the goal of producing medium-mass nuclei beams with higher current for the super heavy element program. The following subsection will describe the details and status of these three components.

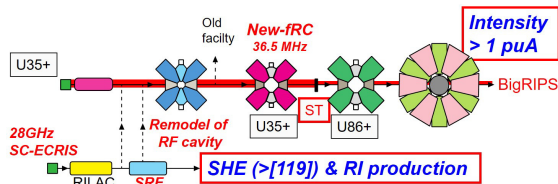


Figure 4: Upgrade plans for the RIBF accelerator complex.

Superconducting RILAC [21]

RILAC consists of an RFQ and 12 DTLs to provide intense heavy ion beams to search for super heavy elements (SHEs). $^{70}\text{Zn}^{14+}$ was accelerated to 5 MeV/u to search for element 113. The SHE experiment is used to probe the 8th row of the periodic table ($A \geq 119$). The accelerating voltage will be upgraded to provide more intense heavier ion beams with higher energy. The goal of the upgrade is to accelerate ions ($A/q = 6$) up to 6.5 MeV/u. The last four DTL tanks in the existing RILAC will be replaced with a superconducting linac that are based on quarter wave resonators. Figure 5 shows the structure of the new superconducting RILAC that consists of three cryomodules, including 4 or 2 superconducting cavities with a liquid helium transfer line. The differential pumping system in the narrow space is very important because the vacuum in the existing linac is ineffective compared to the vacuum required in superconducting cavities. Table 2 lists the SRILAC specifications required to produce an overall acceleration voltage of 18 MV for $A/q = 6$. This project was funded in 2016 and its construction is in progress. Six of ten bulk cavities were successfully validated so far (as of 2018/10/23), exhibiting high Q_0 values compared to the SRILAC goals. Construction will end by the end of March 2019. SHE researchers who cannot wait for completion have started searching for element 119 using RILAC2+RRC this year. This will continue until the completion of SRILAC.

Remodel of RRC RF Cavities

Figure 6 shows the structure of the RF resonator in the RRC. This structure is basically a half wave resonator. A pair of movable boxes in the cavity are used to tune the resonance frequencies by changing the capacitance from 18 to 40

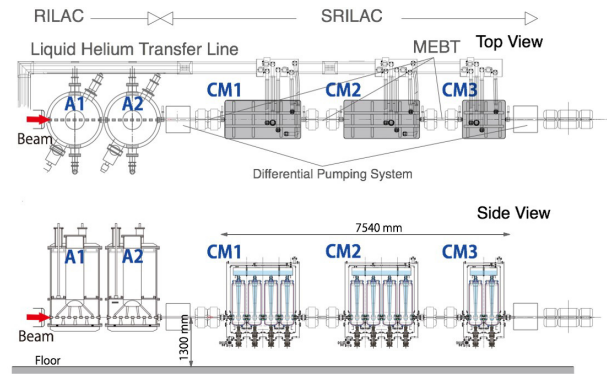


Figure 5: Plan view of SRILAC.

Table 2: SRILAC Specifications

Design Parameters	
Number of cavities	10 QWRs
Frequency (MHz)	73.0 (c.w.)
E_{inj} (MeV/u)	3.6
E_{ext} (MeV/u)	6.5
Gap Voltage (MV)	1.2
Synchronous Phase (deg.)	-25
E_{acc} (MV/m)	6.8
Target Q_0	1×10^9 at 4.5K
Beam Current (μA)	<100
RF bandwidth (Hz)	± 60
Q_{ext}	$1 - 4.5 \times 10^6$
Amplifier Output Power (kW)	7.5

MHz. At the lowest frequency of 18.25 MHz, gaps between the movable box and the Dee electrodes are so close that discharge occurs frequently at higher voltages. The slanted stem in Fig. 7 widens the gaps at 18.25 MHz, making it possible to apply a higher voltage. This remodel is complete and this cavity is operating at 120 kV, thus increasing the space charge limit in the RRC.

Conceptual Design of the New FRC [22]

Figure 8 shows a plan view of the new FRC, and the main specifications are listed in Table 3. The new FRC contains six sector magnets and its K-value is 2200. Four accelerating RF cavities and a flattop cavity are used. The RF acceleration frequency is 36.5 MHz, which is the same as that of RILAC2. This provides wide acceptance in the longitudinal direction. The structure of the RF resonators will be similar to that used in the RIBF accelerator. We can obtain a 15 mm turn separation using similar RF cavities as those used in the RIBF accelerators. This structure looks like a standard ring cyclotron, except for the heavy weight (8000 tons). Unfortunately the budget is not approved.

Content from this work may be used under the terms of the CC BY 3.0 licence (© 2018). Any distribution of this work must maintain attribution to the author(s), title of the work, publisher, and DOI.

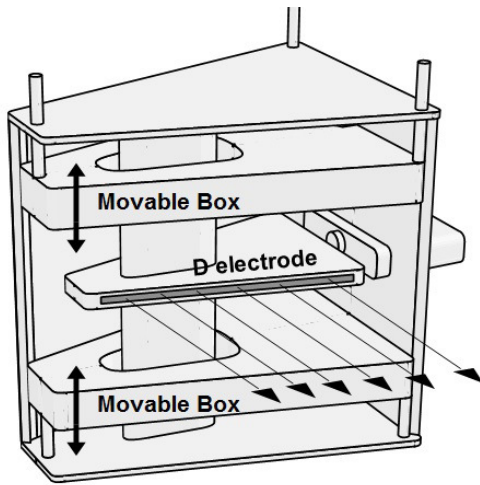


Figure 6: Structure of an RF resonator in the RRC.

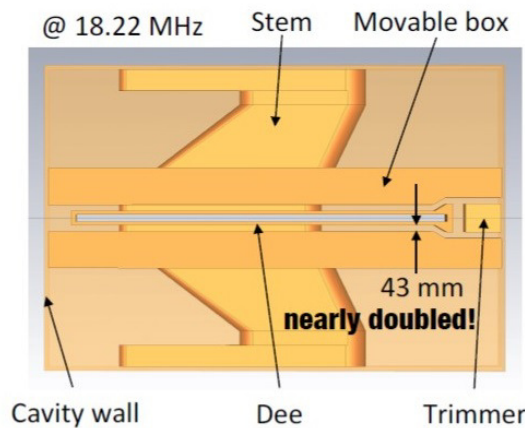


Figure 7: Effective voltages for three harmonics.

Table 3: Specification of the new FRC. The number in parentheses in the weight row is the weight estimated by cutting the edge of the yoke, where iron is not saturated.

Item	new FRC	existing FRC
K-value (MeV)	2200	700
Sectors	6	4
RF Cavities	4+FT	2+T
RF Frequency (MHz)	36.5	54.75
Injection radius (m)	2.76	1.56
Extraction radius (m)	5.67	3.30
Velocity gain	2.1	2.1
Diameter (m)	19	10.8
Height (m)	6.6	3.34
Weight (ton)	8100 (7100)	1320
Δr (cm)*	1.5	1.3

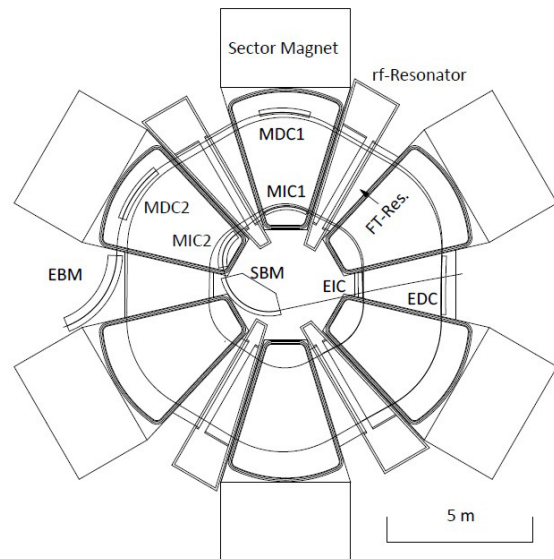


Figure 8: Plan view of new FRC.

BUDGET-FRIENDLY VERSION OF THE UPGRADE PROGRAM

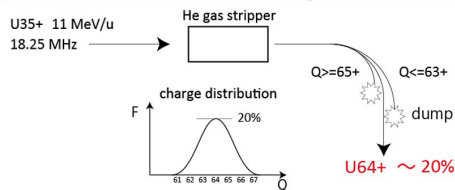
Until the budget for the new FRC is approved, we are pursuing a budget-friendly version of the upgrade program without deviating from the 1 pμA uranium beam goal. The first candidate for upgrade is the charge stripper ring. The goal is to increase the stripping efficiency up to 100%. The second candidate is the high brightness ion source with low charge.

Charge Stripper Ring [23]

20% ~ 30% of ions injected into the charge stripper can survive the normal stripping system due to their charge distribution, as shown in Fig. 9. The total charge conversion efficiency for RIBF is about 6% because RIBF strips charges in two steps for acceleration of uranium ions. FRIB [24] aims to provide an effective efficiency of 85% using multi charge acceleration [25] in the linac, which has large acceptance in the longitudinal direction. The proposed charge stripper ring (CSR) can recycle ions with charge states that do not match the objective charge state until they reach the objective charge, as shown in Fig. 9. Installation of two CSRs in the RIBF accelerator complex could provide a stripping efficiency of nearly 100%.

Figure 10 shows a plan view of the CSR optimized for the second charge stripper at 50 MeV. The ring consists of an isometric ring with quadruple array, charge stripper, and RF cavities for energy compensation. This structure will preserve the bunch structure in order to match to the acceptance of subsequent cyclotrons. Careful analysis of transverse and longitudinal motion in the CSR is underway to minimize emittance growth due to the installation of this ring.

Present scheme at RIBF (conventional)



Stripper-ring scheme

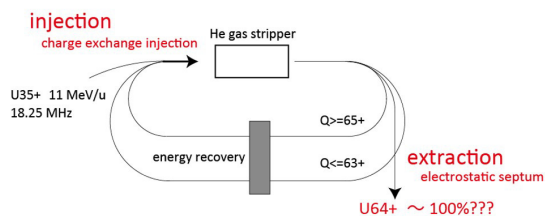


Figure 9: Concept of the charge stripper ring.

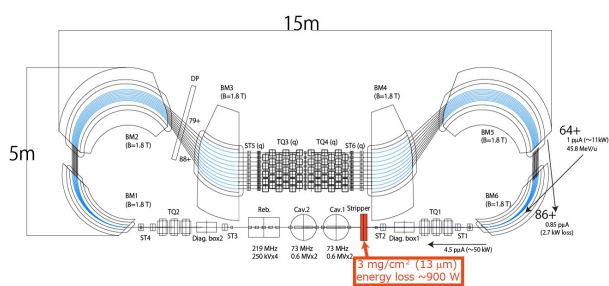


Figure 10: Plan view of the charge stripper ring.

Low Charge Ion Source with High Brightness

The next candidate is the low charge ion source with high brightness. In this idea, the accelerators after the RRC remain unchanged, as shown in Fig.11. Only the input current from the ion source increases up to 1 pμA. Generally speaking, beam emittance from the ion source increases as the beam intensity from the ion source increases. We need a high brightness ion source in order to maintain total transmission through subsequent accelerators. To achieve this goal, we are studying the use of ion sources with such charges as low as 10+, which require another stripper and decelerator. Figure 12 shows a very primitive design of the ion source. This is an EBIS-based ion source. 1+ ion generated by the electron beam in this cell travels with the electron beam to the extraction electrode. The electron density and voltage at the intermediate extraction point are tuned such that the charge state is 10+.

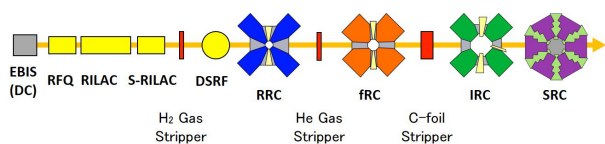


Figure 11: Accelerator scheme for the low charge ion source.

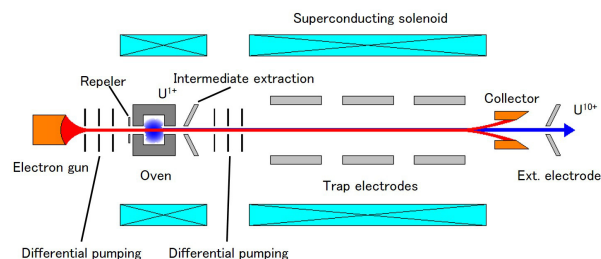


Figure 12: Conceptual design of the DC EBIS for low charge uranium ions.

SUMMARY AND OUTLOOK

Successful operation and many important scientific achievements motivate us to upgrade the RIBF accelerator complex. The first portion of the upgrade program is the installation of a superconducting linac, with the goal of synthesizing superheavy elements (119 and 120). The budget for the SRILAC was approved by the government. Construction will end by March 2019. The other portions involve increasing the space charge limit in the low energy cyclotron in the RRC and skipping the first stripper, requiring replacement the existing FRC. The RF cavities in the RRC were remodelled to increase the space charge limit; this remodel is now complete. The budget for the new FRC has not been approved. Thus, we are pursuing a budget-friendly version of the upgrade program that focuses on upgrading the charge stripper ring and low charge ion source with high brightness.

REFERENCES

- [1] Y. Yano, Nucl. Instrum. Methods Phys. Res., Sect. B 261 (2007) 1009.
- [2] Y. Yano, Proc. 13th Int. Cyclo. Conf. (1992) 102.
- [3] T. Mitsumoto et al., Proc. 17th Int. Conf. on Cyclotrons and Their Applications, (2004) 384.
- [4] J. Ohnishi et al., Proc. 17th Int. Conf. on Cyclotrons and Their Applications (2004) 197.
- [5] H. Okuno et al., IEEE Trans. Appl. Supercond., 17, (2007) 1063.
- [6] M. Odera et al., Nucl. Instrum. Methods A227 (1984) 187.
- [7] O. Kamigaito et al., Rev. Sci. Instrum. 76 (2005) 013306.
- [8] K. Yamada et al., IPAC2012, New Orleans, Louisiana, USA, TUOBA02 (2012).
- [9] A. Goto et al., Proc. 12th Int. Cyclo. Conf. (1989) 51, 439.
- [10] K. Morita et al., J. Phys. Soc. Jpn 81, 103201 (2012).
- [11] Y. Shimizu et al., J. Phys. Soc. Jpn. 87, 014203 (2018).
- [12] D. Steppenbeck et al., Nature 502, 207 (2013).
- [13] H. Wang et al., Progress in Theory and Experiment Physics 2017,021D01 (2017).
- [14] T. Nakagawa et al., Rev. Sci. Instrum. 81 (2010) 02A320.
- [15] Y. Higurashi et al., Rev. Sci. Instrum. 83 (2012) 02A308.

Content from this work may be used under the terms of the CC BY 3.0 licence (© 2018). Any distribution of this work must maintain attribution to the author(s), title of the work, publisher, and DOI.

- [16] H. Kuboki, et al., Phys. Rev. ST Accel. Beams 13 (2010) 093501.
- [17] H. Okuno, et al., Phys. Rev. ST Accel. Beams 14 (2011) 033503.
- [18] H. Imao, et al., Phys. Rev. ST Accel. Beams 15 (2012) 123501.
- [19] H. Hasebe, et al., INTDS2016, Cape town (2016).
- [20] R. Baartman, Proc. 20th Int. Conf. on Cyclotrons and Their Applications (2013) WE2PB01.
- [21] N. Sakamoto et al., Proc. LINAC2018 (2018) WE2A03.
- [22] H. Okuno et al., Proc. 21th Int. Conf. on Cyclotrons and Their Applications (2016) MOA01.
- [23] H. Imao et al., Proc. IPAC2018 (2018) MOZGBE1.
- [24] J. Wei et al., Proc. LINAC2016 (2016) MO1A01
- [25] P.N. Ostroumov et al., Phys. Rev. ST Accel. Beams 3, 030101 (2000).

DEVELOPMENT OF RIKEN 28 GHz SC-ECRISs FOR SYNTHESIZING SUPER-HEAVY ELEMENTS

T. Nagatomo[†], Y. Higurashi, J. Ohnishi, A. Uchiyama, M. Fujimaki, K. Kumagai, N. Fukunishi, N. Sakamoto, T. Nakagawa, and O. Kamigaito, Nishina Center for Accelerator-based Science, RIKEN, Wako, Saitama 351-0198, Japan

Abstract

Production of intense metallic ion beams were required at RIKEN to synthesize new elements with atomic numbers higher than 118. To meet this requirement, we systematically studied the optimization of RIKEN 28 GHz SC-ECRIS performance. Using these results, we produced V^{13+} ion beam of 400 μA at ~ 2 kW microwave power (18+28 GHz) and a B_{ext} (maximum magnetic mirror field at the beam extraction side) of 1.4 T. For long-term operation, we successfully produced an intense and stable beam (100–200 μA). To progress this project, new super-conducting RF cavities are now under construction downstream of the RIKEN heavy-ion linac (RILAC) to increase beam energy. In this project, we also constructed a new 28 GHz SC-ECRIS based on these results to increase beam intensities. In addition, three sets of movable slits were installed in the low energy beam transport (LEBT) to inject the high-quality beam into the upgraded RIKEN heavy-ion LINAC (RILAC) to control the size of the transverse emittance of the beam.

INTRODUCTION

After synthesizing a super-heavy element (with an atomic number of 113), a new project was started at RIKEN for synthesizing a new element with an atomic number higher than 118 [1, 2]. For this project, intense, highly charged metallic ion beams, using ions such as Titanium (Ti^{13+}), Vanadium (V^{13+}), and Chromium (Cr^{13+}), were required. To progress the project, the RIKEN heavy-ion linac (RILAC) is up-graded by adding new super-conducting ratio frequency (RF) cavities. In this project, we also constructed a new SC-ECRIS for increasing beam intensity.

The up-graded RILAC is also used as an injector accelerator for the RIKEN radioactive isotope beam (RIBF) project [2, 3]. To accelerate the heavy ion beam for RIBF, the ion source has to provide it with a mass to charge state ratio smaller than three (e.g., $^{48}Ca^{16+}$ and $^{70}Zn^{24+}$). High electron density (n_e) and long confinement time (τ_i) in the ion source plasma are required to produce these highly charged, heavy ions. Using a crude calculation [4], the required $n_e \tau_i$ for $^{48}Ca^{16+}$ ion production was in the order of 10^9 (sec/cm³), which is one order of magnitude larger than the required $n_e \tau_i$ for the $^{51}V^{13+}$ ion (in the order of 10^8 (sec/cm³)). Therefore, it was necessary to design an ion source that could provide the optimum condition to cover a wide range of $n_e \tau_i$ in the ion source plasma.

In the last three decades, two guidelines (scaling laws [4, 5] and high B mode [6-8]) have been proposed and used to design and develop ion sources. Scaling laws were proposed to describe the effects of the main ion source parameters (microwave power, magnetic field strength, microwave frequency, mass of heavy ions, etc.) on the output beam of highly charged heavy ions. These studies reported that the strength of the magnetic mirror affects the optimum charge state (i.e., a higher mirror ratio yields higher output ion beam charge states). In the middle of the 1990s, the high-B mode, which employs a high magnetic mirror ratio to confine the plasma, was proposed to increase the beam intensities of highly charged heavy ions. To meet the requirement for the project, we systematically studied the effects of a magnetic mirror on beam intensity based on these guidelines.

It was clear that we need to produce enough metallic vapor to produce an intense beam. In addition, high transmission efficiency in the low-energy beam transport line (LEBT) was required for efficient operation of the ion source. Considering these points, we constructed and developed an ion source, a high temperature oven (HTO), and a LEBT for this project.

In the second and third sections of this contribution, the results of optimization of the ion source performance and the metallic ion beam production with HTO are described. In the fourth section, we present the structure of the LEBT and the first results from the new ion source.

OPTIMIZATION OF THE MAGNETIC MIRROR

In the test experiments for magnetic mirror effects, we used two different types of ion sources, Liquid-He-free SC-ECRIS [9] and RIKEN 28 GHz SC-ECRIS [10]. The RIKEN 28 GHz SC-ECRIS has six solenoid coils to produce a flexible mirror magnetic field in the axial direction, and it can produce both classical and flat B_{min} [11].

Generally, as an ECRIS has three magnetic mirrors (B_{inj}/B_{min} , B_r/B_{min} , and B_{ext}/B_{min}) (B_{inj} , maximum magnetic mirror field at the microwave injection side; B_{ext} , maximum magnetic mirror field at the beam extraction side; B_r , the radial magnetic field; and B_{min} , minimum strength of the mirror magnetic field), various combinations of the magnetic mirrors can exist to produce a beam of highly charged heavy ions. Therefore, we needed to carefully study the effects of the magnetic mirror to maximize beam intensity. Figure 1 a) and b) show the normalized beam intensities as a function of B_{inj}/B_{ext} and B_r/B_{ext} with the RIKEN 28 GHz SC-ECRIS (18 and 28 GHz microwaves) and the Liquid-He-free SC-ECRIS (18 GHz microwaves).

[†]nagatomo@riken.jp

Content from this work may be used under the terms of the CC BY 3.0 licence (© 2018). Any distribution of this work must maintain attribution to the author(s), title of the work, publisher, and DOI.

The beam intensity of various charge state heavy ions produced with our ECRISs appeared saturated at $B_r=1-1.2B_{ext}$ and $B_{inj}=1.6-2.0B_{ext}$. The results of RIKEN 28 GHz SC-ECRIS appear similar to the results from the Liquid-He free SC-ECRIS. These results are well-reproduced with high B mode operation (B_{inj}/B_{ext} was ~ 2.0 and B_r/B_{ext} was ~ 1.0) [8].

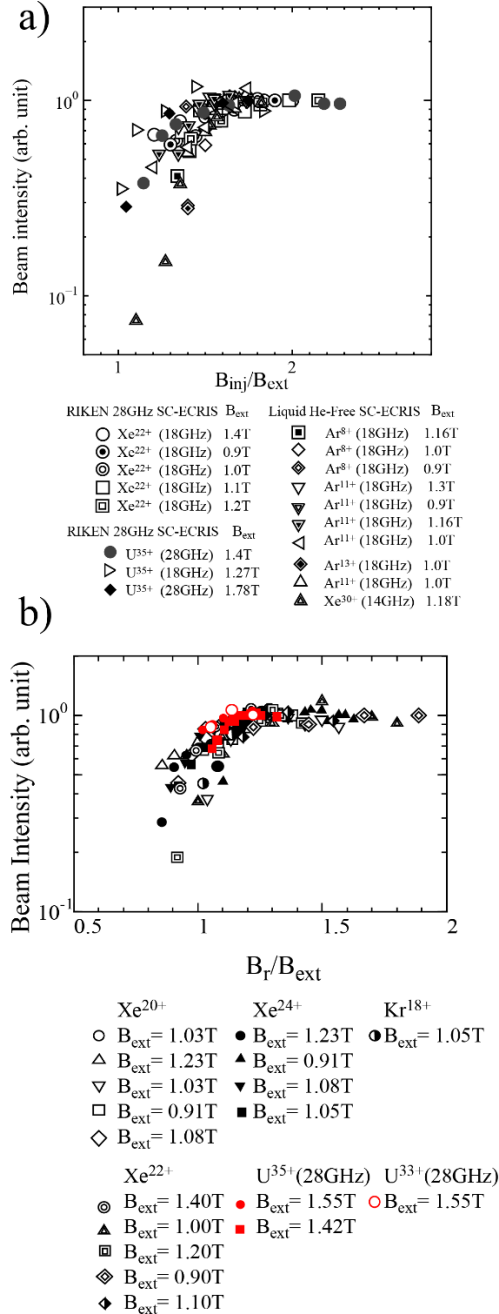


Figure 1: a) Beam intensity of highly charged heavy ions as a function of B_{inj}/B_{ext} and b) beam intensity of highly charged heavy ions as a function of B_r/B_{ext} .

To study the relationship between B_{ext} and B_{inj} (or B_r) in more detail, we provided two-dimensional contour maps (B_r vs. B_{ext} and B_{inj} vs. B_{ext}) for the beam intensity of Xe²²⁺ produced with the RIKEN 28 GHz SC-ECRIS (18 GHz

microwaves injection) (Fig. 2 a) and b)). In these figures, red and blue colors indicate the highest and lowest beam intensities, respectively. B_{min} was set to ~ 0.5 T, which is the optimum strength for maximizing the beam intensity with 18 GHz microwave injection. The extraction voltage and the microwave power were 21 kV and ~ 500 W, respectively. The gas pressure and biased disc condition (negative voltage and position) were changed slightly to maximize beam intensity at the measurement points. In this experiment, we observed that the gas pressure for maximizing beam intensity increased with increasing magnetic field strength. Beam intensity increased with increasing both B_r (or B_{inj}) and B_{ext} , and it became constant above a certain value of magnetic field strength (Fig. 2). To maximize beam intensity, B_r and B_{ext} were ~ 1.5 and ~ 1.2 T, respectively (Fig. 1 a)). The corresponding B_{inj} and B_{ext} values were ~ 2.2 and ~ 1.2 T, respectively (Fig. 1 b)).

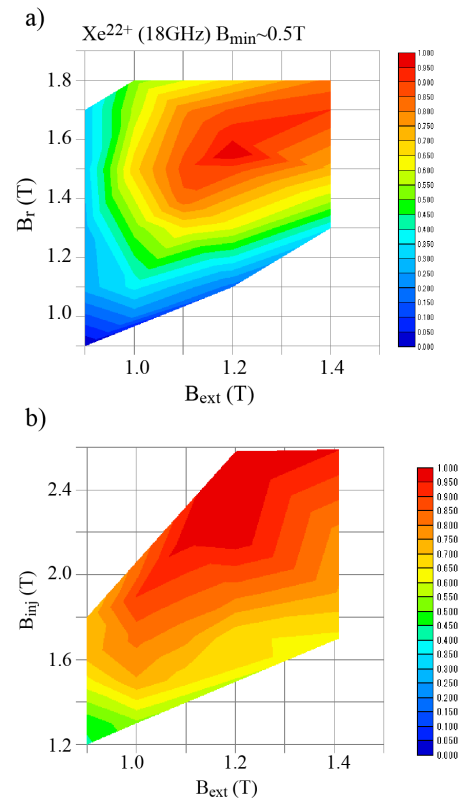


Figure 2: Two-dimensional contour maps (a) B_r vs. B_{ext} and b) B_{inj} vs. B_{ext} for the Xe²²⁺ ion beam.

To investigate the effect of B_{ext} on beam intensity, we measured the optimum B_{ext} for various charge states of Ar and Xe ions with 18 and 28 GHz in the same procedures shown in Fig. 2. As the beam intensity was gradually changed as a function of magnetic field strength, it was difficult to accurately determine the B_{ext} causing beam intensity saturation. Therefore, we chose, as a reference, a B_{ext} that provided ~ 95 % of the maximum beam intensity. We observed that B_{ext} , which provided ~ 95 % of the maximum value (optimum B_{ext}) for highly charged Xe ions, increased from ~ 1.2 to ~ 1.6 T when the charge state increased from

22 to 30. We also observed the same tendency for the highly charged Ar ions with the Liquid-He-free SC-ECRIS. The optimum B_{ext} increased from ~ 1.1 to ~ 1.25 T when the charge state increased from 8 to 13 for the Ar ions.

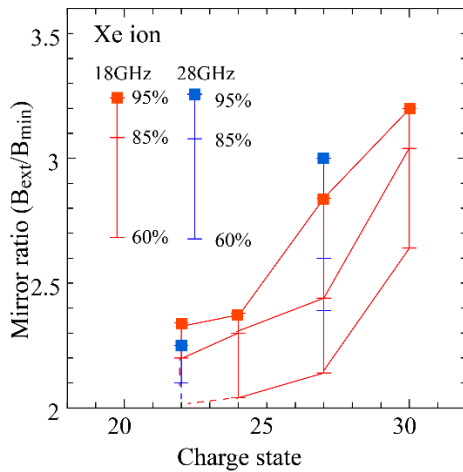


Figure 3: Magnetic mirror ratio ($B_{\text{ext}}/B_{\text{min}}$) as a function of the charge state for Xe ions with 18 and 28 GHz micro-waves.

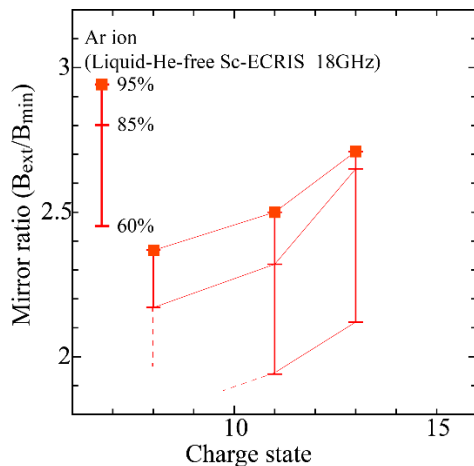


Figure 4: Magnetic mirror ratio ($B_{\text{ext}}/B_{\text{min}}$) as a function of the charge state for Ar ions.

As described in refs. [4, 5], the optimum charge state depends on the mirror ratio when B_{min} is fixed. Figure 3 and 4 show the mirror ratio ($B_{\text{ext}}/B_{\text{min}}$) that provides $\sim 95\%$ of the maximum beam intensity as a function of the charge state of Xe and Ar ions. The results for Xe and Ar ions were obtained from the two-dimensional contour maps (B_r vs. B_{ext} and B_{inj} vs. B_{ext} , respectively). $\sim 85\%$ and $\sim 60\%$ of the maximum beam intensity were also plotted in these figures as a reference. The mirror ratio for the optimum B_{ext} increased from ~ 2.2 to ~ 3.2 with increases in the charge state of the Xe ions. We observed the same tendency for the Liquid-He-free SC-ECRIS when the mirror ratio increased from ~ 2.3 to ~ 2.7 when the charge state increased from 8 to 13. These results were qualitatively reproduced by the scaling law. These experimental results were obtained for a low microwave power density (below several 100 W/L).

We might observe a different tendency at a higher RF power (i.e., 1 kW/L).

METALLIC ION BEAM PRODUCTION

As mentioned in the introduction, since the $n_e \tau_i$ for V^{13+} ions is in the order of 10^8 (sec/cm³), it is assumed that the V^{13+} ions are in the same region ($n_e \tau_i$) as the Xe^{24-27+} ions. As described in ref. [4, 12, 13, 14], $n_e \tau_i$ depends on the mirror ratio. Therefore, from the results shown in Fig. 3, the magnetic mirror ratio ($B_{\text{ext}}/B_{\text{min}}$) for the V^{13+} ions was assumed to be 2.2–2.7. If we chose a B_{min} of 0.6 T for 28 GHz, which is the optimum value for maximizing the beam intensity, the optimum B_{ext} might be 1.3–1.6 T. In the test experiment, we observed that the beam intensity decreased slightly when B_{ext} decreased from 1.6 to 1.4 T. On the bases of these results, we chose $B_{\text{ext}}=1.4$ T in this test experiment.

For production of the vapor, we used the HTO [15]. For long-term operation, we fabricated a new crucible, which had approximately twice the volume of the old crucible [16]. To obtain a sufficient temperature for evaporating the materials, a detailed simulation was carefully performed, and a sufficiently high temperature was obtained to produce the vapor. The detailed results are presented in ref. [15]. Enough metallic vapor should be provided to maximize beam intensity. To optimize the vapor pressure, we measured the beam intensity as a function of oven power at a fixed microwave power, as shown in Fig. 5. The beam intensity increased with increasing oven power and it seems that the intensity was saturated at the highest oven power. We used the same procedure at each microwave power.

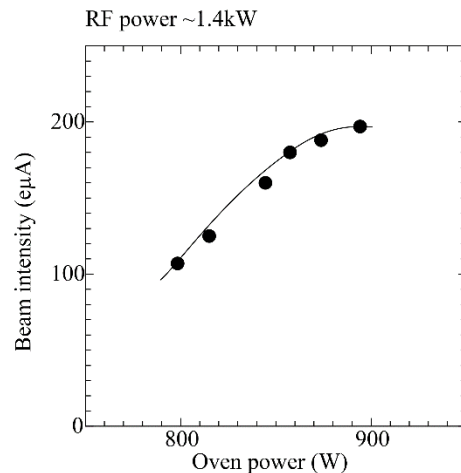


Figure 5: Beam intensity of the V^{13+} ions as a function of oven power at a microwave power of ~ 1.4 kW.

Figure 6 shows that beam intensity and X-ray heat load as a function of microwave power for $B_{\text{ext}} = 1.4$ T. We used the double frequencies injection (18 GHz (maximum power of several 100 W) + 28 GHz) [17] for producing the stable beam. Both the beam intensity and heat load increased with increasing microwave power. At ~ 2 kW we obtained 400 eµA of V^{13+} ions, and the X-ray heat load was ~ 1.2 W, which was sufficiently low for safe operation of

Content from this work may be used under the terms of the CC BY 3.0 licence (© 2018). Any distribution of this work must maintain attribution to the author(s), title of the work, publisher, and DOI.

the ion source. Figure 7 shows the oven power required to maximize beam intensity at each microwave power. The oven power increased linearly with increasing microwave power. The consumption rate of the material was ~ 2.4 mg/h for lower microwave power (~ 1.2 kW), which was sufficiently low to operate the ion source for a long time.

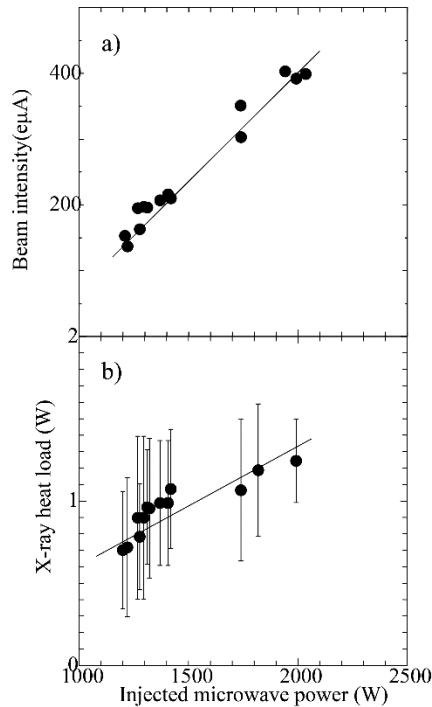


Figure 6: a) Beam intensity of the V^{13+} ions as a function of microwave power and b) X-ray heat load in the cryostat as a function of microwave power.

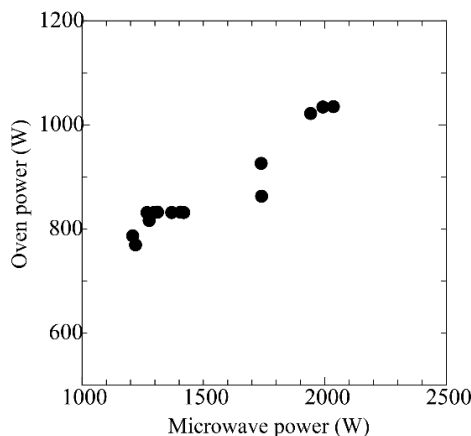


Figure 7: Optimum oven power as a function of microwave power.

For long-term operation, we successfully produced an intense beam (100–200 eμA) of V^{13+} ions. However, we wanted to improve the HTO's performance at higher material consumption for long-term operation, as described in ref. [15].

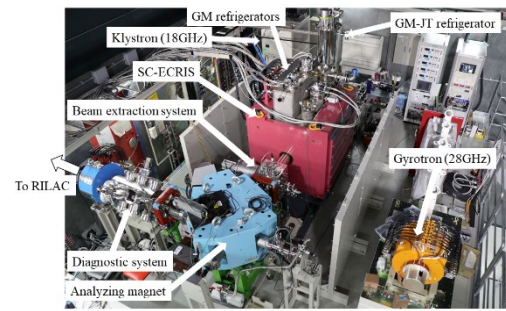


Figure 8: Photograph of the 28 GHz SC-ECRIS.

NEW ION SOURCE AND LEBT

As mentioned in the introduction, the ion source was required to provide a plasma condition of $n_e \tau_i \sim 10^9$ (sec/cm³) to produce Ca^{16+} ions, which is the same order magnitude of $n_e \tau_i$ for Xe^{30+} . To meet this requirement, the mirror ratio (B_{ext}/B_{min}) should be greater than 3. If we chose $B_{min}=0.6$ T for 28 GHz, the optimum B_{ext} may be higher than 1.8 T. Therefore, we decided to construct the same type of ion source as RIKEN 28 GHz SC-ECRIS because the existing ion source could provide a high enough magnetic field for production of both Ca^{16+} and V^{13+} ion beams. In addition, as each ion source could provide the same condition, we could easily apply the results from one ion source to the other ion source. Figure 8 shows a photograph of the ion source installed on the platform of the ion source room. The ion beam produced with the ion source was injected into the radio frequency quadrupole (RFQ) linac installed in the next room through the LEBT.

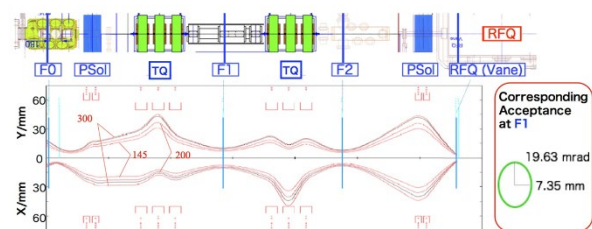


Figure 9: Schematic drawing of the LEBT (upper) and calculated results of beam trajectories (lower).

The detailed structure of the LEBT and its first results are described in ref. [18]. The LEBT consists of several quadrupole magnets, diagnostics systems, and focusing solenoid coils, as shown in Fig. 9. The lower figure shows the calculated trajectories of the ion beam, which had emittances of 145, 200, and 300 π mm*mrاد. The average of four root mean square emittances of the V^{13+} ion beam was ~ 200 π mm*mrاد in the test experiments. It was assumed that most of the produced beam was transported in the LEBT. Furthermore, for safe operation of the intense beam in the long-term, it was important to minimize beam loss

in the accelerators. Therefore, we install the emittance slits (Fig. 10, left) at the beam focus point (F1 in Fig. 9), which shape the beam in the phase spaces (x - x' and y - y'), as shown in the light figure of Fig. 10.

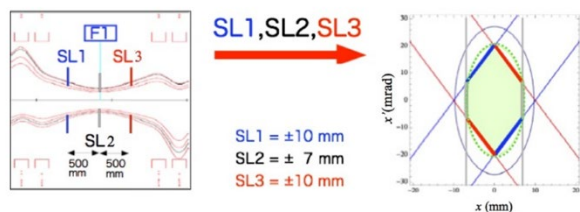


Figure 10: Schematic drawing of the emittance slits (left) and the shape of the emittance cut-off with slits (right).

In July 2018, we extracted the first beam from the ion source. The beam intensity of Ar^{11+} was $90 \mu\text{A}$ at an extraction voltage of 15 kV and an injected microwave power of 600 W. From this autumn, 28 GHz microwaves will be injected into the ion source to further increase beam intensity.

CONCLUSIONS

We systematically studied the effect of the magnetic mirror ratio on beam intensity of various charge state heavy ions with 18 and 28 GHz microwaves. The beam intensity was saturated at $B_{\text{inj}}=1.6-2.0B_{\text{ext}}$ and $B_r=1-1.2B_{\text{ext}}$, which was similar to operation of the high B mode. The optimum B_{ext} to maximize beam intensity depended on the charge state of the heavy ion. It was qualitatively reproduced by the scaling law. We produced an intense V^{13+} ion beam based on our systematic study, and we obtained $400 \text{ e}\mu\text{A}$ of the V^{13+} ion beam with a microwave power of $\sim 2 \text{ kW}$ and a B_{ext} of 1.4 T. For long-term operation, we produced $100-200 \text{ e}\mu\text{A}$ of V^{13+} ions with the new HTO. We used

these results to construct the new ECRIS with the same structure as the existing SC-ECRIS and LEBT. In July 2018, we successfully extracted $90 \mu\text{A}$ of Ar^{11+} ions from the new ECRIS at a microwave power (18 GHz) of 600 W.

REFERENCES

- [1] K. Morita, *Proceedings of the 14th International Symposium on Nuclei in the Cosmos (NIC2016)*, JPS Conf. Proc. 14, 010004, 2017.
- [2] O. Kamigaito et al., *Proceedings of IPAC2016*, Busan, Korea, TUPMR022.
- [3] Y. Yano, *Nucl. Instrum. Methods B261*, 1009, 2007.
- [4] R. Geller, *Electron Cyclotron Resonance Ion Sources and ECR Plasmas*, Institute of Physics, Bristol, 1996, and references therein.
- [5] R. Geller et al., *Proc. 8th Int. Conference on ECR Ion Sources and Their Applications*, NSCL report MSUCP-47, MSU, Dec. 1987, p.1.
- [6] T. Antaya and S. Gammino, *Rev. Sci. Instrum.* 65, 1723, 1998.
- [7] S. Gammino et al., *Rev. Sci. Instrum.* 67, 4109, 1996.
- [8] D. Hitz et al., *Rev. Sci. Instrum.* 73, 509, 2002.
- [9] T. Kurita et al., *Nucl. Instr. and Meth. B* 192, 429, 2002.
- [10] Y. Higurashi et al., *Rev. Sci. Instrum.* 85, 02A953, 2014.
- [11] G. D. Alton and D. N. Smithe, *Rev. Sci. Instrum.* 65, 775, 1994.
- [12] K. Golovanivsky, *Instrum. Exp. Tech.* 28, 989, 1986.
- [13] R. Post, *The course and workshop on Phys. of mirrors*, Vienna, Italy, 1987.
- [14] N. Itagaki, et al., *J. Plasma Fusion Res. SERIES*, 4 305, 2001.
- [15] J. Ohnishi et al., to be published in *Proc. of ECRIS2018*, Catania, Italy, 10-14 Sep 2018.
- [16] J. Ohnishi et al., *Rev. Sci. Instrum.* 87, 02A709, 2015.
- [17] Z.Q. Xie, and C.M. Lyneis, *Rev. Sci. Instrum.* 66, 4218, 1995.
- [18] T. Nagatomo et al, to be published in *Proc. of ECRIS2018*, Catania, Italy, 10-14 Sep 2018.

HIGHLY CHARGED ECR ION SOURCE DEVELOPMENT AT IMP*

L. Sun[†], W. Lu, J. W. Guo, L. X. Li, Z. Shen, L. B. Li, W. Huang, X. Z. Zhang, H. Y. Ma, Y. Yang, J. Q. Li, Y. Cao, W. H. Zhang, X. Fang, Y. M. Ma, Y. C. Feng, B. M. Wu, W. Wu, L. Z. Ma, H. W. Zhao

Institute of Modern Physics, CAS, Lanzhou, 730000, China

Abstract

Highly charged ECR ion source development plays an important role in the heavy ion accelerators advancement at IMP, such as HIRFL upgrade, heavy ion treatment complex HIMM, future heavy ion facility HIAF, and so on. As requested by those projects, many high performance highly charged ECR ion sources with different technologies have been built, or under development. The representative ion sources are superconducting ECR ion sources SECRAL and recently built SECRAL-II, room temperature LECCR4 ion source with an innovative evaporative cooling method, permanent magnet ECR ion sources of LAPECR series, and a 45 GHz 4th generation ECR ion source FECCR. In this talk, a general review of highly charged ECR ion sources will be presented. The typical performances, operation status, as well as the future developments will be discussed.

INTRODUCTION

Requested by the development of cyclotrons at IMP, Electron Cyclotron Resonance (ECR) ion source had been incorporated to HIRFL dated to the late 1980s, when the first ECR ion source a Caprice type 10 GHz machine was bought from Grenoble, France in 1987 [1]. This ion source was lately modified and became the so called LECCR0 source in the IMP highly charged ECR ion source series. Based on the experience of LECCR0, a 10 GHz ECR ion source that was lately renamed as LECCR1 had been developed and also put into routine operation during the years from 1995 to 2005. Since then, series of LECCR type room temperature ECR ion source have been developed and put into operation for HIRFL successively, which has a fundamental impact to the performance of the facility and multiple discipline scientific goals (Fig. 1). The development of permanent magnet ECR ion sources was started after year 2000. The main goal of this type of compact machine is to prove intense multiple heavy ion beams for industrial applications and small-scale platforms that provide convenient beam time and ion species for users from diversity of fields. The development of superconducting ECR ion source is fundamentally boosted by the needs from the HIRFL upgrade, especially the heavy ion cooler storage ring synchrotron CSR program [2], and the nuclear sciences therein. The first superconducting ECR ion source SECRAL (Superconducting ECR ion source with Advanced design in Lanzhou) is also the 2nd so-called the 3rd generation ECR ion source after the VENUS ion source completed in 2002. Operated typically with the microwave power from a 24 GHz gyrotron generator and an 18 GHz klystron amplifier, SECRAL is one of the most powerful

ECR ion sources with many world records of highly charged heavy ion beam intensities.

This paper will give a brief review of the highly charged ion sources developed by the Ion Source Group at IMP. The typical features and the performances will be given. In the last section of this paper, a general introduction of the new activities towards the 45 GHz ECR ion source FECCR will also be given.

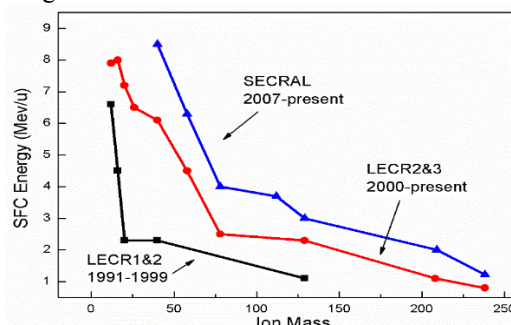


Figure 1: The impact of ion source development to SFC cyclotron performance at HIRFL.

PERMANENT MAGNET ECRIS

All permanent magnet ECR ion sources have many advantages over traditional ECR ion sources composed of several axial room temperature solenoids and one permanent magnet hexapole magnet, which make them the first choice for many heavy ion facilities and platforms. At IMP, three types of all permanent magnet ECR ion sources have been built for diverse applications, i.e. the very compact ECR ion source LAPECR1 for intense mono or multi charge state ion beams' production, the LAPECR2 ion source installed on the 320 kV high voltage multidisciplinary platform [3], and the LAPECR3 ion source dedicated to C⁵⁺ beam production for the cancer therapy facility HIMM [4].

LAPECR1

This ion source is designed with a very compact size of $\varnothing 200$ mm \times 300 mm (including the extraction structure) which makes the source body weighs only 25 kg that can be easily moved around by an adult. Despite of the compactness, the source is equipped with a $\varnothing 40$ mm ID plasma chamber that enables the direct microwave power feeding with a WR62 rectangular waveguide to simplify the injection plug structure. Iron plugs at both the injection and extraction sides have been incorporated to enhance the mirror peaks. The source is designed and operated at 14.5 GHz. Recently a LAPECR1 source has been used for LEAF platform beam commissioning at IMP. With 100~300 W microwave power, 5.0 emA He⁺, 1.5 emA He²⁺, 1.7 emA N²⁺,

*Work supported by CAS (QYDZB-SSW-JSC025), and NSF (contract No. 11427904)

†lun@impcas.ac.cn

160 $\mu\text{A N}^{5+}$, and $\sim 100 \mu\text{A Ar}^{9+}$ have been produced. Fig. 2 shows the picture when LAPECR1 is under commissioning.



Figure 2: LAPECR1 source at test bench.

LAPECR2

LAPECR2 has been built and installed on a 320 kV multi-discipline platform to deliver intense ion beams. Based on the users' requirements, ion beam species from low to high charge states of gaseous or solid elements are required. For the purposes, the source was designed to operate at high magnetic field, high frequency mode with all permanent magnet structure. To produce intense high charge state ion beams, the plasma chamber is intentionally designed as big as possible. A tradeoff between the magnet compactness and the magnetic field strength makes $\varnothing 67\text{mm}$ the final plasma chamber ID value. During the machine commissioning in 2006, the source was fed with maximum 1.1 kW 14.5 GHz microwave power from a klystron amplifier to achieve high power density inside the plasma chamber. For routine operation, a 700 W maximum output TWTA is used as a result of the limited space on the high voltage platform. LAPECR2 is a very powerful permanent magnet ECR ion source. The preliminary performance during source commissioning is given in another paper [5].

LAPECR2 was put into operation on the 320 kV HV multidisciplinary platform in 2007 (shown in Fig. 3). And it has been running on it to delivery various ion beam species for the 6 experimental terminals since then. Up to now, LAPECR2 has been used for routine operation more than 78,000 hours with 53,000 hours on-target beam time. Ion beams from H up to U have been produced. Totally, 13 groups of gaseous elements including H, D, He, C, N, O, Ne, F, Cl, Ar, Kr, and Xe, and ion beams from 14 groups of solid elements including U, Pb, Bi, Au, Ag, Eu, Fe, Ni, Ti, Mg, Cs, I, S, and Li have been delivered. Typically, 11 $\mu\text{A Xe}^{30+}$, 84 $\mu\text{A Ag}^{19+}$, 20 $\mu\text{A Ag}^{24+}$, 6 $\mu\text{A Ag}^{30+}$, 20 $\mu\text{A Bi}^{31+}$, 4 $\mu\text{A U}^{31+}$ and so on have been extracted during routine operation.



Figure 3: LAPECR2 ion source at 320 kV platform.

LAPECR3

Several heavy ion treatment facilities called HMM or Heavy Ion Medical Machine have been initiated in China. The prototyping machines located in Wuwei and Lanzhou have been already started around 2012. The entire facility consists of 2 ECR ion sources, a cyclotron injector, a compact synchrotron and four treatment terminals. For accelerator compactness and lower cost, intense C^{5+} beam from the ECR ion source is needed and pre-accelerated by the cyclotron and injected into the synchrotron with the charge exchange injection scheme. LAPECR3, a permanent magnet ECR ion source operating at 14.5 GHz is developed aiming to be capable of delivering more than 100 $\mu\text{A C}^{5+}$ within the beam emittance of $\leq 75 \pi \cdot \text{mm} \cdot \text{mrad}$ (4 rms). As LAPECR3 is eventually for commercial applications, it should be compact and cost-efficient. The ion source's magnet is mainly composed of the injection magnetic rings, extraction magnetic rings, middle magnetic ring and a 24-segmented Halbach structure hexapole magnet. An iron plug has been employed to boost the injection magnetic field peak to $\sim 1.8 \text{ T}$ which is essential for the high B mode operation for an ECR ion source at 14.5 GHz. Such a magnet can house a $\varnothing 50 \text{ mm}$ ID plasma chamber for intense medium charge state ion beams production.

During source commissioning, C^{5+} ion beam was optimized using CH_4 gas. But beam quality was quite poor as a results of strong space charge effect stemmed from the intense H beams produced as a result of high H proportion in CH_4 . Therefore, C_2H_2 , C_2H_4 , C_3H_8 , C_4H_{10} and so on have been all tried. Among them, C_2H_2 seems to be the best choice in terms of C^{5+} beam intensity and beam quality. But the obvious drawback is the heavy pollution caused by residual carbon. Beam intensity seems to be saturated after 600 W microwave power. About 120 $\mu\text{A C}^{5+}$ beam was produced at 500 W microwave power with CH_4 , and the total drain current was 4.7 emA. Under the same conditions, 262 $\mu\text{A C}^{5+}$ ion beam could be obtained when C_2H_2 was used as the working gas, and the total drain current was 5.5 emA [6]. Totally four LAPECR3 ion sources have been installed and used as the injector ion sources for HMM up to now (Fig 4). The typical routine operation beam currents of 60~70 $\mu\text{A C}^{5+}$ (slightly steered by cyclotron stray fields) have been adopted with the regards of accelerator needs and ion source maintenance service issues. The typical maintenance period is better than 1 month before the plasma chamber is severely contaminated by residual carbon and obvious ion source performance degradation appears.



Figure 4: LAPECR2 ion source on a test bench.

LAPECR series have played important roles in the applications of high charge state ECR ion sources at IMP.

Content from this work may be used under the terms of the CC BY 3.0 licence (© 2018). Any distribution of this work must maintain attribution to the author(s), title of the work, publisher, and DOI.

These 3 types of permanent magnet sources can generally meet a wide diversity of application and scientific program needs. Table 1 gives a general overview of the key parameters of LAPECR series.

Table 1: Comparison of LAPECR Sources

Specs.	LAPECR1	LAPECR2	LAPECR3
ω_{ecr}	14.5 GHz	14.5 GHz	14.5 GHz
Axial Fields	1.3 T*/0.7 T*	1.28 T/1.07 T	1.8 T*/0.9 T
Br	1.1 T	1.2 T	1.1 T
Chamber ID	∅40.0 mm	∅67.0 mm	∅50.0 mm
Mirror Length	78 mm	255 mm	170 mm
Plasma volume	~0.1 L	0.9 L	~0.3 L
U_{max}	~50 kV	~25 kV	~30 kV
Size (mm)	∅204×300	∅650×560	∅450×380
Weight	~25 kg	~650 kg	~157 kg

*with iron plug

ROOM TEMPERATURE ECRIS

Room temperature ECR ion source features one high field hexapole magnet and room temperature solenoids cooled with high pressure deionized water. Bulky iron yokes are usually utilized to minimize stray field and increase the effective mirror fields inside the plasma chamber. As the mirror fields are continuously adjustable, a room temperature ECR ion source can provide optimum magnetic configurations for the operation with microwave frequency from 10 GHz ~18 GHz typically. At IMP, room temperature ion sources of 10 GHz, 14.5 GHz and 18 GHz have been developed over the last 15 years, which is a clear evidence of ECR technology evolution and advancement.

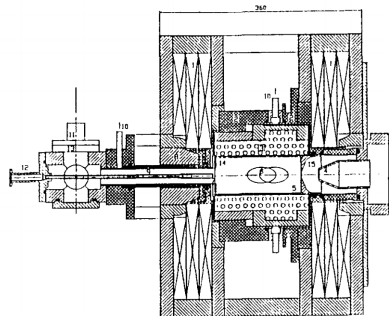


Figure 5: Schematic drawing LECCR1 source.

LECCR1 is still a Caprice type ECR ion source based on the famous 10 GHz Caprice source from CEA/Grenoble. Nevertheless, LECCR1 was not just a duplication of Caprice. Many new ideas and tricks had been tested, and some of them are still widely used among the ECR community. Fig. 5 gives the schematic drawing of LECCR1 source. By moving the plasma electrode position inside the plasma chamber, dependence of ion beam intensities of different charge states on the plasma electrode positions has been demon-

strated. With plasma chamber inner liner, typically an aluminium one, high charge state ion beam yield has been improved. With some tricks on the magnetic structure, B_{min} could be shifted towards the source extraction, which had been verified to be useful for intense beam production. Last but not least, a modified hexapole magnet had been tried as indicated in Fig. 5, and high charge state ion beam intensities had been obviously augmented, which was the first time high B mode applied to LECCR ion source. [7, 8]

The purpose of LECCR2 source was to produce intense ion beams with sufficiently high charge state particularly for heavy elements. This 14.5 GHz ECR ion source was based on the concept of Caprice and GANIL ECR4 [1, 9]. The schematic plot of LECCR2 is shown in Fig. 6. The design of the magnetic field configuration takes into account the latest understanding on the high-B and high frequency modes that are essential to improve the production of highly charged ions. High-B mode had been built with bulky iron yokes surrounding the solenoid pancakes for the axial mirrors, and radially with a very compact and efficient 24-segmented Halbach structure NdFeB hexapole magnet. The traditional diameter and length of the plasma chamber for CAPRICE is about ∅65 mm and 165 mm respectively. The dimensions of the plasma chamber for LECCR2 are ∅70 mm in diameter and 300 mm in length. Higher microwave frequency, bigger plasma volume, and sufficiently high magnetic confinement makes LECCR2 prevailed in intense highly charged ion beams production over LECCR1. Additionally, with a newly developed resistor oven and MIVOC method, metallic ion beams such as Ca^{12+} , Mg^{9+} , Ni^{12+} , Pb^{28+} and so on, could be made with LECCR2 and since then HIRFL was able to deliver to the users metallic beams. [10]

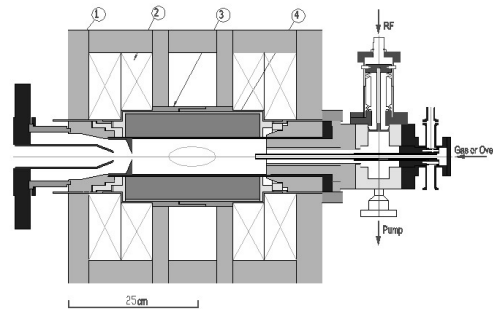


Figure 6: Schematic drawing LECCR2 source.

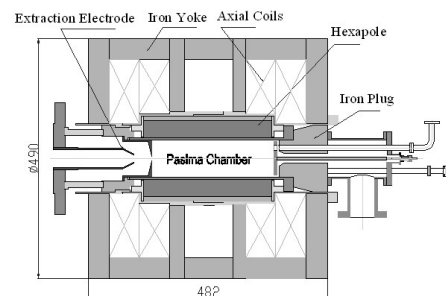


Figure 7: Schematic drawing LECCR3 source.

Inspired by the performance of LECR2, an upgraded version ECR ion source was proposed soon after LECR2 was used for routine operation. Obviously, higher fields and bigger plasma volume are favourable for highly charged ion beam production. LECR3 was designed with higher axial fields and bigger plasma chamber. The success of AECR [11] with a rectangular waveguide as microwave coupling scheme also gave LECR3 design good reference in terms of simpler ion source injection plug design and also sufficient room for iron plug to boost injection field peak. The schematic plot of LECR3 source is shown in Fig. 7. By adopting better NdFeB material with higher remanence and 36-segmented Halbach structure, the hexapole produces 1.0 T at the inner wall of a $\varnothing 76$ mm diameter plasma chamber [12]. LECR3 can produce very high intensity ion beams as well as ion beams of high charge states, for instance 1.1 e mA Ar⁸⁺, 0.5 e μ A Ar¹⁷⁺ and so on.

As LECR3 challenges almost the limit of room temperature technologies with regards to the water cooled copper pancakes that provide the axial mirror fields, we therefore collaborated with IEE/CAS to develop a higher field axial mirror that equips a high performance ECR ion source somehow comparable with an 18 GHz superconducting ECR ion source for intense beam production, such as SECRAL. Typically, the room temperature magnets cooled with de-ionized pressured water can barely work with excitation current density above 10 A/mm². Evaporative cooling method using a proprietary evaporative cooling medium developed by IEE, has some advantages over the conventional de-ionized pressured-water cooling: (1) Pressured de-ionized water free, and (2) average current density up to 12 A/mm² is possible. The detailed technical description can be found in references [13] and [14]. Incorporated with ECR ion source, axial solenoids immersed in Evaporative Cooling medium can provide much higher axial fields that can be optimum for the operation at 18 GHz microwave frequency. Based on this concept, LECR4 was developed based on the joint work between IMP and IEE. Fig. 8 is the layout of the LECR4 test bench. With higher mirror fields, even at a little bit low radial field, this prototyping ion source have produced many inspiring results that can prevail over any room temperature ECR ion sources and even competitive with those achieved with 18 GHz SECRAL.

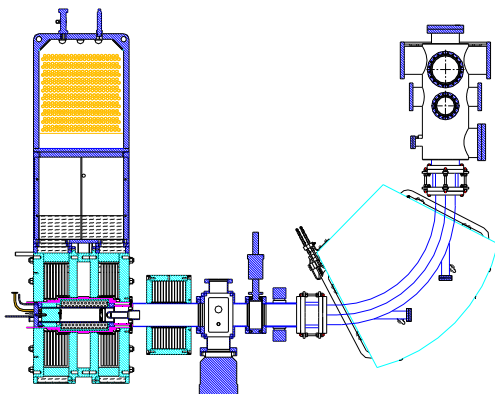


Figure 8: LECR4 source test bench layout.

Table 2 gives a comparison of the LECR series of ion sources. Obviously, the progress of ion source technologies and the understanding towards better performing machine is evidenced. Fig. 9 gives an overview of the ion source performance comparison with Xe ion beam production.

Table 2: Comparison of LECR Sources

Specs.	LECR1	LECR2	LECR3	LECR4
ω_{ecr}	10 GHz	14.5 GHz	14.5 GHz	18 GHz
Fields (T)	1.04 / 0.8	1.5 / 1.0	1.7 / 1.1	2.5 / 1.3
Br (T)	0.8	1.0	1.0	1.0*
Chamber ID	$\varnothing 65.0$ mm	$\varnothing 70.0$ mm	$\varnothing 76.0$ mm	$\varnothing 76.0$ mm
Mirror Length	165 mm	300 mm	300 mm	300 mm
Plasma volume	~ 0.7 L	1.1 L	~ 1.3 L	~ 1.3 L
RF Power	0.5 kW	1.0 kW	1.0 kW	2.0 kW

*with a salvaged hexapole magnet

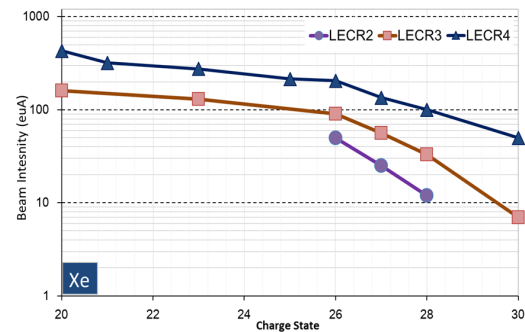


Figure 9: Evolution of Xe beam intensities with room temperature ion sources.

UPERCONDUCTING ECRIS

Superconducting ECR ion sources are representing the state of the art ECR ion source technologies. Typically operated at the microwave frequency of 24~28 GHz, superconducting ECR ion sources can produce ion beam intensities that are several times of an conventional 2nd generation machine. At IMP, the increasing needs of highly charged heavy ion beams to boost the performance of HIRFL, especially the CSR storage ring, are the driving force to build a high performance superconducting source. Two superconducting ECR ion sources have been successively developed at IMP, i.e SECRAL in 2005 and SECRAL-II in 2015.

SECRAL

The design of SECRAL has been optimized for maximum ion source performance at 24-28 GHz microwave frequency for very high charge state heavy ion beam production as well as for developing a compact fully superconducting ECR ion source with a magnet structure which is easier to build without great technical challenge. The fully superconducting ECR ion source SERSE [15] and VENUS

Content from this work may be used under the terms of the CC BY 3.0 licence (© 2018). Any distribution of this work must maintain attribution to the author(s), title of the work, publisher, and DOI.

[16] gave many useful references for design of the 3rd generation ECR ion sources. To satisfy the requirements of running at 24-28 GHz, the magnet of SECRAL should be able to excite on the axis the mirror peaks of more than 3.6 T at the injection side and 2.0 T at the extraction side, and a radial sextupole field more than 2.0 T at plasma chamber wall. Different from the traditional design, such as the VENUS/LBNL, SuSI/MSU [17] and SCECRIS/Riken [18], the axial solenoid coils of the SECRAL magnet are located inside of the sextupole. This innovative magnet structure design of SECRAL reduces the interaction forces between the sextupole coils and the solenoid coils which makes the cold mass clamping much easier and also a more compact structure. Fig. 10 gives the schematic structure of SECRAL cold mass.

To keep the cost within the budget limit, SECRAL magnet was completed with only one-stage cooling system that preserves the thermal shield at 70 K. Without LHe recondensation system, LHe must be refilled every day to keep the cold mass immersed safely inside the 4.2 K liquid. When the source was designed, bremsstrahlung radiation damage to the main insulator was not considered (or fully understood within the ECR community), therefore the lately inserted Ta shield tube made the plasma chamber ID size shrink down from $\varnothing 126$ mm to $\varnothing 120$ mm that makes SECRAL is only optimum for the operation at 24 GHz with regards to the radial field strength inside the plasma chamber. Even so, SECRAL is one of the most powerful ECR ion sources in the world and also the first ion source demonstrated >1 emA Ar^{12+} and >0.5 emA Bi^{31+} [19]. SECRAL was fully on-line for HIRFL operation since 2007, and has provided more than 31,000 hours' beam time for HIRFL with intense highly charged heavy ion beams that essential for HIRFL performance.

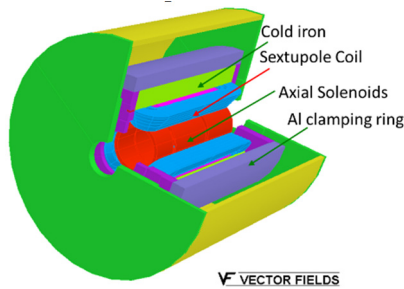


Figure 10: Sketch of SECRAL magnet structure.

SECRAL-II

SECRAL-II magnet is a close copy of SECRAL. The main difference is in the cryogenic system design. The cold mass will be housed in a $\varnothing 817$ mm ID \times 821 mm long LHe tank. Cold mass, LHe and the helium tank all together weighs about 1.54 tons. External to the 4.2 K reservoir, generally two thermal installation stages are designed. The first one is the 60 K copper thermal shield, and the second one is the vacuum buffer between 60 K and room temperature. Evaporated helium gas will be recondensed to LHe by 5 condensers bolted to the 2nd stage of five 1.5 W GM coolers individually. 5 HTS leads are used to minimize the ohmic and conduction heat load between 60 K and 4.2 K

stages. 5 Sumitomo RDK-415 D coolers can provide about 200 W cooling capacity at 60 K that is sufficient for the 60 K thermal shield cooling. A conservative estimate of the total static heat load at 4.2 K is about 1.86 W, which allows a maximum dynamic heat load of 5.64 W according to the calculation and it turned out to be ~ 6.0 W that is sufficient for the routine operation needs of about 5 kW at 28 GHz. Fig. 11 is the sectional plot of SECRAL-II magnet with most of the subsystems integrated. [20]

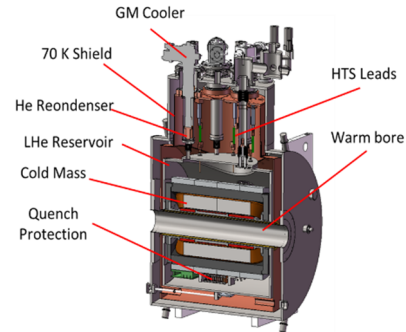


Figure 11: SECRAL-II magnet structure.

Table 3: High Intensity and Highly Charged Ion Beams Production with SECRAL-II

Ion	VENUS 2018	SECRAL 2016	SECRAL-II 2018
$^{16}\text{O}^{6+}$	4750	2300	6700
O^{7+}	1900	810	1750
$^{40}\text{Ar}^{12+}$	1060	1420	1190
Ar^{14+}	840	846	1040
Ar^{16+}	525	350	620
Ar^{17+}	120	50	130
Ar^{18+}	4.0	--	14.6
$^{78}\text{Kr}^{18+}$	770		1030
Kr^{28+}	100		146
Kr^{30+}			20
Kr^{31+}	17		7
Kr^{32+}	8.0		0.5
$^{129}\text{Xe}^{26+}$		1100	
Xe^{30+}		360	365
Xe^{34+}	104	120	102
Xe^{38+}	26	22.6	56
Xe^{42+}	6	12	16.7
Xe^{44+}	2	1	3.9
Xe^{45+}	0.88	0.1	1.3

Robust cryogenic system design enables SECRAL-II to be able to operate at high microwave power. Maximum heated with 12.4 kW microwave power (10 kW@28 GHz + 2.4 kW@18 GHz), this ion source has produced many recorded beam intensities and charge states in recent ion source commissioning. Table 3 lists most of recent results with VENUS@28 GHz [21], SECRAL@24 GHz, and SECRAL-II@28 GHz. As given in the table, emA order ion beams such as Kr^{18+} and so on are achievable now, which is a very important benchmark for next generation heavy ion accelerations composed of either SRF linacs or synchrotrons. Very high charge state ion beams production such as Kr^{3n+} , Xe^{4n+} and so on, has pushed the M/Q dc

beams extracted with an ECRIS from traditionally >4 to presently <3 , which is very attractive to cyclotrons and HCI physics, in terms of machine performance and possible physics investigations. [22]

NEXT GENERATION ECRIS

To meet the highly charged ion beam intensity needs of a next generation heavy ion accelerator, such as HIAF, beam intensity gain by a factor of ~ 2.3 should be made. According to ω_{ecr}^2 scaling, the next generation ECRIS is desired to be operated at $\omega_{ecr} = (2.3)0.5 * 28 \sim 43$ GHz. At IMP, a 45 GHz ECRIS is under construction with this guiding rule. To make an ECR ion source optimum for operation at the frequency of 45 GHz, magnetic fields of two mirror maxima 6.5 T and 3.5 T at source injection and extraction sides respectively, >3.2 T at the ion source plasma chamber wall are desired. For this purpose, approximately $1500 \text{ A/mm}^2 @ 12 \text{ T}$ will be seen inside the superconductor, which will only be made with state of the art superconductors, such as Nb_3Sn , YBCO or Bi-2212. With regards to the technology maturity and cost, Nb_3Sn is so far the feasible choice. Table 4 gives the typical parameters of a 45 GHz ECR ion source.

Table 4: Typical Parameters of FEER Magnet

SPECS.	UNIT	FEER
Frequency	GHz	45
Mirror Fields	T	$\geq 6.4/3.2$
B_{rad}	T	≥ 3.2
Mirror Length	mm	~ 500
Magnet coils	/	Nb_3Sn
Conductor J_c	A/mm^2	$>1500 @ 12\text{T}$
Cooling Capacity	W	≥ 10.0

ity@4.2 K

Supported by LEAF (Low Energy heavy ion Accelerator Facility) project, which is mainly composed by a 45 GHz ECR ion source FEER, a 300 kV high voltage platform, LEBT, a 4-vane 81.25 MHz 0.5 MeV/u CW RFQ L-RFQ [23] and MEFT, a prototype 4th generation ECR ion source is under construction at IMP. Several critical challenges are foreseen and need corresponding solutions, i.e. i. the 45 GHz Nb_3Sn magnet, ii. 45 GHz/20 kW microwave power transmission and coupling for efficient ECRH, iii. strong bremsstrahlung radiation and the resultant issues, iv. intense beam extraction and transmission, v. high power operation with long term stability and reliability. A collaboration work between ATAP/LBNL and IMP has given a feasible design of the FEER cold mass based on bladder and keys assembly (Fig. 12) [24]. A cryogenic system design with 6 KDE-422 cryocoolers from a domestic company Nanjing Cooltech will provide $\sim 13 \text{ W}$ cooling power at 4.2 K state, which is promising for medium power operation at 45 GHz according to our estimate. A 45 GHz/20 kW gyrotron system from GyCOM Inc. has already been delivered to IMP. It has not only been used for long-time stability test, but also connected to SECRAL-II test bench for high power coupling PoP test and intense beam production. Once energized at full power, FEER is believed to deliver

a total current of 20–40 emA for heavy ion beams. As heavy ions have relatively low velocity given the same acceleration voltage, space charge effect will be apparent in such a beam transmission system. A four-electrode extraction system with the ion source floated at 50 kV potential is considered in the draft design. Challenges in v. are still open to the researchers, even for a 3rd generation ECR ion source. Very efficient cooling to the plasma surroundings and understanding of the behaviour of intense hot plasma (electrons) might help to mitigate the problems during high power operation. A 1/2 sized prototyping cold mass of FEER is under development at IMP. It will demonstrate the technologies of Nb_3Sn coils fabrication, bladder & key assembly, active quench protection power supply system and ms order quench detection system.

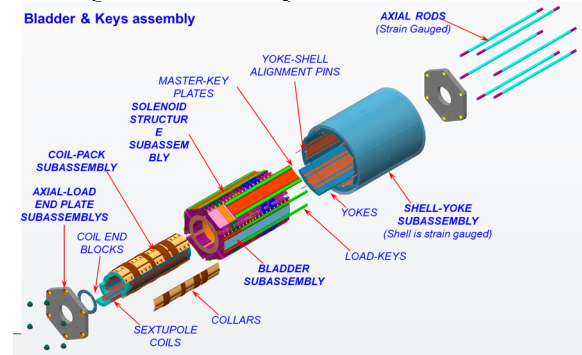


Figure 12: Explosive picture of FEER cold mass.

CONCLUSION

Boosted by the nuclear sciences and applications in China, highly charged ECR ion sources have got remarkable progress in the last 20 years. Typically, more than 5 types of ion sources can provide the highly charged ion beam solutions for versatile needs. For the heavy ion facilities development in China, there are at least 3 higher performance ECR ion sources to be completed in the coming 3 years, among them FEER is the most challengeable one.

ACKNOWLEDGEMENTS

We acknowledge the fruitful collaboration work on FEER cold mass design between ATAP/LBNL and IMP. The intense R&D work on Nb_3Sn prototyping made with IMP and XSMT colleagues is also warmly acknowledged.

REFERENCES

- [1] B. Jacquot and M. Pontonnier, "The new 10 GHz CAPRICE source - Magnetic structures and performances", in *Proc. 10th Int. Workshop on ECR Ion Sources*, ORNL, USA, Nov. 1990, pp.133, CONF-9011136 (1990).
- [2] J. W. Xia *et al.*, "The heavy ion cooler-storage-ring project (HIRFL-CSR) at Lanzhou", *Nucl. Instr. Meth. A*, vol. 488, pp. 11-25, 2002, doi.org/10.1016/S0168-9002(02)00475-8.
- [3] X. Ma *et al.*, "A Progress Report of 320 kV Multi-Discipline Research Platform For Highly Charged Ions", *Journal of Physics: Conference Series* 163 (2009) 012104, doi:10.1088/1742-6596/163/1/012104.
- [4] J. C. Yang, J. Shin, W. P. Chai, J. W. Xia, Y. J. Yuan, Y. Li, "Design of a compact structure cancer therapy synchrotron",

- Content from this work may be used under the terms of the CC BY 3.0 licence (© 2018). Any distribution of this work must maintain attribution to the author(s), title of the work, publisher, and DOI.
- Nucl. Instr. Meth. A*, vol. 756, pp. 19-22, 2014, dx.doi.org/10.1016/j.nima.2014.04.050.
- [5] L. T. Sun *et al.*, “A high charge state all-permanent magnet ECR ion source for the IMP 320 kV HV platform”, *Nucl. Instr. Meth. B*, vol. 163, pp. 503-512, 2007, doi:10.1016/j.nimb.2007.07.012.
- [6] Y. Cao *et al.*, “An all permanent magnet electron cyclotron resonance ion source for heavy ion therapy”, *Rev. Sci. Instrum.*, Vol. 85, 02A960 (2014), doi: 10.1063/1.4852335.
- [7] Liu Zhanwen *et al.*, “Status Report on HIRFL ECR2 Ion Source”, in *Proc. 12th Int. Workshop on ECR Ion Sources*, RIKEN, Japan, April. 1995, pp. 235, INS-J-182 (1995).
- [8] P. Yuan *et al.*, “THE PRELIMINARY EXPLANATION OF A NEW WORKING MODEL ON 10 GHz ECR2 SOURCE”, in *Proc. 15th Int. Conf. on Cycl. and their App.*, CAEN, France, June. 1998, pp. 402, JACoW, <http://www.jacow.org>.
- [9] P. Sortais, “General review of recent developments for electron cyclotron resonance ion sources (invited)”, *Rev. Sci. Instrum.*, Vol. 67, pp. 867 (1996), doi.org/10.1063/1.1146826.
- [10] H. W. Zhao, B. W. Wei, Z. W. Liu, Y. F. Wang, and W. J. Zhao, “Development of ECR ion sources in China (invited)”, *Rev. Sci. Instrum.*, Vol. 71, pp. 646 (2000), doi: 10.1063/1.1150337.
- [11] Zu Qi Xie and C. M. Lyneis, “Production of high charge state ions with the Advanced Electron Cyclotron Resonance Ion Source at LBNL”, *Rev. Sci. Instrum.*, Vol. 67, pp. 886 (1996), doi: 10.1063/1.1146829.
- [12] Z. M. Zhang *et al.*, “A new ECR ion source for atomic physics research at Institute of Modern Physics”, *Rev. Sci. Instrum.*, Vol. 73, pp. 580 (2002), doi: 10.1063/1.1429317.
- [13] B. Xiong *et al.*, “Application of evaporative cooling technology in super-high power density magnet”, *Rev. Sci. Instrum.*, 85, 02A913 (2014); doi: 10.1063/1.4827113.
- [14] W. Lu *et al.*, “High intensity high charge state ion beam production with an evaporative cooling magnet ECRIS”, *Rev. Sci. Instrum.*, 87, 02A738 (2016); doi: 10.1063/1.4936183.
- [15] G. Ciavola and S. Gammino, “The SERSE project”, *Rev. Sci. Instrum.* Vol. 65, pp.1057 (1994), doi.org/10.1063/1.1145060.
- [16] C. Lyneis, Z. Q. Xie Z Q and C. Taylor, “Development of the third generation electron cyclotron resonance ion source”, *Rev. Sci. Instrum.* Vol. 69, pp. 682 (1998), doi.org/10.1063/1.1149169.
- [17] P. A. Závodszky *et al.*, “FIRST COMMISSIONING RESULTS OF THE SUSI ECRIS”, in *Proc. 18th Int. Conf. on Cycl. and their App.*, Giardini Naxos, Italy, Oct. 2007, pp. 283, JACoW, <http://www.jacow.org>.
- [18] T. Nakagawa *et al.*, “First results from the new RIKEN superconducting electron cyclotron resonance ion source (invited)”, *Rev. Sci. Instrum.* Vol. 81, 02A320 (2010), doi: 10.1063/1.3259232.
- [19] L. Sun *et al.*, “Advancement of highly charged ion beam production by superconducting ECR ion source SECRAL (invited)”, *Rev. Sci. Instrum.* Vol. 87, 02A707 (2016), doi: 10.1063/1.4933123.
- [20] L. Sun *et al.*, “SECRAL II ION SOURCE DEVELOPMENT AND THE FIRST COMMISSIONING AT 28 GHz”, in *Proc. 22nd Int. Workshop on ECR Ion Sources*, Busan, Korea, August 2016, pp. 43, JACoW, <http://www.jacow.org>.
- [21] D. Z. Xie, W. Lu, J. Y. Benitez, C. M. Lyneis, D. S. Todd, “RECENT PRODUCTION OF INTENSE HIGH CHARGE ION BEAMS WITH VENUS”, in *Proc. 22nd Int. Workshop on ECR Ion Sources*, Busan, Korea, August 2016, pp. 141, JACoW, <http://www.jacow.org>.
- [22] H. W. Zhao *et al.*, “Superconducting ECR ion source: From 24-28 GHz SECRAL to 45 GHz fourth generation ECR”, *Rev. Sci. Instrum.* Vol. 89, 052301 (2018), doi: 10.1063/1.5017479.
- [23] W. Ma *et al.*, “Design of an 81.25 MHz continuous-wave radio-frequency quadrupole accelerator for Low Energy Accelerator Facility”, *Nucl. Instr. Meth. A*, vol. 847, pp. 130–135, 2017, dx.doi.org/10.1016/j.nima.2016.11.056.
- [24] Liangting Sun, Wang Lu, Enming Mei, GianLuca Sabbi, Wei Wu, Daniel Xie, and Hongwei Zhao, “Superconducting Magnets for High Performance ECR Ion Sources”, *IEEE TRANS. APP. SUPERCON.*, Vol. 28, NO. 3, APRIL 2018, Article No. 4101606, doi: 10.1109/TASC.2018.2791943.

ALL-PERMANENT MAGNET ECR ION SOURCE DECRIS-PM

A. Efremov[†], V. Bekhterev, S. Bogomolov, A. Bondarchenko, A. Lebedev, V. Loginov, V. Mironov,
 FLNR, JINR [141980] Dubna, Moscow reg. Russia
 N. Konev, ITT-Group, [107076] Moscow, Russia

Abstract

Super-heavy-element factory is under construction at the Flerov Laboratory for Nuclear Reactions, JINR, Dubna. The factory will include DC-280 cyclotron, which will be equipped with two 100 kV high voltage platforms. A high charge state all-permanent magnet 14 GHz ECRIS – DECRIS-PM has been designed and fabricated to provide intense multiple charge state ion beams. The request for the source is a production of medium mass ions with $A/q=4\div 7.5$ such as $^{48}\text{Ca}^{8+}$. The conceptual design of DECRIS-PM is presented. During the first tests at the ECR test bench, the source shows a good enough performance for the production of medium charge state ions (such as 900 μA Ar^{8+} , 550 μA Ar^{9+} , 200 μA Ar^{11+} , 160 μA Kr^{15+} , etc.).

INTRODUCTION

One of the basic scientific programs, which are carried out at the FLNR, is a synthesis of new elements requiring intense beams of heavy ions. To enhance the efficiency of experiments for next few years, it is necessary to obtain accelerated ion beams with the parameters listed in Table 1. These parameters have formed the base for the new cyclotron DC-280 [1]. Some required beam currents are collected in Table 2

Table 1: Required Beam Parameters

Ion energy	4÷8 MeV/n
Ion masses	10÷238
Beam intensity ($A\leq 50$)	up to 10 μA
Beam emittance	$\leq 30 \pi \text{ mm}\times\text{mrad}$
Total efficiency	> 50%.

Table 2: Required Beam Intensities

Ion	$^{48}\text{Ar}^{7+}$	$^{48}\text{Ca}^{8+}$	$^{58}\text{Fe}^{10}$
Intensity from ion source μA	300	150	125
Intensity on phys. target pps	3×10^{14}	5×10^{13}	4×10^{13}

The axial injection system of the DC-280 cyclotron will include two high voltage platforms, which will allow for efficient injection of ions from helium to uranium with M/Q ratio in the range of 4÷7. Each HV-platform will be equipped with the low power consuming ECR ion source.

[†] email: aefremov@jinr.ru.

For production of ions with the low and medium masses (from He to Kr) the all-permanent-magnet (PM) ECR ion source will be used. Many good performance all-permanent magnet ECRISs have been built around the world. Most of them are compact versions of ECRIS. Parameters of some PM ECRIS are listed in Table 3.

Table 3: Parameters of PM ECRIS

Ion source	Nanogan 14 GHz	Super Nanogan	LAP ECR2
Frequency	14.5	14.5	14.5
Plasma Chamber \emptyset	28	45	67
Weight	90	200	~500
Ar^{8+}	60	200	460
Ar^{9+}	20	90	455

Nanogan and Supernanogan ion sources are available for purchase from Pantechnik [2]. However, it is obvious that the compact versions of the sources do not provide the required ion beam intensities for our project. The only previously created “full-size” ion source which practically reproduces the structure and ion yields of CAPRICE-type ECRIS is LAPECR2 [3]. For this reason, the following design parameters of DECRIS-PM were selected:

- Microwave frequency – $14 \div 14.5$ GHz
- B_{inj} – ≥ 1.3 T
- B_{min} – 0.4 T
- B_{extr} – $1 \div 1.1$ T
- Plasma chamber \emptyset – 70 mm

SOURCE DESIGN

The main advantages of the all permanent magnet ECRIS are low power consumption, low pressure in the cooling water system, simplified operation, etc. However, there are few significant drawbacks of all permanent magnet ECRIS. First, the magnetic field is fixed and comparatively low. Thus, the designed magnetic configuration should be optimized from the very beginning. Another drawback is strong mechanical force acting on the individual parts of the system. As a result the correction of the magnetic field after the assembly of the magnetic system is practically impossible without demagnetization.

Deviations from the required field distribution can occur for many reasons. The variation in properties of permanent magnets (about of 5%) and the variation of easy axis direc-

Content from this work may be used under the terms of the CC BY 3.0 licence (© 2018). Any distribution of this work must maintain attribution to the author(s), title of the work, publisher, and DOI.

tion for magnets with angular magnetization lead to a difference between the calculated and the actual distribution of the magnetic field.

The magnetic structure and the source assembly are shown in Fig. 1. The magnetic structure consists of five 36-segmented axial magnetic rings with the corresponding axial or radial magnetization. Magnets with angular magnetization were not used. Permanent magnet (PM) rings at the extraction and at the injection sides are inserted into the soft iron rings, which help to slightly increase the magnetic field at maxima and strongly suppress the stray field around the source.

The soft iron plates around the PM rings with the axial magnetization play an important role in the final magnetic field distribution. By changing their thickness, it is possible to tune the minimum field if necessary (magnetic field correction).

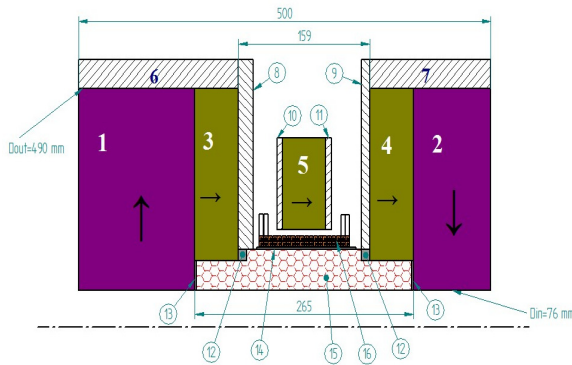


Figure 1: (top) DECRIS-PM at the ECR test bench; (bottom) Magnetic structure of DERIS-PM as follows: numerals 1÷5 – PM rings, 6 and 7 are soft iron rings; 8÷11 are soft iron plates, 12÷14 are auxiliary elements, 15 corresponds to the hexapole, and 16 the coil.

Other specific feature of the source is an additional coil placed at the centre of the structure between the hexapole and central PM ring. The coil is be used to tune the B_{min} value during the source operation. According to [4], the optimal value of B_{min} depends on the level of the injected microwave power and it should be changed on-line for an optimization of the source performance. The coil consumes

less than 1.5 kW of electric power and shares the cooling system with the plasma chamber. When the coil is excited to maximum current, the B_{min} value is shifted by ± 0.075 T depending on the current polarity.

The magnetic field of DECRIS-PM is the superposition of axial and hexapole fields similar to conventional EC-RIS. The hexapole is a 24-segmented Halbach structure magnet, which provides a radial field of 1.05 T at the inner wall of the plasma chamber. The weight of the permanent magnets is around 525 kg and total weight of the system is about 1000 kg.

Calculated and measured axial magnetic field of DECRIS-PM are shown in Fig. 2.

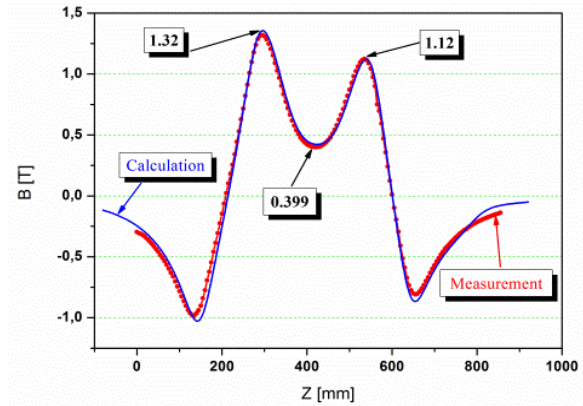


Figure 2: Axial magnetic field distribution of DECRIS-PM (extreme values are indicated at the plot).

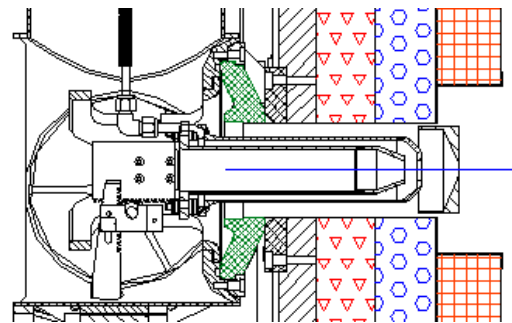


Figure 3: Extraction system.

The three electrode extraction system will be used for beam extraction. Puller electrode is negatively biased and water-cooled (See Fig. 3). Microwave power feeds into the plasma chamber directly through a water cooled rectangular waveguide. Since we are using a TWT rf generator, optimum coupling of the rf power to the plasma by tuning the microwave frequency can be realized.

RESULTS OF THE PRELIMINARY TESTS

The new ion source was tested at the ECR test bench few months ago. During these tests the single gap extraction system was used. The new extraction block could not be installed at the test bench because of its design features.

Table 4: Comparison of Ion Yields of Ar and Xe From Some ECR Ion Sources

Ion	DECRIS-PM	LAPECR2	SuperNanogan	DECRIS-3	ECR-4M
Ar ⁸⁺	920	460	200	720	600
Ar ⁹⁺	500	355	90		450
Ar ¹¹⁺	210	166	35	156	200
Ar ¹²⁺	150	62	12	68	100
Xe ²⁰⁺	75	85		84	
Xe ²⁶⁺	50	40	7 (Xe ²⁵⁺)	23	25 (Xe ²⁵⁺)

Table 5: Ion Yields of Solids

Q ⁺	5+	7+	8+	9+	10+	11+	12+
²⁴ Mg	450	140	40	15			
⁴⁰ Ca				220		158	58
⁵⁰ Ti				90	72	60	23
⁵⁶ Fe				85	80	55	

The Central coil was not used because of the remote control for its power supply was not ready. Normally, the extraction voltage was between 17 kV and 20 kV.

First of all the new ion source was tested by producing argon, krypton and xenon ion beams to investigate the source capacity. The best obtained results were compared to the corresponding results obtained with the all permanent magnet ion sources such as SuperNanogan [2], LAPECR2 [3], and CAPRICE-type room temperature ion sources DECRIS-3 [5] and ECR4m [6]. This comparison is presented in Table 4.

It is obvious that the typical performances of DECRIS-PM are equivalent to those of some typical room temperature ECR ion sources of the same frequency in the world, which demonstrates that design of this source is successful.

In recent years, the reactions of ⁴⁸Ca with different targets have been used to synthesize new superheavy elements with Z = 114–116 and 118. The heaviest target for experiments on synthesis of superheavy elements in heavy ion reactions is ²⁴⁹Cf, so further progress in the synthesis of elements with Z > 118 requires the production of intense beams of accelerated neutron enriched isotopes, such as ⁵⁰Ti, ⁵⁸Fe, ⁶⁴Ni, etc. The use of new isotopes for the production of accelerated beams calls for searching of ways for optimization of the ECR source operation mode and the development of a material feeding technique. For this reason, the new source was also tested by producing Ca, Mg, Ti and Fe ions.

The selection of the best method to feed solids into ECR ion sources strongly depends on specific properties of materials. For producing of Mg and Ca ion beam the traditional method with combination of micro oven and hot screen was applied. The MIVOC method was employed for the production of Ti ((CH₃)₅C₅Ti(CH₃)₃ compound) and Fe (Fe(C₅H₅)₂ compound) ion beams. Table 5 summarizes the results of the Mg, Ca, Ti and Fe ion beam production with DECRIS-PM ion source using the MIVOC method and oven technique

CONCLUSION AND PLANS

Preliminary tests of the source have shown that it is capable of producing intense beams of multi charged ions with intensities comparable or higher than those for tunable Room Temperature ECR sources. DECRIS-PM has already installed at the HV platform of the DC-280 cyclotron. We hope to improve the source performance at the high voltage platform due to the following:

- 3-electrode extraction system (single gap extraction at the test bench);
- effect of the additional coil;
- the larger the gap between poles of the analysing magnet (70 mm at the test bench and 110 mm at the HV platform)

ACKNOWLEDGEMENTS

The advice and help of Prof. H. W. Zhao, Dr. L. T. Sun and whole ECR-team from IMP is warmly acknowledged.

REFERENCES

- [1] G. Gulbekyan *et al.*, “Development of FLNR JINR heavy ion accelerator complex in the next 7 years. New DC-280 cyclotron project”, in *Proc. 2nd Int. Particle Accelerator Conf. (IPAC’11)*, San Sebastian, Spain, Sep. 2011, WEPB2082, pp. 2700-2702.
- [2] <http://www.pantechnik.com/#!sources/vstc2=su-pernanogan>
- [3] L. T. Sun, *et al.*, Nuclear Instruments and Methods in Physics Research B 263 (2007) pp. 503–512
- [4] T. Nakagawa, *et al.*, Rev. Sci. Instrum. 77, 03A304 (2006).
- [5] A. Efremov, *et al.*, AIP Conference Proceedings 2011, 040017 (2018); doi: 10.1063/1.
- [6] P. Sortais, Nuclear Physics News, (1996) 6:4, 6-8, DOI: 10.1080/10506899609

NEW METHOD TO DESIGN MAGNETIC CHANNELS WITH 2D OPTIMIZATION TOOLS AND USING PERMENDUR VANADIUM

L. Neri, L. Calabretta, D. Rifuggiato, LNS-INFN, Catania, Italy
O. Karamyshev, JINR, Dubna, Russia

Abstract

Magnetic channels are used in almost all cyclotrons to focus radially the beam along the extraction path through the coils and yoke region, where the rapid fall off of the magnetic field produces a strong vertical focusing and radial defocusing of the beam. These magnetic channels consist generally of three iron bars. The current sheet approximation has been generally used to evaluate quickly the performance of magnetic channels.

For the new magnetic channels to be used in the upgrade of the LNS-INFN k800 Superconducting Cyclotron, a new method was developed to investigate complex configurations and to achieve higher magnetic gradients in a larger area. The optimization procedure is based on a genetic algorithm implemented on MATLAB code and using the COMSOL code to perform the 2D magnetic field simulations.

Moreover, the use of permendur vanadium in alternative to iron allows to reduce the volume of the bars and mainly the magnetic force.

The results of our simulations are here presented.

INTRODUCTION

The LNS-INFN Superconducting Cyclotron (CS), Catania, has been working for 25 years delivering almost all ion beams in the mass range $2\div 200$ amu and energy range $10\div 80$ AMeV [1].

The CS was designed to perform nuclear physics experiments that generally use low intensity beams. Indeed, due to the compactness of the CS, the last accelerated orbit is not fully separated from the previous one, and the extraction efficiency is under 60%. The beam power dissipated on the septum of the first electrostatic deflector (E.D.) causes issues due to thermal deformation of the septum, extra outgassing, high dark current and E.D. discharges. For these problems the maximum beam power extracted from the cyclotron up to now stays below 100 W.

In 2016 the scientific community and the management of LNS-INFN approved a project to upgrade the CS to allow the extraction of beam power up to 10 kW for the ions with mass below 50 amu [2]. These high power beams are useful to perform the NUMEN experiment and also to drive the facility FRAISE (FRAGMENT In-flight SEPARATOR) [3,4].

To achieve this goal, the beam will be extracted by stripping. This extraction method is based on the sudden change of charge state produced by the crossing of the beam through a thin carbon foil, so called stripper. The consequent decrease of the magnetic rigidity after the stripper produce a strong perturbation of the beam

trajectory that naturally escapes from the cyclotron pole [5].

Although extraction by stripping is very convenient to achieve high extraction efficiency, its application is not trivial when extracting ions with a wide range of masses and/or energies. Indeed, the extraction trajectories are quite different for each different ion type, therefore a large Extraction Channel (Ex.Ch.) is mandatory, by far larger than the one used for electrostatic extraction. A new extraction system for a selected set of ions and energies has been designed [2].

In particular, two big Magnetic Channels (MC1, MC2) are mandatory to focus the beam along the extraction channel, see Fig.1. Moreover, these two channels have to provide large gradient, up to 2 kGauss/cm, over a large area (4×3 cm) to allow for an efficient transmission of the beams that have relatively large transversal sizes [6]. These MC were simulated using the so-called Current Sheet Approximation (CSA) [7]. The size of these channels are quite large and one of the problems, which appeared during the design of these magnetic channels was the magnetic force. As MC's have wide range of positions, according to the ion trajectory, it is very challenging from the mechanical point of view to offset these magnetic forces. In particular, the

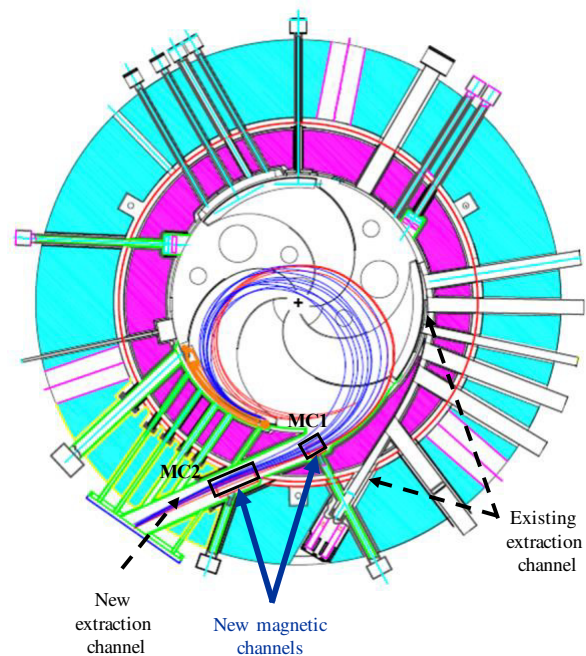


Figure 1: Layout of the two extraction channels from the CS. A set of new extraction trajectories achieved by stripping and the positions of the two new magnetic channels are also shown.

Content from this work may be used under the terms of the CC BY 3.0 licence (© 2018). Any distribution of this work must maintain attribution to the author(s), title of the work, publisher, and DOI.

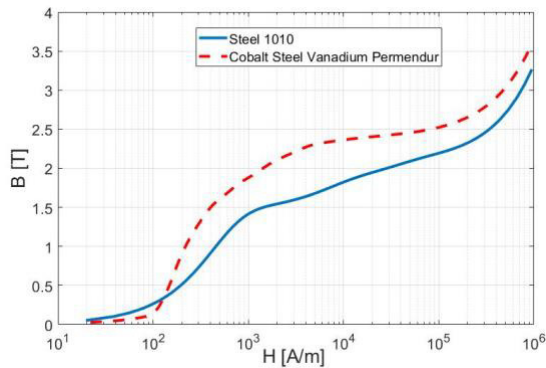


Figure 2: BH chart for Cobalt Steel Vanadium Permendur and Low Carbon Steel 1010.

force acting on MC1 could reach up to 1 ton. For this reason, we investigated the option to build these MC using permendur vanadium material that has a magnetization curve much higher than the pure iron, Fig. 2. Despite the permendur vanadium cost is quite high, it allows to reduce the cross section of the MC of about 10% and accordingly also the magnetic force. The results of these simulations are presented in the next section.

Moreover, we investigated also the option to optimize both the performance and the size of these channel. This method is based on a genetic algorithm which is described in the dedicated section. The results achieved with this optimization method are also presented in the last section.

MAGNETIC CHANNEL PERMENDUR VANADIUM MADE

One way to reduce the size of the MC, while keeping the same gradient, is to replace some parts of the MC's material from "conventional" Low Carbon Steel 1010 (LCS1010), which is widely used in cyclotrons, with Cobalt Steel Vanadium Permendur (CSVP). The magnetic properties of these materials are introduced in the simulation by using Comsol Material Library BH curves. The different magnetic properties of these two materials are shown in Fig 2.

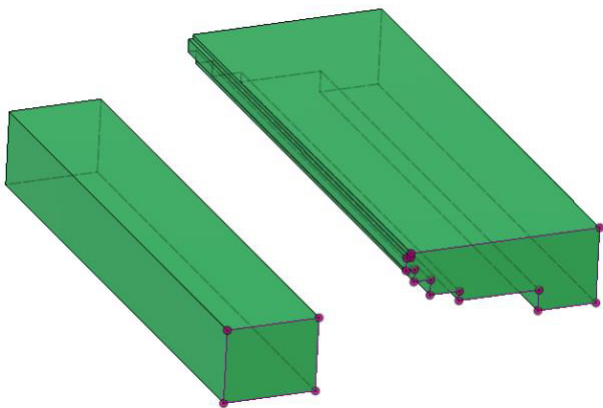


Figure 3: 3D model of magnetic channel, top half.

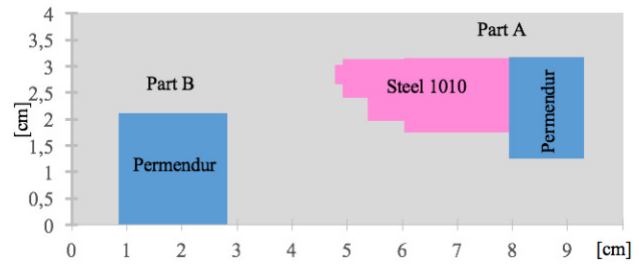


Figure 4: Parts of MC2 replaced with Cobalt Steel Vanadium Permendur (blue) and part kept with Low Carbon Steel 1010 (pink). Only top half part of MC2 is shown.

The preliminary design of the MC, developed by using the current sheet approximation is shown in Fig. 3. Half part is presented as inserted in the simulation that allows to use the middle plane symmetry to simplify the calculation.

As a first step of introducing CSVP in the design of MC we replaced two parts of the conventional MC, made from LCS1010, with CSVP, see Fig. 4. Part B was totally replaced with CSVP while only the right side of Part A was replaced with CSVP. The rationale of this partially material substitution is to preserve the easy manufacturing of a complex part by using LCS100.

The MCs design was studied in the magnetic field produced by the 3D model of the cyclotron. The 3D geometry of the cyclotron was imported in CST Studio software and the magnetic conditions were implemented to evaluate the magnetic field map. Middle plain magnetic field distribution is shown in Fig. 5.

We have adjusted the sizes of CSVP parts in order to maintain the same gradient as the fully LCS1010 magnetic channel. In order to do so, the width of the CSPV elements has been decreased by approximately 20%. The achieved gradients are presented in Fig. 6.

The force, applied on the MC's has been calculated using COMSOL Multiphysics software, as integration of the Maxwell's stress tensor over the surfaces of the MC.

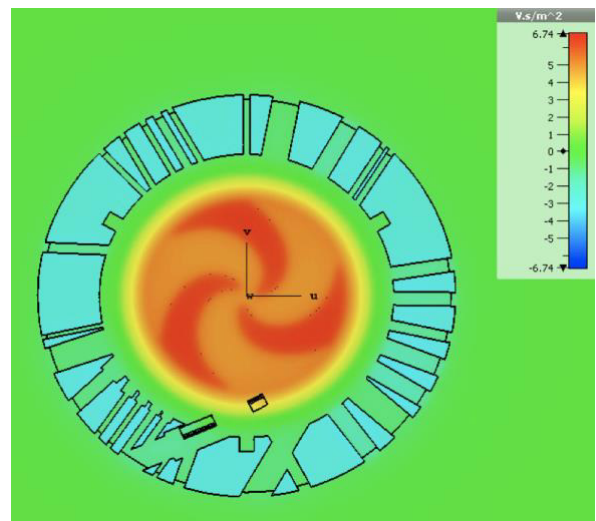


Figure 5: Middle plane magnetic field map achieved by CST Studio 3D model of the cyclotron. MC 1 and MC2 are in the most inner position.

Content from this work may be used under the terms of the CC BY 3.0 licence (© 2018). Any distribution of this work must maintain attribution to the author(s), title of the work, publisher, and DOI.

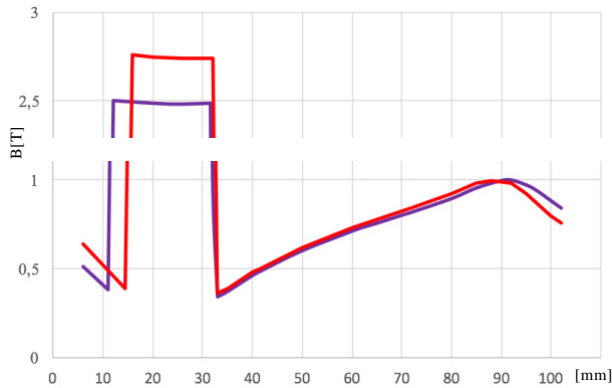


Figure 6: Magnetic field in MC2. Blue line, Low Carbon Steel 1010 made. Red line, partially made with Cobalt Steel Vanadium Permendur.

The positions of the MCs can be adjusted in or out to fit the different trajectories of each different ion beam. The two extreme allowed positions were taken into account for the evaluation of the force calculation and the results are shown in Table 1.

Use of Cobalt Steel Vanadium Permendur can reduce the size and the force on MC1 and MC2 by approximately of 10% and 7.5% respectively, compared to Steel1010. Similar reduction of force was found for both positions, inner

Table 1: Magnetic Forces on MC1 and MC2

MC1	Position	Steel 1010	Steel 1010 + Permendur
Fx Part B	in	-319 N	-294 N
Fy Part B	in	2753 N	2545 N
Fx Part A	in	-192 N	-176 N
Fy Part A	in	2316 N	2109 N
Fz Part A	in	775 N	720 N
Fx Part B	out	-525 N	-488 N
Fy Part B	out	3865 N	3578 N
Fx Part A	out	-268 N	-245 N
Fy Part A	out	2568 N	2362 N
Fz Part A	out	1087 N	1008 N
MC2			
Fx Part B	in	-372 N	-347 N
Fy Part B	in	-2172 N	-2020 N
Fx Part A	in	-317N	-293 N
Fy Part A	in	-3233 N	-3054 N
Fz Part A	in	1560 N	1470N
Fx Part B	out	-265 N	-245 N
Fy Part B	out	-1093 N	-1022 N
Fx Part A	out	-386 N	-349 N
Fy Part A	out	-270 N	-231 N
Fz Part A	out	700 N	712 N

and outer, as result of our simulation, see Table 1. Higher force reduction could be achieved if the full part A is permendur vanadium made.

OPTIMIZATION BASED ON GENETIC ALGORITHM

Genetic algorithm strategy is today a common and well developed method for optimization problems [8]. There are optimization strategies that suffer from high dependence upon the starting conditions and are able to find only local minima around it. Genetic algorithm automatically selects several starting conditions randomly chosen in the full space of the allowed solutions. This procedure deletes the dependency from the user selected starting point and allows the search in the full space of possible solutions.

The optimization procedure based on a genetic algorithm is implemented on MATLAB code [9]. An important variant that we adopted for the optimization of the MC was to use discrete variables instead of continuous. All variables, as it will be described in the following, are related to the geometric parameters of the design. An accuracy of one millimeter was set because solutions that differ of fractions of millimeter do not produce significant changes. In such a way we drastically reduced the space of the possible solutions moving from a continuous to discrete space of solution values. With this choice the computational time was reduced a lot and the capability to search in the whole space of possible solutions was more guaranteed.

The geometry is parametrized with 24 variables, the meaning of 20 of them is shown in Fig. 7. Six variables, identified by blue arrows, are able to change the height of the top part of the rod A. Other six variables, indicated by violet arrows, describe the bottom part. Four variables are used to identify the transverse position of the left side of the rod B and other four the right side. Two more variables are used to wrap and stretch the rod A, and the last two, to do the same for the rod B. Additional different constraints were applied to obtain a geometry compatible with the maximum allowed extension and to preserve the space needed for the beam. To produce a homogenous magnetic field gradient, we decided to remove the corners contribution by applying a rounding shape of all corners.

The genetic algorithm starts with a random selection of one hundred of possible solutions that constitute what is

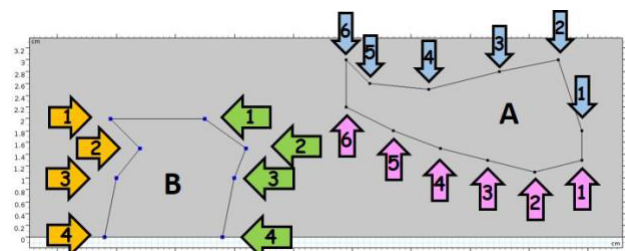


Figure 7: Parametrized design of MC with the identification of almost all variables that define the geometry.

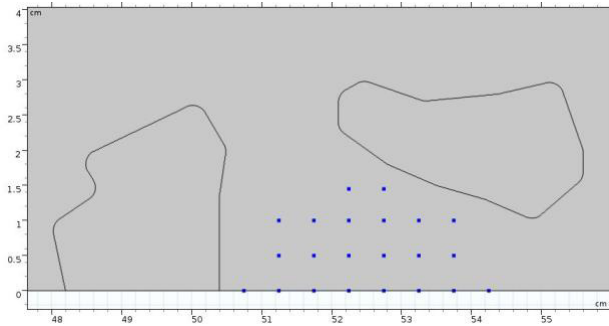


Figure 8: Map of points (blue marked) where the penalty function is evaluated.

commonly called a population.

The goodness function is evaluated for each individual, and good and bad individuals are identified. After the first step the genome constituted by the value of the variables of each individual are mixed between individuals to find the new population to be tested.

Only the best 30 individuals are allowed to share genome between them and 5 of randomly selected worst individuals. The new population is generated with a random mix of genome plus a small possible random variation. After few hundreds of populations, the global minimum is found when no more improvements are found and the goodness of the best individual shows a convergence trend.

The most important requirement that enable the use of a genetic algorithm is the computational time needed for the evaluation of the goodness function. A lot of work was done to identify the computational environment that allowed to compute the goodness function in few second. The geometry was tested by solving a 2D problem with Comsol Multiphysics instead of the 3D problem. This choice reduces the complexity of the problem introducing differences with small impact on the final 3D solution. In the real case we have a linear MC with a defined length inside a magnetic field. The simulated setup is equivalent to a MC of infinite length subjected to a constant external magnetic field. This will give a good agreement for the evaluation of the magnetic field at the center of the MC while will not take into account the fringing field at the two end of the MC. The need to have a fast goodness function evaluation imposed this simplification that will be removed in the last check of the design. The goal of the goodness

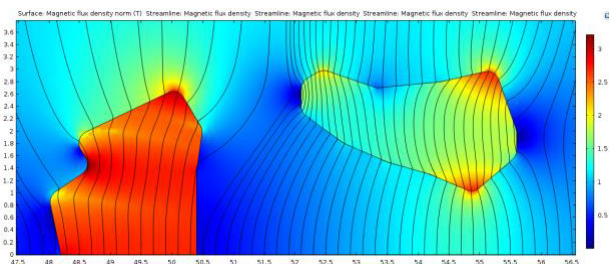


Figure 9: Colour-map and streamlines showing magnetic field value around MC2 after genetic algorithm geometry optimization.

function is the production of a uniform magnetic field gradient in all the beam region. A set of 22 points were taken into account for the calculation of the root mean square deviation. These points of interest are distributed in the area crossed by the beam and are shown in Fig. 8.

The area of the MC surfaces was taken into account to minimize the use of metal. In such a way we minimized the envelope of the MC but more important we reduced the magnetic force acting on the MC. The higher gradient obtained with this optimization procedure allow to use shorter MC that are subject to lower magnetic force.

OPTIMIZATION PROCEDURE RESULTS

The result shown in Fig. 9 was found after several iterations of the optimization procedure that help us to identify the most convenient degrees of freedom to be inserted in the design. Even if a big number of variables can be used with genetic algorithm, this number needs to be always limited to a value corresponding to one day of computational time. With this limitation the set of allowed geometries corresponding to all possible combinations of variables values represent a huge number of different geometries. Nevertheless, they are not comparable to the infinite number of possible geometries. Different tries were needed to identify the most crucial area where to insert higher freedom in the parametrized design. For the final configuration

Table 2: Margin Specifications

r	Z	$\frac{\partial B}{\partial r}$ [mT/cm]	Error [%]
50.75	0	246.2	-1.5
51.25	0	256.8	2.7
51.75	0	254.9	2.0
52.25	0	255.6	2.2
52.75	0	258.4	3.4
53.25	0	261.9	4.8
53.75	0	262.3	4.9
54.25	0	210.2	-15.9
51.25	0.5	248.8	-0.5
51.75	0.5	247.6	-1.0
52.25	0.5	251.6	0.6
52.75	0.5	256.0	2.4
53.25	0.5	259.2	3.7
53.75	0.5	275.1	10.0
51.25	1	218.0	-12.8
51.75	1	224.3	-10.3
52.25	1	242.8	-2.9
52.75	1	252.1	0.8
53.25	1	247.0	-1.2
53.75	1	232.8	-6.9
52.25	1.45	245.0	-2.0
52.75	1.45	249.3	-0.3

shown in Fig.9, 14 parameters for the piece A and 10 for the piece B were used.

The convergence was found after 356 generations in approximated 20 hours of computational time with an Intel I7-3970X CPU.

An average gradient of 250 mT/cm with a mean error of 4.2% was obtained. The evaluated gradients for the set of points in the beam area and shown in Fig. 8, are presented in Table 2.

Each point, identified with its radial and vertical coordinates, its gradient and error are presented in Table 2.

To identify the contribution of different materials, the optimization procedure, using the same parametrized degree of freedom, was tested both with CSVP and LCS1010. Choosing a magnetic field gradient of 250 mT/cm for the two cases, different optimized geometries were found for the two materials. The average deviation over the twenty-two points in the beam area was significant, 4.2% in the case of CSVP and 8.0% for LCS1010.

CONCLUSION

According to our simulations the use of permendur vanadium instead of pure iron steel 1010 allows to reduce the magnetic force applied on the magnetic channel of at least 7%. Moreover, we investigated also complex shapes for the three bars magnetic channels. Using a genetic algorithm, it was possible to optimize the region of uniformity of the gradient and also to maximize the gradient values. Using MCs with higher gradient allows to reduce the length of the channels and consequently the magnetic forces acting on them. This greatly simplifies the handling mechanics of these magnetic channels.

During 2019 a prototype of MC1 and MC2 with the shape achieved by the new optimization procedure will be built. A comparison between the simulations and the experimental measurements will be made.

REFERENCES

- [1] D. Rifuggiato et al., in *Proc. of Cyclotron 2013*, Vancouver, Canada, pp. 52 -54,
<http://accelconf.web.cern.ch/AccelConf/CYCLOTRONS2013/papers/moppt011.pdf>
- [2] L. Calabretta et al.; "Overview of the future upgrade of the INFN-LNS superconducting cyclotron", World Scientific, *Modern Physics Letters*, vol. 32, No.17 (2017) 17400009.
- [3] F. Cappuzzello et al., *Eur. Phys. J. A* (2015) 51: 145.
- [4] P. Russotto et al., "Status and Perspectives of the INFN-LNS In-Flight Fragment Separator", *J. Phys.: Conf. Ser.* vol. 1014.
- [5] G. G. Gulbekyan et al., in *Proc. of Cyclotron 2007*, Giardini-Naxos, Italy, pp. 308-313,
<http://accelconf.web.cern.ch/AccelConf/c07/papers/308.pdf>
- [6] A. Calanna, "High-intensity extraction from the Superconducting Cyclotron at LNS-INFN", *IL NUOVO CIMENTO*, 40 C (2017) 101.
- [7] M. M. Gordon and D. A. Johnson, *Particle Accelerators*, 1980, vol. 10, pp. 217-222.

- [8] W Banzhaf, P Nordin, RE Keller, FD Francone, "Genetic Programming: An Introduction", booksite.elsevier.com, 1998
- [9] Matlab, <https://se.mathworks.com/help/gads/genetic-algorithm.html>

DESIGN OF THE MULTI-ION INJECTOR LINAC FOR THE JLAB EIC (JLEIC)*

B. Mustapha, Z. Conway and M. Kelly, Argonne National Laboratory, Lemont, IL, USA
A. Plastun and P. Ostroumov, Facility for Rare Isotope Beams, East Lansing, MI, USA

Abstract

An Electron Ion Collider (EIC) is the highest priority for future U.S. accelerator-based nuclear physics facility following the completion of the Facility for Rare Isotope Beams (FRIB). Two laboratories are competing to host the future EIC: Brookhaven National Lab. (BNL) and Jefferson Lab. (JLab). The baseline design of JLab's Electron Ion Collider (JLEIC) ion complex comprises a pulsed superconducting (SC) linac injector capable of accelerating all ions from protons to lead, where proton and light ion beams can be polarized. After reviewing the design requirements for the injector linac, important design choices such as the room-temperature (RT) section design, the transition energy between the RT and SC sections and the stripping energy for heavy ions will be discussed. The design of the different linac sections will be presented as well as the results of end-to-end beam dynamics simulations for polarized deuterons and un-polarized lead ions.

INTRODUCTION

The electron-ion collider concept proposed by JLAB (JLEIC) requires a new ion accelerator complex which includes a multi-ion linac capable of delivering any ion beam from hydrogen to lead to the Booster. We have developed a design for a pulsed linac which consists of different ion sources, a room-temperature (RT) front-end, up to 5 MeV/u followed by a superconducting (SRF) section to the full linac energy. This work includes the beam dynamics and electrodynamic studies performed to design efficient and cost-effective accelerating structures for both the RT and SRF sections of the linac. The current design includes two separate RFQs one for heavy ions and one for polarized light-ion beams, and a common RT section with a special IH DTL design downstream of the RFQs. Quarter-wave and half-wave resonators are effectively used in the SRF section of the linac.

DESIGN REQUIREMENTS AND CHOICES FOR JLEIC INJECTOR LINAC

Design Requirements for JLEIC Injector Linac

The baseline design of the JLEIC ion complex [1] calls for the following requirements from the injector linac:

- Capable of accelerating all beams from protons to lead ions, including polarized light ion beams
- Deliver 280 MeV protons and 100 MeV/u lead ions Pb^{67+} for injection to the Booster, and equivalent energies for other ion beams

- Pulsed beam structure with 5-10 Hz repetition rate and 0.2 - 0.5 ms beam pulse length
- Pulsed beam current of ~ 2 mA for light ions and ~ 0.5 mA for heavy ions
- Compact and cost efficient

Important Design Choices for the Linac

In order to satisfy the design requirements listed above, the following design choices were made for the JLEIC injector linac:

- To accommodate the significantly different beam parameters from polarized light-ion and heavy-ion sources, the linac includes two separate RFQs, one for mass-to-charge ratio $A/q \leq 2$ and one for heavy ions with $A/q > 2$.
- As a consequence, two separate low-energy beam transport (LEBT) lines are required. However, this separate front-end choice allows a special LEBT design for polarized light ions to preserve polarization.
- Based on similar pulsed ion linacs [2, 3], a room-temperature (RT) section up to an energy of ~ 5 MeV/u is the most efficient and cost-effective option for the JLEIC linac, followed by a SRF section up to the full linac energy.
- A pulsed SRF linac can be more compact and cost-effective than the full RT option [4, 5]. It also offers wider acceptance and more tuning flexibility for light and heavy ion beams. In addition, taking advantage of state-of-the-art performance of quarter-wave (QWR) and half-wave (HWR) resonators [6, 7], which can deliver higher voltages in pulsed mode, the linac can be even more compact.
- In order to deliver Pb^{67+} at 100 MeV/u, the optimum stripping energy was found to be ~ 13 MeV/u, which is the energy following two QWRs modules made of 7 cavities each.

DESIGN OF THE DIFFERENT SECTIONS OF THE LINAC

Figure 1 shows the layout of the designed JLEIC injector linac with separate front-ends for light ion and heavy-ion beams, a DTL section made of three IH tanks followed by an SRF section made of three QWR cryomodules operating at 100 MHz and nine HWR cryomodules operating at 200 MHz. A stripper section for the heaviest ions is located between the second and third QWR modules.

*This work was supported by the U.S. Department of Energy, Office of Nuclear Physics, under Contract No. DE-AC02-06CH11357

Content from this work may be used under the terms of the CC BY 3.0 licence (© 2018). Any distribution of this work must maintain attribution to the author(s), title of the work, publisher, and DOI.



Figure 1: Layout of the JLEIC multi-ion injector linac.

We should mention that the current design is an extension of the short linac design [8] to the full energy required for injection to the booster ring in the JLEIC baseline design [1]. The short linac was proposed as part of an alternative design approach for the JLEIC Ion complex [9].

Existing Ion Sources and Expected Performance

Table 1 shows the desired polarized proton and deuteron ion beam parameters in comparison to the beams available from existing polarized sources, namely the atomic beam (ABPIS) and the optically pumped (OPPIS) sources [10].

Table 1: Polarized Light Ion Beams: Desired vs. Available H-/D- Beam Parameters

	Units	Desired value	ABPIS value	OPPIS value
Pulse Current	mA	2	3.8	4
Pulse Length	ms	0.5	0.17	0.3
Polarization	%	100	90	85

We notice that while the desired beam parameters are not exactly matched, they are within reach with some R&D effort. For heavy-ion beams, both the electron cyclotron resonance (ECR) and the electron beam (EBIS) ion sources are capable of delivering the desired beam current of 0.5 mA for Pb^{30+} and other ions with equivalent mass-to-charge ratios.

One notable difference between the polarized light ions and heavy ions is the beam emittance at the source, while the 90% emittance is typically 0.5π mm.mrad for heavy ions, it's $\sim 2\pi$ mm.mrad for polarized H-/D- beams [11]. This significant difference in beam emittance is the main reason to have two separate front-ends for polarized light-ion and heavy-ion beams.

LEBTs Design

The design for the polarized light ion LEBT shown in Figure 2 is very similar to the BNL LEBT for polarized H- [12]. It includes two opposite bends to compensate beam polarization. The LEBT is designed for 20 keV/u beams which is the RFQ injection energy.

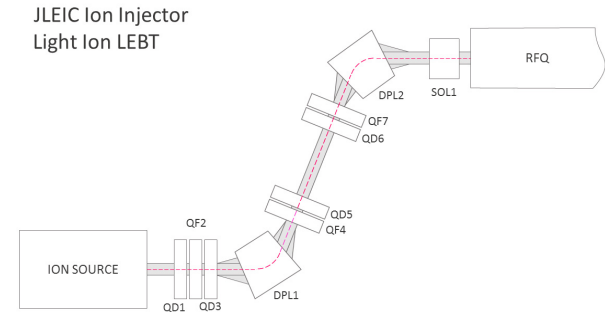


Figure 2: LEBT design for polarized light ion beams.

The heavy-ion LEBT is shown in Figure 3, it is based on the CERN Lead linac-3 injector design [13]. The double-bend is for the selection of the desired charge state for injection into the RFQ. The extraction beam energy from the source is 25 keV/u which is also the RFQ injection energy.

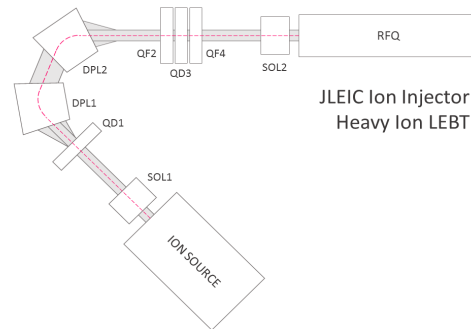


Figure 3: LEBT design for heavy ion beams.

RFQs Design

The design parameters for the light ion and the heavy ion RFQs are listed side by side in table 2. Note the $\sim 100\%$ transmission was achieved for a deuteron beam in order to avoid radio-activation of the RFQ structure by neutrons [14].

Table 2: Design Parameters for the Light-ion and Heavy-ion RFQs

Parameter	Units	Light Ion	Heavy Ion
Voltage	kV	103	70
Average radius	mm	7.3	3.4
Length	m	3	5.6
Quality factor		7200	6600
RF power	kW	150	250
Beam transmission	%	~ 100	99
Design Transverse emittance	π .mm.mrad	2.0	0.5
Output Longitudinal emittance	π .keV.ns	5.0	4.5

For pulsed RFQs, there are different options for the structure design, namely the 4-rod, the 4-vane and the window-coupled design as shown in Figure 4. The

structure can be either brazed or bolted. For the JLEIC RFQs, we propose the brazed 4-vane window-coupled structure for both its mechanical and field stabilities [15].

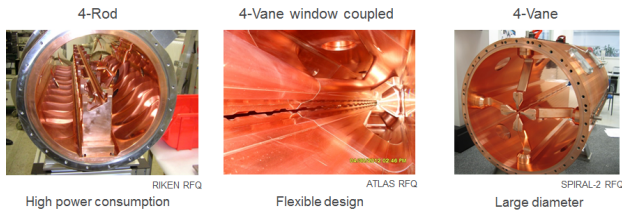


Figure 4: RFQ Design options.

DTL Section Design

During the design of the RT section [16] of the JLEIC linac, we investigated different DTL design options, see figure 5. The first was an IH structure with triplet focusing similar to the BNL EBIS injector [2]. The second option was a special DTL design with RF quadrupole focusing [17]. The third option, which was selected for the JLEIC linac, uses a FODO focusing lattice which offers a large acceptance with minimal emittance growth while preserving a good power efficiency.

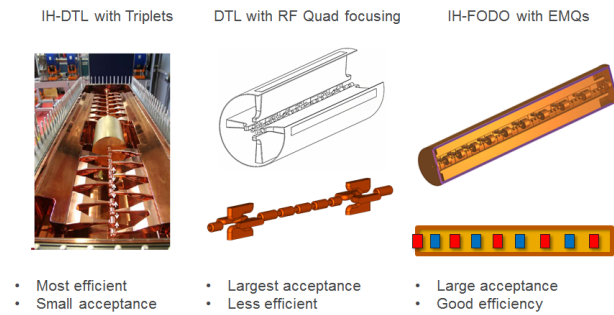


Figure 5: Design options for the DTL section of the linac.

The design parameters for the three DTL tanks required to reach 5 MeV/u energy for all ion beams are listed in Table 3. The DTL section delivers ~ 30 MV over ~ 11 m and requiring ~ 1 MW total power. A schematic of the DTL section showing the three tanks made of 19 accelerating gaps and 20 quadrupoles in a FODO arrangement is shown in Fig. 6.

Table 3: Design Parameters for the Three IH-DTL Tanks with FODO Focusing

Parameter	Units	DTL-1	DTL-2	DTL-3
Input Energy	MeV/u	0.5	2.0	3.6
Output En.	MeV/u	2.0	3.6	5.0
Accel. sections	No.	10	5	4
Length	m	4.3	3.5	3.4
RF power	kW	280	400	620



Figure 6: Layout of the DTL section made of 3 tanks including 19 accelerating gaps and 20 quadrupoles in a FODO lattice arrangement.

SRF Section Design

A schematic layout for the SRF section of the linac is shown in Fig. 7. It is made of three QWR and nine HWR cryomodules. Each cryomodule is made of seven cavities and four solenoids in the arrangement shown in Figure 8 for both the QWR and HWR modules. A stripping section for the heaviest ions is located after the second QWR module at an energy of ~ 13 MeV/u for lead ions.



Figure 7: Schematic layout of the SRF section of the JLEIC including a stripper section after the second QWR module.

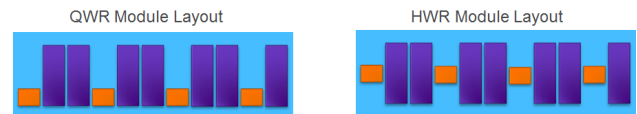


Figure 8: Layouts of the QWR and HWR cryomodules each with seven cavities and four solenoids.

The design of both the QWR and HWR cavities are shown in Fig. 9 along with their electromagnetic field distributions. The corresponding RF design parameters are summarized in Table 4.

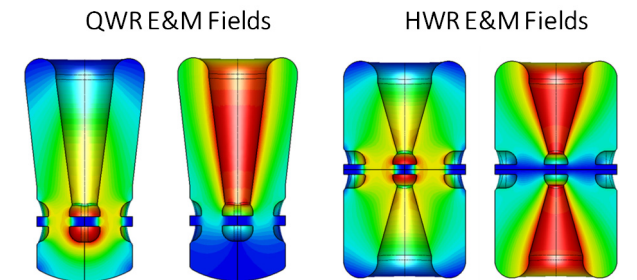


Figure 9: Geometry and electromagnetic field distributions for the QWR and HWR cavities (E-Field on the left and B-Field on the right for each cavity).

Table 4: RF Design Parameters of the QWR and HWR Cavities

Parameter	Units	QWR	HWR
Design β_{opt}	-	0.15	0.3
Frequency	MHz	100	200
Length ($\beta\lambda$)	cm	45	45
E_{peak}/E_{acc}	-	5.5	4.9
B_{peak}/E_{acc}	mT/(MV/m)	8.2	6.9
R/Q	Ω	475	256
G-factor	Ω	42	84
E_{peak} in operation	MV/m	58	52
B_{peak} in operation	mT	86	73
E_{acc}	MV/m	10.5	10.5
Voltage per cavity	MV	4.7	4.7
Cavity phases	Deg	15-30	15-30
No. of Cavities	-	21	63

Stripper Section Design

The Pb beam is used as a reference for the design of the stripper section. The optimum stripping energy on a carbon foil to produce lead ions Pb^{67+} for injection to the JLEIC booster is about 13 MeV/u [18]. This energy maximizes the beam fraction in the desired Pb^{67+} charge state which is about 20% and minimizes the total voltage requirements for the linac up to the full-energy of 100 MeV/u for lead ions as shown in Fig. 10.

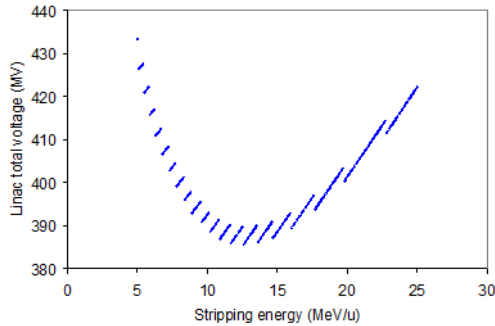


Figure 10: Total linac voltage as function of stripping energy for lead ions.

In order to separate the desired charge state from unwanted charge states and other reaction products, a chicane can be used for a straight linac option or a 180-deg bend for a folded option. Figure 11 shows a preliminary concept of a stripping chicane, where the beam is focused onto the stripper foil using a triplet and the desired charge state is separated and selected using the slits in the middle plane. A rebuncher and another triplet are used at the end of the chicane to longitudinally and transversely match the beam to the following section.

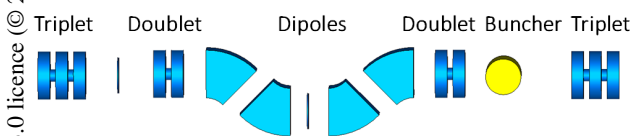


Figure 11: A possible layout for a stripping chicane to be installed between the second and third QWR cryomodules.

BEAM DYNAMICS IN THE LINAC

Beam Dynamics Design

The beam dynamics design is straightforward for the SRF section of the linac, a focusing period made of two accelerating cavities and one solenoid is the main building block. Exception is made at the end of every cryomodule where a missing cavity accounts for the extra drift space between modules where beam diagnostic devices can be installed. The general design rule is to start with a phase advance below 90-deg for the zero current beam and maintain periodic focusing by smoothly decreasing the phase advance along the linac. The accelerating voltage profile in the cavities is shown in Fig. 12. It clearly shows that the HWR covers very well the velocity range from 0.2 to 0.35 and no need for a different cavity type at the higher energies. This simplifies the overall design and fabrication of

the linac with only two cavity types, one QWR and one HWR. The proposed operating voltage per cavity of 4.7 MV which will require 9 Tesla superconducting solenoids for lead beam focusing.

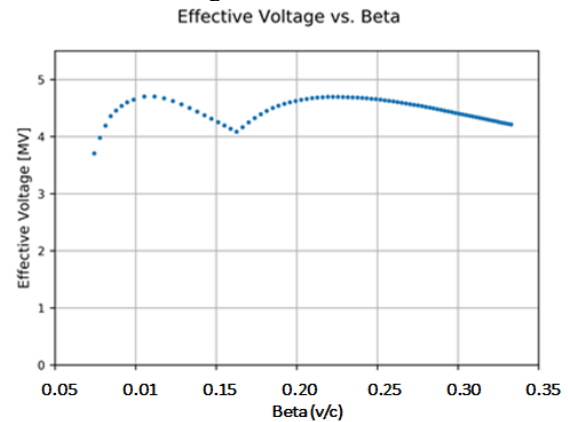


Figure 12: Effective cavity voltage as function of β along the linac showing that the HWR is fairly efficient up to the full energy of the linac.

Beam Dynamics Simulations

The results of end-to-end beam dynamics simulation in TRACK for a 2-mA polarized deuteron beam are shown in Fig. 13. The simulation starts from the ion source through the RT section, and ends with the SRF section at the full linac energy required for injection to the booster. In this case, we note $\sim 100\%$ transmission of the deuteron beam with about 30% emittance growth. Similar results were obtained for a 2-mA polarized proton beam.

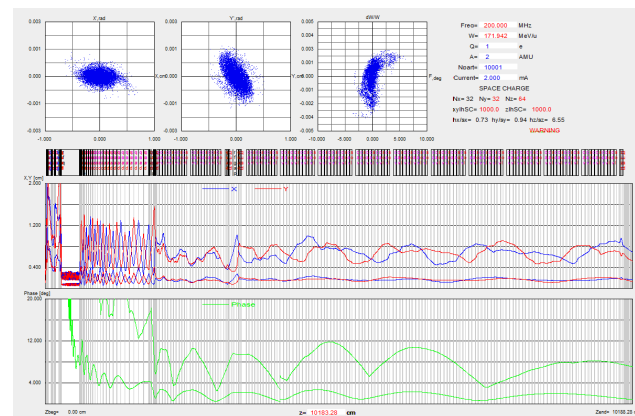


Figure 13: End-to-end beam dynamics simulation results for deuteron beam with $\sim 100\%$ transmission through the whole linac.

For lead ions, the beam dynamics simulation results are shown in Fig. 14.

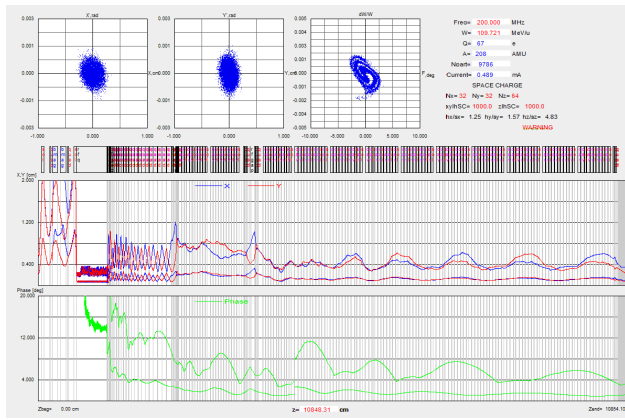


Figure 14: End-to-end beam dynamics simulation results for lead ions with beam stripping at ~13 MeV/u.

SUMMARY

We have designed a pulsed multi-ion injector linac that satisfies all the requirements for the baseline design of the Jefferson Lab EIC concept (JLEIC). The design is based on a 5 MeV/u room-temperature section followed by an SRF linac using QWRs and HWRs taking advantage of the most recent developments of similar structures at Argonne.

ACKNOWLEDGEMENT

The authors would like to thank Jacob Heglund, a SULI Summer Student for his contribution in extending the design of the short linac to the full-energy linac.

REFERENCES

- [1] Y. Zhang *et al*, “JLEIC Ultimate Luminosity with Strong Electron Cooling”, in *Proc. of IPAC17*, Copenhagen, Denmark, May 14-19, 2017
- [2] A. Schempp *et al*, “RFQ and IH accelerators for the new EBIS injector at BNL”, in *Proc. of PAC2007*, Albuquerque, New Mexico, USA
- [3] N. Angert *et al*, “The IH Linac of the CERN Lead Injector”, in *Proc. LINAC-1994*, Tsukuba, Japan
- [4] P. Ostroumov, “Warm and Cold Ion Linac: Comparison and Optimization”, Presentation at the MEIC Collaboration Meeting, JLab, Spring 2015
- [5] R. York, “Status Report on Technology Evaluation for JLEIC Ion Linac”, Presentation at the JLEIC Collaboration Meeting, JLab, Spring 2016
- [6] M. Kelly *et al*, “Low Beta Cavity Development for an ATLAS Intensity Upgrade”, in *Proc. SRF2013*, Paris, France
- [7] Z. Conway *et al*, “Achieving High Peak Fields and Low Residual Resistance In Half-Wave Cavities”, in *Proc. SRF2015*, Whistler, BC, Canada

Table 5 summarizes the beam parameters from the linac for protons, deuterons and lead ions.

Table 5: Important Beam Parameters in the Linac for Protons, Deuterons and Lead Ions

Parameter	H-	D-	Pb ³⁰⁺ → 67+
Input Transverse emittance (π .mm.mrad)	2.0	2.0	0.5
Output energy (MeV/u)	299	172	110
Transmission (%)	99.7	99.9	97.9
Output Transverse emittance (π .mm.mrad)	3.0	3.0	1.0
Output Longitudinal emittance (π .keV/u.ns)	7.5	7.5	7.0
Beam energy spread (%)	0.1	0.1	0.1

- [8] P. Ostroumov *et al*, “Design and Beam Dynamics Studies of a Multi-ion Linac Injector for the JLEIC Ion Complex”, in *Proc. of HB2016*, Malmo, Sweden, July 2016, paper THPM5Y01, p. 559.
- [9] B. Mustapha *et al*, “An Alternative Approach for the JLEIC Ion Accelerator Complex”, in *Proc. NAPAC2016*, October 9-14, Chicago, IL
- [10] A. Sy and V. Dudnikov, “JLEIC Ion Source: Specifications, Design and R&D Prospects”, Presentation at the JLEIC Collaboration Meeting, JLab, Fall 2016
- [11] A. S. Belov, “Polarized ion source with nearly resonant charge-exchange plasma ionizer: parameters and possibility for improvements”, Proceedings of the 15th International Workshop on Polarized Sources, Targets and Polarimetry, September 9-13, 2013, Charlottesville, VA, USA
- [12] J. Alessi *et al*, “Design of a 35 keV LEBT for the new High Intensity OPPIIS at BNL”, in *Proc. PAC1999*, New York, NY, USA
- [13] N. Angert *et al*, “CERN heavy-ion facility design report”, CERN Report 93-01, 28 April 1993, Geneva, Switzerland
- [14] R. Ferdinand *et al*, “Commissioning of SPIRAL2 CW RFQ and Linac”, in *Proc. IPAC-2017*, Copenhagen, Denmark
- [15] P. Ostroumov *et al*, “Development and beam test of a continuous wave radio frequency quadrupole accelerator”, *Phys. Rev. ST Accel. Beams*, 15 (2012) 110101
- [16] A. Plastun *et al*, “Design of the room-temperature front-end for a multi-ion linac injector”, in *Proc. NAPAC2016*, Chicago, IL, USA
- [17] A. Kolomiets and A. Plastun, “Spatially periodic radio-frequency quadrupole focusing linac”, *Phys. Rev. ST Accel. Beams*, 18 (2015) 120101
- [18] A. Leon *et al*, “Charge state distributions of swift heavy ions behind various solid targets”, *Atomic Data and Nuclear Data Tables* 69 (1998) 217-238

INVESTIGATIONS ON KONUS BEAM DYNAMICS USING THE PRE-STRIPPER DRIFT TUBE LINAC AT GSI

C. Xiao*, X.N. Du, and L. Groening

GSI Helmholtzzentrum für Schwerionenforschung GmbH, D-64291 Darmstadt, Germany

Abstract

Interdigital H-mode (IH) drift tube linacs (DTLs) based on KONUS beam dynamics are very sensitive to the rf-phases and voltages at the gaps between tubes. In order to design these DTLs, a deep understanding of the underlying longitudinal beam dynamics is mandatory. The report presents tracking simulations along an IH-DTL using the PARTRAN and BEAMPATH codes together with MATHCAD and CST. Simulation results illustrate that the beam dynamics design of the pre-stripper IH-DTL at GSI is sensitive to slight deviations of rf-phase and gap voltages with impact to the mean beam energy at the DTL exit. Applying the existing geometrical design, rf-voltages, and rf-phases of the DTL were re-adjusted.

KONUS BEAM DYNAMICS DESIGN

A Hamiltonian can be constructed describing the longitudinal particle motion in phase space as

$$H = -\frac{\pi w^2}{\beta_s^3 \gamma_s^3 \lambda} - \frac{q E_{acc} T_n(\beta_r)}{mc^2} (\sin \psi_r - \psi_r \cos \psi_s), \quad (1)$$

since ψ and w are variables canonically dependant on s

$$\frac{d\psi}{ds} = -\frac{2\pi w}{\beta_s^3 \gamma_s^3 \lambda}, \quad \frac{dw}{ds} = \frac{q E_{acc} T_n(\beta_r)}{mc^2} (\cos \psi_r - \cos \psi_s), \quad (2)$$

where q is the electric charge, m is the mass of the particle, c is the velocity of light, λ is the rf-frequency, and γ_s is the relativistic gamma factor. ψ_r is the phase of the field when the particle is at gap center, ψ_s is the synchronous phase, E_{acc} is the accelerating gradient, and T is the transient time factor. The subscripts s and n refer to the synchronous particle and the cell number, respectively. The energy gain of a particle may be expressed through the difference of its individual phase to the synchronous phase. For simplicity this term is normalized to the rest energy of the particle under study, suggesting the substitution

$$w = \frac{W_n - W_{n,s}}{mc^2}. \quad (3)$$

In conventional longitudinal beam dynamics the reference particle and the synchronous particle are identical. Longitudinal focusing is obtained by operating at constant negative rf-phase, such that the reference particle passes the gap center before the crest of the cosine-like gap voltage is reached. In conventional linacs the reference particle with design rf-phase of 0° (on rf-crest) will have maximum energy gain, but

the rf-phase range for stable longitudinal motion vanishes implying longitudinal acceptance of size zero.

In KONUS the reference particle and the synchronous particle are not the same. The gap-to-gap spacings are adjusted such that the synchronous particle arrives at 0° at each gap center. The beam is injected into a KONUS section such that the energy of the reference particle is higher than the synchronous particle energy. Additionally, the rf-phase of the reference particle at the first gap is close to the 0° synchronous phase. As the particle advances from gap to gap, the reference particle position will move counter clockwise in the longitudinal phase space diagram as illustrated in Fig. 1.

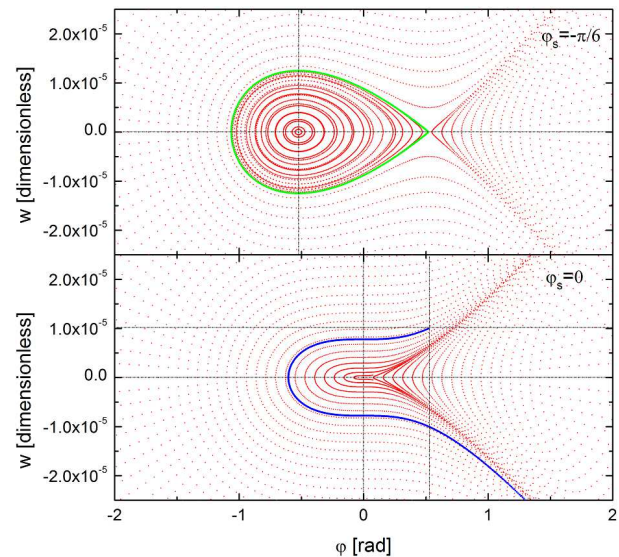


Figure 1: Conventional negative phase structure (upper) and KONUS structure (lower). In conventional designs, the rf-phase of the synchronous (reference) particle is always constant and negative ($\psi_s \approx -30^\circ$). Its energy is equal to the design energy ($w=0$). In KONUS the rf-phase and the energy difference of the reference particle w.r.t. the synchronous particle vary. The reference particle motion is not stable (blue line).

The parameters of the IH-DTL used as a reference in the following are listed in Table 1. This DTL provides transverse and longitudinal beam focusing for a long H-mode linac section, where the defocusing effects of transverse rf-fields and space-charge must be compensated avoiding quadrupole focusing lenses in each drift tube.

Almost all DTLs based on KONUS have been designed with LORASR [1]. One main feature of this code is provision of the gap field map. It builds the field map from

* c.xiao@gsi.de

Table 1: GSI Pre-Stripper IH-DTL Parameter List

Parameter	Value
Frequency	36.136 MHz
Design particle	$^{238}\text{U}^{4+}$
Design intensity	15 emA (electric)
Energy range	0.12 to 1.4 MeV/u
Number of cavities	2
Total length	20 m
Number of sections	4(IH-1)+ 2(IH-2)
Norm. exit rms-emittances	0.1 mm-mrad, 0.45 keV/u-ns

the geometry of gaps and drift tubes and the field map is stored in the code. The front half tube length is assumed equal to the end half tube length. This assumption is not strictly justified as the drift tube lengths increase along the DTL. On-axis longitudinal field distributions for ten types of gap and drift tube geometries are pre-calculated and stored, propagation of single particle coordinates is performed in thirty steps per gap by LORASR.

As input for LORASR the effective voltage and rf-phase at each gap n , $U_{eff,n}$ and ψ_n are used. The energy gain along gap n is calculated as

$$W_{n+1} - W_n = qU_{eff,n} \cos \psi_n, \quad (4)$$

$$U_{eff,n} = U_n T_n, \quad (5)$$

where ψ_n is the reference particle rf-phase at cell number n and U_n is the time dependent voltage between tubes of cell number n . From the given effective voltages and rf-phases LORASR calculates the according lengths of tubes and gaps, i.e., the DTL geometry. Additionally, the corresponding reference particle energies are provided at the exit of each cell.

The beam dynamics design of the UNILAC high current injector (HSI) was done at the IAP of the Goethe University of Frankfurt. According to KONUS beam dynamics, a section is defined as a set of gaps having the same synchronous particle definition. As a consequence each new section comes along with the re-definition of the synchronous particle (usually a transition from 0° to negative synchronous phase, -30° for instance, and vice versa). A complete IH-cavity can comprise one or several sections. The HSI is divided into two IH-cavities. The first cavity, IH-1, contains four sections while IH-2 contains two sections.

The effective gap voltages and the rf-phases serve as input for LORASR. The transient time factors (TTF) of DTL cells are calculated by LORASR and treated as constant values. After the IH-DTL was assembled the real gap voltage distribution along the two cavities has been measured and the measured gap voltages slightly (few percent) differed from the values being initially used for the beam dynamics design [2].

Using measured gap voltages instead of those used for the design, effects the single energy gains after each single cell and in turn the phases along subsequent cells. LORASR neglects this phase deviations in assuming that the phases

remain unchanged. Although the difference between measured and assumed gap voltages are quite small, the large amount of subsequent and phase-locked cells along an accelerating cavity leads to an accumulation of phase deviations and hence to output energy deviation.

Figure 2 shows the longitudinal focusing being simulated with LORASR using measured voltages and designed rf-phases. The initial energy of the reference particle was defined 0.1200 MeV/u, and the final energy of the reference particle was calculated as 1.3837 MeV/u applying Equ. 4. In the pre-stripper IH-DTL design, the longitudinal focussing initially simulated with LORASR is referred to as scenario-0.

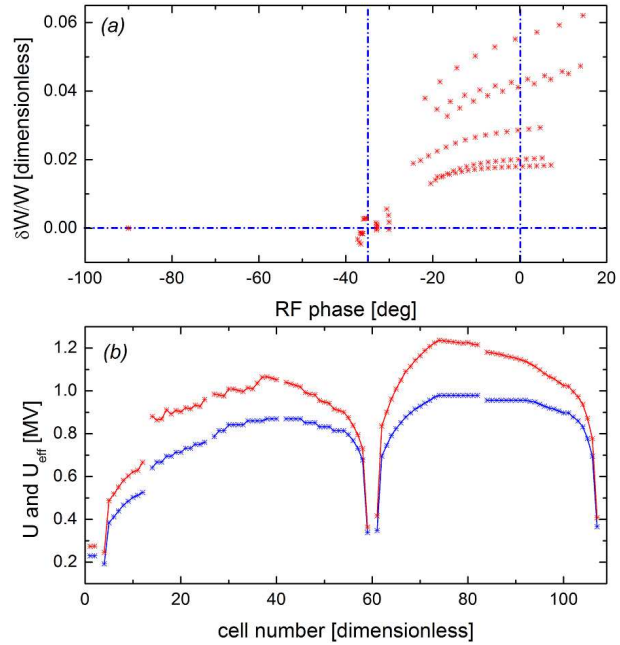


Figure 2: (a): Longitudinal reference particle position at each gap along the KONUS period. Red dots refer to the reference particle. (b): Measured voltage (red) and corresponding effective voltage (blue) at each gap along the IH-DTL (scenario-0).

SINGLE-PARTICLE TRACKING

In the following an estimate of the parameter set ($U_{eff,n}$, ψ_n , and w_n) is performed w.r.t. self consistency of effective gap voltages, rf-phases, and energies by applying the analytical method of Equ. 4. The rf-phase of the reference particle at the subsequent gap $n + 1$ is calculated straightforward. The augmented energy is the previous n_{th} cell's reference energy plus the energy gain across the gap. Each cell is represented as drift-gap-drift (see Fig. 3) and the rf-phase shift across the cell is determined by the distance between two gaps $L_{n,n+1}$ and the particle velocity β_{n+1}

$$\psi_{n+1} - \psi_n = \frac{2\pi L_{n,n+1}}{\beta_{n+1} \lambda} - \pi, \quad (6)$$

where $L_{n,n+1}$ is the distance between gaps n and $n + 1$,

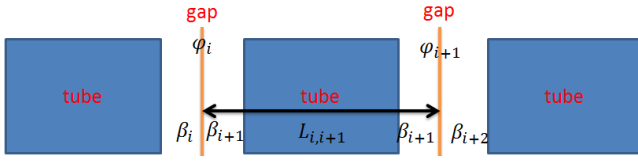


Figure 3: Definition of DTL cell and rf-phase along a drift-gap-drift sequence.

and β_{n+1} is the particle velocity between the gaps. The calculation of the transit time factor T_n by this analytical calculation assumes constant velocity between centers of adjacent gaps. Accordingly, smooth acceleration within the gap is approximated by a instantaneous step of particle velocity at the gap center.

In contrast to LORASR the BEAMPATH [3] code can use external two-dimensional field maps and simulate DTLs applying a consistent procedure. Rf-phases of the reference particle along the DTL are not assigned (except at the entrance gap) but rather calculated from the cell lengths and potential differences between tubes. Phase errors from preceding cells are thus propagated.

In the first simulation, the measured gap voltages from LORASR were taken for input. Initial rf-phases of buncher, IH-1, and IH-2 are chosen in order to ensure that the phases of the reference particle at the first gap of buncher, IH-1, and IH-2 are equal to the values put into LORASR: -90.0° , 14.5° , and 36.7° , respectively. All gap phases of the reference particle obtained from BEAMPATH together with the defined voltages are defined as scenario-1, and they are plotted in Fig. 4 together with the corresponding values from scenario-0.

It is re-iterated that scenario-0 is on the results from LORASR using as input phases and voltages at each single gap. Scenario-1 comprises results from BEAMPATH using as input the same gap voltages as scenario-0 but using just the first gap phase as input identical to scenario-0. In scenario-1 BEAMPATH calculates subsequent gap phases in a self-consistent way rather than using pre-defined values.

Phases of the reference particle are in good agreement along the buncher and the first section of IH-1. However, the phases differ significantly when the reference particle enters into the second section of IH-1 and in the following sections the phases delivered by LORASR and BEAMPATH remain being different. When the particles enters into IH-2 a the phase at its first gap is re-adjusted. In order to judge which result is more reliable, a dedicated routine based on MATHCAD has been established and applied.

In MATHCAD [4], the axially symmetric electric field map inside a gap is described by Fourier-Bessel series (the same as BEAMPATH). The reference particle vector function is defined as [5]

$$Z(t, z) := \begin{bmatrix} z \\ \frac{dz}{dt} \end{bmatrix} = \begin{bmatrix} z \\ \beta c \end{bmatrix}, \quad (7)$$

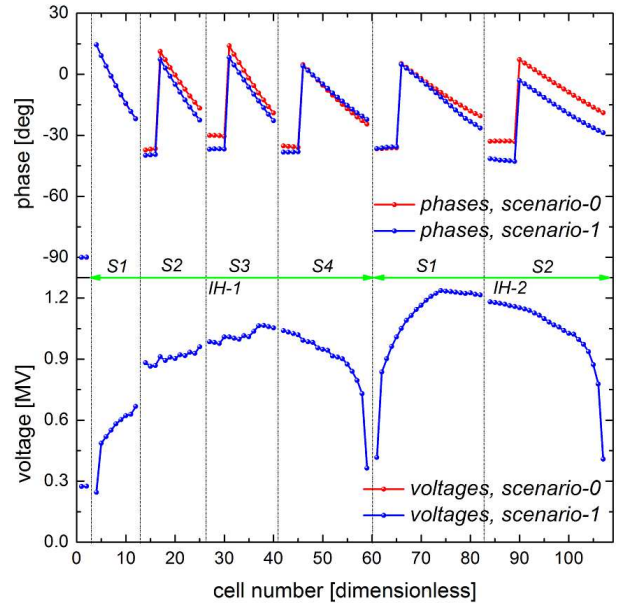


Figure 4: Comparison of scenario-0 and scenario-1. Upper: Rf-phases of the reference particle obtained from LORASR (red) and BEAMPATH (blue) simulations. Lower: Gap voltages used for LORASR (red) and BEAMPATH (blue) simulations (gap voltages are identical for both scenarios).

with βc as velocity. Starting at $t=0$ and $z=0$ (here BEAMPATH is repeated)

$$Z(0, 0) := \begin{bmatrix} 0 \\ \beta_0 c \end{bmatrix}. \quad (8)$$

The derivative DZ is

$$DZ(t, z) := \frac{dZ(t, z)}{dt} = \begin{bmatrix} \beta c \\ \frac{q}{m_0} E_z(z) \cos(\omega t + \psi_0) \end{bmatrix}. \quad (9)$$

This differential equation is non-linear and cannot be solved analytically. MATHCAD provides several routines to solve systems of ordinary differential equations. Each one uses a different integration algorithm and takes the same arguments. The Bulirsch-Stoer method (a very robust method which some prefer over Runge-Kutta) is applied solving Equ. 9 and the results are written as matrix F

$$F = \text{Bulstoer}[Z(0,0), t_i, t_f, s, DZ(t, z)], \quad (10)$$

where $Z(0,0)$ is the vector with initial conditions, t_i and t_f are the starting and ending points of the integration, s is the number of integration steps, and $DZ(t, z)$ is the vector containing the differential equations. At each step

$$F^1 = t_n, F^2 = z_n, F^3 = \beta_n c, \quad n = 1, 2 \dots s. \quad (11)$$

$F^{1,2,3}$ indicates F matrix columns 1, 2, and 3. LORASR output provides rf-phases at the center of each gap and energies at the centers of each tube ($E_z=0$ positions). BEAMPATH outputs the phases and energies at the center of each gap and

hence it is hard comparing energy gains directly between LORASR and BEAMPATH. Therefore, velocity gains from one tube center to the subsequent tube center are compared between LORASR and MATHCAD, and velocity gains from one gap center to the subsequent gap center are compared between BEAMPATH and MATHCAD as shown in Fig. 5.

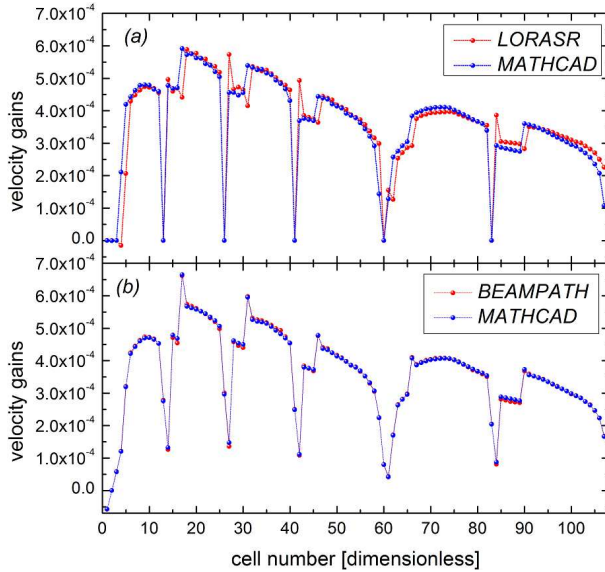


Figure 5: (a): Velocity gains from tube center to following tube center using LORASR and MATHCAD. (b): Velocity gains from gap center to following gap center using BEAMPATH and MATHCAD.

It is concluded that MATHCAD and BEAMPATH deliver quite similar phases at the gap centers and that the calculated velocity gains between gap centers are almost identical. Compared with results from LORASR, simulations with BEAMPATH deliver more reliable results. For the next set of simulations, gap voltages along each cavity and the initial rf-phase of IH-2 are slightly tuned in order to obtain similar phases as provided from LORASR. Gap voltages of the buncher, IH-1, and IH-2 have been multiplied by factors of 1.00, 0.985, and 0.975. Initial phases of the buncher and IH-1 are kept at -48.8° and 105.1° . But the initial phase of IH-2 has been re-changed to 152.4° . Corresponding phases and gap voltages obtained from BEAMPATH simulation are defined as scenario-2 and are plotted in Fig. 6 together with results from scenario-0.

It can be summarized that according to results of single particle tracking using BEAMPATH based on the existing HSI-DTL geometry, rf-phases of the reference particle using gap voltages as assumed in LORASR cannot be fully reproduced.

The final energies of the reference particle were calculated as 1.3837 MeV/u using scenario-0 (LORASR), 1.3992 MeV/u using scenario-1 (BEAMPATH), and 1.4010 MeV/u using scenario-2 (BEAMPATH), respectively.

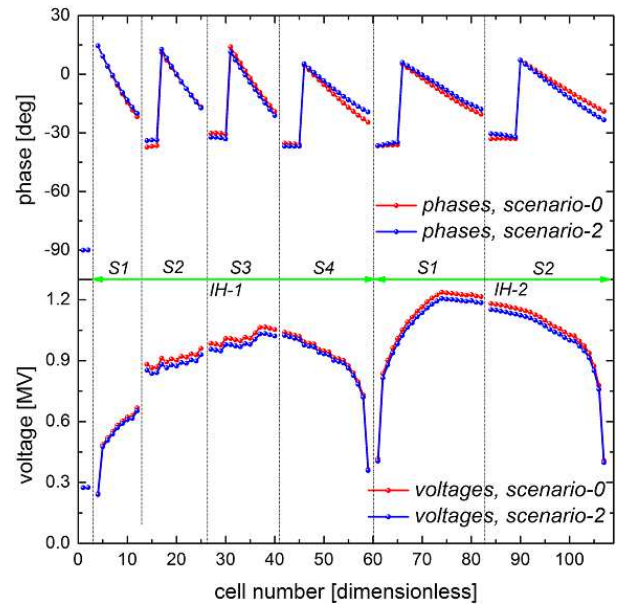


Figure 6: Comparison of scenario-0 and scenario-2. Upper: Rf-phases of the reference particle obtained from LORASR (red) and BEAMPATH (blue) simulations. Lower: Gap voltages used for LORASR (red) and BEAMPATH (blue) simulations.

MULTI-PARTICLE TRACKING

An artificial beam is assumed at the entrance of the MEBT in front of the IH-DTL being captured by the two-gaps buncher. This beam's macro-particles are set on the beam axis, i.e., $x=y=0$, $x'=y'=0$. Longitudinal particle distributions at the entrance and the exit of the MEBT simulated with MATHCAD are shown in Fig. 7.

For the case of the two-gaps buncher with identical gap voltages and initial rf-phases, the particle distributions at $T=14$ applying field-maps of CST and BEAMPATH ($M=1$ and $M=30$) are very similar. In other word, field-maps generated from BEAMPATH are sufficient to simulate the beam dynamics through the rf-gaps.

In the following multi-particle tracking simulations of BEAMPATH, $M=30$ is adopted. In the following simulations along the whole IH-DTL with BEAMPATH and PARTRAN [6] are compared to check and to modify the longitudinal beam dynamics of the HSI-DTL. PARTRAN is a z-code and each DTL cell uses a sequence of quadrupole, drift, and non-linear thin lens to model longitudinal and transverse rf-kicks at the electrical center of each DTL cell. PARTRAN uses pre-calculated TTF.

For further cross-checking between PARTRAN and BEAMPATH, in the following just the self-consistent scenario-2 is focused on. The time transition factor TTF, rf-phase, and effective voltages of each cell are complicated functions of both the field distribution and reference particle velocity, which may change appreciably during the passage through the multiple gap cavity. Another dedicated subroutine based on MATHCAD has been developed to solve these

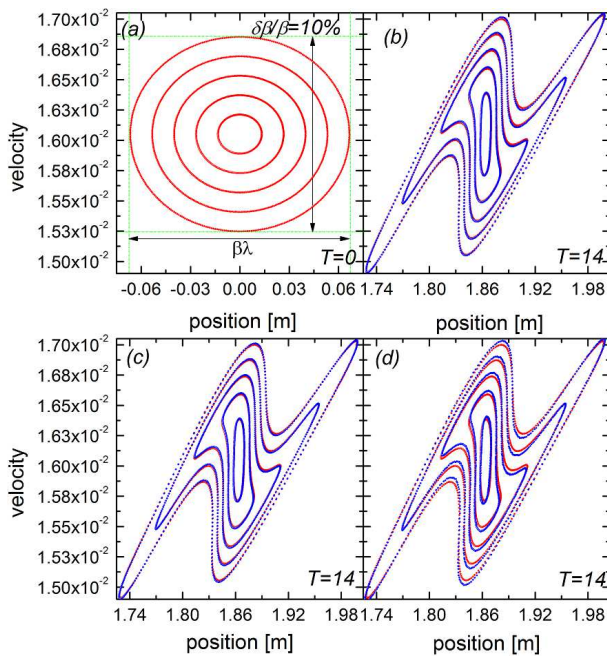


Figure 7: (a): Longitudinal particle distributions at time $T=0$ in scale of one rf-period. (b) and (c): Simulated longitudinal particle distributions at time $T=14$, red dots indicate results using actual longitudinal electric field calculated from CST, and blue dots indicate results using analytical longitudinal electric fields calculated from BEAMPATH ((b): $M=1$ and (c): $M=30$). (d): Simulated longitudinal particle distributions at the time of $T=14$, red dots indicate results using actual longitudinal electric field calculated from CST, and blue dots indicate results using analytical rectangular electric field.

parameters from electrical field map of BEAMPATH simulation for self-consistent scenario-2. Then corresponding effective voltages, rf-phases, and TTF values served as input for PARTRAN simulation. This continuous beam with zero momentum spread is further transported and accelerated through the completed DTL and the resulting longitudinal distributions at its exit are displayed in Fig. 8.

Particle distributions obtained from PARTRAN using scenario-0 and from BEAMPATH using scenario-1 are significantly different, thus indicating significantly different longitudinal beam dynamics. Particle distributions from PARTRAN and BEAMPATH using scenario-2 are not exactly identical but quite similar, thus indicating highly similar longitudinal beam dynamics.

CONCLUSION

As in KONUS beam dynamics the reference particle (bunch center) is not identical to the synchronous particle, the reference particle moves around the synchronous particle in longitudinal phase space. The shift of rf-phase between subsequent gaps (given by the length of drift between them) is used by the designer to adjust the phase relation between the reference particle and the synchronous particle. This

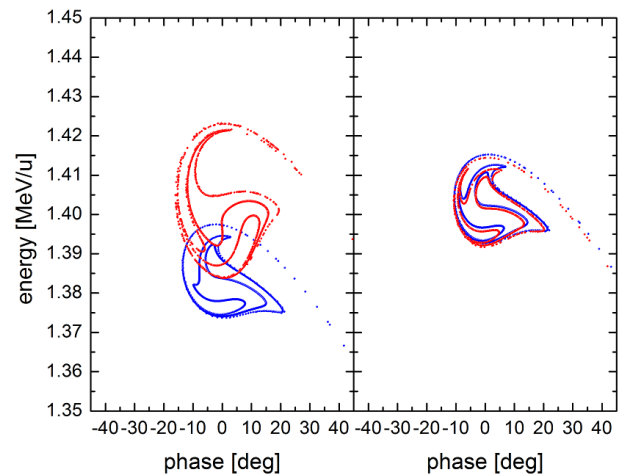


Figure 8: Longitudinal particle distributions at the exit of the DTL. Left: Results simulated from PARTRAN using scenario-0 (blue) and BEAMPATH using scenario-1 (red). Right: Results from PARTRAN (blue) and BEAMPATH (red) using scenarios-2.

adjustment takes place especially during the change of synchronous particle rf-phase from 0° to -30° and vice versa, i.e., during transition from one KONUS section into another. For cavities comprising many gaps small rf-phase errors being neglected may harm further stable acceleration along subsequent cavities and lower the precision of the predicted DTL output energy. The mentioned inconsistencies cannot be modelled by z -codes as PARTRAN for instance. Self-consistent beam dynamics of this IH-DTL optimized with the t -code BEAMPATH (scenario-2). These results could be reproduced very well with PARTRAN using realistic TTF parameters, measured gap voltages, and upgraded rf-phases taking into account unequal lengths of front and end half tubes.

REFERENCES

- [1] R. Tiede. LORASR code development. Proceedings of EPAC2006, Edinburgh, Scotland (2006).
- [2] B. Krietenstein et al. Numerical simulation and RF mode measurements of the new GSI IH-DTL. Particle Accelerator Conference 1997, vol. 2, pp. 2645-2647.
- [3] Y.K. Batygin. Particle-in-cell code BEAMPATH for beam dynamics simulations in linear accelerators and beamlines. Nuclear Instruments and Methods in Physics Research A 539 (2005) 455-489.
- [4] PTC Mathcad, <https://www.ptc.com/en/engineering-math-software/mathcad>
- [5] C. Xiao, X.N DU, and L. Groening. Investigations on KONUS beam dynamics using the pre-stripper drift tube linac at GSI. Nuclear Instruments and Methods in Physics Research A 887 (2018) 40-49
- [6] N. Pichoff, and D. Uriot. PARTRAN, Internal Memorandum, CEA, Saclay.

Content from this work may be used under the terms of the CC BY 3.0 licence (© 2018). Any distribution of this work must maintain attribution to the author(s), title of the work, publisher, and DOI.

STOCHASTIC COOLING SIMULATION OF RARE ISOTOPE BEAM AND ITS SECONDARY*

X. J. Hu[†], J. X. Wu, G. Y. Zhu, Y. Wei, L. Jing, Z. Du, Y. J. Yuan

Institute of Modern Physics, Chinese Academy of Sciences, [730000] Lanzhou, China

Abstract

Stochastic cooling is a broadband feedback system, which is very effective for reducing the beam size without beam loss [1]. It has advantage over electron cooling in cooling low intensity beam with large emittance and momentum spread, and is required for precise study of the decay properties of RIB (Radioactive Ion Beam) by use of the SMS (Schottky Mass Spectrometry) method [2]. This paper mainly concerns on cooling of primary beam and its secondary beam, pointing out the range of mass-to-charge spread that could be cooled for secondary particles. Meanwhile, TOF cooling combined with filter cooling was also studied. The simulation results provide theoretical supports for analysing different ions circulating in the ring at the same time in the experiments.

INTRODUCTION TO HIAF STOCHASTIC COOLING SYSTEM

The High Intensity heavy ion Accelerator Facility (HIAF) was proposed by the Institute of Modern Physics in 2009. As one of 16 large-scale research facilities proposed in China, HIAF is the next-generation high intensity facility for advances in nuclear physics and related research fields.

Stochastic cooling will be built on the Spectrometer Ring (SRing) of the HIAF project. The space for pickups and kickers is reserved in advance for SRing stochastic cooling system. There are 4 m for pickups and 4 m for kickers. All of the electrodes will be installed in the straight section without dispersion, and it has the advantage of preventing the coupling between phase subspaces, especially the transverse heating due to longitudinal kicks. It is planned to have 2 pickup tanks and 2 kicker tanks which would perform both transverse and longitudinal cooling. The betatron phase advances from pickup to kicker are almost 90 deg for both horizontal and vertical cooling.

The kinetic energy was designed to be 400 MeV/u, for the consideration of nuclear physics and atomic physics. The radioactive ion beam injected into SRing has large momentum spread of $\pm 1.5e-2$. If stochastic cooling is used for such kind of beam, the cooling frequency would be small in order to have large cooling acceptance. Fortunately, bunch rotation was proposed to decrease the momentum spread to $\pm 4.0e-3$, which is suitable for stochastic cooling to be cooled to the appropriate values, and then combined with electron cooling for further momentum spread decrease.

* Work supported by National natural science foundation of China (Y862010GJ0)

[†] E-mail: huxuejing@impcas.ac.cn.

COOLING METHODS FOR SRING LONGITUDINAL STOCHASTIC COOLING

By comparisons of different cooling methods, TOF cooling has the maximum cooling acceptance for longitudinal cooling than the others. Therefore, TOF cooling [3,4] was proposed to be used for SRing longitudinal stochastic cooling for beam with large momentum spread. After the beam momentum spread was decreased to a small value stage, filter cooling [5] was used for continuous cooling in order to achieve a reasonable value for subsequent electron cooling.

For the beam energy 400 MeV/u, when the bandwidth was 1-2 GHz, the TOF cooling acceptance was smaller than the initial beam momentum spread $\pm 4.0e-3$. Therefore, the bandwidth was reduced to 0.6-1.2 GHz, and then the TOF cooling could be able to cool this kind of beam with its initial momentum spread within TOF cooling acceptance.

LONGITUDINAL STOCHASTIC COOLING SIMULATION ON SRING

Cooling of Primary Beam

Table 1: Longitudinal Stochastic Cooling parameters

Physical parameters	values
Ion	$^{132}_{50}\text{Sn}$
Kinetic energy	740 MeV/u, 400 MeV/u
Total number of RI	1.0e5, 1.0e8
Initial $\Delta p/p$	$\pm 4.0e-3$ (TOF Cooling) $\pm 7.0e-4$ (Filter Cooling)
γt	3.317
Local γt	2.568
Bandwidth	0.6-1.2 GHz
Number of slot rings for Pickup/Kicker	64/128, 112/224
Number of faltin for Pickup/Kicker(0.75 m)	2/4
Temperature	300 K
Lpk	75.25 m

The SRing stochastic cooling parameters are listed in Table 1. $^{132}\text{Sn}^{50+}$ was chosen for the primary beam. We assumed the beam kinetic energy to be 740 MeV/u or 400 MeV/u for comparisons, and the particle number to be

Content from this work may be used under the terms of the CC BY 3.0 licence (© 2018). Any distribution of this work must maintain attribution to the author(s), title of the work, publisher, and DOI.

1.0e5 or 1.0e8. Two different electrode structures were proposed for the cooling system, and will be involved in the cooling simulation.

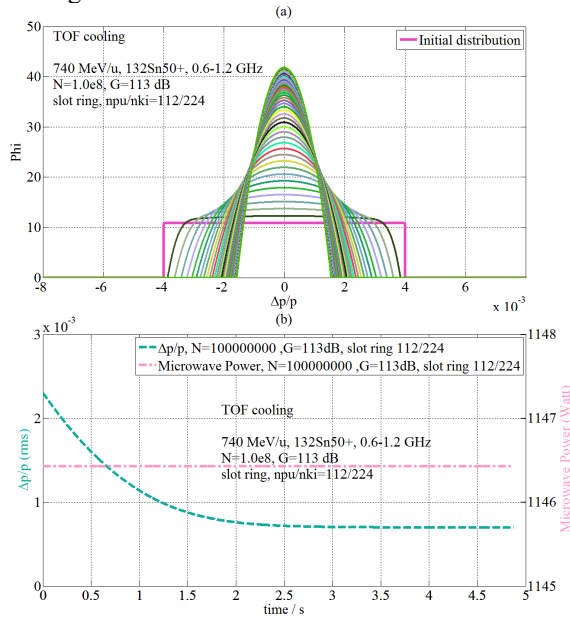


Figure 1: Results of TOF cooling simulation ($E_k=740$ MeV/u). (a) Beam distribution during cooling. (b) Evolution of momentum spread (rms) and microwave power.

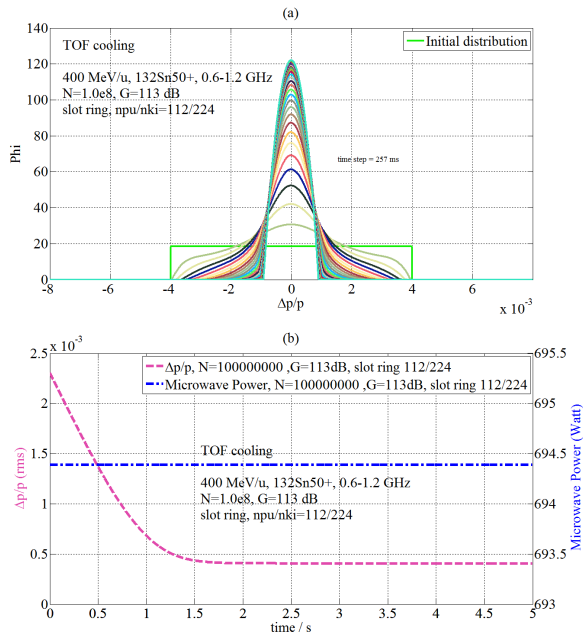


Figure 2: Results of TOF cooling simulation ($E_k=400$ MeV/u). (a) Beam distribution during cooling. (b) Evolution of momentum spread (rms) and microwave power.

Firstly, TOF cooling was used for longitudinal stochastic cooling simulation of two different beam kinetic energies with other beam parameters were kept the same.

When the beam kinetic energy is 740 MeV/u, beam distribution and evolution of momentum spread (rms) and microwave power are shown in Fig. 1, and cooling results

with kinetic energy 400 MeV/u are shown in Fig. 2. From the simulation results, it is clearly that TOF cooling has the ability of cooling the beam to the equilibrium momentum spread of 1.e-4. For lower energy, cooling is a little bit faster and the equilibrium momentum spread is relatively smaller. Meanwhile, the microwave power needed for lower energy is also lower than the higher energy case.

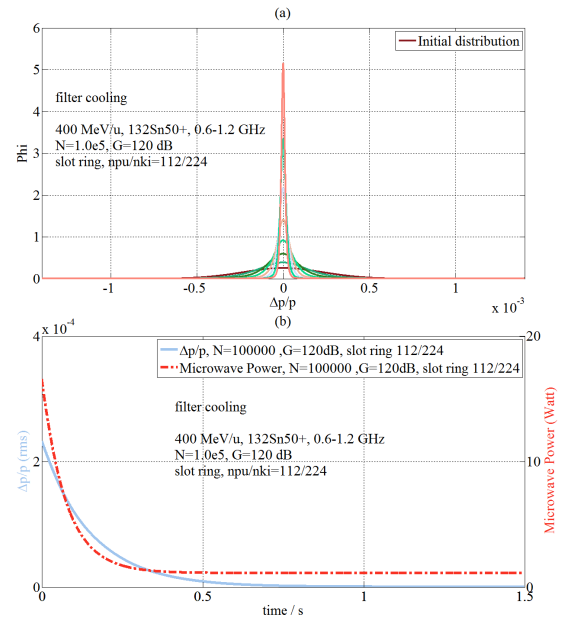


Figure 3: Filter cooling simulation results with particle number 1.0e5 and amplifier gain 120 dB. (a) Beam distribution during cooling. (b) Evolution of momentum spread (rms) and microwave power.

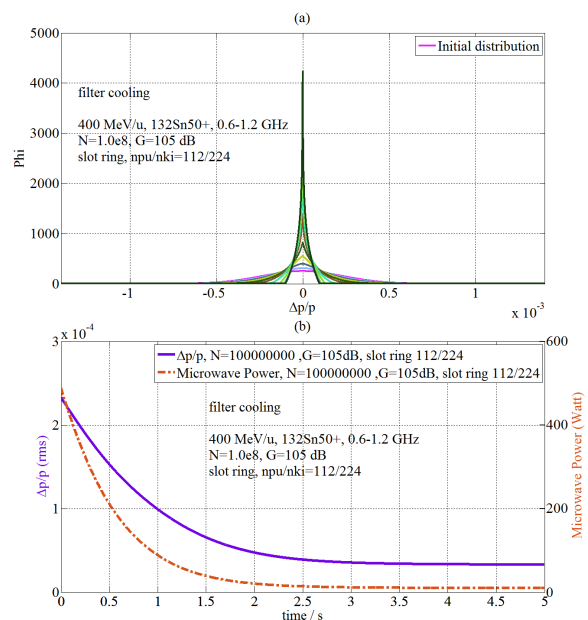


Figure 4: Filter cooling simulation results with particle number 1e8 and amplifier gain 105 dB. (a) Beam distribution during cooling. (b) Evolution of momentum spread (rms) and microwave power.

Then, filter cooling method was used for the simulation comparisons of different particle numbers. As shown in Fig. 3 and Fig. 4, similar to TOF cooling, filter cooling also has the ability of cooling beam to the equilibrium momentum spread of $1.0e-5$, which is smaller than the TOF cooling equilibrium value. Meanwhile, when the particle number is less, cooling is faster, equilibrium momentum spread is smaller as well as the power needed is lower too. Therefore, stochastic cooling is more suitable for cooling beam with low intensity.

For HIAF stochastic cooling, two electrode structures were proposed for the cooling system, one is the slot ring structure and the other one is the falin structure. By simulation of these two different structures in three cases, the results show that if the structure adopts slot ring with 112 and 224 cells for pickup and kicker respectively, cooling is always better than other cases, as shown in Fig. 5.

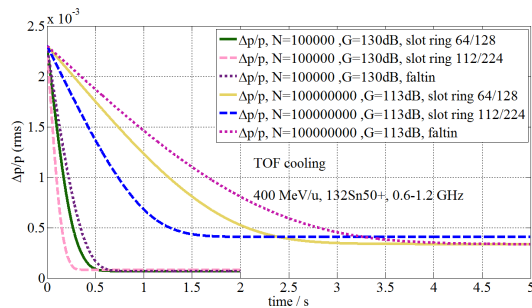


Figure 5: By TOF cooling simulation with two different electrode structures in three cases, slot ring with 112 and 224 cells for pickup and kicker is a better choice.

Cooling of Secondary Beam

For stochastic cooling of secondary beam, we choose $^{132}\text{Sn}^{50+}$ as the primary beam for simulation.

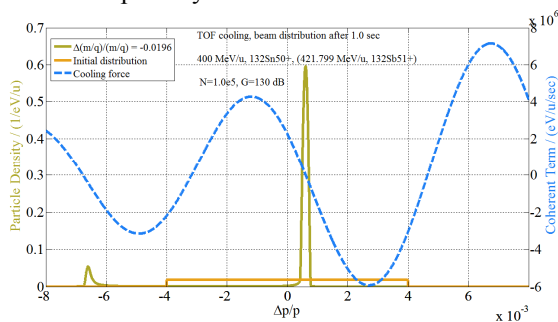


Figure 6: Stochastic cooling of secondary beam $^{132}\text{Sb}^{51+}$ by TOF method.

By simulation, TOF cooling has the ability of cooling the secondary beam such as $^{132}\text{Sb}^{51+}$ with mass-to-charge spread -0.0196 . However, it is worth noting that a small part of beam is lost after cooling due to the TOF cooling acceptance. As shown in Fig. 6.

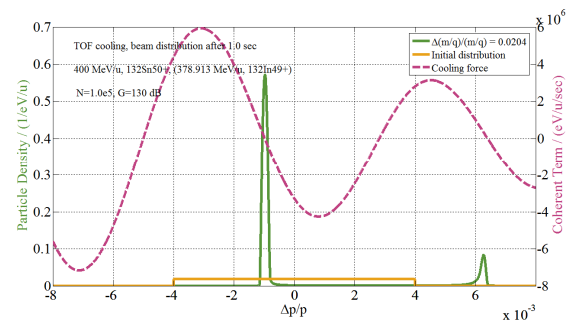


Figure 7: Stochastic cooling of secondary beam $^{132}\text{In}^{49+}$ by TOF method.

In addition, TOF cooling can also be able to cool the secondary beam $^{132}\text{In}^{49+}$ with mass-to-charge spread 0.0204 . Like the Sb case, still a small part of beam is lost after cooling, as shown in Fig. 7.

TOF cooling has the ability of cooling secondary beam for some special cases, and filter cooling could also be able to cool some kind of secondary beam, such as $^{129}\text{In}^{49+}$ with mass-to-charge spread -0.0028 , which is shown in Fig. 8. However, after cooling, the secondary beam lies on the edge of the cooling acceptance and is at risk of loss.

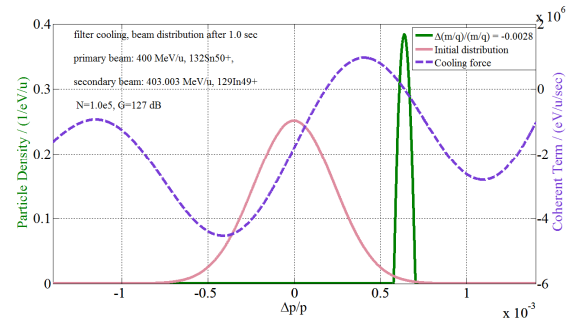


Figure 8: Stochastic cooling of secondary beam $^{129}\text{In}^{49+}$ by filter method.

Furthermore, TOF cooling can be able to scrape out the secondary beams in a range of mass-to-charge spread, $7.5e-4 \leq |r| \leq 1.5e-2$, $r = \Delta(m/q)/(m/q)$, as shown in Fig. 9.

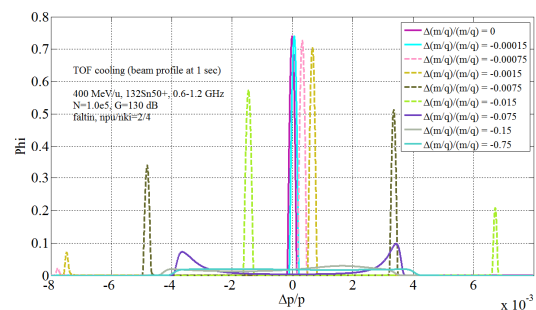


Figure 9: Secondary beam with mass-to-charge spread $7.5e-4 \leq |r| \leq 1.5e-2$ could be scraped out by TOF cooling method after 1.0 sec.

Meanwhile, filter cooling could also be able to scrape out the secondary beams in a range of mass-to-charge spread, $1.5e-4 \leq |r| \leq 1.5e-2$, $r = \Delta(m/q)/(m/q)$, as shown in Fig. 10.

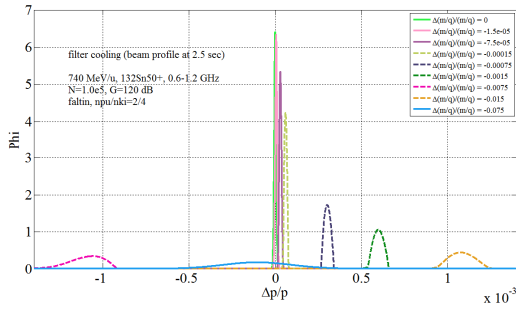


Figure 10: Secondary beam with mass-to-charge spread $1.5e-4 \leq |\Delta(m/q)/(m/q)| \leq 1.5e-2$ could be scraped out by filter cooling method after 2.5 sec.

Combination of TOF and Filter Cooling

For TOF cooling combined with filter cooling, the switch time from TOF to filter is critically important to be considered. When the kinetic energy is 400 MeV/u, the switch time from TOF to filter should be longer than 0.37 s from simulation.

At the same time, different switch times from TOF to filter were also simulated. The results clearly indicate that if the switch time is less than 0.37 s, heating occurs during cooling process. Then, if switch time longer than 0.37 s, cooling effect could not be good enough. Therefore, the optimal switch time from TOF cooling to filter cooling is exactly 0.37 s from the simulation analysis. Result is shown in Fig. 11.

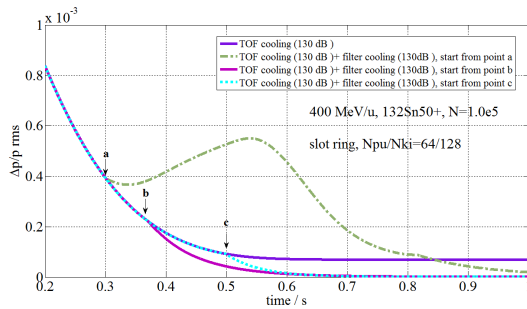


Figure 11: Simulation of different switch times from TOF cooling to filter cooling. Point a is the switch time less than 0.37 s, point b is the switch time 0.37 s and point c is the switch time larger than 0.37s.

It is worth noting that the switch time 0.37 s is not fixed, and depends on many factors, such as the beam kinetic energy, bandwidth, the distance between pickup and kicker and the circumference of the storage ring, and so on. This is because the maximum off-momentum to be cooled by filter method relates to those factors mentioned above, as shown in Eq. (1)-Eq. (6) [6].

$$2m \left| 2x\eta_{pk} + \eta \right| \left| \frac{\delta p}{p} \right| < 1. \quad (1)$$

Here x is the ratio of paths between pickup and kicker and the closed orbit circumference C .

$$m = \frac{f_{min} + f_{max}}{2f_{rev}} \quad (2)$$

$$x = \frac{s_k - s_p}{C} \quad (3)$$

The frequency slip factor is

$$\eta_{pk} = \gamma^2 - \alpha_{pk} \quad (4)$$

With the relativistic Lorentz factor γ and the local momentum compaction factor

$$\alpha_{pk} = \frac{1}{s_k - s_p} \int_{s_p}^{s_k} \frac{D(s)}{\rho(s)} ds \quad (5)$$

$D(s)$ is the dispersion function, and $\rho(s)$ is the local orbit curvature. s_p and s_k are the azimuthal coordinates of pickup and kicker.

Here η stands for the usual frequency slip factor for one revolution around the ring, calculated using Eq. (5) with the usual momentum compaction factor

$$\alpha_P = \frac{1}{C} \int_0^C \frac{D(s)}{\rho(s)} ds \quad (6)$$

Therefore, the optimum switch point from TOF cooling to filter cooling is at the maximum off-momentum where the filter cooling could be able to deal with. In reality, many factors should be taken into consideration for the choice of switch point from TOF cooling to filter, such as amplifier noise, and the delay and so on.

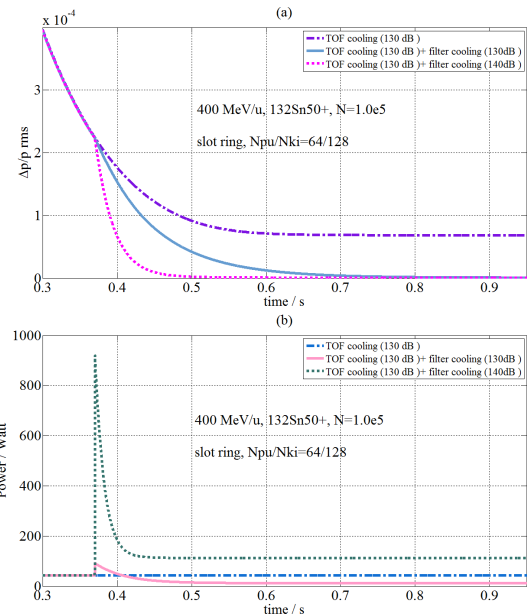


Figure 12: filter cooling simulation with different amplifier gain followed by TOF cooling.

It is clearly from the Fig. 12 that it is a better choice for switching from TOF to filter at an appropriate point during the whole cooling process. This is because after switches,

cooling is obviously faster than before. Besides, after TOF cooling was switched to filter cooling, higher amplifier gain leads to faster cooling, such as 140 dB. However, more microwave power is needed to compensate this optimum cooling process.

CONCLUSION

Stochastic cooling is an effective way to provide a fast precooling of radioactive fragment beams with a large emittance.

For longitudinal stochastic cooling, TOF cooling has maximum acceptance among various methods, and it will be used for SRing stochastic cooling for beams with large momentum spread. Once the momentum spread is reduced to small value stage, filter cooling will be used if the momentum spread could be able to fit into the filter cooling acceptance.

For low beam energy 400 MeV/u, the TOF cooling acceptance is smaller than the initial beam spread $\pm 4.0 \times 10^{-3}$ if the bandwidth is 1-2 GHz. So the bandwidth is changed to 0.6-1.2 GHz, where TOF cooling could be able to deal with.

For lower energy or less particle number, cooling is a little bit faster, equilibrium momentum spread is relatively smaller as well as the power is lower too.

For the electrode structure, cooling would be better if the structure is slot ring with 112 and 224 cell numbers for pickup and kicker respectively.

For TOF cooling combined with filter cooling, the best choice of switch point from TOF cooling to filter cooling is at the maximum off-momentum that fit inside the filter cooling acceptance. In reality, many factors such as amplifier noise, and the delay and so on should be taken into consideration for the choice of switch point from TOF cooling to filter.

TOF cooling can be able to cool the secondary beam but at the expense of losing some particles after cooling.

Both TOF and filter cooling have the ability to scrape out the secondary beam in a range of mass-to-charge spread.

REFERENCES

- [1] Dieter Möhl, Andrew M. Sessler, "Beam Cooling: Principles and Achievements", *Nucl. Instr. and Meth. in Physics Research Section A: Accelerators, Spectrometers, Detectors and Associated Equipment, Volume 532, Issues 1-2, 11 October 2004*, pp. 1-10.
- [2] B. Schlitt, *et al.*, "Schottky mass spectrometry at the heavy ion storage ring ESR", *Hyperfine Interaction. 1996, 99:117-125*.
- [3] H. Stockhorst, R. Stassen, R. Maier, *et al.*, "Experimental Test of Momentum Cooling Model Predictions at COSY and Conclusions for WASA and HESR", *AIP Conference Proceedings, 2007, 950:239-255*.
- [4] T. Katayama, C. Dimopoulou, A. Dolinskii, *et al.*, "Simulation Study of Stochastic Cooling of Heavy Ion Beam at the Collector Ring of FAIR", in *Proc. Int. Workshop on Beam Cooling and Related Topics (COOL'13)*, Mürren, Switzerland, Jun. 2013, paper TUAM1HA04, pp. 52-54.
- [5] John Marriner, "Stochastic Cooling Overview" <https://arxiv.org/ftp/physics/papers/0308/0308044.pdf>
- [6] F. Nolden, I. Nesmiyan, C. Peschke, "On stochastic cooling of multi-component fragment beams", in *Nuclear Instruments and Methods in Physics Research A 564 (2006) 87-93*

COMMISSIONING OF CHINA ADS DEMO LINAC AND BASELINE DESIGN OF CiADS PROJECT*

Shuhui Liu, Zhijun Wang†, Weilong Chen, Weiping Dou, Huan Jia, Yuanshuai Qin, Yuan He, Hongwei Zhao, Institution of Modern Physics, China

Abstract

China Accelerator Driven Subcritical System (C-ADS) program was launched in China in 2011, which aims to design and build an ADS demonstration facility with the capability of more than 10 MW thermal power in multiple phases lasting about 20 years. In the first phase, a demo linac has been constructed and commissioned successfully to demonstrate the key technologies of the high-power CW mode superconducting linac. Followed the China ADS roadmap, a superconducting driver linac with 500MeV and 5mA proton beam is designed for the second phase of China Initiative Accelerator Driven Subcritical System (CiADS) program. The commissioning results of the China ADS 25 MeV demo linac and the RAMI oriented beam physics design of CiADS linac are presented in this paper.

INTRUDUCTION

China Initiative Accelerator Driven Subcritical System (CiADS) program is a strategy project to solve the nuclear waste problem and the resource problem for nuclear power plants in China [1]. It consists three parts, a high-power superconducting proton linac, heavy metal spallation target and the sub-critical nuclear reactor. The high-power superconducting proton linac is comprised of warm temperature front-end accelerator, superconducting section and high energy transportation line, and it will accelerate 10mA proton beam to 1.5GeV [1]. The main design specifications of proton beam at the ultimate stage are shown in Table 1.

Table 1: Specifications of the Required Proton Beams

Particle	Proton	
Energy	1.5	GeV
Current	10	mA
Beam power	15	MW
RF frequency	(162.5)/325/650	MHz
Duty factor	100	%
Beam Loss	<1	W/m
Beam trips/year	<25000	1s<t<10s
	<2500	10s<t<5m
	<25	t>5m

It is extremely challenging to design and build tens of MWs beam power proton linac, and there is no existing machine in the world. To study the key technology and

main factor affecting high reliability and availability of high power accelerator, the accelerator R&D based on a demo linac named China ADS demo linac has been carried out. The China ADS linac has been constructed by the collaborations between Institute of Modern Physics(IMP) and Institute of High Energy Physics(IHEP). This demo linac is composed of an ion source, a low energy beam transport line(LEBT), a 162.5MHz radio frequency quadrupole accelerator(RFQ), a medium energy beam transport line(MEBT), a superconducting accelerating section which contains Half Wave Resonators (HWR) and Spoke resonators and a high energy beam transport line(HEBT). In this paper, the commissioning results of the demo linac and the baseline physics design of CiADS will be presented.

COMMISSIONING OF CHINA ADS DEMO LINAC

China ADS demo linac is operated to accelerate CW proton to 25MeV with beam current of 10mA at 4.5K operation temperature. The total length is about 35m. The schematic view and the photo layout are shown in Fig.1.



Figure 1: The schematic view and the photo layout of China ADS demo linac.

The installation of the demo linac at IMP has been started since August 2014. Up to now, the beam line includes a LEBT, a RFQ, a MEBT, three HWR Cryomodules, a Spoke Cryomodule, a HEBT and a beam dump which can sustain 100 kW beam power.

The 0.2mA CW proton beam with energy of 25MeV and the 12mA pulsed beam with energy of 26.2MeV were achieved in June 2017. The Fig.2 shows the 0.2mA CW beam current. The Time of Flight method is used for the energy measured, the measurement results and the simulation results are coincident as shown in Fig.3.

* Work supported by the National Natural Science Foundation of China (Grant No.11525523 and 11605261)

† email address: wangzj@impcas.ac.cn

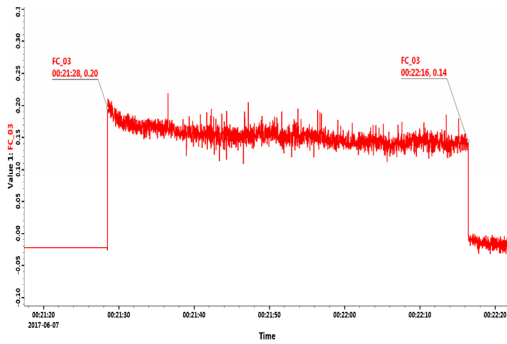


Figure 2: 0.2mA beam current of CW beam.

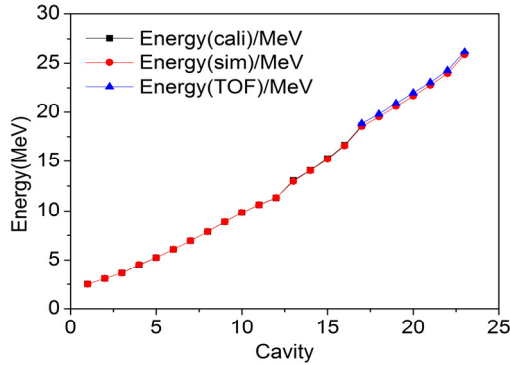


Figure 3: Comparison of measurement and simulated energy results.

For a high-power accelerator, the machine reliability is very important. The machine reliability studies with pulse beam and CW beam were carried out in the China ADS demo facility in December 2017. The fault is defined when the shutdown time duration is more than 10 seconds, and the RF power is CW mode for the pulse beam operation.

Operation Reliability with Pulse Beam

The pulse beam reliability operation study was carried out with two types of beam, 18 MeV proton beam at 1mA with 1Hz and 10us and 18 MeV proton beam at 10mA with 1Hz and 10us. According to the statistical results, for the two types of beam, the demo linac can run continuously for around two hours without fault. It indicates that the effect of beam power to the reliability of demo linac is not serious. From the statistical result as shown in Fig.4, the sources of fault are mainly from ECR ion source, RFQ, power supply, RF system and cryo-plant, and the reliability of the RF system is the lowest. Other systems those are not listed here have no fault.

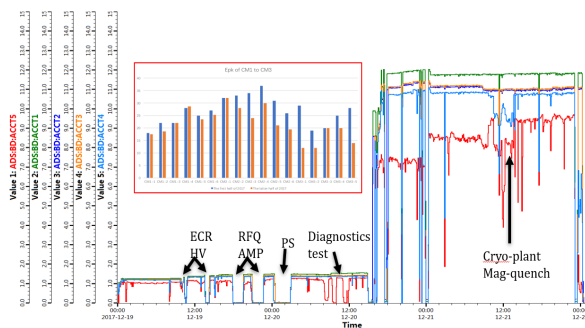


Figure 4: Pulse beam operation reliability test result.

For high power ADS accelerator, high availability is very important. Table 2 shows the availability of China ADS demo linac based on the pulse beam operation reliability test result. The availability is up to 88% [2]. The reasons of the fault maintenance time larger than 5 minutes, such as ECR ion source, Cryo-plant, power supply, are very clear, and they can be avoided in the next stage. However, the reasons of the trips from SRF maintenance time between 10 seconds and 5 minutes, are still under investigation.

Table 2: Availability of China ADS Demo Linac

Operation time (min)	Beam time (min)	Down time (min)	Availability
4050	3566	484	88%

Operation Reliability with CW Beam

Considering the deterioration effect of the high-power beam to superconducting accelerator device, the active protection mode of the machine protection system (MPS) is adopted. According to the beam simulation results, a series of protection conditions for each system of the accelerator are proposed. During the CW beam operation reliability test, The CW proton beam with 0.2 mA beam current can running 1.5 hours without beam trip as shown in Fig.5. The main reasons of beam trips are from RF system and control system. The beam trips from RF systems are mainly caused by phase error, and the beam trips from control system are mainly caused by beam position monitor.

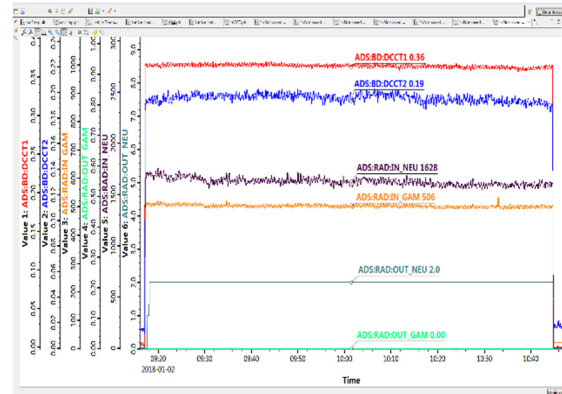


Figure 5: CW beam operation reliability test result.

Reliability analysis forms an important part of designing ADS accelerator. It helps to analyse the performance, and gives insight to the weakness in design based on the predicted failures. Next step, a thorough reliability study at the China ADS demo linac will be continued to master the key physics and technology for high-power machine operation.

PRELIMINARY DESIGN OF CiADS LINAC

CiADS driver linac is defined to be 1.5GeV in energy, 10mA in current and in CW operation mode in three phases. For the first phase, the beam energy is 500MeV, and the beam current is 5mA. The linac consists of a room temperature front end which is considered to do

Content from this work may be used under the terms of the CC BY 3.0 licence (© 2018). Any distribution of this work must maintain attribution to the author(s), title of the work, publisher, and DOI.

the beam quality control, a superconducting linac for highly efficient acceleration and an accelerator to target beam transport line (A2T) which is used to delivering beam to target. The schematic view of the CiADS linac is shown in Fig.6.

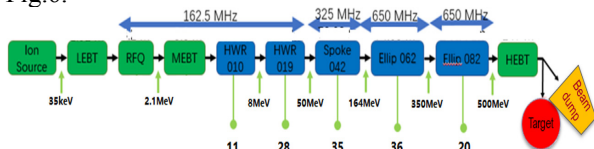


Figure 6: Schematic view of CiADS linac.

Room Temperature Front-end

The room temperature front-end consists of LEBT, RFQ and MEBT. The main function of the front-end accelerator is to guarantee beam quality by beam loss control. First, the design of the LEBT is mainly focus on the transverse beam quality control besides the matching between IS and RFQ. As shown in Fig.7, a 20deg bend magnet is selected to get rid of the H^{2+} and H^{3+} particles to avoid them losing in RFQ cavities. A chopper and diagnostics are included to characterise the beam structure and distribution. What is more, a collimation method is proposed to scrape the outside tail particles just at the end of the ion source to achieve a good transverse beam distribution [3]. The tail particles at the exit of LEBT are tracked back to the entrance of LEBT, and the evolution is shown in Fig.8. It will find that the tail particles exactly the outside ones at the entrance of LEBT. These tail particles can be removed in this way.

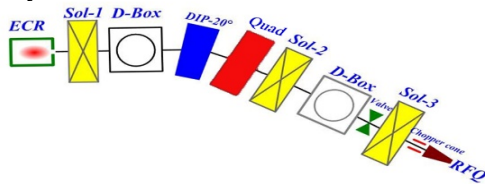


Fig.7 Schematic view of LEBT

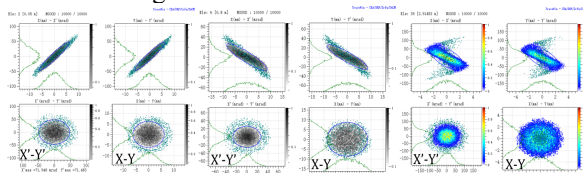


Figure 8: Evolution of the tail particles at the exit of the LEBT.

The 2.1 MeV Radio-frequency Quadrupole (RFQ) is a 4-vane type with a length of 4.57m. As the first RF element, the longitudinal beam distribution is determined by RFQ accelerator to a large extent. The longitudinal beam performance is very critical for beam loss control in the downstream superconducting section. The innovative adaptive-acceptance philosophy is adopted to decrease the 99.9% longitudinal emittance and the probability of beam loss in superconducting section at the cost of low accelerating efficiency. In order to decrease the effect of particle loss on cavity, smaller energy acceptance is kept in the first 150 cells as shown in Fig.9. The final ration of 99.9 % emittance to acceptance of superconducting section is less than $1/5^{[4]}$.

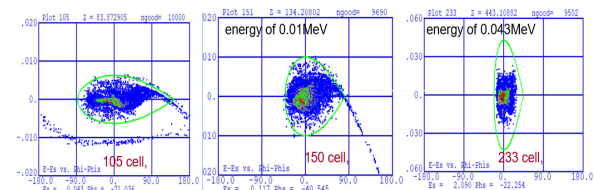


Figure 9: Longitudinal beam space evolution.

Between the RFQ and the superconducting linac, a MEBT, consisting of 7 quadrupoles and 2 RF buncher cavities, is designed to match the beam both in transverse and longitude. Double steering per quadrupole is considered to correct the beam trajectory, and finally there is a selection of beam instrumentation to sufficiently characterise the beam out of the RFQ.

Superconducting Section

The acceleration efficiency and beam loss control are two main issues in the superconducting section. It consists of five families of superconducting cavities which are defined using Particle swarm optimization algorithm (PSO) program based on the cost minimization. Table 3 shows the cavity parameters in CiADS linac.

Table 3 Cavity Parameters of SC Section in CiADS Linac

Cavity type	βg	Frequency MHz	Emax MV/m
Squeezed HWR	0.10	162.5	32
Taper HWR	0.19	162.5	32
3-cell Spoke	0.42	325	33
5-cell Elliptical	0.62	650	33
5-cell Elliptical	0.82	650	33

With the large energy range and the different acceleration structures, it is less effective to design the same focusing structure for the whole linac. Different periodic lattice in both the transverse and longitudinal planes are used for the best-fit to the different energy ranges as shown in Fig.10.

In the low energy part, As the defocusing effect of the RF field and space charge effect are evident, superconducting solenoids are used effectively to compact the lattice structure to increase the acceleration efficiency and acceptance. In addition, superconducting solenoids can be fit well into cryostats together with superconducting cavities, and this can help reduce the total length of the linac. For the high energy part, the quadrupole triplets are placed to increase the reliability and maintainability of this section. In addition, considering the effect of beam loss from beam halo on the superconducting cavities, the quadrupoles with beam pipe of 80mm are used to scraped the uncontrol halo particles, and the beam pipe of elliptical cavities are 100mm. Still full period lattice structure is a good choice to reduce the effect from mismatch. In

addition, optimization at the location of structure transition and frequency jump is concerned seriously to immigrate the longitudinal beam loss.

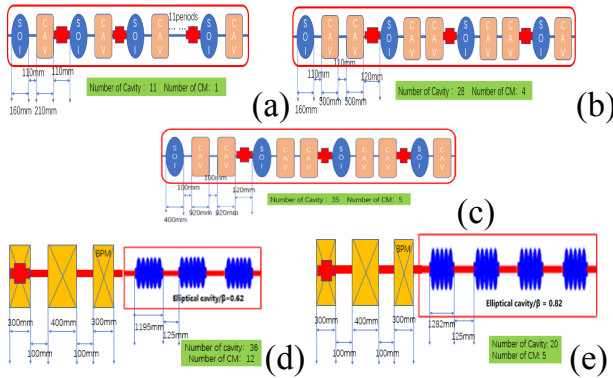


Figure 10: Focusing structure of each accelerating part (a)HWR010 (b)HWR019 (c)Spoke042 (d)Ellip062 with 6cells (e) Ellip082 with 5cells.

Based on the lattice structure mentioned above, design, optimization and multiparticle simulation have been done. The emittance evolution of three planes with different particles are shown in Figs. 11-12. There is no intense emittance oscillation in three planes. The 99.99% emittances growth are 14.3%, 19.9% and 24.4% in these planes respectively.

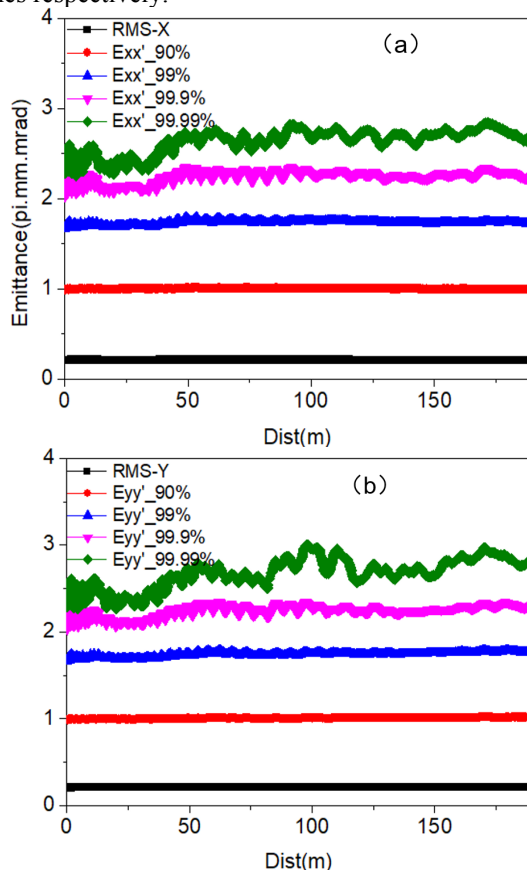


Figure 11: The emittance evolution with different particles along the SC section in the X (a) and Y(b) direction.

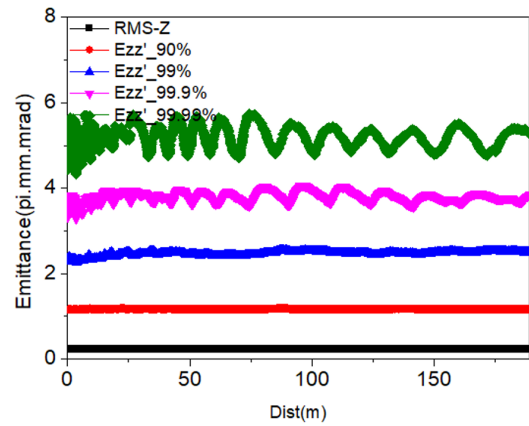


Figure 12: The emittance evolution with different particles along the SC section in the Zdirection.

Accelerator to Target Beam Line

A2T beam line is the coupling section between SC linac and target. Based on the requirements from Target, there are several specifications. The lossless transportation of 2.5 MW proton beam is the basic function. In the physics design, the beam out of superconducting section is matched to a 7 m period transport line which is used to achieve the envelope control by a series of quadrupoles. After the high energy transport line, the beam is horizontally deflected by two 10-degree dipole magnets, and after 25 m of linear transportation, the beam is deflected vertically downward by two 45-degree dipole magnets, and the deflection section is achromatic design. The Fig.13 gives schematic view of the accelerator to target beam transport line.

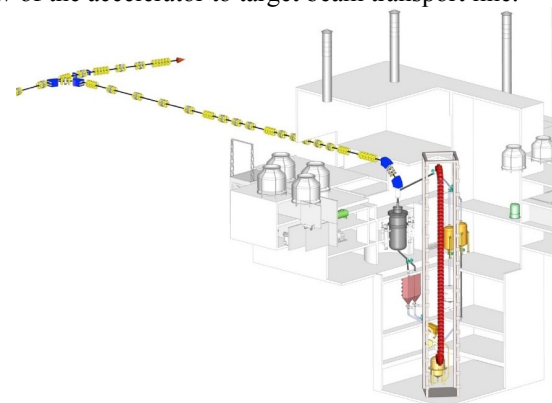


Figure 13: The schematic view of accelerator to target beam transport line.

Second, the homogenization of the beam on the 250 kW thermal power particle flow target is a crucial requirement for this A2T beam line, A radial-angular scanning method is considered to homogenize the power density, and the results of beam scanning for a Gaussian distribution is shown in Fig.14. The peak power density of the beam spot after scanning is $26 \mu\text{A}/\text{cm}^2$.

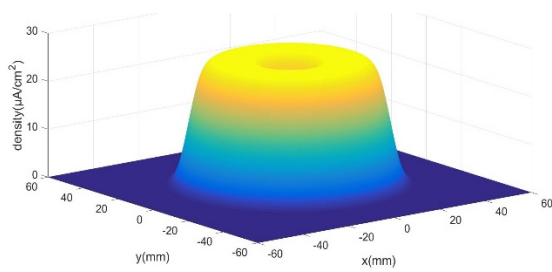


Figure 14: Beam spot density distribution after scanning.

In addition, the beam parameters measurement and reconstruction are critical to beam commissioning of the coupling experiment. So, some beam diagnostic instruments are placed in the periodic transport section to do the beam parameters measurement. Given the upgrade of the accelerator in the future, a 70 m extra space is also considered in this A2T beam transport line.

SUMMARY

The China ADS Front-end demo linac has been constructed, and the CW beam and reliability operation have been done. The 0.2mA CW proton beam with energy of 25MeV and the 12mA pulsed beam with energy of 26.2MeV were achieved. Preliminary reliability studies have been done. The availability is about 88%. Some improvements are considered to improve the reliability and availability.

The baseline physics design of CiADS linac with 500MeV and 5mA has been optimized based on the rules of the thumb in high-power proton linacs. The further engineering optimization and error analysis will be carried out in the next step.

ACKNOWLEDGEMENT

The authors want to express the sincere thanks to all the colleagues in the CiADS accelerator team for the support and discussions, and also the international review committee members for many valuable suggestions and comments during and beyond the reviews.

REFERENCES

- [1] Z. H. Li, P. Cheng, H. P. Geng *et al.*, *Physical Review Special Topics:Accelerators and Beams* 16(2013) 080101
- [2] Y. He, “Beam Dynamic of Accelerator for CiADS & Commissioning of CAFé”, in Proc. HB’2018, Daejeon, Korea, June 2018, MOP1WB01.
- [3] W. L. Chen, “LEBT Design Based on Beam Loss Control”, Master. Thesis, Phys. Dept., Institute of Modern Physics, Lanzhou, China, 2016.
- [4] W. P. Dou, “Beam Dynamics Design of CW RFQ for Chinese ADS”, in Proc. HB’2018, Daejeon, Korea, June 2018, MOP2WB04.

HIGH-BRILLIANCE NEUTRON SOURCE PROJECT

P. Zakalek*, T. Cronert, J. Baggemann, P.-E. Doege, M. Rimmler, J. Voigt, E. Mauerhofer,
U. Rucker, T. Gutberlet, Th. Brückel

Jülich Centre for Neutron Science, Forschungszentrum Jülich GmbH, 52425 Jülich, Germany
H. Podlech, O. Meusel, M. Schwarz, Institut für Angewandte Physik, Goethe-Universität Frankfurt,
60438 Frankfurt am Main, Germany

J. Li, Institut für Energie- und Klimaforschung, Forschungszentrum Jülich GmbH,
52425 Jülich, Germany

S. Böhm, Nuclear Engineering and Technology Transfer,
RWTH Aachen University, 52062 Aachen, Germany

Abstract

The High-Brilliance Neutron Source (HBS) project aims to design a scalable compact accelerator driven neutron source (CANS) which is competitive and cost-efficient. The concept allows one to optimize the whole facility including accelerator, target, moderators and neutron optics to the demands of individual neutron instruments. Particle type, energy, timing, and pulse structure of the accelerator are fully defined by the requirements of a given neutron instrument. In the following, we present the current status of the HBS project.

INTRODUCTION

The neutron landscape in Europe is in a time of change. On the one hand, the European Spallation Source (ESS) is being constructed as world-leading neutron facility but on the other hand many research reactors used for neutron experiments, like the BER-II reactor in Germany or the ORPHEE-reactor in France, are fading out [1]. The European community for neutron research is therefore facing a mixed outlook towards the availability of neutrons in coming decades. As new reactor sources or spallation sources are costly and therefore difficult to realize, new possibilities for neutron production need to be investigated.

In the HBS project we are developing a scalable compact accelerator driven neutron source (CANS) optimized for scattering and neutron analytics. This type of source produces neutrons using nuclear reactions of protons or deuterons in a suitable target material. At these sources, the whole chain ranging from the accelerator to the target / moderator / shielding assembly and the neutron optics can be optimized according to the needs of the neutron experiments. This approach makes such sources very efficient enabling competitive neutron fluxes at the sample position compared to today's research reactors.

Being a scalable neutron source, the performance level can vary from a low power pulsed neutron source designed for universities and industry with an average power at the target of around 1 kW to a high performance neutron source with ~100 kW average power designed as a full-fledged national facility. We have named the low power CANS NOVA

ERA ("Neutrons Obtained Via Accelerator for Education and Research Activities") [2] which is used for basic research, user training and method development, whereas the full-fledged facility compares favorably to nowadays medium flux neutron sources and is operated as a user facility.

In the subsequent text we will describe all basic components of such a source.

HBS LAYOUT

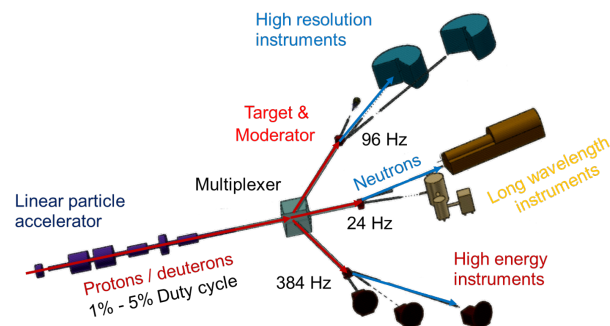


Figure 1: The layout for a high-performance accelerator driven neutron source.

The basic design of a CANS is shown in Figure 1. It consists of a pulsed proton or deuteron accelerator, a multiplexer distributing the protons or deuterons to different target stations each consisting of a target / moderator / shielding assembly and neutron experiments. The neutron experiments with similar requirements for the neutron beam properties are grouped together on the same target station and all upstream elements are optimized to meet these requirements.

This is a general layout which can differ in the specific realization. For example, a low power / low cost CANS like the NOVA ERA will not be equipped with a beam multiplexer and will only maintain one target station.

Accelerator

The protons or deuterons used for the nuclear reaction need to be accelerated to an energy between 10 MeV and 100 MeV. Various types of particle accelerators are available for this purpose, e.g a tandem accelerator, a cyclotron or a

* p.zakalek@fz-juelich.de

Content from this work may be used under the terms of the CC BY 3.0 licence (© 2018). Any distribution of this work must maintain attribution to the author(s), title of the work, publisher, and DOI.

linear accelerator. A tandem accelerator or a cyclotron are limited to a maximal current and are an option for the low power CANS. For the large scale CANS facility, a linear accelerator with dedicated radio frequency quadrupoles (RFQ) is used which delivers peak beam currents up to 100 mA. The specific current and energy values for both types of CANS facilities are summarized in Table 1.

Table 1: Accelerator Parameters used in the HBS Project

	NOVA ERA	Large scale facility
Accelerator	Tandem	Linac
Particle type	Proton / Deuteron	Proton
Energy	10 MeV	70 MeV
Current	1 mA	100 mA
Frequencies	48 - 384 Hz	384, 96, 24 Hz
Duty cycle	4%	~ 4.3 %
Peak beam power	10 kW	7 MW
Average beam power	0.4 kW	~ 3 · 100 kW

The NOVA ERA accelerator employs a low particle beam energy of 10 MeV with 1 mA beam current where commercially available Tandetrans are available. This design uses just one repetition rate which is optimized to the needs of the instruments.

The large scale facility will use a pulsed proton beam with energies up to 70 MeV and a peak current of 100 mA. The accelerator has to provide a pulsed proton beam for at least three target stations with an average beam power of 100 kW each resulting in an average beam power of 300 kW and a total duty cycle of ~ 4.3%. With these parameters a normal conducting accelerator is the preferable choice as similar accelerators already exists like the Linac-4/SPL, the FAIR-p-Linac, the ESS or the SNS accelerators. The advantages of the room temperature (RT), normal conducting, linear accelerator are easy access, a simpler and available technology, lower price and higher reliability.

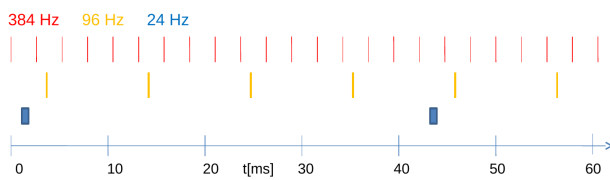


Figure 2: Pulse structure provided by the accelerator for the large scale facility.

Instruments at the different target stations are optimized to use a pulsed proton beam with different frequencies of 24 Hz, 96 Hz and 386 Hz. The pulsing structure needed is shown in Figure 2. The frequencies and duty cycles are chosen in a way that the pulses do not overlap and that the maximal depositable power can be delivered to a dedicated target.

Multiplexer

The three particle beam pulse structures need to be distributed to different target stations. For this reason, a particle beam multiplexer will be used downstream from the linear accelerator. Hereby, a geometric request to the deflection angle from the closed orbit comes from the ion beam dynamics of the setup. In order to avoid divergence and subsequent beam loss, the maximal length of propagation of particles without focusing ion optics is being restricted to ~5 m. This sets a lower limit to the deflection angle provided by a stand-alone kicker magnet. In order to overcome this limitation, a kicker magnet and septum magnet combination will be employed as it is shown exemplarily in Figure 3.

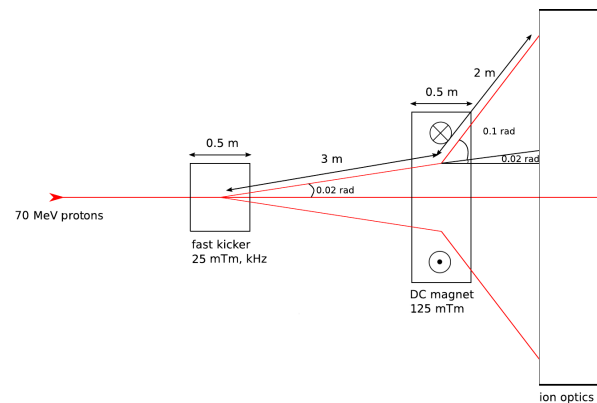


Figure 3: The multiplexer used to separate the different pulse structures.

A fast kicker magnet introduces a 20 mrad kick angle onto the beam's closed orbit which requires an integrated magnetic field strength of 25 mT·m. The field rise time is dominated by the pulse structure shown in Figure 2 and results in less than 800 μs, so that the fast kicker can switch the fields between adjacent pulses. After a well-defined separation of the beam from the closed orbit, a 125 mT·m DC magnet takes over further deflecting the beam. More detailed design studies of the kicker magnet are in progress.

Target / Moderator / Shielding Assembly

The target / moderator / shielding assembly is presented in Figure 4 and consists of the target which is surrounded by a thermal moderator like polyethylene (PE) moderating the fast neutrons with MeV energy to thermal energies between 10 meV and 500 meV. A reflector like beryllium, lead or molybdenum increases the thermal neutron flux inside the moderator due to backscattering. Everything is surrounded by the shielding consisting of borated PE and lead.

Extraction channels directing the thermalized neutrons to the experiments are inserted into this assembly. Their location is optimized in such a way that they extract the neutrons from the maximum of the thermal neutron flux inside the moderator. Into these extraction channels cryogenic one-dimensional finger moderators [3] can be inserted further shifting the thermalized neutron spectrum to cold energies between 1 meV and 10 meV.

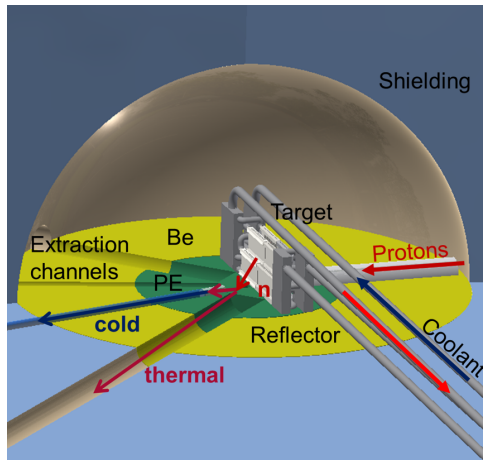


Figure 4: The target / moderator / shielding assembly.

The advantage of the compact design is the possibility to place the first optical elements like neutron guides, filters and choppers close to the target / moderator. Therefore, a large neutron phase space volume can be transferred to the instruments increasing the brilliance. Less neutrons are produced with the nuclear reaction in comparison to spallation or fission, but with this compact design this is compensated by the improved coupling of the moderator and extraction system making the source competitive to modern research reactors.

As the whole target / moderator / shielding assembly is optimized to the needs of the instrument and especially as each instrument can have its own optimized cryogenic source, this approach initiates a paradigm change: "Each instrument has its own source".

Neutron Production

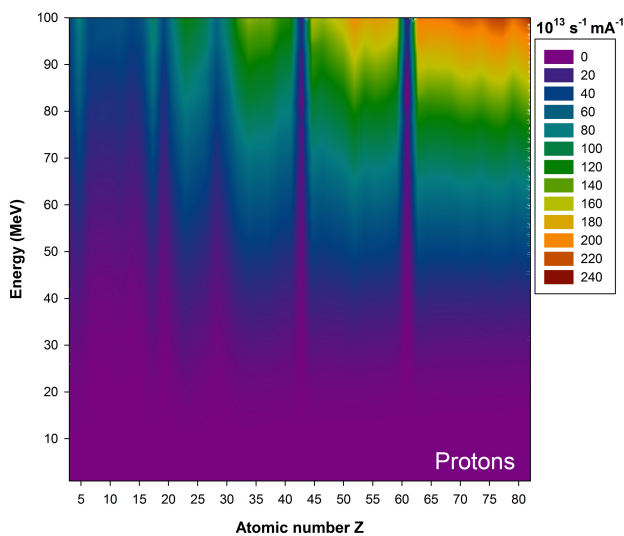


Figure 5: The proton induced neutron yield depending on the primary particle energy for the first 85 elements.

The neutrons are produced by nuclear reaction in a suitable target material. The neutron yield depends on the cross section, the primary particle energy and the stopping power of the target material. Therefore, different target materials are preferable depending on the energy. In Figure 5 the neutron yield for protons at various energies for the first 85 elements is presented.

For energies below 30 MeV, low Z materials are preferable like beryllium or lithium. For energies above 50 MeV, high Z materials like tungsten or tantalum are preferable regarding the neutron yield. As the power depends directly on the energy, a low power CANS like the NOVA ERA will therefore use a beryllium target and the large scale facility will utilize a high Z material like tantalum.

Table 2: Average neutron yield for different power levels, energies and target materials calculated using the TENDL 2017 database [4].

power [kW]	energy [MeV]	target	neutron yield [s ⁻¹]
0.4	10	beryllium	3 · 10 ¹¹
1	16	beryllium	1 · 10 ¹²
10	30	beryllium	2 · 10 ¹³
100	70	tantalum	5 · 10 ¹⁴

The expected average neutron yields are summarized in Table 2 for different power levels, energies and target materials.

Target

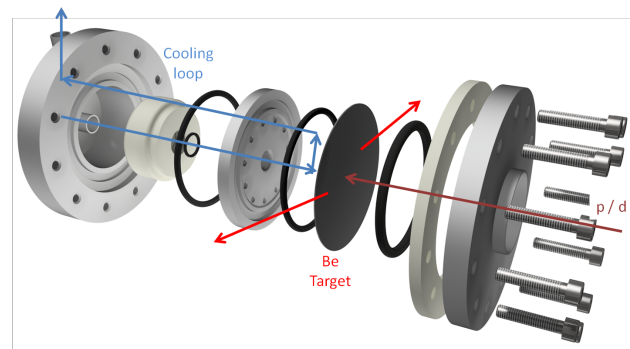


Figure 6: Target design for a NOVA ERA source at a power level of 0.4 kW.

The target design depends on the power it has to withstand, the type and energy of the primary particle and the target material. The target material defines the stopping power and the thermomechanical properties. The energy dependency is related to the stopping range of the primary particles in the target material as the thickness of the target has to be smaller than the stopping range. This will produce most neutrons ($\geq 99\%$) but prevent deposition of hydrogen atoms into the target material ($\leq 0.1\%$) avoiding hydrogen accumulation

Content from this work may be used under the terms of the CC BY 3.0 licence (© 2018). Any distribution of this work must maintain attribution to the author(s), title of the work, publisher, and DOI.

and blistering [5]. With these complex dependencies, each parameter requires its own target design.

The target design for the NOWA ERA source at an average power level of 0.4 kW and a proton energy of 10 MeV is shown in Figure 6. The target is composed of a 0.7 mm thick beryllium window clamped in an aluminum housing [2] and cooled by a water jet. The mechanical simulations with the ANSYS toolkit show that the temperature inside the target is around 50°C and the yield strength around 80 MPa well below the yield strength of beryllium.

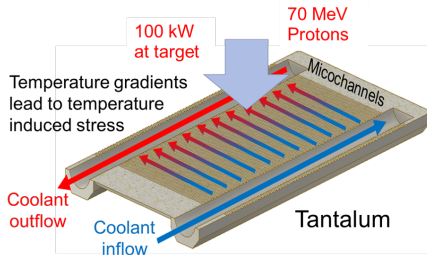


Figure 7: Target design for a large scale facility source at a power level of 100 kW.

The target design for the large scale facility at a power level of 100 kW and a tantalum target is more sophisticated. The power density deposition with a target area of 100 cm² is 1 kW/cm² and cannot be cooled by conventional cooling. In order to cool such a power density it is necessary to use μ -channels which can remove up to 3.5 kW/cm² [6]. The target concept using a direct μ -channel cooling of the tantalum target is shown in Figure 7. With a complex fin-like μ -channel structure, it is possible to remove the heat very efficiently and achieve temperatures inside the target which are below 100°C and a temperature induced stress of around 80 MPa well below the yield strength of tantalum (300 MPa) as calculated using the ANSYS toolkit.

Moderators

The fast energy neutrons in the MeV range need first to be moderated to thermal energies between 10 meV and 500 meV which will be done by a PE moderator with a diameter of about 10 cm surrounding the target.

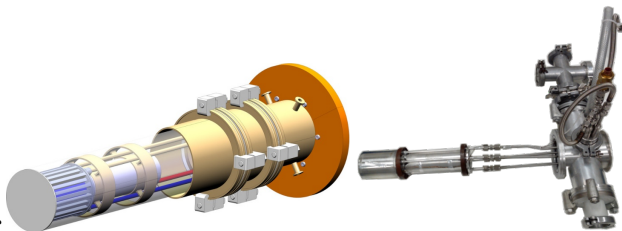


Figure 8: The design and construction of a one-dimensional finger moderator.

Depending on the instrument, a cryogenic moderator shifting the neutron spectrum to energies between 1 meV and 10 meV is needed. For this purpose a one-dimensional finger

moderator as shown in Figure 8 is inserted into the extraction channel positioned at the thermal maximum in the PE moderator. The cryogenic moderator is filled with a suitable material like solid methane, mesitylene or liquid hydrogen with a specific ortho/para ratio at cryogenic temperatures.

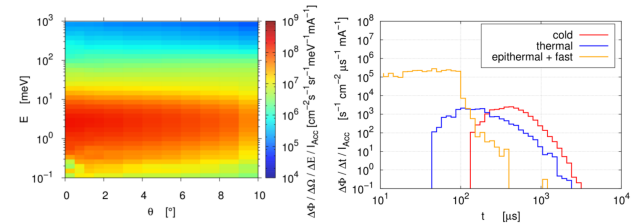


Figure 9: Left: Brilliance as a function of wavelength and divergence for a cryogenic moderator filled with methane [2]. Right: Time structure of this moderator [2].

The dimensions and the moderator material of the cryogenic one-dimensional moderator are optimized to the requirements of the instrument. MCNP6 simulations were used to determine and optimize the neutron phase space volume leaving the extraction channel which is shown in Figure 9. The neutron bandwidth, the pulse width and the divergence is matched to the requirements of the instruments. With this approach, each instruments has its own source.

Instruments

Table 3: Analytically Calculated Instrument Parameters for a NOVA ERA Source [2,7]

	Resolution [Å ⁻¹]	Bandwidth [Å]	Flux [s ⁻¹ cm ⁻²]
Large scale structures			
Reflectometer	0.34	2 - 9.5	5 · 10 ⁴
SANS	0.48	2 - 10.3	7 · 10 ⁴
	0.44	2 - 8.3	2 · 10 ⁴
	0.36	2 - 8.3	4 · 10 ³
	0.31	2 - 7.4	1.5 · 10 ³
Diffractometers			
Powder	0.006	1.1 - 2.0	4.3 · 10 ³
Analytics			
Imaging	0.5 mm, 0.3 Å	1 - 7	2.5 · 10 ³
PDGNAA, NDP	-	-	1.4 · 10 ⁷

The instruments built at a pulsed CANS are designed in a time-of-flight (TOF) setup and can be mainly distinguish by the bandwidth they can use and the resolution they need. The bandwidth and the resolution can be defined by choppers which in most cases results in a loss in neutron flux at the sample position. A more efficient approach is to match the repetition rate of the neutron beam to the instrument length in such a way that the maximal useful phase space volume is filled. For a large scale facility we distinguish at least

three different repetition rates, eg. 24 Hz, 96 Hz and 384 Hz. Instruments using these repetition rates are grouped together and built at the same target station.

Table 4: Analytically Calculated Instrument Parameters for a Large Scale Facility

	Resolution [Å ⁻¹]	Bandwidth [Å]	Flux [s ⁻¹ cm ⁻²]
Large scale structures operating at 24 - 48 Hz			
Reflectometer	0.2	1.2 - 5.7	1.3 · 10 ⁸
SANS	0.31	3 - 8.4	2.4 · 10 ⁷
	0.27	3 - 7.7	5.3 · 10 ⁶
	0.23	3 - 7	1.5 · 10 ⁶
	0.2	3 - 6.4	6 · 10 ⁵
Diffractometers operating at 96 Hz			
Powder	0.003	1.3 - 2.6	6 · 10 ⁶
Spectrometers operating at 100 - 400 Hz [8]			
Backscattering	1	1.84	2.5 · 10 ⁷
Cold ToF	2	5	1.3 · 10 ⁵
Thermal ToF	5	45	1 · 10 ⁵
Analytics operating at 24 - 96 Hz			
Imaging	0.5 mm, 0.2 Å	1 - 7	4.4 · 10 ⁶
PDGNAA, NDP	-	-	2.5 · 10 ¹⁰

At the highest repetition rate of 384 Hz, short length secondary spectrometers for inelastic neutron scattering experiments will be built. As the flight path is short, the phase space volume can be filled with a high repetition rate so that the flux is maximized. The target station with the intermediate repetition rate of 96 Hz will provide neutrons for high resolution thermal diffractometers with a larger bandwidth. At the low repetition rate of 24 Hz, instruments with a large bandwidth of cold neutrons with a relaxed resolution will be built like a reflectometer so that these instruments have no resolution problem with long pulses.

Analytic instruments like a prompt and delayed gamma neutron activation analysis (PDGNAA), neutron depth profiling (NDP) or an imaging station will be built at the target station with the low or intermediate repetition rate. The resulting resolution can resolve Bragg-edges for the imaging experiment and the PDGNAA can be operated in ToF-mode giving depth resolved information.

The expected neutron fluxes at the sample position for a NOVA ERA source where all instruments are built at a single target station are presented in Table 3. The neutron fluxes with for the large scale facility with three different target stations and adjusted proton pulse frequencies are presented in Table 4.

TIMELINE

The current aim of the HBS project is to develop and realize the large scale CANS facility. For this, a conceptual design report will be written and published. It will give an

overview about the project and describes all relevant parts. As many different technological challenges are present in the HBS project ranging from accelerator system, neutron targets, moderators up to the instruments, it is necessary to investigate the components individually. A dedicated technical design report will be prepared within the next years.

The project aims to realize a prototype facility to be constructed within the next five years to prove that the concept is working and the full-fledged facility can be constructed within the next decades.

CONCLUSION

The HBS project develops a scalable accelerator driven neutron source optimized for neutron experiments. It ranges from a low power CANS named NOVA ERA which can be built at universities and industry and perform basic experiments to a high power CANS which has competitive fluxes at the sample position to nowadays neutron experiments.

CANS come at a much smaller price tag than research reactors or spallation sources, avoid the problem with nuclear licensing and the nuclear fuel cycle, and allow one to construct instruments fitting to the particular problem at hand, e.g. smaller samples.

The approach of the scalable accelerator driven neutron source enables one to develop a network of large and small neutron sources throughout Europe improving the access to neutrons.

REFERENCES

- [1] ESFRI Scripta Volume I, ESFRI Physical Sciences and Engineering Strategy Working, Group Neutron Landscape Group, June 2016, Editors: Colin Carlile and Caterina Petrillo
- [2] E. Mauerhofer *et al.*, "Conceptual Design Report NOVA ERA (Neutrons Obtained Via Accelerator for Education and Research Activities) A Jülich High Brilliance Neutron Source project", Schriften des Forschungszentrums Jülich Reihe Allgemeine / General, Band/ Volume 7, 2017
- [3] T. Cronert *et al.*, "High brilliant thermal and cold moderator for the HBS neutron source project Jülich", Journal of Physics: Conference Series, vol. 746, no. 1, 2016
- [4] A.J. Koning and D. Rochman, "Modern Nuclear Data Evaluation With The TALYS Code System", *Nuclear Data Sheets*, vol. 113, no. 2841, 2012
- [5] V.T. Astrelin *et al.*, "Blistering of the selected materials irradiated by intense 200keV proton beam", *Journal of Nuclear Materials*, vol. 396, no. 1, 2010
- [6] P. Mastinu *et al.*, "Micro-channel-based high specific power lithium target", *Nuovo Cim.*, vol. C38, no. 6, 2016, doi:10.1393/ncc/i2015-15193-y
- [7] P. Zakalek *et al.*, "Workhorse Scattering Instruments for Low Power Compact Accelerator Driven Neutron Sources", *JPS conference proceedings* vol. 22, no. 011025, 2018, doi:10.7566/JPSCP.22.011025
- [8] J. Voigt *et al.*, "Spectrometers for compact neutron sources", *Nuclear Inst. and Methods in Physics Research, A*, vol. 884, no. 11, 2018

THE DC130 PROJECT: NEW MULTIPURPOSE APPLIED SCIENCE FACILITY FOR FLNR

S. Mitrofanov[†], P. Apel, V. Bashevoy, V. Bekhterev, S. Bogomolov, O. Borisov, J. Franko, B. Gikal, G. Gulbekyan, I. Ivanenko, I. Kalagin, N. Kazarinov, V. Mironov, V. Semin, V. Skuratov, A. Tikhomirov, Joint Institute for Nuclear Research, 141980, Dubna, Russia

Abstract

The main activities of Flerov Laboratory of Nuclear Reactions, following its name - are related to fundamental science, but, in parallel, plenty of efforts are paid for practical applications. Certain amount of beam time every year is spent for applied science experiments on FLNR accelerator complex. For the moment, the main directions are: the production of the heterogeneous micro - and nano-structured materials; testing of electronic components (avionics and space electronics) for radiation hardness; ion-implantation nanotechnology and radiation materials science. Basing on FLNR long term experience in these fields and aiming to improve the instrumentation, the accelerator department start the Design Study for new cyclotron DC130 which will be dedicated machine for applied researches in FLNR. Following the user's requirements DC130 should accelerate the heavy ions with mass-to-charge ratio A/Z of the range from 5 to 8 up to fixed energies 2 and 4.5 MeV per unit mass. The first outlook of DC130 parameters, its features, layout of its casemate and general overview of the new FLNR facility for applied science is presented.

INTRODUCTION

The main point is that for applied science people use powerful machines which were created and developed to solve the wide range of fundamental research. The usage of 'science' accelerators for such activities is connected which high cost of beam time and difficulty to meet quick changes of user's requirements. There is a "time lack" problem when application begin to demand the beam time more than laboratory could provide to it in parallel with its scientific plan's realization. Usually, it means that all technical "bugs" and methodological questions were successfully fixed and answered, and users requesting the time as much as they could. That's why Flerov Laboratory of Nuclear Reaction of Joint Institute for Nuclear Research starts the Design Study of the dedicated applied science facility based on the new DC130 cyclotron. The irradiation facility will be used mainly for the following applications: creation and development of track membranes (nuclear filters) and the heavy ion induced modification of materials; activation analysis, applied radio-chemistry and production of high purity isotopes; ion-implantation nanotechnology and radiation materials science; testing of electronic components (avionics and space electronics) for radiation hardness. From the com-

mon user's requirements, operation simplicity and cost reasons the main parameters of future machine were chosen. The facility will be based on new DC130 isochronous cyclotron: multiparticle, double - energy machine, capable with light and heavy ions up to bismuth (2 and 4.5 MeV/nucleon).

The research works on radiation physics, radiation resistance of materials and the production of track membranes will be carrying out by using the ion beams with energy of about 2 MeV per unit mass and A/Z ratio in the range from 7.58 to 8.0. Besides these, testing of avionics and space electronics by using of ion beams (^{20}Ne , ^{40}Ar , $^{84,86}\text{Kr}$, ^{132}Xe , ^{197}Au or ^{209}Bi) with energy of 4.5 MeV per nucleon and with mass-to-charge ratio A/Z in the range from 5.0 to 5.5, will be proceeded. One of the significant requirements for this application is the "ion cocktail" means mixed of highly charged heavy ions with the same or very close mass/charge ratios produced and injected in the same time. Once the ions will be accelerated, the different species will be separated by the fine tuning of the cyclotron magnetic field. This issue allows to switch the type of ions quick and will reduce the time which user should spent for full scale testing of its samples.

The idea is to effectively use existing stuff to modernize and totally upgrade the old U200 machine which was decommissioned in 2013, because of being outdated physically and technologically. The design will be based on existing systems of IC100 (Fig.1) and U200 (Fig.2) cyclotrons [1].

The working diagram of DC130 cyclotron is shown in Fig.3. The acceleration of ion beam in the cyclotron will be performed at constant frequency $f = 10.622$ MHz of the RF-accelerating system for two different harmonic numbers h . The harmonic number $h = 2$ corresponds to the ion beam energy $W = 4.5$ MeV/u and value $h = 3$ corresponds to $W = 1.993$ MeV/nucleon. The intensity of the accelerated ions will be about 1 μA for lighter ions ($A \leq 86$) and about 0.1 μA for heavier ions ($A \geq 132$).

The axial injection system and its beam line for new accelerator will be adapted from the existing IC100 cyclotron systems.

In the frame of reconstruction of U200 to DC130 it is planned to upgrade the cyclotron magnetic structure, replace the magnet main coil and renovate RF system. Other systems: beam extraction, vacuum, cooling, control electronics and radiation safety will be new.

[†] mitrofanov@jinr.ru



Figure 1: Layout of IC100 cyclotron.



Figure 2: Layout of U200 cyclotron.

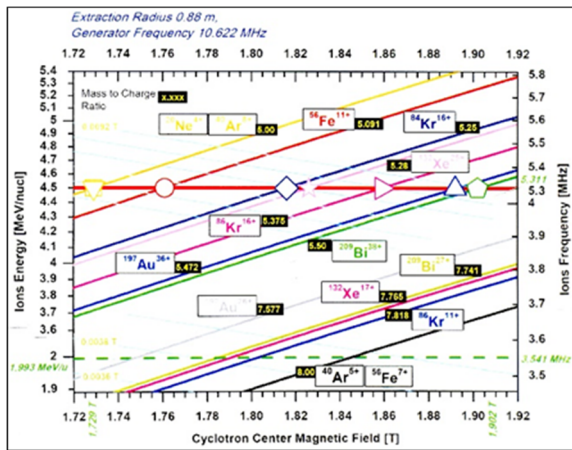


Figure 3: Working diagram of DC130 cyclotron.

The main parameters of DC130 cyclotron are contained in Table.1.

Table 1: DC130 Cyclotron Main Parameters

Pole (extraction) radius, m	1(0.88)	
Magnetic field, T	1.729÷1.902	
Number of sectors	4	
RF frequency, MHz	10.622	
Harmonic number	2	3
Energy, MeV/u	4.5	1.993
A/Z range	5.0÷5.5	7.577÷8.0
RF voltage, kV	50	
Number of Dees	2	
Ion extraction method	electrostatic deflector	
Deflector voltage, kV	60	

ECR SOURCE AND AXIAL INJECTION SYSTEM

The axial injection system [2] of DC130 cyclotron will be adapted from the existing IC100 cyclotron one consisted of the 18 GHz DECRIS-5 ion source which was developed based on sources of the DECRIS-4 (14 GHz) series with copper windings created at FLNR (JINR, Dubna) by intensifying the magnetic structure and changing to a new type of microwave oscillator. The DECRIS-5 ion source was created for industrial application and characterized by increased reliability. It was already successfully commissioned in the framework of DC110 project (mass production of the track membrane) [3]. Also transport beam line will be based on DC110 experience [4].

DC130 MAGNETIC SYSTEM

The magnetic system of DC130 cyclotron will be based on the existing U200 cyclotron one. The magnetic field distribution in the median plane of the DC130 cyclotron magnet has been found by means of computer simulation with 3D OPERA program code [5]. The main parameters of the magnet are contained in Table 2.

Table 2: DC130 Cyclotron Magnet Main Parameters

Size of the magnet, mm	5000×2100×3600
Diameter of the pole, mm	2000
Distance between the poles, mm	160
Number of the sectors pairs	4
Sector angular extent (spirality)	43° (0°)
Sector height, mm	45
Distance between the sectors (magnet aperture), mm	30
Distance between the sector and pole (for correcting coils), mm	20
Number of radial coils	6
Maximal power, kW	≈ 300

The operation mode change will be implemented only by variation the level of the magnetic field in the range from 1.729T to 1.902T and its isochronous distribution will be formed operationally by means of six radial correcting coils. The detail information about magnetic system of DC130 cyclotron contains in report [6].

Content from this work may be used under the terms of the CC BY 3.0 licence (© 2018). Any distribution of this work must maintain attribution to the author(s), title of the work, publisher, and DOI.

RF SYSTEM

The working frequency of RF system is constant and equal to 10.622 MHz. The scheme of RF-resonator is shown in Fig.4. The dashed line designates the placement of the ground plate. Two generators are used for independent feed of two RF resonators.

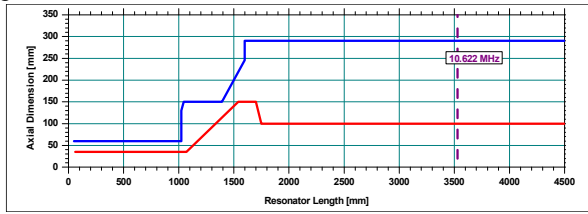


Figure 4: Scheme of RF resonator.

The feedback system ensures precise tuning of RF phase and amplitude at both dees independently. The evaluated power of each RF generator is equal to 11.5 kW.

BEAM EXTRACTION SYSTEM

The scheme of beam extraction system of DC130 cyclotron is shown in Fig. 5. The dashed line is the cyclotron orbit corresponding to average radius of 88 cm. The red line is extraction orbit ending in the object point of the experimental beam lines. The beam extraction system includes the electrostatic deflector ESD and two magnetic static channel MC1,2. In accordance with results of simulation, the maximum voltage at the deflector ESD is equal to 60 kV. The magnetic field gradients in MC1,2 channels are equals to 25 T/m and 8 T/m correspondingly.

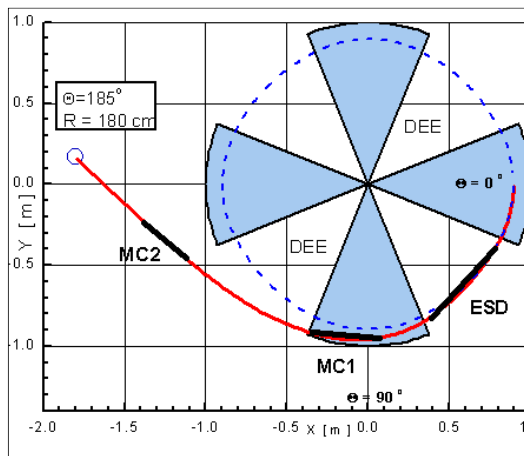


Figure 5: Scheme of DC130 extraction system.

EXPERIMENTAL BEAM LINES

The set of the experimental beam lines includes track membrane line, SEE testing line and radiation physics line. The scheme of the experimental beam lines is shown in Fig.6. The common part of the channel consists of extraction bending magnet, the quadrupole lens triplet and commuting magnet. The centre of the extraction bending magnet is an object point for all beam line. The exper-

ience of working at U400, U400M cyclotrons will be used during developing the experimental channels for these applications.

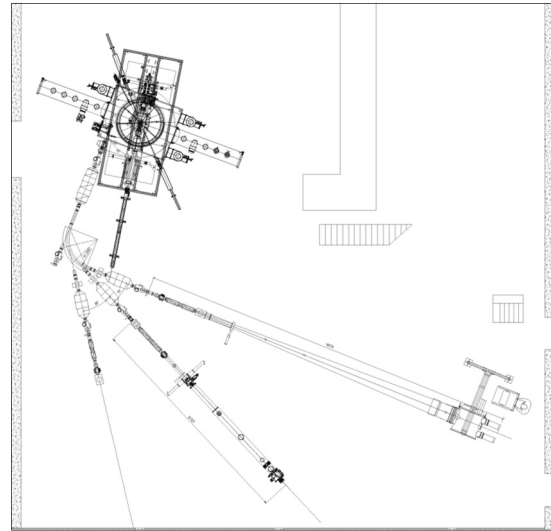


Figure 6: Scheme of experimental beam lines. From left to right: RP line; SEE testing line; TM line

CONCLUSION

Flerov Laboratory of Nuclear Reaction begins the works under the conceptual design of the dedicated applied science facility based on the new DC130 cyclotron. The main characteristics of it are defined and fit main user requirements well. The detailed project will be ready in December'2018.

REFERENCES

- [1] G. Gulbekyan, B. Gikal, I. Kalagin, N. Kazarinov, "Status Report and Future Development FLNR JINR Heavy Ions Accelerators Complex", in *Proc. HIAT09*, 8-12 June 2009, Venezia, Italy, p.59-63, <http://www.jacow.org>
- [2] N. Kazarinov, J. Franko, G. Gulbekian, I. Ivanenko, I. Kalagin, "Simulation of the Axial Injection Beam Line of the Reconstructed U200 Cyclotron of FLNR JINR", presented at HB2018, Daejeon, Korea, June 18-22, 2018, paper WEP2PO027.
- [3] A.A. Efremov, V.V. Bekhterev, S.L. Bogomolov et al., "DECRI5-5 ion source for DC-110 cyclotron complex results of the first tests", in *Proc. ECRIS2012*, Sydney, Australia.
- [4] B. Gikal, S. Dmitriev, G. Gulbekian, N. Kazarinov, et al., "Cyclotron Based Complex IC-100 for Scientific and Applied Research", in *Proc. 18-th Int. Conf. on Cyc. and their App.*, CYC07, 1-5 October 2007, Giardini Naxos, Italy, <http://www.jacow.org>
- [5] "OPERA-3D Reference Manual", Oxford OX5 1JE, England, October 2012.
- [6] G. Gulbekian, I. Kalgin, N. Kazarinov, I. Ivanenko, J. Franko, "The Choosing of Magnetic Structure of Isochronous Cyclotron DC-130 for Applied Application", presented at HB2018, Daejeon, Korea, June 18-22, 2018, paper THPW003.

Content from this work may be used under the terms of the CC BY 3.0 licence (© 2018).

MECHANICAL DESIGN OF SINGLE SPOKE RESONATOR TYPE-2 (SSR2) SUPERCONDUCTING CAVITY FOR RISP*

M. O. Hyun[†], H. Jung, Y. W. Jo, Y. Kim, RISP, IBS, Daejeon, Korea

Abstract

Superconducting linear accelerator and many beam experimental devices for the future of basic science research in Korea are being made and prepared for installation in Sindong linac tunnel north side of Daejeon, Korea. The key components of superconducting linac are the superconducting cavities and RISP linac has four types of superconducting cavities such as quarter-wave, half-wave, and single spoke resonator type-1 and 2. In this paper, we introduce about the initial RF/EM design of single spoke resonator type-2 (SSR2) superconducting (SC) cavity, and explain about mechanical design. Afterwards, we analyze mechanical design parameters of SSR2 SC cavity using ANSYS 18.0 structural solver and material properties of RRR 300 pure-niobium and stainless steel.

INTRODUCTION

From 2011 to now, RISP proceeded enormous research and development of superconducting linac and experimental devices. In our group - Accelerator System Team (AST) – four types of SC cavity, RF coupler, tuner, and cryomodule are designed, fabricated, and tested in the Munji SRF test facility. At the low energy linac region, quarter-wave (QWR) and half-wave (HWR) resonator will be installed, and single spoke resonator type-1 (SSR1) and type-2 (SSR2) also will be installed into the high energy linac region [1]. Between 2012 and 2014, we proceeded first prototyping of every SC cavity types and tested using different SRF facility like TRIUMF, Canada, or Cornell Univ., USA. Unfortunately, we didn't reach our target performance of both SSR1 and SSR2 SC cavity. Therefore, we tried to find out proper design of SSR1 SC cavity with the collaboration of TRIUMF, Canada. Based on the MOU and general contracts, TRIUMF invented a new concept of SSR1 SC cavity called 'Balloon Variant' [2,3]. TRIUMF also proceeded fabrication with PAVAC and 4K/2K cold test using their test facilities [4]. The essential advantage of balloon variant SC cavity shape is the suppression of multi-pacting effects. We decided to apply same balloon variant concept to the SSR2 SC cavity after SSR1 2K cold test was satisfied our expected performances.

SSR1/2 SPECIFICATIONS AND RF DESIGN

Table 1 shows the design specifications of SSR1/2 SC cavity for RISP. For satisfying our high energy SC linac beam lattice, we should evaluate our design specifications.

Figure 1 shows the SSR2 RF volume design for EM simulations. Balloon variant concept was applied same as SSR1 due to its high suppression effect for multi-pacting.

Table 1: Design Specifications of SSR1/2

	Unit	SSR1	SSR2
Operating Frequency	MHz	325	
Beta		0.3	0.51
Operating Temperature	K	2.05	
Q Factor		>5E9	
Epeak	MV/m	35	
Vacc	MV	>2.4	>4.1
df/dp	Hz/mbar		<10
Beam bore	mm	50	
Pressure Envelope @ 300K	bar	2	
Pressure Envelope @ 5K	bar		5

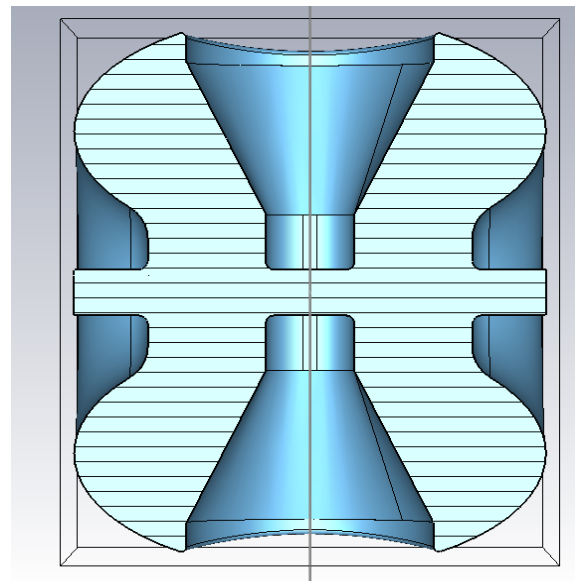


Figure 1: RF volume design done by RF engineer.

With this shape, RF engineer proceeded multi-pacting simulation with CST PIC-solver code, and Fig. 2 shows that the multi-pacting is reduced comparing with RISP SSR2 first prototype and modified RISP SSR2 with double radius corners from the ideation of FNAL [5].

* Work supported Ministry of Science and ICT (MSIT)

[†] atikus43@ibs.re.kr

Content from this work may be used under the terms of the CC BY 3.0 licence (© 2018). Any distribution of this work must maintain attribution to the author(s), title of the work, publisher, and DOI.

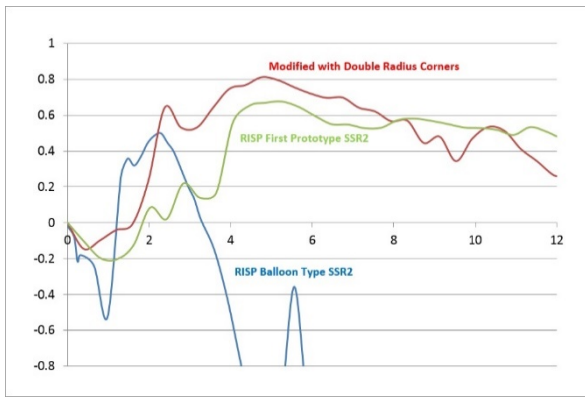


Figure 2: Multi-pacting simulation results.

With some considerations about fabrication capability and peak magnetic field, RF volume design of SSR2 SC cavity was finalized.

STRUCTURAL ANALYSIS

From the initial RF design of SSR2 SC cavity, the mechanical design was proceeded. First of all, we should set-up the material properties of SC cavity. In our project, we usually use RRR 300 pure niobium sheet for cavity and stainless steel(STS) 316L as liquid helium jacket(vessel) outside of SC cavity. Table 2 shows the material properties of RRR 300 pure niobium and STS 316L. We choose the sheet thickness of pure niobium and STS as 3mm, which are same with QWR and HWR.

Table 2: Material Properties of Pure Niobium and Stainless Steel 316L

	Unit	RRR300 Niobium	STS 316L
Young's Modulus	GPa	107	193
Poisson's Ratio		0.36	0.25
Density	g/cm ³	8.56	7.99
Tensile Strength	MPa	134	483
Yield Strength	MPa	51	170
Allowable Stress	MPa	34	113

Tensile strength/3.5 or yield strength/1.5 should be chosen as allowable stress so that niobium allowable stress is 34 MPa and STS316L allowable stress is 113 MPa. We applied these properties into the ANSYS 18.0 WB project file before structural analysis [6]. Figure 3 shows the initial shell design exploded view of SSR2 SC cavity.

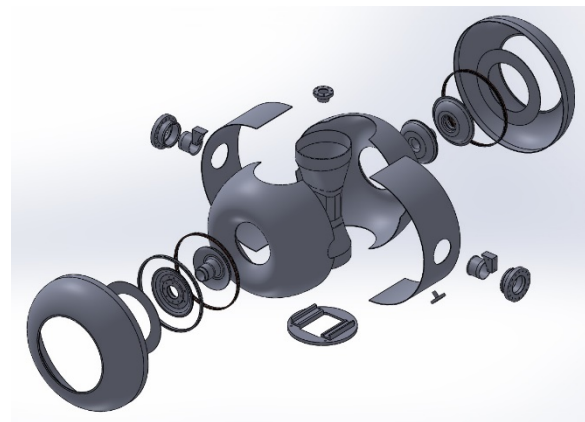


Figure 3 : Exploded view of initial SSR2 SC cavity.

Initially SSR2 SC cavity had no reinforcements so that we added the reinforcement after first structural analysis. For more realistic structural analysis we applied liquid helium jacket with STS316L material. Figure 4 and 5 shows about the difference of spoke deformation between without and with spoke stiffeners. We used ANSYS 18.0 Mechanical WB code for the structural analysis of SSR2 SC cavity.

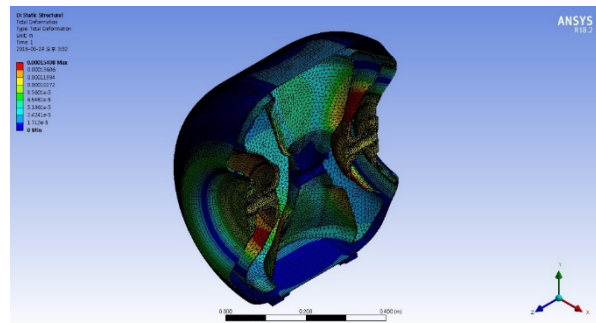


Figure 4 : Deformation shape without Spoke Stiffeners.

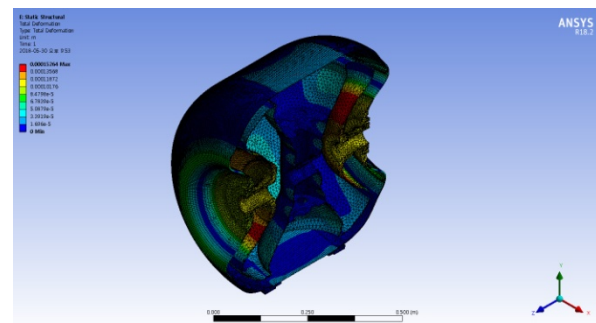


Figure 5 : Deformation shape with Spoke Stiffeners.

For initial structural analysis, we applied rough mesh size as 5mm which is comparably coarse but useful to estimate the tendency of deformation and stress with reducing calculation resources and time. We applied 1.3 bar liquid helium pressure between SSR2 SC cavity and liquid helium jacket for the boundary conditions.

As we expected, deformation around spoke is reduced after applying spoke stiffener. The spoke stiffeners are attached to both side - upper and lower - for avoiding stress

asymmetric shape. We should find optimal position of spoke stiffener in the further research.

Also, we should apply the transition ring between SC cavity and liquid helium jacket for tuning the cavity by pressing and releasing the beam port flanges. Figure 6 shows the deformation of SSR2 SC cavity with spoke stiffeners and transition ring which interconnected one side of SC cavity and adjacent side of liquid helium jacket. As shown in figure, attached side deformation is comparably reduced with that is shown in Fig. 5.

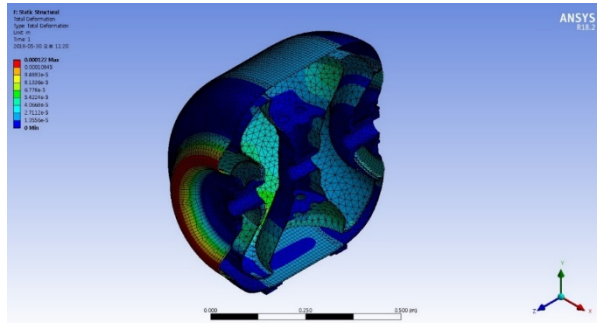


Figure 6 : Deformation shape with Spoke Stiffeners and Transition Ring.

For more robust design, we applied helium pressure up to 2 bar on the SSR2 SC cavity outside surface. With this pressure, maximum deformation of initial shell design is more than 0.2 mm and maximum stress was almost 103 MPa. To avoid the large stress and deformation, we designed the shell stiffener as Fig. 7. This figure shows the double-ring stiffeners which is already applied to the previous SSR2 SC cavity model at 2016 [1], but the composition is changed from niobium to niobium-copper with TIG welding.

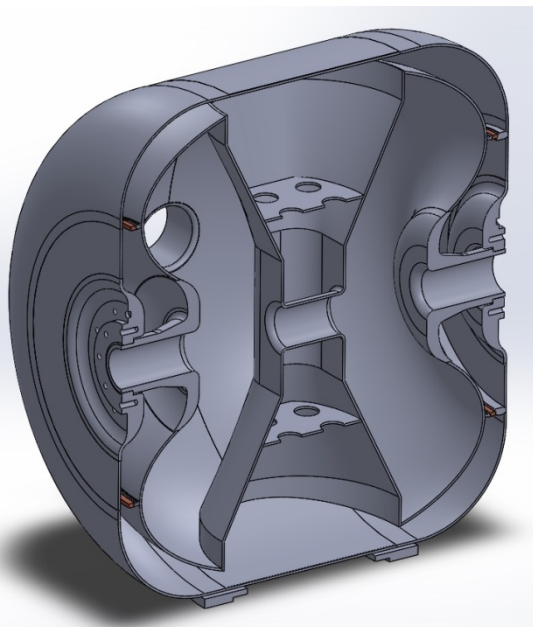


Figure 7 : Nb-Cu Stiffener Ring attached to SSR2 Shell Front and Rear Side.

MODAL ANALYSIS & INTERFACES

For checking the vibration disturbance we should check the natural frequency of SSR2 SC cavity as well. We used ANSYS 18.0 Mechanical WB modal analysis solver for analysing natural(eigen) frequencies at low frequency range. Figure 8 shows the resonance map of SSR2 SC cavity as well.

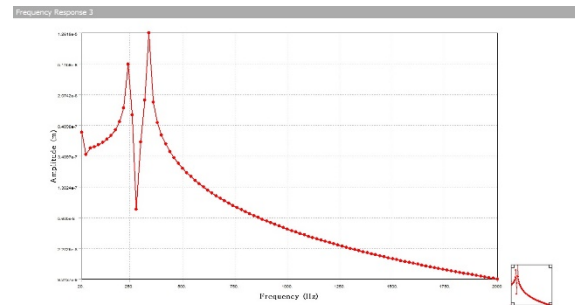


Figure 8: Resonance Map of Dressed SSR2 SC Cavity.

With this figure, we can see that there is some resonance possibility between 240Hz and 250Hz (simulation results was 245.45Hz) with the front beam flange disturbance and fixed point at the spoke beam tube as boundary conditions. Figure 9 shows the deformation and stress shape of SSR2 SC cavity with 245.45Hz resonance.

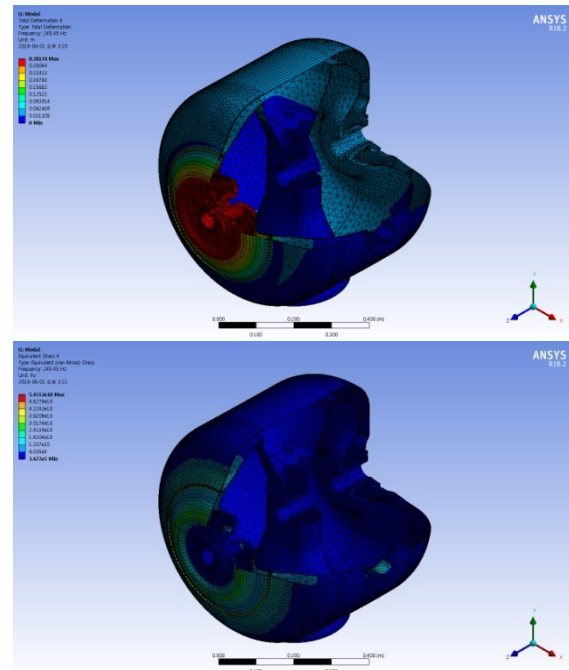


Figure 9: Deformation(a) and Stress(b) shape of SSR2 SC cavity with 245.45Hz resonance.

Considering about general external disturbance due to the motor rotation speed frequency such as 50Hz or 60Hz, 240Hz is same as 4 times of 60Hz and 250Hz is same as 5 times of 50Hz, so that the resonance can be happened with this natural frequency. Therefore, we should consider the

Content from this work may be used under the terms of the CC BY 3.0 licence (© 2018). Any distribution of this work must maintain attribution to the author(s), title of the work, publisher, and DOI.

reinforced structure for avoiding resonance. We will investigate the robust design for solving resonance issues at the future works. Furthermore, we will apply different type of external disturbance to the dressed SSR2 cavity as well.

For the consistency of interfaces of SSR2 SC cavity and those of SSR2 SC cavity, we applied the same type and size of flange connection. Figure 10 shows the interfaces of SSR2 SC cavity and Table 3 shows about the key dimensions.

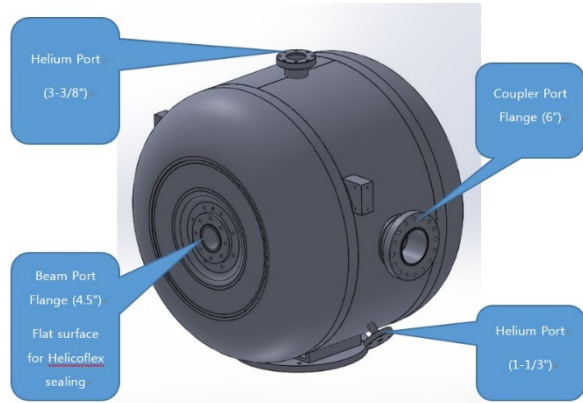


Figure 10: SSR2 Cavity Interface.

Table 3: Key Dimension of SSR2 SC Cavity

	SSR1	SSR2
Outer Diameter	568mm	612mm
Iris-to-iris Length	190mm	320mm
Beam Flange Length	400mm	538mm
Stiffener Diameter	327mm	345mm
Spoke Stiffener Length	376mm	200mm
Coupler Ports Width	718mm	716mm
Stiffener Thickness	5mm	5mm
Jacket Diameter	590mm	626mm
Jacket Length	400mm	546mm
Jacket Thickness	3mm	3mm

We are now under researching about our design parameters of SSR2 SC cavity like end curvature radius of helium jacket and width of stiffener ring. The main purpose of mechanical design parameter is to satisfy the design performance like df/dp or target frequency. Another reason of mechanical design parameter is to follow pressure vessel code [7] so that we guarantee the safety of our SC cavity with operating circumstances. With this purposes, we setup the design objectives as follows:

- minimize df/dp (STB)
- minimize stress (STB)
- frequency target is 325MHz (NTB)

First of all, we will proceed our structural analysis with this objectives and all design parameters. After analyzing parameter sensitivity and parameter correlation, we will select important parameters and make an experimental table with the design of experiment (DOE) method.

CONCLUSIONS

According to the mechanical design and analysis, we can find a proper shape of SSR2 as above. Our institute already contracted with domestic company for the prototyping of SSR2 with this design. We will finalize our SSR2 engineering design after many discussions and considerations with the contractor soon. Also, we can show the fabrication process and the test result in the future.

ACKNOWLEDGEMENTS

This paper was supported by the Rare Isotope Science Project (RISP), which is funded by the Ministry of Science and ICT (MSIT) and National Research Foundation (NRF) of the Republic of Korea.

REFERENCES

- [1] H.J. Kim, H.C. Jung, W.K. Kim, "Progress on Superconducting Linac for the RAON Heavy Ion Accelerator", in Proceedings of IPAC2016, Busan, Korea, 2016, paper MOPOY039, pp. 935-937.
- [2] Z. Yao, R.E. Laxdal, V. Zvyagintsev, "Balloon variant of Single Spoke Resonator", in Proceedings of SRF2015, Whistler, Canada, 2015, paper THPB021, pp. 1110-1114.
- [3] Z. Yao, R.E. Laxdal, B. Waraich, V. Zvyagintsev, R. Edinger, "Design and Fabrication of Beta=0.3 SSR1 for RISP", in Proceedings of LINAC2016, East Lansing, MI, USA, 2016, paper MOPLR041, pp.226-228.
- [4] RISP SSR1 Pre-Fabrication Design Report, written by TRIUMF SRF Group and PAVAC, July 2016.
- [5] Gennady Romanov, Paolo Berrutti, Timergali N. Khabibouline, "Simulation of Multipacting in SC Low Beta Cavities at FNAL", in Proceedings of IPAC2015, Richmond, VA, USA, 2016, paper MOPMA018, pp.579-581.
- [6] ANSYS2018, www.ansys.com
- [7] The American Society of Mechanical Engineers ASME Boiler and Pressure Vessel Code, Section II – Part D, 2000.

FIRST ACCELERATION OF HEAVY ION BEAMS WITH A SUPERCONDUCTING CONTINUOUS WAVE HIM/GSI CW-LINAC*

M. Basten[†], M. Busch, H. Podlech, M. Schwarz, IAP Goethe-Universität Frankfurt, Germany
 K. Aulenbacher¹, W. Barth, F. Dziuba, V. Gettmann, T. Kürzeder, M. Miski-Oglu, Helmholtz Institute Mainz, Germany, also GSI Helmholtzzentrum für Schwerionenforschung, Darmstadt, Germany
 M. Heilmann, A. Rubin, A. Schnase, S. Yaramyshev, GSI Helmholtzzentrum für Schwerionenforschung, Darmstadt, Germany
¹ also Johannes Gutenberg-Universität Mainz, Germany

Abstract

In the future a new superconducting (sc) continuous wave (cw) high intensity heavy ion Linac should provide ion beams with a max. beam energy above the coulomb barrier for the Super Heavy Element (SHE) program at GSI Helmholtzzentrum für Schwerionenforschung. As a first step a newly developed superconducting 15-gap Crossbar H-cavity (CH-cavity) operated at 217 MHz has been successfully tested with heavy ion beam up to the design beam energy of 1.85 MeV/u for the first time. The design energy gain of 3.5 MV within a length of less than 70 cm has been validated with heavy ion beams of up to 1.5 μ A. The measured beam parameters showed excellent beam quality, while a dedicated beam dynamics layout provides beam energy variation between 1.2 and 2.2 MeV/u. The beam commissioning is a milestone of the R&D work of Helmholtz Institute Mainz (HIM) and GSI in collaboration with Goethe University Frankfurt (GUF) and the first step towards a sc heavy ion cw-Linac with variable beam energy. The first tests under cryogenic conditions of the next two CH-cavities have already been started at GUF in a vertical cryostat. The results of the first successful heavy ion beam acceleration with a superconducting CH-cavity will be presented.

INTRODUCTION

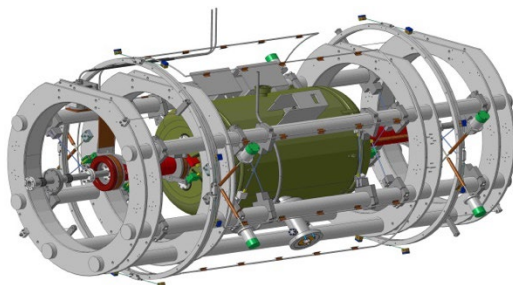


Figure 1: Demonstrator CH-cavity (CH0) with two solenoids inside the support frame.

The design and construction of cw high intensity Linacs is a crucial goal of worldwide accelerator technology development [1]. Above all, compactness of a particle accelerator is a beneficial demand for the development of

*Work supported by the BMBF, project number 05P15RFBA, MYRTE which is funded by the European Commission under Project-ID 662186 and Helmholtz International Center for FAIR.

[†]Basten@iap.uni-frankfurt.de

high intensity cw proton and ion Linacs [2]. The study and investigation of the design, operation and optimization of a cw-Linac, as well as progress in elaboration of the superconducting technology [3] is of high relevance.

For the HIM/GSI cw-Linac HELIAC (HElmholtz Line- ar ACcelerator) several superconducting CH cavities operated at 217 MHz are used to provide acceleration of ions with a mass to charge ratio of up to 6 to beam energies between 3.5 MeV/u and 7.3 MeV/u, while the energy spread should be kept smaller than ± 3 keV/u. For proper beam focusing superconducting solenoids have to be mounted between the CH cavities. The general parameters are listed in Table 1 [4]. R&D and prototyping (demonstrator project) [5] in preparation of the proposed HELIAC is assigned to a collaboration of GSI, HIM and GUF. The demonstrator setup is located in straightforward direction of the GSI-High Charge State Injector (HLI).

Table 1: Design Parameters of the cw-Linac

Mass/charge		6
Frequency	MHz	216.816
Max. beam current	mA	1
Injection energy	MeV/u	1.4
Output energy	MeV/u	3.5 – 7.3
Output energy spread	keV/u	± 3
Length of acceleration	m	12.7
Sc CH-cavities	#	9
Sc solenoids	#	7

The demonstrator comprises a 15 gap sc CH-cavity (CH0) embedded by two superconducting solenoids; all three components are mounted on a common support frame (see Fig. 1) [6]. The beam focusing solenoids consist of one main Nb₃Sn-coil and two compensation coils made from NbTi that shield the maximum magnetic field of 9.3 T within a longitudinal distance of 10 cm down to 30 mT. The solenoids are connected to LHe ports inside the cryostat by copper tapes allowing dry cooling. The sc CH structure CH0 is the key component and offers a variety of research and development [7].

PREPARATION OF RF-CAVITY AND SUPPLY SYSTEM

The sc 15 gap CH-cavity is directly cooled with liquid helium, supported by a helium jacket made from titanium. The first performance test of the cavity was conducted without helium jacket at GUF in a vertical cryostat with low RF power after high pressure rinsing (HPR) at the vendor Research Instruments GmbH (RI). Gradients up to 7 MV/m could be achieved. After the final assembly of the helium vessel and further HPR preparation at RI, the cavity was tested in a horizontal cryostat at GSI. As depicted in Fig. 2, the cavity showed improved performance due to an additional HPR treatment. The initial design quality factor Q_0 has been exceeded by a factor of four, a maximum accelerating gradient of $E_a = 9.6$ MV/m at $Q_0 = 8.14 \times 10^8$ has been achieved [8-10]. Prior beam commissioning of the cavity, the RF power couplers [11-12] were tested and conditioned with a dedicated test resonator [13].

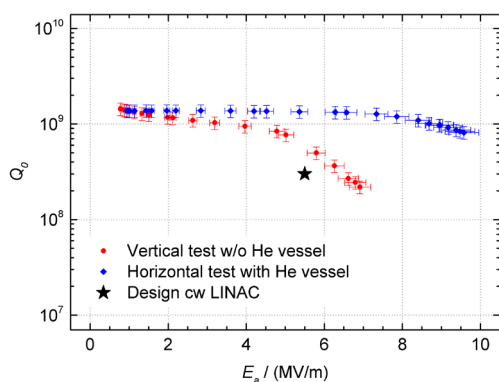


Figure 2: RF-testing of CH-demonstrator cavity - improved performance (add. HPR), low field emission rate, high field gradient, therm. quenching beyond 9.6 MV/m.

For this the couplers were equipped with sensors to control the temperature of the ceramic windows and Langmuir probes to detect multipacting currents. First conditioning [14] has been performed up to 5 kW with pulsed power and up to 2 kW in cw-mode. Further increase of the forward cw-RF power results in a temperatures rise of more than 80°C at the ceramic window, potentially sufficient to damage the coupler. During the operation, the "cold" coupler window has been anchored to the liquid nitrogen supply tube by copper ribbons. The power couplers as well as three frequency tuners, developed at IAP [15] and manufactured at GSI have been integrated in the RF-cavity in a clean room of class ISO4. Furthermore, the CH-cavity and both solenoids were assembled on a string. After leak testing of the accelerating string the complete cold mass was integrated [16] into the cryostat outside of the clean room.

DEMONSTRATOR-BEAM DYNAMICS

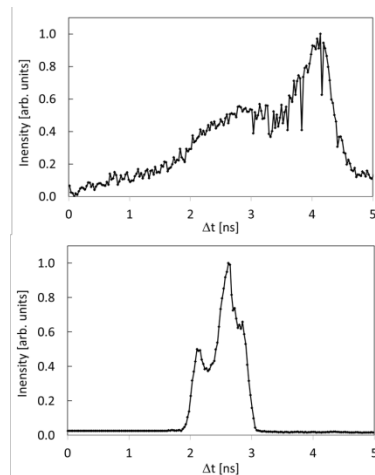


Figure 3: Bunch shape measurement for HLI beam at 1.366 MeV/u (top) and at same energy for matched case with rebuncher R1 and R2 (down).

The beam dynamics layout behind the HLI at 1.4 MeV/u has been simulated in advance. In a preparing beam test run, it could be confirmed, that the room temperature focusing quadrupoles (triplet and two duplets) and two rebuncher cavities are sufficient to provide for full 6D-matching to the demonstrator [17]. At the same time, the input beam is axially symmetric for further solenoid focusing due to especially chosen gradients, while bunch length (see Fig. 3) and momentum spread are matched as well.



Figure 4: Layout of matching line to the Demonstrator and beam diagnostics test bench; QT/QD = quadrupole triplet/duplet, R = rebuncher, X/Y = beam steerer, G = SEM-grid, T = current transformer, P = phase probe, BSM = bunch shape monitor, EMI = emittance meter.

The transport line (see Fig. 4) provides also for beam instrumentation. Moreover, beam transformers, Faraday cups, SEM-profile grids, a dedicated emittance meter, a bunch structure monitor and phase probe pickups (beam energy measurements applying time of flight) provide for proper beam characterization behind the demonstrator.

The beam dynamics layout of the sc cw-Linac is based on the EQUUS (EQUidistant mULTigap Structure) concept, as proposed in [18]. It features high acceleration efficiency with longitudinal and transversal stability, as well as a straightforward energy variation by varying the applied RF-voltage or the RF-phase of the amplifier. Highly charged ions with a mass-to-charge ratio of maximum 6 will be accelerated from 1.4 MeV/u up to 3.5 - 7.3 MeV/u. Energy variation while maintaining a high beam quality is the core issue with respect to beam dynamics, simulated using advanced software [19-20] and previously developed algorithms [21-23]. The constant

Content from this work may be used under the terms of the CC BY 3.0 licence © 2018). Any distribution of this work must maintain attribution to the author(s), title of the work, publisher, and DOI.

cell length inside an EQUUS designed cavity is fixed for a higher (geometrical) β compared to the injection beam energy (constant- β structure). As a consequence of constant- β structure leads to a sliding movement in longitudinal phase space. Trajectory and energy gain depend strongly on the initial phase at the first gap centre and the difference between particle energy and design energy. The corresponding transversal emittance evolution has been measured in a broad range with small emittance growth. Beam dynamics behind the HLI has been carried out with the LORASR code (see Fig. 5) [24]. The quadrupole triplet and duplets provide for an axially symmetric input beam for further solenoid focusing. The beam is matched to the demonstrator in the 6d phase space.

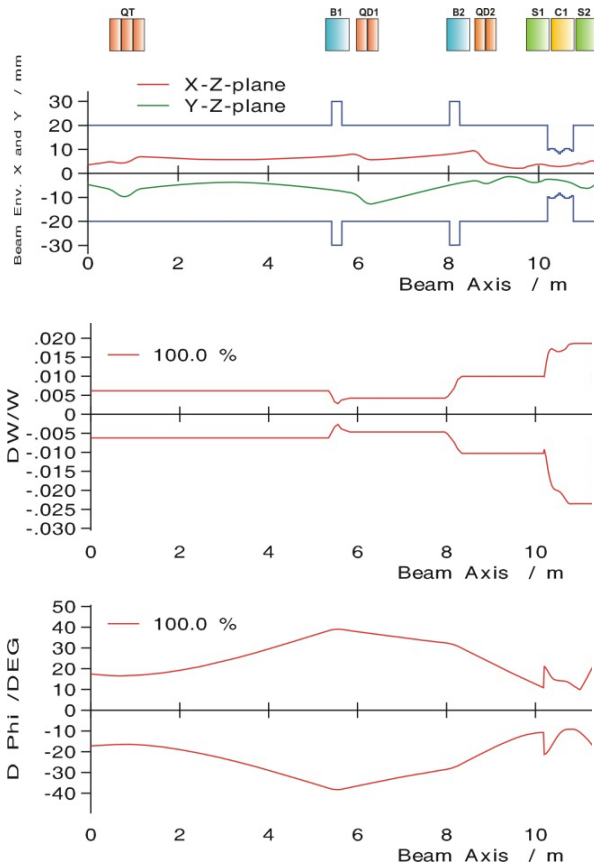


Figure 5: Beam envelopes (matching the demonstrator).

FIRST BEAM ACCELERATION

At June 2017, after successful RF-testing of the sc RF-cavity in 2016, set up of the matching line to the demonstrator and a short commissioning and ramp up time of some days, the CH0-cavity first time accelerated heavy ion beams (Ar^{11+}) with full transmission up to the design beam energy of 1.866 MeV/u ($\Delta W_{\text{kin}} = 0.5 \text{ MeV/u}$) [25], as shown in Fig. 6. For the first beam test the sc cavity was powered with 10 Watt of net RF power, providing an accelerating voltage of more than 1.6 MV inside a length of 69 cm. Further on the design acceleration gain of 3.5 MV has been verified and even exceeded by accelera-

tion of beam with high rigidity ($A/q = 6.7$). As summarized in Table 2, argon and helium ion beams with different charge state from an Electron Cyclotron Resonance ion source ($^4\text{He}^{2+}$, $^{40}\text{Ar}^{11+}$, $^{40}\text{Ar}^{9+}$, $^{40}\text{Ar}^{6+}$) were accelerated at HLI with the demonstrator. For longitudinal beam matching the rebuncher settings were adapted according to the mass-to-charge ratio A/q , as well as the acceleration voltage.

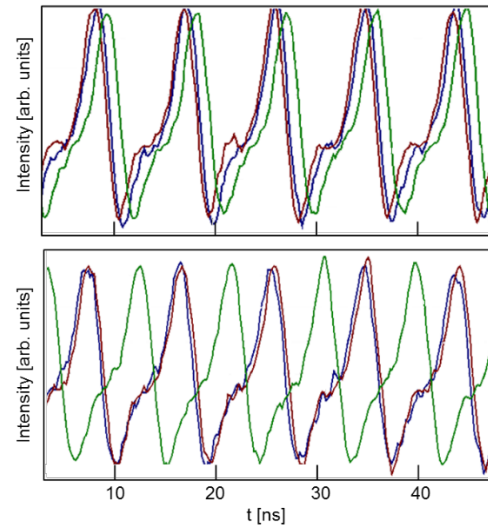


Figure 6: First RF-acceleration with the 216.816 MHz-CH-cavity; measured Ar^{11+} -phase probe signals from HLI beam at 1.366 MeV/u (top), HLI-RF-frequency is 108.408 MHz ($T = 9.224 \text{ ns}$). By acceleration up to the nominal beam energy (down), the coarse time of flight between blue and red signal is slightly reduced. The time of flight for the fine measurement between red and green signal is significantly shifted, according to the beam energy of 1.866 MeV/u.

Table 2: RF- Parameters for Matched Case

	He^{2+}	Ar^{11+}	Ar^{9+}	Ar^{6+}
A/q	2.0	3.6	4.4	6.7
$U_{\text{Reb1,eff.}}$ [kV]	8.3	15.0	18.3	27.9
$U_{\text{Reb2,eff.}}$ [kV]	22.7	40.8	49.9	75.9
$E_{\text{acc,CH}}^*$ [MV/m]	1.8	3.2	3.9	5.9
U_0 [MV]	1.2	2.2	2.7	4.0

$$^* E_{\text{acc}} = \text{transit time factor} \times \text{total accelerating voltage} / (n \times 0.5 \times \beta \lambda)$$

A maximum average beam intensity of 1.5 μA has been achieved, limited only by the beam intensity of the ion source and maximum duty factor (25%) of the HLI, while the CH-cavity was operated in cw-mode. All presented measurements were accomplished with high duty factor beam and maximum beam intensity from the HLI.

SYSTEMATIC BEAM INVESTIGATIONS

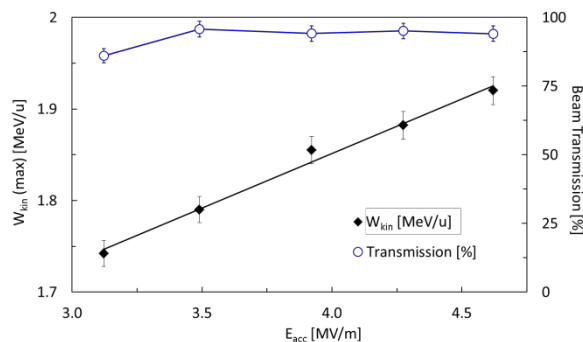


Figure 7: Acceleration of an Ar^{9+} -beam; maximum achieved beam energy and transmission as function of the (eff.) accelerating gradient [25].

A full measured 2D-scan of beam energy and beam transmission for a wide area of different accelerating fields and RF-phases has been performed. The linear increase of beam energy with ramped accelerating gradient (as shown in Fig. 7) could be observed for different RF-phase settings, while the beam transmission is kept above 90 %. In general these measurements confirm impressively the EQUUS beam dynamics, featuring effectively beam acceleration up to different beam energies without particle loss and significant beam quality degradation. As measured with helium beam, for lighter ions a maximum beam energy of up to 2.2 MeV/u could be reached with the demonstrator cavity, but with reduced beam quality.

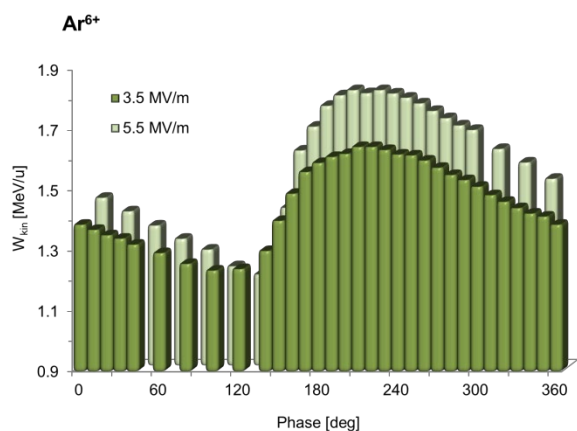


Figure 8: Phase-scan of Ar^{6+} -beam energy for 3.5 MV/m and 5.5 MV/m [25].

With Ar^{6+} -beam ($A/q = 6.7$), an energy gain above 0.5 MeV/u could be reached with an accelerating gradient of 6 MV/m. As an example, Fig. 8 shows a fully measured 360° phase scan for two different accelerating gradients (3.5 MV/m and 5.5 MV/m). All individual data as well as the characteristic shapes of the phase scans are in good agreement according to the accelerating gradient. For an increased gradient the maximum beam energy at an RF-phase of 210° boosts as well, while the minimum

beam energy at 130° could be decreased down to 1.2 MeV/u. The bunch length detected with a bunch shape monitor (BSM) [26-27] was measured as very sensitive to RF-phase changes. A change of RF-phase by 30° only, leads to a significant change of bunch length (by more than a factor of four), while the beam transmission is not affected. For further matching to another CH-cavity, the adjustment of the beam energy setting by changing the RF-amplitude is more favourable - compared to changing the RF-phase - as no significant bunch shape change could be observed.

PHASE SPACE MEASUREMENTS

At first the beam quality has been characterized by measuring the phase space distribution for different energies [25]. The measured emittance of the argon beam, delivered by the HLI, is adequately low. The total 90% horizontal beam emittance is measured for 0.74 μm , while the vertical emittance is 0.47 μm only. All measurements have been performed without solenoidal field, therewith any additional emittance degradation effects by different beam focusing could be avoided. The measured (normalized) beam emittance growth at full beam transmission is sufficiently low: 15 % (horizontal plane) and 10% (vertical plane). Selective measurements at other RF-amplitudes and -phases, as well as for other beam rigidities confirmed the high (transversal) beam performance in a wide range of different parameters.

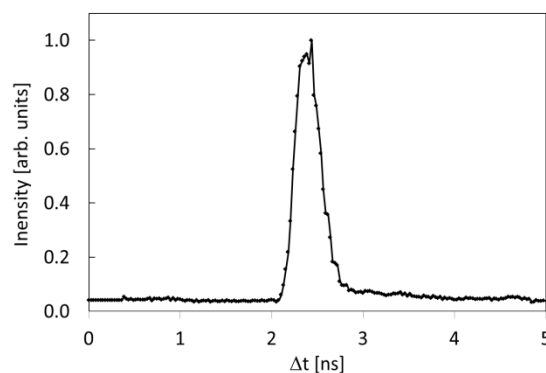


Figure 9: Bunch shape of Ar^{9+} -beam fully matched after acceleration to 1.85 MeV/u [25].

Besides beam energy measurements the bunch shape for the matched case was measured with the Feschenko monitor [27] (see Fig. 9). As shown, an impressive small minimum bunch length of about 300 ps (FWHM) could be detected, sufficient for further matching to and acceleration in future RF-cavities.

ADVANCED R&D

Up to now, the reference design for the cw-Linac dates back to [4]. Meanwhile many experiences have been gained in design, fabrication and operation of sc CH-cavities and the associated components. In this context, a revision of the Linac layout was recommended. Opti-

Content from this work may be used under the terms of the CC BY 3.0 licence (© 2018). Any distribution of this work must maintain attribution to the author(s), title of the work, publisher, and DOI.

mized cavity layouts [28] resulted in modified voltage distributions. Furthermore, the layout - now with three CH-cavities and a sc rebuncher (see Fig. 10) [29] per cryo module - has been specified with more details. It features high acceleration efficiency with longitudinal and transversal stability, as well as a straightforward energy variation. Highly charged ions with a mass-to-charge ratio of maximum 6 will be accelerated from 1.4 MeV/u up to 3.5- 7.3 MeV/u. High beam quality and beam energy variation is the core feature of the cw-Linac to be noticed especially at beam dynamics layout [19-21, 23, 30-32].

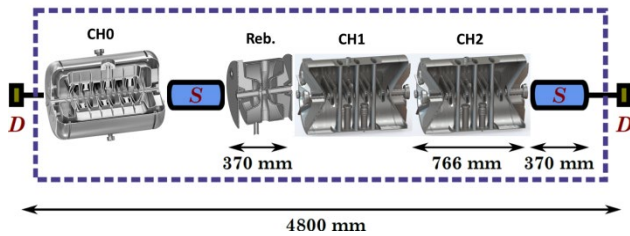


Figure 10: Advanced cryo module layout containing demonstrator CH0 cavity, two short CH cavities, a rebuncher and two solenoids.

Meanwhile the next two CH cavities CH1 and CH2 have already been constructed and CH1 has already been tested under cryogenic conditions (see Table 3). After a fast cooldown with 1.8 K/min, to avoid hydrogen related Q-disease and several days of RF conditioning, all multipacting barriers could permanently be surmounted and the RF performance of the cavity could be determined. Fig. 11 shows the resulting Q_0 vs. E_a curve of the vertical test without helium vessel [33]. The Q-value dropped from $Q_0^{\text{low}} = 1.02 \cdot 10^9$ at low field levels down to $Q_0^{\text{high}} = 2.43 \cdot 10^8$ at a maximum gradient of $E_a = 9$ MV/m. This corresponds to a total voltage of $U_{\text{eff}} = 3.32$ MV inside the cavity. The design Q-value of $3 \cdot 10^8$ is reached at an accelerating gradient of $E_a = 8.52$ MV/m, which is 55% above the design gradient of $E_a = 5.5$ MV/m. Field emission started at field gradients above $E_a = 5$ MV/m; the Fowler-Nordheim plot resulted in a field enhancement factor of about 80 [33].

Table 3: Main Results of the First RF Test of CH1 [33]

Q_0^{low}		$1.02 \cdot 10^9$
R_{BCS}	$n\Omega$	12.6
R_{mag}	$n\Omega$	9.78
R_0	$n\Omega$	26.02
E_a	MV/m	9
U_{eff}	MV	3.32
Q_0^{high}		$2.43 \cdot 10^8$

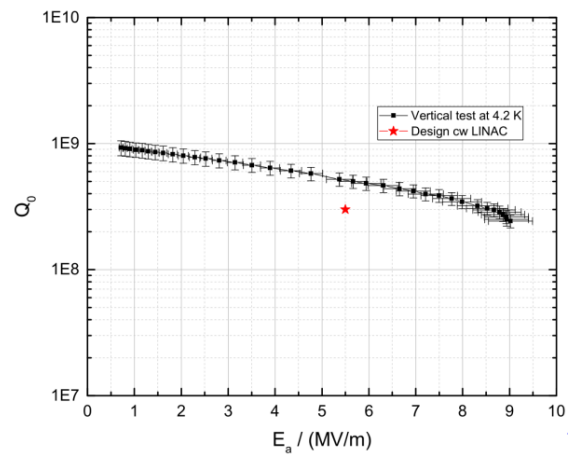


Figure 11: RF-testing of CH1 in a vertical cryostat without helium vessel; a maximum field gradient E_a of 9 MV/m has been measured.

SUMMARY

An advanced cw-Linac approach, based on a standard cryomodule equipped with three CH-cavities and a sc-rebuncher, demonstrates the high capabilities due to energy variation preserving the beam quality, as shown in the first beam test. The design acceleration gain of the first sc CH-cavity was achieved with heavy ion beams even above the design mass to charge ratio at full transmission and maximum available beam intensity [34]. The beam quality was measured as excellent in a wide range of different beam energies, This new design could provide beam acceleration for ions with different mass-to-charge ratio even above the design beam energy, featuring the ambitious GSI-user program, while the GSI-UNILAC is upgraded for short pulse high current FAIR-operation. [35]. The achieved demonstrator beam commissioning confirms the capabilities of the applied EQUUS beam dynamics design and is a major milestone paving the way to the cw-Linac HELIAC. First extensive tests under cryogenic conditions with CH1 showed promising results with an accelerating gradient of up to $E_a = 9$ MV/m and low field emission rates [33] confirming the optimized cavity layout [28].

ACKNOWLEDGEMENTS

Successful beam testing could not be accomplished without strong support of highly committed people from different GSI-departments. The beam test is a milestone of the R&D work of HIM and GSI in collaboration with GUF preparing a superconducting heavy ion cw Linac.

REFERENCES

- [1] C. Prior, Overview of High Intensity Accelerator Projects, Proceedings of HB'10, Morschach, Switzerland, pp. 6-10 (2010).
- [2] S.M. Polozov *et al.*, Beam dynamics study and electro-dynamics simulations for the cw RFQ, Proceedings of IPAC2017, Copenhagen, Denmark, pp. 1333-1336 (2017).
- [3] R. Laxdal, Physica C-Superconductivity and its Applications, Volume: 441, Issue: 1-2, Pages: 13-20, (2006), doi: 10.1016/j.physc.2006.03.096
- [4] S. Minaev *et al.*, "Superconducting, energy variable heavy ion linac with constant β , multicell cavities of CH-type", Phys. Rev. ST Accel. Beams 12, 120101, (2009). doi: 10.1103/PhysRevSTAB.12.120101
- [5] W. Barth *et al.*, "A superconducting CW-LINAC for heavy ion acceleration at GSI", EPJ Web of Conferences, vol. 138, article number 01026, (2017). doi: 10.1051/epjconf/201713801026
- [6] F. Dziuba *et al.*, "First Cold Tests of the Superconducting cw Demonstrator at GSI", in *Proc. of RuPAC'16*, St. Petersburg, Russia, Oct. 2016, paper WECBMH0, pp. 83-85.
- [7] T. Kürzeder *et al.*, Infrastructure for Superconducting CH-Cavity Preparation at HIM *Proc. of IPAC'18*, Vancouver, Canada, 2018, Paper WEPML045, p.p.2796-2799, doi: 10.18429/JACoW-IPAC2018-WEPML045
- [8] F. Dziuba *et al.*, First Performance Test on the Superconducting 217 MHz CH Cavity at 4.2 K, Proceedings of LINAC'16, East Lansing, MI, USA, pp. 953-955 (2016).
- [9] F. Dziuba *et al.*, First Cold Tests of the Superconducting cw Demonstrator at GSI, Proceedings of RuPAC'16, St. Petersburg, Russia, p. 83-85 (2016).
- [10] F. Dziuba *et al.*, "RF Commissioning of the Superconducting 217 MHz CH Cavity for Heavy Ions and First Beam Operation", Proc. of LINAC2018, paper THPO073, this conference.
- [11] M. Heilmann *et al.*, High power RF coupler for the cw-linac demonstrator at GSI, in proceedings of IPAC'17, Copenhagen, Denmark, pp. 990-992 (2017).
- [12] J. List *et al.*, "High Power Coupler R&D for Superconducting CH-cavities", Proc. of LINAC2018, paper THPO107, this conference
- [13] M. Busch *et al.*, Update on the sc 325 MHz CH-cavity and power coupler processing, proceedings of LINAC'16, East Lansing, MI, USA, pp. 913-915 (2017).
- [14] F. Dziuba *et al.*, "Performance tests of the superconducting 217 MHz CH cavity", in *Proc of SRF'17*, Lanzhou, China, 2017, paper TUPB024.
- [15] M. Amberg *et al.*, The fast Piezo-based frequency tuner for sc CH-cavities, Proceedings of LINAC'14, Geneva, Switzerland, pp. 214-216 (2014).
- [16] V. Gettmann *et al.*, "Commissioning of a superconducting cw heavy ion Linac@GSI", in *Proc of SRF'17*, Lanzhou, China, 2017, paper MOPB094.
- [17] M. Schwarz *et al.*, "Beam Dynamics for the sc cw heavy ion Linac at GSI", in *Proc of IPAC'15*, Richmond, VA, USA, 2015, p. 3742-3744.
- [18] M. Miski-Oglu *et al.*, "Steps towards superconducting cw-Linac for heavy ions at GSI", in *Proc of SRF'17*, Lanzhou, China, 2017, paper MOPB024.
- [19] R. Tiede *et al.*, "LORASR Code Development", in *Proc of EPAC'06*, Edinburgh, Scotland, 2006, pp. 2194-2196.
- [20] S. Yaramyshev *et al.*, Nucl. Instr. Meth. Phys. Res., Sect. A, vol. 558/1 (2006), pp. 90-94. doi: 10.1016/j.nima.2005.11.018
- [21] S. Yaramyshev *et al.*, "An advanced procedure for longitudinal beam matching for sc cw heavy ion linacs", in *Proc of HB'16*, Malmö, Sweden, 2016, pp. 571-574.
- [22] M. Schwarz *et al.*, "Beam Dynamics Simulations for the New Superconducting CW Heavy Ion Linac at GSI", in *Proc of SRF'17*, Lanzhou, China, 2017, paper MOPB005.
- [23] S. Yaramyshev *et al.*, "Virtual charge state separator as an advanced tool coupling measurements and simulations", Phys. Rev. ST Accel. Beams 18, 050103, (2015). doi: 10.1103/PhysRevSTAB.18.050103
- [24] W. Barth *et al.*, "Advanced superconducting cw heavy ion linac R&D", in *Proc of IPAC'13*, Shanghai, China, 2013, pp. 3770-3772.
- [25] W. Barth *et al.*, "First heavy Ion Beam Test with a superconducting multi gap CH-cavity", Phys. Rev. ST Accel. Beams 21, 020102, (2018). doi: 10.1103/PhysRevAccelBeams.21.020102
- [26] T. Sieber *et al.* 2018 Bunch Shape Measurements at the GSI cw-Linac Prototype, *Proc. of IPAC'18*, Vancouver, Canada, may 2018, paper WEPAK006 pp.2091-2094, doi: 10.18429/JACoW-IPAC2018-WEPAK006
- [27] A.V. Feschenko, "Technique and instrumentation for bunch shape measurements", in *Proc of RuPAC'12*, St. Petersburg, Russia, Oct. 2016, pp. 181-185, paper FRXOR01.
- [28] M. Basten *et al.*, "First measurements of the next sc CH-cavities for the new superconducting cw heavy ion LINAC@GSI", Proc. of SRF2017, TUPB022
- [29] M. Gusarova *et al.*, Multipactor discharge in superconducting accelerating CH cavities, IOP Conf. Series: Journal of Physics: Conf. Series 1067 (2018) 082007 doi: 10.1088/1742-6596/1067/8/082007
- [30] S. Yaramyshev *et al.* 2018 Advanced approach for beam matching along the multi-cavity sc cw Linac at GSI, IOP Conf. Series: Journal of Physics: Conf. Series 1067 (2018) 052005 doi: 10.1088/1742-6596/1067/5/052005
- [31] M. Schwarz *et al.*, "Further steps towards the superconducting CW-linac for heavy ions at GSI", in *Proc. of IPAC'16*, Busan, South Korea, May 2016, paper MOPOY023, p. 896-898.
- [32] S. M. Polozov *et al.*, "Beam dynamics study and electro-dynamics simulations for the cw RFQ", in *Proc. of IPAC'17*, Copenhagen, Denmark, May 2017, paper TUPAB013, pp. 1333-1336.
- [33] M. Basten *et al.*, "Cryogenic Tests of the superconducting beta=0.069 CH-cavities for the HELIAC-project", Proc. of LINAC2018, paper THPO072
- [34] W. Barth *et al.*, Superconducting CH-Cavity heavy ion beam testing at GSI, IOP Conf. Series: Journal of Physics: Conf. Series 1067 (2018) 052007 doi: 10.1088/1742-6596/1067/5/052007
- [35] W. Barth *et al.*, "High brilliance uranium beams for the GSI FAIR", Phys. Rev. ST Accel. Beams 20, 050101, (2017). doi: 10.1103/PhysRevAccelBeams.20.050101

DESIGN AND BEAM COMMISSIONING OF THE LEAF-RFQ*

L. Lu[†], W. Ma, H. Jia, Y. H. Zhai, Y. Yang, L. P. Sun, L. B. Shi, L. T. Sun, Y. He, H. W. Zhao
 Institute of Modern Physics (IMP), CAS
 509 Nanchang Rd., Lanzhou, Gansu 730000, China

Abstract

An 81.25 MHz continuous wave (CW) radio frequency quadrupole (RFQ) accelerator has been designed and fabricated for the Low Energy Accelerator Facility (LEAF) by the Institute of Modern Physics (IMP) of the Chinese Academy of Science (CAS). The operation frequency is 81.25 MHz and the inter-vane voltage is a constant of 70 kV. It took about 44 hours continuous conditioning to reach RF power of 75 kW which is 1.1 time of the maximum designed operational power, and the successful CW acceleration of 150 μ A He⁺ beam to the designed energy of 0.5 MeV/u. Both the results of the high power test and the beam test will be reported in this paper.

INTRODUCTION

The LEAF project was launched as a pre-research facility for the high intensity Heavy Ion Accelerator Facility (HIAF) project and a heavy ion irradiation facility for material research at IMP [1] [2]. The LEAF will consist of a 2 mA U³⁴⁺ electron cyclotron resonance ion source, a low energy beam transport line, a CW 81.25MHz RFQ accelerator [3], a medium energy beam transport line and an experimental platform for nuclear physics. The layout of the LEAF project is shown in Fig. 1. The LEAF-RFQ shown in Fig. 2 will operate as a CW injector with the capability of accelerating all ion species from proton to uranium from 14 keV/u up to 500 keV/u. The design goal

is to design a compact type cavity with lower power loss and high operation stability. Considering the LEAF-RFQ will operate in CW mode, a four-vane structure is a better choice than four-rod type, because the four-vane structure is a more stable structure for water cooling. The PISL (Pi-mode stabilizing loop) structure is adopted to suppress the dipole effect. In addition, tuners and undercuts are used for frequency tuning and field flatness. The main parameters of the LEAF-RFQ are listed in the table 1. In this paper, we report the designs and results of the low power test and the high power test.

Table 1: Main Parameters of the LEAF-RFQ

Parameters	Value
A/q	7
Operation	CW/pulsed
Vane type	Four vane
Frequency (MHz)	81.25
Input energy (keV/u)	14
Output energy (MeV/u)	0.5
Inter-vane voltage (kV)	70
Kilpatrick factor	1.55
Peak current (emA)	2
Transmission efficiency (%)	97.2
Acceleration efficiency (%)	81.7
Length of vane (mm)	5946.92
Average radius of aperture (mm)	5.805

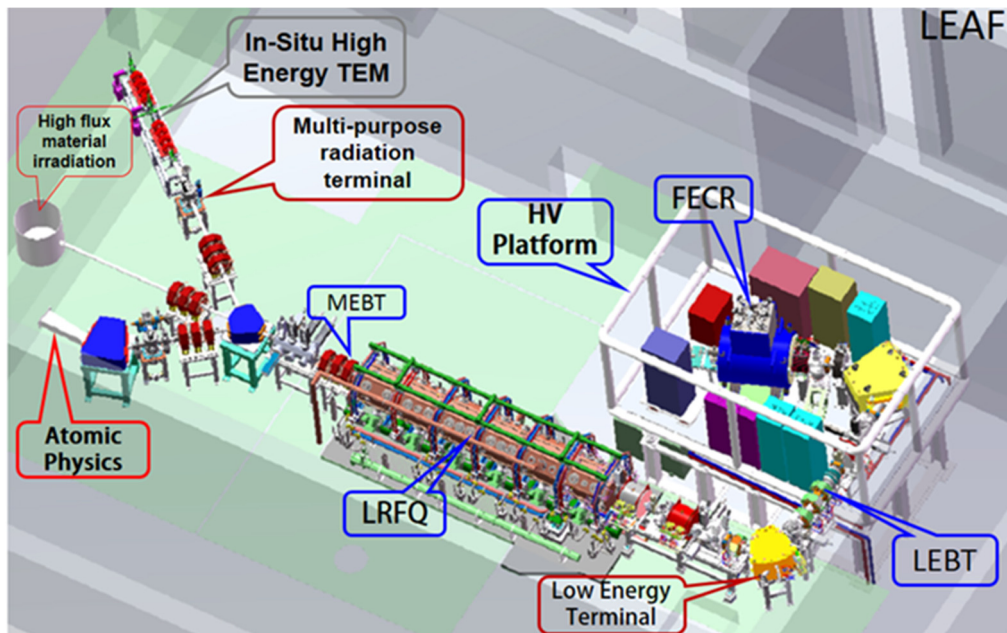


Figure 1: Layout of LEAF facility.

*Work supported by the NSFC under Grant No. 11427904, No. 11475232 and No. 11535016.

[†]luliang@impcas.ac.cn

Content from this work may be used under the terms of the CC BY 3.0 licence (© 2018). Any distribution of this work must maintain attribution to the author(s), title of the work, publisher, and DOI.



Figure 2: Side view of installed RFQ after full assembly on site.

DESIGN AND LOW POEWR TEST

The LEAF-RFQ is an octagon normal 4-vane structure with uniform-distributed 48 tuners and 12 pairs PISLs. The RFQ is 6m long and adopts two RF couplers. Based on our simulation of the thermal analysis and multipacting, the RFQ could operate very stable. For fabrication, the RFQ was divided 6 segments. Each segment was connected by screws. The low power tests and tuning of the whole cavity were carried out through three steps. Firstly, frequencies, Q factor and fields were measured in the cavity with aluminum end-plates and aluminum tuners inserted into the cavity 26mm, the same situation as the simulation. Secondly, through the tuning code LRFQtuning (a code developed for LEAF RFQ tuning based on the Matlab), the depths of the tuners were adjusted to meet the requirements of frequency and fields. After a few iterations, a satisfactory resonant frequency and field distribution will be achieved. Lastly, the copper tuners with the final insertion and copper end-plates replaced aluminum those. This step was to check the resonant frequency and field distribution, meanwhile, the Q factor was measured.

The LEAF-RFQ low power test consists of each section test and the whole cavity test. The low power tests of single section were carried out to check the machining and brazing quality. The average frequency difference between the simulated and the measured after brazed is 10.15 kHz. The average frequency difference between the measured before brazed and after brazed is 23.35 kHz. Shown in table 2, the low power test of the full length RFQ showed that the final quadrupole mode frequency is 81.253 MHz which meets well with the design value of 81.25 MHz, the measured Q factor is 16230 which is 90.3% of the simulated value and the measured frequency separation was 5.54 MHz which is enough for safe operation. Figure 3 shows the measured longitudinal field distributions of the quadrupole, two dipole fields in the cavity with the tuned tuners [4]. The relative error of the quadrupole field is less than 1% and the admixtures of the two dipole modes are within 1.5% of the quadrupole field. Therefore, the

frequency and field distribution meet the operation requirement.

Table 2: Main Parameters of the LEAF-RFQ

Measured results	Value
Quadrupole frequency (MHz)	81.253
Q factor	16230 (90.3%)
Q field relative error (%)	0.8
Admixture of dipole field (%)	1.5
Separated Δf (MHz)	5.587

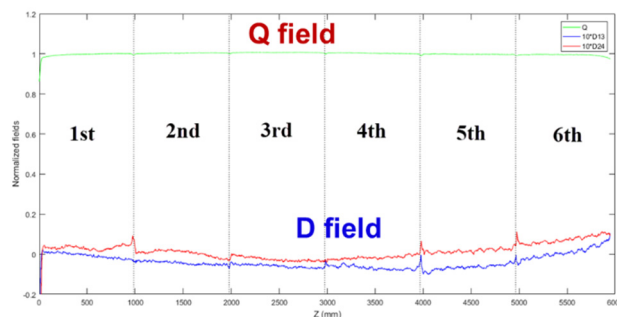


Figure 3: Measured Q and D field of the LEAF-RFQ.

RF CONDITIONING AND BEAM COMMISSIONING

After installing the equipment of vacuum, couplers, cooling routers, ARC detectors and pick-ups, and connecting with two 60kW solid state type RF source, the RF commissioning was started from Feb. 3rd 2018 aiming to 75 kW (1.12 times of necessary power). With a base vacuum condition of $\sim 1 \times 10^{-5}$ Pa, it took about 44 hours continuous conditioning to reach the goal of 75 kW.

The LEAF-RFQ was designed for $2 \leq A/q \leq 7$ ion acceleration, and the designed Kilpatrick factor was 1.54. The He⁺ beam was adopted for beam commissioning. The first pulse beam used 100 μ A He⁺ ions passed the RFQ in Feb. 9th 2018. Under the condition of pulse beam, the beam energy was measured as 0.5 MeV which meet the designed value. And two hours late, the first CW He⁺ beam passed

the RFQ. The current of the CW beam was measured 150 μ A. With supplying of correction magnet, the beam conditioning was restarted in June 1st 2018, the beam transmission and acceleration efficiency were measured 97.21% and 50.11%, respectively. The measured transmission agreed with the design. The acceleration efficiency is lower than the design because an upstream multi-harmonic buncher is not installed yet.

Shown in Fig. 4 and Fig. 5, in Sep. 5th 2018, the first N^{2+} beam was successfully accelerated 110 μ A up to the designed 500 keV/u with 97.97% transmission and 56.45% acceleration efficiency measured in pulse mode (5 μ s), and, the CW 110 μ A N^{2+} beam pass 15 minutes. The high current N^{2+} beam will be operated in one month when the multi-harmonic buncher is installed.

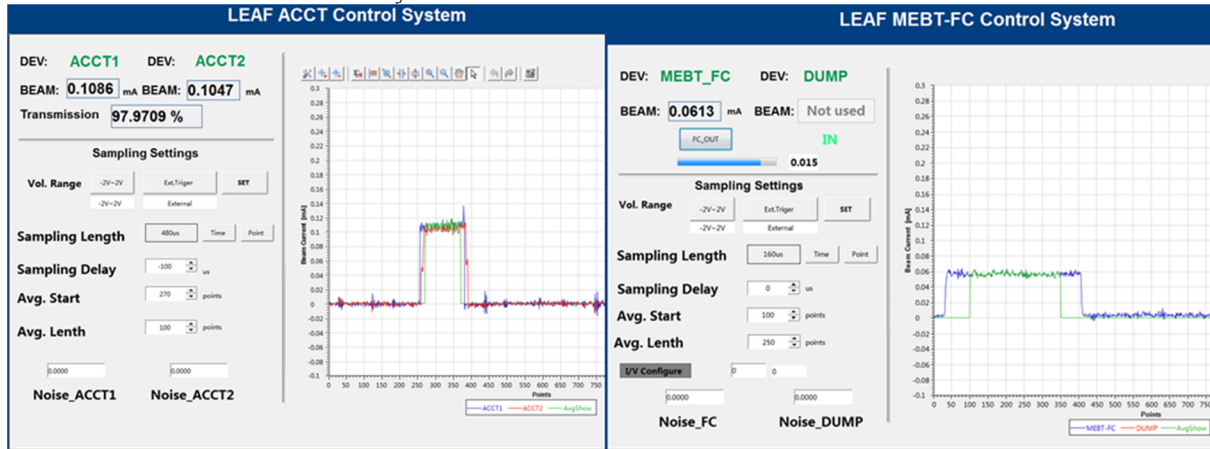


Figure 4: Measured signals of N^{2+} beam current form ACCTs and a Faraday Cup.

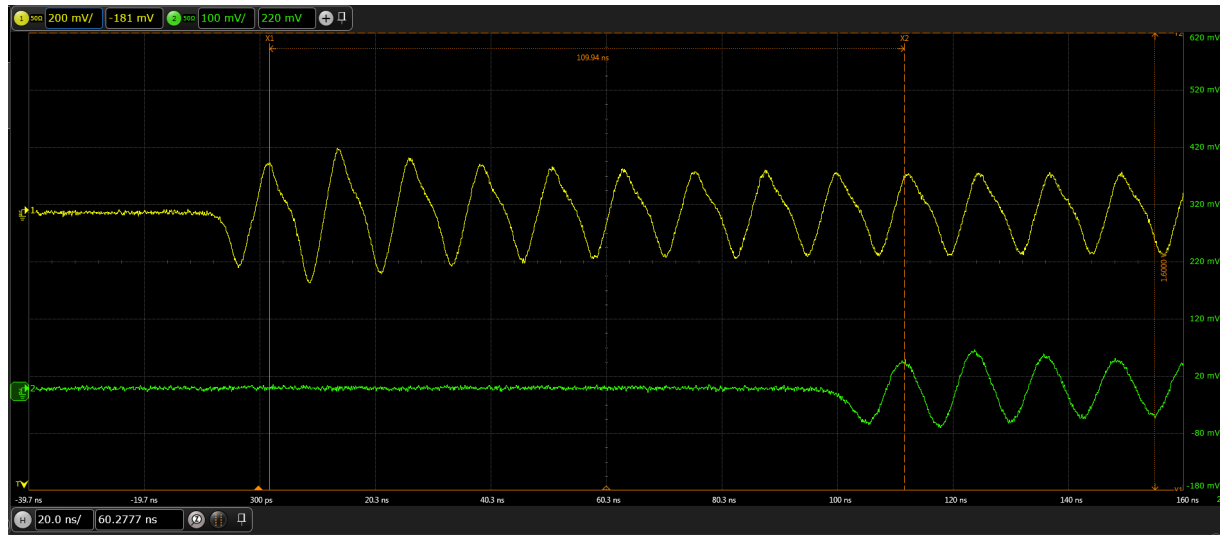


Figure 5: Measured signals of N^{2+} beam current from two BPMs.

CONCLUSION AND FUTURE PLAN

The LEAF-RFQ has been designed and simulated, and the beam test was successfully performed. The RFQ is an octagon four-vane type with 48 tuners and 12 pairs PISLs. It is about 6 m long with a good mode separation and a flat field distribution between inter-vanes. According to the high power test, several milestone goals have been achieved, such as the successful RF commissioning of LRFQ to its maximum designed power, and the successful CW acceleration of He^+ beam and N^{2+} beam to the designed energy of 0.5 MeV/u with matched transmission. For the

next, high intensity N^{2+} beam will be tested because the multi-harmonic buncher was installed already.

REFERENCES

- [1] J. Yang, J. Xia, G. Xiao, H. Xu, H. Zhao, *et al.*, *Nucl. Instr. Meth. B*, 317 (2013) 263-5.
- [2] C. Li, LP. Sun, Y. He, *et al.*, *Nucl. Instr. Meth. A* 729 (2013) 426-33.
- [3] Wei Ma, L. Lu, Xianbo Xu, Liepeng Sun *et al.*, *Nucl. Instr. and Meth. in Phys. Res. A*, 847 (2017) 130-135.
- [4] Wei Ma, L. Lu, Ting Liu, Longbo Shi, *et al.*, *Nucl. Instr. and Meth. in Phys. Res. A*, 901 (2018) 180-188.

MULTI-PHYSICS ANALYSIS OF A CW FOUR-ROD RFQ *

Z. S. Li¹, J. W. Xia¹, Y. J. Yuan, J. C. Yang, Y. He, Y. Q. Yang, Z. Xu, Y. Cong, J. Meng, L. Jing, H. Du¹, Z. J. Wang, Y. Zhang, H. N. Wang, X. N. Li¹, K. D. Wang¹, W. J. Xie, W. Yuan, H. M. Xie¹, X. W. Xu, G. D. Shen¹, Q. Y. Kong¹, X. J. Yin^{1,†}, J. X. Wu^{1,‡}

Institute of Modern Physics of Chinese Academy of Sciences, [730000] Lanzhou, China
 Y. R. Lu[§], K. Zhu

State Key Lab of Nuclear Physics and Technology, Peking University, [100871] Beijing, China
¹also at Huizhou Research Center of Ion Sciences, [516003] Huizhou, China

Abstract

The new injector SSC-LINAC is under design and construction to improve the efficiency and intensity of beams for the Separated-Sector Cyclotron (SSC). This will be accomplished with a normal conducting radio-frequency quadrupole (RFQ) accelerator. To match with the SSC, the RFQ must be operated on Continuous Wave (CW) mode with a frequency of 53.667 MHz. A four-rod structure was adopted for small dimensions of the cavity. While, it was a huge challenge on CW mode. A multi-physics theoretical analysis, including RF, thermal, structural and frequency shift coupling analysis, have been completed in response to the security and stable operation of the RFQ. The experimental measurement of frequency shift was also completed, which is consistent with the simulation. In this paper, the results of theoretical analysis and experiment are reported in detail.

INTRODUCTION

To achieve excellent performance in nuclear and atomic physics, the Heavy Ion Research Facility in Lanzhou (HIRFL) was upgraded successfully with a multifunctional Cooler Storage Ring (CSR) [1]. As the only injector of the HIRFL, the Sector Focusing Cyclotron (SFC) has to provide ion beams for both SSC and CSR. The SSC has to be shut down when the SFC provides the beams to the CSR, which causes the low utilization of the HIRFL. Furthermore, a higher beam intensity, which cannot be satisfied by the SFC, is required by several new experiments such as the super heavy element and precise mass measurement experiments. In order to solve the two problems, a linear accelerator called SSC-LINAC was proposed as a new injector of the SSC to replace the SFC [2]. The SSC-LINAC consists of a superconducting high-charge-state electron cyclotron resonance (ECR) ion source, a low energy beam transport (LEBT) line, a four-rod RFQ, a medium energy beam transport (MEBT) line, three DTLs and a high energy beam transport (HEBT) line [3], as shown in Fig. 1.

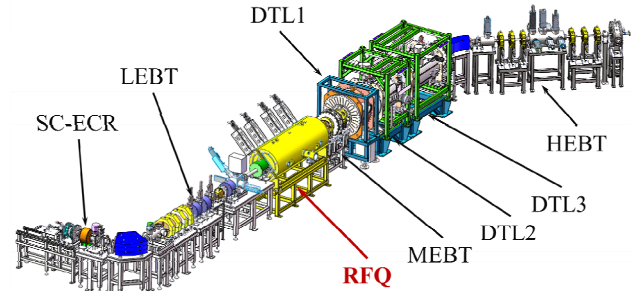


Figure 1: Layout of the SSC-LINAC.

The RFQ accelerator is a critical component of the SSC-LINAC. It accelerates intense beams and operate in CW mode, which was the greatest challenge for a four-rod structure. To control the emittance growth and beam losses caused by intense beams, a quasi-equipartitioning design strategy was applied in beam dynamics [4]. The main parameters of the RFQ are listed in Table 1. Furthermore, cooling channels design have been finished carefully. The bottom plate, stems and mini-vanes are all cooled by deionized water to ensure the CW mode operation [5].

Table 1: Main Parameters of the SSC-LINAC RFQ [4]

Parameters	Values
Frequency	53.667 MHz
Ratio of Mass to Charge	3~7
Design Beam Current	0.5 pA
Input Energy	3.728 keV/u
Output Energy	143 keV/u
Inter-Vane Voltage	70 kV
Cavity Length	2.527
Transmission efficiency	94.1%

MULTI-PHYSICS THEORETICAL ANALYSIS

To demonstrate the security and stable operation of the RFQ, a multi-physics theoretical analysis was finished by using the Computer Simulation Technology (CST) [6] code. The analysis consists of RF, thermal, structural and frequency shift coupling analysis. The RF analysis determine the power losses of the RFQ cavity. In the thermal analysis, the power losses are used as heat loads to determine temperatures. Displacements and stresses are deter-

* This work was supported by the National Natural Science Foundation of China (Nos. 11375243, 11405237, and 11475235) and the Guangdong Innovative and Entrepreneurial Research Team Program (No. 2016ZT06G373).

† yinxj@impcas.ac.cn

‡ wujx@impcas.ac.cn

§ yrlyu@pku.edu.cn

mined by the structural analysis with temperatures and pressure boundary conditions. A frequency shift is obtained in the second RF analysis with displacements. The effects of the coupler and the plungers were ignored in the multi-physics analysis to get more efficient.

RF Analysis

To match with the SSC and get a high accelerating gradient, the RFQ frequency was chosen as 53.677 MHz, which is four times of the SSC. A four-rod structure is very suit for this frequency, because of its small dimensions. It consists of a cylinder wall, 4 mini-vane rods, 12 stems and a bottom plate, as shown in Fig. 2.

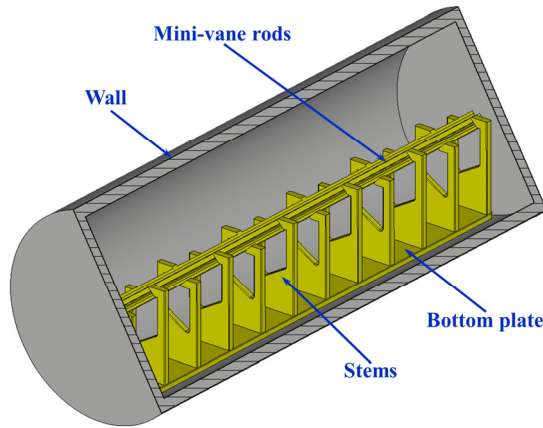


Figure 2: The CST model of the SSC-LINAC RFQ for the multi-physics analysis.

The RF analysis was completed to get the RF power loss fields on cavity surfaces, which is determined from the magnetic field distribution. Figure 3 shows RF simulation results of surface power loss. These fields are used as the heat loads on to the thermal model. A RF power of 30 kW is needed to accelerate ion beams with a mass-to-charge ratio of 7, such as $^{238}\text{U}^{34+}$ beams.

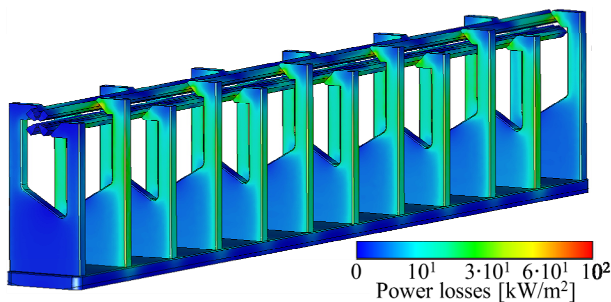


Figure 3: The power loss distribution of the cavity with a total power loss of 30 kW.

Thermal Analysis

In the thermal analysis, heat loads of the cavity, cooling channels and convection coefficients of cavity surfaces must be determined at the first step.

RF power loss fields were transferred to the thermal model and applied to the surfaces as heat loads. Power losses of cavity parts are shown in Fig. 4.

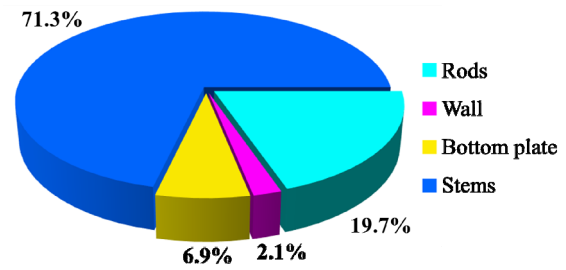


Figure 4: Power losses of cavity parts [7].

As shown in Fig. 5, cooling channels of the cavity consist of two parts: one part is the cooling channel of four rods, and the other is the cooling channel of the bottom plate and stems. The heat load of the cylinder wall account for only 2.1% of the total load. It can be cooled well by the heat transfer between the surface of the cylinder wall and the ambient air. Therefore, the wall has no more cooling requirement.

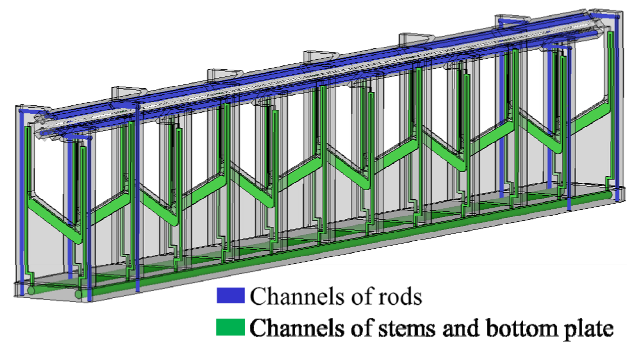


Figure 5: Cooling channels of the cavity.

The convection coefficient of the cooling channels was evaluated by the following formulae [7]:

$$h = \frac{\kappa \cdot Nu}{D} \quad (1)$$

Where κ is the thermal conductivity of the water, D is the diameter of channels, Nu is the Nusselt number defined as:

$$Nu = \frac{(f/8)(Re-1000)Pr}{1+12.7(f/8)(Pr^{2/3}-1)} \quad (2)$$

where f is the Darcy friction factor calculated by the following formula:

$$f = (0.79 \ln(Re) - 1.64)^{-2} \quad (3)$$

Re is the Reynolds number given by

$$Re = \frac{vD\rho}{\mu} \quad (4)$$

v is the flow velocity, ρ is water density and μ is the absolute viscosity. Pr is the Prandtl number given by

$$Pr = \frac{\mu C_p}{\kappa} \quad (5)$$

C_p is the specific heat of water.

The temperature of the ambient air and the cooling water was set to 20°C. Temperatures of the cavity with

Content from this work may be used under the terms of the CC BY 3.0 licence (© 2018). Any distribution of this work must maintain attribution to the author(s), title of the work, publisher, and DOI.

kinds of RF powers were simulated in the thermal analysis. Figure 6 shows surface temperature results with a RF power of 30 kW. The maximum temperature is 41.95°C. It exists at the top of stems, where there isn't any cooling channel.

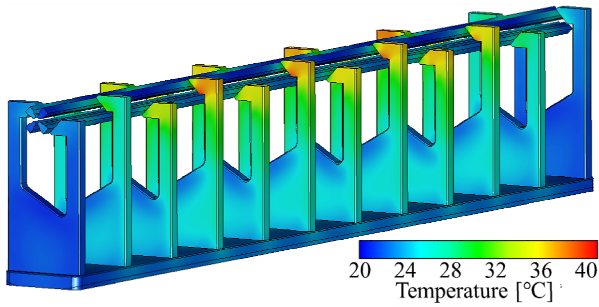


Figure 6: The temperatures of the cavity with a total power loss of 30 kW.

Structural Analysis

The temperatures of the cavity from the thermal analysis were transferred to the structural model. Displacement results are shown in Fig. 7. Displacements caused by the thermal expansion are below 0.105 mm. The stress level is below 14 MPa as shown in Fig. 8. It is safe for full power operation on CW mode.

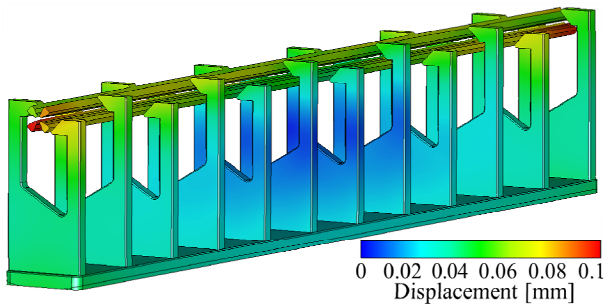


Figure 7: Displacement results of the cavity with a total power loss of 30 kW.

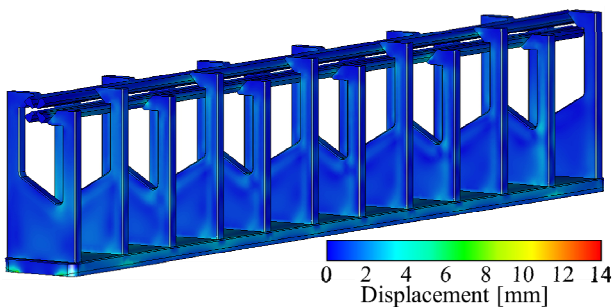


Figure 8: Stress contours of the cavity.

Frequency Sensitivity Analysis

The frequency shift, which caused by the change of cooling water temperature and RF power, must be controlled at reasonable range for the stable operation of the RFQ with full power. So, it is necessary to make a frequency sensitivity analysis.

Figure 9 shows the result of frequency shift caused by RF power. A frequency shift rate of -2.48 kHz/kW was obtained by a linear fit. Frequency shifts caused by temperature change of the cooling water were given by Fig. 10. The frequency shift rate is -1.06 kHz/°C.

A RF power of 35 kW with an appropriate margin and a water temperature variation range of ± 5 °C were used to evaluate the total frequency shift, which was -97.4 kHz. The shift can be tuned by automatic RF controlling system with a maximum tuning capacity of 191.5 kHz, so that the RFQ can operate with a stable resonance frequency.

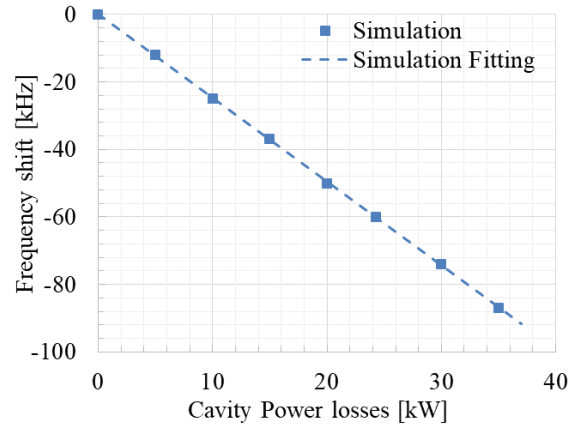


Figure 9: Frequency shift caused by RF power.

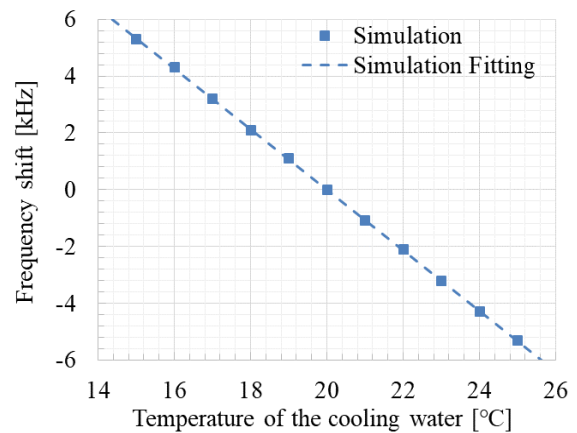


Figure 10: Frequency shift caused by temperature change of the cooling water.

FREQUENCY SHIFT EXPERIMENT

The frequency shift experiment has been finished during the RF power conditioning. Figures 11 and 12 show results of frequency shift measurements. Frequency shift rates caused by the RF power and the temperature change of the cooling water were -2.58 kHz/kW and -0.987 kHz/°C, respectively. Comparing with simulation and experiment results, the deviation value of Frequency shift rates caused by the RF power is less than 5%. Frequency shift rates caused by the temperature change of the cooling water agreed well with the simulation ones within less

than 7% relative error. this proves that multi-physics simulation results with the CST code is credible.

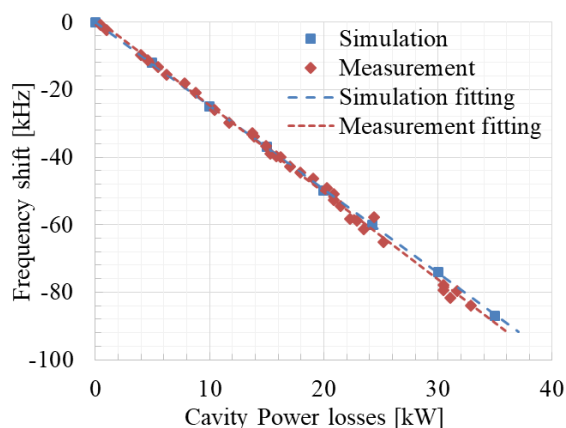


Figure 11: Comparison of frequency shift caused by RF power in simulation and measurement.

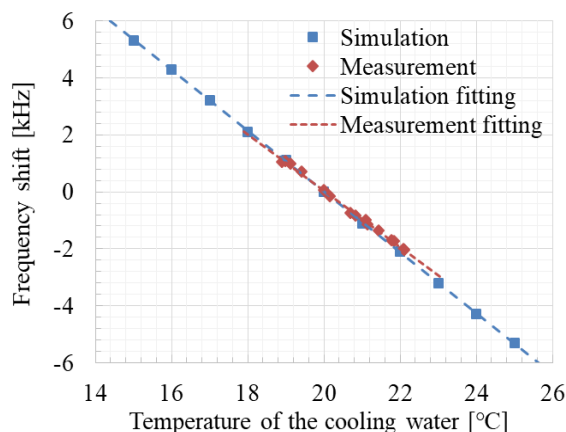


Figure 12: Comparison of frequency shift caused by temperature change of the cooling water in simulation and measurement.

CONCLUSION

A multi-physics theoretical analysis, including RF, thermal, structural and frequency shift coupling analysis, was finish for the CW four-rod RFQ of the SSC-LINAC by using the CST code. Displacements caused by the thermal expansion are below 0.105 mm. The stress level is below 14 MPa, which is safe for full power operation on CW mode. A total frequency shift caused by the change of cooling water temperature and RF power is below 100 kHz, which can be tuned by automatic RF controlling system in stable operation. The experimental measurement of frequency shift was also completed, which agreed with the simulation within less than 7% relative error. This can verify the reliability of the CST code.

REFERENCES

- [1] J.W. Xia *et al.*, “The heavy ion cooler-storage-ring project (HIRFL-CSR) at Lanzhou”, *Nucl. Instrum. Meth. A*, vol. 488, no. 1-2, p. 11, Aug. 2002, doi: 10.1016/S0168-9002(02)00475-8
- [2] Y. He *et al.*, “Conceptual Design of Linear Injector for SSC of HIRFL”, in *Proc. LINAC’10*, Tsukuba, Japan, Sep. 2010, pp. 482-484,
- [3] X. Yin *et al.*, “The R&D Status of SSC-LINAC”, in *Proc. IPAC’14*, Dresden, Germany, Jul. 2014, pp. 3277-3279, doi.org/10.18429/JACoW-IPAC2014-THPME026
- [4] G. Liu *et al.*, “Design of a CW high charge state heavy ion RFQ for SSC-LINAC”, *Nucl. Instrum. Meth. A*, vol. 701, p. 186, Feb. 2013, doi: 10.1016/j.nima.2012.11.017
- [5] Y. R. Lu *et al.*, “A CW High Charge State Heavy Ion RFQ for SSC-LINAC”, in *Proc. IPAC’13*, Shanghai, China, May 2013, pp. 3878-3880,
- [6] CST, <https://www.cst.com/>
- [7] X.J. Yin *et al.*, “Design, Fabrication, and Beam Commissioning of a Continuous-wave Four-rod RF Quadrupole”, *Phys. Rev. ST Accel. Beams*, vol. 19, p. 010402, Jan. 2016, doi: 10.1103/PhysRevAccelBeams.19.010402

NEW TYPE OF INJECTOR FOR CANCER THERAPY

Chaochao Xing^{†1}, Liang Lu, Lei Yang¹, Tao He¹, Chenxing Li, Xianbo Xu,
 Institute of Modern Physics, Chinese Academy of Sciences, Lanzhou 730000, China
¹also at University of Chinese Academy of Sciences, Beijing 100049, China

Abstract

We performed a compact design for 100 MHz Hybrid Single Cavity (HSC) for injector of cancer therapy. The proposed designs are conventional four-rod structure and DTL in a single IH cavity. This compact linac injector, running in frequency of 100 MHz, accelerates C⁶⁺ beams with 20 mA from 0.02 MeV/u up to 4 MeV/u. The total length of HSC is designed less than 4 meters.

INTRODUCTION

Compared with traditional structure, firstly, the HSC model consists of RFQ structure and DT structure without MEBT. Secondly, the IH structure provides the higher shunt impedance and acceleration gradient. In the structure, E-field is focused in the connection parts of 4-rod and first DT.

For DTL section, the section adopts the Alternative Phase Focus (APF). The DTL section with APF can achieve three-dimensional focusing without the installation of quadrupole lenses into the drift tubes.

Further, traditional injector has a complex control system and huge injector. Compared with traditional types, HSC adopts Direct Plasma Injection Scheme (DPIS). The DPIS could easily create enough C⁶⁺ ions to the linac by adjusting the distance from target to laser.

BEAM DYNAMICS

In this part, the beam dynamics were divided into 3 sections, RFQ section, DTL section, and HSC section [1][2]. For RFQ section, it accelerates the C⁶⁺ with 20 mA from 0.02 MeV/u up to 0.6 MeV/u. The DTL section accelerates C⁶⁺ from 0.6 MeV/u up to 4 MeV/u. For RFQ section was designed by RFQGen code. DTL section and HSC were designed by PIMLOC code. More details will be given in the next.

RFQ Section and DTL Section

The RFQ section is divided into 4 section: radial matching section (RMS), shaper section (SH), gentle buncher section (GB), and accelerator section (ACC) [3]. The length of IH-RFQ is short 1 m. The original main parameters were given in the Fig. 1.

We want the length of RFQ to be as short as possible, meanwhile, ensure the acceptable transmission and beam quality. To achieve the aims and realize an efficient bunching for RFQ section, we adopt some basic ideas, as follows: Firstly, we must vary the transverse focusing strength B along the beam direction because of the corresponding space-charge conditions at different positions.

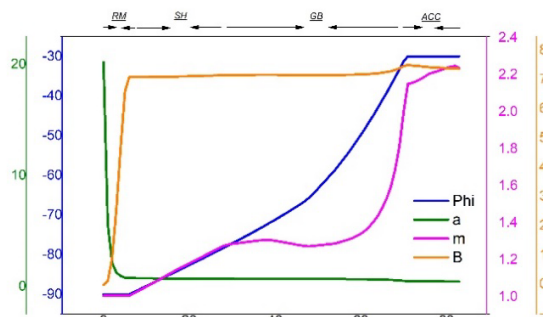


Figure 1: The original parameters in RFQ section.

Traditionally, the transverse B should be increasing with the space-charge force until the transverse defocusing force is weakened. After that it should go down. Secondly, the evolution speeds of the synchronous phase and the modulation parameters can also improve the bunching process.

When we followed the important conditions. We can get the optimized parameters, shown in Fig. 2.

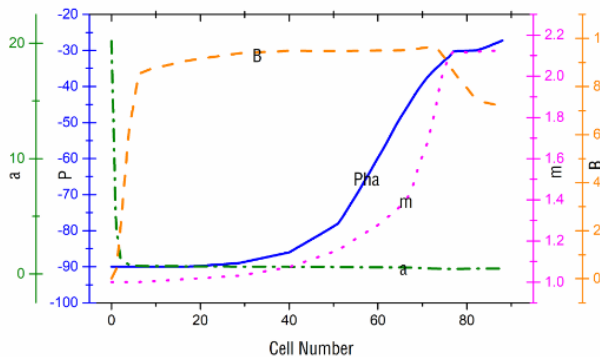


Figure 2: The optimized parameters in RFQ section.

Figure 3 gives the transmission efficiency, which is almost over 95%, at last cell.

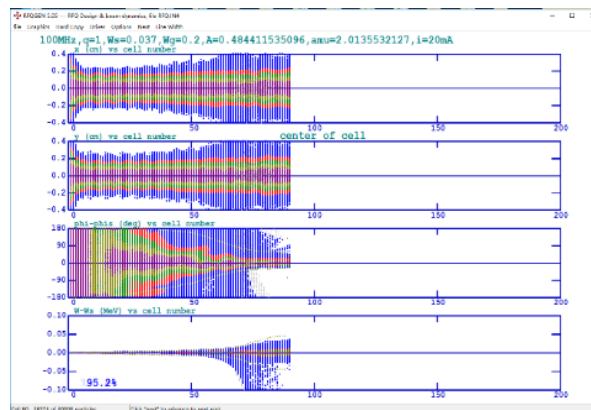


Figure 3: Transmission efficiency at last cell.

Content from this work may be used under the terms of the CC BY 3.0 licence (© 2018). Any distribution of this work must maintain attribution to the author(s), title of the work, publisher, and DOI.

[†]ccxing@impcas.ac.cn

And, we can't ignore the beam losses, both longitudinal and transverse losses. In order to reduce the beam losses, increasing the longitudinal acceptability in the first several cells is effective way. As shows in Fig. 4, beam loss have been significantly reduced after optimized.

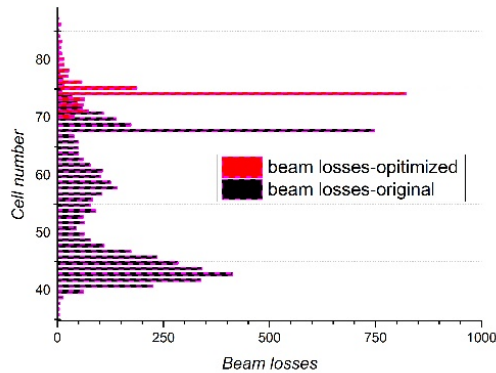


Figure 4: Beam losses of original and optimized designs.

The main parameters of RFQ and the final parameters are summarized in Table 1.

Table 1: Design Parameters of the RFQ Section

Parameters	Value
Inter-vane voltage	85 (kV)
Vane length	1050 (m)
Synchronous phase	-90° to -30°
Modulation factor	1 to 2.1
Transmission efficiency	95.2 %
Ellipse parameters (Alpha x, y)	1.8456, -1.3395
Ellipse parameters (Beta x, y)	18.0319, 13.0393 (cm/rad)
Ellipse parameters (Emit, u, rms x, y)	0.9089, 0.8803 (cm-mrad)
Ellipse parameters (Emit, u, rms z)	0.0712 (MeV-deg)

The output of RFQ section is adopted convergent design for following DT injection, shown in Table 2.

The most important theory in DTL section is Alternative Phase Focus (APF) principle. Drift tube linac (DTL) with APF is a compact version, which was discovered in 1953, compared with the traditional DTL. It can achieve three-dimensional focusing without the installation of the quadrupole lenses into the drift tube. It means that inter-gap RF field is used to achieve not only acceleration but also beam focusing in APF DTL [4][5][6]. On the one hand, if the synchronous phase greater than 0 degree, it will mainly offer transverse focusing, which is higher than longitudinal focusing. On the contrary, it mainly offers longitudinal focusing. But, we can't deny the fact that it is small longitudinal acceptance in DTL. So, the number and value of negative phase must be increased in the first several gaps. The Fig. 5 gives the phase in each gap.

Table 2: The Input Parameters of DTL

Parameters	Value
Ellipse parameters (Alpha x, y)	1.8456, -1.3395
Ellipse parameters (Beta x, y)	18.0319, 13.0393 (cm/rad)
Ellipse parameters (Emit, u, rms x, y)	0.9089, 0.8803 (cm-mrad)
Ellipse parameters (Emit, u, rms z)	0.0712 (MeV-deg)
Δw	0.03 (MeV)
Δp	30 (Deg)

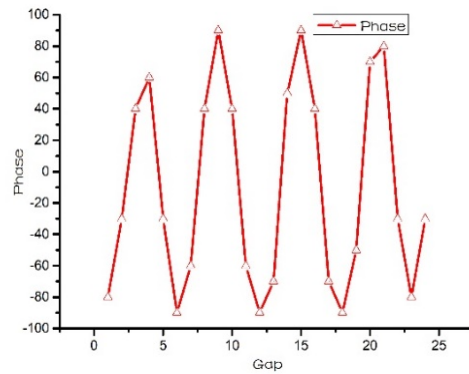


Figure 5: The phase in each gap.

The voltage in each gap and the length of each gap were given in Fig. 6. when we change the length of gap and coefficient, the length of DT is changed subsequently. To insure the minimum length of DT over 1 mm, length of gap was restricted no more than 40 mm.

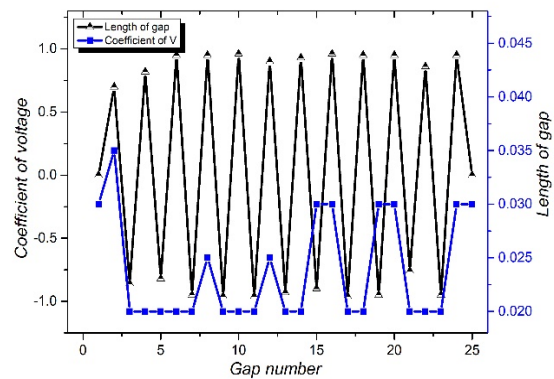


Figure 6: The voltage and length of gap in each cell.

The number of simulated particles is 10000. After setting the basic parameters in PIMLOC and tracing the particles, we could get the results of simulations, shown in Table 3, which was calculated by PIMLOC to satisfy the whole design requirements.

Content from this work may be used under the terms of the CC BY 3.0 licence (© 2018). Any distribution of this work must maintain attribution to the author(s), title of the work, publisher, and DOI.

Table 3: The Parameters in DTL

Parameters	Value
Voltage	199.2 kV
Cell number	24
Length	1853 mm
Bore radius	13 mm
DT radius	30 mm
Minimum length of DT	13 mm

The minimum length of DT is over 1 cm, which is satisfied to Engineering requirements. The output at the end was given in Fig. 7. Transmission efficiency is over 90%.

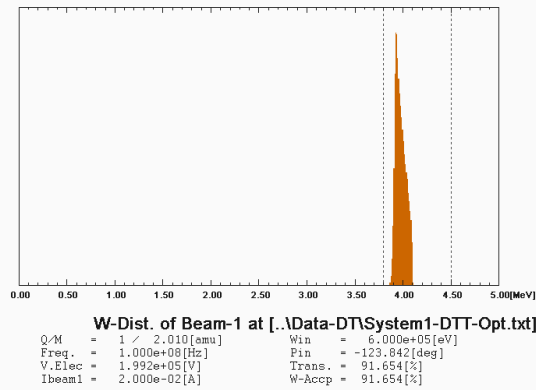


Figure 7: The output at the last gap.

HSC Section

The parameters of HSC were determined by the output parameters of RFQ section and DTL section. But, the distance between exit of RFQ section and first DT (L-RFQ-DT) is the vital important for the transmission efficiency. The transmission efficiency was changed along with the distance. In our research, the maximum transmission efficiency occurred at range of 30 mm to 60 mm.

Secondly, Length of ion source to RFQ section (L-IS) is also an important factor. The injection phase is related to the two factor, L-RFQ-DT, L-IS. So, the appropriate length is vital important to the whole HSC.

The output of HSC was shown in Fig. 8, which was satisfied the design aims. The transmission efficiency is over 80%.

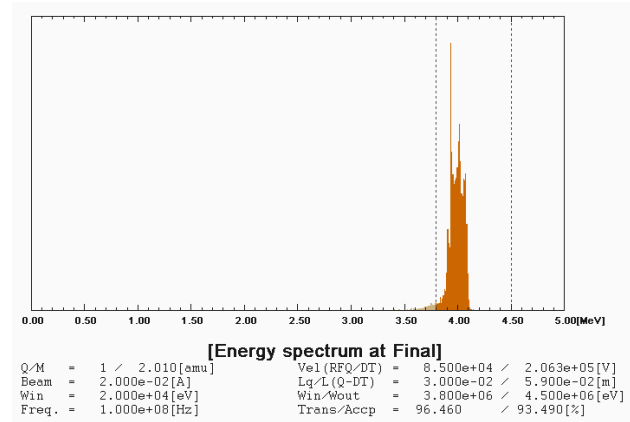


Figure 8: The results of HSC.

After optimizing the main parameters of HSC, the final parameters are summarized in Table 4.

Table 4: The Final Parameters in HSC

Parameters	Value
L-IS	10 (mm)
L-RFQ-DT	59 (mm)
L-Pure-Q	30 (mm)

SUMMARY AND FUTURE PLAN

We have studied a new HSC type linac which is a practical and efficient machine to accelerate high intense ion beam. We discussed the E matching designs for reducing the concentrated electric field distribution and investigated relation of meth and power & frequency.

In the next step, we will optimize multi-physical fields of HSC by ANSYS.

REFERENCES

- [1] I.M. Kapchinskii and V.A. Teplyakov, "A linear ion accelerator with spatially uniform hard focusing", *Prib. Tekh. Eksp.* 1970, 19 (1969).
- [2] T.P. Wangler, Los Alamos Report No. LA-8388, 1980.
- [3] T. Ito, L. Lu, *et al*, *Nucl. Instrum. Methods Phys. Res. B* 261 (2007) p.p.17-20.
- [4] L. Lu, T. Hattori, *et al*, *Nucl. Instrum. Methods Phys. Res. A* 688 (2012) p.p.11-21.
- [5] L. Lu, T. Hattori, H.Y. Zhao, *et al*, "High Power Test of An Injector Linac For Cancer Therapy Facilities", *Phys. Rev. ST Accel. Beams* 18, 111002 (2015) p.p.1-8.
- [6] CC. Xing, L. Lu, T. He, L. Yang, W. Ma, *et al*, "Design of Practical HSC Type Injector for Cancer Therapy", in proceeding of LINAC2018, Beijing, China, 2018, paper TUPO101.

Nb SPUTTERED 325 MHz QWR CAVITIES FOR CiADS*

F. Pan[†], T. Tan, P. Xiong, H. Guo, C. Zhang, T. Jiang, and Y. He,
Institute of Modern Physics, [730000] Lanzhou, China

Z. Li, H. Wang, Northwest Institute for Non-ferrous Metal Research, [710016] Xi'an, China

Abstract

The possibility for adopting niobium thin film coated copper (Nb/Cu) quarter wave resonators (QWRs) in the low energy section of CiADS project [1] is being evaluated. Comparing with bulk niobium cavities, the Nb/Cu cavities feature a much better thermal and mechanical stability at 4.5 K. Two 325 MHz Nb/Cu QWR cavities have been fabricated at IMP, to demonstrate whether the niobium coated copper cavity technique can meet the requirements of CiADS. The cavity is coated with biased DC diode sputtering technique. This paper covers resulting film characters, vertical tests with the evolution of the sputtering process, and improvements to mitigate issues we met.

INTRODUCTION

The operational stability of SRF cavities is one of the foremost challenges that hinder CiADS linear accelerator from continuous running [2]. Let Nb/Cu cavities replace the bulk niobium cavities could be an effective solution, because Nb/Cu cavities come up with advantages in terms of both thermal stability and mechanical stability [3]. At 4.2 K, the heat conductance of high purity bulk Nb is about 75 W/(m·K), while the number is as high as 300-2000 W/(m·K) for high purity oxygen free copper [3]. The poor thermal conductivity of Nb put an upper limit for SRF cavity wall thickness, in order for the inner surface to be effectively cooled, which impairs the robustness of the cavity's mechanical structure. The use of a copper cavity as a substrate can effectively solve the major problems of poor thermal conductivity and sensitivity to external pressure and vibration at the same time, because the thicker copper wall can provide rigid stiffening in the SRF cavity. Furthermore, Nb/Cu cavity is economical than bulk Nb cavity in terms of fabrication and processing cost. The material cost of OFHC copper is only about 4% of the price for SRF grade bulk Nb. In addition, copper is easier to anneal, polish, and machine than niobium, the cavity processing cost for Nb/Cu cavities would be much lower than that for bulk Nb cavities [3].

IMP launched its Nb/Cu cavity project in 2016. Up to now, the film characters, including thickness profile along the cavity, structure and morphology tests have been performed at IMP. Two dummy QWR cavities had been produced and coated to understand and optimize the sputtering setup and process.

THIN FILM COATING SETUP

The coating system employed in this project is modify from an existed equipment at NIN with biased DC diode sputtering [4] ability. Figure 1(a) showed the side view of this very system. For the purpose of R&D tests, a 325 MHz QWR dummy cavity without a beam line has been designed at IMP. The dimension of the dummy cavity is shown in Fig. 1(b). For simplicity, two dummy cavities were machined directly from OFHC ingot to avoid any difficulties brought by welding seams inside the cavity [5]. S.S. flanges were brazed onto the cavities. Before coating process, surfaces were treated with mechanical and electrical polishing. From electromagnetic simulation, the unloaded quality factor (Q_0) for an uncoated copper cavity is 1×10^5 , and is 8×10^8 for a superconducting Nb/Cu cavity.

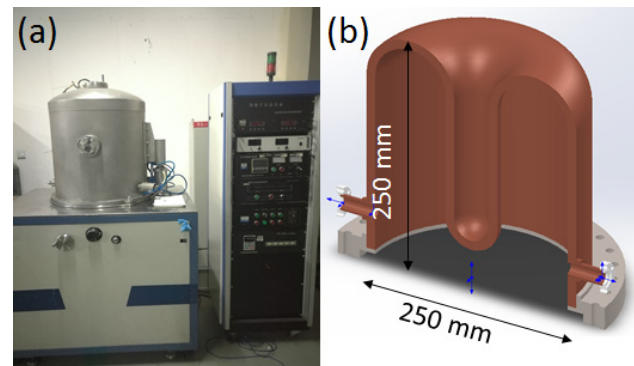


Figure 1: (a) the deposition system and (b) the dimension of the 325 QWR cavity.

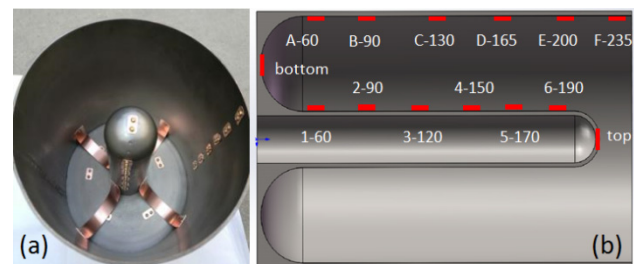


Figure 2: The sample holder's (a) appearance and (b) the exact location of the samples' locations.

A QWR-like sample holder with 16 samples positions along the outer and inner conductors had been used before the actual cavity coating. This setup allows access to the film properties in different positions by small sample characterizations. Thus the thickness and T_c distribution of the coating film could be investigated from clipped samples. The surface treatment of small sized samples is similar to the dummy cavity. The samples' locations and their distance to the bottom plate are marked on Fig. 2(b).

* Work supported by Key Research Program of Frontier Sciences, CAS, Grant NO. QYZDY-SSW-JSC019.

[†] email address: pan2015@impccas.ac.cn

SAMPLES RESULTS

The thickness of the niobium film deposited on copper samples is measured by a step profiler. The critical transition temperature (T_c) is measured by Superconducting QUantum Interference Device (SQUID) through standard susceptibility measurement.

Initially, the sputtering utilized a tube-target sitting right in the middle of the inner and outer conductor. Such layout generated a non-uniform growth rate distribution, which is specified in Table 1. The ratio of average growth rate between inner conductor and outer is about 10:1. The experiment also reveals that the coating rate at cavity top was one-fifth of the rate at bottom area. With a maximum ratio of 50:1, the niobium film coated on the sample at point F couldn't be thick enough before the film at point 1 started to break-off. The thickness limit test show film starts to break when the thickness of film greater than 60 μm . Then the shape of the Nb target was re-designed to ensure a maximum deposition ratio below 10:1.

Table 1: Average Growth Rate at Beginning

	Location	Growth rate (nm/h)
Outer Conductor	Top	20
	Bottom	100
Inner Conductor	Top	200
	Bottom	1000

With optimization between each run, 3 test runs with copper samples were performed before the cavity coating. The T_c s of selected samples are presented in Table 2. Samples along the inner conductor exhibit better T_c above 9.3 K. But samples on the top of the outer conductor are with poor properties. The film properties are improved gradually. However, point F remains a weak point of our coating. This agrees with the growth rate distribution and implies the T_c of F sample is still limited by the thickness.

Results from the last run of experiments showed an almost complete superconducting coating was achieved on the QWR-like sample holder, except for point F. Due to the limit of current deposition system size, the optimization of growth rate ratio cannot be further reduced. To solve this problem, a new deposition system with a larger vacuum chamber to tune the sputtering layout is being built.

Table 2: Summary of Samples' T_c s in Each Test Run*

Run	A	F	Bot- tom	1	3	Top
1	7.3	X	9.0	9.3	N/A	#
2	<6	X	X	9.3	9.3	9.3
3	9.3	<7	9.4	N/A	9.3	9.3

*: T_c unit in K.

#: Large visible defect on the surface, unable to measure.

N/A: Not measured.

X: not superconducting down to 4 K.

CAVITY TEST

After the first cavity coating test, it was observed the film on the top of the outer conductor wasn't silver shining, implying the film there could be very thin or contaminated. And particles falling from the target produced several defects at the bottom part, because the cavity is under the target. The cloudy film and defects are shown in Fig. 3.



Figure 3: The first QWR Cu/Nb Cavity made in NIN.

Ultrasonic cleaning and high pressure rinsing (HPR) are used in the first coated cavity post-treatment processing. Film peeled off at a few spots on the outer conductor after ultra-sonic cleaning, with typical size 1~2 mm (Fig. 4(a)). Optical investigation suggests it may result from the fall-outs from the target or contaminated substrate surface. After HPR, no more defects are detected, no matter there was or wasn't ultrasonic cleaning before it. In order to avoid more damage to the film, ultrasonic cleaning is no longer used in the post treatment processing for the second coated cavity. An SRF grade Nb plate is used as the end-plate, sealed by indium wire, because the QWR is designed to work under isolated vacuum. In the first cryogenic RF test, the microwave power was coupled from the sides (Fig. 4(b)), and this configuration gave us a lot of problems including MP and difficulty in feeding power into the cavity, because the size of the coupling tube is too small and the tube inner surface is rough.

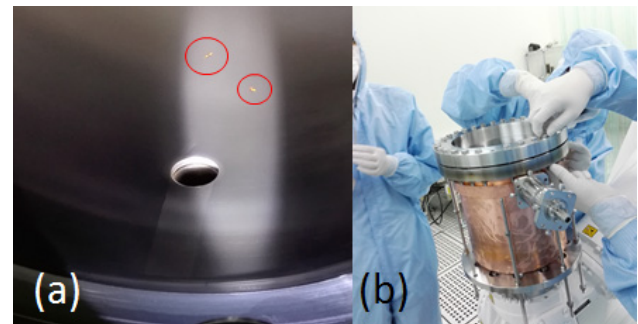


Figure 4: The first QWR Cu/Nb Cavity made in NIN. (a) A few spots peeled off after ultrasonic cleaning. (b) The first film cavity is coupling from the sides.

The vertical test of the first film cavity is very lossy at 4.2 K. The Q_0 cannot be measured from the damping curve. Four temperature probes were installed on the bottom and top of the outer cavity surface and near the tube. The temperature reading showed that, there was little power fed into the cavity and most of power was consumed by the MP

at the coupling tube. The temperature near the tube is much higher than the top and bottom when we turned on the input RF power. The loaded quality factor (Q_L) of the 1st cavity is about 2.5×10^5 measure by FWHM, in heavily over-coupled condition. The Q_L value is much higher than the OFHC copper cavity at low temperature ($\sim 6 \times 10^4$), indicating at least part of the cavity was in superconducting status.

The RF power feeding configuration for the vertical test of the 2nd cavity was switched to bottom-coupled (Fig. 5). The 2nd cavity has the same behavior: $Q_L \sim 4E5$ at 4.2 K. However, in the 2nd test, the temperature rising occurred all over the cavity. The heating was more uniform comparing with the first test, and the temperature increase was less than the maximum value observed on the first cavity. In the 2nd test, the temperature sensor near the cavity top area always heats up faster than the others, indicating the film near the cavity opening does not transfer into the superconducting state.



Figure 5: The vertical test of the 2nd cavity is switch to bottom-coupled.

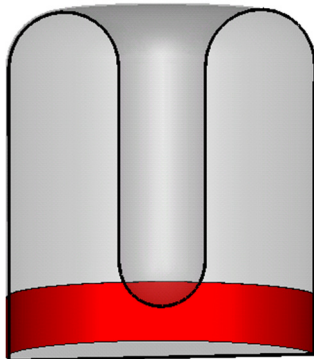


Figure 6: Non-SC part at the bottom is the main contribution for loss.

Calculation for the loss source was made based on the assumption that there was non-superconducting defects on the cavity wall, either (a) a Φ -1 mm exposed copper spot like the ones in Fig. 4(a), or (b) a normal conducting niobium ($RRR \sim 4$) ring near the opening (Fig. 6). The results indicated that the loss from a type (a) defect was about the same order as the loss from a whole superconducting cavity, while type (b) defect can dramatically reduce the cavity's Q by 2 orders of magnitude. Comparing with the measured

Q_L , the appearance of a normal conducting Nb ring may explain why we were having a degraded RF performance. To mitigate this problem, additional efforts need to be imposed to ensure the film near the cavity opening to be good. Such efforts include extending the Nb cathode out of the cavity to get uniform coating near the cavity opening, and flipping the deposition set up upside down to avoid any particles falling from the target depositing on the cavity surface.

CONCLUSION

The results of samples tests and vertical tests of the cavity showed that we are close to the final production of Nb/Cu QWR cavities with acceptable SRF performance. With proper optimization of our deposition system, we will demonstrate the feasibility for adopting Nb/Cu cavities at the low energy section of the CIADS linear accelerator.

REFERENCES

- [1] Y. He, "Successful Beam Commissioning of Chinese ADS Injector-II", in *Proc. SRF'17*, Lanzhou, China, July. 2017, paper MOXA01.
- [2] W. M. Yue, "Conditioning and Operation of Superconducting Half-wave Resonators for C-ADS Injector", in *Proc. SRF'17*, Lanzhou, China, July. 2017, paper THXA01.
- [3] V. -F. Anne-Marie, "Superconducting RF materials other than bulk niobium: a review", *Supercond. Sci. Technol.*, vol. 29, no. 11, p.113002, Sep. 2016, doi:10.1088/0953-2048/29/11/113002.
- [4] V. Palmieri, V. L. Ruzinov, S. Yu. Stark *et al.*, "Niobium sputtered quarter wave resonators", *Nuclear Inst. and Methods in Physics Research*, vol. 328(1-2), pp. 280-284,1993, doi: 10.1016/0168-9002(93)90642-U.
- [5] L. Alberty, G. Arnau-Izquierdo, I. Aviles Santillana *et al.*, "The Copper Substrate Developments for the HIE-ISOLDE High-Beta Quarter Wave Resonator", in *Proc. SRF'16*, Paris, France, Sep. 2013, paper TUP069, pp. 596-598.

Content from this work may be used under the terms of the CC BY 3.0 licence (© 2018). Any distribution of this work must maintain attribution to the author(s), title of the work, publisher, and DOI.

DYNAMICS STUDY OF A DRIFT TUBE LINAC FOR BOTH HEAVY IONS AND PROTON*

H. Du^{†,1}, X. J. Yin¹, J. C. Yang, Y. J. Yuan, J. W. Xia, X. N. Li¹, Z. S. Li¹, K. D. Wang, Q. Y. Kong,
 Institute of Modern Physics, Chinese Academy of Sciences, 730000 Lanzhou, China
¹also at Huizhou Research Center of Ion Sciences, 516003 Huizhou, Guangdong, China

Abstract

An accelerator complex for Space Environment Simulation and Research Infrastructure (SESRI) has been designed by Institute of Modern Physics (IMP) and will be constructed in Harbin Institute of Technology (HIT). This accelerator consists of an ECR ion source, a linac injector, a synchrotron and 3 research terminals. As an important part of the complex, the linac injector should provide both proton and different kinds of heavy ions, from helium to bismuth, with energy of 5 MeV and 1 MeV/u respectively for the synchrotron. In order to provide beams with the mass to charge ratio (A/Q) range from 1 – 6.5 (for proton to ²⁰⁹Bi³²⁺) by only one linac injector, a special solution of the main acceleration section DTL is carried out. The relevant dynamics calculations, such as beam matching, stripping process of the hydrogen molecule ion and beam energy spread reducing, are performed by Particle in Cell (PIC) method.

INTRODUCTION

In order to simulation and research the damage to the electronic equipment and organism on the spacecraft by high-energy particles in the universe, Harbin Institute of Technology (HIT) proposed building an accelerator based nuclear irradiation source named Space Environment Simulation and Research Infrastructure (SESRI). The accelerator complex of SESRI is designed and constructed by Institute of Modern Physics (IMP) which contains an ECR ion source, a linac injector, a synchrotron and 3 research terminals [1] as shown in Fig. 1. The ECR ion source can provide mostly all stable ions from proton to bismuth. These ions are accelerated by the linac injector to the injection energy of the synchrotron. The synchrotron accelerates different kinds of ions to specific energy and then slowing extracts them to the experiment terminals. The design of the linac injector must meet the preliminary requirements of the synchrotron, which can be seen in Table 1. For this linac injector, the main problem is how to accelerate very heavy ions like ²⁰⁹Bi³² and lightest ion proton and make it more compact. Between the linac injector and the synchrotron, there is a long beam transport line used for vacuum degree transition.

According to the project requirement, preliminary dynamics design of the DTL is finished. And then, Beam dynamics tracking with a PIC simulation code for different operation mode alone the main acceleration section is accomplished. The simulation takes beam matching into

account and verifies the preliminary design. On the other hand, effects of stripping foil on the hydrogen molecule ion are studied. A short beam transport line used for reducing the beam energy spread of proton and heavy ion is also designed in the PIC simulation.

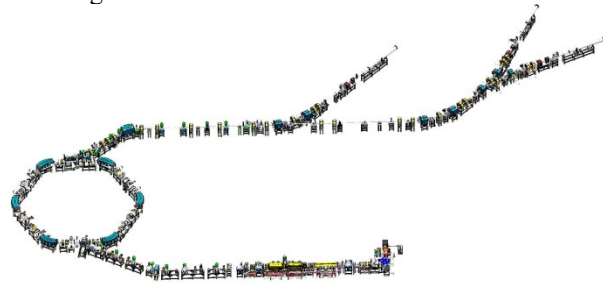


Figure 1: Integrated layout of SESRI accelerator complex.

Table 1: Inject Beam Parameters of the Synchrotron

Parameter	Value
Beam energy	1 MeV/u(²⁰⁹ Bi ³²⁺), 5 MeV (proton)
Energy spread	±0.3%
Transverse emittance	≤13πmm·mrad
Beam current	30 eμA(²⁰⁹ Bi ³²⁺), 300 eμA(proton)

PRELIMINARY DYNAMICS DESIGN OF THE DTL

The R/Q of the injection ion for the synchrotron ranges from 1 to 6.5 and it is too large for a normal conducting muticell linac which is because the cavity power range is squared of the R/Q. The whole RF system cannot operate stably in such a large power range. So in order to provide proton beam to the synchrotron, H₂⁺ is accelerated to 1MeV/u by RFQ and DTL1 firstly and then be stripped to proton to continue accelerate by DTL2. In this way, the R/Q range of the RFQ and the first section of the DTL will be only from 2 to 6.5. Beam extract energy of the RFQ is set to 300 keV/u for H₂⁺ and other heavy ions. The RF frequency is 108 MHz for the whole linac injector.

KONUS dynamics [2] concept and LORASR code [3] are adopted to make the preliminary dynamics design of the DTL for the linac injector. On the basis of the injection energy requirements of the synchrotron for proton and heavy ions, this linac injector contains two DTL cavities. All heavy ions including H₂⁺ can be accelerated to 1 MeV/u by the DTL1 which contains an inner focusing quadrupole triplet. And DTL2 is only used to accelerate the proton from 1 MeV to 5 MeV. For heavy ions, the DTL2 is just regard as a drift section. Between the two

* Work supported by National Natural Science Foundation of China (11375243, 11405237) and Guangdong Innovative and Entrepreneurial Research Team Program (2016ZT06G373).

[†] duheng@impcas.ac.cn

DTLs, there must be a foil for stripping H_2^+ to proton. For simplicity, the effects of stripping foil on the H_2^+ are ignored in the preliminary design.

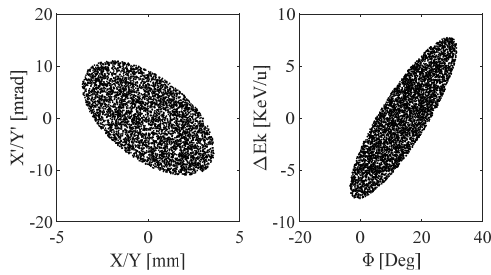


Figure 2: Phase space distribution at the entrance of DTL1.

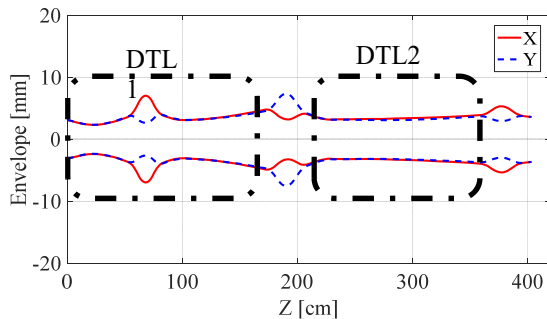


Figure 3: Beam transverse envelope in DTL1 and DTL2.

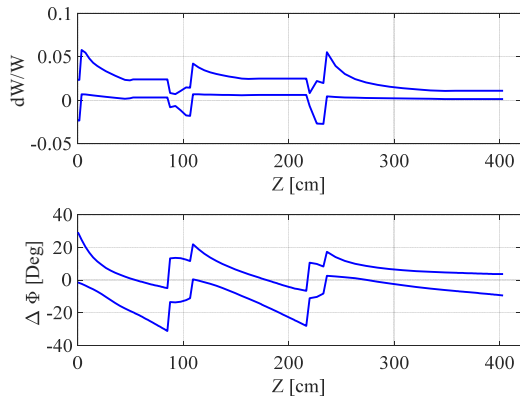


Figure 4: Energy spread and bunch length boundary along DTL1 and DTL2.

In the dynamics calculation, the tracking particle is set to be proton, but the maximum values of gap voltage and quadrupole magnet strength about DTL1 must be reasonable when $^{209}\text{Bi}^{32+}$ is accelerated. Kilpatrick factor is less than 2.1 and the maximum pole face electric field of all quadrupole magnets is not larger than 0.9T. Beam transverse and longitudinal phase space distribution at the entrance of DTL1 is set to uniform distribution which the RMS emittance is $0.2\pi\text{mm}\cdot\text{mrad}$ and $0.45\pi\text{ns}\cdot\text{keV/u}$ respectively as shown in Fig. 2. Transverse envelope of 90% beam is shown in Fig. 3. DTL2 is followed by a quadrupole triplet. Energy spread and bunch length boundary of the beam relative to the synchronous particle can be seen in Fig. 4. The normalized RMS emittances relative increment is small in transverse but a little larger for the longitudinal as shown in Fig. 5. Nevertheless, the

synchrotron cares more about the transverse emittance, especially the horizontal one, and beam energy spread. As Fig. 6, the minor axis of longitudinal phase ellipse is short and it will benefit for reducing the beam energy spread which will be discuss later.

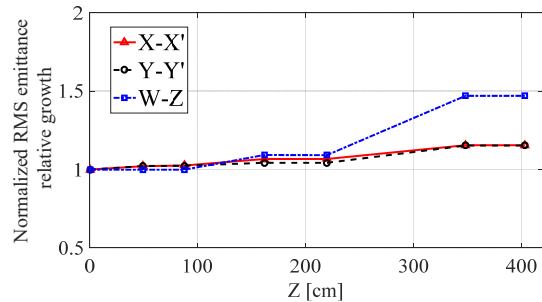


Figure 5: Normalized RMS emittances relative increment.

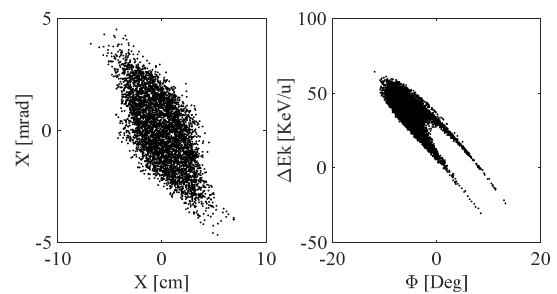


Figure 6: Phase space distribution at the exit of DTL2.

BEAM DYNAMICS TRACKING FOR $^{209}\text{Bi}^{32+}$

The dynamics preliminary design of the RFQ has been finished and the phase space distribution of the extraction beam of the RFQ is shown in Fig. 7. Transverse and longitudinal normalized RMS emittance is $0.15\pi\text{mm}\cdot\text{mrad}$. Between the RFQ and DTL1, there is a 1.5 meter long beam transport line including 5 quadrupole magnets and a 2 gap buncher named Buncher1. When doing the simulation of $^{209}\text{Bi}^{32+}$, DTL2 is treated as a drift section. The second buncher behind DTL2 is used for reducing the beam energy spread of heavy ions extracted from DTL1. The PIC simulation is performed by Beampath code.[4]

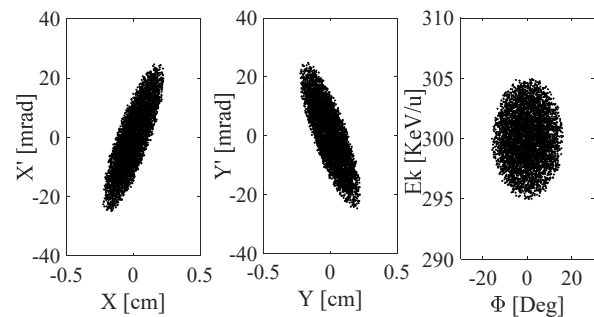


Figure 7: Beam phase space distribution at the exit of RFQ.

The transverse beam envelope, bunch length and energy spread along the main acceleration section are shown in Fig. 8. At the exit of the linac injector, energy spread of

Content from this work may be used under the terms of the CC BY 3.0 licence (© 2018). Any distribution of this work must maintain attribution to the author(s), title of the work, publisher, and DOI.

$^{209}\text{Bi}^{32}$ is less than $\pm 0.3\%$. In this simulation, transverse normalized RMS emittance increases about 28% which is a little larger than preliminary design result. On the basis of the requirement of synchrotron, the normalized RMS emittance of heavy ion beam extracted from RFQ must be not more than $0.125\pi\text{mm}\cdot\text{mrad}$.

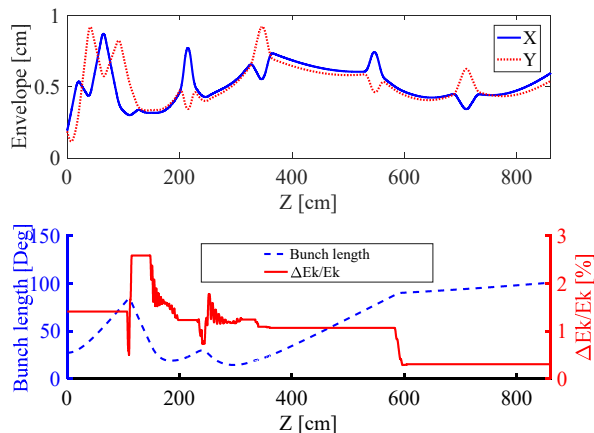


Figure 8: Beam envelope and energy spread along the main acceleration section.

BEAM DYNAMICS TRACKING FOR H_2^+ /PROTON

Because the RFQ and DTL1 are designed for H_2^+ and the DTL2 is designed for proton, a stripping foil is needed to convert H_2^+ to proton. It will enlarge the transverse beam emittances and energy spread. On the other hand, the holistic beam energy would be lower slightly. These situations must be considered in dynamics tracking. According to literature research [5], a $15\mu\text{g}/\text{cm}^2$ carbon foil is chose, and the stripping efficiency approaches 100%. Its influence on H_2^+ is calculated by LISE++ code as Table 2 [6].

Table 2: 1 MeV/u H_2^+ Stripping Results by LISE++

Parameter	Value
Energy loss	1.7 keV/u
Energy straggle	0.6 keV/u(1σ)
Angular straggle	1.47 mrad(1σ)
Lateral spread	$1e-5\ \mu\text{m}$ (1σ)

The dynamics tracking of 500 μA H_2^+ /proton is also performed by Beampath code. Monte Carlo method is adopted at the stripping foil. Buncher3 is placed behind DTL2 with a distance of 2.5 m for reducing the energy spread of proton. The transverse beam envelope, bunch length and energy spread of H_2^+ /proton can be seen in Fig. 9. Energy spread of 100% beam is too large for the synchrotron. But after removing the 20% particles with large energy spread, the rest of beam can satisfy the energy spread requirement of the synchrotron. Transverse emittances of H_2^+ /proton are shown in Fig. 10. Because the injection design of synchrotron demands painting in horizontal direction, vertical emittance growth is accepta-

ble. Based on the dynamics tracking, proton beam extracted by the linac injector can meet the design target.

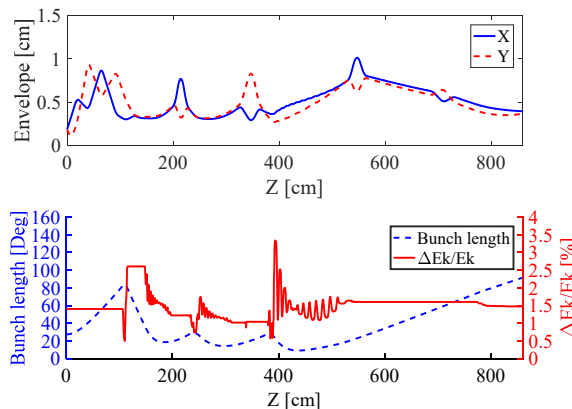


Figure 9: Beam envelope and energy spread of H_2^+ /proton.

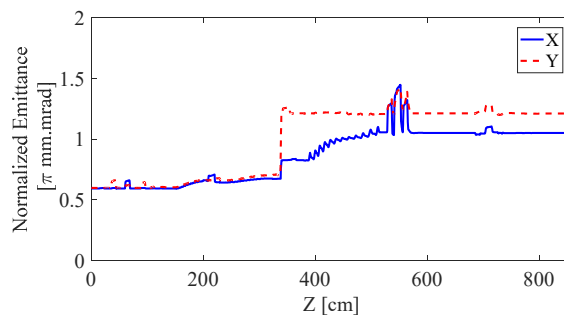


Figure 10: Normalized emittances of H_2^+ /proton.

CONCLUSION

Preliminary design of the DTL for the linac injector of SESRI complex has been finished. Beam matching section between RFQ and DTL1, stripping foil and energy spread reducing section are design and simulated. The transverse emittance and energy spread of extraction beam of this linac injector meet the requirements of synchrotron basically. Formal design scheme and the RF structure design are in the optimization.

ACKNOWLEDGMENTS

We are grateful to Y.R. Lu at PKU for his suggestions.

REFERENCES

- [1] LIU Ming, *et al.*, Nucl. Phys. Rev. 2017, 34(4): 730-734.
- [2] R. Tiede, *et al.*, "Konus beam dynamics designs using H-mode cavities" in *Proc. HB'08*, Nashville, TN, USA, Aug. 2008, paper WGB11, p. 223.
- [3] R. Tiede, *et al.*, "LORASR Code Development", in *Proc. 10th European Particle Accelerator Conf. (EPAC'06)*, Edinburgh, UK, Jun. 2006, paper WEPCH1118, p. 2194.
- [4] Y. K. Batygin, Particle-in-cell code BEAMPATH for beam dynamics simulations in linear accelerators and beamlines, Nucl. Instr. Meth. A, 2005, 539: 455.
- [5] B. T. Meggitt, *et al.*, Equilibrium charge-fractions for H+ and H2+ ions transmitted through carbon foils at 60-300

keV, Journal of Physics B Atomic & Molecular Physics,
1973, 6(12):L362-L364.

- [6] D. Bazin, O. B. Tarasov, M. Lewitowicz, O. Sorlin, "The
code LISE: a new version for 'Windows'", Nuclear Physics
A 701 (2002) 661-665.

STUDY ON A HOM TYPE BUNCHER*

L. Lu[†], X. Xu, L. Shi, L. Sun, Institute of Modern Physics (IMP), CAS, Lanzhou, China
 C. Xing, T. He, L. Yang, University of CAS, Beijing, China

Abstract

Normally, drift tube linacs (DTL) are used following RFQ linacs for beam acceleration in middle and high beam energy region. The acceleration efficiency of DTLs is decreasing with beam energy increasing. Using resonated higher order mode (HOM) of cavity, DTL can achieve higher effective shunt impedance. We proposed a 325MHz DTL with TE₁₁₅ mode. In this paper, the dynamics calculation and electromagnetic design of the HOM-DTL will be reported.

INTRODUCTION

Shown in Fig. 1, in the low energy region, the Interdigital-H (IH) type drift tube linacs (DTLs) have a higher shunt impedance and suitable accelerating structure for heavy ion acceleration, thus the DTLs operated in TE₁₁₁ mode are normal used following the RFQ type linac [1-3]. However, in the medium and high energy region, the Alvarez type DTLs operated in TM₀₁₀ mode are normally used although its shunt impedance reduces rapidly [4,5], shown in Fig. 2, because its shunt impedance is higher than the IH-DTLs in those energy regions.

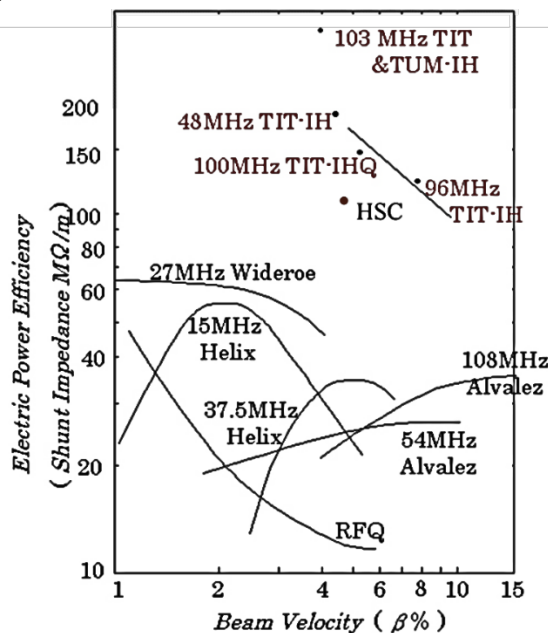


Figure 1: The shunt impedance of the low beta linacs.

Since the DTLs operated in TE_{11n} mode of the higher order mode have a property which is suitable to accelerate

[†]luliang@impcas.ac.cn

*Work supported by the NSFC under Grant No. 11427904, No. 11475232 and No. 11535016.

ions in medium and high energy region [6]. We proposed a 325MHz DTL operated in TE₁₁₅ mode. Our proposed HOM-DTL is designed as a prototype buncher and its structure is shown in Fig. 3.

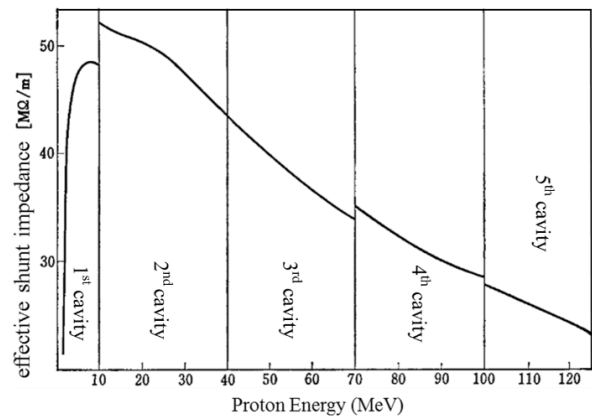


Figure 2: The shunt impedance changing of the Alvarez type DTLs in medium and high energy region.

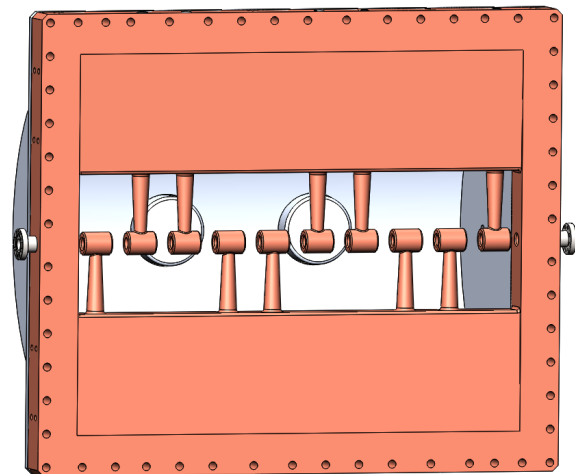


Figure 3: The inner structure of proposed HOM-DTL.

ELECTROMAGNETIC DESIGN

The frequency of proposed HOM-DTL is 325MHz which is 4th harmonic of the frequency of 81.25MHz. This HOM-DTL is a prototype research for future heavy ion buncher. The estimated peak voltage is rather high as several mega-voltages (MV). The Microwave Studio (MWS) code and ANSYS code are used to calculate the cavity electromagnetic simulation and mechanical simulation [7,8].

As shown in Fig. 3, the HOM-DTL has normal DTs and ridges that is same to the normal type IH-DTLs with TE₁₁₁ mode and Alvarez type DTLs with TM₀₁₀ mode,

Content from this work may be used under the terms of the CC BY 3.0 licence (© 2018). Any distribution of this work must maintain attribution to the author(s), title of the work, publisher, and DOI.

however, the resonated frequency of cavity can be tuned to TE₁₁₅ mode by configuring directions of the stems. Shown in Fig. 4 and Fig. 5, the biggest feature of the HOM-DTL is that the axial accelerating e fields of gaps are quite flat, even in the two end gaps. The flat e field distribution makes the field tuning of cavity very easy. The proposed HOM-DTL adopts 10 stems and 11 gaps, and the total length is 1m. Shown in the table 1, when the Kilpatrick factor adopts 1.5, the simulated total voltage of the HOM-DTL is 1.93MV, and the shunt impedance of the HOM-DTL is calculated as 91.8 MΩ/m that is better than other structure linacs in same beam beta region shown in Fig. 1 and normal DTLs shown in Fig. 2. That indicates the 325MHz HOM-DTLs have a better power efficiency in the medium energy region.

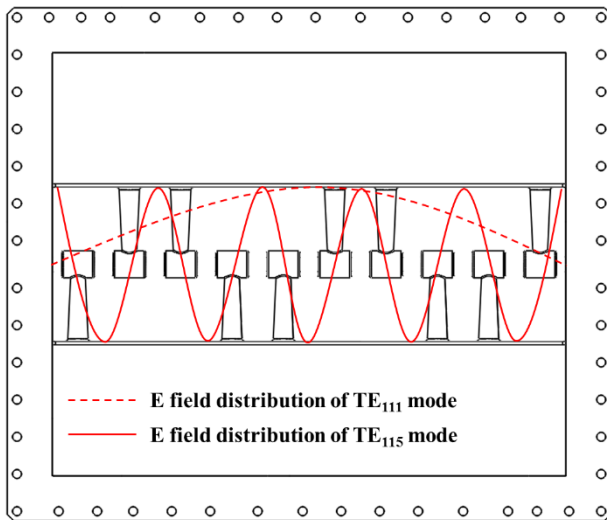


Figure 4: RF property of TE₁₁₅ mode (solid line) in the HOM-DTL. Dot line shows RF property in IH-DTLs.

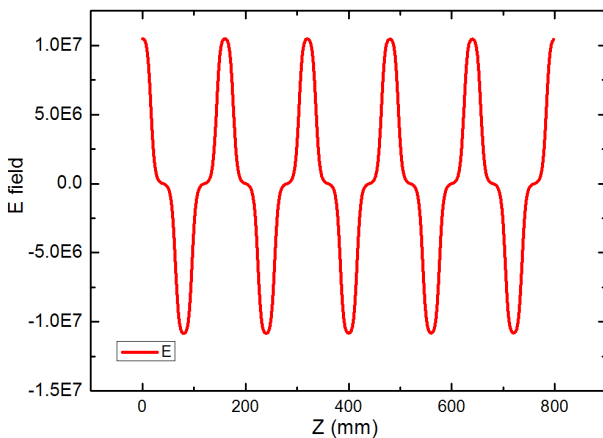


Figure 5: Flat e field distribution of TE₁₁₅ mode in the HOM-DTL.

Because an existing main copper frame (copper-colored part in the Fig. 3) was adopted for simulations and fabrications of the 325MHz HOM-DTL, the optimization of the RF structure design is limited. In our

opinion, the shunt impedance could be increased 1.5 times of the calculated 91.8 MΩ/m.

Table 1: The Simulated Parameters of the HOM-DTL

Items	Value
Frequency / MHz	325.008
Gap No.	11
DT No.	10
Cavity diameter / mm	660
Beam bore / mm	20
DT diameter / mm	40
β (particle energy)	0.173
Inner length / mm	800
Total voltage / MV	1.93 @ 1.5 Kp.
Dissipated power / kW	50.6 @ 1.5 Kp.
Q value	9167
Shunt impedance / MΩ / m	91.8

The RF properties of proposed HOM-DTL are confirmed by MWS, shown in Fig. 6, according to the resonated TE_{11n} order, the frequency shows an uptrend and the Q value shows a downtrend. The downward Q indicates that the RF mode is more higher, the higher RF power is needed. Based on our calculations, the ridges have a big effect on the cavity RF property. The height of the ridges is more higher, meanwhile the stems are more longer, the Q value is more higher. The TE₁₁₄ is 308.223MHz, the desired resonated RF mode is 325MHz which is totally separated from the neighbor mode.

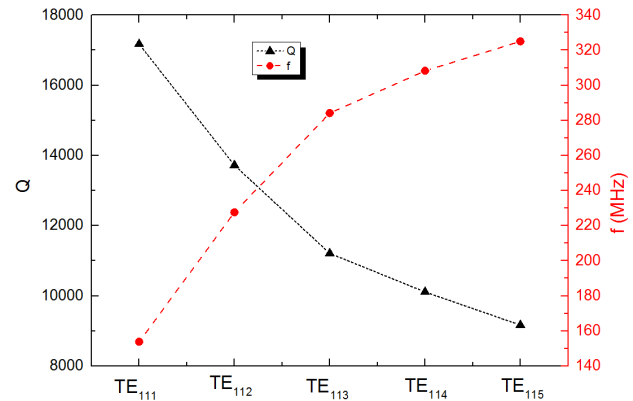


Figure 6: Resonated RF mode and Q values of calculated HOM-DTL. According to the TE_{11n} order, the Q shows a downtrend and the frequency shows uptrend.

And same with the normal IH-DTLs, the hottest part of the HOM-DTL is the stem [9]. Shown in Fig. 7, the surface current concentrates in the stems. Though we are limited by budgets, and the HOM-DTL will be carried out low power test and aimed to test the shaping method without alignment. However, the cooling designs of stems should be considered for possibilities of future use. According to the ANSYS calculations, with 10 water

Content from this work may be used under the terms of the CC BY 3.0 licence (© 2018). Any distribution of this work must maintain attribution to the author(s), title of the work, publisher, and DOI.

routes for stem cooling and 10% duty, the maximum deformation is occurred in the cavity (between two tuners) and the maximum temperature is about 40°C and locates in the first tube.

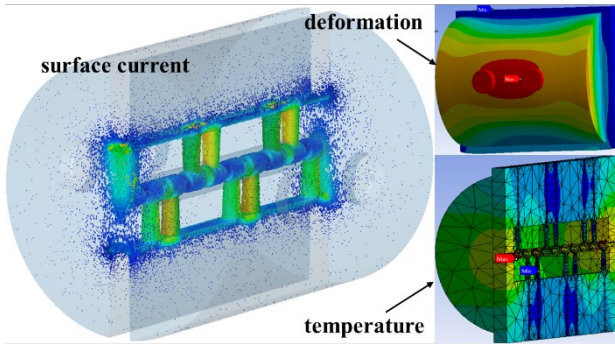


Figure 7: Images of surface current (left part) and multi-physics analysis. The intensity increases as the color changes from blue to yellow and to red.

The frequency tuning is being designed using four tuners. Both sides of the main frame have two tuners, and the tuners are uniform distribution in the beam direction. The diameter of tuners is 60mm, and the preset inserting length of the tuners is 35mm. According to our simulations, the adjustment region of frequency is $\pm 1.56\text{MHz}$ which is enough for frequency tuning.

FABRICATION

The HOM-DTL is being fabricated in manufacturing company. Shown in Fig. 8, although the main frame is being shaped from a block copper by using a numerical-controlled machine tool, the cavity wall is being bent from an aluminum sheet because of the budget limitation. The stand supports the main frame directly by using two stainless holders. And two tuner-supports fixes the four tuners. The tuners are also made from aluminum material.

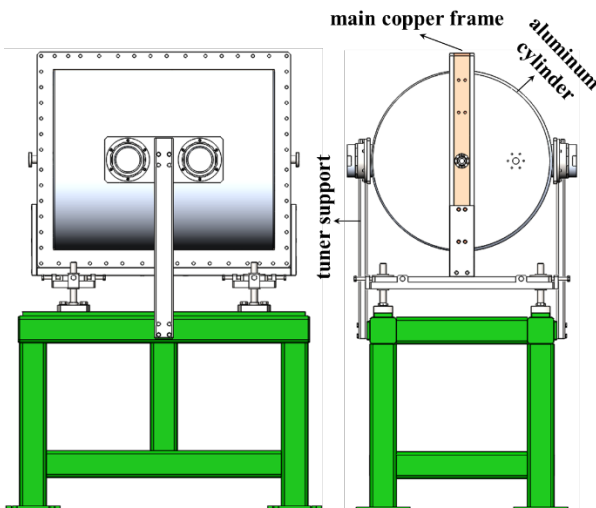


Figure 8: Assembly image of the HOM-DTL. The main frame is made from oxygen-free copper material. The other cavity parts (walls and the tuners) are being made from aluminium material.

SUMMARY AND FUTURE PLAN

A HOM structure cavity driven by TE_{115} RF mode was calculated and simulated for high energy beam bunching. Its shunt impedance is higher than IH-DTLs and Alvarez type DTLs in medium energy acceleration. Along the 800mm axis, the designed 325MHz HOM-DTL buncher could induce 1.93MV with flat e field distribution along the axis. Its shunt impedance is 91.8 $\text{M}\Omega/\text{m}$ with a safe K_p factor of 1.5. The core part of the HOM-DTL is being shaped from a block copper, and other parts are being fabricated from aluminium material.

The fabrication and assembly will be finished by the end of this October. Our team will carry out a low power test for measuring the RF properties such as resonated frequency and e field distribution. Also, we are applying a national natural science foundation of China for future copper fabrication of the cavity wall.

ACKNOWLEDGEMENT

Return to our researcher, the authors would like to convey thanks to Prof. Dacheng ZHANG for fruitful discussions and comments on the cavity designs.

REFERENCES

- [1] T. Ito, L. Lu, et al., Nucl. Instrum. Methods Phys. Res. B 261, 2007, p.17-20.
- [2] L. Lu, T. Hattori, et al., Nucl. Instrum. Methods Phys. Res. A 688, 2012, p.11-21.
- [3] L. Lu, T. Hattori, H.Y. Zhao et al., High Power Test of An Injector Linac For Cancer Therapy Facilities, Phys. Rev. ST Accel. Beams 18, 111002, 2015, p.1-8.
- [4] L.W.Alvarez, Phys. Rev., 70, 799, 1946.
- [5] M. Heilmann, X. Du, P. Gerhard, L. Groening, M. Kaiser, et al., Design Study for A Prototype Alvarez-Cavity for the Upgraded Unilac, in *proceedings of IPAC2017*, Copenhagen, Denmark, 2017, pp.2205-2207.
- [6] N. Hayashizaki, T. Hattori, IH Linac with Higher Order Modes, in *proceeding of EPAC08*, Genoa, Italy, 2008, pp.3419-3421.
- [7] <http://www.cst.com>
- [8] <https://www.ansys.com/>
- [9] L. Lu, L. P. Sun, T. He, L. Yang, W. Ma, et al., Research on A Two-Beam Type Drift Tube Linac, in *proceeding of LINAC2016*, Michigan State University, East Lansing, Michigan, USA, 2016, pp.989-991.

ERROR ANALYSIS AND RF OPTIMIZATION OF A COMPACT RFQ*

K. D. Wang[†], X. J. Yin, Z. S. Li, H. Du, Q. Y. Kong, X. N. Li, Institute of Modern Physics, Chinese Academy of Sciences, Lanzhou, China, also at Huizhou Research Center of Ion Sciences, Huizhou, Guangdong, China

Abstract

A 162.5 MHz, 7.2 MeV 4-rod radio frequency quadrupoles (RFQ) dynamics design has been finished for injector of a carbon ion cancer therapy facility which is promoted by the Institution of Modern Physics (IMP) of the Chinese Academy of Science (CAS). A detailed error analysis was performed after the optimization process. Field flatness error is analysed for determining a RF optimization target. The RF structure is designed based on a new type dynamics design. Electric field of the RF structure is optimized in order to supporting the dynamics design. The error analysis and detailed field flatness optimization of this compact RFQ have been presented and discussed in this paper.

INTRODUCTION

Hadron therapy offers superior dose conformity in the treatment of deep-seated tumours compared with conventional X-ray therapy due to its Bragg-peak feature of energy deposition in organs [1]. So many accelerator facility dedicated to cancer therapies have been constructed in these years. One of them is Heavy Ion Medical Machine in Lanzhou (HIMM), which has been designed and constructed by IMP (Institute of Modern Physics). A linac is designed to replace cyclotron as the accelerator injector in the next generation HIMM, which consists of an ECR ion source, a 162.5 MHz RFQ, a compact Interdigital H-mode Drift-Tube-Linac (IH-DTL), and beam transport lines. The layout is shown in Fig. 1.

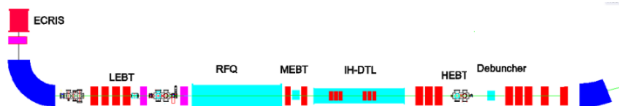


Figure 1: Layout of the linac injector of cancer therapy facility.

A RFQ operated under 162.5MHz as important part of this linac has been designed. It accelerate $^{12}\text{C}^{4+}$ beam from 8keV/u to 600keV/u with 0.1% duty factor. Unlike most research facilities, this RFQ need not running with high current and high duty factor. The optimization of designing this type RFQ is focus on compact structure, high stability and low cost. Based on a traditional setup, a new compact fast-bunching design is introduced to optimize. The whole dynamics design process is supported by PARMTEQM [2]. This method is used to create a more compact structure by ignoring the space-charge effect [3]. Finally, RFQ structure length is shorten from the standard design value 272cm to

230 cm, while effectively regulating the particle loss and emittance growth. The final parameters is shown in the Table 1. And main parameters as a function of position z . is shown in Fig. 2.

Table 1: Main Dynamics Parameters for RFQ

Parameter	Value
Frequency (MHz)	162.5
Beam current (euA)	200
Input energy (keV/u)	8
Output energy (keV/u)	601.45
Duty factor	0.1%
Kilpatrick factor	1.83
Minimum aperture (a)(cm)	0.3
Input trans. emit. ($\pi \cdot \text{mm} \cdot \text{mrad}$)	0.200
Output trans. emit. ($\pi \cdot \text{mm} \cdot \text{mrad}$)	0.199
Output longitudinal emit. ($\pi \cdot \text{MeV} \cdot \text{deg}$)	0.242
Length of the vane (cm)	230.14
Transmission efficiency	99.3%

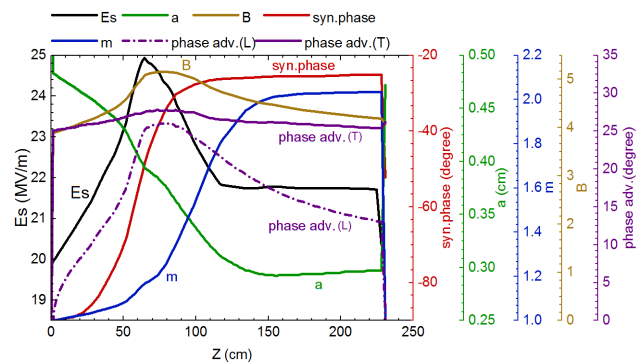


Figure 2: The RFQ beam dynamics parameters as a function of position z .

It can be seen from Fig. 2 that the bunch process is completed in a short time in this design, which shorten overall structure length. Based on the dynamics design, the error is analysed from two aspects: 1. Input beam errors; 2. Errors of field flatness distribution along inter-vane. The dynamic design of RFQ is tested by the tolerance of mismatched beam. And optimization objective of RF design is carried out by the error analysis of field flatness. The RF design has been optimized to meet the requirement of field flatness.

* Work supported by National Natural Science Foundation of China (11375243, 11405237) and Guangdong Innovative and Entrepreneurial Research Team Program (2016ZT06G373).

[†] wangkedong@impcas.ac.cn

ERROR ANALYSIS

Input Beam Errors

The beam injected into RFQ is affected by the stability of ion source and power supply of LEBT transmission line [3]. The beam parameters are usually different from the ideal condition given in the design. The RFQ's compatibility to the undesired beam is researched as a comprehensive consideration of the RFQ front-end device.

For the RFQ dynamics design, beam emittance at entrance of the RFQ is 0.2 π mm-mrad (Norm. RMS), beam current is 0.1 pA, and the energy is 8 keV/u with zero

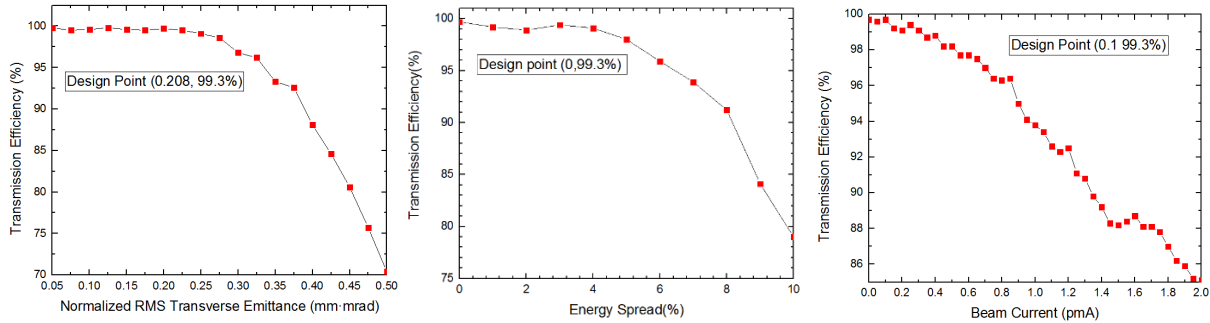


Figure 3: From left to right is transmission efficiency as a function of Norm. RMS transverse emittance, beam energy spread and beam current respectively.

Field Flatness Errors

Four-rod structure is chosen due to the compact structure and low cost. For four-rod RFQ, the optimization of field flatness is very important, which directly affect beam transmission. Field flatness error has been researched here as it is considered as the main error of RF design.

Except for the impact of a non-ideal input beam on the RFQ, there are some errors which result from fabrication, assembling, and operation. These errors are always added in the research process. They are uniformly distributed in the ranges listed in Table 2. The dR value refers to the error of the electrode pole radius, and the d refers to the error of the depth of the modulation curve. The ϕ refers to the error of the RF phase, which is determined by the precision of the RF phase control system. The ΔT and ΔL are the cavity position offsets produced during installing. All of these values are set based on prior experience learned from SSC-Linac fabrication [4].

Table 2: The Setting of the RFQ Errors

Parameter	Range
Distribution	Uniformly
dR (mm)	± 0.1
d (mm)	± 0.1
ϕ ($^\circ$)	± 1
ΔT (mm)	± 0.2
ΔL (mm)	± 0.2

Based on the fabrication, assembling errors, the field flatness error is set as 3.5%, 4% and 5% respectively for

energy spread and 360 $^\circ$ phase width. Through simulation of the PARMTEM, the input error impact is shown in the Fig. 3. During the simulation, one of the parameters such as the emittance, current or energy spread of the input beams is adjusted while the other parameters are kept constant. It could be found that 8% energy dispersion, 1 pA (4 eA) current and 0.375 π mm-mrad (Norm. RMS) emittance can be tolerated under 90% transmission efficiency respectively. The tolerances for three parameters errors are far greater than the actual requirements, because during operation, input beam errors are the superposition effect of these three errors.

researching field flatness impact. Through analysis of 1000 sets of errors, the probability distribution of the beam loss is determined using TraceWin simulations as shown in the Fig. 4. The calculated transmission efficiency is slightly higher than that of PARMTEQM, because the electric field and the beam loss criteria are different [5]. As shown in Fig. 4, the relative frequency of beam loss distribute mainly less than 5%, when the field oscillations is 3.5%. That means the beam transmission efficiency can be maintain upon 95% with 3.5% field flatness.

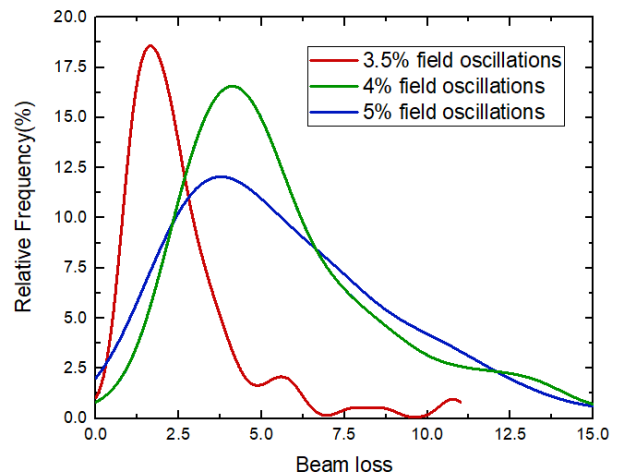


Figure 4: The relative frequency of the beam loss with different field oscillations.

RF DESIGN OPTIMIZATION

4-rod type is chosen for this RFQ, because it has advantages in flexibility for tuning and more convenient for

Content from this work may be used under the terms of the CC BY 3.0 licence (© 2018). Any distribution of this work must maintain attribution to the author(s), title of the work, publisher, and DOI.

maintenance [6]. An initial RF design is carried out by the CST Microwave Studio (MWS) [7], after the cavity type choosing. The field flatness as one of the important characteristics constrain the performance of RFQ. It will influence the beam quality and transmission efficiency badly. For the impact of end effect of 4-ROD RFQ, the inter-vane field along the RFQ forms a shape which the both ends is higher than the midium. The general method to improve this fluctuation of the electric field is changing the resonant frequency of the basic cell through adjusting the height of the tuner block between the stem. While local electric field will decrease with local resonant frequency decrease [8]. Theoretically, the adjustable variables increase with the blocks increase. The numbers of the blocks determines the difficulty and the limit of adjustment. And optimization of the numbers and height of blocks is a process of trial and error. For this RFQ, optimization objective of field oscillations is around 3.5%. Through field flatness error analysis, this field oscillations is enough to guarantee beam transmission. The final block position is shown in the Fig. 5. The Fig. 6 indicates the field flatness comparison between initial structure and structure with tuner block. The field flatness is judged by the formula:

$$\text{Unflatness} = \frac{E - \bar{E}}{\bar{E}}$$

where E is the electric field value in the every quadrant. \bar{E} is the average electric field in corresponding quadrant. Through optimizations, the fluctuation of the electric field is kept less than $\pm 3.5\%$, which could satisfy the operating requirement.

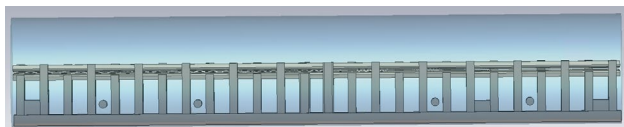


Figure 5: Setting of RFQ block (The right end of figure is beam inlet).

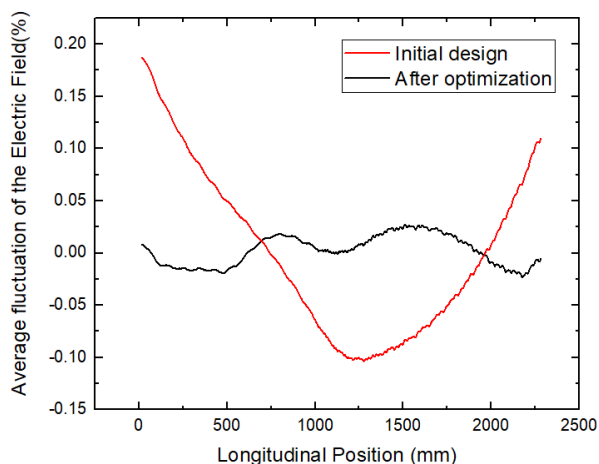


Figure 6: Average fluctuation of the electric field along the longitudinal position.

CONCLUSION

Based on the dynamics design, the input beam errors and the field flatness errors has been analysed. The feasibility of dynamics design was demonstrated by the tolerance of non-ideal input beams. And the optimization objective of the field flatness has been determined through the error analysed. Based on this optimization, the field flatness in RF design is less than 3.5%, which could guarantee beam transmission.

ACKNOWLEDGEMENTS

The authors would like to give special thanks to Prof. Yuanrong Lu at Peking University for his helpful suggestions, and to several other individuals of the Institute of Modern Physics, CAS, for their help and support. This work is supported by the Guangdong Innovative and Entrepreneurial Research Team Program (No.2016ZT06G373).

REFERENCES

- [1] K. Ando, Y. Kase, International Journal of Radiation Biology 85, 2009, p.715.
- [2] K.R. Crandall, T.P. Wangler, L.M. Young, et al., RFQ Design Codes, LA-UR-96-1836.
- [3] X.H. Zhang, Y.J. Yuan, J.W. Xia, et al., Instability Research of 53.667 MHz Heavy Ion RFQ, J. Atomic Energy Science and Technology, 49(5).
- [4] G. Liu, Y.R. Lu, Y. He, et al., Design of a CW high charge state heavy ion RFQ for SSC-LINAC, Nucl. Instr. Meth. A701(3):186193, 2013.
- [5] K. Zhu, Y. R. Lu, X. J. Yin, et al. The beam commissioning of a CW high charge state heavy ion RFQ, Nucl. Instr. Meth. 2015, 794(3):113121.
- [6] T. Wangler, RF Linear Accelerators. 2008.
- [7] CST Simulation Packages <http://www.cst.com>
- [8] Simulation and experiments of rf tuning of a 201.5 MHz four-rod RFQ cavity, J. Chinese Physics C, 2011, 35(11): 1042-1046.

Content from this work may be used under the terms of the CC BY 3.0 licence (© 2018). Any distribution of this work must maintain attribution to the author(s), title of the work, publisher, and DOI.

A NEW RF STRUCTURE: BENT-VANE TYPE RFQ*

L. Yang^{†1}, L. Lu, Z. Zhang, T. He¹, C.C. Xing¹, Y. He,
 Institute of Modern Physics, Chinese Academy of Sciences, Lanzhou 730000, China
¹also at University of Chinese Academy of Sciences, Beijing 100049, China

Abstract

A new cavity structure of RFQ accelerator with bent vanes is proposed to meet the miniaturization requirement of low frequency accelerators. The new structure has a downsized cross section by bending vanes while keeping a certain vane lengths. It also possesses the advantages of simple cooling structure in low frequency field. The new structure has obvious advantages in reducing manufacturing difficulty of cavity, cutting down project cost, enhancing facility reliability and stability.

INTRODUCTION

Radio frequency quadrupole (RFQ) can accelerate, focus and bunch particle beam in the low energy field, which is generally used as an injector for high energy accelerator. Four-rod type and four-vane type are main RFQ accelerator structures. Four-rod RFQ is used in the low frequency field and four-vane RFQ is applied in the high frequency field [1]. However, the cooling structure of four-rod RFQ is quite complex so that it is difficult to design and machine cavity and the lateral dimension of four-vane RFQ is large in the low frequency band which increases machining difficulty and cost [2]. In addition, four vane with windows RFQ can decrease the cross-section length in the low frequency band, but its cooling structure is extremely complicated and the windows can directly influence mechanical strength of the cavity and electric field flatness.

In order to overcome the disadvantages of above three kinds of RFQ accelerators, a new RFQ structure is proposed called bent-vane type RFQ at Institute of Modern Physics (IMP), Chinese Academy of Sciences. It significantly reduces the lateral dimension of the cavity in the low frequency field and has a water-cooled system with a simple structure and sufficient cooling efficiency. The RF structure of bent-vane RFQ is presented in this paper.

THEORETICAL FOUNDATION

Considering an ideal four-vane RFQ with a cloverleaf geometry (Fig. 1), its equivalent circuit is shown in Fig. 2 [1]. According to the equivalent circuit, the cavity quadrupole radius is

$$r^2 = \frac{16}{\mu_0(4 + 3\pi)\omega_0^2 C'}$$

where ω_0 is the resonant frequency, C' is the total capaci-

tance per unit length and μ_0 is the permeability constant. This equation indicates that the lateral dimension can be decreased by increasing the capacitance at a fixed frequency.

Based on the discussion above, the vanes of four-vane RFQ are bent to increase the capacitance for reducing the lateral dimension of cavity. Hence, a new RFQ structure is proposed called bent-vane type RFQ, shown in Fig. 3.

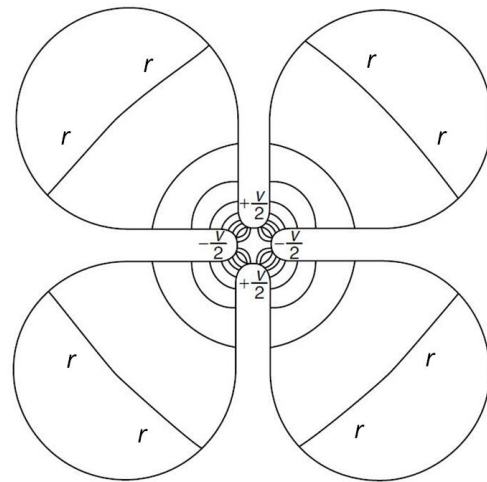


Figure 1: The ideal four-vane RFQ with a cloverleaf geometry.

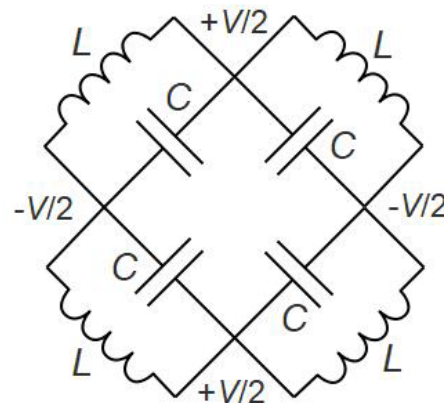


Figure 2: The equivalent circuit of the ideal four-vane RFQ with a cloverleaf geometry.

RF STRUCTURE

In order to obtain suitable lateral dimension and quality factor of bent-vane RFQ, the cross-section profile of bent-vane RFQ is put forward with 13 independent variables, shown in Fig. 4.

* Work supported by Natural Science Foundation of China (Grant No. 11675236, 11475232 and 11535016)

[†] yanglei@impcas.ac.cn

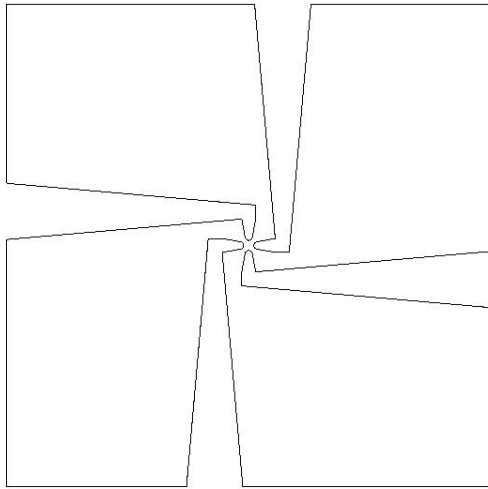


Figure 3: The schematic diagram of the bent-vane type RFQ.

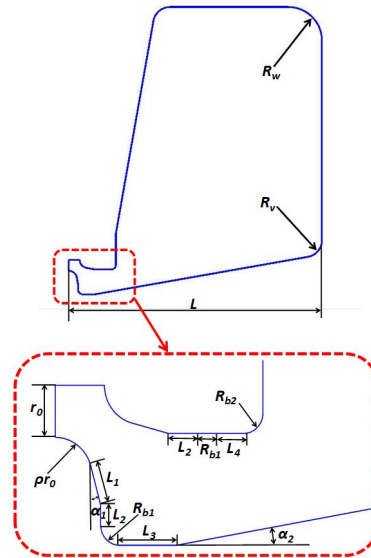


Figure 4: The cross-section of bent-vane RFQ.

r_0 , ρ and α_1 are defined in the code RFQGen [3]. The other parameters can be optimized by ourselves using CST MWS [4]. Keeping frequency constant (81.25 MHz), it is explored that the other ten parameters have an impact on the lateral dimension, quality factor and shunt imped-

ance of cavity, shown in Fig. 5 (only presenting four parameters). The optimization values of the parameters of cross-section are listed in Table 1. The RF structure of bent-vane RFQ is shown in Fig. 6.

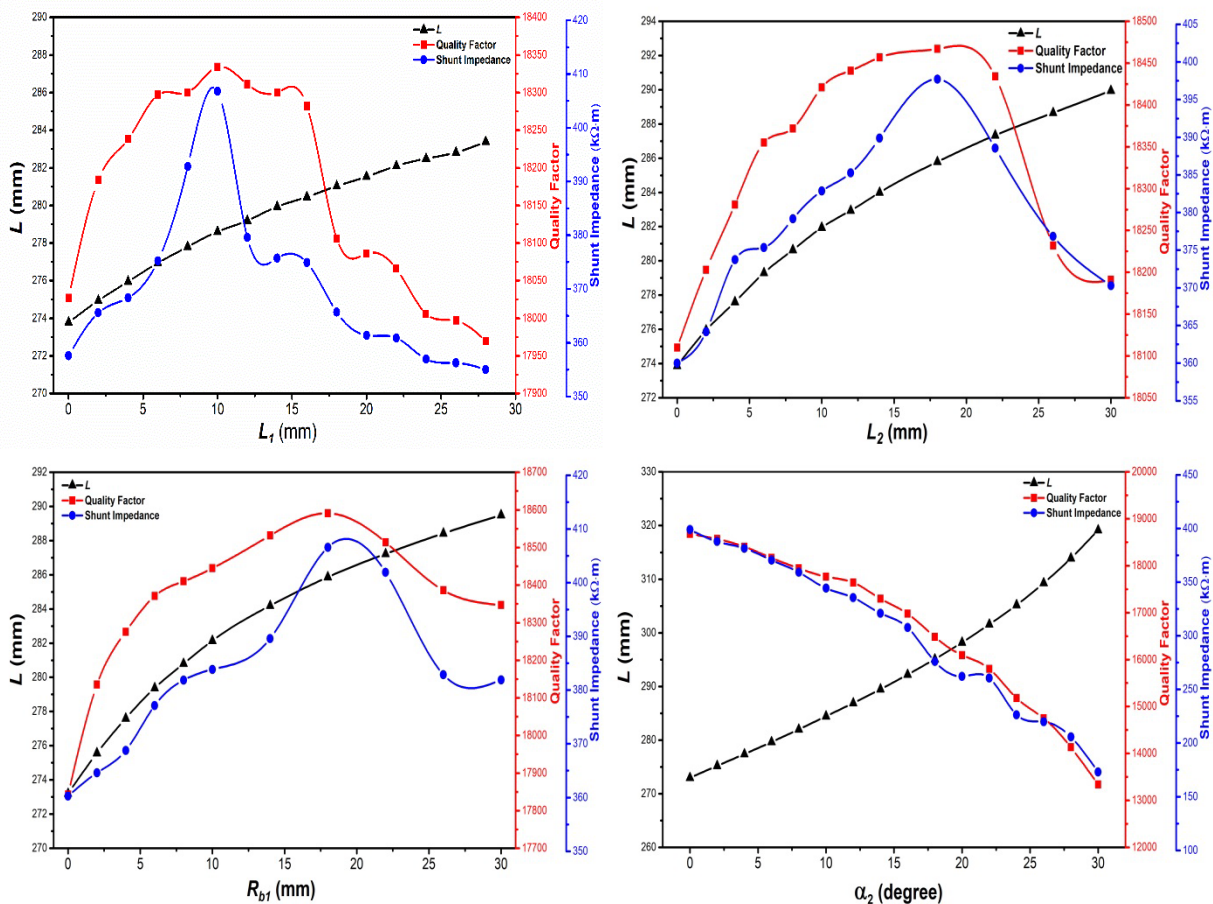


Figure 5: The variation of the lateral dimension, quality factor and shunt impedance of bent-vane RFQ as the functions of the parameters of cross-section profile (only presenting four parameters).

Content from this work may be used under the terms of the CC BY 3.0 licence (© 2018). Any distribution of this work must maintain attribution to the author(s), title of the work, publisher, and DOI.

Table 1: The Cross-Section Parameters of Bent-vane RFQ

Parameter	Value	Parameter	Value
r_0	5.347 mm	L	279 mm
ρ	0.75	R_v	20 mm
α_1	10 Deg.	α_2	5 Deg.
L_1	10 mm	R_w	40 mm
L_2	5 mm	L_4	10 mm
R_{b1}	5 mm	R_{b2}	5 mm
L_3	10 mm		

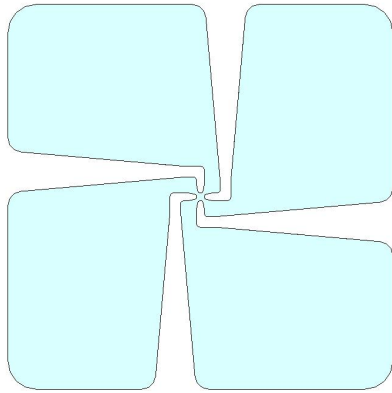


Figure 6: The RF structure of bent-vane RFQ.

CONCLUSION

A new RF structure of RFQ accelerator is proposed called the bent-vane type RFQ. The new structure has a downsized cross section by bending vanes while keeping a certain vane length. It also has the simple cooling structure. The research cavity frequency is 81.25 MHz. The cross-section profile is defined with 13 independent variables. The optimization values of the parameters of cross-section are verified to the RF structure of the bent-vane RFQ.

ACKNOWLEDGEMENTS

This work is supported by the National Natural Science Foundation of China (Grant No. 11675236, 11475232 and 115350).

REFERENCES

- [1] T.P. Wangler, RF Linear Accelerators, John Wiley & Sons, New York, 2008.
- [2] Lei Yang *et al.*, "Research on the New Cavity Structure of RFQ Accelerator with Bent Vanes at IMP", in *Proc. LIN-AC'18*, Beijing, China, Sep. 2018, paper THPO050.
- [3] K.R. Crandall *et al.*, RFQ Design Codes, LA-UR-96-1836, 1998.
- [4] CST Simulation Packages <https://www.cst.com/>

BEAM COMMISSIONING IN THE FIRST CHINESE DEMO CANCER THERAPY SYNCHROTRON*

J. Shi[†], Huizhou Research Centre of Ion Sciences, Huizhou, China
J. C. Yang, J. W. Xia, W. P. Chai, Institute of Modern Physics, Chinese Academy of Sciences, 730000 Lanzhou, China

Abstract

Heavy Ion Medical Machine in Wuwei (HIMM-ww) is the first Chinese heavy ion accelerator facility developed for cancer therapy. After commissioning, the particle number after acceleration reached $1.5e9$ ppp (particles per pulse), while injection exceeded $3e9$ ppp. The slow extraction efficiency reached nearly 90% for all energies from 120 to 400 MeV/u. The spill duty factor exceeded 90% at a sample rate of 10 kHz. This paper reports the results of the synchrotron commissioning.

INTRODUCTION OF THE SYNCHROTRON

Heavy ion medical machine (HIMM) was constructed on the basis of the experience gained from the Heavy Ion Research Facility in Lanzhou-Cooler Storage Ring (HIRFL-CSR) project [1]. HIMM facility consists of an electron cyclotron resonance (ECR) ion source, a cyclotron injector, a compact synchrotron ring, and 5 nozzles [2]. The C5+ beam generated by the ECR ion source is pre-accelerated by the cyclotron to 6.2 MeV/u and then injected into the synchrotron using the charge exchange injection method [3]. The injected beam is accelerated from 6.2 MeV/u to an extraction energy ranging from 120 to 400 MeV/u.

The layout of the synchrotron, which has a two-fold symmetry structure composed by 8 dipoles and 12 quadrupoles, is shown in Fig. 1. Two long straight sections are used for injection and extraction respectively and four medium-long straight sections are occupied by RF cavity, DCCT (DC Current Transformers), ES (Electrostatic Septum), transverse RF, respectively. The parameters of the ring are listed in Table 1.

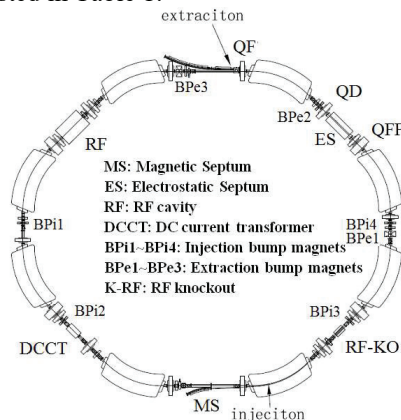


Figure 1: Schematic layout of the HIMM synchrotron ring.

* Work supported by the Pearl River Talent Plan 2017, the Youth Innovation Promotion Association of the CAS (No. 2017453)
[†] email address: shijian@impcas.ac.cn

BEAM COMMISSIONING RESULTS OF THE SYNCHROTRON

Figure 2 shows the current ramping shape of the synchrotron's main quadrupole power supply (the power supply of the dipoles has the same shape as the quadrupoles) and the extraction bump at the extraction flattop [3]. The synchrotron cycle is 7 seconds. The extraction beam energy is 260 MeV/u. The horizontal and vertical axes represent the time and amplitude of the power supply, respectively. The extraction duration is 2 seconds. The ramping time of the extraction bump is less than 10 ms, and the flat-top duration is the same as that of the dipole magnet.

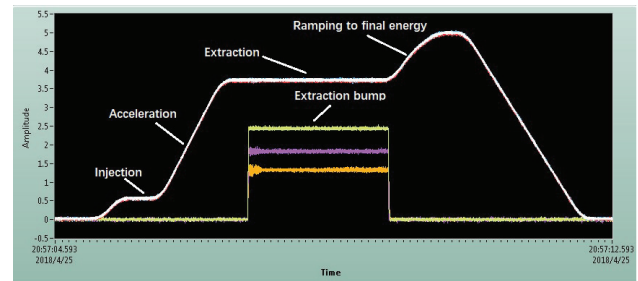


Figure 2: Ramping shape of the quadrupole and extraction bump.

Beam Injection and Acceleration

Different with other cancer therapy facility in the world, the cyclotron is adopted as the injector. The beam intensity of the cyclotron is less than 10 uA. To store enough particles in the ring, the CEI (charge exchange injection) method, which regardless of Liouville's theorem allows beams to be injected at the point of phase space already occupied by previously injected beam [3], is adopted. Therefore, an intense beam can be accumulated in the ring without largely increasing the beam emittance. In addition, the injected beam can be painted in the horizontal phase space by changing the local closed orbit during injection to reduce the hitting probability at the stripping foil, thus increasing the injection efficiency.

Figure 3 is the DCCT signal which shows the beam intensity during the whole cycle. The extraction beam energy is 260 MeV/u in Fig. 3. The beam intensity after injection is 1800uA which corresponding to the particles number of $3e9$. The beam capture efficiency is 50%, and the accelerate efficiency is approximately 95%.

Content from this work may be used under the terms of the CC BY 3.0 licence (© 2018). Any distribution of this work must maintain attribution to the author(s), title of the work, publisher, and DOI.

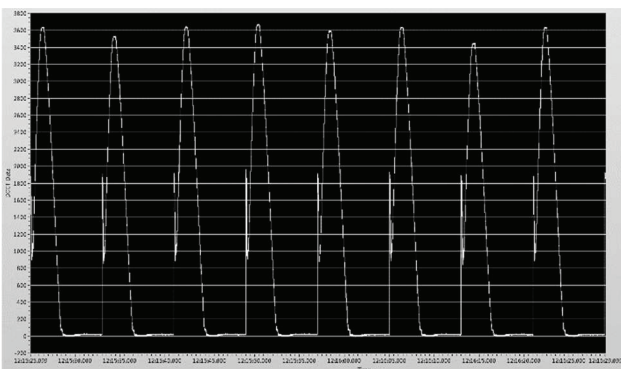


Figure 3: beam intensity of on the DCCT.

Slow Extraction

Five beam energies, 120, 190, 260, 330, and 400 MeV/u, with an energy separation of 70 MeV/u were chosen as the commissioning energies for passive scanning. A total of 123 energies separated by nearly 2.3 MeV/u corresponding to the Bragg peak in water with a range step of 2 mm from 120 to 400 MeV/u were used for active scanning.

The beam duty factor is an important parameter to indicate the spill quality. The duty factor defined as follows [4]:

$$D = \frac{\left[\int_{T_1}^{T_2} I(t) dt \right]^2}{\int_{T_1}^{T_2} dt \cdot \int_{T_1}^{T_2} I^2(t) dt},$$

where $I(t)$ is the spill intensity and T_1 and T_2 define the time range where the duty factor is computed.

To improve the spill duty factor, amplitude modulation [5] and longitudinal RF modulation [6, 7] were adopted. The longitudinal RF voltage keeps in a constant value on the extraction duration to improve the spill duty factor.

To flatten the whole spill, the TRF voltage should be changed exponentially with time [5]. The polynomial function was adopted in our case to save the calculation time in every synchrotron cycle. The beam duty factor is approximately 90%.

The fast quadrupole (FQ) feedback system is adopted to flatten the spill. The FQ feedback system is mainly used for beam flattening in the macroscopic aspect of the spill. The main quadrupole ripple is less than 3×10^{-5} ; therefore, the feedback system for spill microscopic flattening is unnecessary. Inversely, the FQ system may import extra spill ripple because it has the response time during the feedback procedure. Additionally, the beam position in the terminal will change as the FQ causes the separatrix change. Therefore, the beam feedback system was adopted only for the passive scanning. Figure 4 shows the spill with feedback. The beam energy is 400MeV/u. The duty factor exceeded 95%.

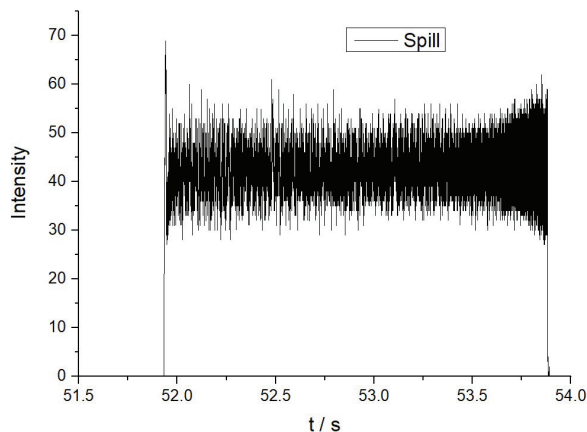


Figure 4: Spill structure with feedback.

Typical spill structures for 4 other passive scanning energies, 120, 190, 260, and 330 MeV/u, are shown in Fig. 5.

The sample rate of the spill is 10 kHz. The extraction flattop is 2 seconds, but in fact the extraction time is usually less than 2 seconds. This is because the particle numbers in every synchrotron cycle fluctuate. The reference intensity must be slightly larger than the actual beam intensity to ensure the beam is extracted completely during the extraction flattop.

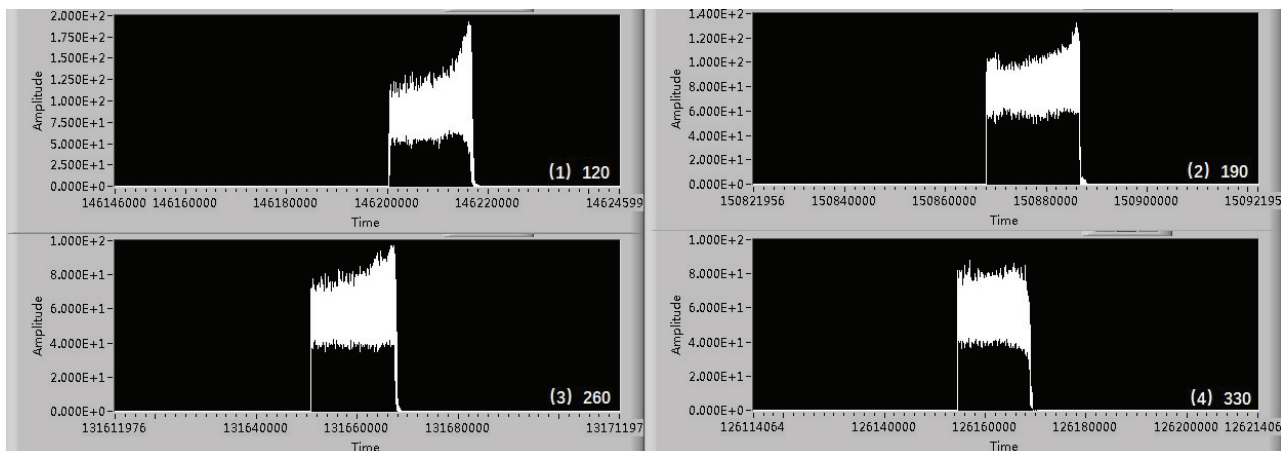


Figure 5: Screenshot of the time structure shown in the ionisation chamber.

Figure 6 shows the 400MeV/u beam signal viewed in the anode-stripped ion chamber in the terminal. The anode-stripped ion chamber has an effective area of

200mm×200mm. There are 200 strips in each of the horizontal and vertical directions. The definition of the beam position is less than 0.2 mm after gaussian fitting. The two

upper figures show the beam profile in x (horizontal) and y (vertical) direction, respectively. The horizontal axis is the position of the beam, while vertical axis is the time duration. The colours represent the relatively beam intensity,

black is 0 while white means great than or equal to 5.0. The lower two figures show the beam profile and the gaussian fitting.

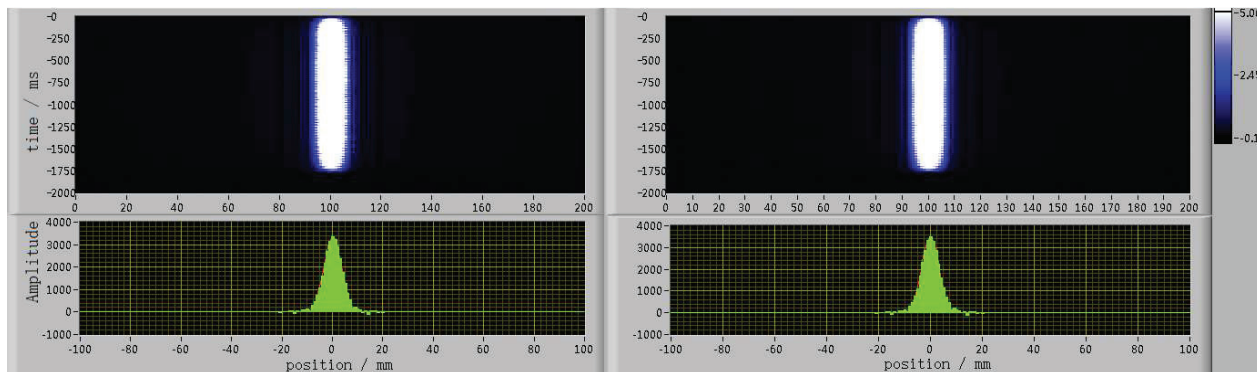


Figure 6: Beam signal viewed in the anode-stripped ion chamber.

Figure 7 shows the extraction efficiency vs energies. The ionisation chamber was installed only in the treatment room. The slow extraction efficiency measured includes the HEBT transfer efficiency. The theoretical extraction efficiency can reach 99% since the step width of the beam is nearly 10 mm at the entrance of the ES, the thickness of the wire is 0.1 mm, and the HEBT efficiency is 100% in theory. Actually, to decrease the spark of the ES, the maximum ES voltage is 115 kV, which is lower than the designed value of 135 kV. The gap of the ES also decreased from the designed value of 15 mm to 12.5 mm to maintain the electrical field strength. The alignment error of the ES wire, the closed orbit, the large horizontal chromaticity, and the large momentum spread vs the narrow gap of the ES will cause beam loss, which decreases the extraction efficiency.

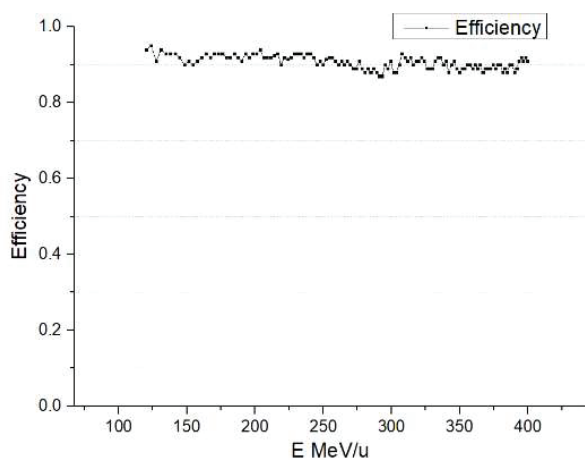


Figure 7: Beam energies vs. extraction efficiency.

SUMMARY

After commissioning, the particle number after acceleration reached 1.5×10^9 ppp (particles per pulse), while

injection exceeded 3×10^9 ppp. The slow extraction efficiency reached nearly 90% for all energies from 120 to 400 MeV/u. The spill duty factor exceeded 90% and 95% at a sample rate of 10 kHz without feedback and with feedback, respectively.

For a square irradiation field, the uniformity was better than 106% after the magnet scanning in treatment rooms. The uniformity defined as D_{max}/D_{min} , where D_{max} and D_{min} are the maximum and minimum lateral dose distribution in the middle line of the horizontal and vertical directions.

REFERENCES

- [1] J.W. Xia, W.L. Zhan, B.W. Wei, et. al., The heavy ion cooler-storage-ring project (HIRFL-CSR) at Lanzhou, NIM A 488, 2002, p.11.
- [2] J.C. Yang, J. Shi, et al., Design of a compact structure cancer therapy synchrotron, NIM A 756, 2014, p.19.
- [3] Weiping Chai, Jiancheng Yang, et al., Stripping accumulation and optimization of HIRM synchrotron, NIM A 763, 2014, pp.272–277.
- [4] M. Tomizawa, T. Adachi status and upgrade plan of slow extraction from the JPARC main ring, Proceedings of IPAC'10, Kyoto, Japan, THPEB014.
- [5] T. Furukawa, K. Noda, M. Muramatsu, et al., Global spill control in RF-knockout slow-extraction, NIM A 522, 2004, pp.196-204.
- [6] R. Cappi. Ch. Steinbach, Low frequency duty factor improvement for the cern ps slow extraction using RF phase displacement techniques, IEEE Transactions on Nuclear Science, Vol. NS-28, No. 3. June 1981.
- [7] T. Furukawa, K. Noda, Contribution of synchrotron oscillation to spill ripple in RF-knockout slow-extraction, NIM A 539, 2005, pp.44-53.

HIGH RESOLUTION MASS SEPARATOR DIPOLE DESIGN STUDIES FOR SPES PROJECT

C. Baltador, M. Comunian, L. Bellan, M. Cavenago, A. Galatà, L. Ferrari, A. De Lorenzi*,
 F.Mosio and A.Pisent

INFN-LNL, [35020] Legnaro, Italy
 *Consorzio RFX,[35127] Padova, Italy

Abstract

The purposes of the SPES (Selective Production of Exotic Species) project at INFN laboratory in Legnaro (Italy) is to study nuclei close to the drip lines. Therefore, a High-Resolution Mass Separator (HRMS) must provide full separation of the ions with a resolution $1/20000$, to be sensible to the proton-neutron mass difference in the fission products. SPES HRMS consists of: two 90° magnet dipoles, one electrostatic multipole in between them, six electrostatic quadrupoles, two electrostatic hexapoles and two electrostatic triplets before and after the slits on the object and image point. All these components will be installed on a high voltage platform with a maximum operating voltage of -240 kV. Before entering the HRMS, a 40 keV energy beam go through an RFQ Cooler, designed to have an output energy spread of 1 eV. Mass separation within target resolution is the most critical part: dipoles must provide a magnetic field homogeneity of $4 \cdot 10^{-5}$ throughout beam occupancy (half magnet pole surface), at a field intensity of 0.562 T for the reference ion ^{132}Sn . Therefore, a very accurate dipole design is mandatory. This contribute will show the studies which lead to a possible dipole design.

INTRODUCTION

The Selective Production of Exotic Species (SPES) project at INFN-LNL Legnaro, Italy is a radioactive ion beam (RIB) facility [1,2]. Many field of interests will characterize its experimental life, ranging from basic research in nuclear physics and astrophysics to interdisciplinary applications, like production of radionuclides of medical interest and the generation of neutrons for material studies, nuclear technologies and medicine. SPES RIB production is based on the ISOL method with an UCx Direct Target able to sustain a power of 10 kW. The primary proton beam is delivered by a high current Cyclotron accelerator, with energy $35-70$ MeV and a beam current of $0.2-0.5$ mA. Neutron-rich radioactive ions will be produced by proton induced Uranium fission in the UCx target at an expected fission rate in the order of 10^{13} fissions per second. The exotic isotopes will be re-accelerated by the ALPI superconducting LINAC at energies of $10A$ MeV and higher, for masses in the region $A=130$ amu at expected rate on the secondary target of $10^7 - 10^9$ pps.

In the framework of the SPES project, the High-Resolution Mass Spectrometer (HRMS) must provide high purification of the ^{132}Sn ion beam and $> 95\%$ transmission. The

design goal is to achieve a mass resolving power $\Delta m/m = 1/20000$.

HRMS LAYOUT

The design choices made for the HRMS are common from the medium mass separator (MRMS) of SPES [3], which is now under installation and will be used as a test stand for the HRMS. Similar optics layout is used in recent projects [4,5,6], with different choice of parameters.

The HRMS general layout, which is perfectly symmetric with respect to the central axis, is presented in Fig. 1.

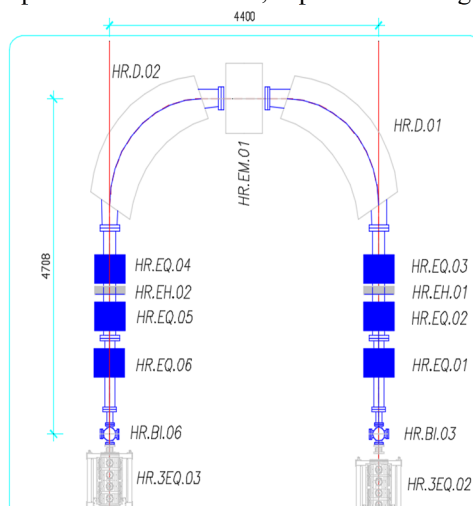


Figure 1: HRMS layout on high voltage platform.

HRMS will be installed on a High Voltage platform (represented by the light blue line) with a maximum operating voltage of -240 kV. The beam, which is extracted from the source with 40 keV energy, enters HRMS from the right-hand side branch of the device. The object and image slits (HR.BI.03-6) delimit separator entrance and exit.

More in details, following the beam path, an accelerating column (HR.AT.01) gradually accelerates the beam to accommodate its energy for the HV platform and then it will pass through the following components:

- an electrostatic triplet (HR.3EQ.02);
- two electrostatic quadrupoles (HR.EQ.01-2);
- one electrostatic hexapole (HR.EH.01-2);
- a single electrostatic quadrupoles (HR.EQ.03);
- a magnetic dipole (HR.D.01-2), H-shaped with bending angle $\varphi = 90^\circ$;
- one electrostatic multipole (HR.EM.01);

After the multipole, the beam will pass through the same array, but with inverted order.

From the optical point of view, the spacing between the elements is set to achieve unit magnification imaging from slit to slit in the horizontal plane. Hexapoles are added to provide dynamics correction aberration: in a separator the horizontal size of the beam is large in the dipoles so that geometrics aberrations occur. The triplet is needed to create a waist into the object point of the separator. All the components, excluding the dipoles, are electrostatic to avoid mass dependences outside the dipoles, for a given energy. Table 1 summarizes the specifications of the various components.

Table 1: HRMS Components Specifications

Element	Nom. Value	Units / Note
HR.3EQ.02/03	-7 / +6 / -7	kV / triplet
HR.BI.03/06	1.1	mm/object-image
HR.EQ.01/06	-9.6	kV
HR.EQ.02/05	+4	kV
HR.EH.01/02	< 1	kV / hexapole
HR.EQ.03/04	-6	kV
HR.D.01/02	0.5623	T
HR.EM.01	< 1	kV / multipole

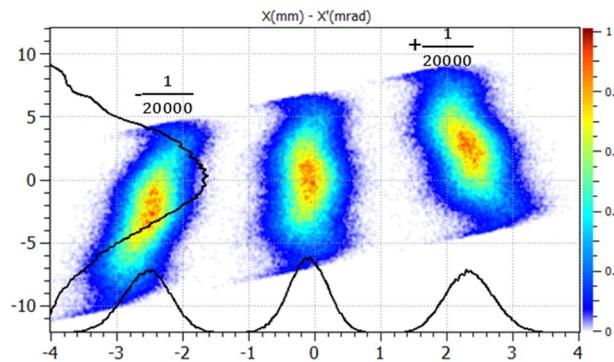


Figure 2: Emittances of three resolved isobars at image slit as from beam optics simulations (Tracewin).

HIGH RESOLUTION ISSUES

Mass resolution relates directly with the displacement Δx of the beam at the image point with respect to the position at the object slit through the relation:

$$\Delta x = D \frac{dm}{m} \quad (1)$$

where D is the dispersion of the separator. In general, the larger Δx the lower the horizontal overlap of the separated isobars at the image point. Large dispersion is therefore needed: in HRMS case 100 m dispersion is expected, leading to 2.5 mm isobar separation at image slit, provided the 1/20000 mass resolution (see Fig. 2).

However, many issues can degrade the resolute power of a separator. In this contribution only general overview is

presented, while a deep study about sources of performance degradation for HRMS is presented in [7].

Magnetic mass separators, like HRMS, discriminates momentum, since deflection of charged particles under an external vertical magnetic field, is described by the magnetic rigidity relation:

$$B\rho = \frac{p}{q} \quad (2)$$

By applying the logarithm derivatives to $p^2 = 2mE$ (m the mass and $E = qV$ the energy of the particle), one has:

$$2 \frac{dp}{p} = \frac{dm}{m} + \frac{dE}{E} \quad (3)$$

This gives the important information that energy variation can have the same effect as a mass variation. Hence, the energy spread of the beam must be in of the same order mass resolution, otherwise HRMS performances would be affected. This immediately translates in terms of voltage stability of the high voltage platform to be in the range of less than 1V for a nominal beam of 260 keV.

Beam emittance also needs to be as small as possible. Emittance ε and mass resolution relates through the relation:

$$\frac{dm}{m} = \frac{2\varepsilon}{D x'}, \quad (4)$$

being x' the beam divergence. Equation (4) shows that a beam featuring small emittance is mandatory for achieving the needed purification level. An RFQ Cooler (currently under development by LPC [8]) is prescribed to be placed before HRMS entrance to reduce energy spread and emittance: its design goals are indeed an output energy spread $>\pm 1\text{eV}$ and transverse emittance reduction by a factor 10. From the combined action of C-RFQ and the acceleration provided by the HV platform a 3.2 mm mrad geometric emittance is expected at object slit.

Anyway, the most critical role to satisfy the requirements for a mass separation resolution of 1/20000 is played by the two dipoles, in terms of mechanical design. This can be easily understood, since the wanted resolution implies a very high magnetic field homogeneity within the poles. From (2), since $v = \sqrt{2mV/q}$, by logarithm derivations one gets:

$$\frac{dB}{B} = \frac{1}{2} \frac{dm}{m} \quad (5)$$

Hence, field deviation from the reference value must lie within a range of the same order of magnitude of the mass separation that has to be resolved. i.e. $5 \cdot 10^{-5}$. Otherwise a field variation would act as a mass variation, in the same fashion as discussed before for the energy spread.

DIPOLE DESIGN

Designing a suitable dipole capable to achieve the field homogeneity needed to preserve the 1/20000 mass

Content from this work may be used under the terms of the CC BY 3.0 licence (© 2018). Any distribution of this work must maintain attribution to the author(s), title of the work, publisher, and DOI.

resolution is therefore mandatory for the HRMS. Table 2 summarizes main beam reference parameters.

HRMS features two H-shaped dipoles with bending angle $\varphi = 90^\circ$. The following relation directly relates the curvature radius to the dispersion generated by a dipole:

$$D = \rho(1 - \cos \varphi) \quad (6)$$

When the bending angle is $\varphi = 90^\circ$ than $D = \rho$. Therefore, two identical dipoles, like in our case, would double the dispersion. Of course, one single 180° dipole would act in the same fashion, but this configuration allows for the installation of the electrostatic multipole for high order aberration corrections [9]. From equation (1), we know that large dispersions values are beneficial for the mass resolution. Unfortunately, practical limitations to the overall HRMS size is due to the small space available on site, for the platform and the overall services around it. The maximum possible curvature radius for the dipoles is $\rho = 1500$ mm.

Table 2: Beam Reference Parameters

Geometric Emittance	3.2	4σ mm*mrad
Ion Mass (q=1)	132	amu
Beam Energy	260	KeV
RMS Energy Spread	1	eV
RMS Spot size at image	0.3	mm
Maximum X range	500	mm

The reference vertical magnetic field inside the dipoles is then derived from the rigidity relation (2) as $B_{y-ref} = 0.562$ T.

The entrance and exit edges of the magnetic dipoles are angled ($\alpha = 27^\circ, 16'$) with respect to the beam trajectory to provide vertical focusing. Edges also feature circular curvatures to correct hexapole aberrations deriving from second order components of the dipole field:

$$r_{edge} = \frac{B_{y-ref}}{2C_{hexapole}} (\sec \alpha)^3 \quad (7)$$

where $C_{hexapole} = 0.163$ T/m is the hexapole term coefficient, given by Tracewin [10] simulations.

From beam optical simulations done with Tracewin, info on beam horizontal and vertical extensions can be obtained (see bottom part of Fig. 3. These information are needed for pole gap and length sizing. The electrostatic components of the HRMS are configured to produce a very narrow beam at the dipole entrance, but despite a 40 mm pole gap of can be enough as vertical acceptance, helping also for power saving, a too complex vacuum chamber installation pushed for a 60 mm gap.

Tuning to the pole length, the choice of an initial 900 mm was made with the rule of thumb to almost double the horizontal beam extension of 500 mm (see upper part of Fig. 3). It was then possible to optimize this value to 860 mm. In more details the density profiles given by Tracewin state that the 68% of the beam lies within ± 115

mm, the 90% within ± 220 mm and the 99% within ± 250 mm, with respect to the optical axis.

The size of the coil cross section, chosen on power saving considerations, and the magnetization level of the iron in working condition, define the return yoke size. It is important to try to keep the magnet working as much as possible, in the linear range of the B-H curve: in our case, we have considered XC06 iron and the magnetization level limit of 1.6 T, which was a good compromise between magnetization level and magnet weight. A summary of the main dipole parameters are listed in Table 3.

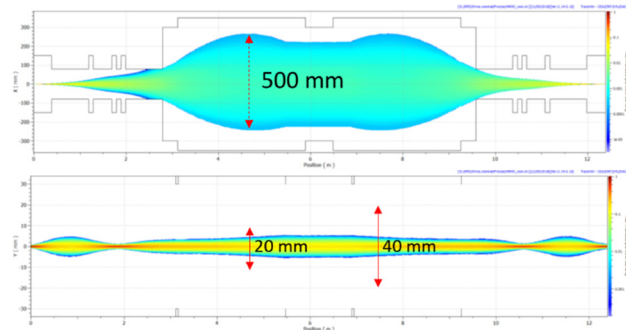


Figure 3: Beam density on horizontal (top) and vertical (bottom) planes, from object slit to image slit (Tracewin).

Table 3: Dipole Parameters

Radius	1500	mm
Bending Angle	90	Deg
Vertical Gap (wrt centre)	± 30	mm
Pole length (wrt centre)	± 430	mm
Nominal Magnetic Field	0.562	T
Edge Angle	27.16	Deg
Edge Hexapole radius	2220	mm
Iron max. magn. level	1.6	T
Coil current density	4.2	A/mm ²
Power	28	kW

FIELD OPTIMIZATION

As discussed before, the most critical aspect for achieving the 1/20000 resolution for the HRMS is the field homogeneity in between the two poles. The challenge arise not only by the homogeneity level $5 \cdot 10^{-5}$, but especially because this goal has to be achieved throughout all the area where the beam is intended to pass inside the dipole that is very large, since the high dispersion inside the dipole (upper part of Fig. 3). The idea is that the magnet must behave like an ideal infinite, hard-edge dipole.

A possible approach that can be followed for the optimization process is to optimize the dipole cross section shape at first, achieving the desired homogeneity along the transverse direction with respect to the optical axis, with 2D simulations. The optimized cross section can then be transposed to the third dimension, where a second optimization process is needed to consider the asymmetry introduced by the dipole-bending angle.

The observable throughout all the process is the field flatness, defined as:

$$\left(\frac{B_y(s)}{B_{y-ref}}\right) - 1 = 0 \pm 4 \cdot 10^{-5} \quad (8)$$

where s is the pole length x -position for the 2D simulations and the longitudinal angular position of the dipole in the 3D simulations. With this definition for the flatness, we are looking for a profile that is zero within the $4 \cdot 10^{-5}$ range.

The following design studies were carried out with the TOSCA package of the commercial fem software OPERA-3D [11].

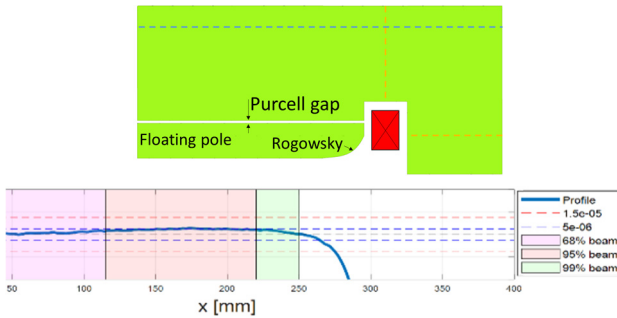


Figure 4: Cross sectional view of $1/4$ dipole (top) and Flatness profile (bottom).

2D Optimization

With 2D simulations, it is possible to investigate the best design solution for the field flatness in the transverse direction with respect to the optical axis. Many solutions were investigated. In the end, the best result was obtained with the Purcell-cell design, in combination with the Rogowsky shaped pole edge.

The Purcell-cell design consists in a fully magnetically detached pole from the rest of the yoke. We can address to the detached pole as the ‘floating pole’, while to the gap in between as ‘Purcell gap’ (see upper part of Fig. 4). The Rogowsky edge profile is a curve given by the following equation:

$$y_{Rog} = G \left(\frac{1}{2} + \frac{1}{\pi} e^{\left(\frac{\pi x}{G} - 1\right)} \right), \quad (9)$$

where y_{Rog} is the y position at which the Rogowsky curve has to stop and G is the full dipole gap.

With a correct choice of Purcell gap vertical position and y_{Rog} , a flatness profile within $5 \cdot 10^{-6}$ was even achievable. The lower part of Fig. 4 show the flatness profile, as defined by equation (8), in function of the pole length. The vertical axis is limited to the reference flatness goal of $4 \cdot 10^{-5}$, while dashed lines are reference flatness values. Lastly, horizontal beam density information are given by the coloured areas: the 68% of the beam is enclosed by the pink area, the 99% by the red and the 99% by the green one.

3D Optimization

Moving to the third dimension the bending angle of the dipole introduces an asymmetry that cannot be considered in the two 2D cross section. This asymmetry generates a

field hot-spot in the dipole ‘elbow’. This is show in the B_y map a) of Fig. 5. This field map corresponds to the simple extrusion of the 2D cross section presented in the upper part of Fig. 4, to which hexapole curvatures to the entrance and exit faces was added only. Note that the colour scale in Fig. 5 ranges within $\pm 10^{-4}$ with respect to B_{y-ref} .

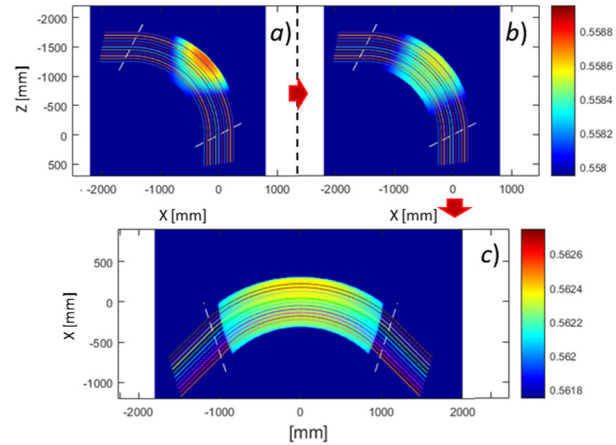


Figure 5: Field homogeneity rough optimization. Field maps inside the dipole after: a) simple extrusion of 2D cross section; b) magnetic flux balance; c) Rogowsky profile extended to the entrance and exit edges.

Therefore, for flatness optimization, the asymmetry has to be counteracted. Since it consists in a different amount of iron between the internal and external curvature of the dipole, a good way to proceed is to balance the magnetic fluxes in the internal and external return yokes. The lack of iron in the internal curvature causes the increase of the magnetization level and consequently of the local relative permeability of the iron: this acts like a bottleneck for the magnetic flux. To restore the flux balance, the internal and external return yoke horizontal and vertical surfaces should be equalized, respectively. The two surfaces are highlighted with yellow dashed lines in the upper part of Fig. 4. This equalization can be done by increasing the amount of iron in the internal curvature for the horizontal surface, while cutting away iron as highlighted by the blue dashed line in Fig. 4, on the external part of the yoke for the vertical one. The latter step causes the magnet top and bottom external surfaces to be not flat as usual. This is also beneficial for dipole weight.

The result of this flux balance can be seen in the field map b) of Fig. 5. In Fig. 5 the field uniformity is now enhanced in the dipole centre, but there still something missing at the entrance and exit of the dipole.

It makes sense, then, to extend the Rogowsky shape also to the entrance and exit faces of the floating pole. Until now, it was applied to the floating pole lateral edges only, as consequence of the extrusion of the 2D cross section. The consequences of this step are shown in the field map c) of Fig. 5, while Fig. 6 shows the model of the dipole, obtained so far.

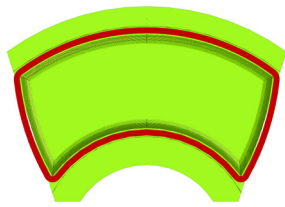


Figure 6: OPERA model of the dipole: view of the pole face.

Let refer to this last step as ‘*opt-0*’. It is now possible to look at the field flatness again but considering a flatness profile along the beam propagation direction, instead of transverse direction, like in the 2D case. In this way, it is possible to have longitudinal information about the field homogeneity. The transversal information can be obtained this time by considering not only the flatness profile at the optical axis ($\rho = 1500 \text{ mm}$) but also at different curvature radius. In the following plots, flatness profiles in 50 mm steps far away from the optical axis are reported, so that the entire beam horizontal extension (99% of the beam lie within $\pm 250 \text{ mm}$ wrt ρ) is observed. The trajectories of these profiles are visible in the field maps of Fig. 5. In the flatness profiles in Fig. 7 the vertical axis gives information about the homogeneity level, the horizontal axis now gives longitudinal information, while the different lines give transversal information.

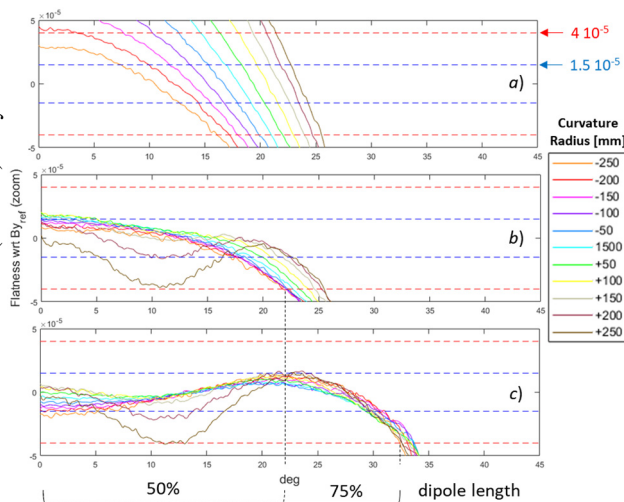


Figure 7: Flatness profiles at different curvature radius: a) *opt-0*; b) *opt-1*; c) *opt-3*.

The upper plot *a*) of Fig. 7 refers to the flatness of the *opt-0* step. It is clear that further optimization is still needed, since a vertical field hot-spot at the dipole ‘elbow’ is still present even if strongly weakened than before.

By applying a net cut to the floating pole ‘elbow’ only, it is possible to damp the hot-spot with high accuracy (*opt-1* step). Flatness is now within the reference range (red dashed line), enclosing the 99% of the beam for the 50% of the dipole length (Fig. 7b).

A further extension of the flatness along the longitudinal direction is possible by introducing some field reinforcement inside the Purcell-gap, at the entrance and

exit faces (*opt-2* step). A correct sizing of the reinforcements can extend field flatness up to the 75% of the pole length, as shown by *c*) plot of Fig. 7.

Lastly, fringe field effect must be taken into account as well. Fringe field causes the magnetic length of the dipole to be different with respect to the hard-edge model, given by $L_{hard-edge} = \frac{\pi}{2}\rho$. The effective magnetic length can be obtained with:

$$L_{eff} = \frac{\int_{-\infty}^{\infty} B_y(s) ds}{B_y(0)} \quad (10)$$

, where s is the curvilinear coordinate along the dipole length. To have $L_{hard-edge} = L_{eff}$ condition, field clamps can be added to the entrance and exit dipole faces (see lhs of Fig. 8). By placing the clamp at the proper distance from the pole face, it is possible to cancel the difference between the two lengths (see rhs of Fig. 8).

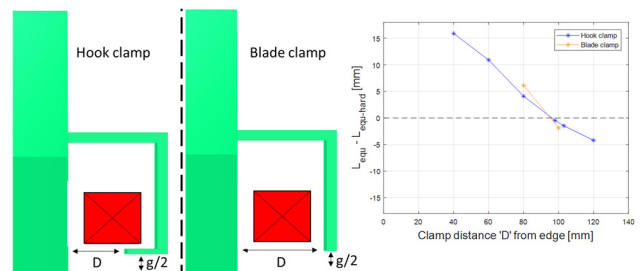


Figure 8: Two possible field clamp configurations (left), both capable to cancel the fringe field effect (right).

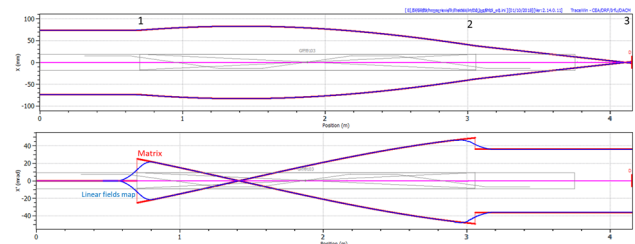


Figure 9: Beam optics inside dipole simulations with Tracewin: comparison between theoretical hard-edge matrix model (red line) and field map (blue line) from dipole final design with OPERA simulation.

It is now possible to check dipole field, obtained from this study, with beam optics simulations. Figure 9 shows a perfect agreement between a theoretical, matrix-modelled, hard-edge dipole (doubled checked with COSY-infinity [2]) and the same simulation done using the field map obtained with OPERA simulations.

CONCLUSIONS

The design studies performed with OPERA simulations demonstrate that a dipole with a field flatness suitable for a separator with a resolution of 1/20000 is feasible. Mechanical and electrical tolerances are currently under investigation and preliminary studies are giving encouraging results with very strict tolerances, but anyhow reasonable. Since the engineering of the design here presented was not done yet, this can be considered a feasibility study only.

REFERENCES

- [1] G. Bisoffi, *et al.*, “Progress in the realization and commissioning of the exotic beam facility SPES at INFN-LNL”, 2018 J. Phys.: Conf. Ser. 1067 052017.
- [2] M. Comunian, *et al.*, “Status of the SPES Exotic Beam Facility”, presented at the 14th Int. Conf. on Heavy Ion Accelerator Technology (HIAT’18), Lanzhou, China, Oct. 2018, paper MOYAA02, this conference.
- [3] A. Galata, *et al.*, “ADIGE: the radioactive ion beam injector of the SPES project”, in *Proc. 8th Int. Particle Accelerator Conf. (IPAC’17)*, Copenhagen, Denmark, May 2017, pp. 2281, doi:10.18429/JACoW-IPAC2017-TUPVA087
- [4] C.N. Davids, *et al.*, “A compact high resolution isobar separator for the CARIBU project” in *Proc. PAC’09*, Vancouver, Canada, May 2009, paper FR5REP116, pp. 5050.
- [5] J.A. Maloney, *et al.*, “New design studies for TRIUMF’s ARIEL High Resolution Separator”, Nucl. Instrum. and Methods Phys. Res. Section B, 376 (2016) <https://doi.org/10.1016/j.nimb.2015.11.023>.
- [6] T. Kurtukian-Nieto, *et al.*, “SPIRAL2/DESIR high resolution mass separator” Nucl. Instrum. and Methods. Phys Res. Section B, 317 (2013)
- [7] M. Comunian, *et al.*, “Design of high resolution mass spectrometer for SPES”, in *Proc. IPAC’18*, Vancouver, Canada, Apr.-May 2018, pp. 3252, doi:10.18429/JACoW-IPAC2018-THPAK021
- [8] A. Nieminen, *et al.*, “Beam Cooler for Low-Energy Radioactive Ions”, Nuclear Instruments and Methods in Physics Research A 469, ELSEVIER, August 2001, p. 244-253; <http://www.elsevier.org>
- [9] L. Bellan, INFN-LNL annual Report 241 (2015) ISSN 1828-8561;
- [10] D. Utriot and N. Pichoff, “TraceWin”, CEA Saclay, website: <http://irfu.cea.fr/Sacm/logiciels/index3.php>.
- [11] <https://operafea.com>

Content from this work may be used under the terms of the CC BY 3.0 licence (© 2018). Any distribution of this work must maintain attribution to the author(s), title of the work, publisher, and DOI.

MULTIPOLE MAGNETS FOR THE HIAF FRAGMENT SEPARATOR USING THE CANTED-COSINE-THETA (CCT) GEOMETRY*

W. Wu[†], Y. Liang, L.C. Zhou, E. M. Mei, D.S. Ni, S.J. Zhen, X.J. Ou, W.J. Yang,
 Institute of Modern Physics, Lan-zhou, China

Abstract

The fragment separator of the HIAF (High Intensity Heavy Ion Accelerator Facility) project called HFERS requires quadrupoles with high gradients (11.4 T/m) and large bores (gap width of 420 mm). The iron dominated magnets with superconducting coils have been widely used in the similar facilities such as A1900, BigRIPS, Super-FRS and RISP with the advantages of low request for coils installation precision, simple fabrication and low cost, but they have large cold mass and helium containment, which result in long time cooling down and high pressure rise during a quench. In addition, due to iron saturation, it is hard to guarantee on the field quality in the operated field range. A new coil dominated design based on the Canted-Cosine-Theta geometry is presented for HFERS, which is expected to overcome these problems. The design superimposes several layers of oppositely wound helical windings to generate high quality quadrupole. Sextupole, octupole and steering dipole can also be easily integrated to reduce the length of cryostat. This paper reports the detailed design of HFERS multiplets based on the CCT concept and the construction of a sub-scale prototype.

INTRODUCTION

The **High Intensity Accelerator Facility** is a new project to pursue nuclear physics research and is under construction at the Institute of Modern Physics in China [1]. As shown in Fig. 1, it consists of a 45 GHz superconducting ECR ion source, a superconducting Linac, a fast cycling booster ring, a fragmentation separator and a spectrometer ring. The fragmentation separator of HIAF called HFERS is an important connection between BRing and SRing. It is used to produce, separate, purify, and identify the desired exotic nuclei. The field rigidity is 25 T · m. It has a big beam acceptance of ±160 mm. For similar facilities, such as A1900 [2], BigRIPS [3],[4], SuperFRS [5] and RISP [6], to meet the magnetic field requirement within a large aperture, the superferric design with cold iron have been widely used. They are easy to fabricate and wind, while their coils require lower positioning precision. But because of the iron saturation, it is hard to achieve good field quality at both low and high field with the superferric design. And large cold mass also brings about new challenges, such as long-time cooling-down, high pressure during a quench and difficulties of supports and alignments. Air-core type magnets have the advantages of light weight and good field linearity and are

used in BigRIPS as the first element near the target to lower the radiation heat load [7]. Walstrom type coil with better field quality are used in the S³ device of SPIRAL2 project [8]. But their magnetic field are more sensitives to coil positioning error and they are difficult to fabricate and wind, especially Walstrom type coil [9].

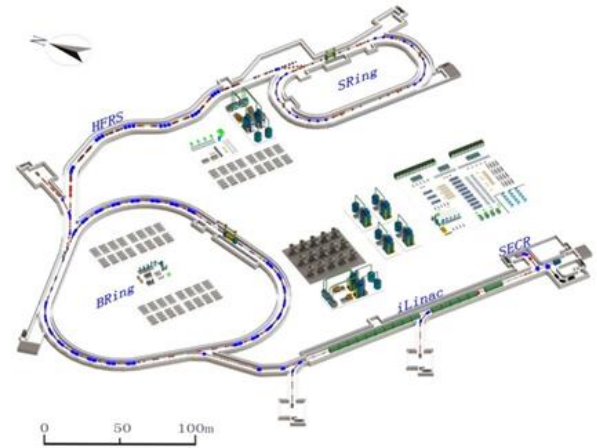


Figure 1: Layout of HIAF project.

CANTED-COSINE-THETA MAGNET

The basic idea of Canted-Cosine-Theta was firstly published by D. I. Meyer and R. Flasck in 1970 [10]. As shown in Fig. 2, by the superposition of two oppositely tilted solenoids with respect to the bore axis, the azimuthal component of the magnetic field is cancelled and the high-quality dipole field can be generated.

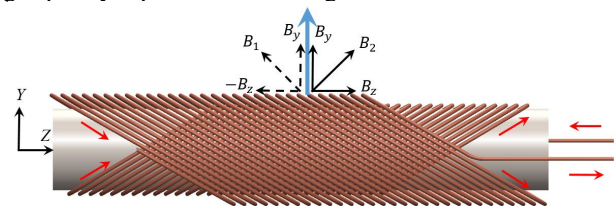


Figure 2: Conceptual view of CCT dipole windings.

Higher order multipole fields can also be obtained by superimposed current with an z direction oscillation as shown in following equations. For example, n=2 produces a quadrupole field as shown in Fig. 3, and so forth.

$$x(\theta) = R \cdot \cos(\theta) \quad (1)$$

$$y(\theta) = R \cdot \cos(\theta) \quad (2)$$

$$z(\theta) = \frac{h}{2\pi} \theta + \sum_n A_n \sin(n\theta + \varphi_n) \quad (3)$$

* Work supported by the National Natural Science Foundation of China (Grant No. 11575266)

[†] wuwei@impcas.ac.cn

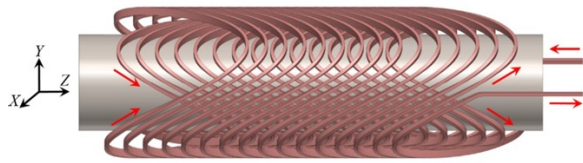


Figure 3: Conceptual view of CCT quadrupole windings.

Because of its flexibility and field quality in comparison to convectional superconducting magnets, CCT magnet gained new traction. Meinke *et al.* described their studies in a series of publications [11 – 14]. More recently, Caspi *et al.* have successfully developed a series of CCT dipole prototypes with NbTi and Nb₃Sn [15 – 17] and also presented a Proton gantry design based on CCT coils [18]. At CERN, for Hi-Lumi LHC orbit correctors, the CCT solution was finally retained for the advantages of easier assembly and lower cost, compared with the classical cos-theta design [19]. It was also an option for the 16-T FCC-hh main dipole which is under development in PSI [20]. In a word, the CCT coil is at a balance point between field quality and cost, thus, our HFRS complex also chose the CCT as baseline solution.

MAGNETIC DESIGN

As shown in Fig. 4 is the layout of HFRS. Totally 39 superconducting singlets are grouped into 13 triplets and cryostat modules. Fig. 5 shows a typical lattice of HFRS singlet consists of three quadrupoles with different effective length, sextupole, octupole and steering dipole.

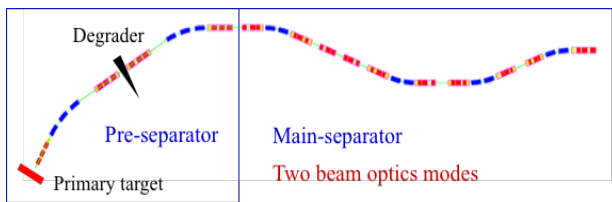


Figure 4: Layout of HFRS.

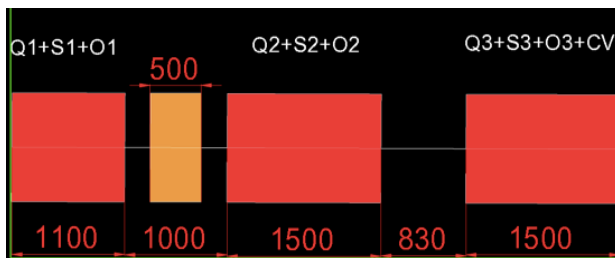


Figure 5: A typical lattice of HFRS singlet.

Table 1: Magnet Specifications

	Quadrupole	Sextupole	Octupole
Aperture	320 mm	320 mm	320 mm
Gradient	11.43 T/m	30 T/m ²	105 T/m ³
Effective length	0.8/ 1.1/1.5 m	0.8/ 1.1/1.5 m	0.8/ 1.1/1.5 m
Field quality	< ±8·10 ⁻⁴	< ±5·10 ⁻⁴	< ±5·10 ⁻⁴

The usable magnet aperture is 320 mm and the field gradient is 11.43 T/m. Field requirements for quadrupole, sextupole and octupole field are summarized in Table 1. In addition, dipole coils are used for two directions' steering corrections. The quadrupole coil, which experience the highest field, is the most demanding coil. Thanks to the good features of CCT coil, octupole, quadrupole, sextupole and dipole fields can be nested to reduce the mechanical length of the cryogenic modules.

Comparison of Different Conductor Placement Methods

For complicate coil like CCT, two types of conductor placement methods can be considered. First is the **direct placement with adhesive**, such as BNL's direct winding technology [21] with ultrasonic adhesive system. Recently, techniques that thermally embedded wire into thermal plastic material have also been applied in the fabrication of RF smart card coils and 3D printing of electromechanical devices [22]. But this method requires special equipment.

Another is **conductor placement in grooves**. Superconducting wires or cables can be placed into machined grooves from metal or composite mandrel. With cable, the CCT magnet's operation current is high and its inductance is low, which is suitable for powering in a string of magnets. With wire, its operation current is low while the inductance is high, which is a good choice for magnets powered with standalone converters. But it needs more mandrels if the grooves can only accommodate one wire. More mandrels mean higher cost, in order to lower the cost, CERN winds several insulated wires (2 x 5) into one groove and then connects them in series as shown in Fig. 6 (a). This method could be named **coil placement in grooves**. In order to improve the positioning accuracy, simplify the winding process and eliminate the insulation thickness of each wire, we come up with a variant that puts mini round cable with 7 insulated wires into groove as shown in Fig. 6 (b). Compared with CERN's solution, this design has more flexibility of insulation design that wire insulation is for turn to turn and cable insulation is for ground. Due to the transposition of wires, the coupling loss can be reduced.

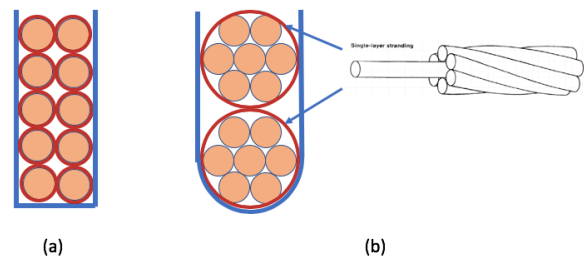


Figure 6: Conceptual drawing of coil placement in grooves and its variant with mini round cable.

Conductor Selection and Insulation System

In order to reduce the power supply and current leads costs, operational current lower than 500 A is chosen.

Content from this work may be used under the terms of the CC BY 3.0 licence (© 2018). Any distribution of this work must maintain attribution to the author(s), title of the work, publisher, and DOI.

When the peak field is about 3.5 T, the Nb-Ti wire is selected. Its specifications are summarized in Table 2. In order to withstand high radiation dose while maintaining voltage insulation levels > 1 kV, polyimide coating are used. The mini round cable is stranded by 7 insulated wires and wrapped with two layers of polyimide tapes for insulation (see Table 3). The voids between two adjacent cable can be filled with copper alloy wire as heater and glass fibre, then vacuum impregnated with CTD101K resin system. The impregnation also provides a support for the cables inside the grooves.

Table 2: NbTi Superconductor Specifications

	Units	
Wire diameter	mm	0.85
Diameter with insulation (polyimide coating 0.025mm)	mm	0.90
Number of NbTi filaments		630
Filament diameter	µm	22
Cu RRR		>100
n-value		>30
Cu/Sc		1.3
Ic@4.2K 4 T	A	>750

Table 3: Mini Round Cable Specifications

	Units	
Number of strands		6+1
Cable diameter	mm	2.70
Cable diameter with insulation (Polyimide tape wrapped)	mm	2.80

CCT Coil Design of HFRS Singlet

For each singlet, a set of multipole coils are nested concentrically with their mandrels. In order to reduce the cold mass and transfer function non-linearity, room temperature iron yoke outside of cryostat is used. The coils are designed to generate lower field which can be enhanced by the iron yoke. Table 4 list the design parameters of quadrupole and sextupole CCT coils with the effective length of 0.8 m.

Table 4: Overview of Magnet Parameters

Characteristics	Quadrupole	Sextupole
Gradient Field	10 T/m	30 T/m ²
I/wire	440 A	330 A
Layers	2×(6+1)	1×(6+1)
CCT skew angle	30°	40°
Turns per layer	66	64
ID of mandrel	420 mm	453.2 mm
Pitch	12.2 mm	12.6 mm
Groove size	2.8mm×5.8mm	2.8mm×3mm
Conductor length	6.4 km	3.4 km
Bpeak	3.5 T	3.0 T
Io/Iss	54%	37.5%

The quadrupole and sextupole coils are modelled in OPERA-3D as shown in Fig. 7 and the peak field located in the inner quadrupole coil is about 3.5 T as shown in Fig. 8. The octupole (Fig. 9) and steering dipole coil are designed in the pattern of discrete Cosine-Theta coil and will be mounted inside the quadrupole coil and outside the sextupole coil, respectively.

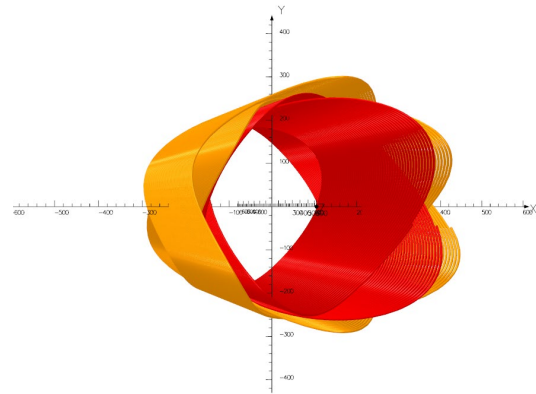


Figure 7: CCT coil model created by OPERA.

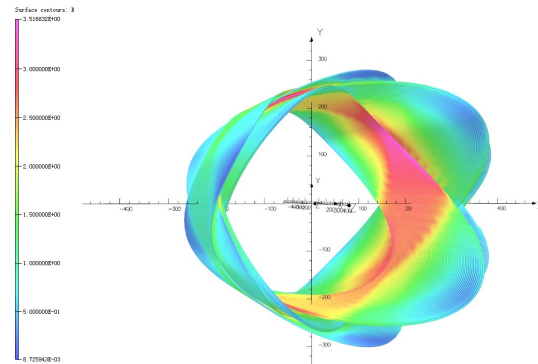


Figure 8: B map of the CCT coil model.

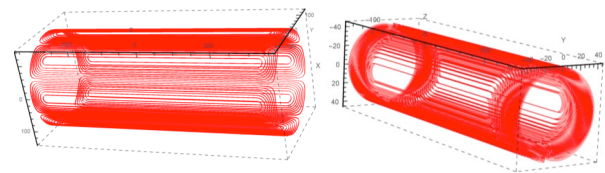


Figure 9: Octupole coil (left) and dipole coil (right).

MECHANICAL DESIGN

The coil winding is embedded in aluminium alloy coil formers with CNC machined slot. The machined formers are hard anodized for insulation. As shown in Fig. 10 and Fig. 11, the singlet assembly is comprised of two formers for quadrupole and two formers for sextupole, GFRP former for steering dipole, aluminium outer support tube, two end plates, and two joint boxes for quadrupole and sextupole coils' connections. In order to guarantee the field quality, the positional accuracy of the grooves need to be controlled within 0.05 mm. According to the prelim-

Opera

Opera

inary error analysis, the concentricity of four formers is not as strict as that of slots. The assembly is then vacuum impregnated with CTD101K resin. Finally, three singlets are inserted into a central stainless bobbin as triplets. The bobbin also serves as a part of the helium vessel.

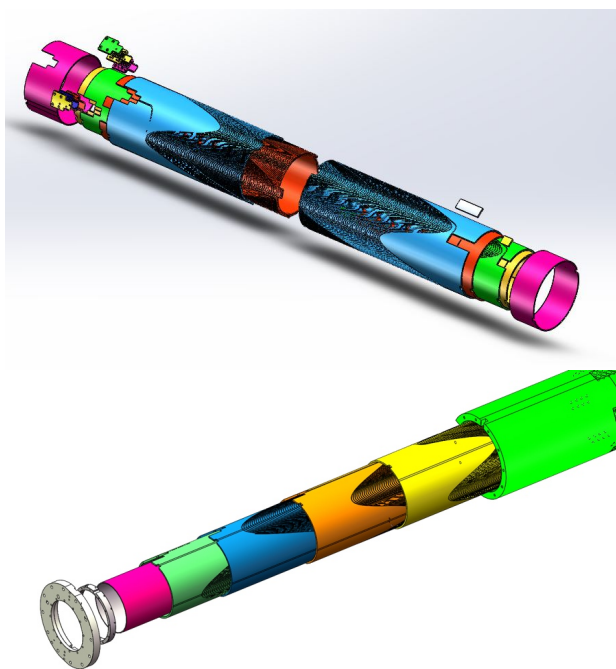


Figure 10: 3D drawing of the singlet assembly.

SUBSCALE MODEL COIL

In order to study the feasibility of the CCT design. We designed and fabricated a subscale quadrupole coil (see Fig. 11). As listed in Table 5, the field gradient is 40 T/m within a 60mm cold bore. The effective length is 160 mm. The NbTi conductor as described in Table 6 was used. The groove size is 2 x 5 mm for ten turns of conductor as shown in Fig. 6 (a). Same method of coil placement in grooves as CERN's was adapted. Figure 12 shows the process of winding 10 turns of wires into grooves. After winding, assembly, instrumentation, splicing and vacuum impregnation, the coil was successfully energized to design current without a quench. Fig. 13 shows the measured radial field increased linearly with operated current.

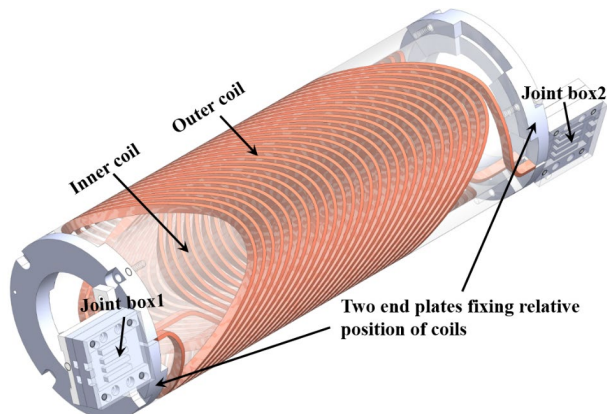


Figure 11: 3D drawing of the subscale model coil.

Parameter	Unit	Value
Gradient	T/m	40
Effective length	Mm	160
Operation current	A	400
Winding pitch	mm	6
Tilt angle	Deg	45
Inductance	mH	10
Aperture	mm	60
Good field	mm	± 20

Table 6: Specifications of the Superconductor Used in the Subscale Model Coil

Wire type	Monolith
Insulation	Formvar + Polyester braid
Bare size	ϕ 0.72 mm
Insulated size	ϕ 0.77 mm (Formvar) ϕ 0.9 mm \pm 5 μ m (Polyester braid)
Cu/SC	1.3:1
RRR (293 K/10 K)	> 100
Ic (6 T, 4.2K)	442.7 A



Figure 12: Winding process of the subscale quadrupole coil.

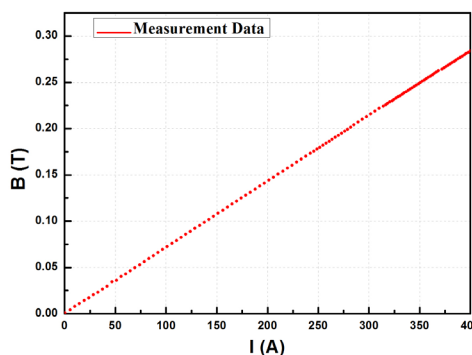


Figure 13: Measured transfer function (B_r at radius of about 7 mm).

PROJECT PLANING

IMP plans to fabricate and test a model singlet with nested quadrupole, sextupole, octupole and steering dipoles by the June of 2019. The effective length is 0.8 m and the bore diameter is 200 mm. And then the full size prototype singlet and triplets will be built by the middle of 2020. Totally 13 sets of multiplets need to be produced and tested before the end of 2023.

CONCLUSION

The novel CCT geometry coil structure has been adapted to the multiple magnets design of HFRS spectrometer. It reduces significantly size, weight of cold mass, cryogenic system and magnet installation requirements and cost of fabrication and operation. However, further error analysis of field quality, quench simulation and stress analysis are now under way to ensure the field quality and safety operation of the full-size magnets.

ACKNOWLEDGEMENTS

The authors would like to express their sincere acknowledge to Prof. Lucio Rossi (CERN), Prof. Glyn Kirby (CERN), and Prof. Shlomo Caspi's (LBNL) for their comments and useful suggestions.

REFERENCES

- [1] J.C.Yang, et al. High Intensity heavy ion Accelerator Facility (HIAF) in China. <https://www.sciencedirect.com/science/article/pii/S0168583X13009877>
- [2] A.F.Zeller, et al., "Magnetic elements for the A1900 fragment separator", *Adv. In Cryo. Eng.*, vol. 43, pp. 245-252, 1998.
- [3] T. Kubo, "In flight RI beam separator BigRIPS at RIKEN and elsewhere in Japan", *Nuclear Instruments and Methods in Physic Research B* 204 (2003) 97.
- [4] K. Kusaka et al., "Prototype of superferric quadrupole magnets for the BigRIPS separator at RIKEN", *IEEE Trans. Appl. Superconductivity* 14 (2004) 310.
- [5] Leibrock H. et al. "Prototype of the Superferric Dipoles for the Super-FRS of the FAIR-Project" *IEEE Trans. App. Supercond.*, Vol.20, No.3, June 2010
- [6] H. C. Jo, D. G. Kim, S. Choi, H. M. Jang, K. Sim and S. Kim, "Prototype HTS Quadrupole Magnet for the In-Flight Fragment Separator of RISP," in *IEEE Transactions on Applied Superconductivity*, vol. 28, no. 6, pp. 1-6, Sept. 2018, Art no. 4008906.
- [7] K. Kusaka et al, "An Air-Core Type Superconducting Quadrupole Triplet for the BigRIPS Separator at RIKEN" *IEEE Trans. Appl. Superconductivity* 18(2008) 240.
- [8] S. Manikonda et al, "Multipole Magnets with High Field Uniformity over Full Length for Super Separator Spectrometer" *IEEE Trans. Appl. Superconductivity* 18(2008) 240.
- [9] P. Walstrom, "Soft-edged magnet models for higher-order beam-optics map codes," *Nuclear Instruments and Methods in Physics Research Section A: Accelerators, Spectrometers, Detectors and Associated Equipment*, vol. 519, no. 1-2, pp. 216-221, 2004.

- [10] D. I. Meyer and R. Flashck, "A new configuration for a dipole magnet for use in high energy physics applications" in *Nuclear Settlements and Methods*. Amsterdam, The Netherlands: North Holland Pub. Co., 1970, pp. 339-341.
- [11] C.L.Goodzeit, M.J.Ball and R.B.Meinke, "The double-helix dipole - a novel approach to accelerator magnet design," *IEEE Trans. Appl. Superconduct.*, vol. 13, no. 2, pp. 1365-1368, Jun. 2003.
- [12] R. B. Meinke et al., "Superconducting double-helix accelerator magnets," in *Proc. Particle. Acc. Conf.*, 2003, pp. 1996-1998.
- [13] A.V.Gavrilin et al., "New concepts in transverse field magnet design," *IEEE Trans. Appl. Superconduct.*, vol. 13, no. 2, pp. 1213-1216, Jun. 2003.
- [14] A.V.Gavrilin et al., "Conceptual design of high transverse field magnets at NHMFL," *IEEE Trans. Appl. Superconduct.*, vol. 12, no. 1, pp. 465-469, Mar. 2002.
- [15] S. Caspi et al., "Test results of CCT1 a 2.4 T canted cos theta magnet," *IEEE Trans Appl. Supercond.*, vol. 25, no. 3, Jun. 2015, Art. no. 4002304.
- [16] S. Caspi, F. Borgnolutti, L. Brouwer, D. Cheng, D.R.Dietderich, H. Felice, A. Godeke, R. Hafalia, M.Martchevskii, S. Prestemon, E. Rochepault, C. Swenson and X. Wang, "Canted-Cosine-Theta Magnet (CCT) - a Concept for High Field Accelerator Magnets," *IEEE Trans. Appl. Superconduct.*, vol. 24, no. 3, p. 4001804, JUNE 2014.
- [17] L. Brouwer, "Canted-cosine-theta superconducting accelerator magnets for high energy physics and ion beam cancer therapy," Ph.D. dissertation, Univ. California, Berkely, CA, USA, 2015, ISBN 978-83-7814-491-5.
- [18] S. Caspi, D. Arbelaez, L. Brouwer, D. Dietderich, R.Hafalia, D. Robin, A. Sessler, C. Sun, and W. Wan, "Progress in the Design of a Curve Superconducting Dipole for a Therapy Gantry," *Proceedings of IPAC2012*, New Orleans, Louisiana, p. 4097-4099 (2012).
- [19] G. A. Kirby et al., "Hi-Lumi LHC Twin-Aperture Orbit Correctors Magnet System Optimisation," in *IEEE Transactions on Applied Superconductivity*, vol. 27, no. 4, pp. 1-5, June 2017.
- [20] B. Auchmann et al., "Electromechanical Design of a 16-T CCT Twin-Aperture Dipole for FCC," in *IEEE Transactions on Applied Superconductivity*, vol. 28, no. 3, pp. 1-5, April 2018, Art no. 4000705.
- [21] Parker, B., Anerella, M., Escallier, J., Ghosh, A., Jain, A., Marone, A., et al. (2007). BNL Direct Wind Superconducting Magnets. *IEEE Transactions on Applied Superconductivity*, 22(3), 4101604-4101604.
- [22] Saari, M., Cox, B., Richer, E., Krueger, P. S., & Cohen, A. L. (2015). Fiber Encapsulation Additive Manufacturing: An Enabling Technology for 3D Printing of Electromechanical Devices and Robotic Components. *3D Printing and Additive Manufacturing*, 2(1), 32-39.

NOVEL METHODS FOR THE PRODUCTION OF RADIONUCLIDES OF MEDICAL INTEREST WITH ACCELERATORS

S. Corradetti[†], A. Andrichetto, F. Borgna, M. Ballan¹, INFN - Laboratori Nazionali di Legnaro, 35020 Legnaro (PD), Italy

V. Di Marco, Università degli Studi di Padova – Dipartimento di Scienze Chimiche, 35131 Padova, Italy

G. Marzaro, N. Realdon, Università degli Studi di Padova – Dipartimento di Scienze del Farmaco, 35131 Padova, Italy

¹also at Università degli Studi di Ferrara - Dipartimento di Fisica e Scienze della Terra, 44122 Ferrara, Italy

Abstract

Radionuclides for radiopharmaceuticals preparation are currently produced in cyclotrons, generators or nuclear reactors. However, none of these modes is free from serious issues, like: high costs of targets, production of undesired radionuclide contaminants, long and expensive separation methods and formation of long-lived radioactive wastes. For this purpose, novel methods are being developed for the production of highly pure radionuclides. The ISOL (Isotope Separation On-Line) method can be applied to produce high purity radionuclides of medium and heavy masses. ISOL is nowadays established as a major method for the production of high intensity and high quality radioactive ion beams for nuclear physics studies. The SPES-ISOLPHARM project at INFN-LNL (Istituto Nazionale di Fisica Nucleare – Laboratori Nazionali di Legnaro) aims to provide a feasibility study for an innovative technology for the production of high specific activity radionuclides based on the ISOL method. The ongoing experimental activities on primary and secondary (ion collectors) targets production, construction and testing of the selection and transport apparatus is here presented.

INTRODUCTION

Radiopharmaceuticals are medicines that deliver a pre-defined amount of radiation to a target tissue for diagnostic or therapeutic purposes depending on the mechanism of decay. Radiopharmaceuticals are usually made of two parts: a “radioactive core” and a “carrier system”; the latter allows the irradiation of malignant cell populations, avoiding damage to healthy tissues [1].

Beta-emitting radionuclides are usually produced mainly by direct reaction in dedicated targets using neutrons from nuclear reactors. By means of those reactions it is possible to produce a large number of isotopes and different nuclei in the target. The chemical methods to extract the desired radionuclide leads to the presence of a considerable amount of carrier. In this case, the specific activity, which is the ratio between the activity of the radioisotope and the mass of the element taken into account, is very low.

The global network of accelerators used for the production of medical radioisotopes, in particular cyclotrons, has

seen a rapid expansion over the last decade, with a huge increase on the number of installed machines [2].

The accelerators based on the ISOL (Isotope Separation On-Line) technique [3] might be an efficient way to produce radioisotopes for radiopharmaceuticals application, thanks to the mass separation, which guarantees the possibility to produce radioisotopes with high specific activity, close to theoretical value.

THE ISOLPHARM PROJECT

At INFN-LNL (Istituto Nazionale di Fisica Nucleare – Laboratori Nazionali di Legnaro), the SPES (Selective Production of Exotic Species) facility will allow the production of radioactive ion beams of neutron-rich nuclei with high purity, in the range of mass between 80 and 160 amu [4].

At SPES the production of the radioactive isotopes is obtained by nuclear reactions induced by 40 MeV protons, accelerated by a cyclotron, recently installed at LNL, that will collide a multi-foil target with discs of different materials, mostly uranium carbide [5], properly spaced to dissipate the heat (8 kW) generated by the reaction. Most of the produced nuclides will be neutron-rich (uranium fission) but using different target materials it could be possible to produce proton-rich isotopes. The reaction products will be extracted from the target by evaporation at high temperature (about 2000 °C), and then forced to pass through a transfer tube towards an ionization cavity, where they will be ionized to the 1+ state. Once ionized, these isotopes will be accelerated through an electrode at high potential (up to 40 kV).

The ground-breaking idea of the ISOLPHARM method was granted an International patent (INFN). The driving idea is the obtainment of carrier-free radioisotopes, to be used as radiopharmaceutical precursors, thanks to the extreme purity of ISOL radioactive beams.

The formed beam will be focused using different electromagnetic systems and purified in order to have a pure isotope beam without any contaminants. It will therefore be possible to collect the radionuclides of interest using a proper substrate placed at the end of the experimental line. In Fig. 1 a general scheme of the process is shown.

[†] stefano.corradetti@lnl.infn.it

Content from this work may be used under the terms of the CC BY 3.0 licence (© 2018). Any distribution of this work must maintain attribution to the author(s), title of the work, publisher, and DOI.

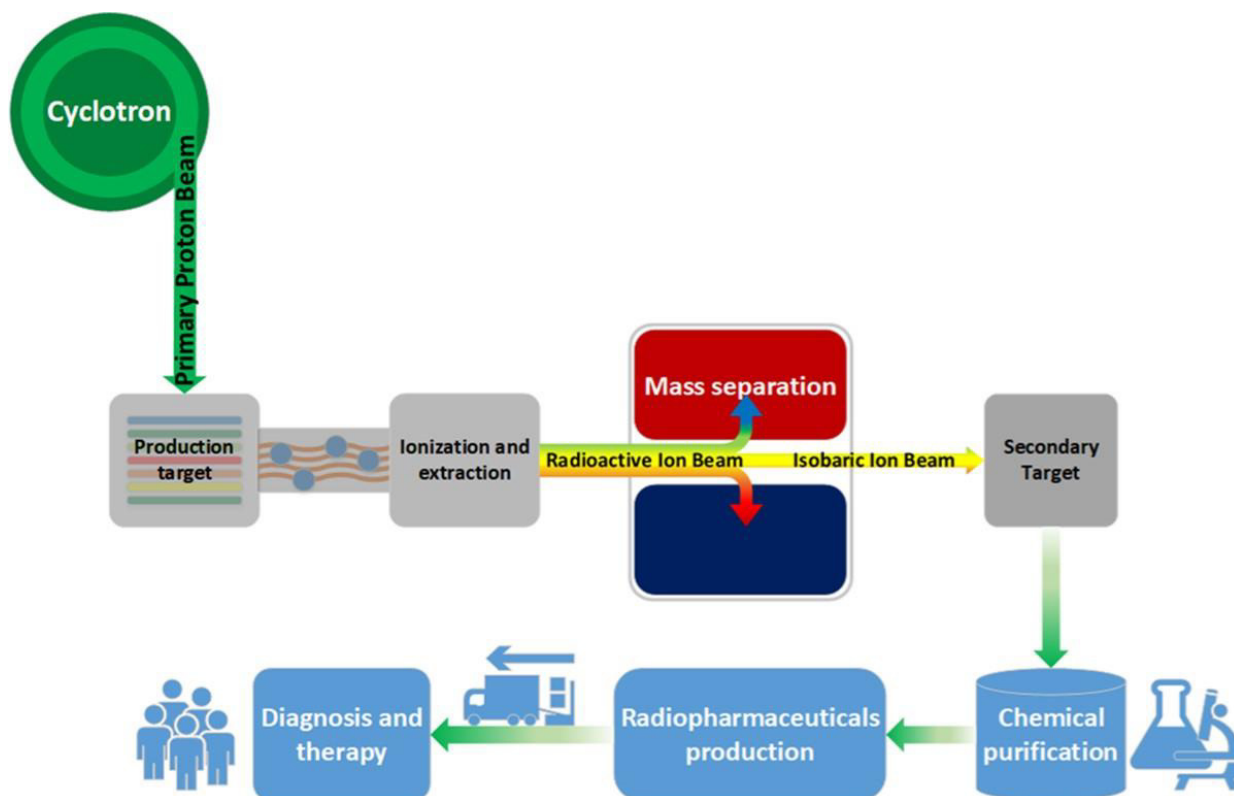


Figure 1: The ISOLPHARM process.

THE SPES FRONT END

The experimental apparatus present at LNL allowed the performance of some preliminary tests. A SPES test bench was used, referred to as offline Front End (FE). This apparatus, shown in Fig. 2, has been designed and developed for the SPES project.

To study the production of a radionuclide with the ISOL technique for the obtainment of a radiopharmaceutical product, stable isotopes of the same element can be used, since they have the same chemical behavior. For this reason, the FE was used to produce stable ion beams and carry out the feasibility tests here reported. The FE is made of five different functional subsystems: the ion source complex, the beam optics subsystem, the Wien filter and two diagnostic boxes.

In offline mode, different methodologies can be used to introduce the stable isotopes to be ionized and accelerated, depending on the physical state of the element. In the case of gases, they are introduced through a controlled gas flow and injected in the ionization source thanks to a calibrated leak; in case of solid materials, they are in the form of soluble salts, dissolved in acidic media and quantitatively deposited and solvent evaporated on a tantalum foil, called mass marker (MM) [6].

The ionization sources used in the FE are of two kinds [7], according to the first ionization potential of the element. For elements of the 1st and 2nd groups, a Surface Ion

Source (SIS) is adopted; for elements with higher electro-negativity, a Plasma Ion Source (PIS) is necessary.

For the simulation of the radionuclide production, at the end of the line, immediately after the second diagnostic box, a substrate of pharmaceutical grade (usually sodium chloride, “irradiation target” in Fig. 2) is positioned in order to collect the desired accelerated stable ions.

COPPER IONIZATION AND DEPOSITION TESTS

Among the radioisotopes that can potentially be produced in the framework of the ISOLPHARM project, ^{64}Cu and ^{67}Cu are a promising theranostic pair [8].

In order to evaluate the capability of the SPES FE to efficiently ionize copper isotopes and extract them into a beam, ionization tests were performed by loading precise amounts of stable natural copper into the ion source, by means of the MM technique which foresees the surface deposition of a small amount of the desired element on a thin tantalum foil that is lately accurately folded and inserted inside a small tubular oven, that replaces the production target. Such oven can be heated by Joule effect, allowing the atomization of the substrate previously deposited on the foil, and the migration of the neutrals towards the ion source. In the case of copper, the PIS was used.

We could verify copper ionization thanks to the analysis of masses composing the beam. A typical mass scan for copper is reported in Fig. 3A. Copper is clearly identified thanks to the two peaks of masses 63 and 65.

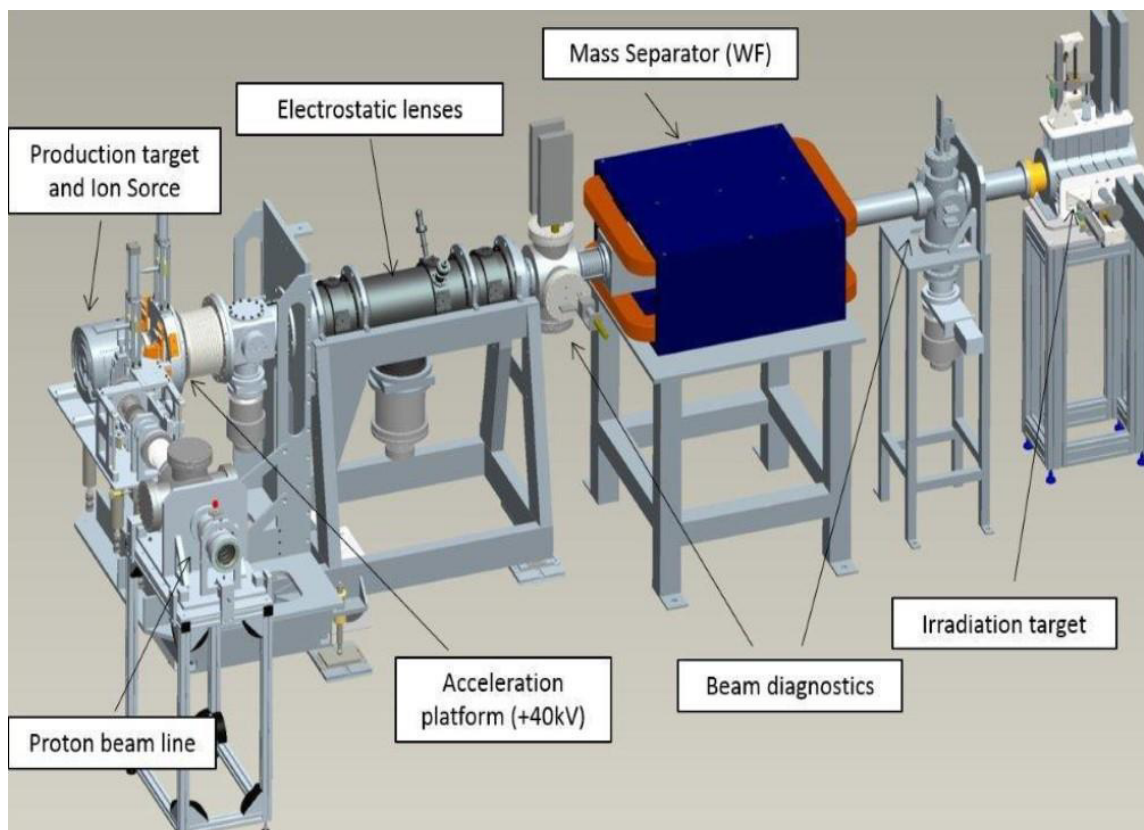


Figure 2: The off-line Front End.

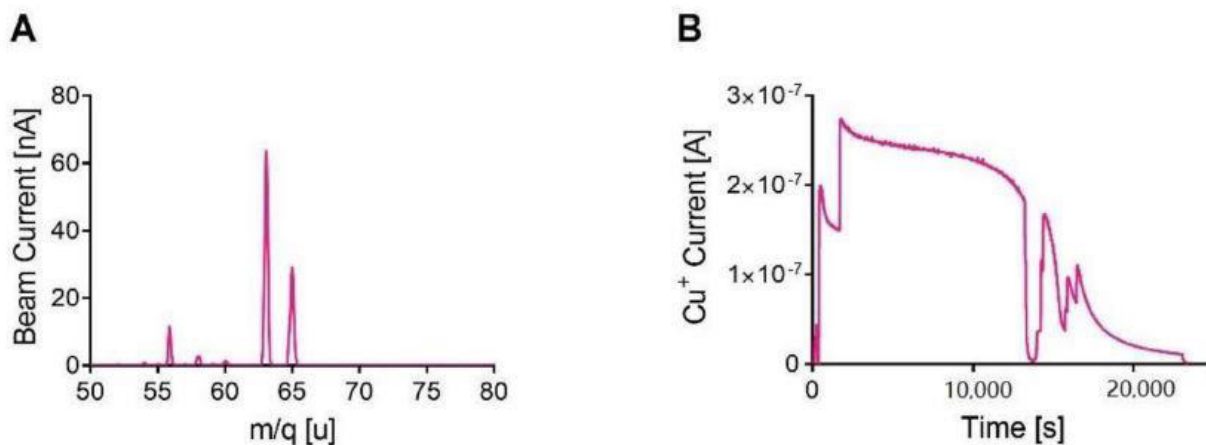


Figure 3: (A) Mass scan of copper beams and (B) trend of copper beam in time during ionization tests.

The ionization efficiency, i.e., the total amount of ^{nat}Cu ionized out of the amount of ^{nat}Cu in the MM, was $7.7 \pm 1.3\%$. In Figure 3B the copper beam current trend is reported.

After the removal of the secondary target at the end of several hours of irradiation, its appearance was as shown in Fig. 4, clearly showing the implantation of the two different masses composing ^{nat}Cu , 63 and 65..

The quantification of copper after the recovery from the beam was made possible thanks to the dissolution of the targets in acidic medium. When diluted nitric acid was used, only a low amount of copper was measured, so the

dissolution in concentrated nitric acid and at high temperatures was then applied. In this case the amount of copper recovered was higher (about 50%), but still not the 100% of the copper which was foreseen on the targets. For this reason, further studies are going to be carried out to improve the efficiency of the chemical recovery process.

CONCLUSION

The ISOLPHARM project aims to develop a technique which opens the possibility to produce a wide range of radionuclides with extremely high levels of purity. This is related to the intrinsic high specific activity, because of the

Content from this work may be used under the terms of the CC BY 3.0 licence (© 2018). Any distribution of this work must maintain attribution to the author(s), title of the work, publisher, and DOI.

lack of isotopic contaminants, and radionuclidic and chemical purity, since impurities coming from the beam and from the targets are very limited, compared to those of traditional methods.



Figure 4: The ^{63}Cu and ^{65}Cu spots on the secondary target from right to left.

REFERENCES

- [1] F. Azaiez *et al.*, *Nuclear Physics for Medicine*. NUPECC 2014. ISBN: 978-2-36873-008-9
- [2] M. A. Synowiecki, L. R. Perk, and J. F. W. Nijssen, “Production of novel diagnostic radionuclides in small medical cyclotrons”, *EJNMMI Radiopharm. Chem.*, vol. 3, no. 1, p. 3, 2018.
- [3] T. Nilsson, “European RIB facilities – Status and future”, *Nucl. Instruments Methods Phys. Res. Sect. B Beam Interact. with Mater. Atoms*, vol. 317, no. PART B, pp. 194–200, Dec. 2013.
- [4] A. Monetti *et al.*, “The RIB production target for the SPES project”, *Eur. Phys. J. A*, vol. 51, no. 10, p. 128, Oct. 2015.
- [5] S. Corradetti, M. Manzolaro, A. Andrighetto, P. Zanonato, and S. Tusseau-Nenez, “Thermal conductivity and emissivity measurements of uranium carbides”, *Nucl. Instruments Methods Phys. Res. Sect. B Beam Interact. with Mater. Atoms*, vol. 360, pp. 46–53, Oct. 2015.
- [6] F. Borgna *et al.*, “A preliminary study for the production of high specific activity radionuclides for nuclear medicine obtained with the isotope separation on line technique”, *Appl. Radiat. Isot.*, vol. 127, pp. 214–226, 2017.
- [7] M. Manzolaro, G. Meneghetti, A. Andrighetto, G. Vivian, and F. D’Agostini, “Thermal-electric coupled-field finite element modeling and experimental testing of high-temperature ion sources for the production of radioactive ion beams”, *Rev. Sci. Instrum.*, vol. 87, no. 2, pp. 2–5, 2016.
- [8] F. Borgna *et al.*, “Early evaluation of copper radioisotope production at ISOLPHARM”, *Molecules*, vol. 23, no. 10, pp. 1–12, 2018.

PRELIMINARY DESIGN AND SIMULATION RESULTS OF Ne⁺ BEAM SOURCE*

Y. H. Xie[#], C. D. Hu, Y. J. Xu, J. Li, Y. L. Xie,
 Institute of Plasma Physics, Chinese Academy of Sciences, 230031 Hefei, China

Abstract

An ion source of Ne beam was designed for basic physical research in the Institute of Plasma Physics, Chinese Academy of Science (ASIPP). The ion source was designed with hot cathode plasma source with three electrodes accelerator. The designed beam energy is 10-20 keV, the beam power is 50 kW, beam size is 250 mm × 250 mm and beam duration is 2 seconds. The three electrodes accelerator with slit type was designed. The extracted beam current and beam divergence angle was simulated. The maximum beam power of 40 kW can be extracted when the divergence angle less than 5 degree with beam energy of 10 keV and the beam power of 28 kW can be extracted with minimum divergence angle of 2.2 degree. When the beam energy is 20 keV, the maximum beam power of 180 kW can be extracted when divergence angle less than 5 degree. And the beam power is 130 kW with minimum beam divergence angle is 2.2 degree too. The results shown that, the maximum beam power can't got 50 kW with beam energy of 10 keV, but the beam power can achieve 130 kW with beam energy of 20 keV.

INTRODUCTION

In order to support the basic physical research in Institute of Plasma Physics, Chinese Academy of Sciences (ASIPP), a fast ion source was needed. The desired fast ions with beam energy of 10-20 keV, beam power of 50 kW with beam duration of 2 seconds. A Ne⁺ beam system was designed based on the R&D experiences of high power neutral beam injector on Experimental Advanced Superconducting Tokamak (EAST) [1-7].

The ion beam system contains a Ne⁺ beam source, vacuum vessel, calorimeter, power supply system, water cooling system, control system and gas pumping system. The Ne⁺ beam source was designed and the beam performance was simulated. The preliminary simulation results were presented in this manuscript.

THE Ne⁺ BEAM SOURCE

The Ne⁺ beam source contains a hot cathode plasma generator and an accelerator with three electrodes. The schematic map of beam source is shown in Fig. 1. The designed parameters of the beam source are shown in Table 1. The plasma generator has a rectangle cross

section arc chamber with dimension of 400 mm × 400 mm × 300 mm (W×L×H). There are three lines of permanent magnets installed on the back electron dump plate and 36 lines on the arc chamber body to form axial line-cusp configuration. Each Sm-Co permanent magnet has the magnet intensity of 3500G, and can form a large magnetic-free-area region to generate plasma. In the opposite direction of accelerate grids, 16 pure tungsten filaments are installed near the back electron plate, which to provide sufficient primary electrons. The filaments are made of pure tungsten with hairpin shape and each of them is 160 mm long with the diameter of 1.5 mm. The multiple slit type apertures are used in the accelerator system, which have the transparence of 60%. Each layer of the two accelerator grids have 28 rails, which has cavity structure and made of molybdenum.

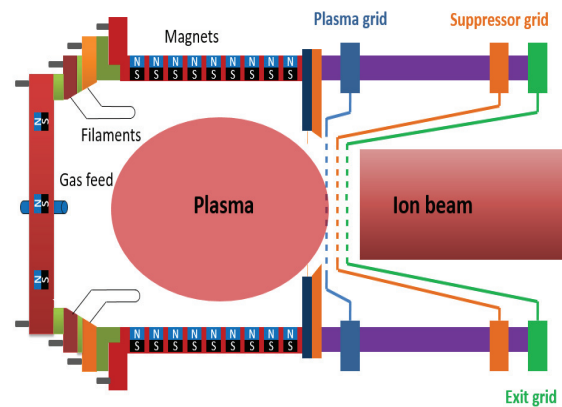


Figure 1: Schematic of high current ion source.

Table 1: The Designed Parameters of Beam Source

Source Species	Ne ⁺
Source type	Hot cathode
Beam energy	10-20keV
Beam power	50 kW
Beam duration	2s
Beam cross section	250 mm × 250 mm
Number of accelerator	3
Extraction sort	Multi-slot
Transparence	0.6
Divergence angle	Less than 5°

*Work supported by National Natural Science Foundation of China (Contract No. 11675215, 11575240, 11675216)
[#]xieyh@ipp.ac.cn

THE ACCELERATOR OF BEAM SOURCE

The accelerator system is slot type and has a three stage electrode grids, which are plasma grid, suppressor grid and exit grid, which is shown in Fig. 2. Each stage has two modules, and each module has 14 rails and which is made of molybdenum. The plasma grid and exit grid are circular cross type with diameter of 3.6 mm. The gradient grid is water-drop cross type with width of 4.57 mm and depth of 5.99 mm. The distance between two rails is 5.4 mm and the accelerator has a beam transparency of 60%. The gap between plasma grid and suppressor grid is 10.67 mm, between suppressor grid and exit grid is 1.73 mm. The extraction area is confine in 250 mm × 250mm with the mask plate.

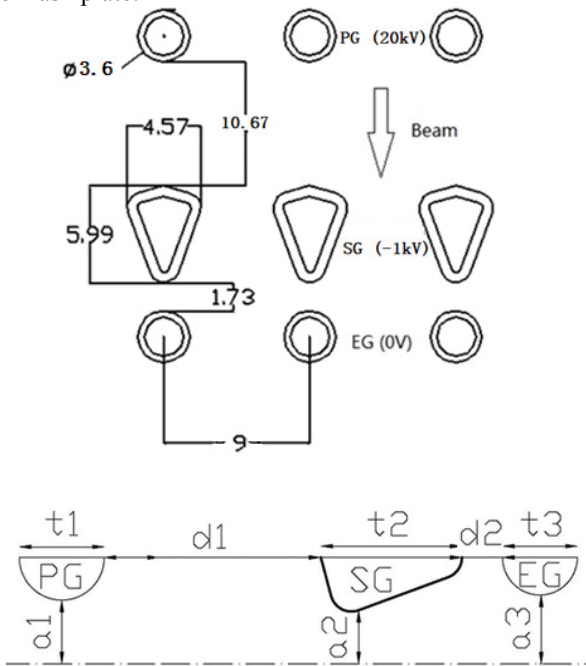


Figure 2: Schematic map of accelerator for the Ne beam source.

The performances of beam source, such as beam divergence angle, extracted beam current, beam profile are simulated. The simulation picture of accelerator grids is shown in Fig. 2 too.

PRELIMINARY SIMULATION RESULTS OF BEAM SOURCE

The beam divergence angle and beam power were simulated with different beam energy of 10 keV and 20 keV. The results are shown in Fig. 3 and Fig. 4, respectively. From Fig. 3, it can be seen that, the beam power increased from 15 kW to 40 kW with the beam divergence angle less than 5 degree. The beam power is around 27 kW when the beam in the optimum beam divergenc angle of 2.25 degree. The results also shown that, the beam power can not achieve 50 kW with beam energy of 10 keV.

The Fig. 4 tells us the beam power with different divergence angle with beam energy of 20 keV. The beam power increased from 85 kW to 188 kW when the beam

divergence angle changed from 5 degree to 2.25 degree and then 5 degree too. The beam power is much larger than the beam with 10 keV, which can meets the requirement of 50 kW extracted beam power. The beam power is around 130 kW with the optimum beam divergence angle of 2.25 degree.

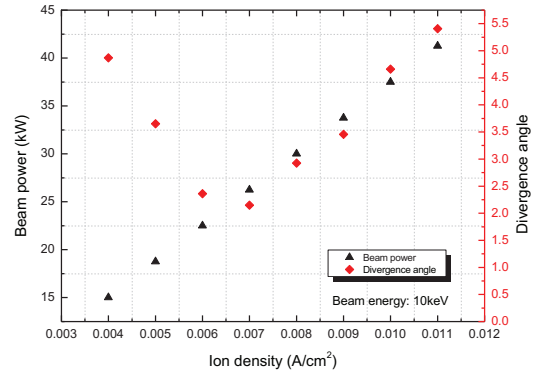


Figure 3: The beam power and beam divergence angle as a function of ion density with beam energy of 10 keV.

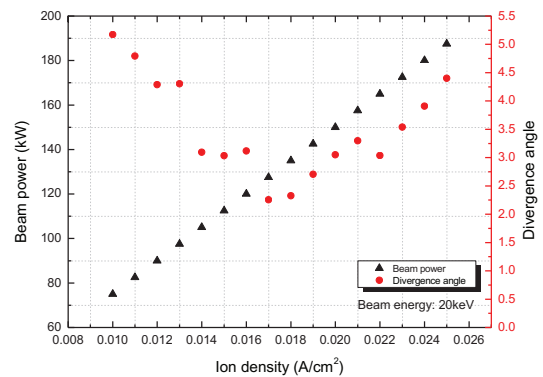


Figure 4: The beam power and beam divergence angle as a function of ion density with beam energy of 20 keV.

Consider the beam divergence angle is very high, the beam profile during the beam transmission was simulated too. In order to decrease the beam divergence angle, the beam extract surface was simulated with two tructures, which is shown in Fig. 5. The left one is the two pieces of grids are arranged in the same plane, and the right one is the two pieces of grids are arranged with angle of 1 degree, which can form the mechanical focus.

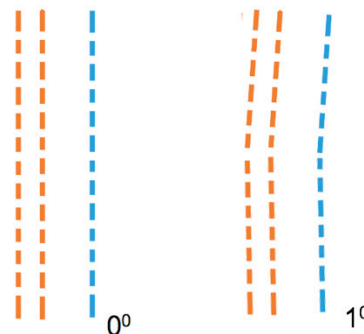


Figure 5: Layout of two pieces of accelerator.

Content from this work may be used under the terms of the CC BY 3.0 licence (© 2018). Any distribution of this work must maintain attribution to the author(s), title of the work, publisher, and DOI.

The beam system was designed with length of 150 cm and the beam will injected into the plasma in the position of 180 cm. The beam profiles in the position of 50 cm, 100 cm, 150 cm and 180 cm downstream the exit grid were simulated with two structures. The results are shown in Fig. 6 and Fig. 7. It can be seen from Fig. 6 that, the beam power profile is much smooth during the beam transmission, it is good to achieve uniform beam power among the beam extraction area. But the beam power is not uniform when the accelerator has a angle, which is

shown in Fig. 7. The beam is overlaped and like Gaussian distribution. The power density in the middle is about two times compare with it in the mergin of beam. In this case, the beam loss is smaller compare with the accelerator with flat sturcture. The beam transmission efficiency with minimum divergence angle of 2.25 degree and beam energy of 20 keV is simulated and shown in Fig. 8. When the beam transmitted into the plasma, the beam transmission efficiency is estimated about 88% for flat accelerator and about 93% for the accelerator with angle.

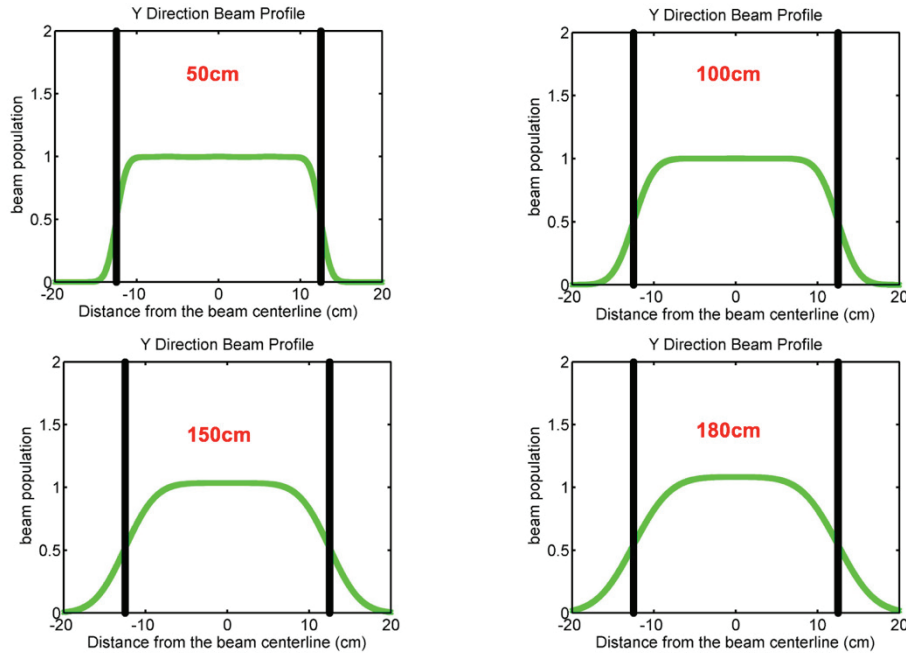


Figure 6: Beam profiles in differnt postions when accelerator grid arranged in the same plane.

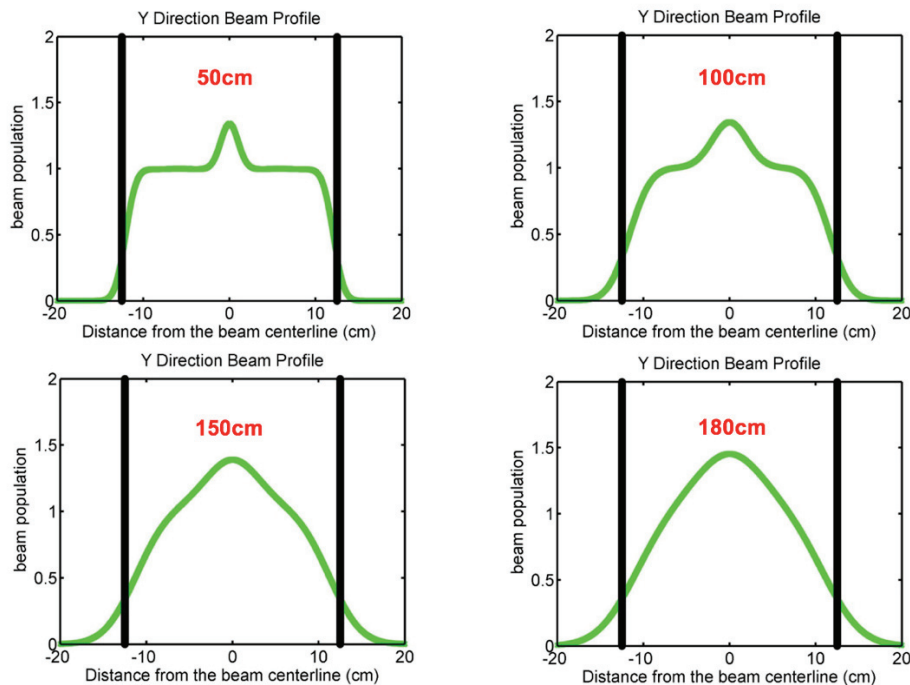


Figure 7: Beam profiles in differnt postions when the accelerator grids arranged with angle of 1 degree.

Content from this work may be used under the terms of the CC BY 3.0 licence (© 2018). Any distribution of this work must maintain attribution to the author(s), title of the work, publisher, and DOI.

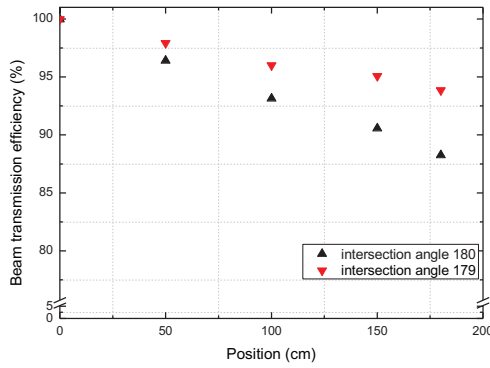


Figure 8: Beam transmission efficiency with two different structures.

STRUCTURE DESIGN OF ACCELERATOR FOR Ne⁺ BEAM SOURCE

The three layers of accelerator has the same structure. Each layer of accelerator contains grids, holds, grid support, side plate and water cooling pipes, which shown in Fig. 9. The module of grids is installed on the grid support can be adjusted to flat or has a angle. The cooling water is connected with the cooling pipes and goes through the inner pipe of each grid, which can takes away the heat deposited on the grids.

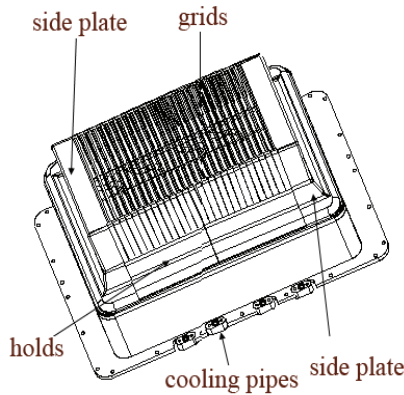


Figure 9: Structure of accelerator for Ne beam source.

CONCLUSION

An Ne⁺ beam source with hot cathode plasma generator and three electrodes accelerator is designed to supply the fast ions for basic physical research. The designed beam power is 50 kW and beam cross section is

250 mm × 250 mm. The beam energy was designed from 10 keV to 20 keV.

The beam divergence angle, beam power and beam profiles were simulated with beam energy of 10 keV and 20 keV. The results shown that the maximum beam power of 40 kW and 180 kW can be extracted when the divergence angle less than 5 degree with beam energy of 10 keV and 20 keV, respectively. The beam power is 28 kW and 130 kW can be extracted with minimum divergence angle of 2.25 degree when the beam energy is 10 keV and 20 keV, respectively. The divergence angle can be decreased by fold the accelerator grids. But the beam power density will change to Gaussian distribution.

Under this design, the maximum beam power can not achieve 50 kW with beam energy of 10 keV, but the beam power can achieve 130 kW with beam energy of 20 keV.

REFERENCES

- [1] Y. X. Wan, J. G. Li and P. D. Weng, “First engineering commissioning of EAST tokamak”, Plasma. Sci. Technol. 8, 253 (2006).
- [2] C. D. Hu and NBI Team, “Conceptual Design of Neutral Beam Injection System for EAST”, Plasma Sci. Technol. 14, 567 (2012).
- [3] Y. H. Xie, C. D. Hu, S. Liu, Y. L. Xie, Y. J. Xu, L. Z. Liang, C. C. Jiang, P. Sheng, Y.M. Gu, J. Li, Z. M. Liu, “R&D progress of high power ion source on EAST-NBI”, Plasma. Sci. Technol. 13, 541 (2011).
- [4] C. D. Hu, Y. H. Xie and NBI Team, “The Development of a Megawatt-Level High Current Ion Source”, Plasma Sci. Technol. 14, 75 (2012).
- [5] C. D. Hu, Y. H. Xie, S. Liu, Y. L. Xie, C. C. Jiang, S. H. Song, J. Li and Z. M. Liu, “First plasma of megawatt high current ion source for neutral beam injector of the experimental advanced superconducting tokamak on the test bed”, Rev. Sci. Instrum. 82, 023303 (2011).
- [6] Y. H. Xie, C. D. Hu, S. Liu, J. Li, Y.J. Xu, Y.Q. Chen, L.Z. Liang, Y.L. Xie, C.C. Jiang, P. Sheng, Z.M. Liu, “Upgrade of accelerator of high current ion source for EAST neutral beam injector”, Fusion Eng. Des., 100,265(2015)
- [7] Y.H. Xie, C.D. Hu, H.W. Zhao, NBI Team. “Analysis of ion beam optics of tetrode accelerator for neutral beam injector on the experimental advanced superconducting Tokamak”, Nucl. Instrum. Meth. A, 791,22 (2015).

JINR HEAVY ION ACCELERATORS APPLICATION FOR SEE TESTING IN ISDE

V. S. Anashin[†], P. A. Chubunov, Branch of JSC United Rocket and Space Corporation - Institute of Space Device Engineering (ISDE), Moscow, Russia

V. A. Skuratov, S.V. Mitrofanov, Joint Institute for Nuclear Research (JINR), Dubna, Russia

Abstract

Thousands satellites and spacecrafts are launched worldwide every year. All of them, without exception, are exposed to space ionizing radiation. The radiation consists of galactic cosmic rays, solar energetic particles, as well as electrons and protons from Earth's radiation belts. Radiation environment results in upsets and even failures of spacecraft system electronics. To ensure mission success, electronic engineers must perform a series of operations to validate the radiation hardness level of electronic components used. For modern electronic parts the most hazardous upsets and failures are due to the impact of single high-energy particles. Such radiation effects are called as SEEs – Single Event Effects – since undesirable event is induced by a single particle strike. The spectrum of space radiation environment is extremely wide, but as the measure for the single particle environment with particular energy Liner Energy Transfer (LET) can be used. Ground tests are unable to reproduce the space environment, yet heavy-ion accelerators allow us to create experimental environment simulating LETs similar to space radiation. LET spectrum is from a few MeV cm/mg up to one hundred MeV cm/mg. The goal of SEE tests is to obtain the dependence of SEE cross-section from LET for each type of effects (upsets and failures). To ensure energy deposition in a sensitive region and register SEEs, particles with at least 30-40 μm range in Device Under Test (DUT) die are required. To meet the test requirements, the wide range of ions – from O to Bi and energies from 3 MeV/nucleon – shall be used, while a lid should be removed from a DUT. A number of devices, due to their design, require the longer-range, and hence the higher-energy ions, while maintaining the requirements for LET. To meet the needs of Russian space equipment designers and manufacturers of integrated circuits and other semiconductor devices, ISDE in collaboration with JINR have created the unique in Russia SEE Test Facilities. In this paper, we introduce readers the test facilities specifications, ion beam formation and monitoring techniques, certified methods for ion energy and fluence measurement and technical means for their implementation. The paper presents statistics on the use of test facilities, directions for their further development and upgrade.

GENERAL INFORMATION ABOUT TEST FACILITIES

Since 2010, we have been acting in the field of SEE testing. Up to now, 3 test facilities on the basis of U-400 and

U-400M accelerators that provide all types of SEE radiation tests of electronic components of any functional class are in operation. The test facilities allow to irradiate DUTs in the following test environments: range of ions from C to Bi; initial energy from 3 to 60 (for light ions) MeV/A; LETs (Si) from 1 to 100 MeV \times cm²/mg; ranges (Si) from 0.03 to 2 mm (depending on the energy); adjustable fluxes from 10 to 10⁵ particles/(cm² \times s); irradiation area up to 200 \times 200 mm; beam nonuniformity less than 10 % [1]. The general structure of SEE Test Facilities is shown in Fig. 1. Equipment in green belongs to the heavy ion accelerator, and all others have been designed especially for SEE testing.

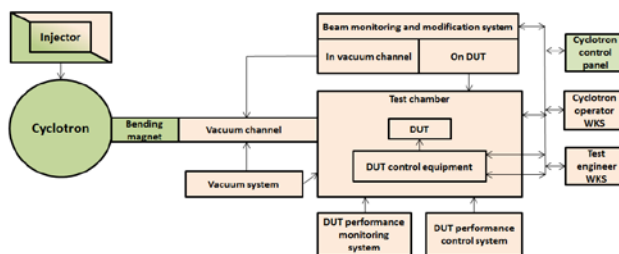


Figure 1: General structure of SEE Test Facilities based on ion sources.

In Fig. 2 we can see a layout of a beam transfer channel with a large number of tools which are used for beam formation, monitoring and measurement. To provide the high accuracy of the beam in a test chamber (on DUT) we use multistage control of the beam parameters [2].

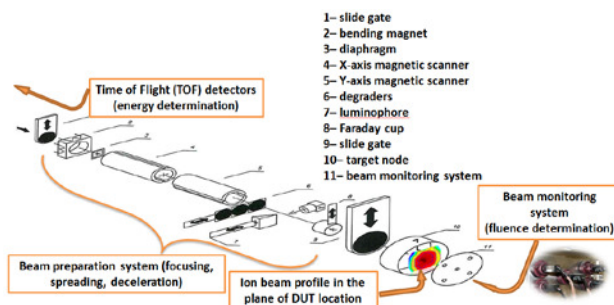


Figure 2: Beam transfer channel layout.

SEE tests are considered to be one of the most expensive parts of ground testing of spacecraft electronic equipment. And the largest expenses are related to the ion accelerators operation. Thus, it is essential to optimize the test procedure. A key advantage of our test facility is a

[†] npk1@niikp.org

Content from this work may be used under the terms of the CC BY 3.0 licence (© 2018). Any distribution of this work must maintain attribution to the author(s), title of the work, publisher, and DOI.

large beam area that allows several items to be irradiated simultaneously. This provides the high levels of beam fluxes, which in turn allows the fast fluence production corresponding to the test standards. Also, test engineers to reduce the time for vacuum pumping must comply with the regulations of vacuum equipment operations for eliminating the extra gassing sources. Large amounts of test equipment are recommended to be preliminary outgassed in a special chamber.

To obtain a large irradiation area considering the specific structure and length of each test facility several beam modification systems have been designed. The beam spot from the heavy ion accelerator goes through two magnet scanners, which in turn move the beam in two directions (see Fig. 3). Using this technique, we scan the area in a vacuum chamber and seed the irradiation area with the heavy ions with low nonuniformity. For different facilities we use different scan frequency in X- and Y-axis and different current waveforms (saw-shape, sinus). The maximum amplitude of magnetic fields is about 300-350 Gs.

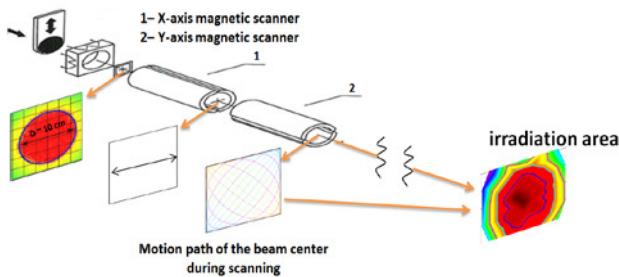


Figure 3: Beam modification system.

Examples of beam profile are shown in Fig. 4.

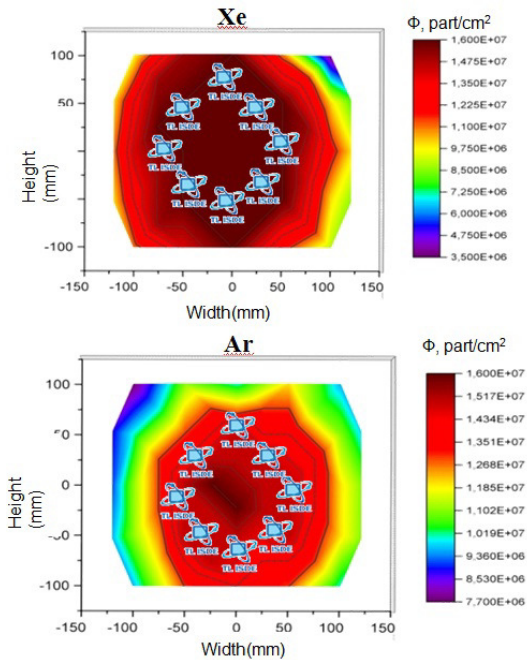


Figure 4: Typical shapes of ion beam profile & best location of DUTs.

CERTIFIED BEAM CONTROL TECHNIQUES

The main parameters of the heavy ions during SEE testing are the beam fluence and LET. To calculate fluence we use old and reliable method of holes calculation on irradiated track detector. Also, we have the scintillator-based detection system (orange spots in Figs. 5, 6), but it is used only for estimation of fluence value. To meet the dosimetry support requirement of each irradiation we put the track detectors nearby the DUT (Figs. 5,6). The fluence evaluation method is quasi-online (online: scintillators, off-line: track detectors), and yet it shows the excellent accuracy. The online detectors are used to determine the moment for stopping the irradiation after the fluence reaches $>10^7$ (3×10^5 for Power MOSFETs). To obtain a precise value, the track detectors placed close to the DUTs are used (Fig. 7). The measurement method is based on the calculation of etched holes formed due to the differences in etching rates of the damaged and undamaged areas of the plastic track detector after its irradiation with heavy ions, and then dividing this amount by the area of field on which holes were calculated.

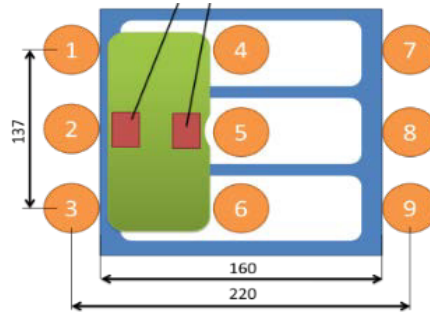


Figure 5: Track detectors (TD) mounting.

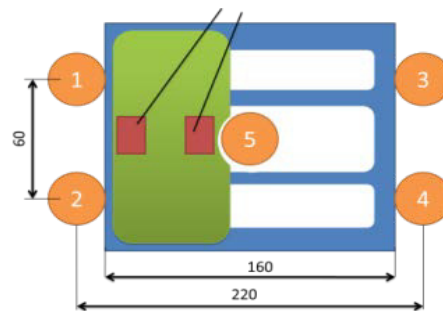


Figure 6: TD irradiation.



Figure 7: Holes calculation.

To obtain the LET value we need to know the ion energy and after that it is easy to calculate LET using SRIM software. For energy measurements we use Time of Flight (TOF) technique and system based on scintillation detectors and high resolution electronics. Schematic of TOF technique is shown in Fig. 8. TOF technique based on one-to-one correspondence between the kinetic energy and the particle velocity. During the test campaign, energy measurements are performed once after each ion ejection (may be repeated if required). This method provides energy determination with up to 2% accuracy.

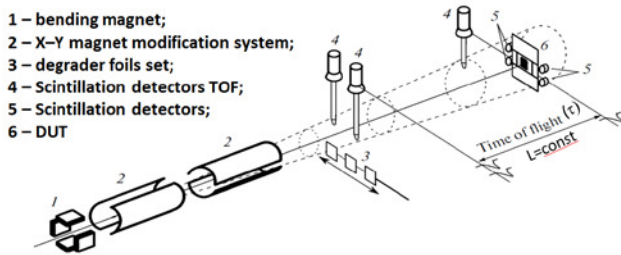


Figure 8: The energy measurements.

An important feature of the high-energy facility is the opportunity to use special thin aluminum or nickel stacked degrader in the beam line (Fig. 9). The use of degraders allows us to change the ion energy, and therefore, the ion LETs and ranges without changing its species (Fig. 10). As a result, we can obtain a number of LETs while irradiating with one ion. Thus, using degraders with all ion species, we obtain quasi-continuous LET spectrum in almost the whole required range (Fig. 11).

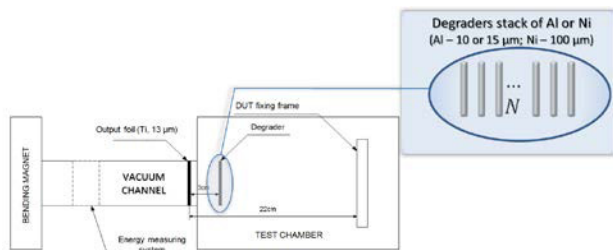


Figure 9: Special features of beam parameters determination for the High-Energy Test Facilities.

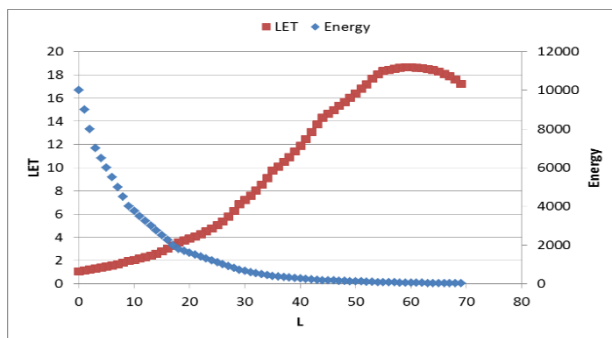


Figure 10: An example of dependence between ion energy, LET and range.

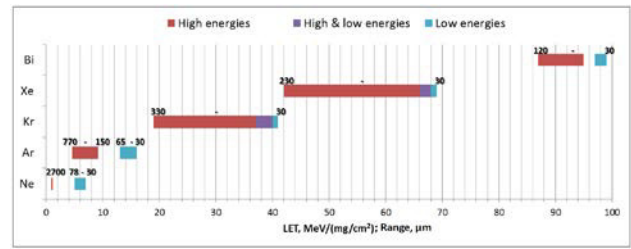


Figure 11: Quasi-continuous LET spectrum at the high-energy facility using degraders – LET & Range for different type of ions.

CONCLUSION

The ISDE & JINR collaboration have created and now successfully operates the unique in Russia test facilities for certification of microelectronics for space applications. Their application allow us to perform the comprehensive single event effect tests and failure analysis, and ensure the fault- and failure-free operation of spacecraft electronics in harsh space radiation environment. Since 2010, more than 4200 parts of electronic components for space application have been tested. To meet the growing demands of test customers, we do our best for the test facilities development and enhancement. We are looking forward to cooperating fruitfully in the field of SEE testing and space device engineering.

ACKNOWLEDGEMENTS

The authors thank Aleksey Konyukhov from ISDE for his assistance in translating the article into English.

REFERENCES

- [1] V. S. Anashin, P. A. Chubunov, S. A. Iakovlev, A. E. Koziukov, G. G. Gulbekyan, V. A. Skuratov, and S. V. Mitrofanov, "Typical Facilities and Procedure for Single Event Effects Testing in Roscosmos" in *Proc. 15th European Conference on Radiation and Its Effects on Components and Systems (RADECS 2015)*, Moscow, Russia, Sep. 2015, paper DW-14, pp. 382-387.
- [2] V.S. Anashin, P.A. Chubunov, S.V. Mitrofanov, G.A. Protopopov, V.A. Skuratov, and Yu.G. Teterev, "Estimation of Heavy Ion Beam Parameters During Single Event Effects Testing", in *Proc. 6th Int. Beam Instrumentation Conf. (IBIC'17)*, Grand Rapids, MI, USA, Aug. 2017, paper MOPCF10, pp. 94-97, ISBN: 978-3-95450-192-2, doi:10.18429/JACoW-IBIC2017-MOPCF10

List of Authors

Bold papercodes indicate primary authors; ~~crossed-out~~ papercodes indicate 'no submission'

— A —			
Amemiya, N.	FRXAA01	Chen, W.L.	WEYAA01
Anashin, V.S.	THOEA01	Chubunov, P.A.	THOEA01
Andrighetto, A.	MOYAA02 , THYAA01	Cogan, S.	MOYAA01
Antoine, S.	WE0AA01	Compton, C.	MOYAA01
Antonini, P.	MOYAA02	Comunian, M.	MOYAA02 , THOAA01
Antonio, A.	THOAA01	Cong, Y.	WEPB03
Ao, H.	MOYAA01	Conway, Z.A.	TUOPA01
Apel, P.Yu.	WEOXA01	Corradetti, S.	MOYAA02 , THYAA01
Arai, H.	FRXAA01	Cronert, T.	WEZAA01
Aulenbacher, K.	WEOYA02	Cui, Y.	MOPB07
		Curtin, J.	MOYAA01
— B —		— D —	
Back, B.	TUXAA01	Dalesio, L.R.	MOYAA01
Baggemann, J.	WEZAA01	Dantsuka, T.	TUYAA01
Bakulin, M.I.	TH0CA01	Davidson, K.D.	MOYAA01
Ballan, M.	THYAA01	de Ruvo, L.	MOYAA02
Baltador, C.	MOYAA02 , THOAA01	Delahaye, P.	TUYBA01
Barth, W.A.	WEOYA02	Denisov, G.G.	TH0CA01
Bashevoy, V.	WEOXA01	Di Marco, V.	THYAA01
Basten, M.	WEOYA02	Dickerson, C.	TUXAA01 , TUZCA01
Battisson, S.T.	MOOYA01	Dixon, K.	MOYAA01
Bechtold, A.	TUXAA03	Dmitriev, S.N.	WEXAA01
Beeckman, W.	WE0AA01	Dmitriev, S.N.	MOOXA01
Beher, S.	MOYAA01	Doege, P.-E.	WEZAA01
Bekhterev, V.	TUOXA01 , WEOXA01	Dou, W.P.	MOZAA01 , MOPB05 , WEYAA01
Bellan, L.	MOYAA02 , THOAA01	Du, H.	MOPB16 , WEPB03 , WEPB08 , WEPB12
Bellato, M.A.	MOYAA02	Du, X.	WE0AA02
Benini, D.	MOYAA02	Du, Z.	WE0AA03
Bermudez, J.	MOYAA02	Dziuba, F.D.	WEOYA02
Bilbrough, D.G.	TUXAA01		
Bisoffi, G.	MOYAA02	— E —	
Bockwinkel, J.A.	MOOYA01	Efremov, A.A.	TUOXA01
Böhm, S.	WEZAA01	Eremeev, A.G.	TH0CA01
Bogdashov, A.A.	TH0CA01		
Bogomolov, S.L.	MOOXA01 , TUOXA01 , WEOXA01	— F —	
Bondarchenko, A.E.	TUOXA01	Facco, A.	MOYAA01 , MOYAA02
Borgna, F.	THYAA01	Fagotti, E.	MOYAA02
Borisov, O.N.	WEOXA01	Fang, X.	MOPB05 , MOPB10 , MOPB15 , TUZAA02
Bortolato, D.	MOYAA02	Favaron, P.	MOYAA02
Brückel, Th.	WEZAA01	Feng, Y.C.	TUZAA02
Bultman, N.K.	MOYAA01	Ferrari, L.	MOYAA02 , THOAA01
Busch, M.	WEOYA02	Forest, F.	WE0AA01
Bykov, Yu.V.	TH0CA01	Franko, J.	WEOXA01
		Fu, Q.	MOZAA01
— C —		Fujimaki, M.	TUYAA01 , TUZAA01
Calabretta, L.	TUOZA01	Fujimoto, T.	FRXAA01
Calderolla, M.	MOYAA02	Fujita, T.F.	FRXAA01
Cao, Y.	MOPB10 , MOPB15 , TUZAA02	Fukunishi, N.	TUYAA01 , TUZAA01
Casagrande, F.	MOYAA01	Furukawa, T.	FRXAA01
Cavenago, M.	MOYAA02 , THOAA01		
Chai, W.P.	WEPB15	— G —	
Chen, J.	MOYAA01	Galatà, A.	MOYAA02 , THOAA01
Chen, R.F.	MOPB15		

Content from this work may be used under the terms of the CC BY 3.0 licence (© 2018). Any distribution of this work must maintain attribution to the author(s), title of the work, publisher, and DOI.

Galtarossa, F.	MOYAA02
Gan, P.P.	MOZAA01
Ganni, V.	MOYAA01
Ganshyn, A.	MOYAA01
Gao, D.Q.	MOZBA01, MOPB04, MOPB07
Gao, J.	MOPB04
Gao, S.L.	MOZAA01
Gettmann, V.	WE0YA02
Giacchini, M.G.	MOYAA02
Gibson, P.E.	MOYAA01
Gikal, B.	MO0XA01, WE0XA01
Glasmacher, T.	MOYAA01
Glyavin, M.Yu.	TH0CA01
Graham, B.W.	MO0YA01
Gramegna, F.	MOYAA02
Groening, L.	TUXAA03, WE0AA02
Gulbekyan, G.G.	MO0XA01, WEXAA01, WE0XA01
Guo, H.	WEPB06
Guo, J.W.	MOPB10, TUZAA02
Guo, Y.H.	MOPB05
Gutberlet, T.	WEZAA01

— H —

Hao, Y.	MOYAA01
Hara, Y.	FRXAA01
Hasebe, H.	TUYAA01
He, M.	THXAA01
He, T.	MOPB08, WEPB04, WEPB10, WEPB13
He, Y.	MOZAA01, WEYAA01, WE0YA03, WEPB03, WEPB06, WEPB13
Heighway, J.K.	MO0YA01
Heilmann, M.	WE0YA02
Hendricks, M.R.	TUZCA01
Higurashi, Y.	TUYAA01, TUZAA01
Hodges, L.	MOYAA01
Hoffman, C.R.	TUXAA01
Holland, K.	MOYAA01
Holoptsev, V.V.	TH0CA01
Hosoyama, K.	MOYAA01
Hseuh, H.-C.	MOYAA01
Hu, C.D.	THODA01
Hu, X.J.	WE0AA03
Huang, W.	TUZAA02
Huang, Y.Z.	MOPB07
Hussain, A.	MOYAA01
Hyun, M.O.	WE0YA01

— I —

Ikegami, M.	MOYAA01
Ikezawa, E.	TUYAA01
Ikoma, N.	TUYAA01
Imao, H.	TUYAA01
Ivanenko, I.A.	MO0XA01, WE0XA01
Ivanov, G.N.	MO0XA01
Iwata, Y.	FRXAA01

— J —

Jehanno, P.J.	WE0AA01
Jia, H.	MOPB05, WEYAA01, WE0YA03
Jiang, P.	MOPB05
Jiang, T.C.	WEPB06
Jiang, X.L.	MOPB03
Jing, L.	MOPB05, WE0AA03, WEPB03
Jivkov, P.	WE0AA01
Jo, Y.W.	WE0YA01
Jones, S.	MOYAA01
Jung, H.C.	WE0YA01

— K —

Kalagin, I.V.	MO0XA01, WEXAA01, WE0XA01
Kamigaito, O.	TUYAA01, TUZAA01
Kanemura, T.	MOYAA01
Karamyshev, O.	TU0ZA01
Kazarinov, N.Yu.	MO0XA01, WE0XA01
Kelly, M.P.	MOYAA01, TU0PA01
Kidera, M.	TUYAA01
Kim, Y.	WE0YA01
Knudsen, P.	MOYAA01
Komiyama, M.	TUYAA01
Konev, N.N.	TU0XA01
Kong, Q.Y.	WEPB03, WEPB08, WEPB12
Kopelovich, E.A.	TH0CA01
Kürzeder, T.	WE0YA02
Kumagai, K.	TUYAA01, TUZAA01

— L —

Laxdal, R.E.	MOYAA01
Lebedev, N.	TU0XA01
Leray, M.J.	WE0AA01
LeTourneau, J.	MOYAA01
Li, C.X.	WEPB04
Li, H.P.	MOZAA01
Li, J.	THODA01
Li, J.	WEZAA01
Li, J.Q.	MOPB10, TUZAA02
Li, J.Q.	MOPB07
Li, L.B.	MOPB10, TUZAA02
Li, L.X.	TUZAA02
Li, X.N.	WEPB03, WEPB08, WEPB12
Li, X.X.	MOPB15
Li, Z.S.	WEPB03, WEPB08, WEPB12
Li, Z.X.	WEPB06
Liang, Y.	TH0BA01
Lidia, S.M.	MOYAA01
Linardakis, P.	MO0YA01
Litvinov, Yu.A.	MOXAA01
Liu, S.	MOZAA01
Liu, S.H.	WEYAA01
Liu, W.P.	TUXAA02
Liu, X.J.	MOPB05
Liu, Y.	MOPB04
Lobanov, N.R.	MO0YA01
Loginov, V.N.	TU0XA01

Lombardi, A. MOYAA02
 Lu, L. MOPB05, MOPB08, WE0YA03,
 WEPB04, WEPB10, WEPB13
 Lu, W. MOPB10, TUZAA02
 Lu, W. MOPB05, MOPB15
 Lu, Y.R. MOZAA01, WEPB03
 Luchinin, A.G. TH0CA01
 Luo, J. TU0ZA02

— M —

Ma, B.H. MOPB10, MOPB15
 Ma, H.Y. TUZAA02
 Ma, L.Z. MOZBA01, MOPB02, TUZAA02
 Ma, W. MOPB05, MOPB08, WE0YA03
 Ma, X. MOXAA01
 Ma, Y.M. TUZAA02
 Machicoane, G. MOYAA01
 Maggiore, M. MOYAA02
 Maie, T. TUYAA01
 Maier, M.T. TUXAA03
 Malloch, I.M. MOYAA01
 Manzolaro, M. MOYAA02
 Mao, L.J. MOZBA01, MOPB16
 Mao, R.S. MOZBA01
 Marcato, D. MOYAA02
 Marchi, T. MOYAA02
 Marti, F. MOYAA01
 Marzaro, G. THYAA01
 Mastinu, P. MOYAA02
 Matsuba, S. FRXAA01
 Mauerhofer, E. WEZAA01
 Maus, J.M. TUXAA03
 Mei, E.M. TH0BA01
 Mei, E.M. MOPB02
 Meng, J. MOZBA01, WEPB03
 Meusel, O. WEZAA01
 Miller, S.J. MOYAA01
 Milpied, X. WE0AA01
 Mironov, V. TU0XA01, WE0XA01
 Miski-Oglu, M. WE0YA02
 Mitrofanov, S.V. WE0XA01, TH0EA01
 Mizushima, K. FRXAA01
 Modanese, P. MOYAA02
 Moisis, M.F. MOYAA02, TH0AA01
 Momozaki, Y. MOYAA01
 Monetti, A. MOYAA02
 Montis, M. MOYAA02
 Morozkin, M.V. TH0CA01
 Morris, D.G. MOYAA01
 Murakami, T. FRXAA01
 Mustapha, B. TUXAA01, TU0PA01, WEYAA02

— N —

Nagase, M. TUYAA01
 Nagatomo, T. TUYAA01, TUZAA01
 Nakagawa, T. TUYAA01, TUZAA01
 Nakamura, M. TUYAA01
 Neri, L. TU0ZA01

Ni, D.S. MOPB02, TH0BA01
 Nignol, C. WE0AA01
 Noda, K. FRXAA01
 Nolen, J.A. WEYAA02

— O —

Obana, T. FRXAA01
 Oganessian, Y.T. MO0XA01, WEXAA01
 Ogitsu, T. FRXAA01
 Ohnishi, J. TUYAA01, TUZAA01
 Okuno, H. TUYAA01
 Orikasa, T. FRXAA01
 Osipov, N.F. MO0XA01
 Ostroumov, P.N. MOYAA01, TU0PA01
 Ou, X.J. TH0BA01
 Ozeki, K. TUYAA01

— P —

Palmieri, A. MOYAA02
 Pan, F. WEPB06
 Pavinato, S. MOYAA02
 Pedretti, D. MOYAA02
 Pisent, A. MOYAA02, TH0AA01
 Plastun, A.S. TU0PA01
 Plotnikov, I.V. TH0CA01
 Podlech, H. WEZAA01, WE0YA02
 Poggi, M. MOYAA02
 Popeko, A.G. WE0AA01
 Popielarski, J.T. MOYAA01
 Popielarski, L. MOYAA01
 Prestemon, S. MOYAA01
 Prete, G.P. MOYAA02
 Priller, J. MOYAA01

— Q —

Qian, C. MOPB15
 Qiao, Y. MOPB03
 Qin, Y.S. WEYAA01

— R —

Realdon, N. THYAA01
 Ren, H.T. MOYAA01
 Rifuggiato, D. TU0ZA01
 Rimmler, M. WEZAA01
 Roncolato, C.R. MOYAA02
 Rossignoli, M. MOYAA02
 Rubin, A. WE0YA02
 Russo, T. MOYAA01
 Rucker, U. WEZAA01

— S —

Saito, K. MOYAA01
 Sakamoto, N. TUYAA01, TUZAA01
 Saotome, N.S. FRXAA01
 Saraya, Y. FRXAA01
 Sarchiapone, L. MOYAA02
 Sato, S. FRXAA01
 Savard, G. TUXAA01, TUZCA01, WEYAA02
 Scarpa, D. MOYAA02

Content from this work may be used under the terms of the CC BY 3.0 licence (© 2018). Any distribution of this work must maintain attribution to the author(s), title of the work, publisher, and DOI.

Schnase, A. **WEOYA02**
 Schwarz, M. **WEZAA01, WEOYA02**
 Scott, R.H. **TUZCA01**
 Semin, V.A. **MOOXA01, WEOXA01**
 Shangguan, J.B. **MOPB04**
 Shen, G.D. **MOPB16, WEPB03**
 Shen, Z. **TUZAA02**
 Shi, J. **WEPB15**
 Shi, L.B. **WEOYA03, WEPB10**
 Shirai, T. **FRXAA01**
 Shmelev, M.Yu. **THOCA01**
 Skuratov, V.A. **WEOXA01, THOEA01**
 Sobolev, D.I. **THOCA01**
 Sokolov, E.V. **THOCA01**
 Soluyanova, E.A. **THOCA01**
 Stanley, S. **MOYAA01**
 Stöhlker, T. **MOXAA01**
 Su, Y.W. **MOZBA01**
 Suda, K. **TUYAA01**
 Sun, L.P. **MOPB05, MOPB08, WEOYA03, WEPB10**
 Sun, L.T. **MOZBA01, MOPB05, MOPB10, MOPB15, TUZAA02, WEOYA03**

— T —

Tai, E.M. **THOCA01**
 Takayama, S. **FRXAA01**
 Tan, Q.Y. **MOZAA01**
 Tan, T. **WEPB06**
 Tan, Y.L. **MOPB07**
 Tansho, R. **FRXAA01**
 Tasset-Maye, O. **WEOAA01**
 Tikhomirov, A. **WEOXA01**
 Troitsky, M.M. **THOCA01**
 Tsifakis, D. **MOOYA01**
 Tsvetkov, A.I. **THOCA01**
 Tunningley, T. **MOOYA01**

— U —

Uchiyama, A. **TUYAA01, TUZAA01**
 Utyonkov, V.K. **WEOAA01**

— V —

Voigt, J. **WEZAA01**
 Vondrasek, R.C. **TUZCA01**

— W —

Wang, C. **MOZAA01**
 Wang, H. **MOPB10, MOPB15**
 Wang, H.N. **WEPB06**
 Wang, H.N. **WEPB03**
 Wang, K.D. **WEPB03, WEPB08, WEPB12**
 Wang, X.W. **MOPB03**
 Wang, Y.Y. **MOZBA01**
 Wang, Z. **MOZAA01**
 Wang, Z.J. **MOZAA01, WEYAA01, WEPB03**
 Watanabe, S. **TUYAA01**
 Watanabe, T. **TUYAA01**
 Watanabe, Y. **TUYAA01**

Weij, J. **MOYAA01**
 Wei, Y. **MOPB05, WEOAA03, WEPB03**
 Wiseman, M. **MOYAA01**
 Wu, B.M. **MOPB02, TUZAA02**
 Wu, J.X. **MOZBA01, MOPB15, WEOAA03, WEPB03**
 Wu, Q. **MOZAA01**
 Wu, W. **MOPB02, TUZAA02, THOBA01**

— X —

Xia, J.W. **MOZBA01, WEPB03, WEPB08, WEPB15**
 Xiao, C. **TUXAA03, WEOAA02**
 Xiao, G.Q. **MOZBA01, FRXBA01**
 Xie, H.M. **WEPB03**
 Xie, W.J. **WEPB03**
 Xie, Y.H. **THODA01**
 Xie, Y.L. **THODA01**
 Xing, C.C. **MOPB08, WEPB04, WEPB10, WEPB13**
 Xiong, P.R. **WEPB06**
 Xu, T. **MOYAA01**
 Xu, X.B. **MOPB08, WEPB04**
 Xu, X.W. **WEPB03, WEPB10**
 Xu, Y. **THODA01**
 Xu, Z. **MOZBA01, MOPB03, WEPB03**

— Y —

Yamada, K. **TUYAA01**
 Yamaguchi, T. **MOXAA01**
 Yamasawa, H. **TUYAA01**
 Yamazaki, Y. **MOYAA01**
 Yang, J.C. **MOXBA01, MOZBA01, MOPB16, WEPB03, WEPB08, WEPB15**
 Yang, L. **MOPB08, WEPB04, WEPB10, WEPB13**
 Yang, W.J. **MOPB02, THOBA01**
 Yang, W.Q. **MOZBA01**
 Yang, Y. **MOPB05, MOPB10, MOPB15, TUZAA02, WEOYA03**
 Yang, Y.Q. **WEPB03**
 Yao, Q.G. **MOZBA01**
 Yaramyshev, S. **WEOYA02**
 Yin, D.Y. **MOPB16**
 Yin, X. **MOZBA01, WEPB03, WEPB08, WEPB12**
 Yuan, Y.J. **MOZBA01, MOPB15, WEOAA03, WEPB03, WEPB08**

— Z —

Zafiroopoulos, D. **MOYAA02**
 Zakalek, P. **WEZAA01**
 Zhai, Y.H. **MOPB05, MOPB10, WEOYA03**
 Zhang, B. **MOZBA01**
 Zhang, C. **WEPB06**
 Zhang, H. **MOPB07**
 Zhang, S. **MOPB07**
 Zhang, W. **MOZBA01**

Zhang, W.H.	TUZAA02	Zhao, Y.T.	TU0YA01
Zhang, X.Z.	MOPB10, MOPB15, TUZAA02	Zheng, S.J.	TH0BA01
Zhang, Y.	WEPB03	Zhou, L.	TH0BA01
Zhang, Y.H.	MOXAA01	Zhou, Z.Z.	MOZBA01
Zhao, H.W.	MOZBA01, MOPB05, MOPB10, MOPB15, TUZAA02, WEYAA01, WEOYA03	Zhu, G.	WEOAA03
Zhao, J.	MOPB04	Zhu, K.	MOZAA01 , WEPB03

Institutes List

AEC

Chiba, Japan

- Arai, H.
- Fujimoto, T.

ANL

Lemont, Illinois, USA

- Back, B.
- Bilbrough, D.G.
- Conway, Z.A.
- Dickerson, C.
- Hendricks, M.R.
- Hoffman, C.R.
- Kelly, M.P.
- Momozaki, Y.
- Mustapha, B.
- Nolen, J.A.
- Savard, G.
- Scott, R.H.
- Vondrasek, R.C.

ASIPP

Hefei, People's Republic of China

- Hu, C.D.
- Li, J.
- Xie, Y.H.
- Xie, Y.L.
- Xu, Y.

CIAE

Beijing, People's Republic of China

- He, M.
- Liu, W.P.

Consorzio RFX

Padova, Italy

- Antonio, A.

Dalian University

Liaoning Province, People's Republic of China

- Luo, J.

FRIB

East Lansing, Michigan, USA

- Ao, H.
- Beher, S.
- Bultman, N.K.
- Casagrande, F.
- Chen, J.
- Cogan, S.
- Compton, C.
- Curtin, J.
- Dalesio, L.R.
- Davidson, K.D.

- Facco, A.
- Ganni, V.
- Ganshyn, A.
- Gibson, P.E.
- Glasmacher, T.
- Hao, Y.
- Hodges, L.
- Holland, K.
- Hseuh, H.-C.
- Hussain, A.
- Ikegami, M.
- Jones, S.
- Kanemura, T.
- Knudsen, P.
- Laxdal, R.E.
- LeTourneau, J.
- Lidia, S.M.
- Machicoane, G.
- Malloch, I.M.
- Marti, F.
- Miller, S.J.
- Momozaki, Y.
- Morris, D.G.
- Ostroumov, P.N.
- Plastun, A.S.
- Popielarski, J.T.
- Popielarski, L.
- Priller, J.
- Ren, H.T.
- Russo, T.
- Saito, K.
- Stanley, S.
- Wei, J.
- Xu, T.
- Yamazaki, Y.

FZJ

Jülich, Germany

- Zakalek, P.

GANIL

Caen, France

- Delahaye, P.

GSI

Darmstadt, Germany

- Barth, W.A.
- Du, X.
- Groening, L.
- Heilmann, M.
- Litvinov, Yu.A.
- Maier, M.T.
- Rubin, A.
- Schnase, A.
- Stöhlker, T.
- Xiao, C.

- Yaramyshev, S.

GYCOM Ltd

Nizhny Novgorod, Russia

- Bakulin, M.I.
- Sokolov, E.V.
- Soluyanov, E.A.
- Tai, E.M.

HIJ

Jena, Germany

- Stöhlker, T.

HIM

Mainz, Germany

- Aulenbacher, K.
- Dziuba, F.D.
- Gettmann, V.
- Kürzeder, T.
- Miski-Oglu, M.

HSRC

Higashi-Hiroshima, Japan

- Matsuba, S.

IAP

Frankfurt am Main, Germany

- Basten, M.
- Busch, M.
- Meusel, O.
- Podlech, H.
- Schwarz, M.

IAP/RAS

Nizhny Novgorod, Russia

- Bogdashov, A.A.
- Bykov, Yu.V.
- Denisov, G.G.
- Ereemeev, A.G.
- Glyavin, M.Yu.
- Holoptsev, V.V.
- Kopelovich, E.A.
- Luchinin, A.G.
- Morozkin, M.V.
- Plotnikov, I.V.
- Shmelev, M.Yu.
- Sobolev, D.I.
- Troitsky, M.M.
- Tsvetkov, A.I.

IBS

Daejeon, Republic of Korea

- Hyun, M.O.
- Jo, Y.W.
- Jung, H.C.
- Kim, Y.

IEK

Jülich, Germany

- Li, J.

IMP/CAS

Lanzhou, People's Republic of China

- Cao, Y.
- Chai, W.P.
- Chen, R.F.
- Chen, W.L.
- Cong, Y.
- Cui, Y.
- Dou, W.P.
- Du, H.
- Du, Z.
- Fang, X.
- Feng, Y.C.
- Gao, D.Q.
- Gao, J.
- Guo, H.
- Guo, J.W.
- Guo, Y.H.
- He, T.
- He, Y.
- Hu, X.J.
- Huang, W.
- Huang, Y.Z.
- Jia, H.
- Jiang, P.
- Jiang, T.C.
- Jiang, X.L.
- Jing, L.
- Kong, Q.Y.
- Li, C.X.
- Li, J.Q.
- Li, L.B.
- Li, L.X.
- Li, X.N.
- Li, X.X.
- Li, Z.S.
- Liang, Y.
- Liu, S.H.
- Liu, X.J.
- Liu, Y.
- Lu, L.
- Lu, W.
- Ma, B.H.
- Ma, H.Y.
- Ma, L.Z.
- Ma, W.
- Ma, X.
- Ma, Y.M.
- Mao, L.J.
- Mao, R.S.
- Mei, E.M.
- Meng, J.
- Ni, D.S.
- Ou, X.J.
- Pan, F.
- Qian, C.
- Qiao, Y.

- Qin, Y.S.
- Shangguan, J.B.
- Shen, G.D.
- Shen, Z.
- Shi, J.
- Shi, L.B.
- Su, Y.W.
- Sun, L.P.
- Sun, L.T.
- Tan, T.
- Tan, Y.L.
- Wang, C.
- Wang, H.N.
- Wang, H.
- Wang, K.D.
- Wang, X.W.
- Wang, Y.Y.
- Wang, Z.J.
- Wei, Y.
- Wu, B.M.
- Wu, J.X.
- Wu, Q.
- Wu, W.
- Xia, J.W.
- Xiao, G.Q.
- Xie, H.M.
- Xie, W.J.
- Xing, C.C.
- Xiong, P.R.
- Xu, X.B.
- Xu, X.W.
- Xu, Z.
- Yang, J.C.
- Yang, L.
- Yang, W.J.
- Yang, W.Q.
- Yang, Y.Q.
- Yang, Y.
- Yao, Q.G.
- Yin, D.Y.
- Yin, X.
- Yuan, Y.J.
- Zhai, Y.H.
- Zhang, B.
- Zhang, C.
- Zhang, H.
- Zhang, S.
- Zhang, W.H.
- Zhang, W.
- Zhang, X.Z.
- Zhang, Y.H.
- Zhang, Y.
- Zhao, H.W.
- Zhao, J.
- Zheng, S.J.
- Zhou, L.
- Zhou, Z.Z.
- Zhu, G.

- Bellato, M.A.

INFN/LNL

Legnaro (PD), Italy

- Andrichetto, A.
- Antonini, P.
- Ballan, M.
- Baltador, C.
- Bellan, L.
- Benini, D.
- Bermudez, J.
- Bisoffi, G.
- Borgna, F.
- Bortolato, D.
- Calderolla, M.
- Cavenago, M.
- Comunian, M.
- Corradetti, S.
- de Ruvo, L.
- Facco, A.
- Fagotti, E.
- Favaron, P.
- Ferrari, L.
- Galatà, A.
- Galtarossa, F.
- Giacchini, M.G.
- Gramegna, F.
- Lombardi, A.
- Maggiore, M.
- Manzolaro, M.
- Marcato, D.
- Marchi, T.
- Mastinu, P.
- Modanese, P.
- Moisis, M.F.
- Monetti, A.
- Montis, M.
- Palmieri, A.
- Pavinato, S.
- Pedretti, D.
- Pisent, A.
- Poggi, M.
- Prete, G.P.
- Roncolato, C.R.
- Rossignoli, M.
- Sarchiapone, L.
- Scarpa, D.
- Zafiroopoulos, D.

INFN/LNS

Catania, Italy

- Calabretta, L.
- Neri, L.
- Rifuggiato, D.

ISDE

Moscow, Russia

- Chubunov, P.A.

INFN- Sez. di Padova
Padova, Italy

ITT-Group

Moscow, Russia
• Konev, N.N.

JCNS

Jülich, Germany
• Baggemann, J.
• Brückel, Th.
• Cronert, T.
• Doege, P.-E.
• Gutberlet, T.
• Mauerhofer, E.
• Rimmler, M.
• Rucker, U.
• Voigt, J.

JINR

Dubna, Moscow Region, Russia
• Apel, P.Yu.
• Bashevoy, V.
• Bekhterev, V.
• Bogomolov, S.L.
• Bondarchenko, A.E.
• Borisov, O.N.
• Dmitriev, S.N.
• Efremov, A.A.
• Franko, J.
• Gikal, B.
• Gulbekyan, G.G.
• Ivanenko, I.A.
• Ivanov, G.N.
• Kalagin, I.V.
• Kazarinov, N.Yu.
• Lebedev, N.
• Loginov, V.N.
• Mironov, V.
• Mitrofanov, S.V.
• Oganessian, Y.T.
• Osipov, N.F.
• Semin, V.A.
• Skuratov, V.A.
• Tikhomirov, A.

JINR/DLNP

Dubna, Moscow region, Russia
• Karamyshev, O.

JINR/FLNR

Moscow region, Russia
• Popeko, A.G.
• Utyonkov, V.K.

JLab

Newport News, Virginia, USA
• Dixon, K.
• Wiseman, M.

KEK

Ibaraki, Japan
• Hosoyama, K.
• Ogitsu, T.

Kyoto University

Kyoto, Japan
• Amemiya, N.

LBNL

Berkeley, California, USA
• Prestemon, S.

MMRC

Fukui-ken, Japan
• Li, Z.X.
• Wang, H.N.

National Institute of Radiological Sciences

Chiba, Japan
• Fujita, T.F.
• Mizushima, K.

NET

Aachen, Germany
• Böhm, S.

NIFS

Gifu, Japan
• Obana, T.

NIRS

Chiba-shi, Japan
• Furukawa, T.
• Hara, Y.
• Iwata, Y.
• Matsuba, S.
• Murakami, T.
• Noda, K.
• Saotome, N.S.
• Sato, S.
• Shirai, T.

NTG Neue Technologien GmbH & Co KG

Gelnhausen, Germany
• Bechtold, A.
• Maus, J.M.

PKU

Beijing, People's Republic of China
• Fu, Q.
• Gan, P.P.
• Gao, S.L.
• Li, H.P.

- Liu, S.
- Lu, Y.R.
- Tan, Q.Y.
- Wang, Z.
- Zhu, K.

QST-NIRS

Chiba, Japan

- Saraya, Y.
- Tansho, R.

Research School of Physics and Engineering, Australian National University

Canberra, Australian Capitol Territory, Australia

- Battison, S.T.
- Bockwinkel, J.A.
- Graham, B.W.
- Heighway, J.K.
- Linardakis, P.
- Lobanov, N.R.
- Tsifakis, D.
- Tunningley, T.

RIKEN

Saitama, Japan

- Ikoma, N.

RIKEN Nishina Center

Wako, Japan

- Dantsuka, T.
- Fujimaki, M.
- Fukunishi, N.
- Hasebe, H.
- Higurashi, Y.
- Ikezawa, E.
- Imao, H.
- Kamigaito, O.
- Kidera, M.
- Komiyama, M.
- Kumagai, K.
- Maie, T.
- Nagase, M.
- Nagatomo, T.
- Nakagawa, T.
- Nakamura, M.
- Ohnishi, J.
- Okuno, H.
- Ozeki, K.
- Sakamoto, N.
- Suda, K.
- Uchiyama, A.
- Watanabe, S.
- Watanabe, T.
- Watanabe, Y.
- Yamada, K.
- Yamasawa, H.

Saitama University

Saitama, Japan

- Yamaguchi, T.

Sigmaphi

Vannes, France

- Antoine, S.
- Beeckman, W.
- Forest, F.
- Jehanno, P.J.
- Jivkov, P.
- Leray, M.J.
- Milpied, X.
- Nignol, C.

SIGMAPHI S.A.

Vannes, France

- Tasset-Maye, O.

Toshiba

Yokohama, Japan

- Orikasa, T.
- Takayama, S.

TRIUMF

Vancouver, Canada

- Laxdal, R.E.

UNIFE

Ferrara, Italy

- Ballan, M.

United Rocket and Space Corporation, Institute of Space Device Engineering

Moscow, Russia

- Anashin, V.S.

University of Chinese Academy of Sciences

Beijing, People's Republic of China

- Yang, L.
- Yang, W.J.

Università degli Studi di Padova

Padova, Italy

- Di Marco, V.
- Marzaro, G.
- Realdon, N.

Xi'an Jiaotong University

People's Republic of China

- Zhao, Y.T.

Participants List

— A —

Ao, Dante
Pfeiffer Vacuum

— B —

Baltador, Carlo
INFN-LNL

Basten, Markus
Institute for Applied Physics

Beeckman, William
SigmaPhi

Bisoffi, Giovanni
INFN/LNL

— C —

Chen, Chunhui
WXHK

Chubunov, Pavel
Branch of JSC URSC-ISDE

Comunian, Michele
INFN/LNL

Cong, Yan
IMPCAS

Corradetti, Stefano
INFN-LNL

— D —

Delahaye, Pierre
GANIL

Dickerson, Clayton
Argonne National Lab

Dong, Jin
Leybold (Tianjin) International
Trade Co., Ltd.

Dong, Yi
Shenyang Huiyu Vacuum Technics
Co., Ltd.

Dong, Xiaohui
Kaiteng Sifang

Du, Heng
IMPCAS

— E —

Efremov, Andrey
FLNR JINR

— F —

Fang, Yuchao
HCM

— H —

He, Ming
CIAE

He, Shengkan
WXHK

Hu, Xuejing
IMPCAS

Huang, Yulu
IMPCAS

Huang, Rachel
WATTSINE

— I —

Iwata, Yoshiyuki
National Institute of
Radiological Sciences (NIRS)

— J —

Ji, Luo
Dalian University

Jia, Yongzhi
IMPCAS

Jiang, Bin
Agilent

— K —

Kang, Mingtao
ShangHai PUSU Tech Co., Ltd.

Karamyshev, Oleg
JINR

Kester, Oliver
TRIUMF

Komarov, Pavel
Flerov Laboratory of
Nuclear Reactions JINR

Kuzin, Maksim
BINP

— L —

Lei, Yang
IMPCAS

Li, JiaQing
IMPCAS

Li, Jinhai
CIAE

Li, Lu
IMPCAS

Li, Min
IMPCAS

Li, Peng
IMPCAS

Content from this work may be used under the terms of the CC BY 3.0 licence (© 2018). Any distribution of this work must maintain attribution to the author(s), title of the work, publisher, and DOI.

Li, Zhongshan
IMPCAS

Li, Larry
WATTSINE

Li, Weilin
HCM

Li, Lori
LUVATA

Linardakis, Peter
Australian National University

Litvinov, Yury
GSI Helmholtzzentrum für
Schwerionenforschung

Liu, Huiping
IMPCAS

Liu, Yan
IMPCAS

Liu, Yi
Kaiteng Sifang

Lu, Liang
IMPCAS

— M —

Maier, Michael
GSI Helmholtzzentrum für
Schwerionenforschung

Mitrofanov, Semen
FLNR JINR

Mustapha, Brahim
Argonne National Laboratory

— N —

Nakagawa, Takahide
RIKEN

Neri, Lorenzo
INFN-LNS

— O —

Okuno, Hiroki
RIKEN

— P —

Pan, Feng
IMPCAS

— Q —

Qiao, Jian
SINAP

— S —

Shi, Jian
IMPCAS

Shirkov, Grigory
Joint Institute for Nuclear Research

Sun, Liangting
IMPCAS

SUN, Liepeng
IMPCAS

— T —

Tan, Teng
IMPCAS

Tan, Yulian
IMPCAS

Tang, Meitang
IMPCAS

Tang, Tongsheng
Shanghai Kelin

Tao, He
IMPCAS

Thomson, Jana
TRIUMF

Tsvetkov, Aleksandr
Institute of Applied Physics,
Russian Academy of Sciences

— V —

Vondrasek, Richard
Argonne National Laboratory

— W —

Wang, Guicai
IMPCAS

Wang, Jinchuan
IMPCAS

Wang, Kedong
IMPCAS

Wang, Xianwu
IMPCAS

Wang, Jiping
Shenyang Huiyu Vacuum
Technics Co., Ltd.

Wang, Kun
KJTJ

Wang, Nankai
ShangHai PUSU Tech Co., Ltd.

Wang, Chaozhan
Pfeiffer Vacuum

Wei, Jie
Michigan State University
Facility for Rare Isotope Beams

Wei, Shidong
BGTC

Wu, Wei
IMPCAS

— X —

Xiao, Chen
GSI Helmholtzzentrum für
Schwerionenforschung

Xie, Yahong
IMPCAS

Xing, Chaochao
IMPCAS

Xing, Fang
IMPCAS

Xu, Zhe
IMPCAS

— Y —

Yang, Yao
IMPCAS

Yang, Fan
Edwards Technologies Trading
(Shanghai) Co., Ltd

Yao, Qinggao
IMPCAS

Yin, Dayu
IMPCAS

Yin, Xuejun
IMPCAS

Yu, Xingyun
BBEF

Yue, Xiaolu
SigmaPhi

— Z —

Zakalek, Paul
Forschungszentrum Jülich GmbH

Zhai, Haoyin
Rui Yan

Zhang, Xiaoqi
KJTJ

Zhang, Huan
BGTC

Zhang, Honghui
Shanghai Kelin

Zhang, Wentao
XSMT

Zhang, Jianhua
BBEF

Zhou, Ying
SKY

Zhou, Eric
LUVATA

Zhu, Kun
Peking University

Zhu, Sihua
XSMT